# Static and dynamic collapse behaviour of cylindrical tubes and tube assemblies.

Ghani, Eskandar

To

my parents

and in memory of my distinguished teacher,

Professor Kevin Nash

# STATIC AND DYNAMIC COLLAPSE BEHAVIOUR OF CYLINDRICAL TUBES AND TUBE ASSEMBLIES

by

Eskandar Ghani

B.Sc.(Eng) London, A.K.C.

A thesis submitted for the degree of

Doctor of Philosophy

in the Faculty of Engineering of the University of London

Department of Civil Engineering

King's College

London

1982

# STATIC AND DYNAMIC COLLAPSE BEHAVIOUR OF CYLINDRICAL TUBES AND TUBE ASSEMBLIES

by

Eskandar Ghani

B.Sc.(Eng) London, A.K.C.

## ABSTRACT

The work reported here summarizes and reviews studies of the axial collapse behaviour of cylindrical tubes. Quasi-static tests are performed on tubes of differing sizes in order to establish a classification chart relating the mechanism of axial collapse to non-dimensional tube geometry. By comparing the level of energy absorption of these mechanisms for tubes of similar geometry, an optimum collapse mode is determined. Consequently, a design method is presented by which the geometry of an assembly of tubes may be optimized for maximum energy absorption. Optimum solutions are provided to a specific design problem relating to a protective device designed to contain a dynamic malfunction within a nuclear power plant reactor.

Theories on the axial collapse behaviour of cylindrical tubes are examined and their validity judged against the experimental results obtained. In some cases discrepancies are noticed, the sources of which are located within the theory and modified.

Finally, the influence of elevated temperatures and dynamic loading are studied for the specific application considered.

# ACKNOWLEDGMENTS

I would like to express sincere gratitude to my supervisors Dr G. L. England , Reader in Engineering Mechanics and Mr K. R. F. Andrews , Lecturer, Department of Civil Engineering, University of London King's College, for their advice and guidance in the course of the research work reported herein.

The help provided by the workshop staff of the above Department under the counsel of Mr R. Earll , Chief Technician, is gratefully acknowledged; my appreciations extend in particular to : Mr C. St. C. Blakey for technical assistance in the laboratory, ex-workshop assistant, Mr C. Mordi for preparing the tube specimens used in the experimental testing program, and Messrs R. Hunt and M. Collins who prepared the photographs presented in the thesis.

I also wish to thank the Health and Safety Executive , London, for sponsoring my research study.

# CONTENTS

## Glossary

| | |
|---|---|
| Axial failure /collapse/ /buckling | crumpling of a cylindrical tube in the axial direction |
| E.A. | energy absorber/dissipater : a device constructed to dissipate most of the kinetic energy that is applied to it by irreversible conversion to another form of energy |

### Mechanisms of tubular axial collapse (see Chapter 2 : Plates 2.25-2.29)

| | |
|---|---|
| Concertina | axisymmetric collapse in the form of 'bellows'/rings which form sequentially |
| Euler | strut-like failure with the development of a characteristic 'kink' at or near midlength of tube |
| Diamond | multi-lobe, non-axisymmetric but sequential collapse accompanying a change in the circular shape of the cross-section of tube |
| Crushing | non-sequential collapse; simultaneous failure along the length of tube |
| Simple compression | crushing of very short tubes in the form of limited 'barrelling' without formation of a fold |

### Other definitions

| | |
|---|---|
| Stroke efficiency | ratio of the absorbing portion to total length of an EA device |
| Specific energy absorption | energy absorbed per unit weight of an absorber |
| Energy absorption capacity | total energy absorption (in Joules) |

Glossary (continued)

| | |
|---|---|
| Energy dissipation density | maximum energy absorbed/dissipated per unit bulk volume of absorber |
| Operating stress/pressure | average resisting force per unit area of an EA |
| Design efficiency | energy absorbed per unit material volume of absorber |
| Axial compression | shortening of a tube in the axial direction |
| Ultimate stress | peak/critical stress of a tube in axial compression |
| Fold energy indices (Chapter 4) | These define a measure of energy absorption of tubes in units of Joules. They define the energies absorbed in the formation of an axial fold for tubes failing in the sequential modes of collapse |
| energy dissipated per unit volume of absorber material | |
| Euler energy index (Chapter 4) | For Eulerian collapse, this index defines the energy absorbed by a tube up to the peak compression load applied |
| Imperfections, initial deviations (Chapter 6) | geometric irregularities in tubes deviating from perfect cylindrical form |
| Lower bound design curves (Chapter 7) | Because of the boundary conditions introduced, discrete functions are obtained between various design parameters, e.g. energy absorption capacity, and geometries of tubes. The term 'lower bound curve' denotes a curve drawn through the lowest local points in each of these functions, thus providing in each case a 'safe' design relationship |

## Basic Notation

Tube geometry

| | | |
|---|---|---|
| $D$ | = | internal diameter |
| $D'$ | = | external diameter |
| $L$ | = | length |
| $T, t$ | = | thickness |
| $R$ | = | mean radius |
| $A$ | = | net cross-section area |

Other variables

| | | |
|---|---|---|
| $E_s^c$ | = | specific energy absorption of tube in axial compression |
| $L_t$, $L_t^*$ | = | nominal, true axial shortening of tube over n (integer) folds |
| $V_{no}$, $V_{tr}$ | = | nominal, true mean volume of an axial fold |
| $E_f$ | = | energy dissipated in the development of an axial fold |
| $h$ | = | length of one half-wave of a concertina fold |
| $\lambda$ | = | proportion of a concertina fold that lies 'external' to the original tube |
| $D^o$ | = | external tube diameter after collapse in the concertina mode |
| $\theta, \alpha, \phi$ | = | angles |
| $\Delta, \Delta_1$ | = | geometric parameters |

defining the configuration of tube at various stages of collapse

| | | |
|---|---|---|
| $\varepsilon_x$, $\sigma_x$ | = | strain, stress at position x along tube |
| $\varepsilon_{x\theta}$, $\sigma_{x\theta}$ | = | circumferential strain, stress at position x due to rotation of relevant collapsed portion of tube through $\theta$ |
| $\varepsilon_A$, $\sigma_A$, $M_A$ | = | rotational strain, stress and moment at plastic hinge A |

Notation (continued)

$Y$ = direct yield stress in compression

$Y_u$ = ultimate stress of material in compression

$E$ = modulus of elasticity

$E_p$ = modulus of strain hardening

$E_r$ = reduced modulus of elasticity

$P_o$ = load at yield of material in compression

$P_{cr}$ = critical axial load at collapse

$\bar{P}$ = mean postbuckling axial load (see page 107 for definition)

$\sigma_{cr}$ = critical axial stress at collapse

$\sigma_{max}$ = critical axial stress at collapse

$\sigma_n$ = nominal postbuckling axial stress

$\bar{\sigma}$ = mean postbuckling axial stress ($= \bar{P}/A$)

$\sigma_{cl}$ = critical axial stress from the classical theory (101)

$S$ = critical stress ratio : $\sigma_{cr}/\sigma_{cl}$

$\rho$ = density of tube material (weight/unit volume)

$\nu$ = Poisson's ratio

$\psi$ = ratio of the amplitude of initial deviations (imperfections) to the thickness of tube

# FOREWORD

The past few decades have witnessed distinct advances in worldwide technology within a broad spectrum of subjects, the more notable amongst which include, transport, defence, space research programs and nuclear energy. In these and associated fields, the greater efficiencies offered by current technology in satisfying particular needs in society are observed to be reflected in : higher speed vehicles, e.g. the motor car, ships and the submarine, aircraft and the supersonic jet, more versatile and sophisticated missiles and other weaponry, space vehicles, e.g. moon probes, and finally, the elaborate designs of nuclear power stations with increasing capacity to generate and accommodate nuclear energy.

However, in spite of the resulting desirable trend, whether it be an economic, social or a political advantage, viewed globally, the above and other similar examples are capable of inflicting serious injury to the public and damage to the environment as well as themselves, in the event of an accident. Hence because of these potential sources of threat to public safety, there is now an ever-increasing demand for the design and installation of protection devices that are crashworthy and collapse in a predictable fashion, should an unintentional impact take place.

The design requirement of such a mechanism is to absorb the kinetic energy at collision in an irreversible manner. This may be achieved either through permanent material

deformation of the device in the form of plastic flow, or friction, or alternatively, through viscous flow and discharge of a liquid or a gas enclosed within a fluid container device. In all cases, the cushioning effect obtained by suitable design of the device may serve as a safety measure in assimilating the damage that could be caused to personnel, the surrounding medium, or both, in a given application. The importance of cost has created an apparently persisting need to find simpler structural devices and elements, in particular those that possess high energy absorbing capacities per unit material weight or bulk volume. However, the emphasis on minimum cost has not inevitably been the prime design aim in situations where potential dangers to human safety or structural integrity are too great and occurrence of a tragedy has had to be fundamentally avoided.

The work presented in this thesis constitutes the result of investigations carried out by the author as part of a research contract between the Health and Safety Executive and King's College, University of London. The contract is based on a study of the collapse behaviour of simple structural elements suitably chosen for their potential use as energy dissipating safety systems in a nuclear power plant. More specifically, a crushing layer has been allocated for the accommodation of these collapsing elements to act as load-limiters within the central rotating shield; this is intended to reduce the effect of the impulse by the coolant material on the roof of the primary containment, in the case of a dynamic malfunction.

The criteria used in assessing the suitability of a device to dissipate energy are discussed first. Following this, a review is presented of various types of elements or structural devices used in this function, and their merits and disadvantages in this field are highlighted. For suitable material and geometry, the cylindrical tube in axial compression is selected as the suitable element for the specific application considered.

In this study the experimental program focuses on quasi-static collapse conditions under ambient temperatures. This approach is considered to be a fundamental initial step for the specific application here, prior to the assessment of the influence of the real conditions incorporating dynamic effects and the operating temperatures (~500 ˚C) in the final analysis. Axial collapse tests are carried out on a series of cylindrical tubes of varying geometry for a particular metallic material. A design chart is established which correlates the modes of collapse observed with the different geometries selected. Subsequently, the energy absorption capacities of the potentially useful collapse modes are evaluated and compared, in an effort to determine an optimum failure mode for design.

With the above and other necessary parameters in a design program identified, a design method is presented together with optimum solution to a given problem : For a particular crushing layer, it is required to select suitable geometry for tubes and consequently to obtain their quantity, material volume and total energy dissipation capacity, with the aim

of optimizing their geometry such that maximum energy may be absorbed by the layer, for a given total weight of crushing tube material. As well as identical tubes, consideration is also directed towards employing tube assemblies in the form of concentric tube sets and the possibility of subdividing the prescribed layer into 'rows' of sublayers (each packed with tubes), in an attempt to locate the optimum arrangement of size and quantity of tubes for maximum energy dissipation.

The experimental data obtained are also inspected against the solutions of certain established theories, reviewed here, on particular mechanisms of collapse. Discrepancies are noticed in the comparisons made. Factors responsible for these discrepancies are identified and alternative empirical solutions are proposed in particular cases, for better description of the experimental behaviour.

Finally, as regards the real conditions in a nuclear reactor containment, the effects of the dynamic nature of loading and operating thermal conditions are discussed. These are recognized to be worthy of detailed study in a future research program, since they would influence the final design of tubes as energy absorbers for the particular application considered.

# CHAPTER 1

## INTRODUCTION

An energy absorber (E.A.) is herein defined as a device constructed to dissipate most of the energy (usually kinetic) it receives by irreversible conversion to another type of energy, but of a 'degraded' nature, e.g. heat. In this process it produces a resistive force over some stroke and must be capable of accommodating large permanent deformations without structural failure. The irreversible property eliminates restitution, so that, for example, a spring or a pneumatic damper which mainly stores potential (elastic) energy for conversion later in the same kinetic form cannot therefore be classified under this category.

## 1.1 Criteria used in the Assessment of E.A. Systems

The parameters comprising the performance characteristics of E.A. Systems are considered individually below.

### 1.1.1 The Load - Deformation Curve

The shape of the load-deformation curve for an E.A. provides a measure of its reliability and controlled behaviour. A favourable EA is one which is associated with a reasonably constant operating force throughout deformation. The ideal design aim would be to obtain an optimal rectangular shape load-deformation curve, offering an ideally smooth deceleration response.

### 1.1.2 Stroke Efficiency

This is the ratio ($< 1$) of the absorbing portion to total length of an EA device. It provides as estimate of the geometric suitability of the EA element to absorb energy in

relation to the direction of loading. There is often a preferred orientation of the device in its alignment with the applied load.

A high ratio indicates participation of a large portion of the element in this function and thus promotes a favourable and efficient use of material. Systems which exhibit excessive local deformation, as in tension devices, reduce the available stroke length and consequently the material efficiency. However, in the case of the tension device, suitable end-fittings may be installed for its alignment with the load, whereas, depending on the particular application considered, alignment could be a practical problem for those devices that operate under unidirectional compressive loading.

### 1.1.3 Specific Energy Absorption

As discussed in detail in Chapter 3 in its application to the circular tube, this parameter is essentially the ratio of the maximum energy that can be absorbed, to specimen weight. It constitutes a significant index in design and is particularly noteworthy in the design of aircraft where weight minimization is important. The energy is calculated from the area under the load-deformation curve for the absorber.

A valuable EA exhibits a high specific energy and necessarily a high stroke efficiency.

### 1.1.4 Energy Dissipation Density

This is the maximum energy dissipated per unit bulk volume

of the absorber and is a particularly useful quantity (as observed in the design study of Chapter 7) in applications where the device, or a group of them, is required to fit within a confined space.

### 1.1.5 Operating Pressure

This is the average resisting force per unit of net area of the dissipator subjected to loading and presents the pressure level at which it functions. In this context the choice of an EA is dependent on its capability to produce the required level of resistance for a given application.

### 1.1.6 Cost

The importance of cost evidently may not be ignored in any design task. In this field the inevitable aim is at gaining maximum energy absorption per unit cost. This does not necessarily imply maximum specific energy or maximum dissipation density, since the cost quantity must include the additional costs attached to the supporting mechanisms that may be required to adapt the EA for the particular use or safety conditions in mind. The latter costs may well exceed those for the EA itself. Thus, in a design program, the global cost of the device and all its associated accessories must be considered.

## 1.2 Classification of Energy Absorbing Systems

All E.A. devices are grouped into two broad classes :

(i) Non-Destructive devices

(ii) Destructive devices.

### 1.2.1 Non-destructive/'Multicycle'/Re-usable Devices

These mechanisms convert the incoming kinetic energy of impact fully or mainly into heat (by friction) or into the kinetic energy of an escaping fluid (by controlled flow). As their category name signifies, they can be used repeatedly for several cycles. The class is subdivided as follows :

(i) solid friction devices

(ii) hydraulic/viscous friction types, e.g. dashpots

(iii) discharge types, e.g. gas bags (Figure 1.1) and liquid-filled devices

The first type above consists of surfaces designed to rub together, an action which provides a resisting pressure between them. However, they invariably require a method of controlling this contact pressure in order to provide the desired resistance. Whereas in the automobile brake the driver controls the frictional resistance in deceleration by the use of a pedal, because of general variations in the coefficients of friction, velocity of contacting surfaces and their nature, an elaborate control system is often not feasible.

E.A. systems conforming to the other two types above have the advantage of saving space and possessing a high stroke efficiency. They are especially reliable in applications not requiring high specific energy. Their low operating pressures makes them suitable for use in promoting low deceleration of large but low-density vehicles. Coppa (15)(16) has discussed

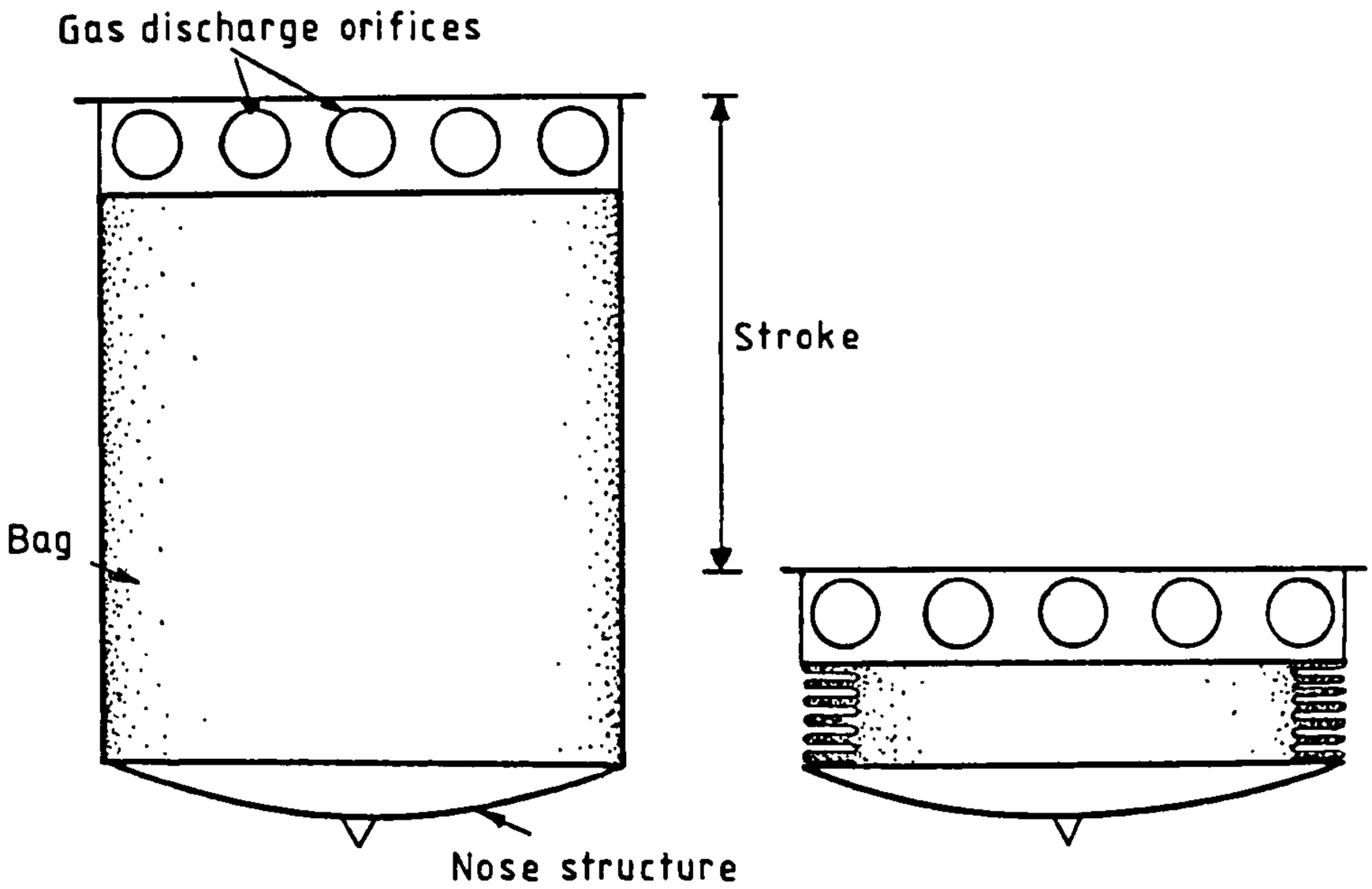


The gas-bag energy dissipator [Ref.(16)]

Figure 1.1

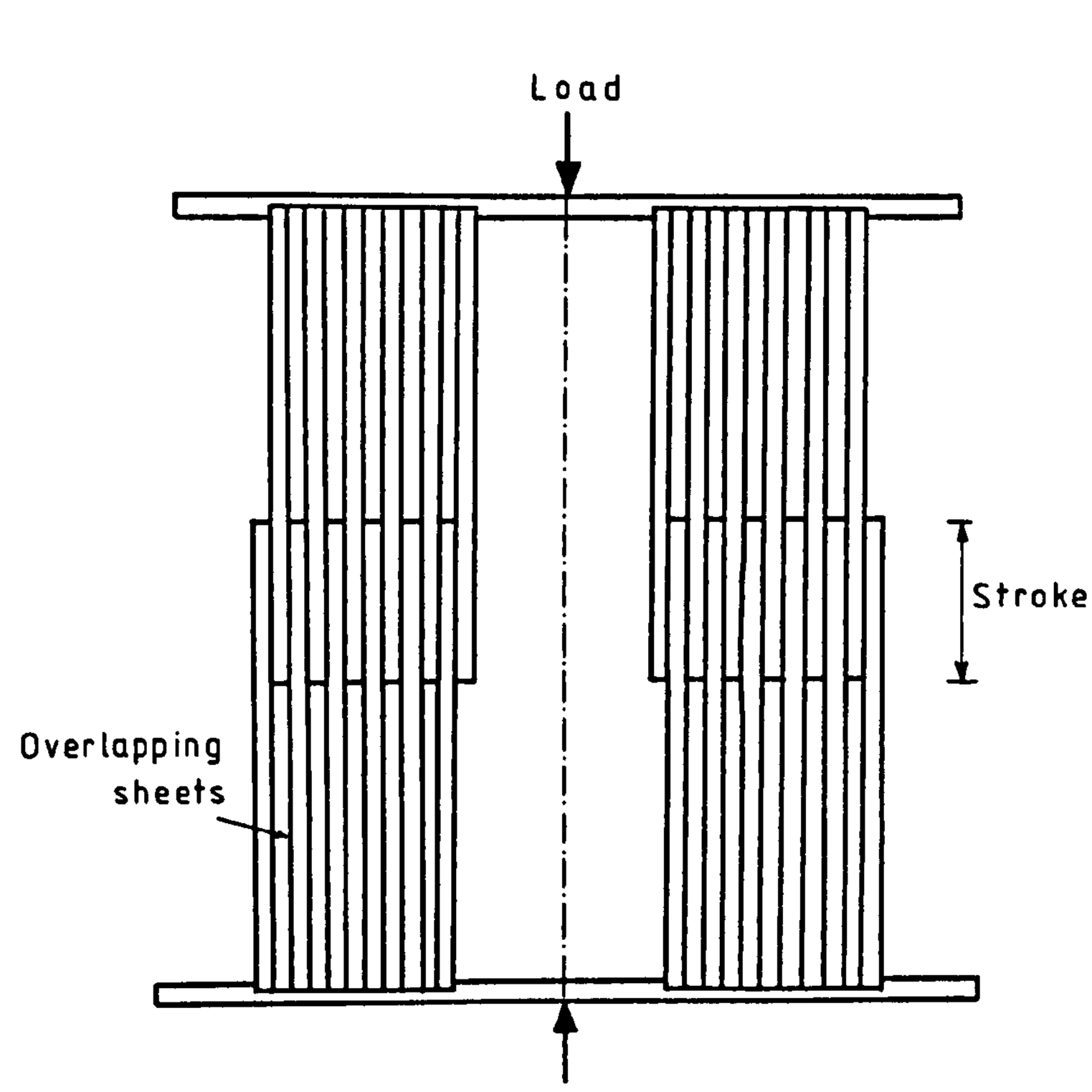


A non-reuseable friction device [Ref.(12)]

Figure 1.2

the influential parameters in the concept of the discharge valve and applications where gas bags have been recognized to be of potential use. Rich (86) has described the operation of a shock proof buffer assembly also based on the principle of the controlled flow of an escaping fluid.

However, not all solid friction type absorbers are re-usable; Conrad (12) has illustrated a remarkably simple device consisting of partially overlapping sheets wrapped over a cylindrical core as shown in Figure 1.2 . The resulting radial compressive forces between the sheets provides a source of frictional contact pressure resisting against axial loading of the core. However, performance is greatly affected by temperature and surface conditions of the plates and the system generally suffers from a low stroke and a very low absorption capacity.

Multicycle devices tend to be rather elaborate in design as compared with most other EA elements. Furthermore, they often require proper maintenance whether it be re-adjustment of the components of the system before re-use as in a friction device, or, refilling of the container in the liquid types. Thus, allowance must be made for depreciation and loss of efficiency of these systems in terms of their energy absorption capacity after several application cycles.

### 1.2.2 Destructive/'One-Shot'/Non-reusable Devices

The kinetic energy of impact is converted to heat through permanent deformation of this class of devices. The majority

of EA systems with simple geometry of fabrication in the finished design belong to this category. Ductile and brittle deformation constitute the two broad sub-classes by which these devices operate.

### 1.2.2.1 Ductile deformation

This involves permanent material deformation of the EA system in the form of plastic work and constitutes the basis of a large number of absorbers. These devices exhibit one of several, or more typically, a combination of different modes of ductile behaviour which include extension, compression, bending, shear and torsion. But normally a particular mode in a combination predominates. These modes are considered individually below for further classification of the absorber systems that will be discussed.

#### (i) Extension

Wires, rods, tubes, cables, etc. undergoing uniaxial tension as a means of absorbing energy constitute the simplest elements under this mode. The tensile energy absorption capacity of cylindrical tubes of various sizes, materials and heat treatment conditions have been described in detail by Thornton and Magee (98), as referred to in Chapter 3. They have shown that the specific energy depends upon the ultimate tensile strength and strain of the material which properties are used in the ranking of materials for use in energy absorption.

Several restraint systems designed to reduce the effect of pipe-whip in the case of failure of high pressure piping

systems make use of the plastic deformation of tensile elements.

Kirk (52) has described the design of a safety rod and its applications to a subway system. The kinetic energy of the subway vehicle is dissipated by tensile behaviour of this rod through a circular cutting tool with the aim of applying a constant retarding force to the vehicle.

Tension devices have the characteristic disadvantage of a reduced stroke length because of excessive local deformation. However, directionality of loading is no major issue since suitable end-fittings may be installed for the alignment of these devices with the tensile load.

(ii) Compression

This mode is restricted to those absorbers that deform under direct compression only, as a means of absorbing energy. Struts and metallic rods in axial compression constitute perhaps the simplest types of elements that have been examined for their potential as energy absorbers. Postlethwaite and Mills (76) have analyzed the behaviour of simple steel struts under dynamic conditions. They have found that collapse occurs in two phases. Initially, in a condition called the pre-failure phase, the strut fails elastically whilst the end-masses attached to it experience a transient deceleration this being a function of strut shape. This is followed by the development of plastic hinges forming at the points of maximum moment in the buckled configuration. The energy absorption in this post-failure phase is independent of

velocity, so that the behaviour of the strut directly compares to its static collapse characteristics. An inherent assumption in this theory is that the mass of the body retarded by the strut greatly exceeds that of the strut itself. It is claimed that these struts have suitable applications in the design of the frontal structure of an automobile.

Other examples of compression devices include metallic and plastic bumpers, cellular bodies like metal sponges and foams, crushing materials, like wood (Balsa, fibreboard, straw, woodchip, sawdust, woodwool), polystyrene, corrugated and moulded cardboard and thermoplastics.

Thiele (95) has described the chemical process by which aluminium sponge and foam may be produced and the methods by which their properties may be varied. Their low-density advantage has implied suitable application of these structures in automobile design and in lifting and conveying systems. Thermoplastics, in particular, are associated with high energy dissipation densities and high operating pressures but the performance of these absorbers is sensitive to loading rate about which relatively little is known. A particular advantage of these crushable materials is that they are omnidirectional and may be used as padding, cartridges in a tube or as elements of a structure.

Spherical shells have gained an important position in the design of crash-helmets. Since the latter are designed specifically not to deform under impact, then strictly speaking

these structures do not classify as E.A. systems. However, their widespread and everyday use as a means of avoiding human injury in collisions makes them unique in this field. Johnson et al (41)(43)(45) and Simpson and Goldsmith (90) as described by Johnson (45), have examined in detail the mechanisms of head injury caused and the subsequent factors that must be incorporated for safety in the design of crash--helmets. Kitching et al (53) have analyzed the compression of hemispherical shells between rigid plates. Flattening in deformation accompanies the development of planar compressive radial forces causing 'dimpling' with the production of a set of plastic lobes with increasing load. Other applications of spherical absorbers include uses in submarine and ocean--liner impacts with quay structures. These systems, too, have the advantage of a high omnidirectionality of loading.

(iii) Bending

The most commonly used type of E.A. element in this category is the cylindrical tube under lateral compression. Two types of failure are distinguished as indicated in Figure 1.3 ;

(a) Complete lateral compression or tube flattening - crushing of a tube between rigid plates

(b) Local lateral loading of a tube - a simply-supported tube undergoes local failure due to an indenter load.

These mechanisms have been studied in detail by : Thomas, Reid and Johnson (97), Watson et al (102)(103), Mutchler (69), Burton and Craig (11), Redwood (81) and De Runtz and Hodge (18). The latter proposed a rigid-plastic limit state theory for

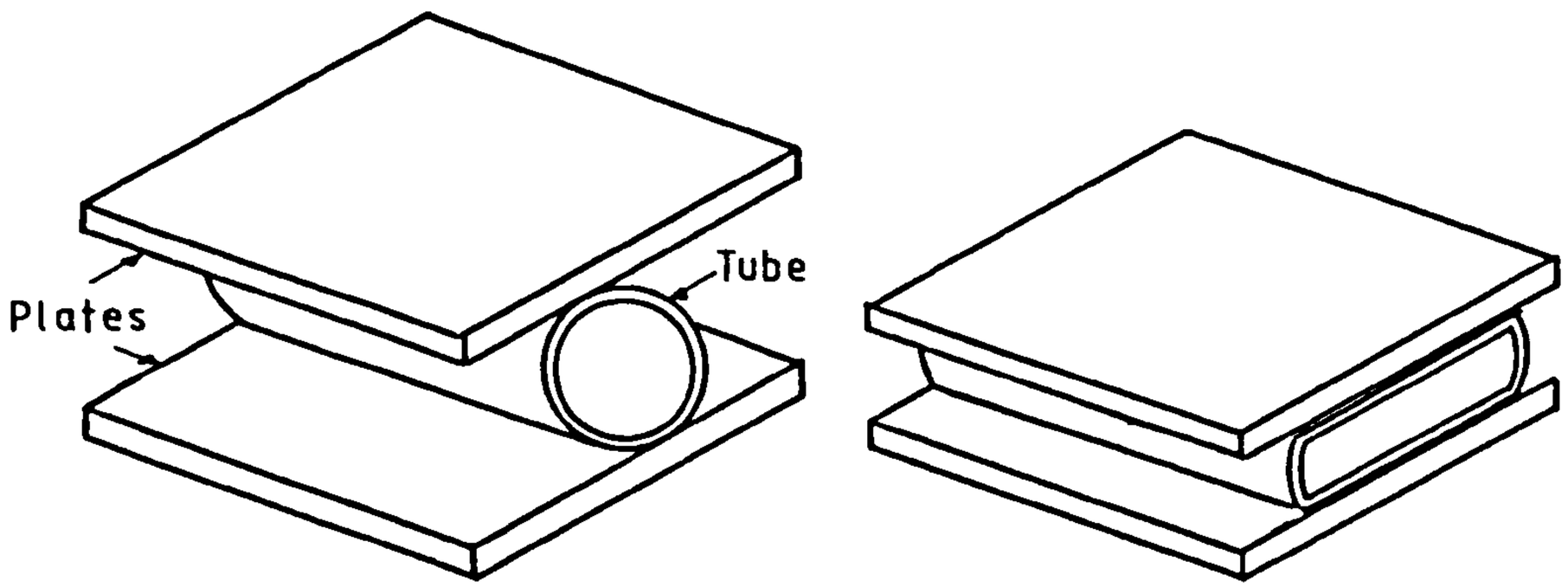


[i]
Crushing of a tube between rigid plates
[Ref.(18)]

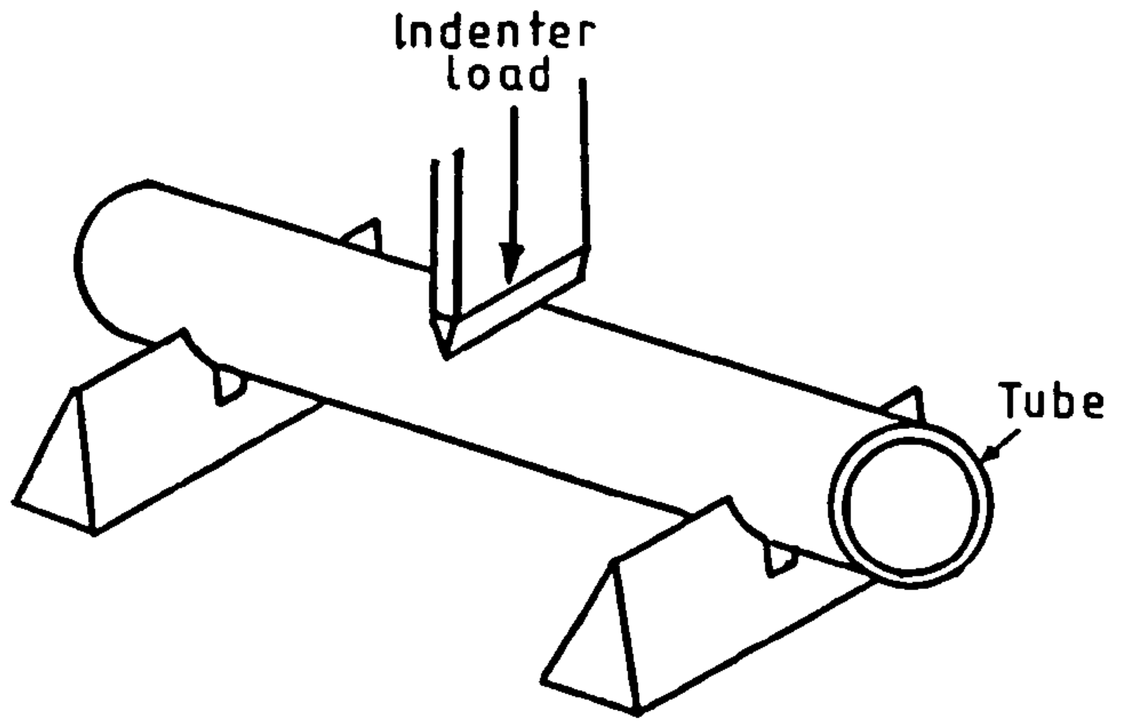


[ii]
Bending of a simply-supported tube
[Ref.(97)]

Figure 1.3

the first case above in which collapse consists of the development of a set of plastic hinge lines along the length of the tube. These hinges are assumed to be stationary in relation to the rigid portions of the tube which simply rotate in deformation of the tube. This is essentially a two dimensional problem of plastic collapse and the theory indicates the increase in load required to continue deformations beyond the initial collapse. Redwood (81), Reid and Yella Reddy (84) have elaborated on this theory by incorporating the effects of strain hardening in the hinges.

In the second mechanism above, i.e. that of the locally loaded tube, the length of the tube is found to govern the mode of deformation for a given section geometry. Short struts behave essentially as rings whereas long tubes fail smoothly in the absence of a pronounced limit load under continuously changing curvature. The length of the overhang of the tube is known to add considerable constraint against bending of the tube between the supports. For suitable support conditions this tube may be made to possess a longer stroke than the flattening tube for which the stroke is limited to the size of its diameter, even though they both have a high stroke efficiency since the solid height is only twice the thickness of the tubes. However, the local nature of failure in the former case indicates a less materially-efficient system since only the dented portion of the tube develops a plastic hinge. The plastic deformations decay rapidly with distance away from this region. Advantages of both systems include simplicity, effectiveness, low cost and ease of operation without the need for close control of

the direction of loading. The absorption capacity, however, is significantly lower than that for the axially loaded tube.

Johnson, Reid and Yella Reddy (46) have analyzed the behaviour of assemblies of laterally loaded tubes. In arrangements where there is no interference between the adjacent tubes the behaviour of the system resembles clearly that of a single tube. Where interaction does occur, as in the case of mutually orthogonal rows of tubes, the geometry of the contact zone and ductility of the tubes are of particular importance. However, the energy absorption capacity depends very little on the diameter, D, of the tubes so long as suitable wall thicknesses t, are chosen to reduce the t/D ratio sufficiently for each element of the system to behave as a thin-walled tube.

Another example of a bending device comprises the single or alternate bending deformation of a strip drawn through a fixture - the so called 'metal bender'. By suitable choice of geometry and material the operating force for this type of absorber can be reasonably adjusted for a particular application.

(iv) <u>Cyclic bending</u>

The most prominent example of an absorber device offering cyclic plastic deformation is the rolling torus or the wire helix. Described and analyzed in detail by Johnson et al (42)(44)(47) and Platus (75), this comprises a length of wire coiled in the gap between two concentric tubes such that the wire is gripped. As the cylinders interpenetrate axially, their

opposite motion causes the wire to be rotated and rolled in the gap without sliding. The wire thus behaves as a series of toroids which are inverted cyclically. For metal wire assemblies the incoming energy is absorbed through dissipation of plastic work in the elastic-plastic hoop strain cycles within the wire. The force level at which rolling initiates is governed primarily by the dimensions of the system, mechanical properties of the wire and the frictional interaction between the wire and the tubes. These factors are adjusted in accordance with a given application.

Mazelsky (65) has illustrated an alternative cyclic method of energy dissipation as shown in Figure 1.4 . A ratchet is used to precipitate cyclic plastic deformation of four small metallic elements linked to it perpendicularly by a set of pins, as the ratchet is loaded longitudinally. However, only a small portion of the whole structure absorbs energy in deformation thus presenting a rather inefficient system.

A metal strip bending device similar to that of the metal bender has been introduced by Jackson (40). A long metal bar in the form of a coil is deformed plastically as it is pulled at one end between a set of non-aligned pins, as shown in Figure 1.5 . In this primarily linear device the stroke is governed by the length of the metal coil.

Generally, in the design of cyclic plastic bending devices of the types described, undesirable effects like possible corrosion and metal fatigue must be assessed. These are the

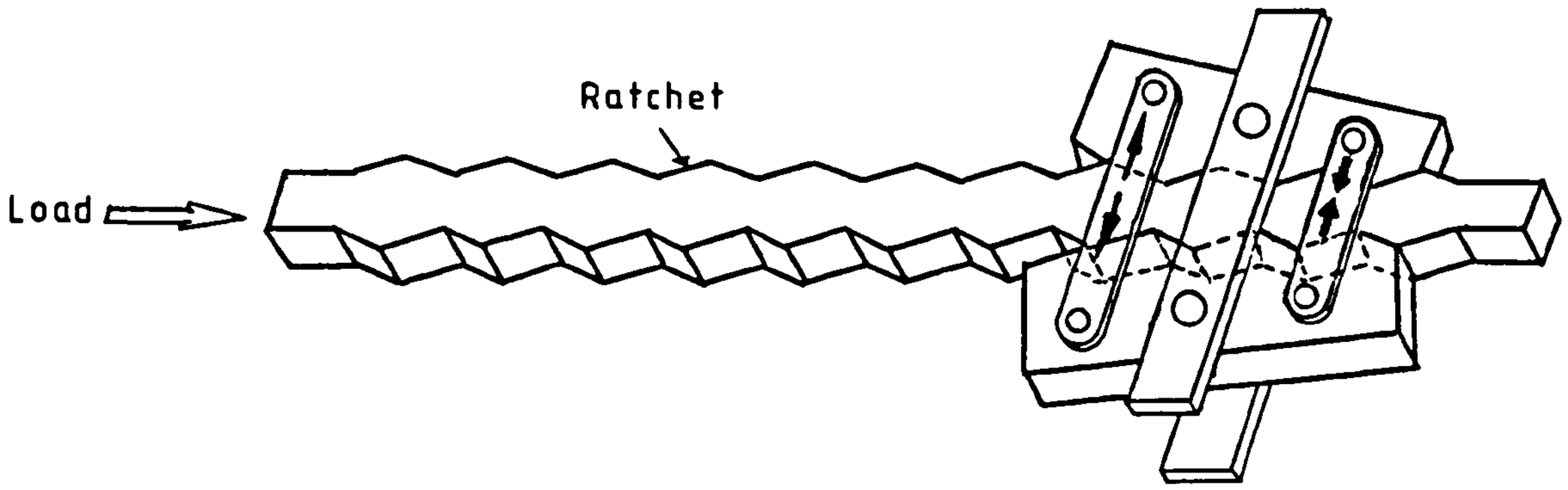


Cyclic deformation [Ref.(65)]

Figure 1.4

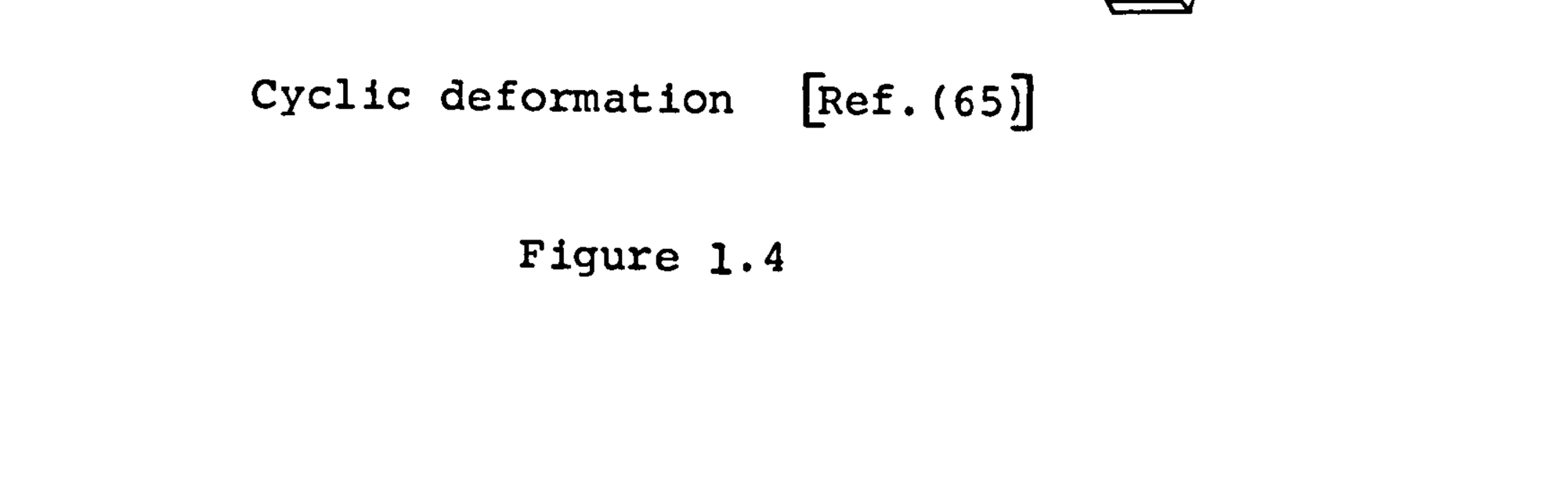


Metal strip bending device [Ref.(40)]

Figure 1.5

consequence of cyclic stressing and must be accounted for if premature failure of the device is to be avoided.

(v) Shear and torsion

Absorbers that operate by means of developing plastic torsion or a torsional hinge belong to this group, e.g. ductile shafts such as mild steel which may undergo significant plastic torsions before rupture. Considering the door hinge as an analogy, a device can be made which has a fixed pin instead such that rotation produces torsional strains in the pin. Rawlings (79) has analyzed the behaviour of elbow-type hinge elements and Miller et al (67) have described the application of this principle to automobile structures. However, these devices typically suffer from the disadvantage of fracture at the hinge joint and the inability to produce a reasonably constant decelerating force in operation.

Moberg (68) has illustrated how the shearing of the edges of metal strips in machining processes may be directed as a method to absorb energy. Similarly, Tiesenhausen (99) has made use of cutting processes in the design of an E.A. device where energy is absorbed by the development of grooves along the length of a metal tube. These have the advantage of providing a steady resisting force but are associated with low stroke, low absorption capacity and tend to be fairly expensive in terms of design and cost/weight effectiveness. In this category, too, the rolling torus previously described is worthy of mention as it exhibits considerable shear deformation in its operation.

(vi) Mixed mode

This comprises the class of absorbers which are associated with more than one mode of deformation without a distinct dominant mode. The cylindrical tube in axial compression constitutes one such example in which the folding process accompanies stretching, bending and compression deformation of the material. Its combination of high performance, high stroke and high absorption capacity for suitable geometry and material have made this element a particularly simple, reliable and efficient means of absorbing kinetic energy. But directionality and off-axis loading have considerable influence on the performance of this tube. Nevertheless, as noted by Wirsching and Slater (104) in their summary of the application of tin cans as car bumpers, some protection is still provided by the cans under oblique loading.

Tubes of other shapes, e.g. square or polygons forming prisms and of various plastic materials as well as metals have been commonly used. Redwood (82) and Johnson (41)(43) have analyzed the behaviour of square tubes in axial compression and the latter has described the potential application of this element in safety design of motor coaches. Similarly, Kukkola (56) has illustrated the use of short square tubes in the protection of equipment within a nuclear power plant.

Tube inversion, as described and analyzed in detail by Al-Hassani et al (2) and Johnson (43)(45), provides a novel example of combined bending and stretching or compression deformation. This involves the turning inside-out or outside-

-in (external or internal inversion) of a thin metal tube as it is pushed axially onto a 'radiused' die. This is shown in Figure 1.6 . Aside from the geometry of the tube itself, effectiveness of the invertube system depends on the die radius, the latter determining the initial peak load required for deformation and the steady-state resistance offered by the tube.

The die angle measured from a line parallel to the axis of the tube, too, has considerable bearing on the behaviour of the system. For angles below 75° Al-Hassani has illustrated that the tube fails primarily by buckling around the point of contact with the inverted tip. For angles between 75° and 120° consistent inversion has been observed, whilst it is seen that generally for angles in excess of about 122° flaring of the tube takes place with a steady increase in the diameter of the tube as it is forced through the die. However, the latter configuration constitutes as essentially extensional deformation mechanism with little bending. Spielman (93) has illustrated a particular application where the concept of the flared tube has been used.

A special case of the inversion tube involving the splitting and curling of the tube for a suitably large fillet radius is the frangible tube. This is discussed under the category of brittle deformations.

The invertube has a high performance and predictability and a rectangular-type (smooth) deceleration response. Its

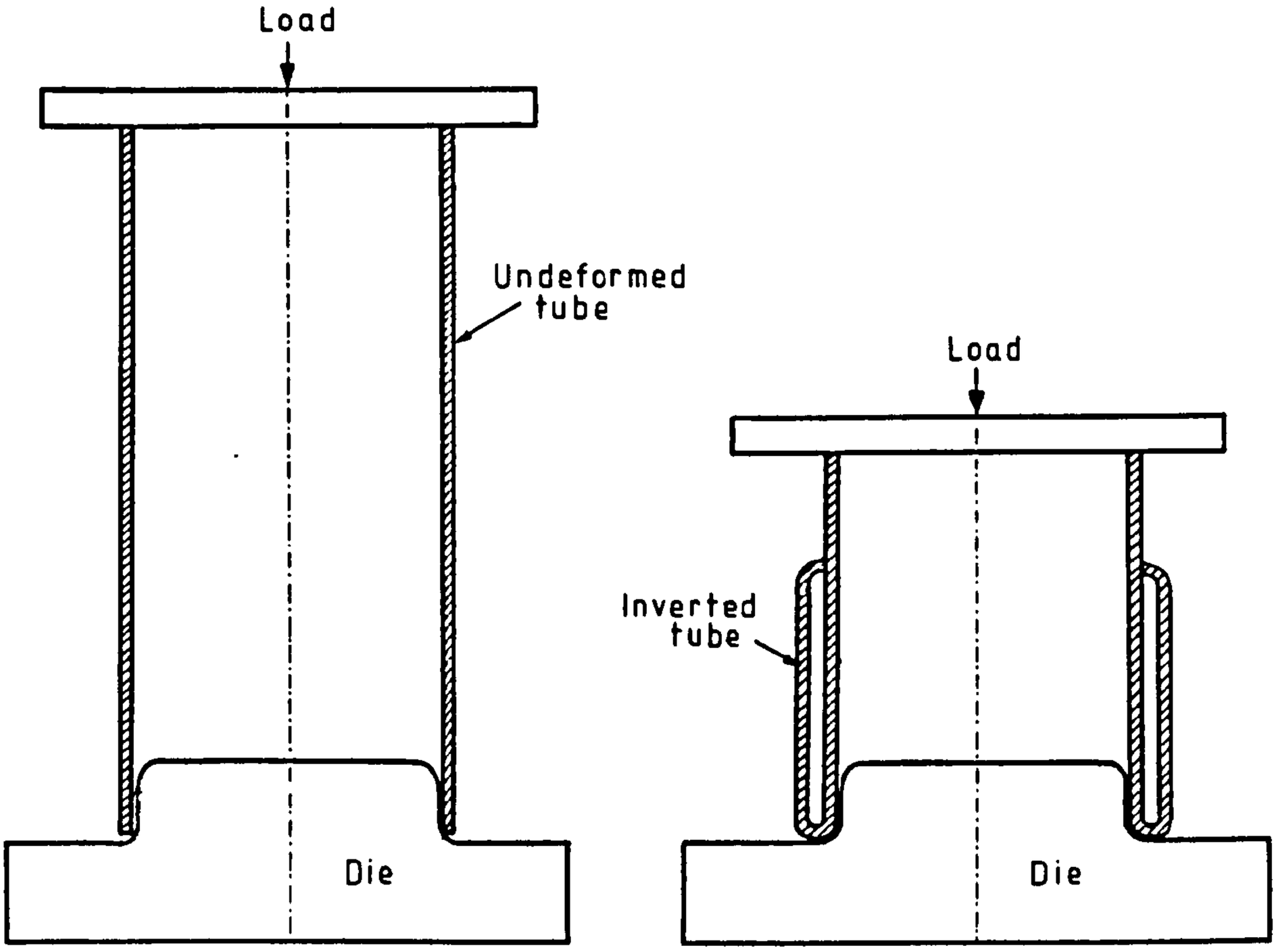


External inversion of a cylindrical tube [Ref.(2)]

Figure 1.6

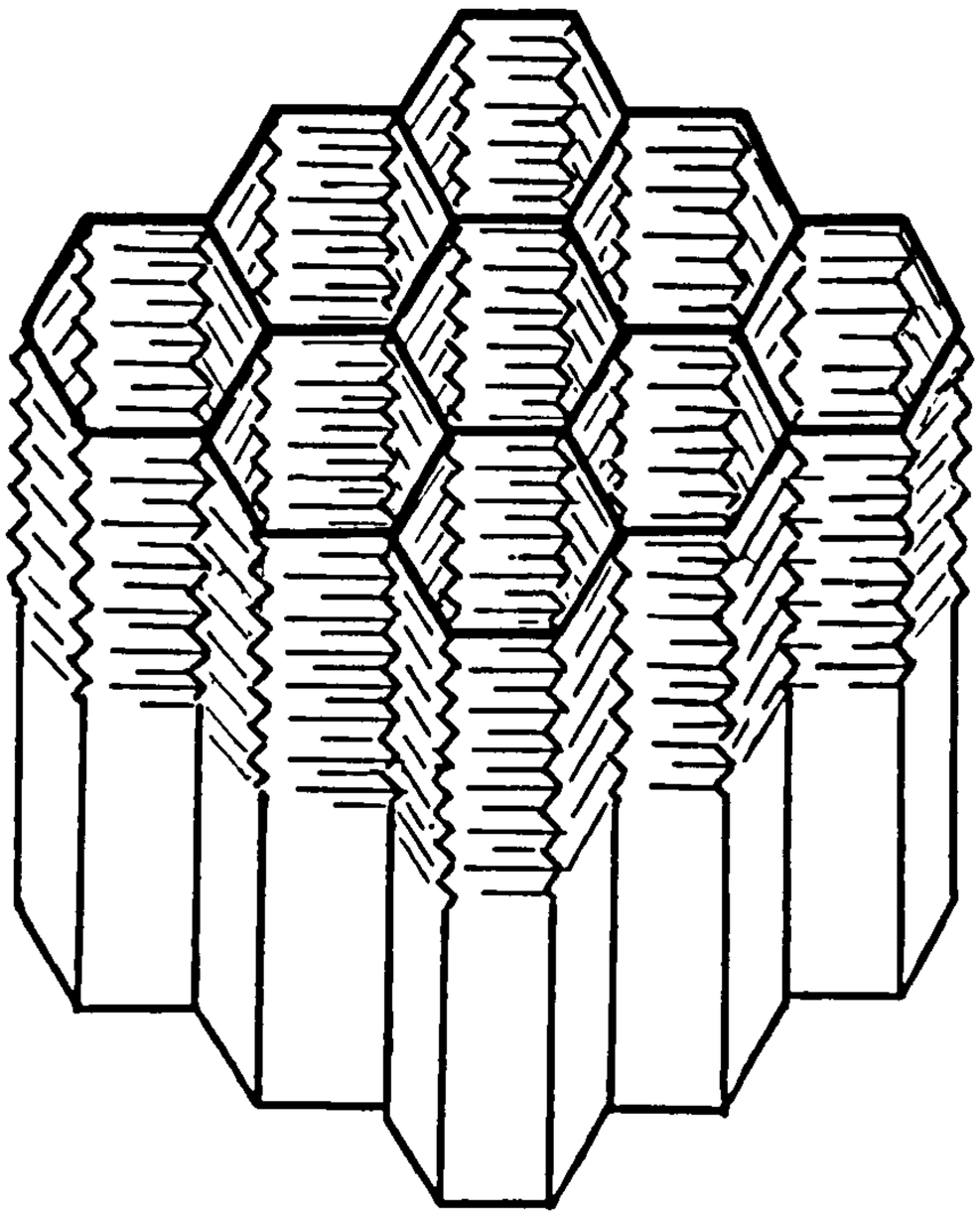

The honeycomb cell structure [Ref.(70)]

Figure 1.7

applications range from lift shaft emergency arrestors to pier fenders and buffer elements for rail vehicles. However, the system suffers from low stroke efficiency which at best is equal to 0.5, as the stroke is limited to the overlapping of the parts of the tube.

Honeycomb core as an assemblage of hexagonal cylinders has also been shown in the past to possess a high potential for energy absorption in the axial direction. These are manufactured from several metals, plastics and even paper. The range of densities offered by these materials permits wide applications where different operating pressures are required since their resistance to crushing is nearly linearly related to their densities. The impact energy is absorbed by plastic deformation and bulging of the honeycomb webs in an 'accordion' fashion, as shown in Figure 1.7 .

McFarland (70) has analyzed the collapse behaviour of the honeycomb core and presents a method by which the crushing stress of the structure may be obtained. Coppa (16) has compared their performance in different materials. A particularly favourable type is the aluminium honeycomb which is considered to be reliable and provides a constant resisting force over a long stroke. Thiele (95) has described how the latter is manufactured. The specific energy of the aluminium honeycomb increases with strain rate, because

(i) The air columns under compression in the voids increase the resistance

(ii) The material resistance increases slightly with defor-

mation rate

(iii) Some of the energy absorbed is converted to heat.

The honeycomb device is claimed to have potential use in protection of strut elements of aircraft undercarriages and as described in detail by Jones (49), in the protection of nuclear-powered ships. However, as with the axially loaded cylinder, proper performance of the system requires minimum deviation of the stress direction from the axis of the core.

The conical tube is worthy of special mention in this category as it produces a particularly high stroke ratio. Here the folding of the material proceeds inwards in stabilizing the structure. This is distinct from the cylindrical tube where the folds pile axially. Johnson and Mamalis (43) have described applications of this element in the protection of the bow of a ship in collision.

(vii) Extrusion

This constitutes devices that are based on the principle of extruding a solid or a fluid through an orifice. The common examples in this group include mechanisms possessing a piston which provides the stroke in the metal container, e.g. the automobile shock absorber which is an example of a multicycle device. A similar type has been described by Peterson (74) where a solid material is extruded. The piston component, however, is not a necessary requirement in devices where the container changes geometry in the extrusion process; example of an analogy is extraction of paste from a tube.

A particular advantage of extrusion devices is their sensitivity to impact velocity. They exhibit low resistance to low impact speeds and are capable of absorbing higher energy at higher impact velocities. Robinson and Greenbank (87) have used this property to an advantage in the design of one such device, with lead as the extruding medium, for use in protection of structures against earthquake damage.

### 1.2.2.2 Brittle deformation

Devices exhibiting brittle deformation or fracture must not necessarily be eliminated from the class of E.A. systems, as may be suggested, on the grounds of possible contravention of the 'no structural failure' property in the definition of an E.A. .

Fracture need not be synonymous with structural failure in the sense of ineffectiveness of the system to absorb energy if the device is designed to undergo brittle failure in a reasonably controlled and reliable manner. So long as a reasonably steady resistance in the development of fractures over a certain stroke is offered by the device, it may find suitable application as an E.A. system.

The frangible tube, discussed in 1.2.2.1 to be a special case of the inversion tube, provides an example of a brittle-type E.A. system. The tube is pushed axially onto a die which has a suitably large radius in relation to the tube diameter. In this process the tube splits and curls in the vicinity of the die, as shown in Figure 1.8 and the energy absorbed accompanies

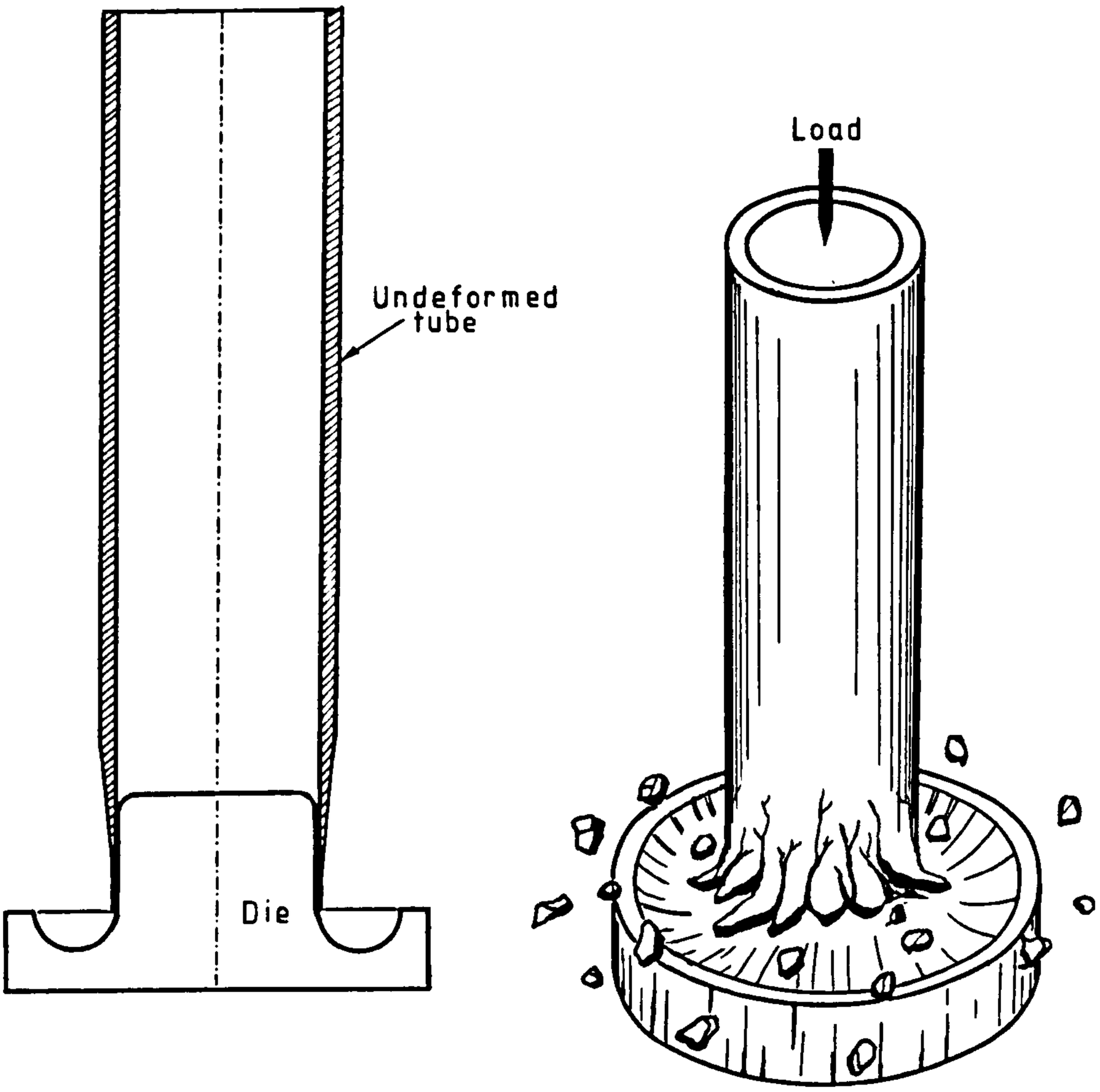


The Fragmenting tube energy dissipator [Ref.(16)]

Figure 1.8

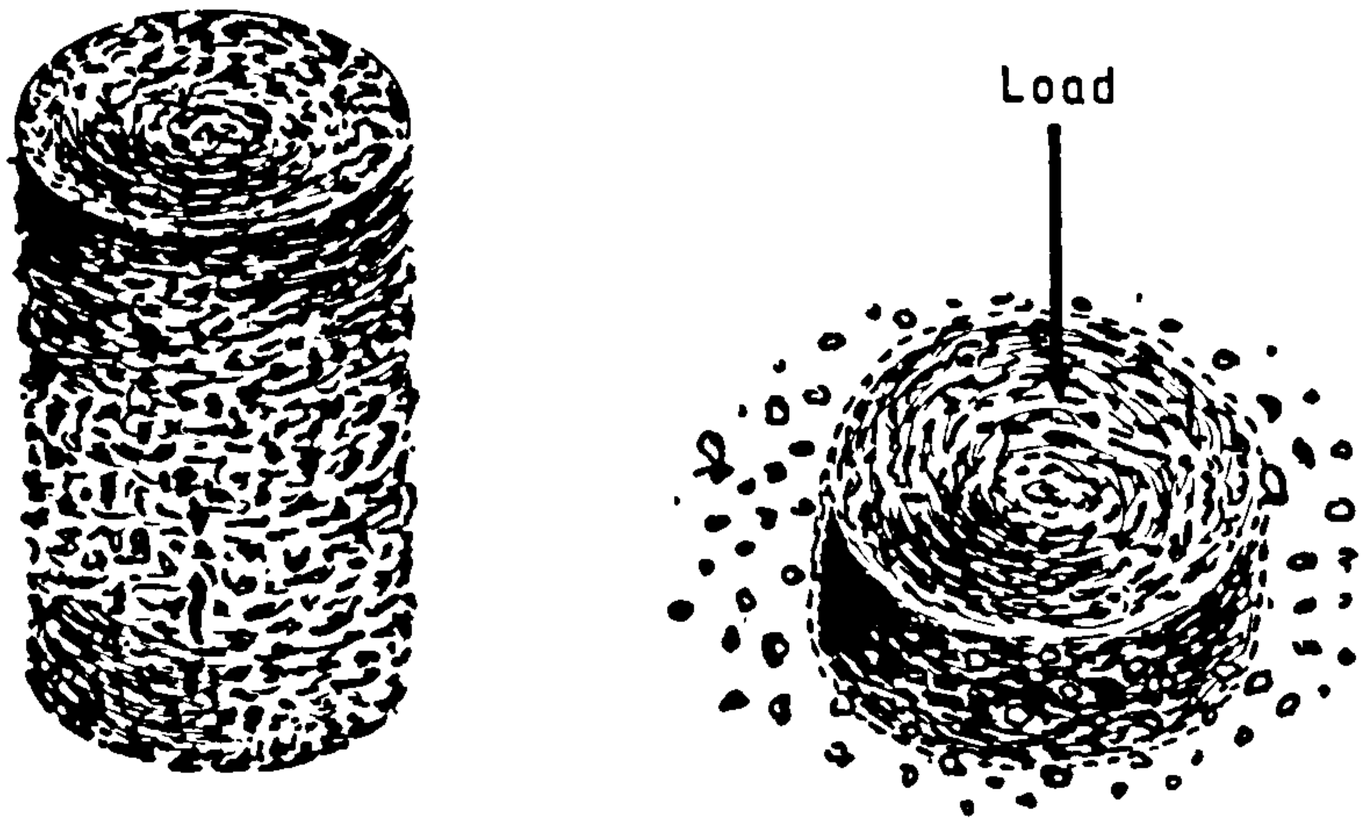


Crushable material, e.g. cellular (lightweight) concrete

Figure 1.9

the development of the resulting fractures. Some energy is also absorbed by friction between the tube and the die. The device has been analyzed notably by Coppa (16) and McGehee (71). Coppa has shown a measure of the characteristic force fluctuations observed in the aluminium fragmenting tube. This is an undesirable feature as it inhibits a smooth deceleration of the kinetic energy and its uniform dissipation throughout collapse. Nevertheless, it can provide a high specific energy for suitable geometry and die proportions.

Machining and cutting processes, e.g. grooving of a metallic bar provide other means by which energy may be absorbed by brittle failure. Rayfield (80) has illustrated the operation of one such device where grooves are made to develop in a metal tube. This offers a steady resistive force but suffers from a low stroke efficiency and a low absorption capacity.

Other examples include cellular (lightweight) concrete and some refractory materials which absorb energy under the action of crushing or punching. These have applications in the protection of ships and quay-side structures in collisions or as highway restraint safety systems.

## 1.3 Relative Merits and Disadvantages of Different Absorption Devices

An extract from Reference 21 is represented identically in Table 1.1 to provide a comprehensive summary of the relative advantages and drawbacks of the E.A. types discussed in the preceding section. In this particular classification fluid--filled and hydraulic systems previously distinguished from

Comparison of different systems in their performance as energy absorbers

| Device | Stroke to length ratio s/l (Approx) | Force - Stroke characteristics | Specific Energy (Approx) ft.lb/lb X $10^3$ | Comments |
|---|---|---|---|---|
| Tension stainless steel strap | 0.5 | strain dependent | 5 | Simple, inexpensive, fractures if overextended |
| Flattening tube array | 0.7 | nearly constant for s/l 0.7 | 1.5 - 5 | Reliable |
| Inside-out tube | 0.5 | constant | 2 - 4 | Reliable - can resist rebound loads |
| Contracting tube | 0.5 | constant | - | - |
| Expanding tube | 0.5 | constant | 8 | Reliable, accepts some off axis loading, inexpensive |
| Folding tube | 0.7 - 0.8 | nearly constant (sinusoidal) | 10 | Reliable, inexpensive, can accept rebound loads |
| Tube mandrel | | | | |
| 1. Franging | 0.8 | large variations (average nearly constant) | 15 - 35 | Large fluctuation in load |
| 2. Splitting and curling | 0.8 | nearly constant | 15 | Reliable, inexpensive if conical mandrel is used |

Table 1.1 {Ref.(21)}

| Device | Stroke to length ratio s/l (Approx) | Force - Stroke characteristics | Specific Energy (Approx) ft.lb/lb X $10^3$ | Comments |
|---|---|---|---|---|
| Metal strip or wire bender | 1.0 | constant | - | Commercially available, reliable, long stroke, works in tension |
| Rolling torus (wire helix) | 0.3 | constant | 10 | Commercially available, worked in tension or compression. Each device must be 'tuned' by adding or subtracting wire |
| Plastic hinge (pin) | 0.8 | Function of geometry | - | Very simple, reliable, resists rebound |
| Extrusion devices | | | | |
| 1. Piston type | 0.3 | velocity sensitive | - | Hydraulic and viscoelastic are reuseable |
| 2. Changing geometry | 0.8 | velocity sensitive | - | Very simple, an example of this is a water bumper |
| Crushing materials | | | | |
| 1. Balsa wood | - | - | 10 - 25 | Omnidirectional load capacity |
| 2. Aluminium honeycomb | 0.7 | constant for s/l 0.7 | 5 - 10 | Omnidirectional load capacity, reliable |
| 3. Thermoplastics | 0.5 - 0.7 | exponential | 10 - 20 | Omnidirectional load capacity, reliable |

1 ft.lb /lb = 30 mm kN /kN



Table 1.1 (Continued)

other types appear to be amalgamated with extrusion devices, if not missing altogether. As has been discussed, however, the former are associated with characteristic low operating pressures and are thus suitable in applications requiring low specific energy.

## 1.4 The Cylindrical Tube Element in Axial Compression

From the review presented of the various EA elements commonly used, the cylindrical tube for collapse in axial compression is selected here as a simple, cheap, reliable and efficient means of dissipating energy for the particular application considered.

As illustrated in later chapters, this element develops, for suitable geometry and material, a repetitive pattern of folds under axial collapse. In this case, despite the load fluctuations that accompany the folding and stretching, the average collapse load is constant throughout failure, thus promoting deformation in a coordinated manner. Consequently, the cylindrical tube possesses a high stroke efficiency, high specific energy and may be made to acquire a desired operating pressure by suitable variations in its geometry; Its manner of collapse has implied that the energy absorption capacity of the axially loaded tube exceeds, to an appreciable extent, that for the laterally compressed tube element. Furthermore, amongst all cross-sectional shapes, the circular tube is unique in possessing the same mechanism of axial collapse under both impact and quasi-static loading conditions (Johnson(45)).

In isolation, the circular tube is recognized to be a simple EA device possessing a particularly favourable cost/weight effectiveness. This is in contrast to many EA systems including tubes in inversion, flaring and fragmentation processes, as reviewed here, which require at additional expense, the construction of specific mandrels, dies or cutting methods for proper operation. Its use is deduced to be ideal in a large-scale application such as that studied here, where a number of EA elements are employed within a specified crushing layer.

Aside from its suitability as an energy absorber, the cylindrical tube represents the most important body element of the structure of the modern aeroplane, missiles and re-entry vehicles and to some extent motor and railway coaches. Thus a study of its collapse behaviour is observed to have manifold applications.

## 1.5 Experimental Program

A summary is presented in this section of (i) the type and properties of the material of the tubes tested, (ii) the experimental loading equipment, and (iii) practical details concerning the testing procedure. Details of the specimens themselves as regards their geometry and collapse behaviour are presented and illustrated in Chapter 2.

### 1.5.1 Tube Material

The material used in the experimental testing program was HT-30 - aluminium alloy, chosen for its suitable ductility,

non-corrosive property and its commercial abundance. The alloy composition and some mechanical properties of the material in the as-received condition are shown in Table 1.2 .

### 1.5.2 Annealing

This is the process of heating a material in an air furnace at a suitable temperature and over a suitable period of time followed by slow cooling to ambient temperature. It is used as a method of releasing the stresses that are locked within the material and are associated with its manufacture. The treated material is consequently expected to exhibit more ductile behaviour even though its mechanical strength may have reduced in this process. The increase in ductility was seen to be a particularly desirable property if collapse of a tube in axial compression is to take place in a controlled manner with minimum brittle failure of the tube specimen.

A temperature of 350 ℃ was used within the annealing range : 330 ℃ - 420 ℃ for the aluminium used. In order to determine the required period of annealing time for the alloy tubing which is also a function of tube wall thickness, the author annealed a set of identical tubes (3.175 mm thick) in an oven for different periods ranging from 1 hour to 7 hours and varying in steps of 1 hour. These tubes were subsequently tested in axial compression and all collapsed in an identical manner. The corresponding load-compression curves were found to be identical in trend and magnitude for tubes annealed beyond 3 hours, indicating completion of the annealing process

Chemical composition and some properties of HT30-aluminium alloy tubing

| Alloy element | Cu | Mg | Si | Fe | Mn | Zn | Cr | Others |
|---|---|---|---|---|---|---|---|---|
| % Composition | 0.1 | 0.4 - 1.5 | 0.6 - 1.3 | 0.6 | 0.4 - 1.0 | 0.1 | 0.5 | 0.2 |

| Manufacturing treatment | Tensile strength | 0.1 % proof stress | Percentage elongation on 2 inches |
|---|---|---|---|
| Solution treatment + precipitation treatment | 20 tons/(in.$^2$)<br>0.304 KN/mm$^2$ | 15 - 16 tons/(in.$^2$)<br>0.228 - 0.243 KN/mm$^2$ | 7 - 9 |

| | | |
|---|---|---|
| Melting range (°C)<br>570 - 660 | Coefficient of linear expansion within temperature range<br>20 °C - 100 °C<br>23 X 10$^{-6}$ | Resistance to atmospheric corrosion<br>Cold forming<br>Machining<br>Weldability<br>} Good |
| Annealing range (°C)<br>330 - 420 | | |

Table 1.2

over this period. The results were in marked contrast to that of the single test performed on an as-received (non--annealed) tube of the same geometry which collapsed in a brittle manner and fragmented. The annealing period was increased in accordance with the wall thickness of tubes beyond 1/8 in. (3.175 mm) thick, in the experimental program. The time variations were typically chosen to incorporate ½-hour to 1-hour time safety margins, e.g. 5 hours for 3/16 in. (4.76 mm) tubes, to ensure complete annealing through to the midsurface of the tubes.

### 1.5.3 Test Equipment

An Instron testing machine, model 1195, with a 100 KN load cell capacity was used for most tests, as illustrated in Plate 1.1 . Loading was applied by means of a moving cross-head onto the tube at pre-selected speeds. In each case, the tube was held between rigid and parallel steel platens and its position matched against a pattern of concentric rings on the load cell platen, in order to ensure axial loading with minimum eccentricity.

Variations in load with axial deformation of the tube (crosshead displacement) were recorded as a curve plotted directly onto a grid chart providing a measure of the axial load/Axial compression (pll) of the tube. As will be seen in the following chapters, this graph was used in a number of ways to characterize tubes in relation to a variety of parameters.

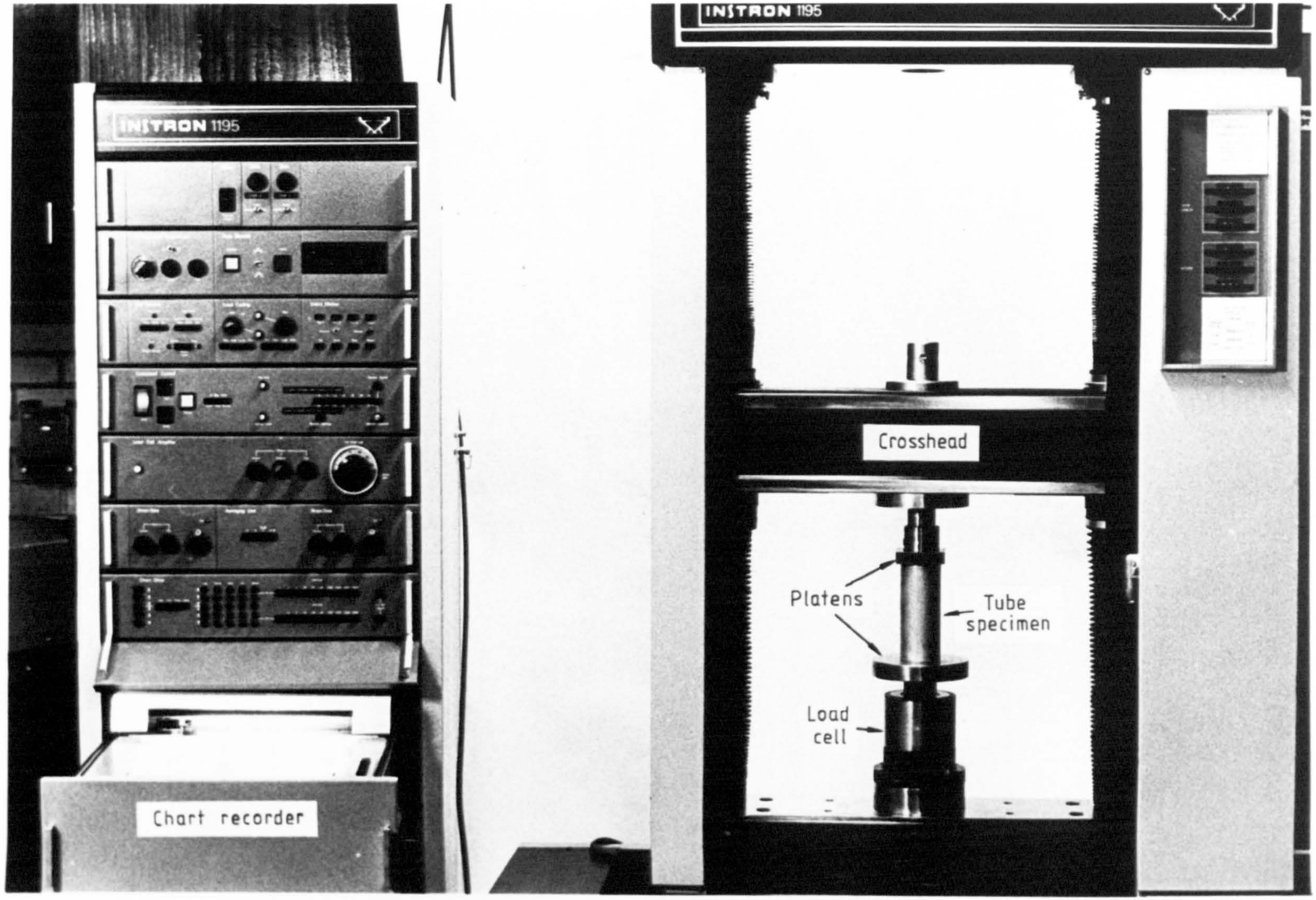


Plate 1.1 Instron testing equipment

For tubes failing at axial loads beyond 100 KN, Losenhausen testing equipment was used, as shown in Plate 1.2 . Here, too, loading was applied by a moving crosshead operated by a hydraulic pump. An X-Y plotter was used to establish as a curve, the corresponding load-compression behaviour of the tubes tested.

In order to determine the yield stress of the annealed aluminium material used, strain gauged axial tests were performed on a set of annealed tubes. A pair of type PL-5 strain gauges recording a maximum of 2% strain were located, in each case, on 2 diametrically opposed generators at the midlength of the tube. These constituted the 'active' pair in the electrical terminology. A second ('dummy') pair of gauges were mounted on a piece of conducting metal and connected together with the active pair to a high sensitivity digital galvanometer, namely a Peekel Strain Recorder. The connections were made by thin flexible wires and were done in a particular combination so as to construct a 4-arm Wheatstone resistance bridge. The strains subsequently recorded were the mean of the individual strains on the two gauge lengths on the tube. These were recorded as a microstrain scale on the X-axis of the X-Y plotter along with the axial load on the Y-axis of the recorder. The trend of the resulting stress-strain curves together with the yield stresses obtained are presented and discussed in Chapter 5 (see P.158 & P. 349). Plate 1.3 shows the strain recording equipment used.

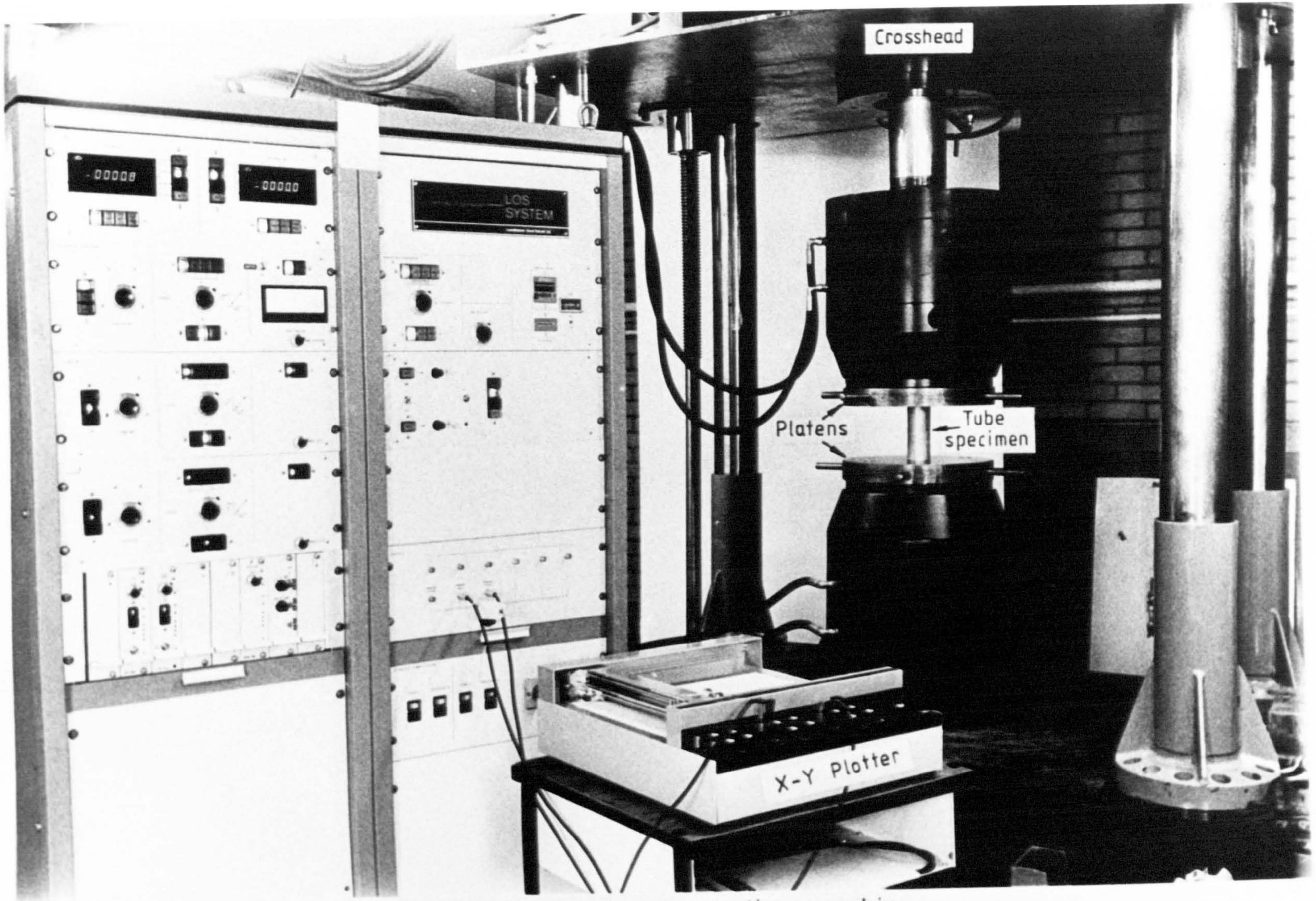


Plate 1.2 Losenhausen testing machine

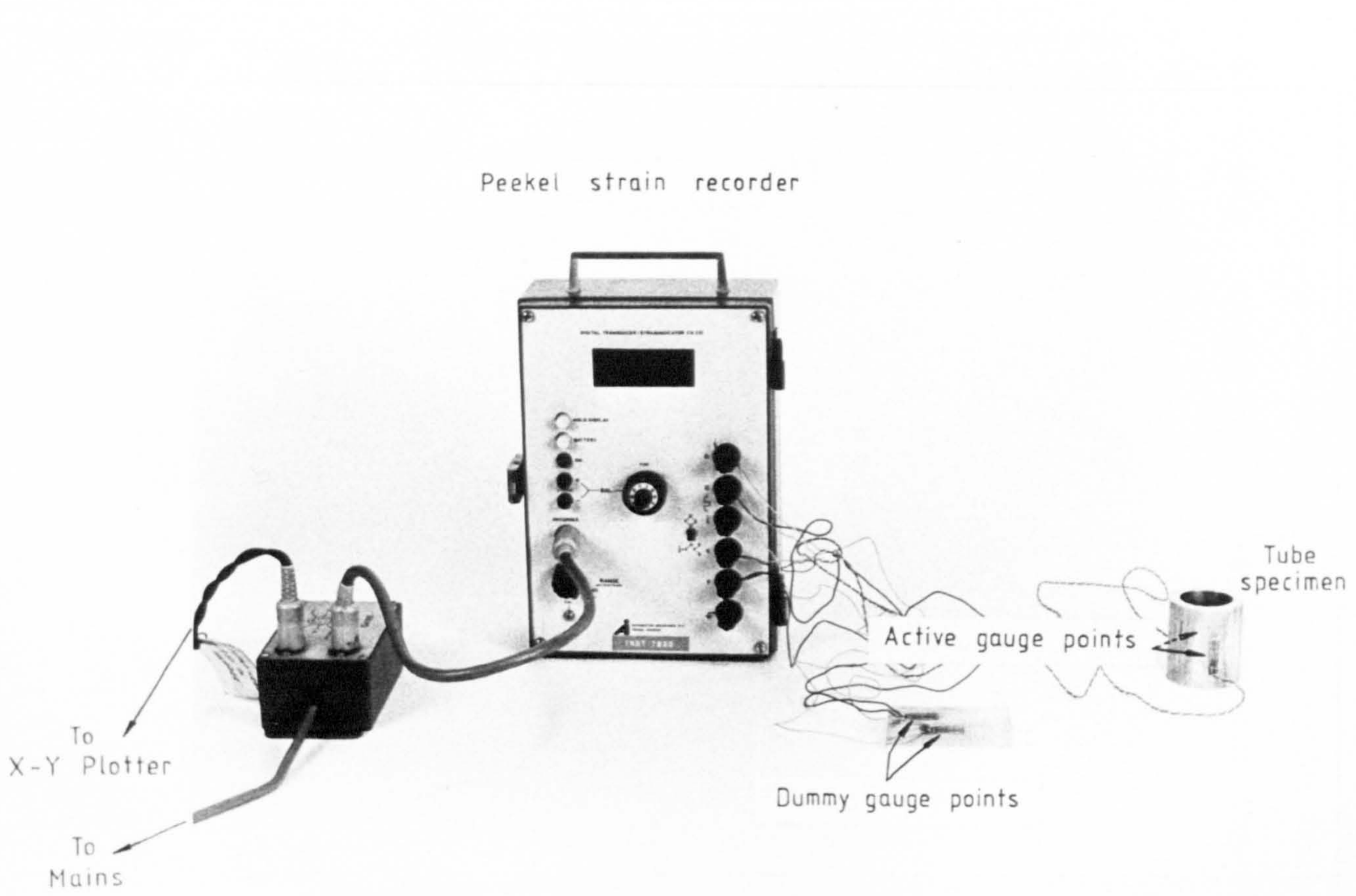


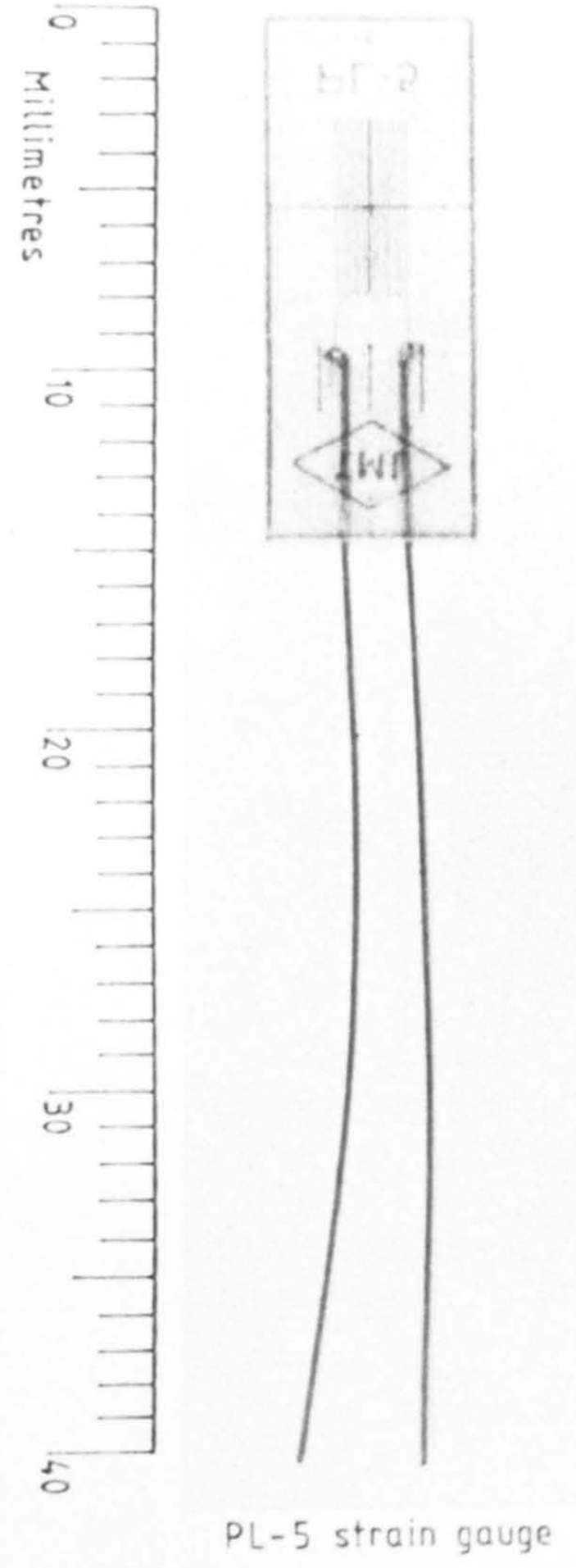


Plate 1.3 Strain recording equipment

### 1.5.4 Deformation Rate

The rates of axial compression selected for the tests performed in the experimental program were in the range : 2 - 10 mm/minute, and frequently a rate of 5 mm/minute was used. For strain gauged tests, lower rates, e.g. ½ mm/minute were chosen.

The above strain rates constitute purely quasi-static loading conditions and their variations within the indicated range were observed to have no influence on any aspect of failure of the tubes tested.

# CHAPTER 2

# CLASSIFICATION OF AXIAL COLLAPSE MODES OF CYLINDRICAL TUBES

# Chapter 2 - Synopsis

Experimental results for the collapse of axially loaded aluminium tubes are presented in the form of a chart based on two dimensionless parameters relating to the tube dimensions, length L, diameter D, and wall thickness t. Zones of this chart are identified with particular modes of collapse. It is inferred that absolute size does not influence the modes of collapse. This is governed simply by the ratios L/D and t/D.

The use of this chart in conjunction with the shapes of the axial load-compression curves permits an explanation to be given as to why a change-over from one collapse mode to another takes place as the magnitude of t, D, or L is varied.

## 2.1 Introduction

In the conventional design of components in an engineering structure that are specifically chosen not to deform under a prescribed loading, concern centres primarily on the limit state or critical stress conditions of the elements, upon which their design is based. However, in the present study of circular tubes for use as energy absorbing elements in axial compression, it is observed that large-scale deformations and the postbuckling behaviour constitute an important aspect of their design for collapse. To this end, there is a need to know the mechanism of collapse for any tube prior to its use in the final energy dissipating application.

The cross-section geometry of a circular tube is important in determining the mode of collapse. Thick-walled tubes have been observed to fail in a concertina (ring-type) mode; whereas thin-walled cylinders collapse predominantly in the asymmetric diamond configuration. However, little investigation has been directed towards establishing the influence of tube length on the mode of axial collapse. It is evident that for a given section geometry, if the tube specimen is sufficiently long, it may behave essentially as a strut failing in the Eulerian manner; whilst a very short tube cannot develop a pattern of axial folds and is forced to crush into a barrel-shaped configuration under compression. Furthermore, between these extremes, a tube may exhibit a combination of several modes, e.g. concertina & diamond.

The dearth of information relating to the effect of specimen length caused the author to investigate the influence of this parameter in collaboration with section geometry. An attempt has been made to correlate, from experiments, the mode of axial collapse with all tube dimensions, i.e. thickness, diameter and length. A 'zone' chart is consequently obtained which identifies the modes of collapse with non-dimensional tube geometry.

For the different modes of collapse observed, the corresponding load-compression curves typically obtained are shown,
(Section 2.3 (p2) and p.96 et.seq.)

## 2.2 Collapse Classification Chart

The results of the experimental investigation are presented in this section. The three geometric variables of a tube, i.e. thickness t, internal diameter D and length L are combined into the two ratios, L/D and t/D, and are then related to the actual failure mechanisms.

The method implies that similar tubes as defined by their L/D and t/D ratios, collapse in identical manner. Thus, for a given material, tube size in the absolute sense is considered to have no influence on the mechanism of failure. This is shown to be so in the axial tests performed.

Tubes of identical section dimensions (& hence fixed t/D) were of HT30-aluminium alloy. In order to vary ratio L/D, they were cut to different lengths; their ends were machined

to form smooth and parallel end surfaces. The tubes were annealed and tested to collapse in axial compression. This procedure was repeated with tubes of other section dimensions but the same t/D ratio. Also, in order to vary ratio t/D for a fixed L/D, the thickness of a set of identical tubes (i.e. fixed L, t, D) was varied by machining these tubes on the outside. The ranges of tube dimensions considered in the experimental program are as follows:

| | | |
|---|---|---|
| Thickness, t | : | ½ mm - ¼ in. (6.35 mm) |
| External Diameter, D' | : | ¾ in. (19.1 mm) - 6 in. (152.4 mm) |
| Length, L | : | ¼ in. (6.35 mm) - 21 in. (533.4 mm) |

The results of all the tests to establish the failure trends on the classification chart discussed are summarized in Figure 2.1 . For the range of the L/D and t/D ratios considered, nine modes of collapse have been identified. These comprise:

| | |
|---|---|
| (a) concertina | axisymmetric and sequential folding starting at one end of tube |
| (b) diamond | non-axisymmetric but sequential collapse accompanying a change in the cross-section shape of tube |
| (c) Euler | bending of tube as a strut |
| (d) concertina + 2-lobe diamond<br>(e) concertina + 3-lobe diamond<br>(f) concertina + 2-lobe & 3-lobe diamond | collapse first in the concertina mode which changes over to diamond configuration<br>2-lobe ⟶ square X-section pattern<br>3-lobe ⟶ hexagonal X-section shape |

---

A single test on a mild steel tube : 6 in.(L) X 1 in.(D') X 20 SWG(t) (t/D = 0.0388, L/D = 6.466) produced collapse in the concertina + 3-lobe diamond mode.

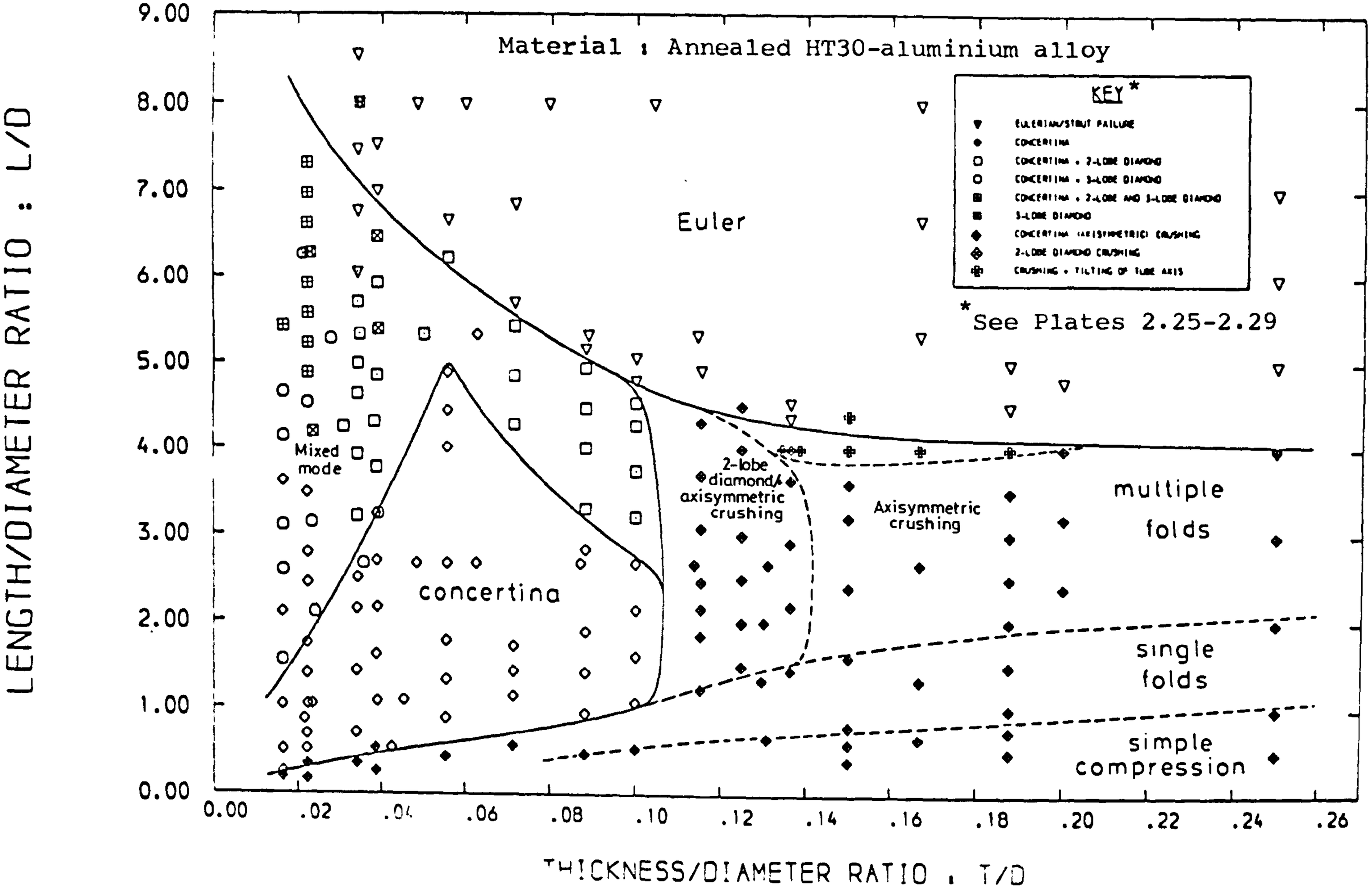


CLASSIFICATION CHART OF AXIAL COLLAPSE MODES IN CYLINDRICAL TUBES

Figure 2.1

| | |
|---|---|
| (g) axisymmetric/ /concertina crushing | simultaneous collapse along the length of tube; axisymmetric 'barrelling' of tube; barrelling may be 'single' or 'multiple' depending on tube length |
| (h) 2-lobe diamond crushing | simultaneous collapse along the length of tube in the form of the 2-lobe diamond configuration |
| (i) tilting of tube axis | shearing of tube on the platen surface in the form of displacement at one end from the original position |

The above modes are categorized into 3 broad mechanisms as follows:

(i) Euler : bending as a strut

(ii) Sequential folding : concertina/diamond/mixed concertina and diamond

(iii) Crushing : simultaneous collapse throughout the entire tube

In order to identify the various forms of collapse, boundaries have been drawn in Figure 2.1 to separate, as groups, the different mechanisms encountered.

Plates 2.1 - 2.24 * show the range of tube sets tested to obtain the above chart. They are shown in the order of increasing t/D ratio as far as the different sets permit and illustrate the collapse configuration of individual tubes within each set. Tables 2.1 - 2.24 * present details of the corresponding tube geometries and modes of collapse

---

* These are presented at the end of chapter

for the individual tubes tested in each set. Results are shown again in the order stated above and may be used with the plates to facilitate the matching of a particular data point in Figure 2.1 with a unique set of tube dimensions.

## 2.3 The Load-Compression Curve and Mode of Axial Collapse

A plot of the axial load vs axial compression was obtained for each of the tests. These curves illustrate certain trends depending on the particular mechanism of collapse. Plates 2.25 - 2.29 show schematically the variation of axial load with shortening of the tube alongside the collapse mechanisms, for various types of collapse. Plates 2.30 - - 2.34 show a selection of actual test results. Plate 2.31 also shows the stages of the folding process for concertina collapse, in relation to the load-compression curve.

The importance of the load-compression plot of a collapsing element has been mentioned in Chapter 1, in the context of energy dissipating systems. It was noted that a nearly constant or uniform load response throughout collapse is a desirable characteristic since it signifies a uniform and controlled dissipation of energy. Although none of the collapse mechanisms observed here is associated with a constant postbuckling load, some collapse modes are clearly 'good' energy dissipators; these are the sequential mechanisms. The repetitive variations in postbuckling loads for the concertina and diamond modes fluctuate about a mean value of the load. This shows that collapse is in a well controlled manner.

In contrast, for Eulerian failure, a continuously declining load throughout buckling is observed, this often leading to catastrophic failure with decreasing capacity to dissipate energy. Crushing modes, too, are considered to be undesirable. Although they appear to exhibit a fairly uniform load response in the case of long thick-walled tubes, the exact nature of the load fluctuations is unpredictable and further, the overall range of deformations is limited, in comparison with the sequential modes of failure. This indicates a low stroke efficiency and therefore a reduced capacity to dissipate energy.

Considering the mixed concertina and diamond modes of collapse, a rise in the successive peaks of loads on the load-compression curves was observed in certain tests before transition from concertina to diamond folding took place. Moreover, subsequent inspection of individual tubes (in a given set) has revealed that they have developed a fairly constant number of concertina folds before changing to diamond collapse. Figure 2.2 indicates the ranges for the number of concertina folds obtained in the different sets of tubes tested. This feature is further examined in the next section.

## 2.4 Discussion of Collapse Modes and Their Boundaries on Classification Chart, Figure 2.1

### (a) Thick Tubes

The test results obtained have indicated that the concertina mechanism, associated with failure of thick-walled tubes, is bounded at a value of $t/D = 0.10$ beyond which crushing

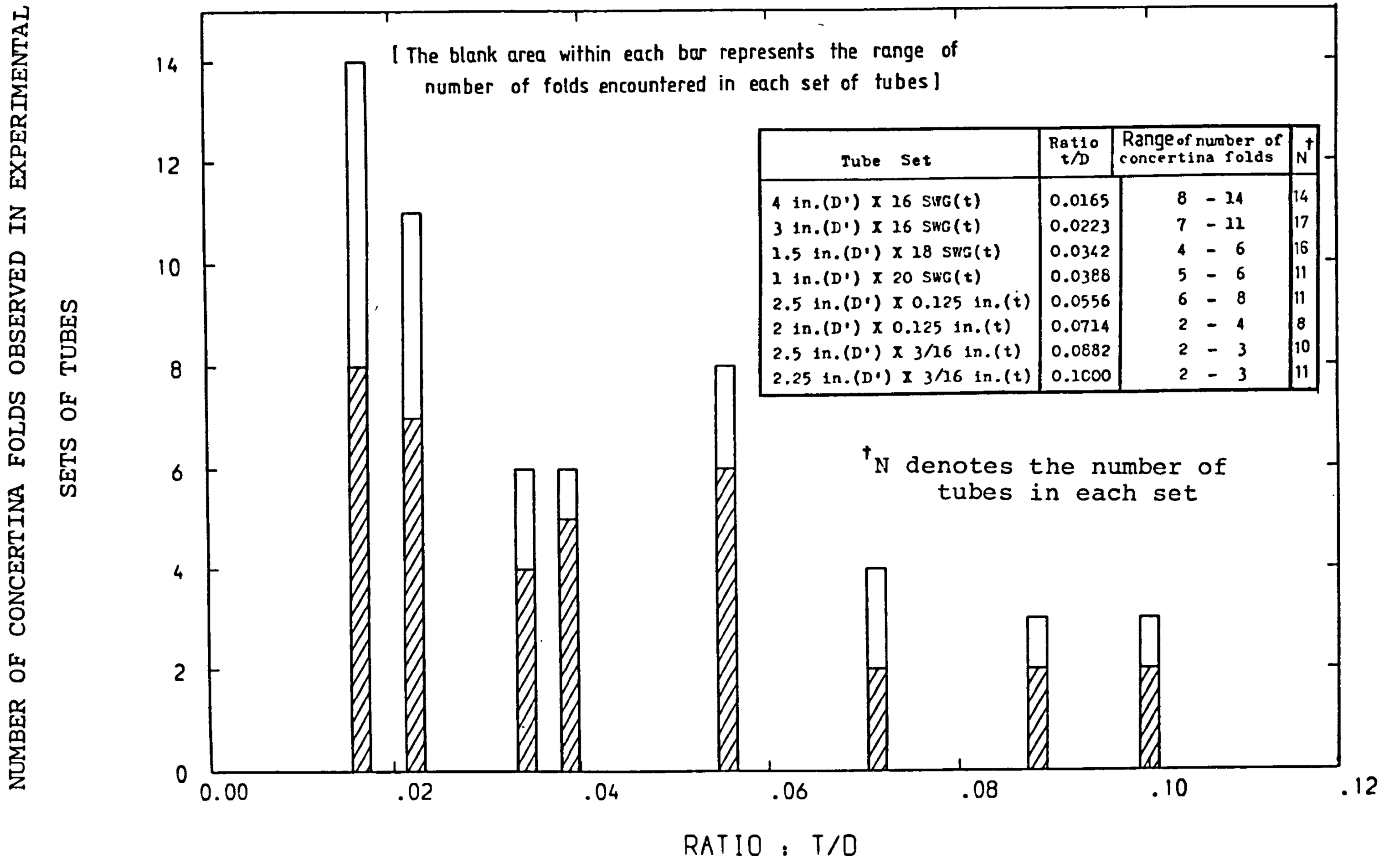


| Tube Set | Ratio t/D | Range of number of concertina folds | †N |
|---|---|---|---|
| 4 in.(D') X 16 SWG(t) | 0.0165 | 8 - 14 | 14 |
| 3 in.(D') X 16 SWG(t) | 0.0223 | 7 - 11 | 17 |
| 1.5 in.(D') X 18 SWG(t) | 0.0342 | 4 - 6 | 16 |
| 1 in.(D') X 20 SWG(t) | 0.0388 | 5 - 6 | 11 |
| 2.5 in.(D') X 0.125 in.(t) | 0.0556 | 6 - 8 | 11 |
| 2 in.(D') X 0.125 in.(t) | 0.0714 | 2 - 4 | 8 |
| 2.5 in.(D') X 3/16 in.(t) | 0.0682 | 2 - 3 | 10 |
| 2.25 in.(D') X 3/16 in.(t) | 0.1000 | 2 - 3 | 11 |

CONCERTINA/CONCERTINA + DIAMOND MECHANISM OF COLLAPSE

**Figure 2.2**

modes take over.

In the concertina mode an appreciable internal work in the form of plastic deformation is involved in bending and stretching of the tube during the sequential development of folds. This is in contrast to the crushing modes where collapse is a simultaneous event along the whole length of the tube and results in considerable thickening of the specimen. Axisymmetric crushing folds involve little or no development of compressive hoop stresses, their occurrence being mainly in the form of limited radial expansion. They are thus distinct from their concertina counterparts both in configuration and the reduced internal work expended in their formation. The changeover from the 2-lobe crushing mode to axisymmetric crushing at higher values of ratio t/D suggests a preference of the tube for axisymmetric thickening instead of changing its cross sectional shape in the formation of the 2-lobe crushing (diamond) mode. n. Tilting of tube axis during deformation from the original vertical direction implies significant shearing between the ends of the tube and the platens of the testing equipment. This feature is also seen as a means of reducing the internal work required for simultaneous crushing of the entire tube. It is predicted that the above crushing modes would persist for thicker-walled tubes and that no new mechanisms would be encountered at higher ratios of t/D beyond the range examined.

(b) Thin Tubes

For thin-walled tubes with t/D ratios smaller than the range $t/D < 0.016$ studied here, it is believed that a whole spectrum of purely diamond modes of collapse exists. Previous studies, notably by Johnson et al (48), Pugsley and Macaulay (78) and Allan (4) have indicated that within this diamond zone (i.e. the region to the left of the test range in Figure 2.1), a reduction in tube ratio t/D would result in an increase in the number of circumferential diamond lobes in the failure configuration. Due to unavailability of ready-made thin-walled tubes of the alloy tested, and in the absence of fabrication methods to construct thin-walled tubes using a mandrel and thin sheets of the alloy material, only one successful result has been obtained by the author to indicate the above trend. This was a test on a 3 in. (76 mm) long X 2¼ in. (57.2 mm) inside diameter tube with a thickness machined to a nominal ½ mm , giving a ratio of $t/D \simeq 0.009$ . As shown in Plate 2.35 this particular tube failed in a regular 4-lobe diamond pattern.

However, as will be observed in later chapters, the concertina mechanism constitutes the optimum choice of collapse mode for a tube on the grounds of energy dissipation. To this end, the chart of Figure 2.1 is considered to be complete in enabling suitable geometry to be selected for cylindrical tubes of the aluminium tested, in their optimum design as energy dissipators. Chapter 7 presents details of a design program in which this optimum or concertina zone is used.

Considering the case of mixed concertina and diamond modes, the previously noted rise in successive peaks† in the concertina region is believed to be associated with axial stiffening of the undeformed portion of the tube,prior to its subsequent deformation in the folding process. The mean level of collapse resistance in the concertina mode is shown in later chapters to exceed that for diamond failure. Thus the above mode changeover in the mixed mode is viewed as a preference of the tube to assume a more stable configuration, particularly if it is argued that the rise in successive load peaks signifies the accumulation of internal work up to a critical condition. For a shorter tube this condition would not be reached so that the tube, expectedly, fails in the concertina mode alone. This would explain why the number of concertina folds in the mixed modes remained largely constant and irrespective of tube length, within certain sets of tests.

The presence of Eulerian buckling as the upper limiting region for all tube section geometries is recognized to be inevitable, since a tube must fail as a strut if it is suitably long. Similarly, the 'simple compression' zone is deduced to be a limiting region at the lower extreme, since a suitably short tube cannot develop a pattern of folds at all. The rising trend of the boundary of this zone with increasing ratios of t/D is explained by the fact that as thickness t is increased, a longer length is required for the formation of an axial fold, implying an increase in ratio L/D.

The curvilinear trend of the boundary of the Euler zone in

---

† on the load/deformation plots (see Plates 2.27 & 2.32).

Figure 2.1 is confirmed as follows. Let us consider a point on the boundary in the region of, say, t/D = 0.08. If the thickness of this tube is reduced by, say, machining it on the outside, the t/D ratio is decreased but ratio L/D remains unaffected. This reduction in thickness alone is believed to be the governing factor at the tube ends which triggers the sequential modes of collapse; hence a greater likelihood may be attached to the new tube failing in the mixed mechanism, implying that a longer length is required for its collapse in the Eulerian fashion. Since the original internal diameter remains unaltered, this signifies an increase in ratio L/D, in harmony with the ascending trend of the boundary.

The slenderness ratio, L/k (k = radius of gyration) has been incorporated in the above discussion, since, $k \simeq \frac{D}{2}$, so that $L/k \simeq 2L/D$. This is verified below.

By definition, $k = (I/A)^{\frac{1}{2}}$ where I = 2nd moment of area
A = net section area

For a cylindrical tube, $A = \pi t(D+t)$ and it can be shown that,

$$I = \frac{1}{4}\pi\left[D^3t + 3D^2t^2 + 4Dt^3 + 2t^4\right] \qquad (2.4.1)$$

$$\text{Thus,} \quad I/A = \frac{D^2\left[1 + 3(t/D) + 4(t/D)^2 + 2(t/D)^3\right]}{4\left[1 + (t/D)\right]} \qquad (2.4.2)$$

Neglecting the term involving $(t/D)^3$,

$$I/A \approx \frac{D^2\left[1 + 2(t/D)\right]^2}{4\left[1 + (t/D)\right]}, \text{ so that } k \approx \tfrac{1}{2}D\left[1 + 2(t/D)\right] \left(=\frac{D}{2}+t\right) \qquad (2.4.3)$$

Hence, for the range of t/D considered here, $k \simeq \frac{D}{2}$.

## 2.5 Concluding Remarks

The existence of failure zones on the dimensionless plot of Figure 2.1 confirms the initial assumption that for a cylindrical tube of ductile material, absolute size has no influence on its mechanism of collapse. What governs the type of failure is the initial shape, i.e. the length of the tube, its thickness and diameter.

The collapse zones obtained in Figure 2.1 in conjunction with their corresponding load-compression curves have made it possible to explain, on a qualitative basis, why a change-over from one mode to another takes place as the magnitude of L/D or t/D is varied.

The repetitive patterns of load-compression curves for the sequential collapse modes are a desirable feature in the context of energy dissipation.

Hence Figure 2.1 may be used in the design of tubes for this function.

# Tables 2.1 - 2.24

## Notation

### Tube geometry

D' = external diameter

D = internal diameter

L = length

t = thickness

$t_{nominal}$ = nominal thickness - this refers to those tubes whose original thicknesses were machined (reduced) to desired nominal values. The individual thickness recordings denote the actual values subsequently recorded with the use of a micrometer screw-gauge.

SWG = Standard Wire Gauge units conversion to millimetres :

| SWG number | mm |
|---|---|
| 16 | 1.63 |
| 18 | 1.22 |
| 20 | 0.91 |

### Other notes

in. = inches

X2 = repeat of an individual test

For descriptions of the mechanisms of collapse, see Section 2.2 (P.59) and Plates 2.25 - 2.29 (PP 96-98).

See Plate 2.1

| Section geometry of tube set | t (mm) | D (mm) | Ratio t/D |
|---|---|---|---|
| 4 in.(D') X 16 SWG(t) | 1.63 | 98.35 | 0.0165 |

| L inches | L mm | Ratio L/D | Mechanism of collapse |
|---|---|---|---|
| 21 | 533.4 | 5.423 | concertina + 2-lobe and 3-lobe diamond |
| 18 | 457.2 | 4.649 | concertina + 3-lobe diamond |
| 16 | 406.4 | 4.132 | concertina + 3-lobe diamond |
| 14 | 355.6 | 3.616 | concertina |
| 12 | 304.8 | 3.099 | concertina + 3-lobe diamond |
| 10 | 254 | 2.583 | concertina + 3-lobe diamond |
| 8 | 203.2 | 2.066 | concertina |
| 6 | 152.4 | 1.550 | concertina, concertina + 3-lobe diamond X2 |
| 4 | 101.6 | 1.033 | concertina |
| 2 | 50.8 | 0.517 | concertina X2 |
| 1 | 25.4 | 0.258 | concertina |
| 0.75 | 19.1 | 0.194 | concertina crushing |

Table 2.1

See Plate 2.2

| Section geometry of tube set | t (mm) | D (mm) | Ratio t/D |
|---|---|---|---|
| 3 in.(D') X 16 SWG(t) | 1.63 | 72.95 | 0.0223 |

| L inches | L mm | Ratio L/D | Mechanism of collapse |
|---|---|---|---|
| 21 | 533.4 | 7.312 | concertina + 2-lobe and 3-lobe diamond |
| 20 | 508 | 6.964 | concertina + 2-lobe and 3-lobe diamond |
| 19 | 482.6 | 6.615 | concertina + 2-lobe and 3-lobe diamond |
| 18 | 457.2 | 6.267 | concertina + 2-lobe and 3-lobe diamond |
| 17 | 431.8 | 5.919 | concertina + 2-lobe and 3-lobe diamond |
| 16 | 406.4 | 5.571 | concertina + 2-lobe and 3-lobe diamond |
| 15 | 381 | 5.223 | concertina + 2-lobe and 3-lobe diamond |
| 14 | 355.6 | 4.875 | concertina + 2-lobe and 3-lobe diamond |
| 13 | 330.2 | 4.526 | concertina + 3-lobe diamond |
| 10 | 254 | 3.482 | concertina |
| 8 | 203.2 | 2.785 | concertina |
| 7 | 177.8 | 2.437 | concertina |
| 5 | 127 | 1.741 | concertina |
| 4 | 101.6 | 1.393 | concertina |
| 2 | 50.8 | 0.696 | concertina |
| 1 | 25.4 | 0.348 | concertina crushing |
| 0.5 | 12.7 | 0.174 | concertina crushing |

Table 2.2

See Plate 2.3

| Section geometry of tube set | L inches | L mm | t (mm) | D (mm) | Ratio t/D | Ratio L/D | Mechanism of collapse |
|---|---|---|---|---|---|---|---|
| 1 in. (D') X 0.5 mm (nominal t) | 6 | 152.4 | 0.56 | 24.28 | 0.0230 | 6.276 | 3-lobe diamond (irregular) |
| | 4 | 101.6 | 0.57 | 24.26 | 0.0236 | 4.189 | 3-lobe diamond |
| | 3 | 76.2 | 0.57 | 24.26 | 0.0234 | 3.140 | concertina + 3-lobe diamond |
| | 2 | 50.8 | 0.59 | 24.23 | 0.0242 | 2.097 | concertina + 3-lobe diamond |
| | 1 | 25.4 | 0.58 | 24.25 | 0.0237 | 1.047 | concertina |
| | 0.5 | 12.7 | 0.54 | 24.32 | 0.0222 | 0.522 | concertina |
| | Tube with L = 5 inches failed in a very irregular pattern. | | | | | | |

Table 2.3

See Plate 2.4

| Section geometry of tube set | L inches | L mm | t (mm) | D (mm) | Ratio t/D | Ratio L/D | Mechanism of collapse |
|---|---|---|---|---|---|---|---|
| 1 in. (D') X 1/32 in. (nominal t) | 6 | 152.4 | 0.52 | 24.36 | 0.0213 | 6.256 | concertina + 3-lobe diamond |
| | 5 | 127 | 0.67 | 24.06 | 0.0278 | 5.278 | concertina + 3-lobe diamond |
| | 4 | 101.6 | 0.74 | 23.92 | 0.0309 | 4.247 | concertina + 2-lobe diamond |
| | 1 | 25.4 | 0.55 | 24.30 | 0.0226 | 1.045 | concertina |
| | Tubes with lengths L = 3 inches and L = 2 inches failed in regular 3-lobe diamond mode but their thicknesses were non-uniform. | | | | | | |

Table 2.4

See Plate 2.5

| Section geometry of tube set | t (mm) | D (mm) | Ratio t/D |
|---|---|---|---|
| 1.5 in.(D') X 18 SWG(t) | 1.22 | 35.66 | 0.0342 |

| L inches | L mm | Ratio L/D | Mechanism of collapse |
|---|---|---|---|
| 12 | 304.8 | 8.547 | Eulerian bending |
| 10.5 | 266.7 | 7.479 | Eulerian bending |
| 9.5 | 241.3 | 6.767 | Eulerian bending |
| 8.5 | 215.9 | 6.054 | Eulerian bending X2 |
| 8 | 203.2 | 5.698 | concertina + 2-lobe diamond |
| 7 | 177.8 | 4.986 | concertina + 2-lobe diamond |
| 6.5 | 165.1 | 4.630 | concertina + 2-lobe diamond |
| 5.5 | 139.7 | 3.918 | concertina + 2-lobe diamond |
| 4.5 | 114.3 | 3.205 | concertina + 2-lobe diamond |
| 3.5 | 88.9 | 2.493 | concertina ←(See Plate 2.31) |
| 3 | 76.2 | 2.137 | concertina |
| 2 | 50.8 | 1.425 | concertina |
| 1 | 25.4 | 0.712 | concertina X2 |
| 0.5 | 12.7 | 0.356 | concertina crushing |

Table 2.5

See Plate 2.6

| Section geometry of tube set | t (mm) | D (mm) | Ratio t/D |
|---|---|---|---|
| 1 in.(D') X 20 SWG(t) | 0.91 | 23.57 | 0.0388 |

| L inches | L mm | Ratio L/D | Mechanism of collapse |
|---|---|---|---|
| 7 | 177.8 | 7.543 | Eulerian bending |
| 6.5 | 165.1 | 7.005 | Eulerian bending |
| 5.5 | 139.7 | 5.927 | concertina + 2-lobe diamond |
| 4.5 | 114.3 | 4.849 | concertina + 2-lobe diamond |
| 3.5 | 88.9 | 3.772 | concertina + 2-lobe diamond |
| 3 | 76.2 | 3.233 | concertina |
| 2.5 | 63.5 | 2.694 | concertina |
| 2 | 50.8 | 2.155 | concertina |
| 1.5 | 38.1 | 1.616 | concertina |
| 0.5 | 12.7 | 0.539 | concertina crushing |
| 0.25 | 6.35 | 0.269 | concertina crushing ← See Plate 2.34 |

Table 2.6

See Plate 2.7

| Section geometry of tube set | L inches | L mm | t (mm) | D (mm) | Ratio t/D | Ratio L/D | Mechanism of collapse |
|---|---|---|---|---|---|---|---|
| 1 in.(D') X 1 mm (nominal t) | 6 | 152.4 | 0.91 | 23.58 | 0.0387 | 6.464 | 3-lobe diamond (irregular) |
| | 5 | 127 | 0.92 | 23.56 | 0.0390 | 5.390 | 3-lobe diamond (irregular) |
| | 4 | 101.6 | 0.90 | 23.60 | 0.0382 | 4.306 | concertina + 2-lobe diamond |
| | 3 | 76.2 | 0.93 | 23.55 | 0.0393 | 3.236 | concertina + 3-lobe diamond |
| | 2 | 50.8 | 0.92 | 23.56 | 0.0390 | 2.156 | concertina |
| | 1 | 25.4 | 0.92 | 23.55 | 0.0392 | 1.078 | concertina |
| | 0.5 | 12.7 | 1.00 | 23.40 | 0.0222 | 0.522 | concertina |

Table 2.7

See Plate 2.8

| Single tubes | L inches | L mm | t (mm) | D (mm) | Ratio t/D | Ratio L/D | Mechanism of collapse |
|---|---|---|---|---|---|---|---|
| 5 in.(L) X 6 in.(D') X 0.125 in.(t) | 5 | 127 | 3.18 | 146.1 | 0.0217 | 0.870 | concertina |
| 6 in.(L) X 6 in.(D') X 0.25 in.(t) | 6 | 152.4 | 6.35 | 139.7 | 0.0455 | 1.091 | concertina |

Table 2.8

See Plate 2.9

| Section geometry of tube set | t (mm) | D (mm) | Ratio t/D |
|---|---|---|---|
| 2.5 in.(D') X 0.125 in.(t) | 3.18 | 57.15 | 0.0556 |

| L inches | L mm | Ratio L/D | Mechanism of collapse |
|---|---|---|---|
| 15 | 381 | 6.667 | Eulerian bending-(See Plate 2.30) |
| 14 | 355.6 | 6.222 | concertina + 2-lobe diamond X2 |
| 11 | 279.4 | 4.889 | concertina |
| 10 | 254 | 4.444 | concertina |
| 9 | 228.6 | 4.000 | concertina |
| 6 | 152.4 | 2.667 | concertina |
| 4 | 101.6 | 1.778 | concertina |
| 3 | 76.2 | 1.333 | concertina |
| 2 | 50.8 | 0.889 | concertina |
| 1 | 25.4 | 0.444 | concertina crushing |

Table 2.9

See Plate 2.10

| Section geometry of tube set | t (mm) | D (mm) | Ratio t/D |
|---|---|---|---|
| 2 in.(D') X 0.125 in.(t) | 3.18 | 44.45 | 0.0714 |

| L inches | L mm | Ratio L/D | Mechanism of collapse |
|---|---|---|---|
| 10 | 254 | 5.714 | Eulerian bending |
| 9.5 | 241.3 | 5.429 | concertina + 2-lobe diamond |
| 8.5 | 215.9 | 4.857 | concertina + 2-lobe diamond |
| 7.5 | 190.5 | 4.286 | concertina + 2-lobe diamond |
| 3 | 76.2 | 1.714 | concertina |
| 2.5 | 63.5 | 1.429 | concertina |
| 2 | 50.8 | 1.143 | concertina |
| 1 | 25.4 | 0.571 | concertina crushing |

Table 2.10

See Plate 2.11

| Section geometry of tube set | t (mm) | D (mm) | Ratio t/D |
|---|---|---|---|
| 2.5 in. (D') X 3/16 in. (t) | 4.76 | 53.98 | 0.0882 |

| L inches | L mm | Ratio L/D | Mechanism of collapse |
|---|---|---|---|
| 11 | 279.4 | 5.176 | Transition between Eulerian bending and concertina + 2-lobe diamond |
| 10.5 | 266.7 | 4.941 | concertina + 2-lobe diamond |
| 9.5 | 241.3 | 4.470 | concertina + 2-lobe diamond |
| 8.5 | 215.9 | 4.000 | concertina + 2-lobe diamond |
| 7 | 177.8 | 3.294 | concertina + 2-lobe diamond |
| 6 | 152.4 | 2.823 | concertina |
| 4 | 101.6 | 1.882 | concertina |
| 3 | 76.2 | 1.412 | concertina |
| 2 | 50.8 | 0.941 | concertina |
| 1 | 25.4 | 0.471 | concertina crushing |

Table 2.11

See Plate 2.12

| Section geometry of tube set | t (mm) | D (mm) | Ratio t/D |
|---|---|---|---|
| 2.25 in. (D') X 3/16 in. (t) | 4.76 | 47.63 | 0.100 |

| L inches | L mm | Ratio L/D | Mechanism of collapse |
|---|---|---|---|
| 9.5 | 241.3 | 5.066 | Eulerian bending |
| 9 | 228.6 | 4.800 | Eulerian bending |
| 8.5 | 215.9 | 4.533 | concertina + 2-lobe diamond |
| 8 | 203.2 | 4.266 | concertina + 2-lobe diamond |
| 7 | 177.8 | 3.733 | concertina + 2-lobe diamond |
| 6 | 152.4 | 3.200 | concertina + 2-lobe diamond |
| 5 | 127 | 2.666 | concertina |
| 4 | 101.6 | 2.133 | concertina |
| 3 | 76.2 | 1.600 | concertina |
| 2 | 50.8 | 1.067 | concertina |
| 1 | 25.4 | 0.533 | concertina crushing |

Table 2.12

See Plate 2.13

| Geometry of tube set | t Nominal (mm) | t Recorded (mm) | D (mm) | Ratio t/D | Mechanism of collapse |
|---|---|---|---|---|---|
| 6 in.(L) X 0.75 in.(D) | 2 | 1.98 | 19.05 | 0.1039 | Eulerian bending |
| Ratio L/D 8.000 | 1.5 | 1.51 | 19.05 | 0.0793 | Eulerian bending |
| | 1 | 1.14 | 19.05 | 0.0598 | Eulerian bending |
| | 0.75 | 0.92 | 19.05 | 0.0483 | Eulerian bending |
| | 0.50 | 0.66 | 19.05 | 0.0346 | Eulerian bending, 3-lobe diamond X2 |

Table 2.13

See Plate 2.14

| Geometry of tube set | t Nominal (mm) | t Recorded (mm) | D (mm) | Ratio t/D | Mechanism of collapse |
|---|---|---|---|---|---|
| 4 in.(L) X 0.75 in.(D) | 2 | 2.18 | 19.05 | 0.1144 | Eulerian bending |
| Ratio L/D 5.333 | 1.5 | 1.69 | 19.05 | 0.0887 | Eulerian bending |
| | 1 | 1.19 | 19.05 | 0.0625 | concertina |
| | 0.75 | 0.95 | 19.05 | 0.0499 | concertina + 2-lobe diamond ← See Plate 2.32 |
| | 0.50 | 0.66 | 19.05 | 0.0346 | concertina + 2-lobe diamond |

Table 2.14

See Plate 2.15

| Geometry of tube set | t Nominal (mm) | t Recorded (mm) | D (mm) | Ratio t/D | Mechanism of collapse |
|---|---|---|---|---|---|
| 2 in.(L) X 0.75 in.(D) | 2 | 2.17 | 19.05 | 0.1139 | 2-lobe diamond crushing X2 |
| Ratio L/D | 1.5 | 1.66 | 19.05 | 0.0871 | concertina |
| 2.667 | 1 | 1.19 | 19.05 | 0.0625 | concertina |
| | 0.75 | 0.92 | 19.05 | 0.0483 | concertina |
| | 0.50 | 0.68 | 19.05 | 0.0357 | concertina + 3-lobe diamond |

Table 2.15

See Plate 2.16

| Section geometry of tube set | | | L inches | L mm | Ratio L/D | Mechanism of collapse |
|---|---|---|---|---|---|---|
| 2 in.(D') X 3/16 in.(t) | | | 8 | 203.2 | 4.922 | Eulerian bending |
| | | | 7 | 177.8 | 4.307 | 2-lobe diamond crushing |
| t (mm) | D (mm) | Ratio t/D | 6 | 152.4 | 3.692 | 2-lobe diamond crushing |
| | | | 5 | 127 | 3.077 | 2-lobe diamond crushing |
| 4.76 | 41.28 | 0.1154 | 4 | 101.6 | 2.461 | 2-lobe diamond crushing |
| | | | 3.5 | 88.9 | 2.154 | 2-lobe diamond crushing |
| | | | 3 | 76.2 | 1.846 | 2-lobe diamond crushing X2 |
| | | | 2 | 50.8 | 1.231 | concertina crushing |

Table 2.16

See Plate 2.17

| Section geometry of tube set | | | L | | Ratio | Mechanism of collapse |
|---|---|---|---|---|---|---|
| | | | inches | mm | L/D | |
| 2.5 in.(D') X 0.25 in.(t) | | | 9 | 228.6 | 4.500 | 2-lobe diamond crushing |
| t (mm) | D (mm) | Ratio t/D | 8 | 203.2 | 4.000 | 2-lobe diamond crushing |
| | | | 6 | 152.4 | 3.000 | 2-lobe diamond crushing |
| | | | 5 | 127 | 2.500 | concertina crushing |
| 6.35 | 50.8 | 0.1250 | 4 | 101.6 | 2.000 | 2-lobe diamond crushing |
| | | | 3 | 76.2 | 1.500 | concertina crushing |

Table 2.17

See Plate 2.18

| Section geometry of tube set | L | | t | D | Ratio | Ratio | Mechanism of collapse | |
|---|---|---|---|---|---|---|---|---|
| | inches | mm | (mm) | (mm) | t/D | L/D | | |
| 0.75 in.(D) X 2.5 mm (nominal t) | 3 | 76.2 | 2.64 | 19.05 | 0.1386 | 4.000 | crushing + tilting failure | |
| | 3 | 76.2 | 2.56 | 19.05 | 0.1344 | 4.000 | as above X2 | |
| | 2 | 50.8 | 2.50 | 19.05 | 0.1312 | 2.667 | concertina crushing ← See | Plate 2.34 |
| | 1.5 | 38.1 | 2.48 | 19.05 | 0.1302 | 2.000 | concertina crushing | |
| | 1 | 25.4 | 2.47 | 19.05 | 0.1297 | 1.333 | concertina crushing | |
| | 0.5 | 12.7 | 2.49 | 19.05 | 0.1310 | 0.667 | concertina crushing ← See | Plate 2.33 |

Table 2.18

See plate 2.19

| Section geometry of tube set | t (mm) | D (mm) | Ratio t/D |
|---|---|---|---|
| 1.75 in.(D') X 3/16 in.(t) | 4.76 | 34.93 | 0.1360 |

| L inches | L mm | Ratio L/D | Mechanism of collapse |
|---|---|---|---|
| 6.25 | 158.8 | 4.545 | Eulerian bending |
| 6 | 152.4 | 4.364 | Eulerian bending |
| 5.5 | 139.7 | 4.000 | 2-lobe diamond crushing |
| 5 | 127 | 3.636 | concertina crushing |
| 4 | 101.6 | 2.909 | concertina crushing |
| 3 | 76.2 | 2.182 | 2-lobe diamond crushing |
| 2 | 50.8 | 1.455 | concertina crushing |

Table 2.19

See Plate 2.20

| Section geometry of tube set | t (mm) | D (mm) | Ratio t/D |
|---|---|---|---|
| 1 ¾ in.(D') X 3/16 in.(t) | 4.76 | 31.75 | 0.1500 |

| L inches | L mm | Ratio L/D | Mechanism of collapse |
|---|---|---|---|
| 5.5 | 139.7 | 4.400 | crushing + tilting failure |
| 5 | 127 | 4.000 | crushing + tilting failure |
| 4.5 | 114.3 | 3.600 | concertina crushing |
| 4 | 101.6 | 3.200 | concertina crushing |
| 3 | 76.2 | 2.400 | concertina crushing |
| 2 | 50.8 | 1.600 | concertina crushing |
| 1 | 25.4 | 0.800 | concertina crushing |
| 0.75 | 19.1 | 0.600 | concertina crushing - compression |
| 0.5 | 12.7 | 0.400 | concertina crushing - compression |

Table 2.20

See Plate 2.21

| Section geometry of tube set | t (mm) | D (mm) | Ratio t/D |
|---|---|---|---|
| 1 in.(D') X 0.125 in.(t) | 3.18 | 19.05 | 0.1667 |

| L inches | L mm | Ratio L/D | Mechanism of collapse |
|---|---|---|---|
| 6 | 152.4 | 8.000 | Eulerian bending |
| 5 | 127 | 6.667 | Eulerian bending |
| 4 | 101.6 | 5.333 | Eulerian bending |
| 3 | 76.2 | 4.000 | crushing + tilting failure X2 |
| 2 | 50.8 | 2.667 | concertina crushing |
| 1 | 25.4 | 1.333 | concertina crushing |
| 0.5 | 12.7 | 0.667 | concertina crushing - compression |

Table 2.21

See Plate 2.22

| Section geometry of tube set | t (mm) | D (mm) | Ratio t/D |
|---|---|---|---|
| 1 ¼ in.(D') X 3/16 in.(t) | 4.76 | 25.40 | 0.1875 |

| L inches | L mm | Ratio L/D | Mechanism of collapse |
|---|---|---|---|
| 5 | 127 | 5.000 | Eulerian bending |
| 4.5 | 114.3 | 4.500 | Eulerian bending |
| 4 | 101.6 | 4.000 | crushing + tilting failure |
| 3.5 | 88.9 | 3.500 | concertina crushing |
| 3 | 76.2 | 3.000 | concertina crushing |
| 2.5 | 63.5 | 2.500 | concertina crushing |
| 2 | 50.8 | 2.000 | concertina crushing |
| 1.5 | 38.1 | 1.500 | concertina crushing |
| 1 | 25.4 | 1.000 | concertina crushing |
| 0.75 | 19.1 | 0.750 | concertina crushing - compression |
| 0.5 | 12.7 | 0.500 | concertina crushing - compression |

Table 2.22

See Plate 2.23

| Section geometry of tube set | t (mm) | D (mm) | Ratio t/D |
|---|---|---|---|
| 1.75 in. (D') X 0.25 in. (t) | 6.35 | 31.75 | 0.2000 |

| L inches | L mm | Ratio L/D | Mechanism of collapse |
|---|---|---|---|
| 6 | 152.4 | 4.800 | Eulerian bending |
| 5 | 127 | 4.000 | concertina crushing |
| 4 | 101.6 | 3.200 | concertina crushing |
| 3 | 76.2 | 2.400 | concertina crushing |

Table 2.23

See Plate 2.24

| Section geometry of tube set | t (mm) | D (mm) | Ratio t/D |
|---|---|---|---|
| 0.75 in. (D') X 0.125 in. (t) | 3.18 | 12.70 | 0.2500 |

| L inches | L mm | Ratio L/D | Mechanism of collapse |
|---|---|---|---|
| 3.5 | 88.9 | 7.000 | Eulerian bending |
| 3 | 76.2 | 6.000 | Eulerian bending |
| 2.5 | 63.5 | 5.000 | Eulerian bending |
| 2 | 50.8 | 4.000 | concertina crushing |
| 1.5 | 38.1 | 3.000 | concertina crushing |
| 1 | 25.4 | 2.000 | concertina crushing |
| 0.5 | 12.7 | 1.000 | concertina crushing - compression |
| 0.25 | 6.35 | 0.500 | concertina crushing - compression |

See Plate 2.33

Table 2.24

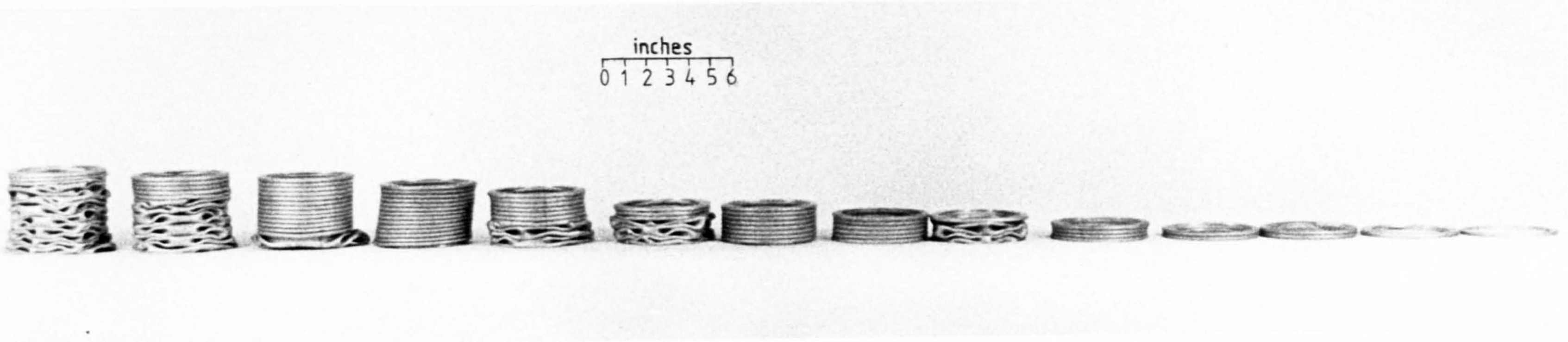


Plate 2.1

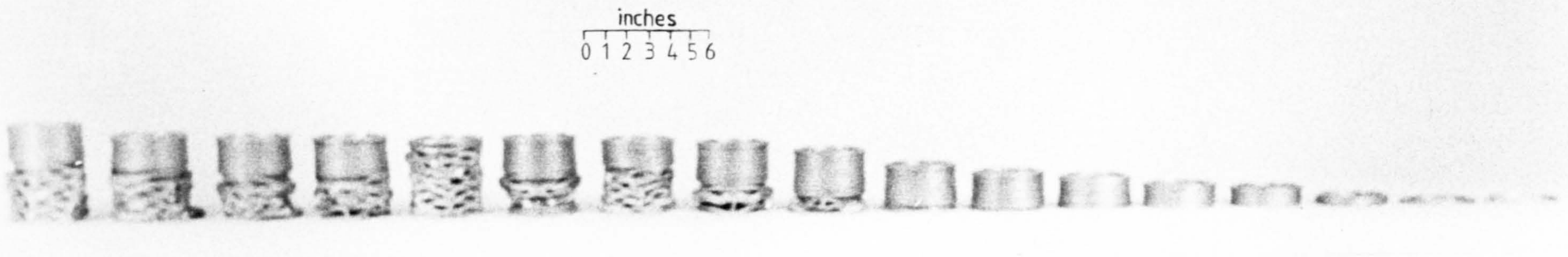


Plate 2.2

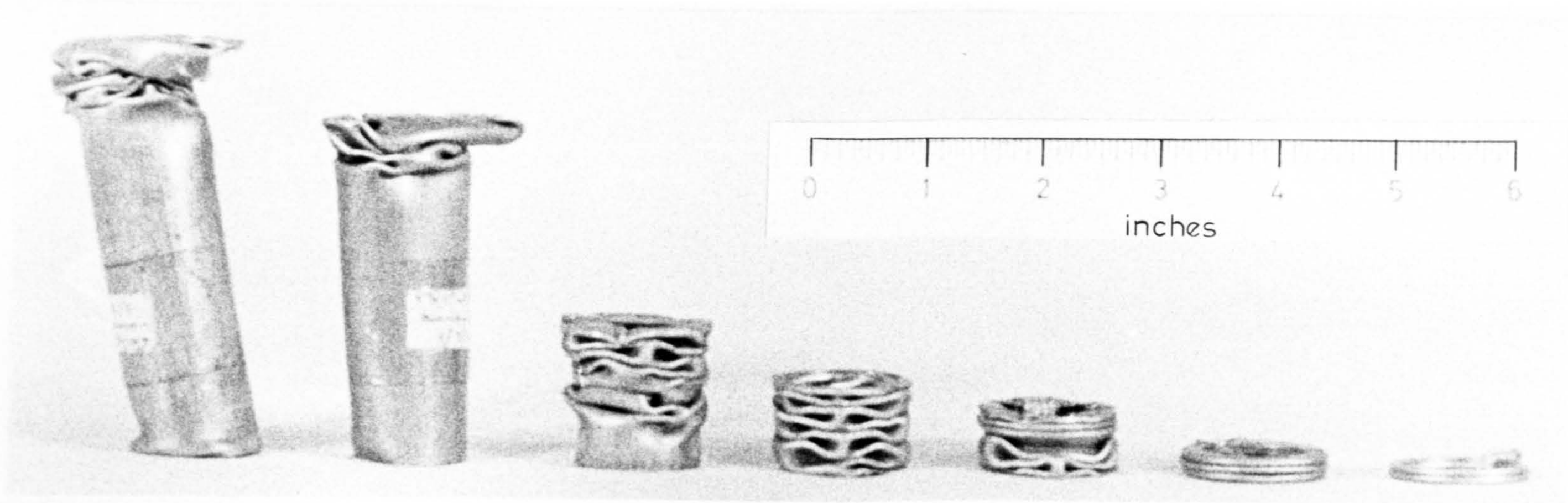


Plate 2.3

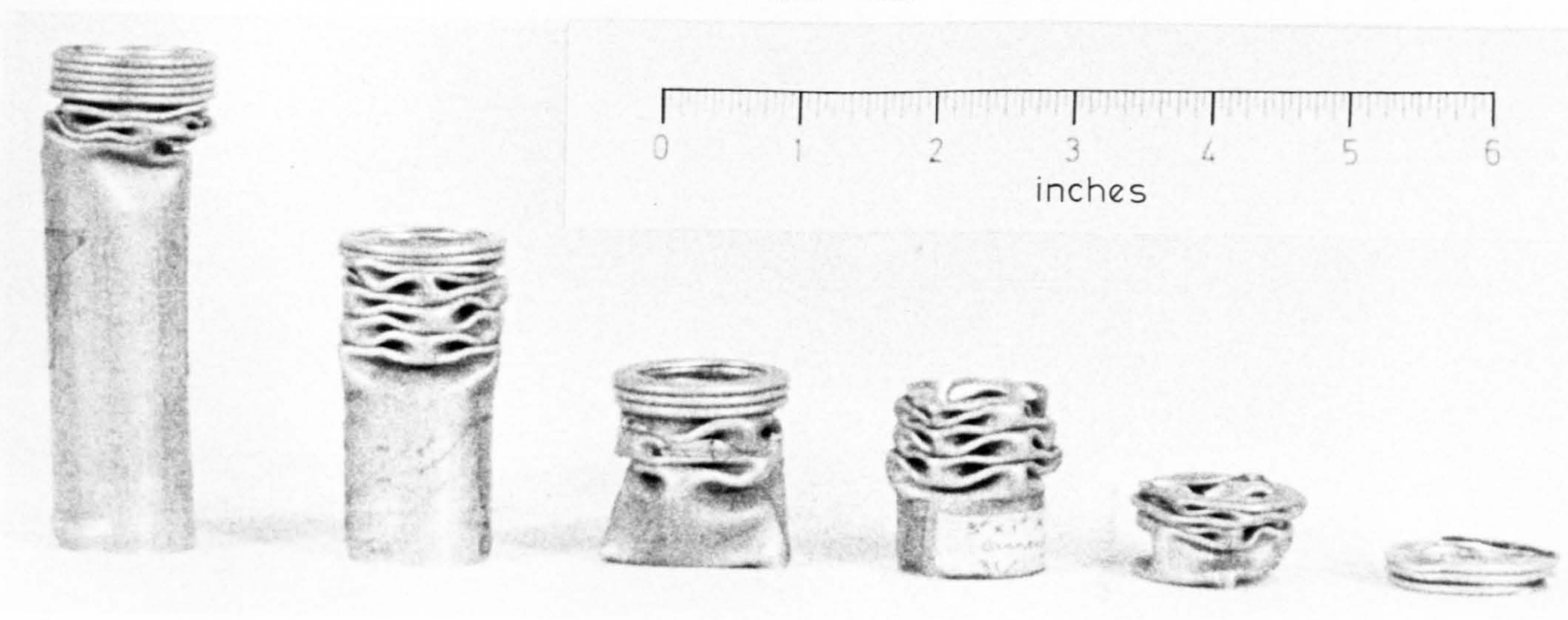


Plate 2.4

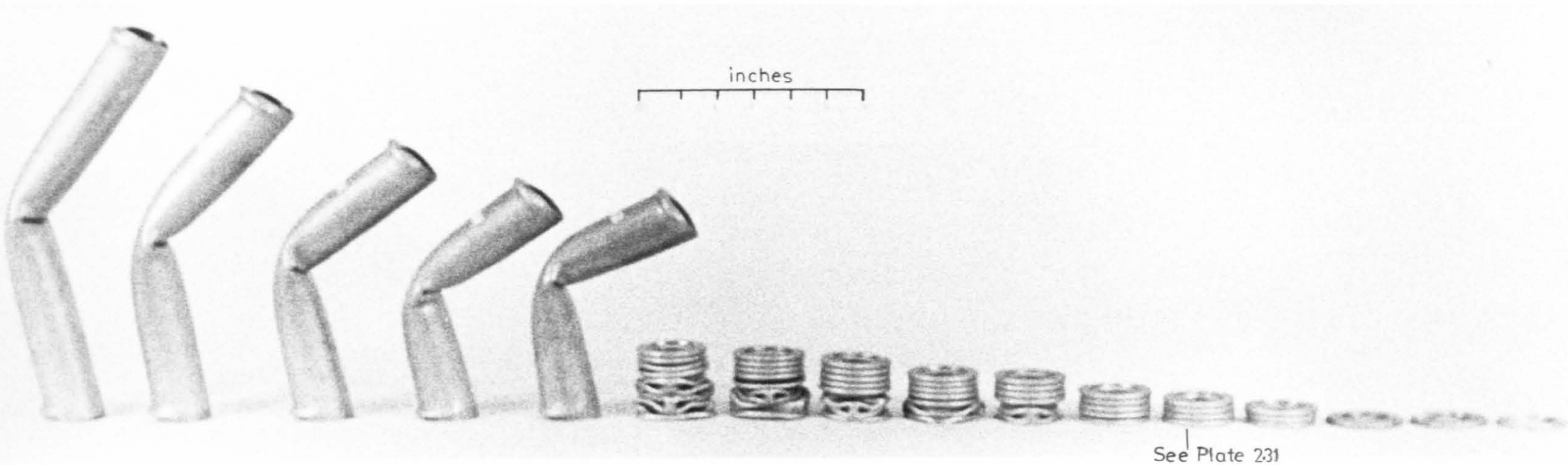


Plate 2.5

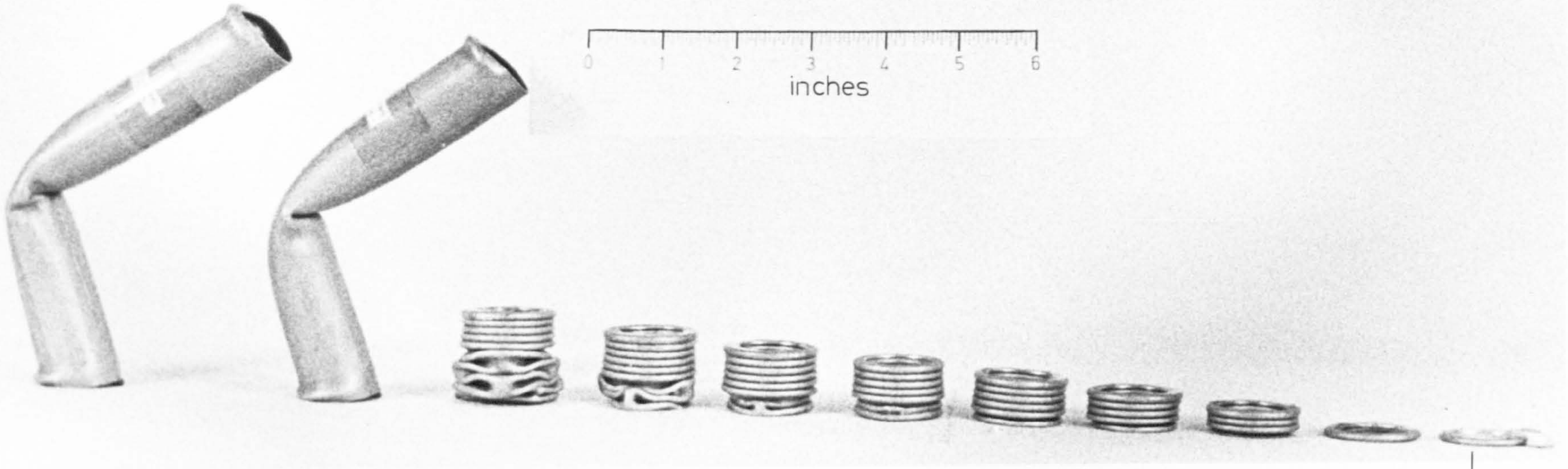


Plate 2.6

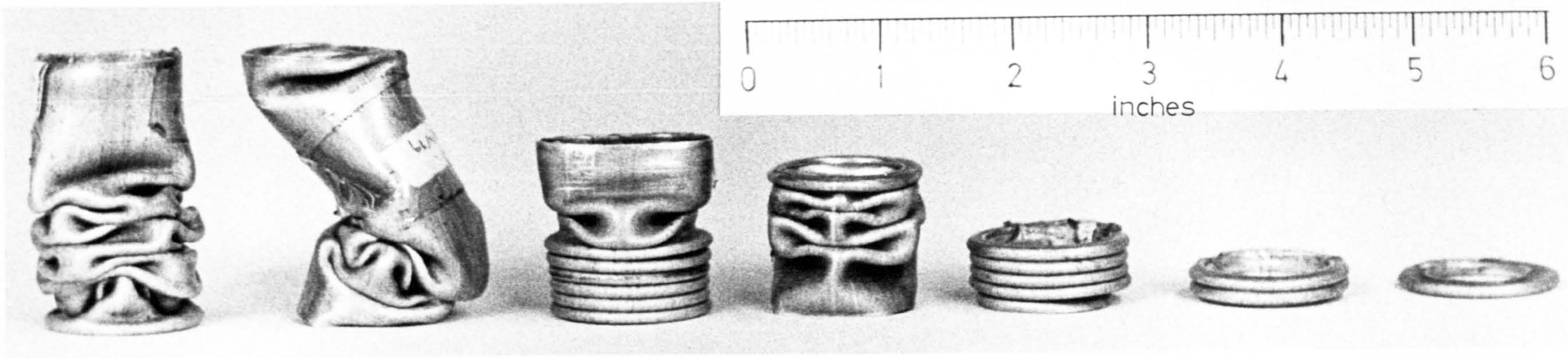


Plate 2.7


Plate 2.8


See Plate 2.30

Plate 2.9

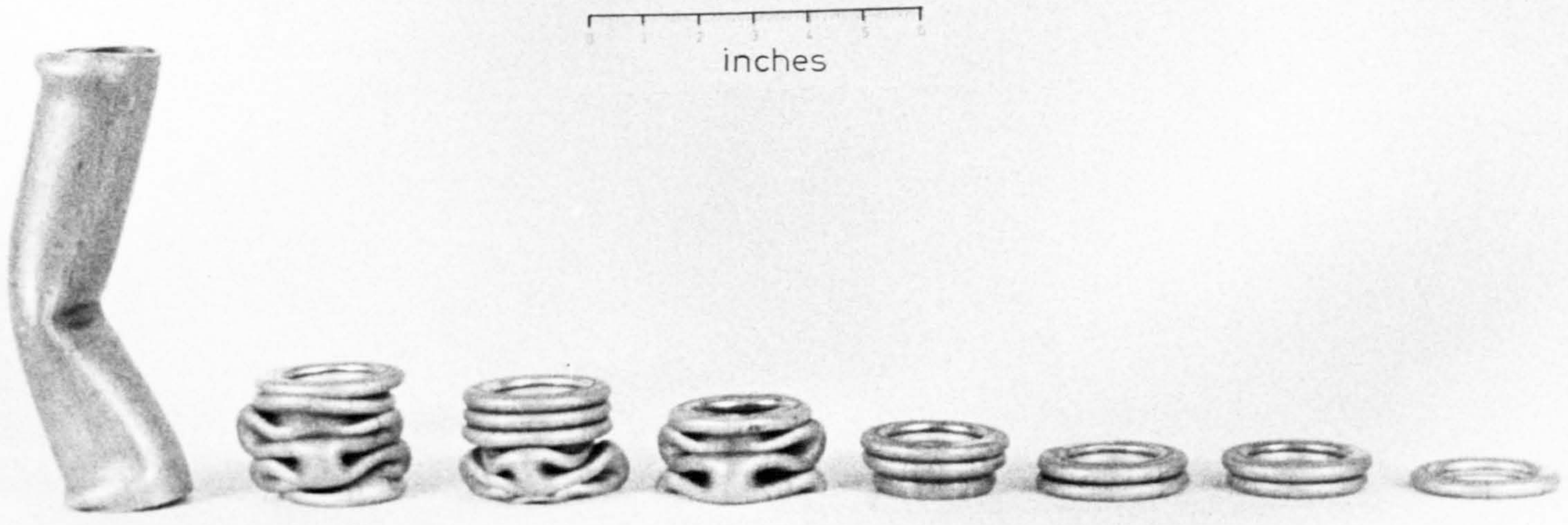


Plate 2.10

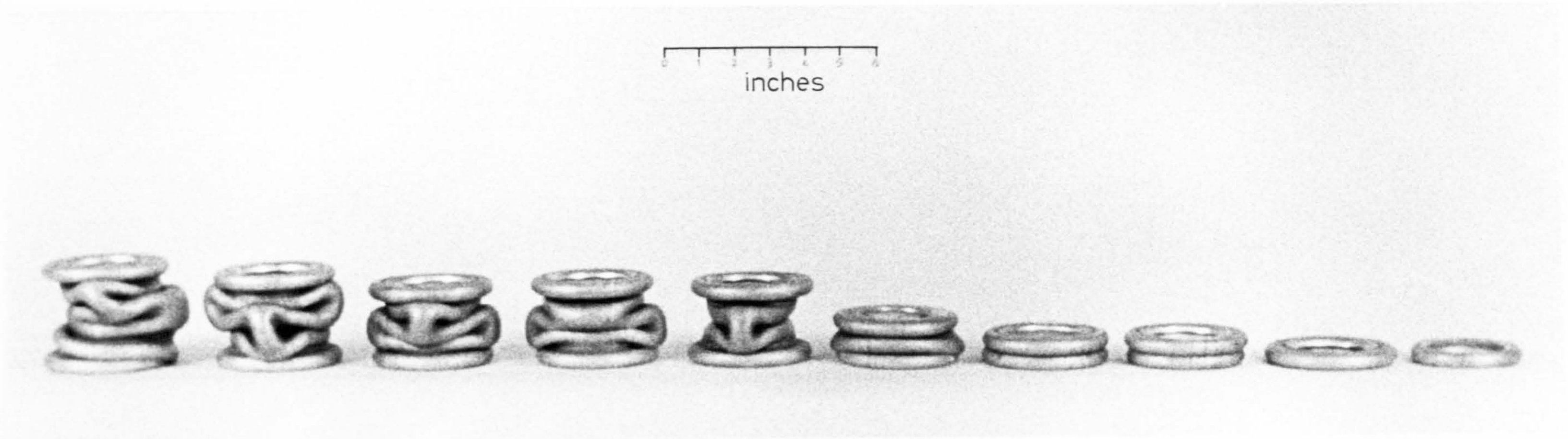


Plate 2.11

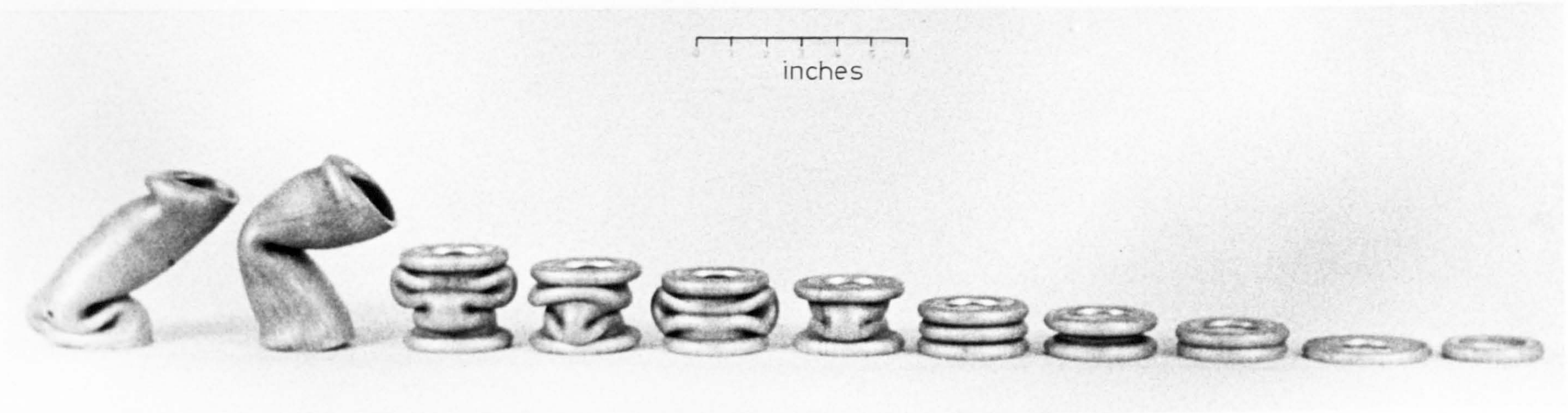


Plate 2.12

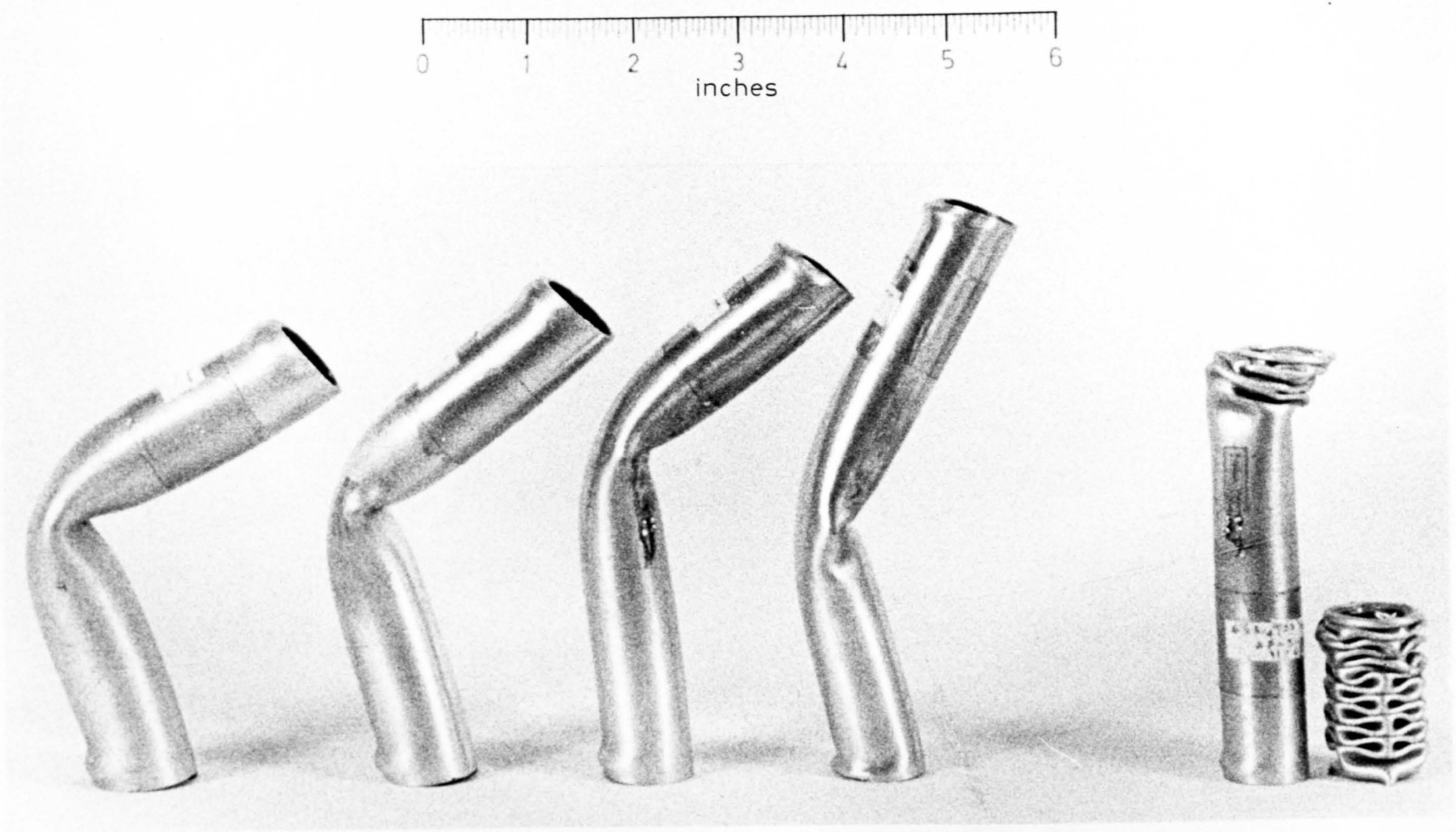


Plate 2.13

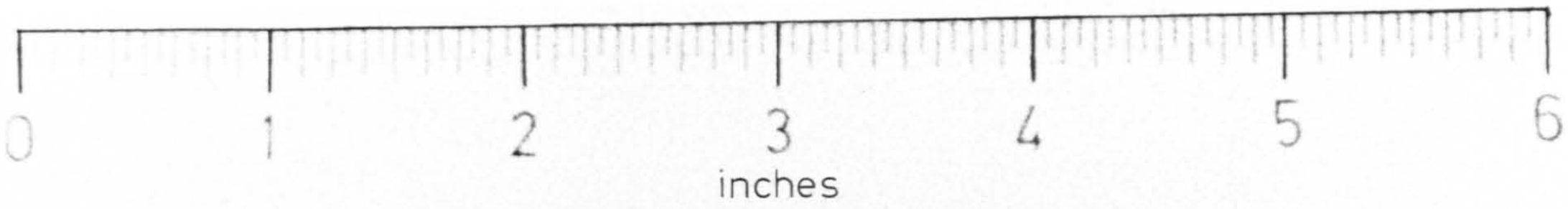



See Plate 2.32

Plate 2.14


Plate 2.15

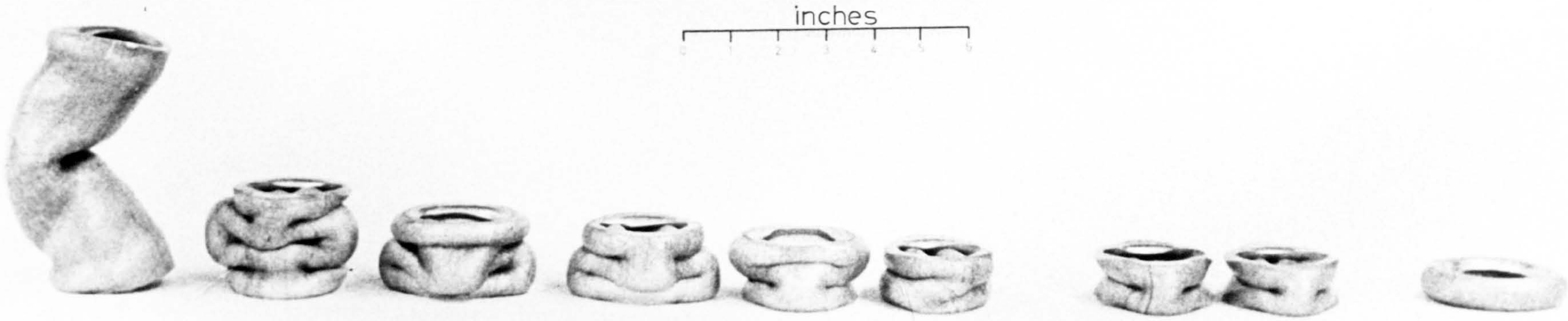


Plate 2.16


Plate 2.17

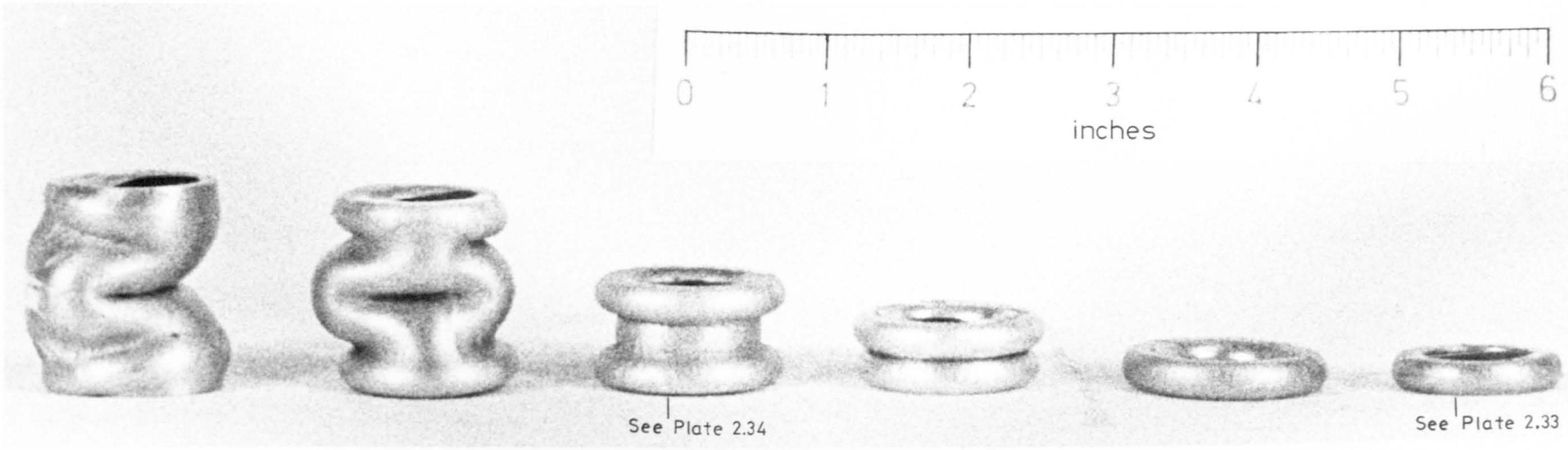


Plate 2.18

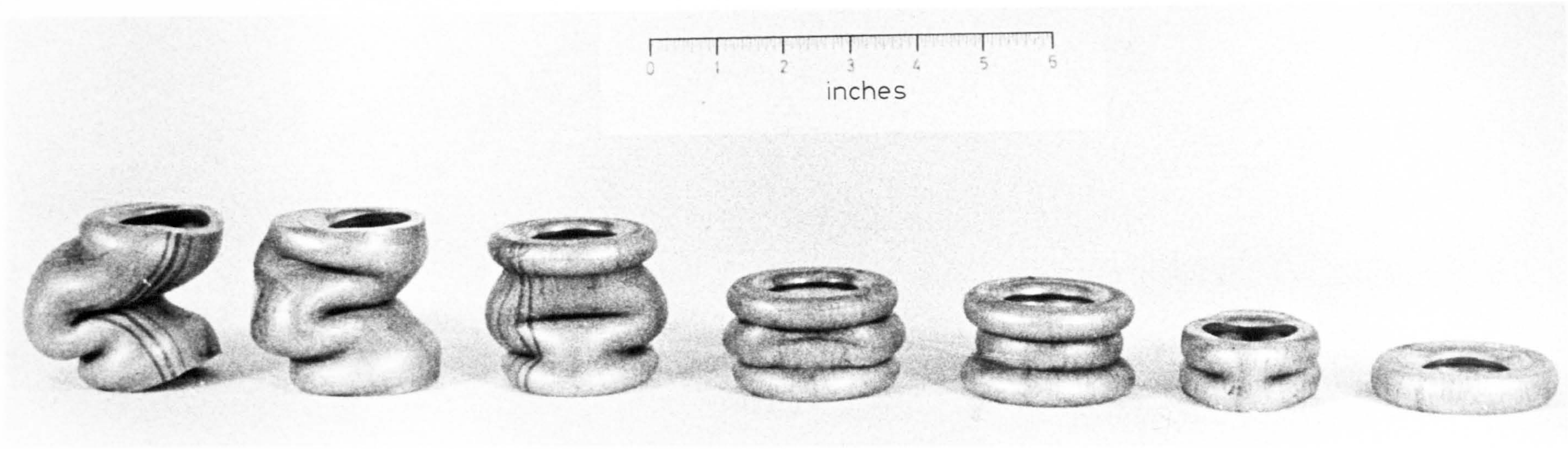


Plate 2.19

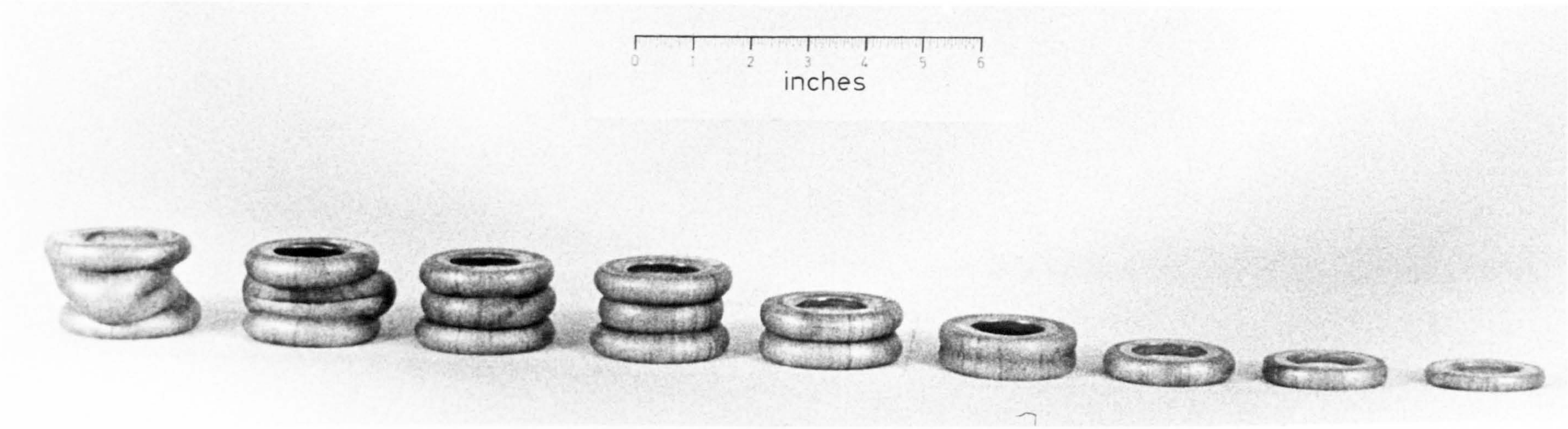


Plate 2.20

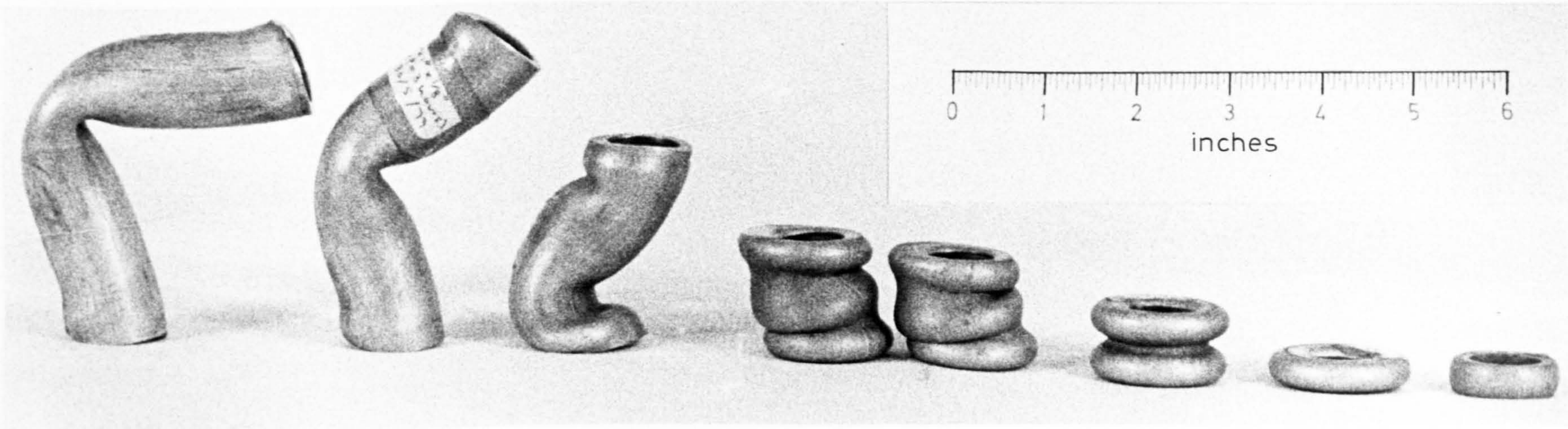


Plate 2.21

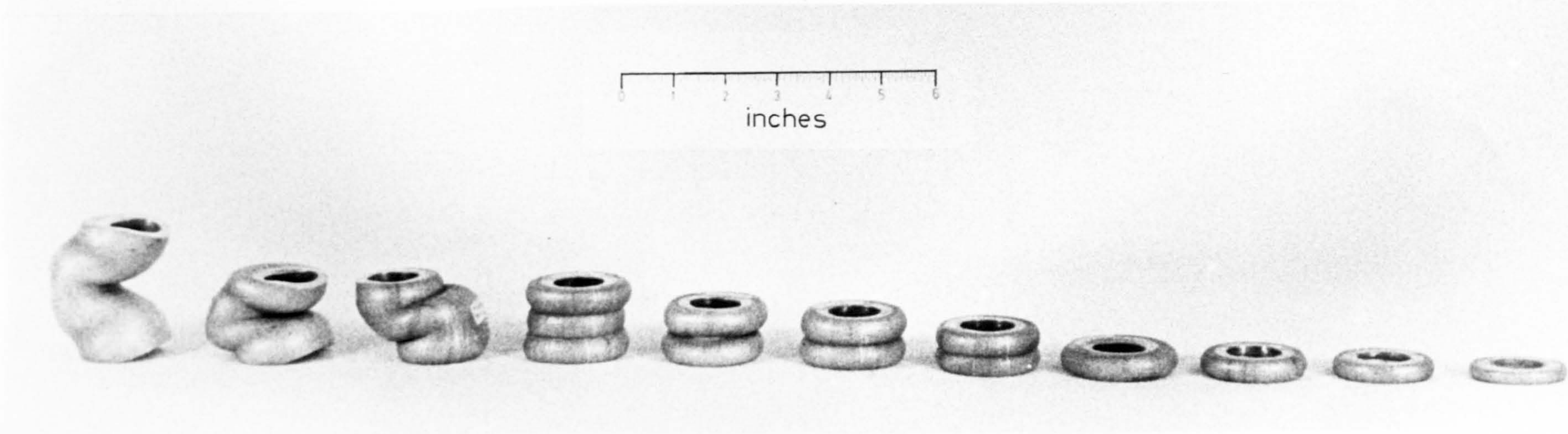


Plate 2.22

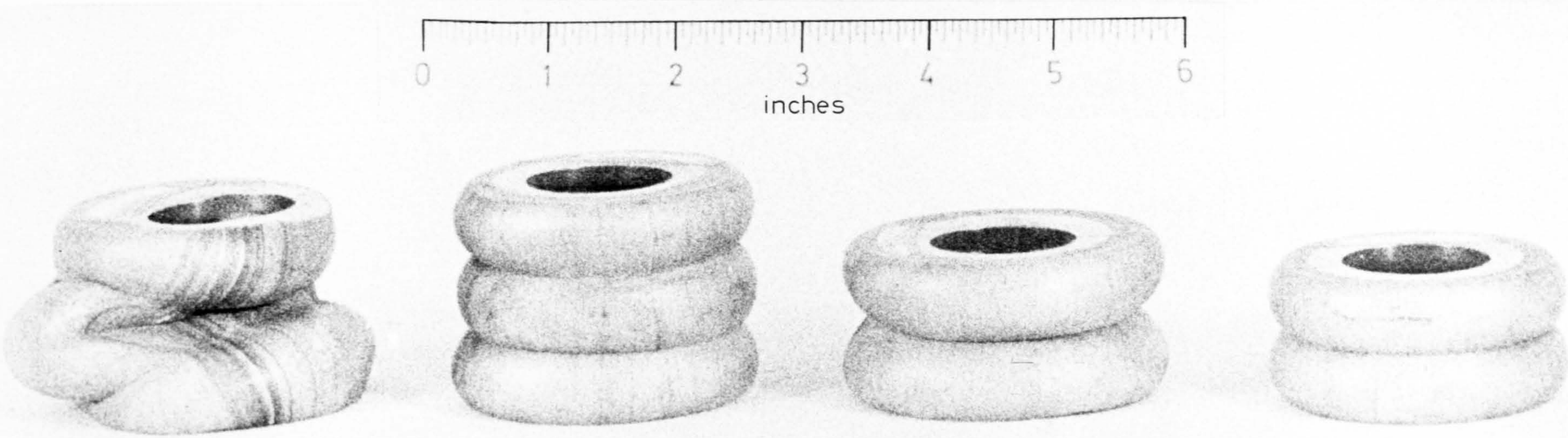


Plate 2.23

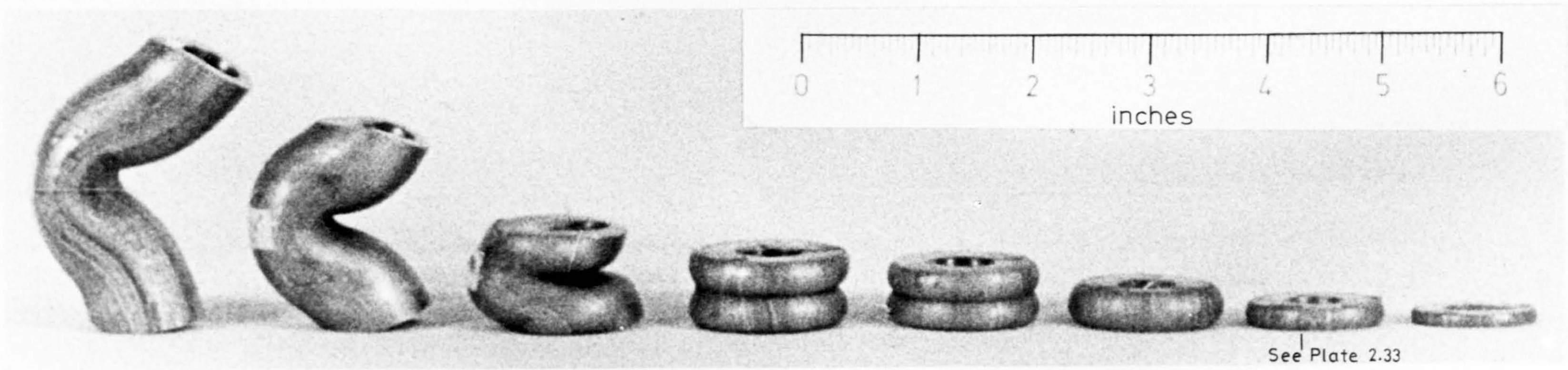


Plate 2.24

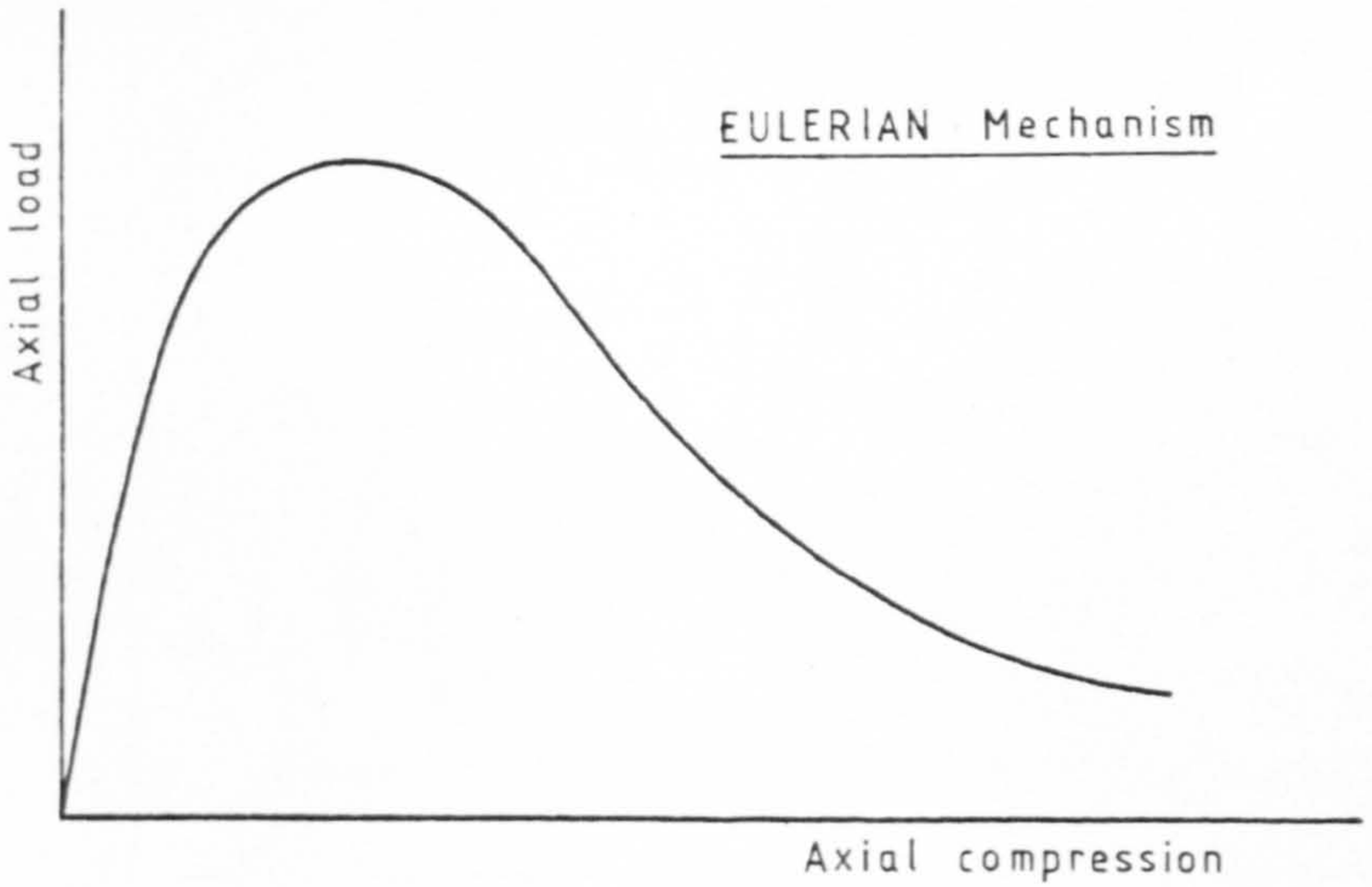


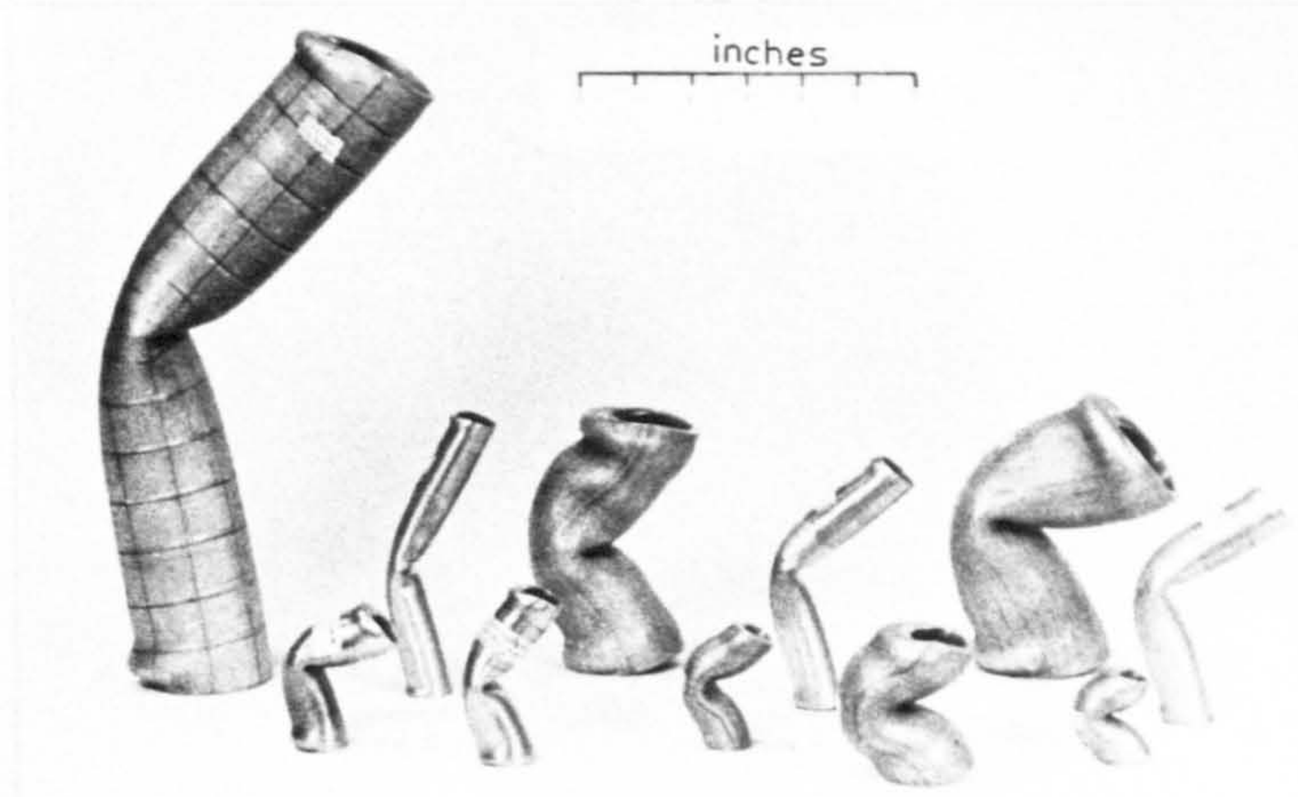


Plate 2.25

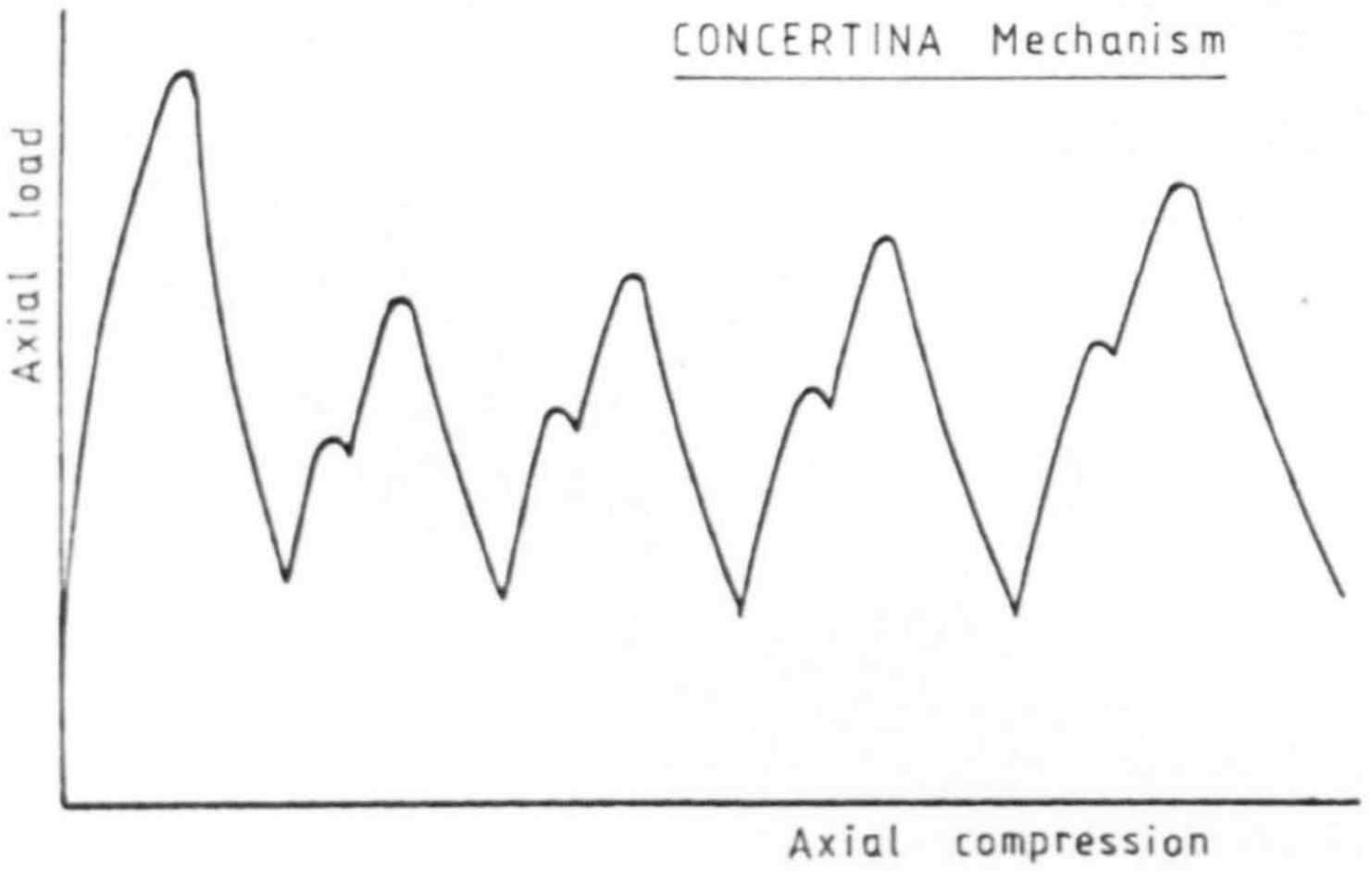


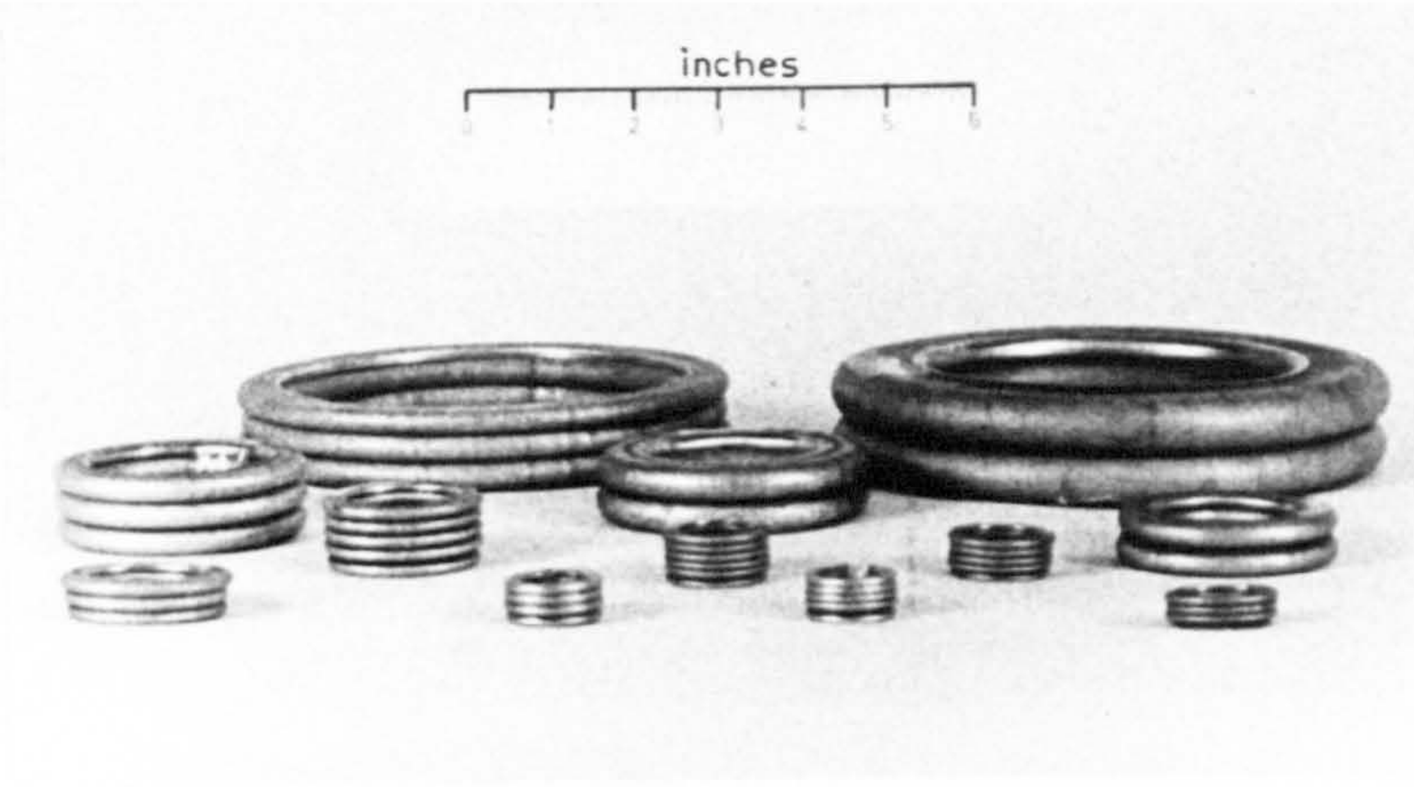


Plate 2.26

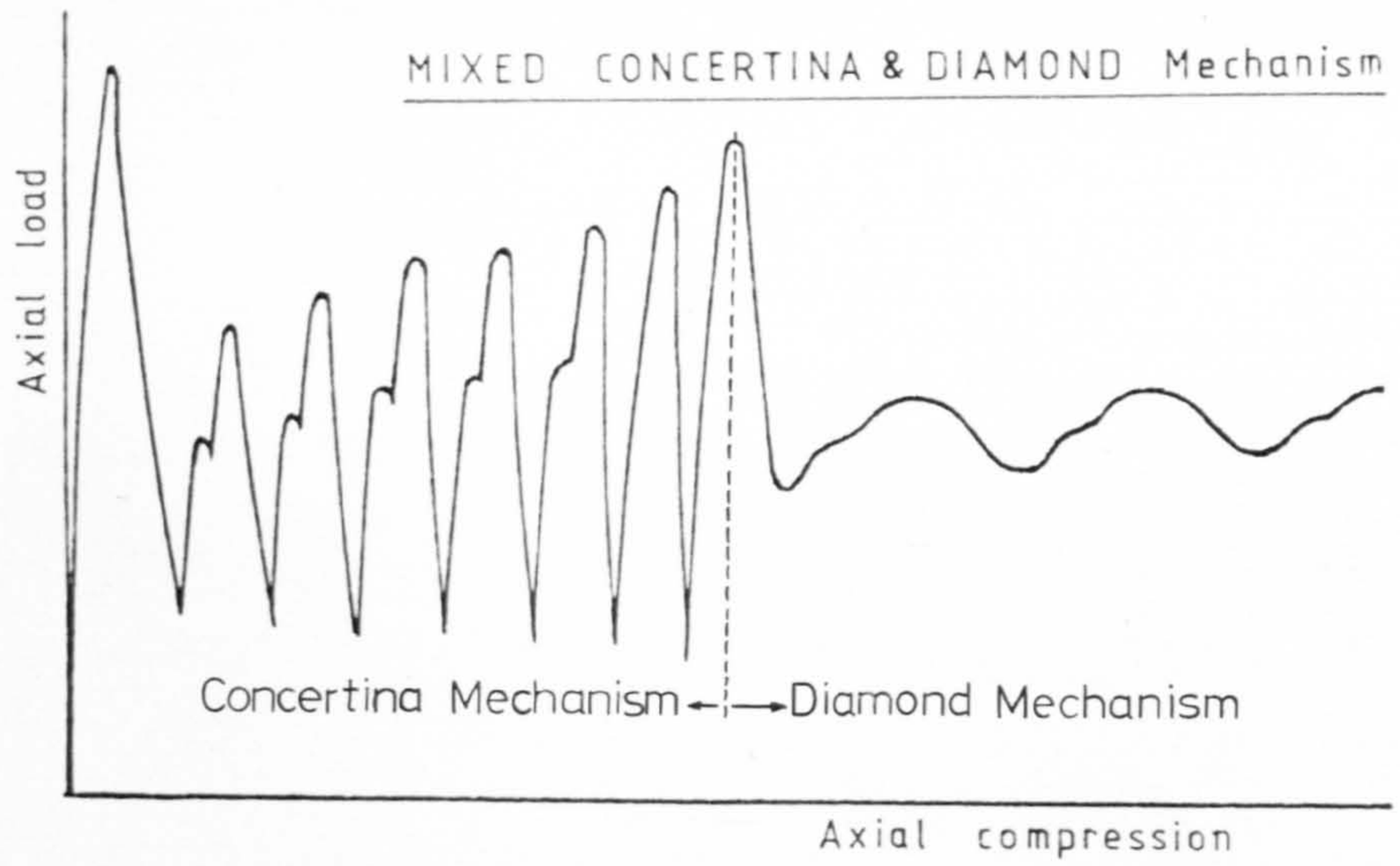


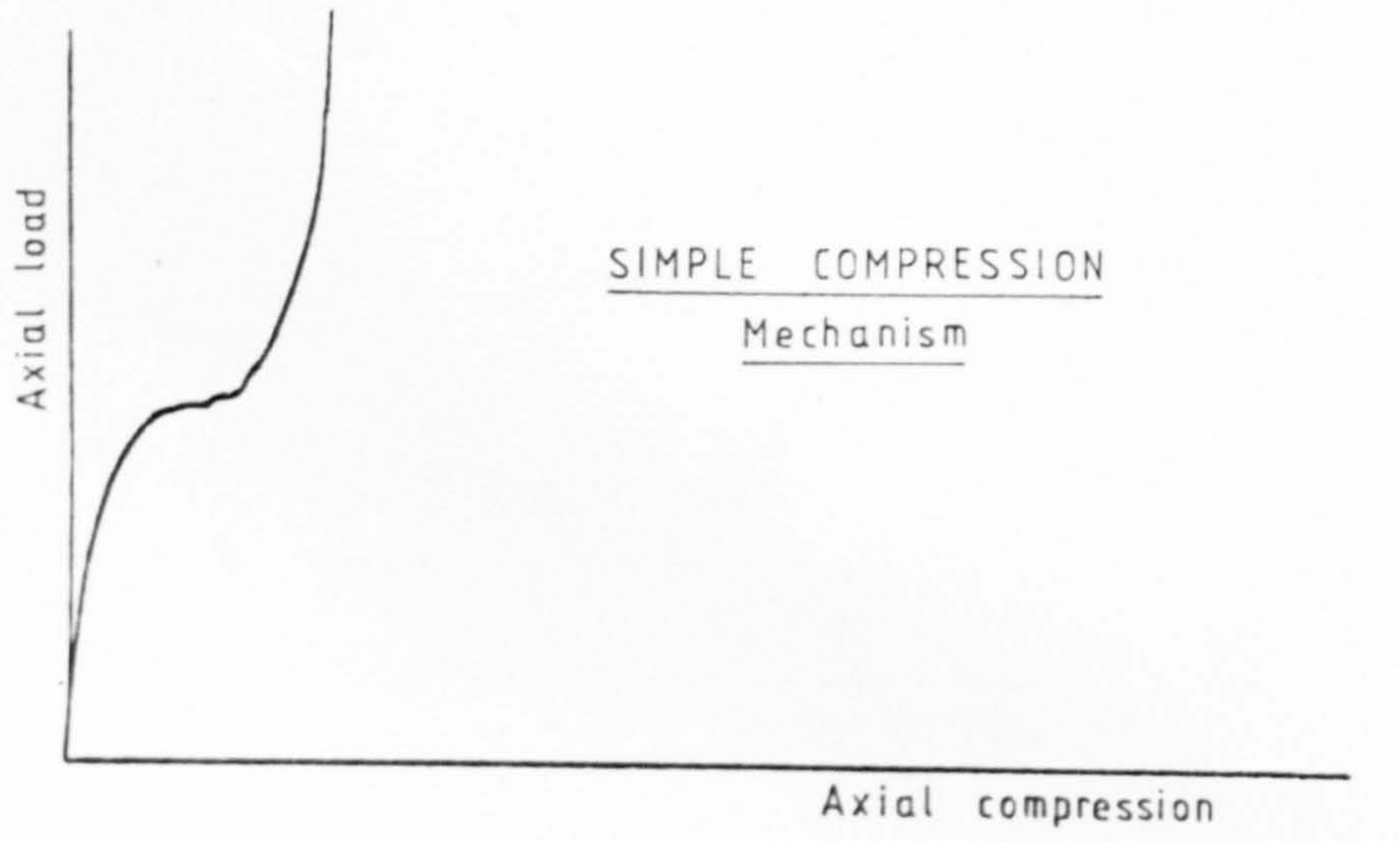



Plate 2.27

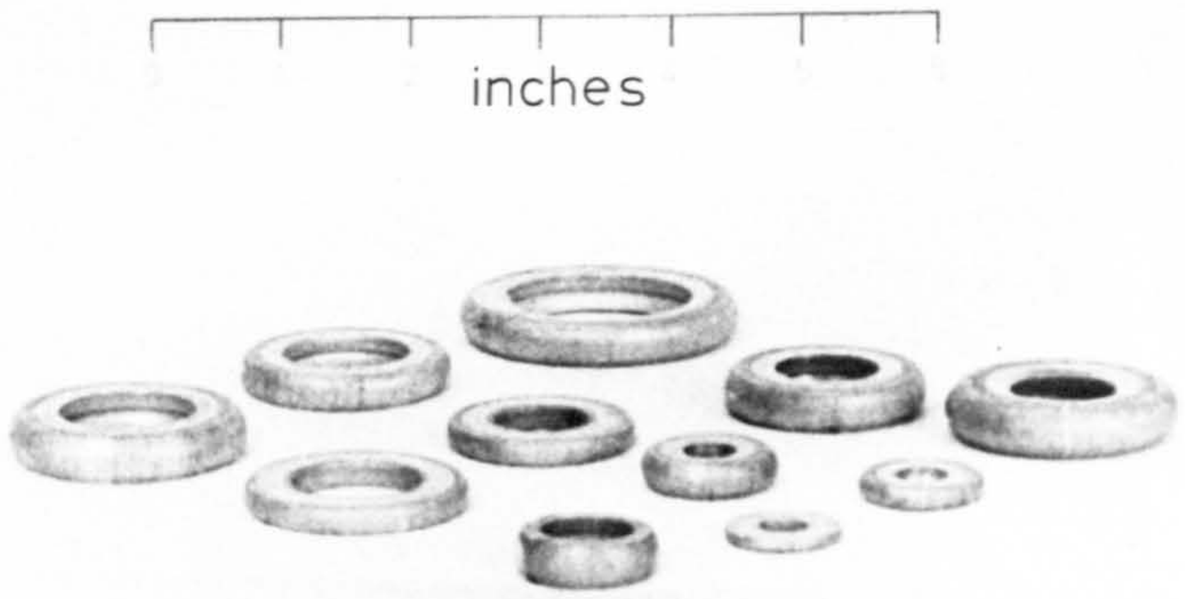


Plate 2.28

CRUSHING / AXIS-TILTING

Mechanisms




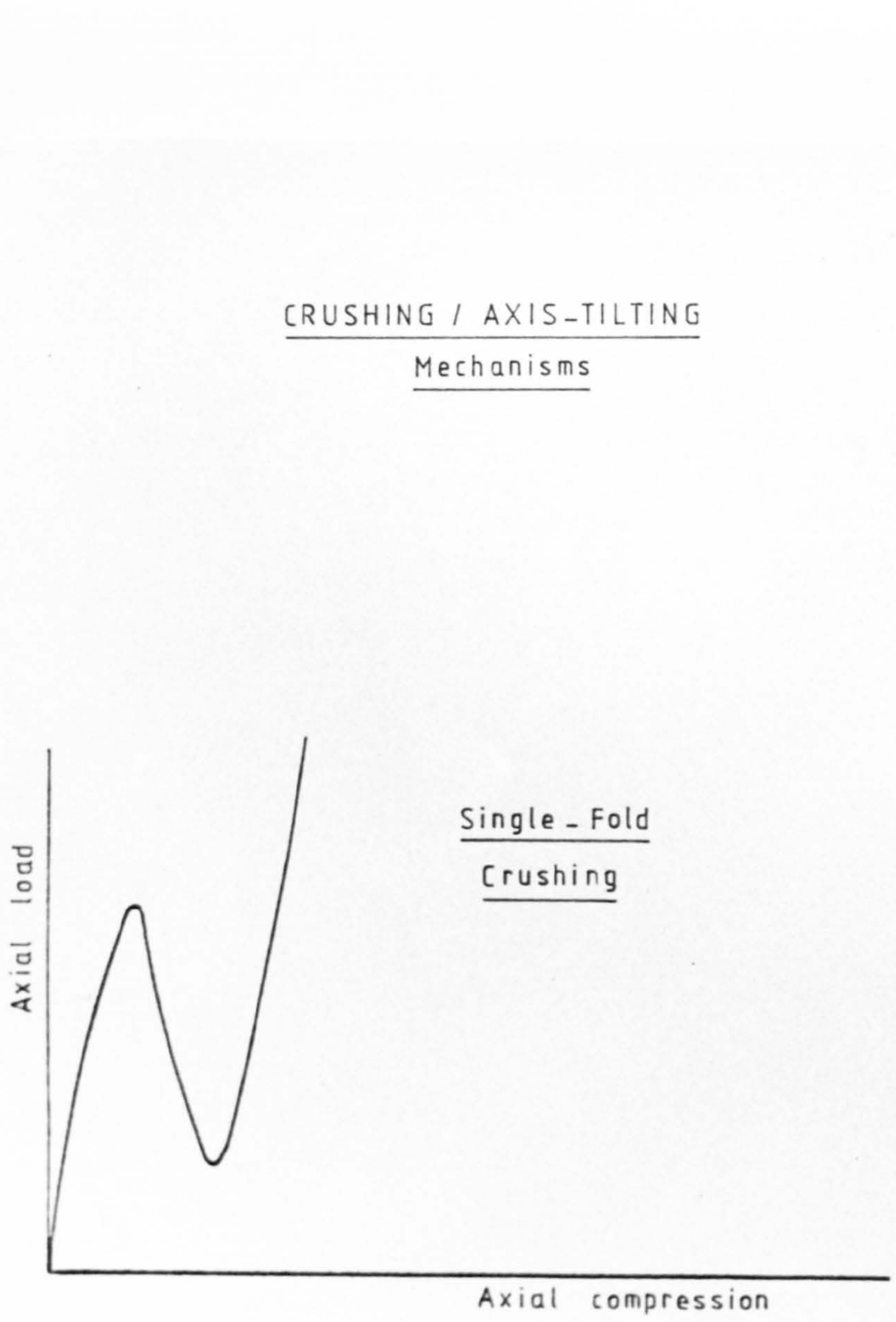


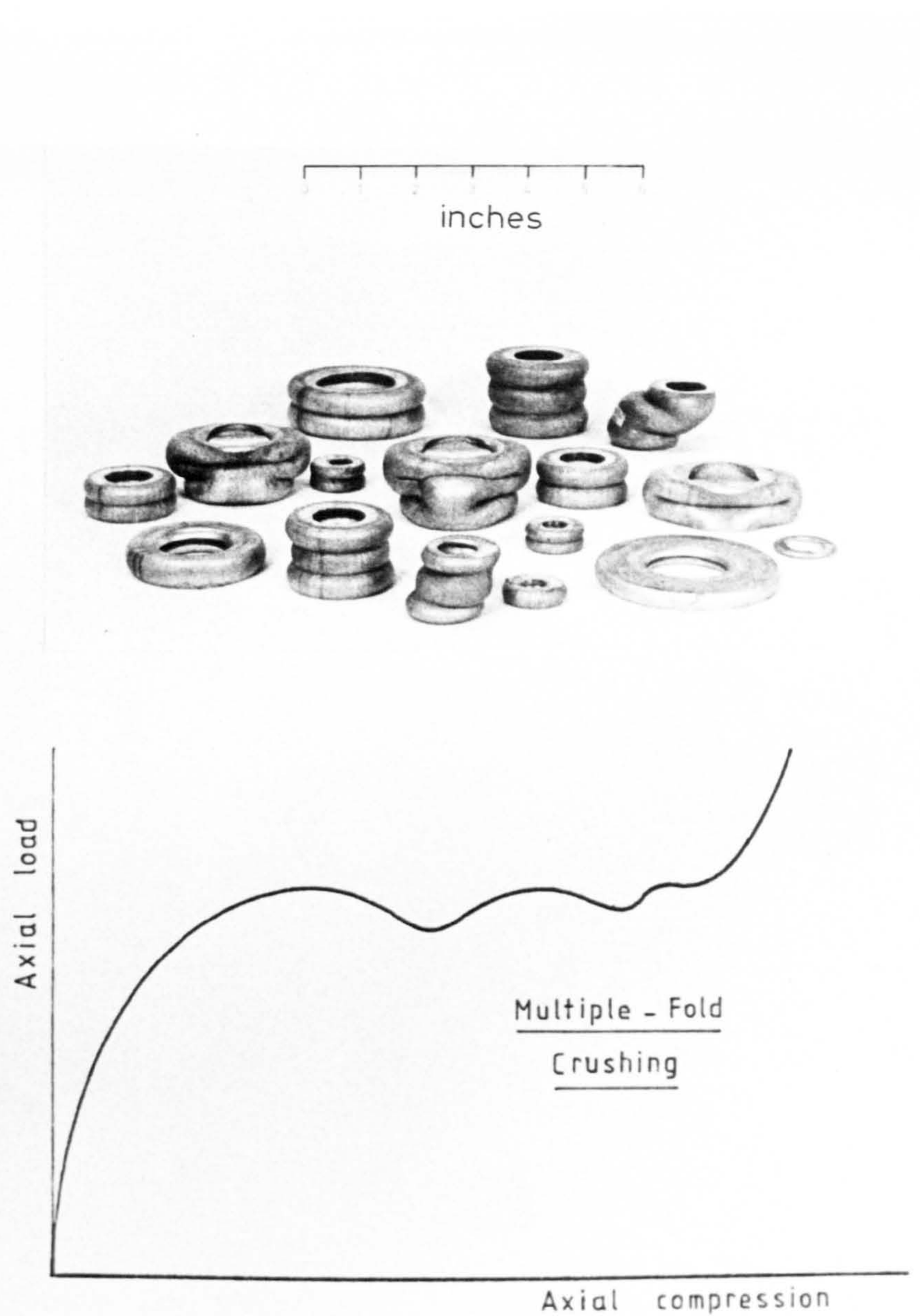


Plate 2.29

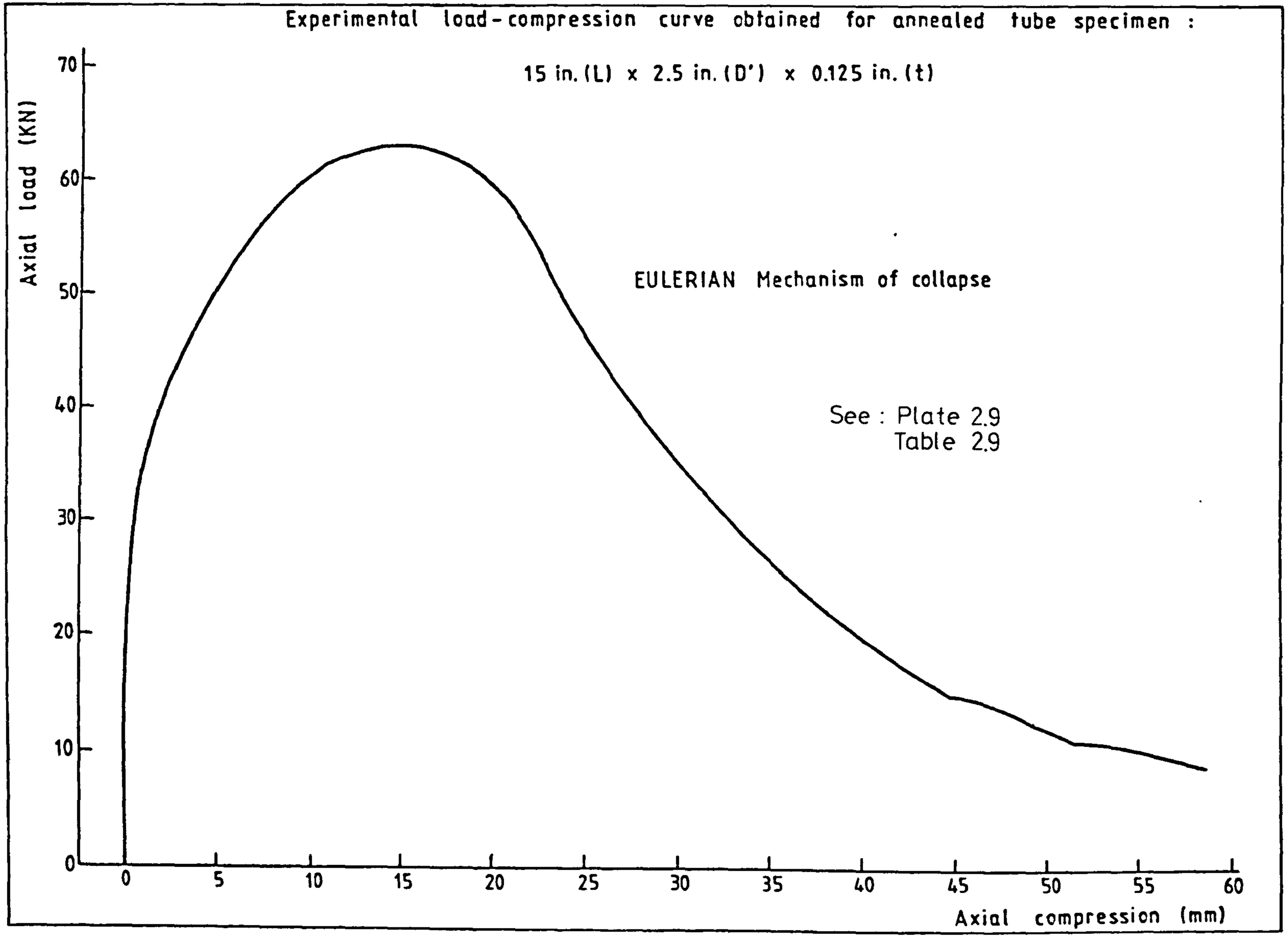
Experimental load-compression curve obtained for annealed tube specimen :
15 in. (L) x 2.5 in. (D') x 0.125 in. (t)
EULERIAN Mechanism of collapse
See : Plate 2.9
Table 2.9
Axial load (KN)
70
60
50
40
30
20
10
0
0
5
10
15
20
25
30
35
40
45
50
55
60
Axial compression (mm)

Plate 2.30

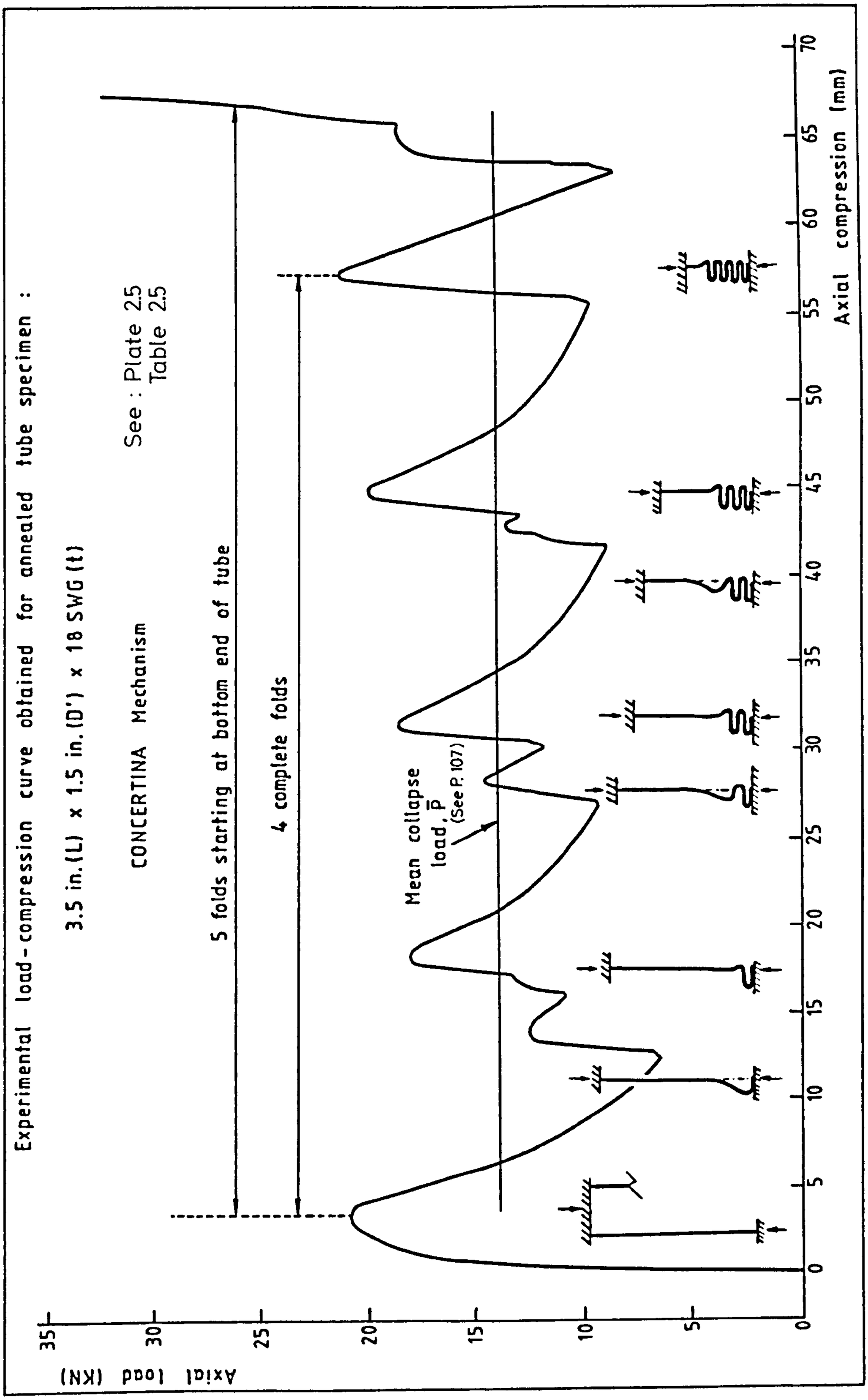
Experimental load-compression curve obtained for annealed tube specimen :
3.5 in.(L) x 1.5 in.(D') x 18 SWG (t)
CONCERTINA Mechanism
5 folds starting at bottom end of tube
4 complete folds
See : Plate 2.5
Table 2.5
Mean collapse load, $\bar{P}$ (See P. 107)
Axial load (KN)
Axial compression (mm)
0
5
10
15
20
25
30
35
40
45
50
55
60
65
70

Plate 2.31

Experimental load-compression curve obtained for annealed tube specimen :

4 in.(L) x 0.75 in.(D) x 0.75 mm (nominal t)

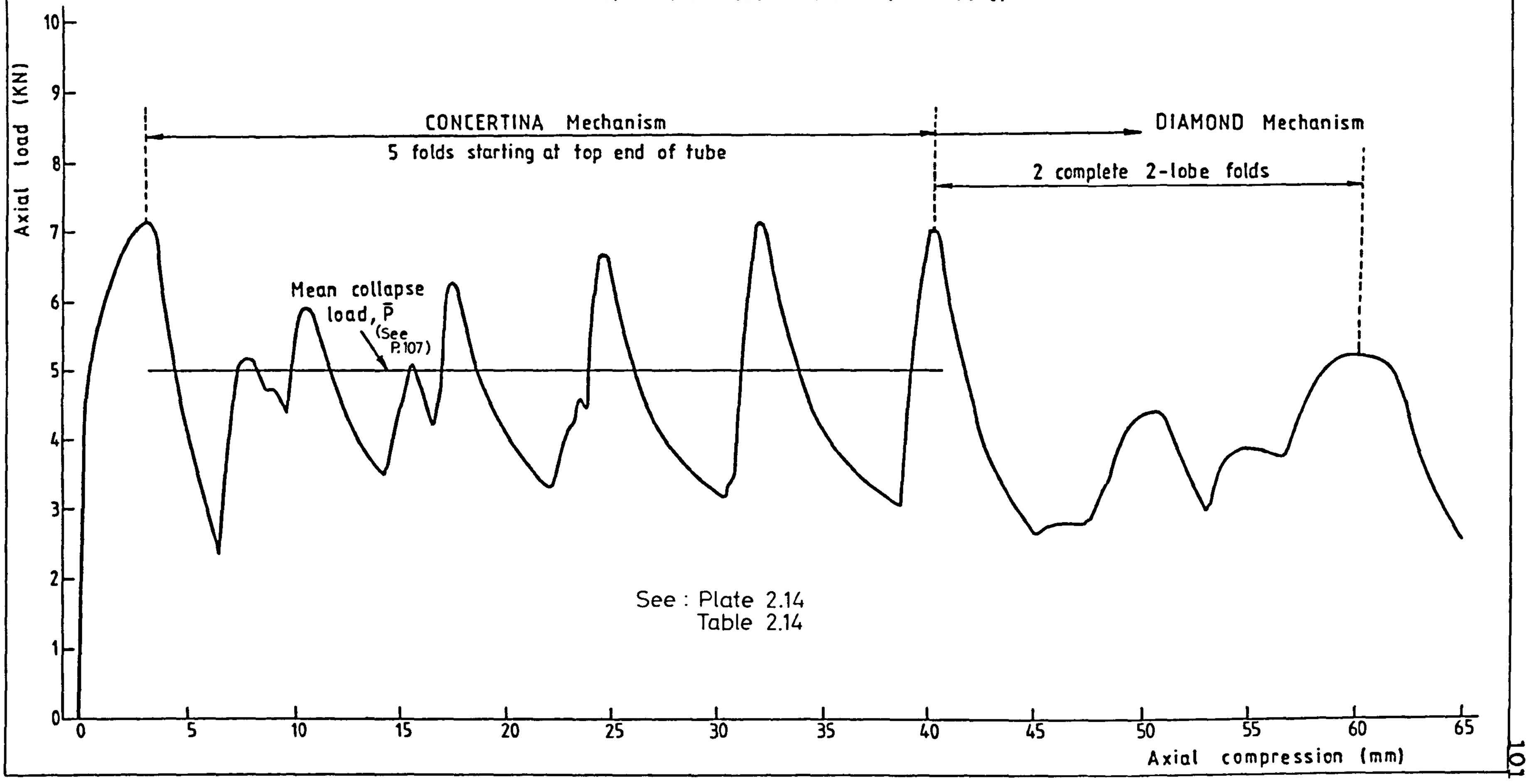


See : Plate 2.14
Table 2.14



Plate 2.32

SIMPLE COMPRESSION Mechanism of collapse

Experimental load-compression curves obtained for annealed tube specimens :

0.5 in. (L) x 0.75 in. (D') x 0.125 in. (t)

0.5 In. (L) x 0.75 in. (D) x 2.5 mm (nominal t)

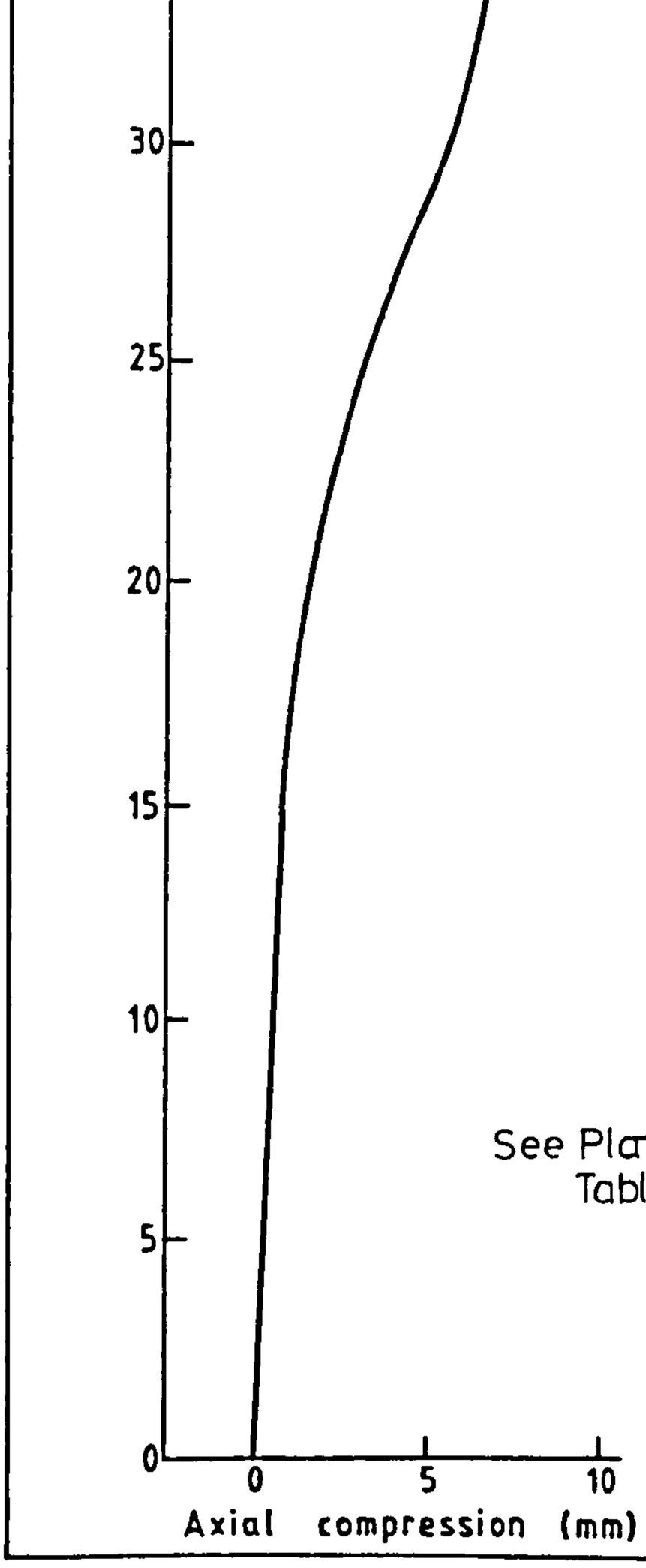


See Plate 2.18
Table 2.18

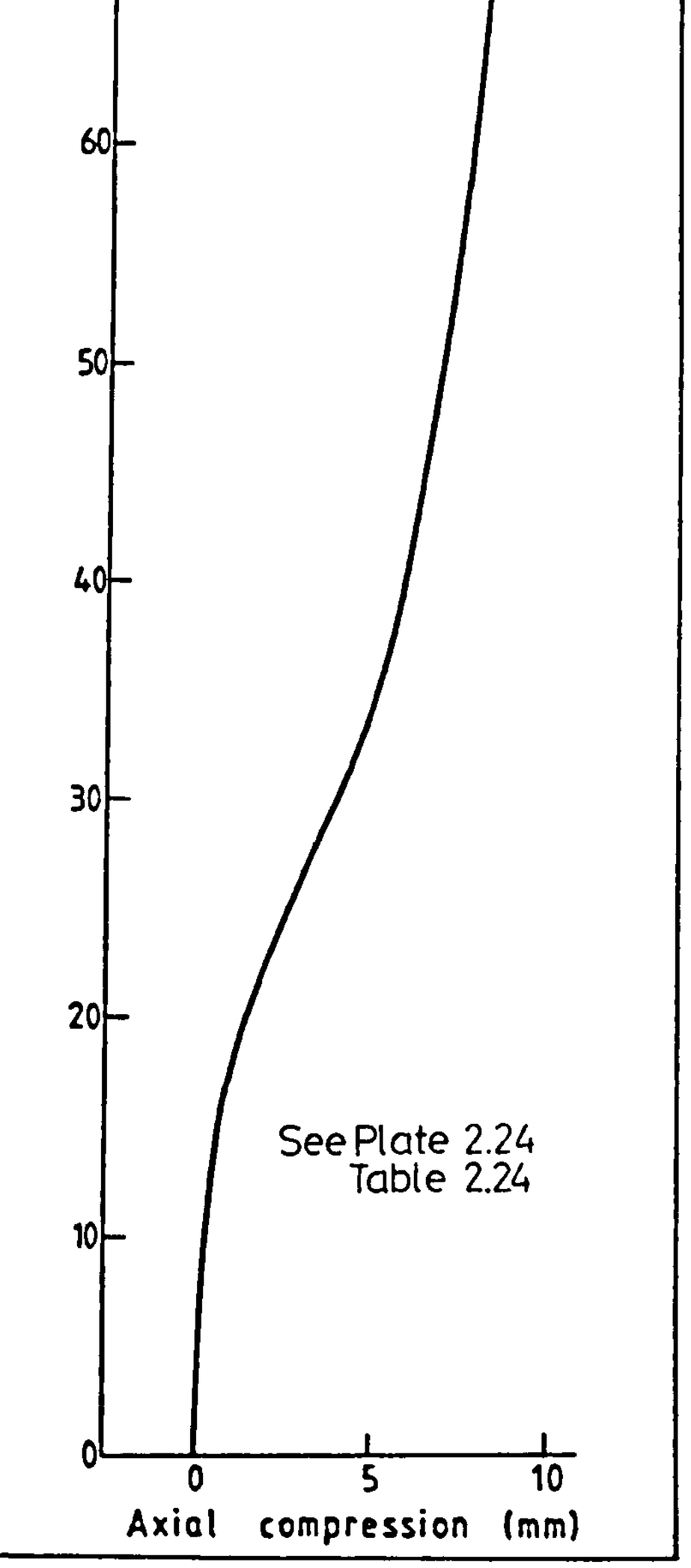


See Plate 2.24
Table 2.24

Plate 2.33

CRUSHING Mechanism of collapse

Experimental load-compression curves obtained for annealed tube specimens :

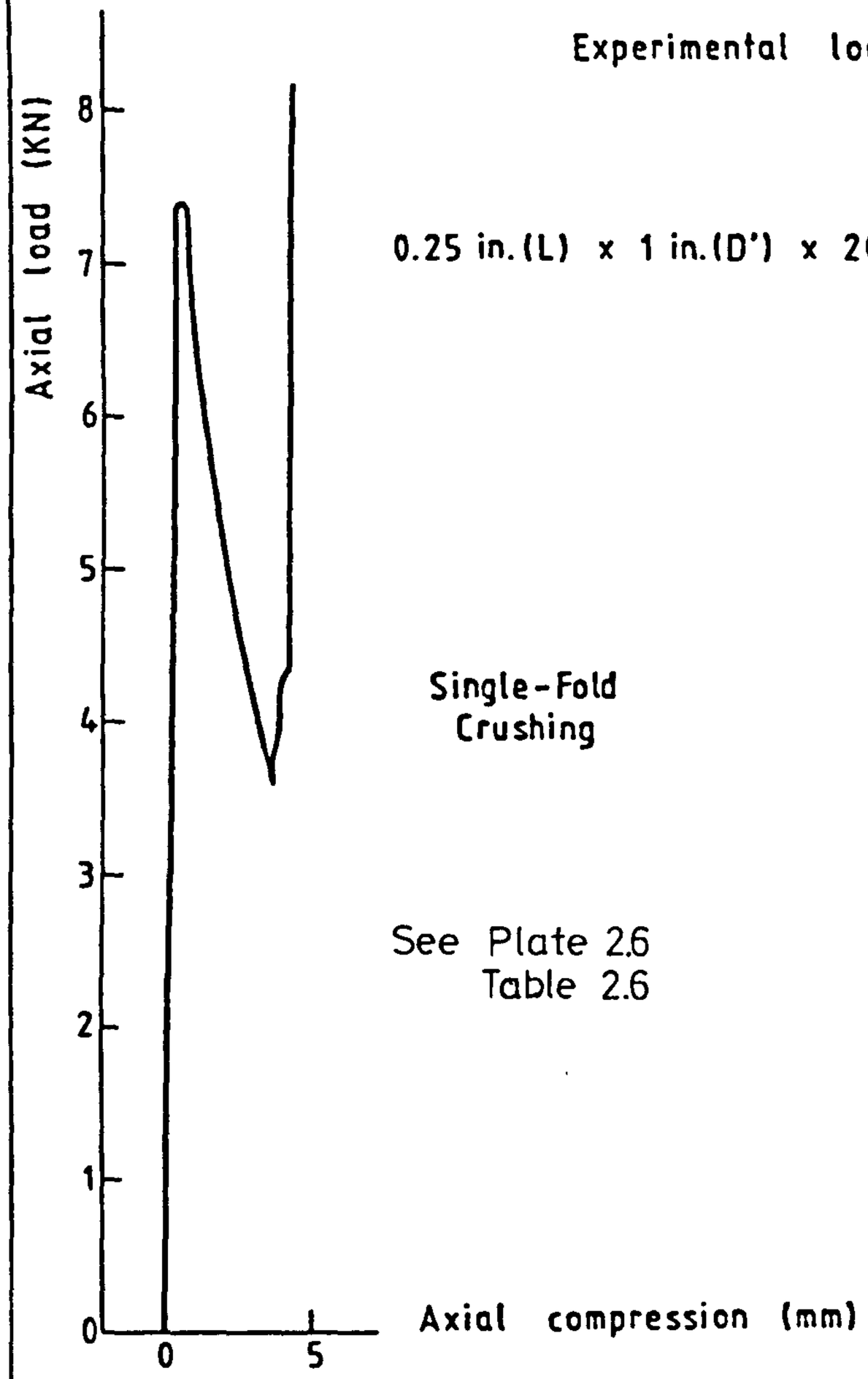


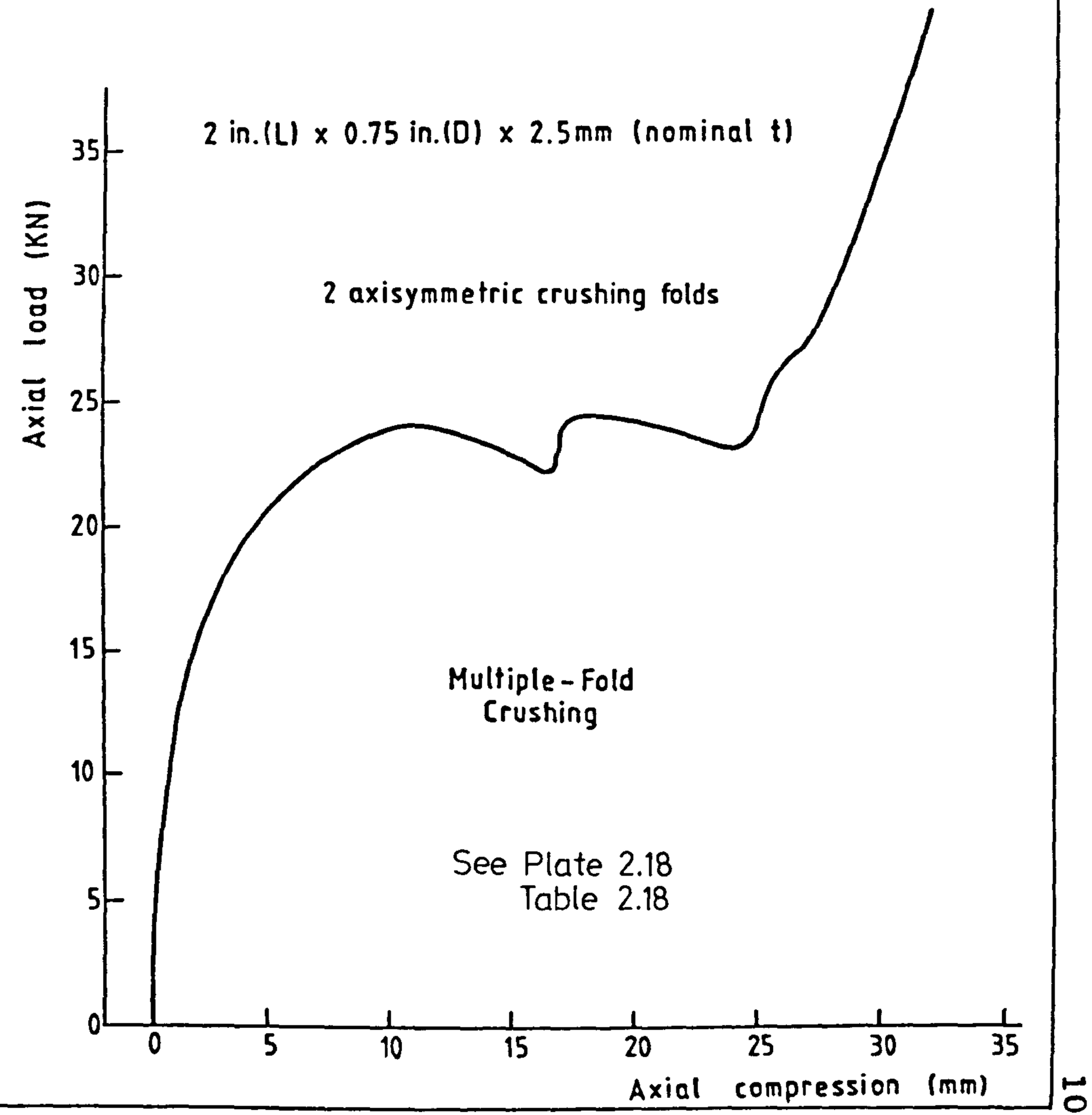


Plate 2.34

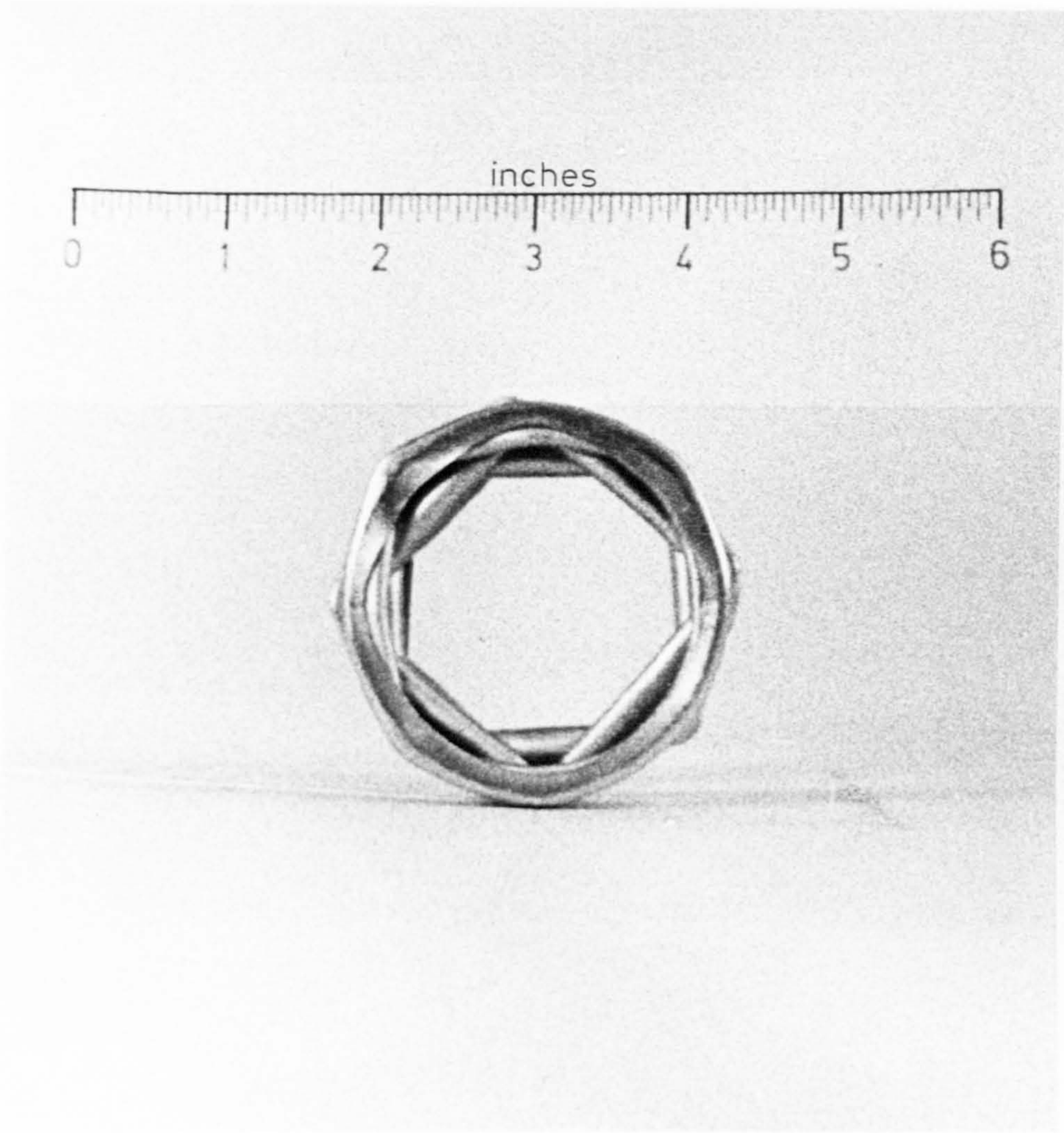



Plate 2.35 The 4-lobe diamond collapse mechanism
(See P. 66)

# CHAPTER 3

# SPECIFIC ENERGY ABSORPTION OF CYLINDRICAL TUBES

## Chapter 3 - Synopsis

For collapse of a cylindrical tube in axial compression, 'specific energy absorption', $E_s^c$, is the energy dissipated over the available stroke divided by the weight of the tube specimen. By providing a logarithmic relationship between $E_s^c$, tube geometric ratio, t/D' and a material constant m, theory (98) indicates how parameter $E_s^c$ can be used to rank materials and tube geometries in the elements' capacity to dissipate energy. Results for $E_s^c$ obtained here for the aluminium alloy tubes tested are shown to confirm this logarithmic relation. It is also shown that for a tube collapsing in two or more failure modes, the use of parameter $E_s^c$ may be extended to compare different modes of collapse for 'specific energy absorption'. Comparison of relative values of $E_s^c$ for concertina and diamond collapse reveals the concertina mode as the favourable mode for dissipation of energy.

## 3.1 Introduction

The concept of "specific energy absorption" has been regarded in the past few decades as a key performance index for structural elements and materials in ranking their suitability for mechanical energy dissipation. It is defined as the absorbed or dissipated energy per unit specimen weight.

This chapter presents comparisons of the experimental results obtained with those reported by Thornton & Magee (98) on this concept. In their paper distinction is made between energy absorption in tensile and compressive deformations of circular tubes of differing geometries, for two materials in various heat treatment conditions. For compressive loading, however, considered here, applied to an axially loaded tube, specific energy absorption, $E_s^c$, is defined as

$$E_s^c = \frac{\text{energy dissipated in axial compression}}{\text{weight of tube specimen}} \qquad (3.1.1)$$

The total energy absorbed may be obtained by integration of the area under the axial load-compression curve for the collapsed tube for compressions up to about 75% of the original specimen length. Parameter $E_s^c$ is then determined by dividing this energy by the compression distance (giving a figure for the mean collapse force, $\bar{P}$) and then by the weight of a unit length of the tube. The mean force $\bar{P}$ is the mean of the characteristic load fluctuations on the axial load-compression curve for the concertina and diamond modes of collapse (see Chapter 2, Plates 2.31 & 2.32) Thus,

$$E_s^c = \frac{\bar{P}}{A\,\rho} \qquad \text{where} \quad \begin{array}{l} A = \text{net section area} \\ \rho = \text{density of tube material} \end{array} \qquad (3.1.2)$$

## 3.2 Specific Energy and Tube Geometry

In their effort to rank materials and tube geometry for specific energy absorption, the above authors (98) proposed the following power law relationship;

$$E_s^c = C\,(t/D')^m \qquad (3.2.1)$$

where t and D' denote respectively the wall thickness and outside diameter of the tube; C and m are parameters that are constant for a particular material and its treatment condition, and

$0.02 < t/D' < 0.1$

$0.5 < m < 1.0$ for different materials

Only the diamond mechanism of collapse has been considered in theory (98), reported here. In order to achieve repeatability of the exact collapse configuration in this mechanism, the authors used tubes bearing specific indentations imposed prior to testing which set up a triggering mechanism thus promoting a particular (3-lobe) type of diamond collapse. The large initial load required for collapse was eliminated by this process.

Figure 3.1 inspects on a logarithmic plot the experimental data obtained for the aluminium alloy tested in relation to equation (3.2.1). Concertina and the diamond mechanisms of collapse are distinguished for the different tubes tested, in some of which the combined modes of collapse took place

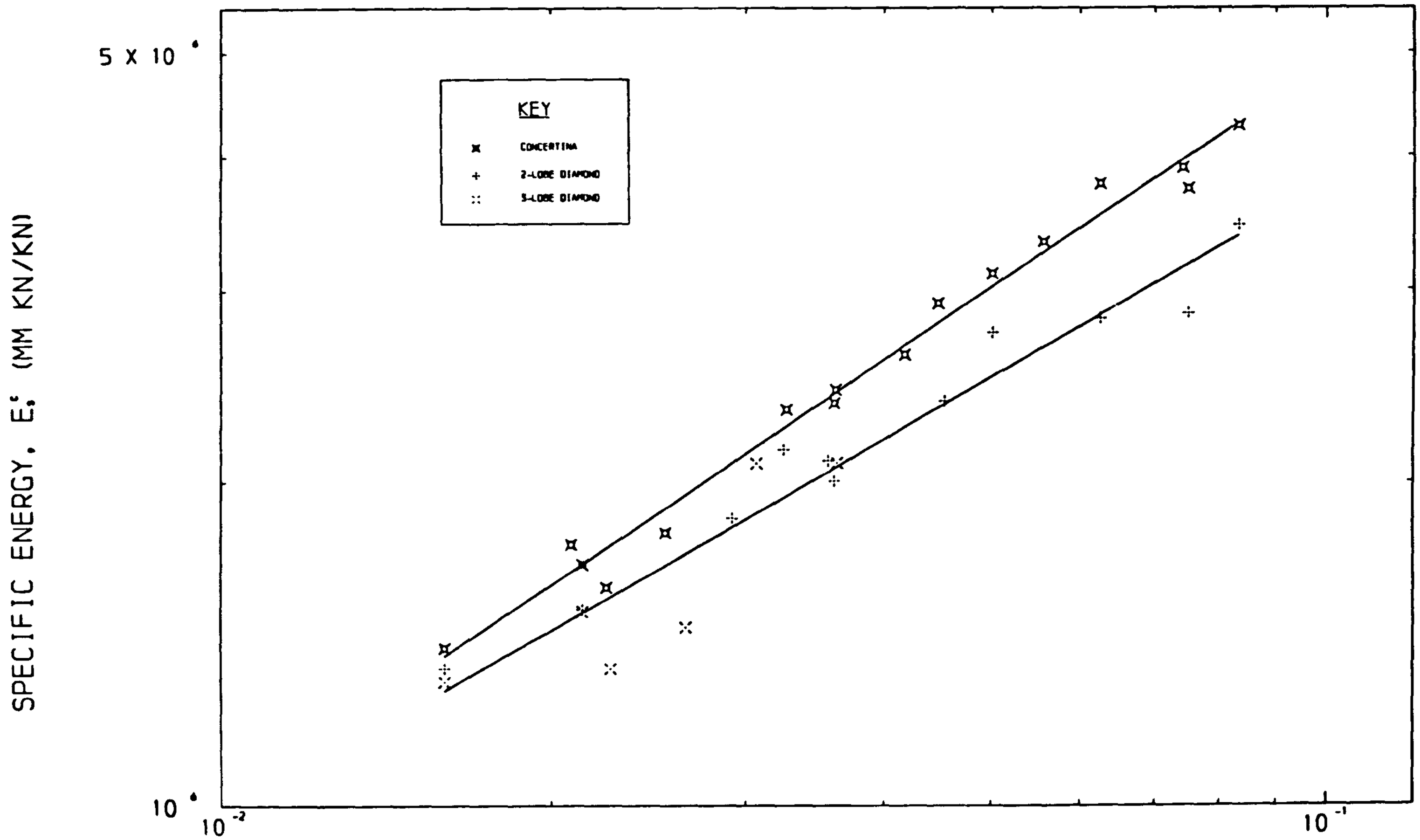


SPECIFIC ENERGY ABSORPTION IN COMPRESSION, $E_s^c$, OF ANNEALED HT-30 ALUMINIUM ALLOY TUBES

Figure 3.1

and each mode separately analyzed. Distinction is also made between the 2-lobe and the 3-lobe diamond modes and their distribution appears to indicate little difference in relative energy absorption, though the test data for the 3-lobe mode appear to be confined to the lower region of the t/D' ratio, i.e. for thinner tubes. The corresponding test data are shown in Tables A1.1 and A1.2, Appendix I.

For the range considered the best-fit linear regressions after transformation yield the following data :

Concertina mode :

$$E_s^c = 10^{7.3763} (t/D')^{0.689} \quad \text{mm KN/KN}$$

Diamond modes : (3.2.2)

$$E_s^c = 10^{7.1607} (t/D')^{0.587} \quad \text{mm KN/KN}$$

Hence, m = 0.689 and 0.587 respectively denoting the gradient of each graph. C = 23.78 km and 14.48 km denoting the intercept of each graph on a vertical line through the ordinate t/D' = 1.0 .

Although the aluminium alloy tested is different from that in the work reported in Reference (98), the above results compare with values of C = 25.2 km and m = 0.772 for an annealed 6061-aluminium alloy. Furthermore, strict comparison is not valid since the latter values also refer to a particular (3-lobe) mode of diamond collapse.

However, the dependence of specific energy on tube section geometry is clearly evident. For the range of t/D' considered, parameter $E_s^c$ varies by a factor of three, signifying an increase in the capacity of thick-walled tubes to dissipate energy.

By distinguishing the two collapse mechanisms, Figure 3.1 indicates that the concertina mode is associated with a higher specific energy absorption than the diamond collapse modes for any t/D' ratio of tubes. The underlying reason is believed to be associated with the relative changes in material state brought about during collapse. The concertina configuration accompanies a substantial degree of plastic deformation together with work hardening for the alloy tested. On the one hand this is due to axisymmetric changes in the original circumference of the tube and the development of hoop stresses, and on the other, due to rotation at the fold hinges. This is in contrast to the diamond mechanism which is widely regarded as an inextensional collapse with minor or no changes in the magnitude of the midsurface circumference of the original tube; c.f. Pugsley and Macaulay (78), Mallock (64), Johnson et al (48) and Yoshimura (107).

Although the present author believes that a fair degree of plasticity is inherent in diamond modes and opposes the notion that the mechanism is inextensional, particularly in the case of the 2-lobe diamond mode where prominent plastic nodal regions have been repeatedly observed, he confirms that the degree of plasticity and material stiffening is lower than that present in the concertina mechanism. The

larger plasticity associated with the latter mode gives rise to collapse at a higher mean collapse load, $\bar{P}$ (hence an increase in area under the load-compression curve). This results in a subsequent increase in specific energy absorption, for a given tube (c.f. Plate 2.32).

The observed pattern implies that paramter C (and possibly m) in equation (3.2.1) not only depend on the type of material and its heat treatment (as stated in ref.98), but also on the mode of collapse. If m is only material dependent, then in theory the two linear relations of Figure 3.1 should be parallel even though for the diamond mechanism the exact lobe configurations are not separately analyzed here. The scatter of recordings for this mechanism is associated largely with the inherent irregularities in the configuration patterns encountered during collapse; hence the presence of some regions of unevenness in the otherwise repetitive pattern of the corresponding load-compression curves resulting in variations in values of the mean load, $\bar{P}$. This was expected since the tubes were tested in their original cylindrical configuration with no indentations initially imposed to trigger the repetition of an exact pattern of folding.

The present author believes that even if sets of ideally 'indented' tubes (for each diamond lobe configuration) were to be tested, and the data separately checked against equation (3.2.1), then variations in m and C would still be observed. The values of m and C are thus believed to

differ not only from concertina to diamond collapse, but also to depend on the collapsed shape in the diamond mechanism.

The percentage variation in the magnitude of C from one collapse mode to another exceeds the corresponding variation in the magnitude of m. For the results of Figure 3.1, these variations from concertina to diamond mode are 39% & 15% respectively, denoting the greater sensitivity of C to the mode of collapse. This correlates with the trend reported(98) for different materials where variations in m are quoted to be on a smaller scale than those for C, particularly for different heat treatments of a material where changes caused in strain-hardening properties of the material result in little variation in the value of index m.

In the referred paper(98), the authors found no relationship between specific tensile energy, $E_s^T$, and the specific energy in compression, $E_s^C$ dealt with here, implying that the former does not properly rank materials for specific energy absorption in relation to tube geometry, particularly where strain hardening is prominent in a material. For collapse in compression it is claimed that as well as parameters C and m in equation (3.2.1), the specific ultimate tensile strength* is an important indicator of the capacity of a material to absorb energy over a wide range of tube geometries. This parameter is in direct relationship to the absorption variable, $E_s^C$ and governs variations in parameter C for different materials. Hence no single parameter alone can fully characterize a material's capacity

* This is the ratio of ultimate tensile stress to density of material

to absorb energy for all tube geometries within the indicated range and all the modes of collapse considered.

In summary, it is concluded that in equation (3.2.1), parameters C and m are constant not only for a particular material and its heat treatment condition (as stated in Ref.(98)), but constant also for a particular mode of collapse. Reference (16) provides a comparison of specific energy absorptions for different materials and types of energy absorbers.

## 3.3 Specific Energy and Nominal Collapse Stress

In their paper (98), the authors define the nominal collapse stress, $\sigma_n$, for a cylindrical tube as follows :

$$\sigma_n = \frac{4\,\bar{P}}{\pi D'^2} \qquad (3.3.1)$$

The following power law relationship is proposed in the reported work (98) :

$$E_s^c = K\,(\sigma_n)^n \qquad (3.3.2)$$

### 3.3.1 Comparison with Experiment

Figure 3.2 indicates the test data obtained here for the relationship of equation (3.3.2) with the concertina and diamond collapse modes again differentiated.* The concertina mode is favoured in this context, too. From Figure 3.2, K = 17.60 km and K = 13.52 km respectively denoting the

* Details of individual data points are presented in Tables A1.1 & A1.2, Appendix I

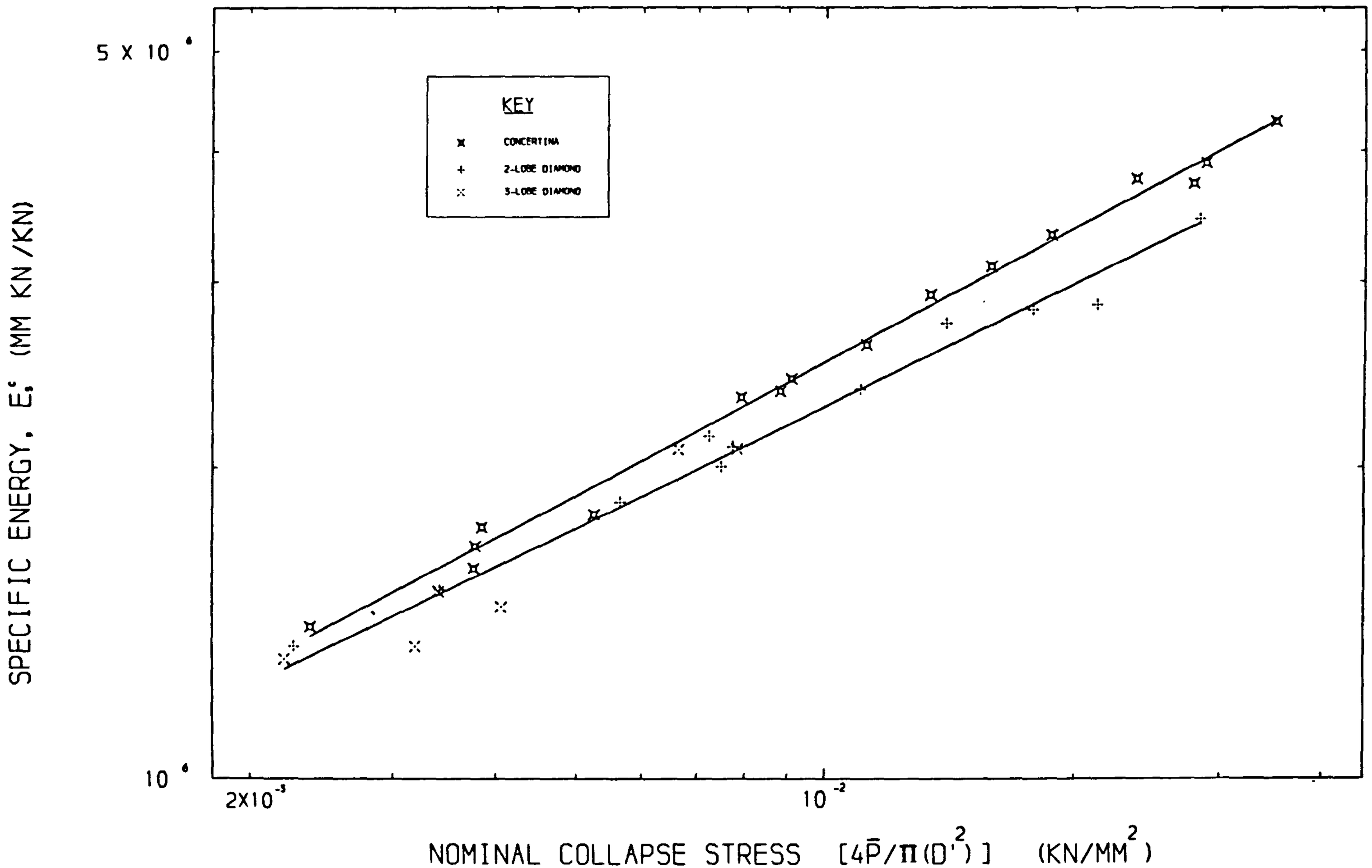


SPECIFIC ENERGY ABSORPTION IN COMPRESSION, $E_s^c$, OF ANNEALED HT-30 ALUMINIUM ALLOY TUBES

Figure 3.2

intercept of each graph with a vertical line through the ordinate, $\sigma_n = 1$ KN/mm$^2$. Parameter n assumes values of 0.422 and 0.386 respectively indicating the gradient of each linear relation (in the logarithmic plot).

It is thus demonstrated here that parameters K and n are constant not only for a particular material but also for a particular collapse mode and that variations in power index n are smaller than for K.

However, the use of this relationship is limited in comparing the absorption levels of different materials, since nominal stress is both a function of material properties and tube geometry, so that, as rightly pointed out in the reported work (98), a direct comparison of absorption capacities for different materials is possible only if identical tubes are considered.

### 3.3.2 Extension of Theory (98)

Following equation (3.3.2) an extension of this theory is presented with the aim of determining an expression for the mean load, $\bar{P}$ in terms of tube geometry and parameters $\rho$ (density), K and n which characterize the properties of the material. The knowledge of the magnitude of $\bar{P}$ for a given material and a particular mode of collapse permits the evaluation of the actual energy (in units of work) that may be absorbed by a tube for a given axial deformation during collapse.

From the definition of Parameter $E_s^c$ in equation (3.1.2), and using equations (3.3.1) and (3.3.2), it is seen that

$$E_s^c = \frac{\bar{P}}{\rho A} = \frac{\bar{P}}{\rho \pi t(D' - t)} = K(\sigma_n)^n = K\left\{\frac{4\bar{P}}{\pi D'^2}\right\}^n \qquad (3.3.3)$$

where $A = \pi t(D'-t)$ denoting the net section area of the tube and $\rho$ is material density.

Rearrangement of the above equation gives,

$$\bar{P}^{(1-n)} D'^{2n} = K_1 t (D' - t) \qquad (3.3.4)$$

where $$K_1 = (4/\pi)^n \rho \pi K \qquad (3.3.5)$$

Equation (3.3.4) is a quadratic in $t$ giving

$$t = \tfrac{1}{2} D' \left\{1 \pm (1 - J)^{\frac{1}{2}}\right\} \qquad (3.3.6)$$

where $$J = \frac{4}{K_1}\left\{\frac{\bar{P}}{D'^2}\right\}^{1-n} \qquad (3.3.7)$$

Positive sign of the radical in equation (3.3.6) reveals that if $J$ is large (comparable to unity) then $t \simeq \frac{1}{2} D'$ and if $J$ is small (negligible), $t \simeq D'$. Both of these results are invalid in view of the experimental range of $t/D'$ in equation (3.2.1). Thus, only negative sign of the radical is meaningful. Hence

$$t = \tfrac{1}{2} D' \left\{1 - (1 - J)^{\frac{1}{2}}\right\} \qquad (3.3.8)$$

If D is chosen as before to denote the internal diameter of the tube, then $D' = D + 2t$ from which the following geometrical identity is observed;

$$t = \tfrac{1}{2} D' \left( 1 - \frac{D}{D'} \right) \qquad (3.3.9)$$

Equation (3.3.9) is written in the above form so that it may be equated to the preceding equation thus giving

$$D = D' \left( 1 - J \right)^{\frac{1}{2}} \qquad (3.3.10)$$

with J defined in (3.3.7). Hence from equations (3.3.8) and (3.3.10),

$$t/D = \tfrac{1}{2} \left\{ \left( 1 - J \right)^{-\frac{1}{2}} - 1 \right\} \qquad (3.3.11)$$

From the collapse mode classification chart of Figure 2.1 (Ch.2, P.60), it is seen that $0.016 < t/D < 0.1$ (approx.) for collapse in concertina or mixed concertina and diamond modes of collapse. This range is in close agreement with the proposed range of validity of equations (3.2.1) & (3.3.2) as indicated in Sections 3.2 and 3.3 (from Ref.(98)), where the external diameter, D' has been used instead of D. Hence equation (3.3.11), too, is valid in the proposed range as follows;

$$0.02 < \tfrac{1}{2} \left\{ \left( 1 - J \right)^{-\frac{1}{2}} - 1 \right\} < 0.1 \qquad (3.3.12)$$

$$\text{i.e.} \qquad 0.0755 < J < 0.3056 \qquad (3.3.13)$$

so that from equation (3.3.7),

$$0.0755 \quad < \quad \frac{4}{K_1}\left\{\frac{\bar{P}}{D'^2}\right\}^{1-n} \quad < \quad 0.3056 \qquad (3.3.14)$$

With parameters $K_1$ and n fixed for a material and a particular sequential mode of tube collapse, the above inequality provides bounds on the magnitude of the mean load, $\bar{P}$ in terms of the square of the external diameter of the tube. If the thickness of the tube is also a known quantity, i.e. ratio t/D is known, equation (3.3.11) may be shown to reveal the following expression for the mean load, $\bar{P}$.

$$\bar{P} = D'^2\left[\tfrac{1}{4}K_1\left\{1 - \frac{1}{\{1 + 2\,(t/D)\}^2}\right\}\right]^{\frac{1}{1-n}}\dagger \qquad (3.3.15)$$

For a given material and a particular mode of collapse considered, parameters $K_1$ and n assume appropriate values in the above equation.

As an alternative to the above equation, an expression for $\bar{P}$ may be obtained directly from the relationship of equation (3.2.1) as follows,

$$E_s^c = \frac{\bar{P}}{\rho\pi t(D'-t)} = C\,(t/D')^m \qquad \text{giving}$$

$$\bar{P} = C_1\,t\,(D' - t)\,(t/D')^m \dagger \qquad (3.3.16)$$

where $C_1 = \rho\,\pi\,C$

Similar to $K_1$ and n in equation (3.3.15), parameters $C_1$ and m assume appropriate values for the particular mechanism of failure under consideration.

---

†These expressions provide the same value for $\bar{P}$ for known tube geometry and given $K_1$, n, $C_1$ and m

## 3.4 Conclusion

1. Experimental results confirm equation (3.2.1) relating specific energy absorption, $E_s^C$, to tube ratio, t/D', over the range : $0.02 \leqslant t/D' \leqslant 0.10$ .

2. In addition to its use in ranking materials and tube ratios, t/D', parameter $E_s^C$ may be used to compare the energy absorptions associated with concertina and diamond modes of collapse, for a given tube. Thus indices C and m in equation (3.2.1) refer also to a specific collapse mode.

3. By comparing the values of $E_s^C$ for concertina and diamond collapse, the former mode is found to be associated with a higher specific energy absorption. On this basis, tubes may be designed to collapse in the 'favourable' concertina mode for maximum dissipation of energy.

# CHAPTER 4

# NEW INDICES FOR DIRECT MEASUREMENT OF THE ENERGY ABSORPTION CAPACITY OF CIRCULAR TUBES

# Chapter 4 - Synopsis

For the concertina and diamond modes of collapse, new indices are introduced defining the energies dissipated in the formation of an axial fold, for a given tube. They are derived from experimental data and provide a direct means of relating the axial energy absorption of cylindrical tubes (in Joules) to their dimensions. A separate energy index is introduced for Eulerian (strut-type) collapse which defines the energy dissipated up to the peak axial load applied. For a given tube, comparison, on an empirical basis, of the energy relationships for concertina and diamond collapse reveals the concertina mode as the favourable/optimum mode for dissipation of energy.

## 4.1 Introduction

The preceding chapter focused on specific energy absorption, $E_s^c$ as a key parameter used in selection of material and geometry for tubes designed as energy absorbers. However, since $E_s^c$ (measured in units of length) is the ratio of mean axial collapse stress, $\bar{P}/A$ to material density, $\rho$ and is a function of tube ratio, t/D' (see Chapter 3), it does not relate the magnitude of absorbed energy to the absolute size of the absorber tube element.

This chapter presents a more direct method of estimating the capacity of tubes to dissipate energy by relating dissipated energy (in Joules) to tube geometry (in units of area/volume). Concertina and the diamond modes of collapse are considered here and differentiated, as in Chapter 3. It was illustrated in Chapter 2 that each of these modes is associated with a repetitive fluctuating axial load during collapse, these fluctuations occurring about a mean value and providing a state of 'stable' postbuckling equilibrium *; the reader is reminded that it was on account of this controlled deformation and high material participation (i.e. high stroke efficiency) that these modes were suggested as suitable in the design of tubes as energy dissipators.

For the above modes of collapse, the energy indices introduced define the energies absorbed for the complete development of an axial fold. This is obtained by integrating the area under the axial load-compression curve between salient points featuring the initiation and completion of a fold. A Hoff planimeter (No. 317) is used for this purpose. The recorded

*as distinct from the 'catastrophic' Eulerian mode in which the axial load rapidly drops beyond initial buckling

energy is then related to the net section area of the tube and subsequently, to the material volume of the fold. For the annealed aluminium alloy tested, the resulting relationships provide a direct estimate of the energies absorbed by tubes of different section geometries, collapsing in the concertina or diamond modes. These relationships are used in Section 4.5 as criteria for relative comparison of the energies that are associated with these collapse mechanisms. For theoretical interest, an energy index is introduced for Eulerian (strut-type) collapse.

## 4.2 Concertina Mechanism

Figure 4.1 illustrates on a logarithmic plot, the relation obtained between the energy absorbed in formation of the first concertina fold and the net cross-section area of the tubes tested.* The area that was measured under the load--compression curve in each case to define and evaluate this energy is indicated schematically in Figure 4.2 . The curvilinear trend of test data in Figure 4.1 has been made distinct by application of a linear regression for those test data not exceeding area $A = 120\ mm^2$, and for the complete range, a square-root regression of the following form :

$$Y = a\,(X)^{\frac{1}{2}} + b \qquad (4.2.1)$$

where $Y = \log_{10}$ (recorded energy)

$X = \log_{10}$ (net cross section area, A)

---

* Details of all individual test data in the relationships shown in this chapter are presented in Tables A1.5, A1.6 and A1.7, Appendix I

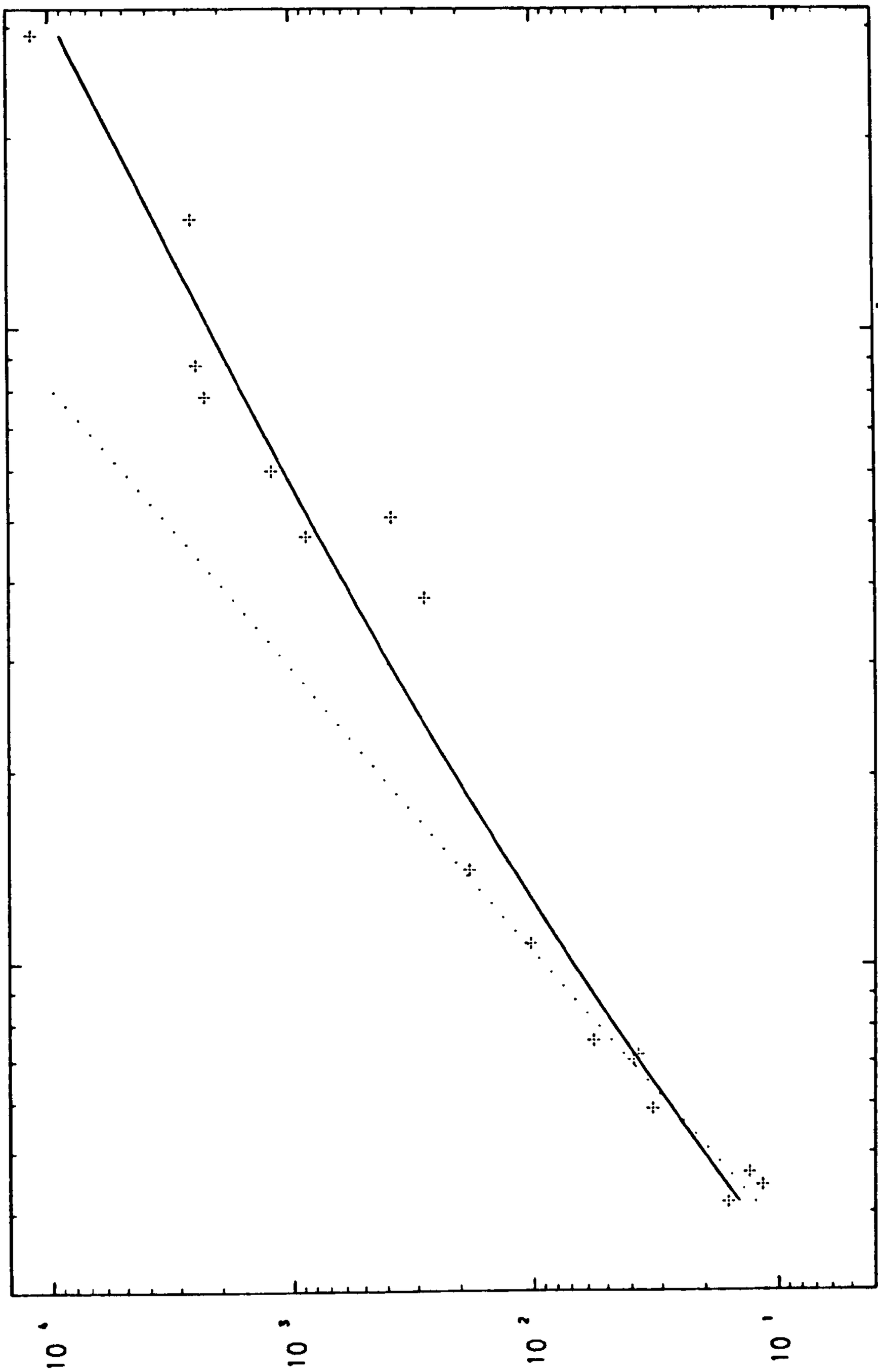
ENERGY ABSORBED IN FIRST FOLD (JOULES)
10⁰
10⁻¹
10⁻²
10⁻³
CROSS-SECTIONAL AREA OF TUBE, A (MM²)
CONCERTINA MECHANISM OF COLLAPSE

Figure 4.1

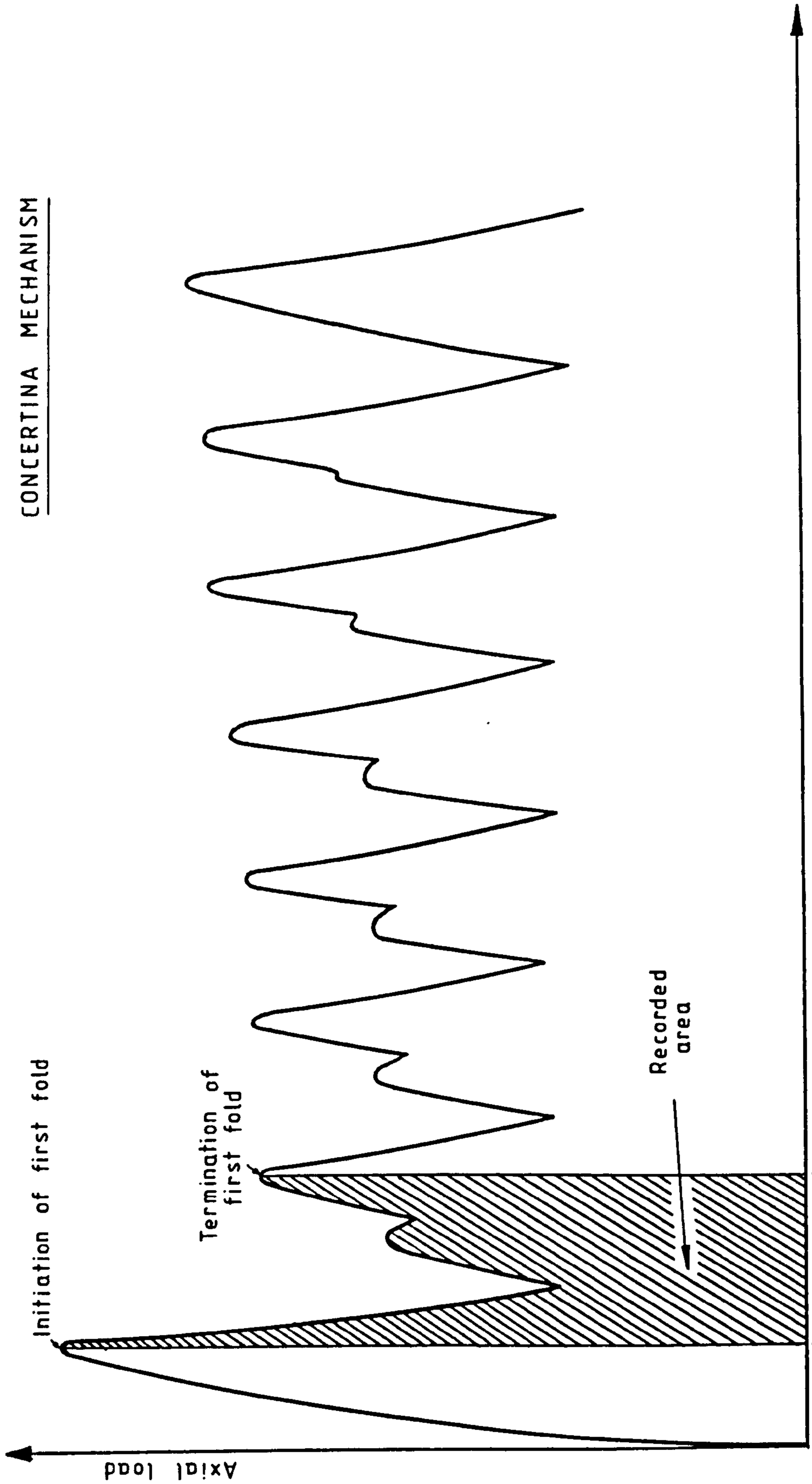


Sketch of the typical experimental load-compression curve defining the area recorded for the first fold-energy index

Figure 4.2

The latter regression has been chosen only for its mathematical simplicity. To this end, the relationship shown remains empirical. The numerical values of the regression constants in (4.2.1) are presented in Section 4.5 collectively with the other relationships obtained in similar manner, which are to follow.

Figure 4.3 indicates a plot of the energy against the volume of the tube used in formation of the first fold, defined as 'energy index', (see P.11). The volume is defined as the axial shortening of the tube for the development of one fold (marked as $L_f$ in Figure 4.2) multiplied by the net cross section area, A, of the tube.

Figures 4.1 and 4.3 suggest the existence of power laws directly linking the absorbed energy (in Joules) to tube geometry (in units of area/volume); they are distinct from the 'indirect' logarithmic energy relations of Chapter 3 . However, because of the curvilinear trend, the index of the power law in each case is a function of the geometric abscissa.

Considering the spread of the test data in Figures 4.1 and 4.3, inspection of individual data in Appendix I (Table A1.5) reveals that, in each case, the three points situated below the regression curves at larger geometries correspond to tubes having large diameters but proportionately smaller thicknesses than those representing points on or above the curves. These denote values for the geometric ratio t/D

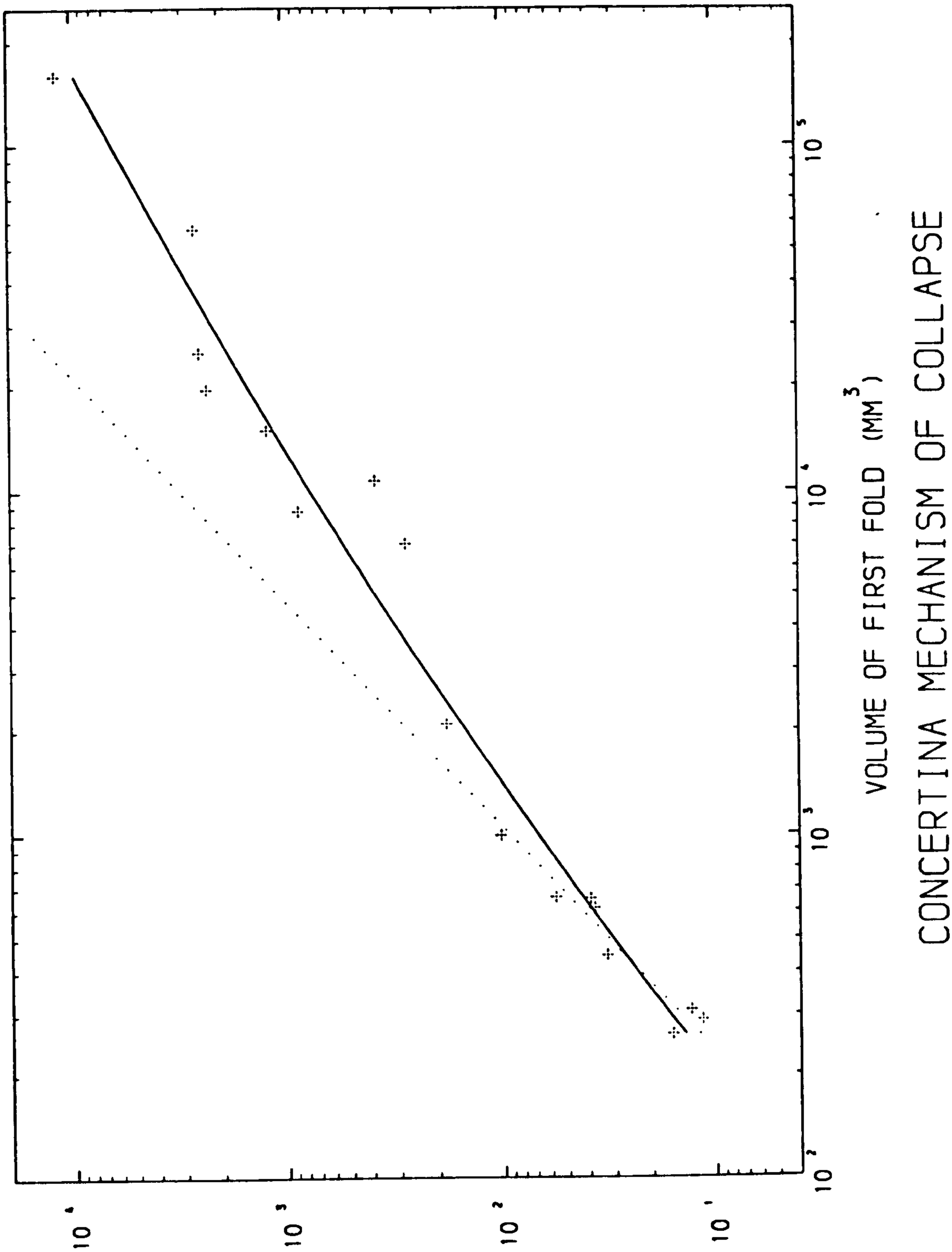
CONCERTINA MECHANISM OF COLLAPSE
VOLUME OF FIRST FOLD (MM$^3$)
ENERGY ABSORBED IN FIRST FOLD (JOULES)
$10^{-1}$
$10^{0}$
$10^{1}$
$10^{2}$
$10^{3}$
$10^{4}$
$10^{5}$

Figure 4.3

in the low range : $0.0165 \lessapprox t/D \lessapprox 0.0223$ for concertina mechanism. The drop from the expected absorbed energy is seen to be associated with this geometric phenomenon. As will be observed in Chapter 5, the mean collapse load, $\overline{P}$ is related to the square root of the internal diameter D and to the thickness t raised to the power of 1.5 . Hence the internal work done in bending at the fold hinges (reflecting the magnitude of the 'energy index') is observed to be sensitive to variations in t for a given diameter.

Next, as distinct from conditions for the first fold, a mean value for the 'fold energy index' introduced is obtained by evaluating the total energy absorbed by a tube over an integral number of folds and dividing this figure by the number of folds, n. This defines the mean energy absorbed per fold. The relevant area recorded under the load-compression curve in each case is illustrated schematically in Figure 4.4 . The procedure is performed for tubes failing either purely in concertina or in the mixed concertina and diamond mode (as in Figure 4.4) in which case the concertina portion is considered only.

Figures 4.5 and 4.6 indicate the similar trends obtained for mean energy vs. tube section area and the mean nominal volume of a fold, respectively. The latter volume, $V_{no}$ is evaluated * by measuring the axial shortening of a tube over n integral folds, marked $L_t$ in Figure 4.4, and dividing this quantity by n to yield a figure of mean axial shortening; this is then multiplied by the section area, A of the tube. It is defined here as the nominal mean volume of a fold (as

---

* This is subject to correction - see P.133

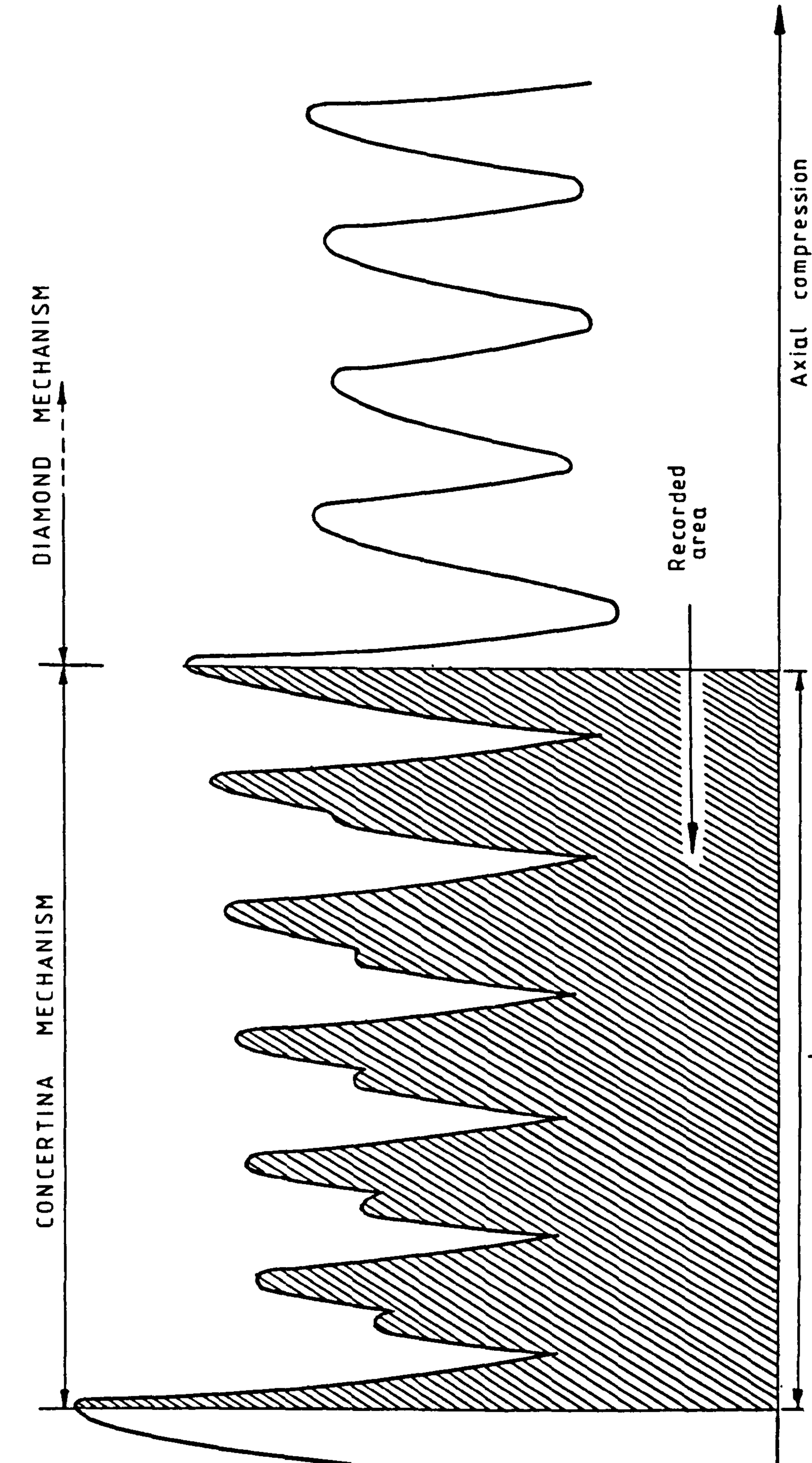


Sketch of the typical experimental load-compression curve defining the recorded-energy index to obtain the concertina mean fold-energy index

Figure 4.4

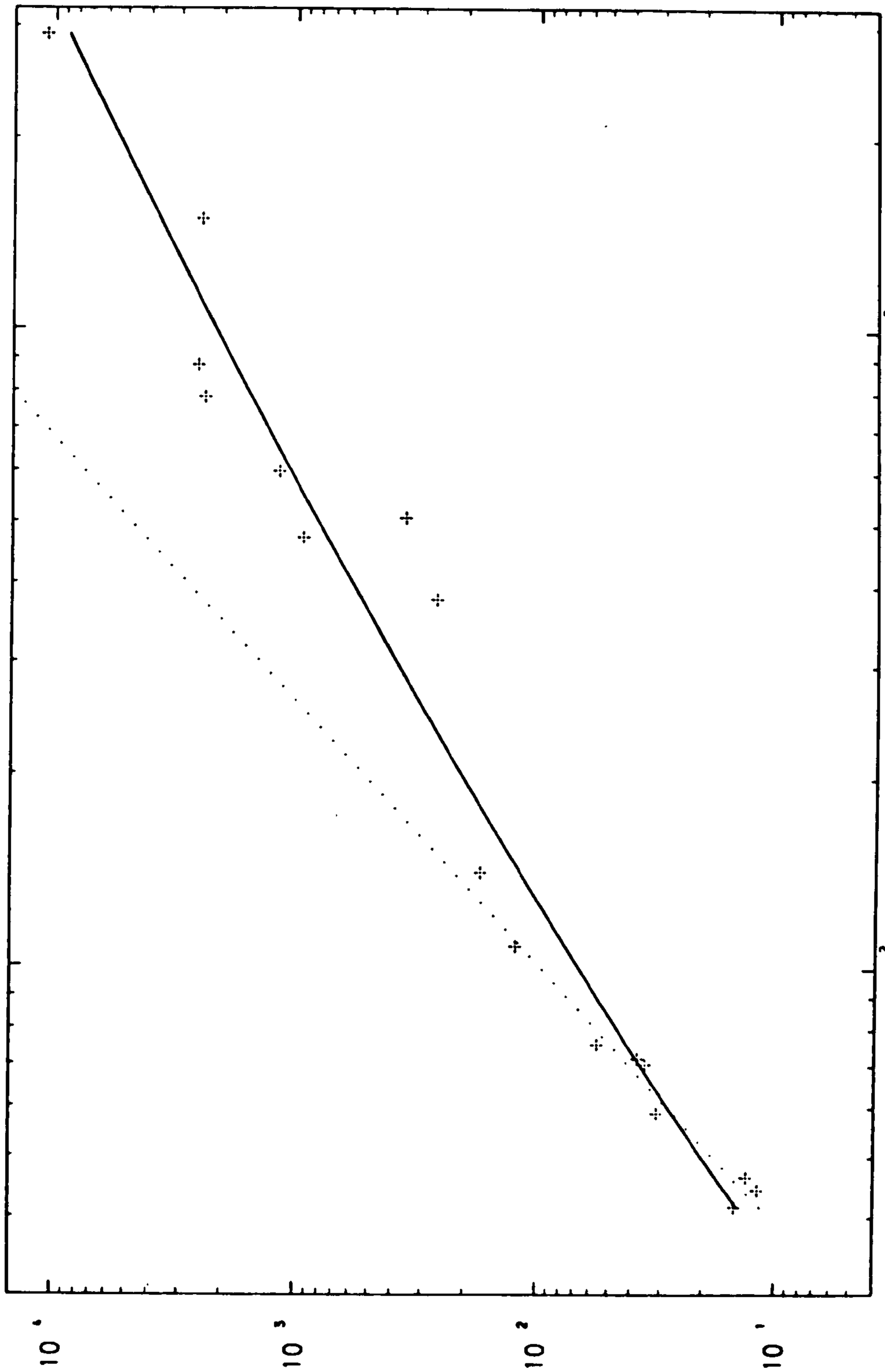
CONCERTINA MECHANISM OF COLLAPSE
CROSS-SECTIONAL AREA OF TUBE, A (MM$^2$)
$10^3$
$10^2$
MEAN ENERGY ABSORBED PER FOLD (JOULES)
$10^0$
$10^1$
$10^2$
$10^3$

Figure 4.5

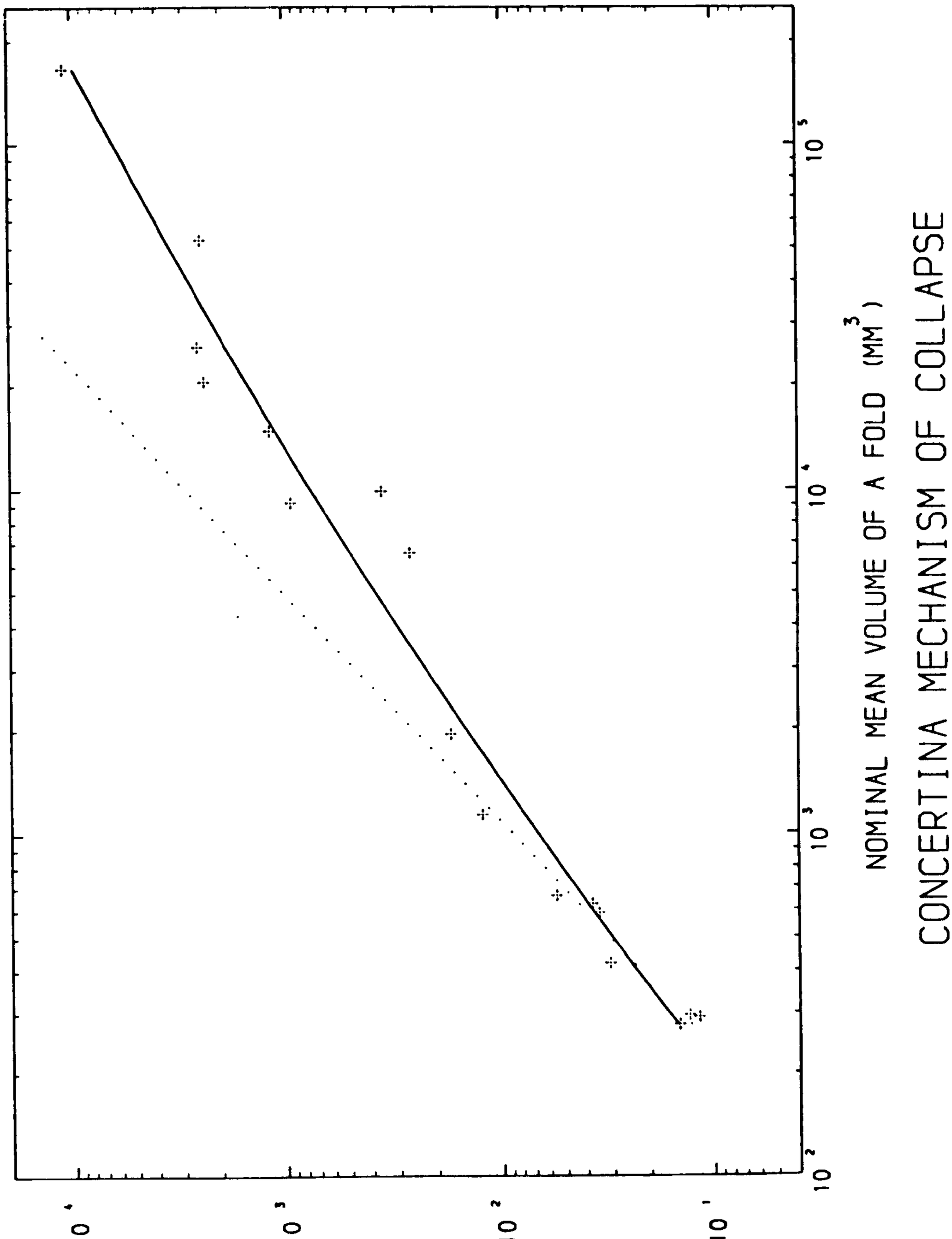
CONCERTINA MECHANISM OF COLLAPSE
NOMINAL MEAN VOLUME OF A FOLD (MM$^3$)
MEAN ENERGY ABSORBED PER FOLD (JOULES)
$10^{-1}$
$10^{0}$
$10^{1}$
$10^{2}$
$10^{3}$
$10^{4}$
$10^{5}$

Figure 4.6

distinct from the 'true mean volume', defined below). Thus

$$V_{no} = \frac{L_t}{n} A \qquad (4.2.2)$$

Since formation of the first fold accompanies the high axial failure load initially required to trigger collapse in this mechanism, it is expected that for a given geometry, the energy absorbed in this fold is higher than the above mean energy considered over a number of folds. The comparison is made in Section 4.5 in discussion of group results.

CORRECTION TO NOMINAL VOLUME

The nominal mean volume of a fold defined above is smaller than the true mean volume of a concertina fold. This is explained with the aid of Figures 4.4 and 4.7 . Let us assume that initially the length of the tube is an integer multiple of the length of one half-wave of a concertina fold, h, say 14 h , for a given section geometry; also, 5 complete concertina folds are to develop in the tube before initiation of collapse in the diamond configuration or even before a further concertina fold develops. Then upon completion of these 5 concertina folds, a total axial length of 10 h of the tube must have been utilized in deformation leaving an undeformed length of 4 h remaining intact, as indicated in Figure 4.7 . Therefore, the total axial shortening over these folds is $L_t^*$ , as marked. However, it is seen that the axial shortening previously recorded in Figure 4.4 is a measure of the relative displacement of one platen from its original position (i) to its new position after collapse (ii), in Figure 4.7 . Thus, the difference between $L_t$ and $L_t^*$ provides

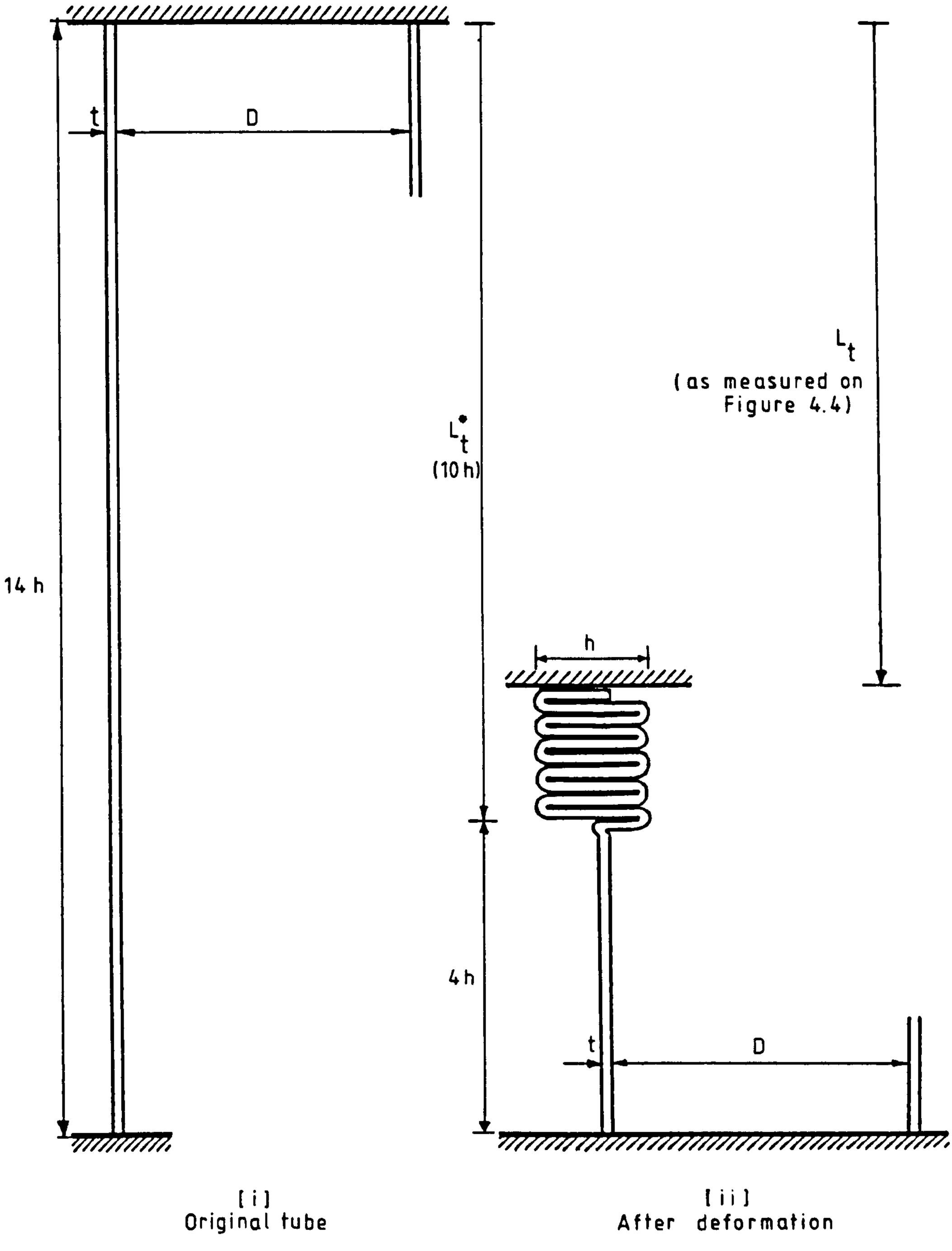


$$L_t^* = L_t + 2nt \quad (n=5 \text{ in this case})$$

$$\text{Nominal volume, } V_{no} = \frac{L_t}{n} \cdot A$$

$$\text{True volume, } V_{tr} = \frac{L_t^*}{n} \cdot A = \left[\frac{L_t}{n} + 2t\right] A$$

Illustration of the geometric difference between nominal mean and true mean volume of a concertina fold

Figure 4.7

a measure of error associated with the nominal mean volume in its representation of the true mean volume of a fold. It is observed that because of the geometry of folding,

$$L_t^* = L_t + 2nt \qquad (4.2.3)$$

where $n$ = number of folds considered

$t$ = tube wall thickness

Hence the true mean volume of a fold, $V_{tr}$ is

$$V_{tr} = \frac{L_t^* A}{n} = (\frac{L_t}{n} + 2t) A \qquad (4.2.4)$$

Comparison of equations (4.2.2) and (4.2.4) reveals that in each case a quantity of two thicknesses must be added to the mean axial shortening per fold in computation of the nominal volume, in order to obtain the true mean volume of a fold. Figure 4.8 indicates the relationship between the same mean energy per fold index and the true mean volume of a fold as described above. The volume in Figure 4.3 showing the energy relationship of the first fold represents the nominal volume of the first fold. With the energy indices introduced and applied to the concertina collapse mode, investigation next centres upon the diamond collapse mechanism.

## 4.3 Diamond Mechanism

In the axial tests performed, it was frequently observed that the folding process and consequently the axial load-compression graphs for the diamond modes of collapse did not exhibit the

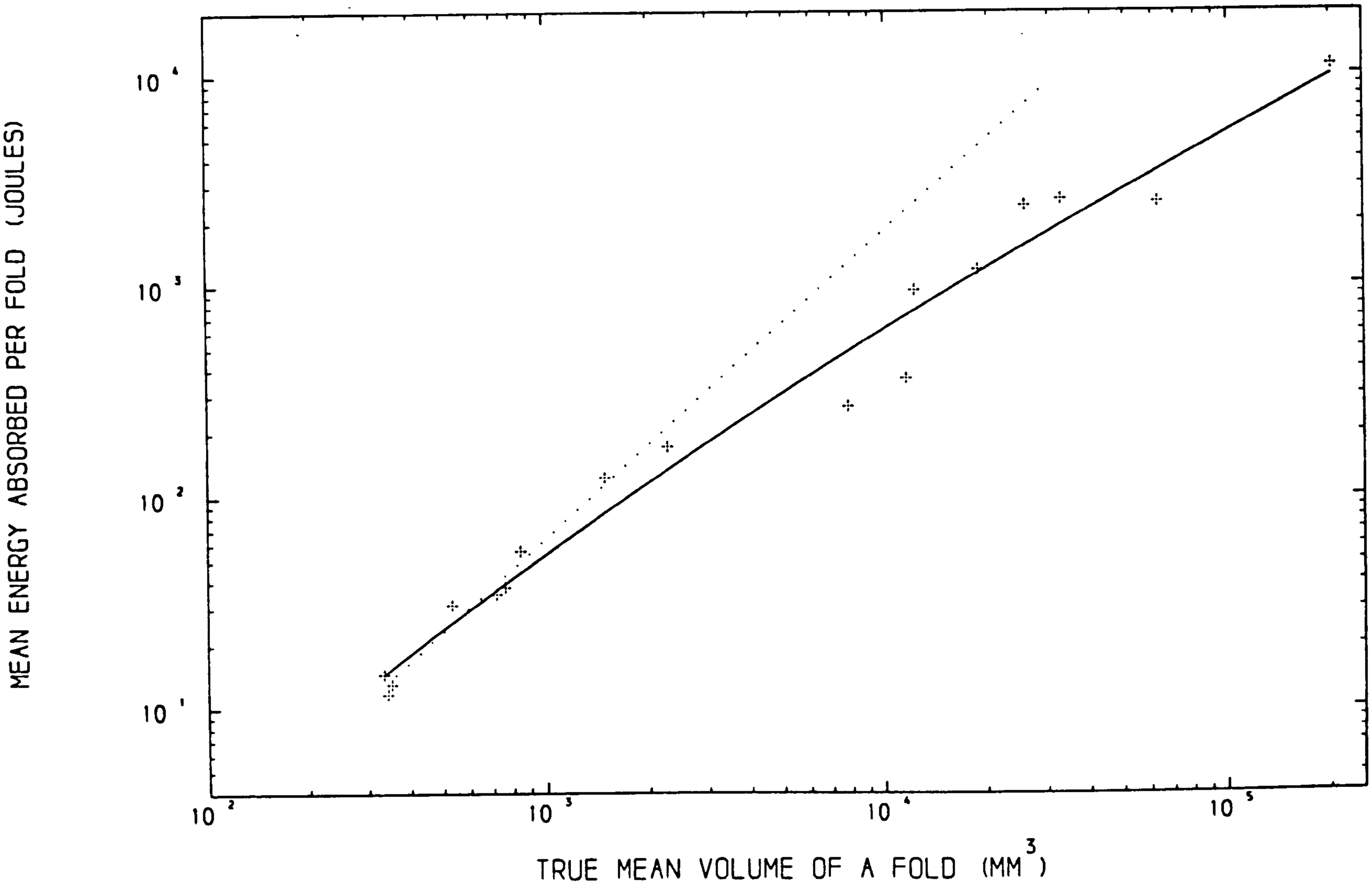
MEAN ENERGY ABSORBED PER FOLD (JOULES)
10 4
10 3
10 2
10 1
10 2
10 3
10 4
10 5
TRUE MEAN VOLUME OF A FOLD (MM 3)
CONCERTINA MECHANISM OF COLLAPSE

**Figure 4.8**

same level of regularity in pattern as those obtained for the concertina mode. To this end, the energy computations per fold for the diamond mode are confined to the regular portion of the load-compression curve in each case, operating as before over an integral number of folds. The area recorded is shown schematically in Figure 4.9 for tubes failing in the mixed modes of collapse.

Figures 4.10 and 4.11 establish the trends obtained in Figures 4.1 and 4.3, for the diamond mechanism. The 2-lobe and the 3-lobe diamond folds are distinguished in these figures and it is concluded that they do not reveal any significant difference in energy absorption. An attempt was made to apply the 'mean energy index' to the 2-lobe crushing mode by evaluating, where possible, the specific area under the deformation curve in each case. However, because of the general lack of any marked salient features in the trend of these characteristic curves and the part simultaneous (as distinct from sequential) formation of these folds, as observed in Chapter 2, these recordings do not possess the same level of accuracy as that for diamond modes in Figures 4.10 and 4.11 . Their apparent tendency to be associated with higher energies is incidental (since crushing modes are unfavourable in design - see Chapter 2), so that these data points are not included in the regression process, and are plotted only for passing interest.

Only the nominal mean volumes of a fold are considered for the diamond mechanism. This is because of the complicated

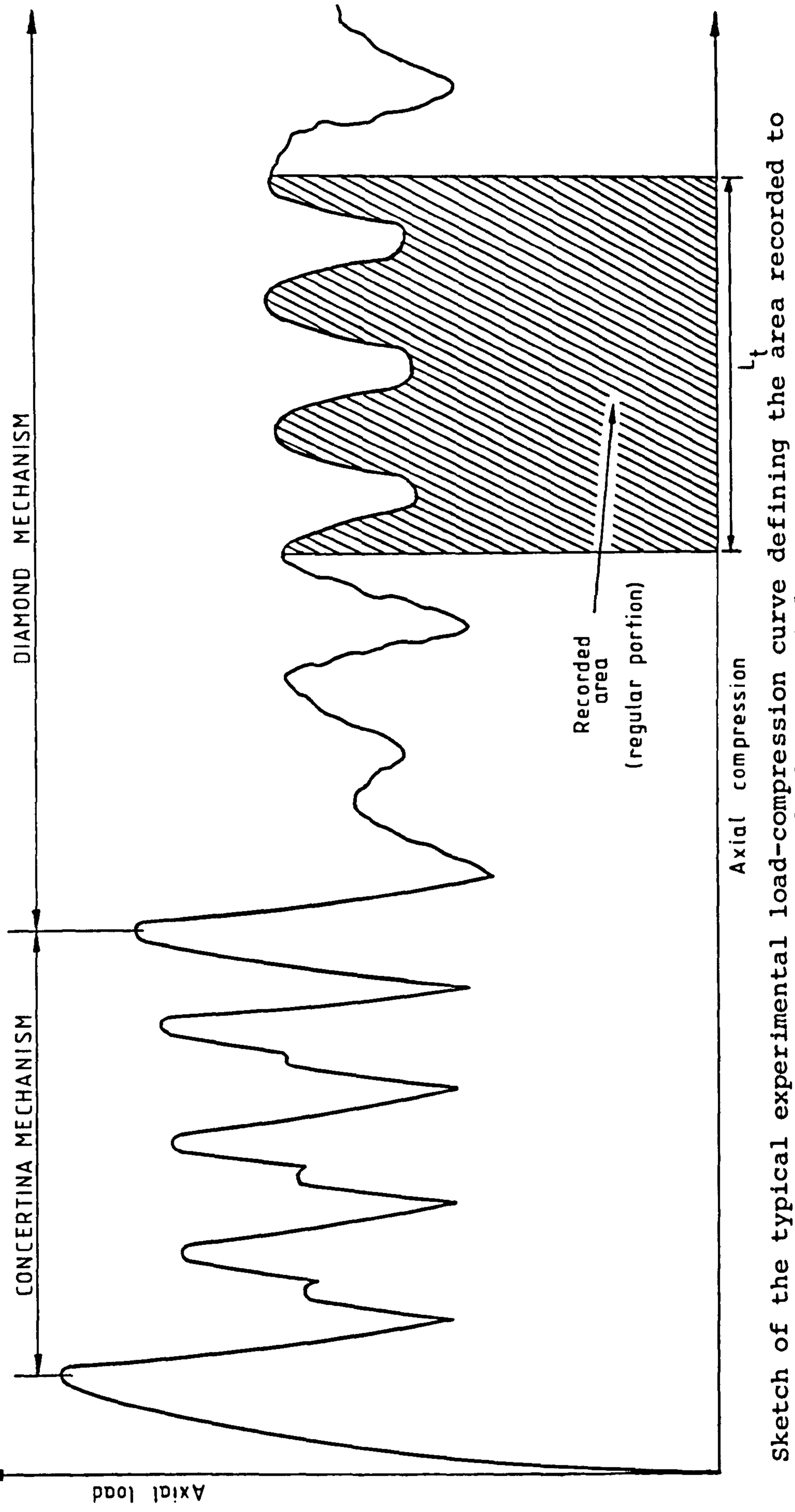


Sketch of the typical experimental load-compression curve defining the area recorded to obtain the diamond mean fold-energy index.

Figure 4.9

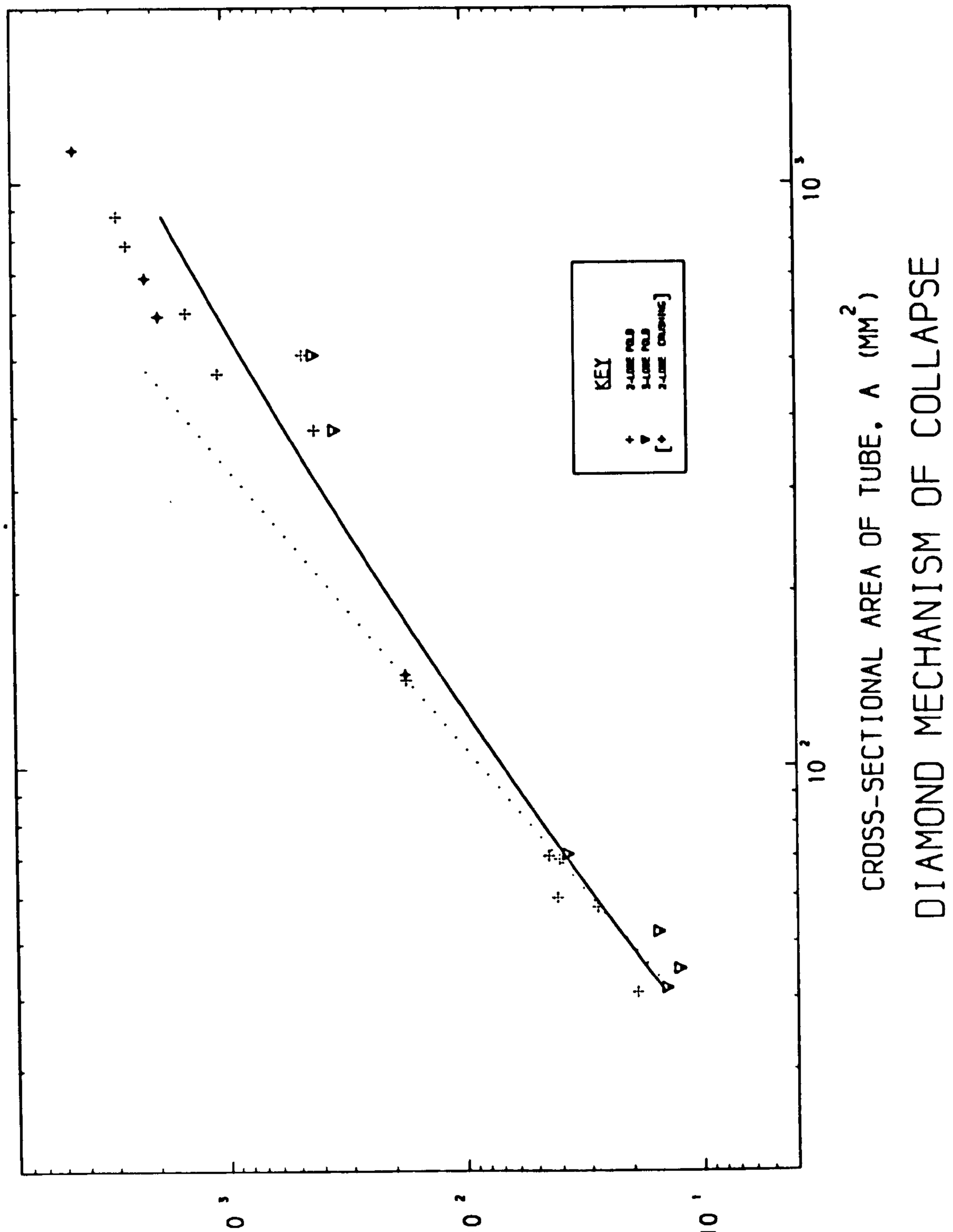


DIAMOND MECHANISM OF COLLAPSE

Figure 4.10

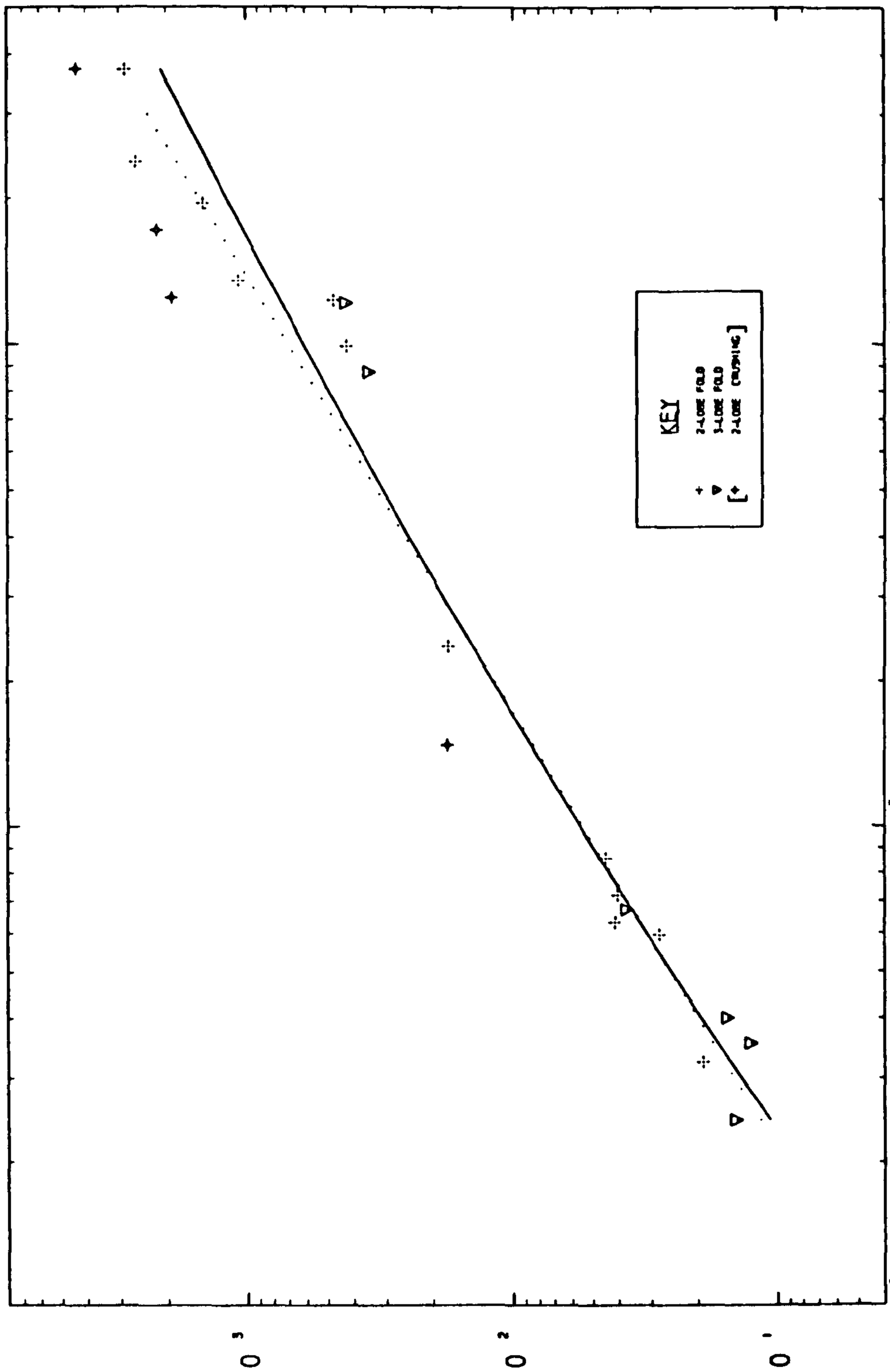
KEY
MEAN ENERGY ABSORBED PER FOLD (JOULES)
NOMINAL MEAN VOLUME OF A FOLD (MM³)
DIAMOND MECHANISM OF COLLAPSE

Figure 4.11

geometric configuration of folding. Whereas in the concertina mode a quantity of two thicknesses was added to the axial shortening for each fold in computation of the true mean fold volume, in the diamond mechanism any extra quantity to be added must encompass not only the wall thickness correction term, but also the volume of the voids present within and between the lobes. Corrections have not been applied for this mechanism of collapse.

## 4.4 Eulerian Mechanism

A new 'energy index' is introduced to describe the relation between absorbed energy and tube geometry for this mode of collapse. This parameter is chosen to denote the energy absorbed up to the peak load applied and the initiation of buckling, when the tube fails in this manner. Hence the index represents the maximum energy absorbed by a tube in deformation without any large-scale change from its original cylindrical configuration. Figure 4.12 indicates schematically the relevant area under the load-compression curve integrated in each test to obtain the above energy. (The peak load here provides the only salient point ('datum') on the curve for measuring areas under it to define an 'energy index'; otherwise, in order to obtain the total energy absorbed, it is necessary to define an arbitrary point, as reference ,on the continuously declining portion of the curve).

Figure 4.13 shows the relationship between this energy and the net section area of the tubes tested. It is realised

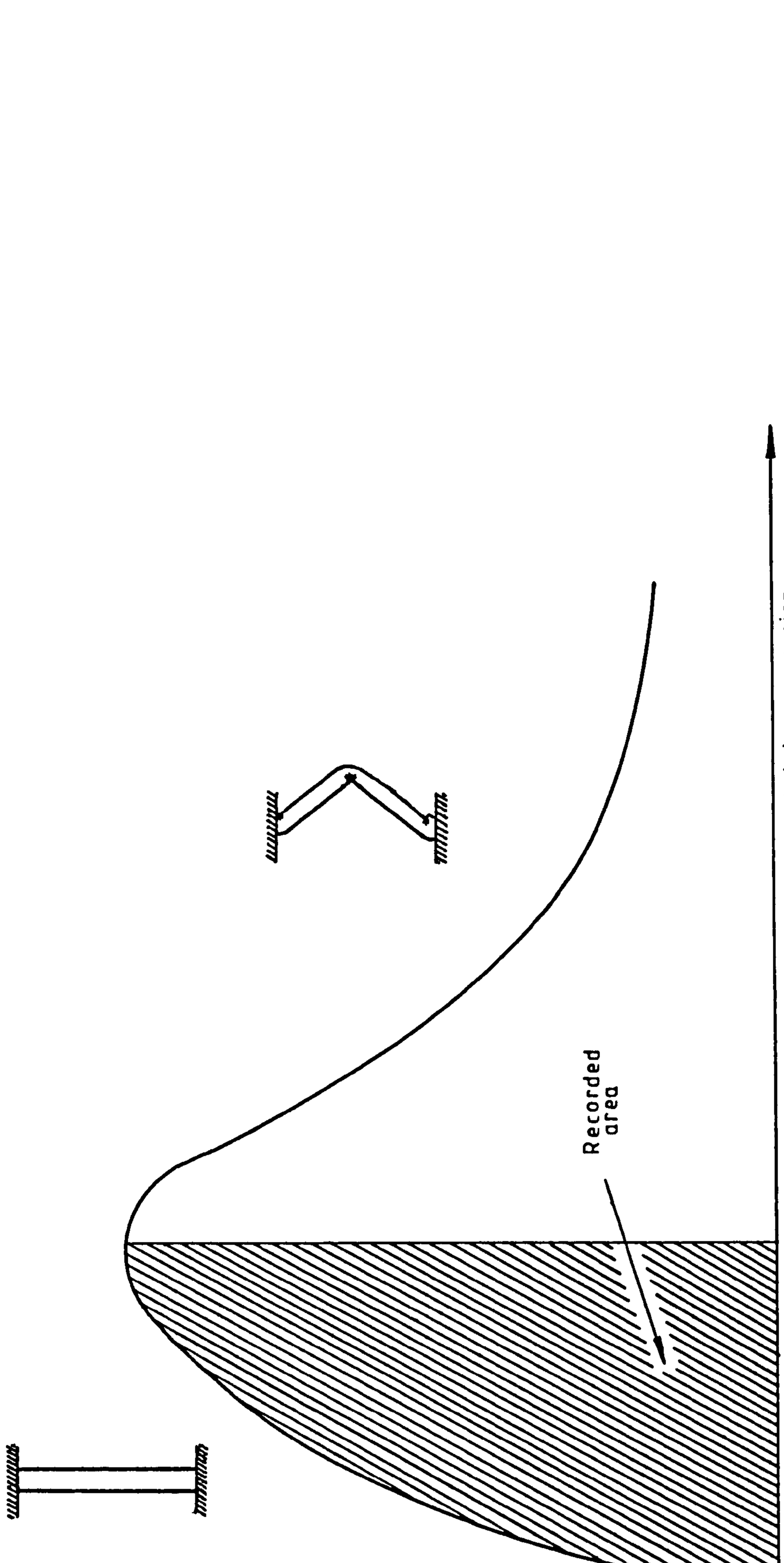


Sketch of the typical experimental load-compression curve defining the area recorded for the energy index in the Eulerian mechanism of collapse

Figure 4.12

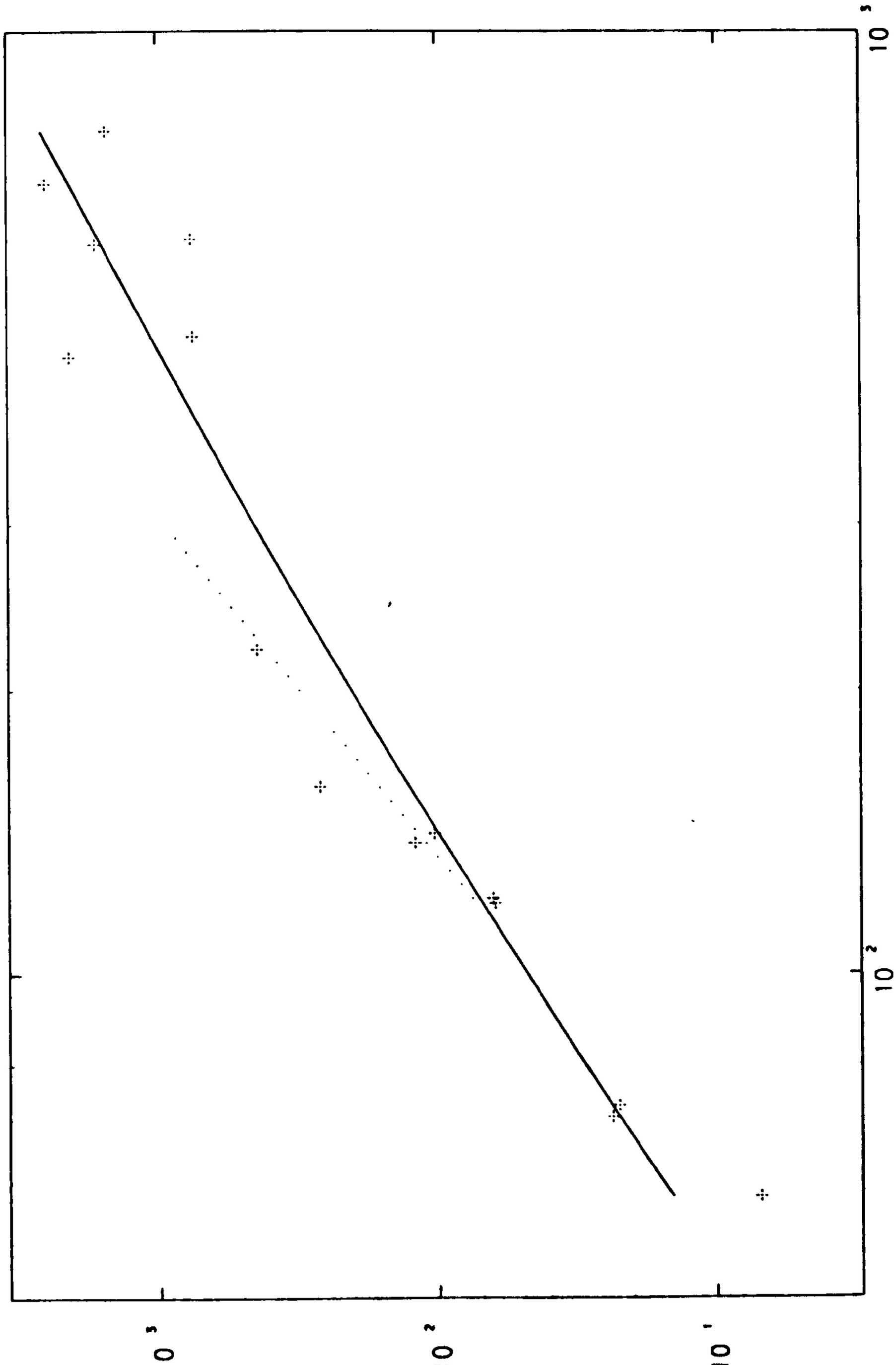
EULERIAN MECHANISM OF COLLAPSE
CROSS-SECTIONAL AREA OF TUBE, A (MM$^2$)
ENERGY ABSORBED UP TO PEAK / FAILURE LOAD (JOULES)
$10^{-1}$
$10^{0}$
$10^{1}$
$10^{2}$
$10^{3}$

**Figure 4.13**

that such a relationship has limited use in design since, as stated in Chapter 2 , the mechanism itself is associated with progressive catastrophic failure and does not possess a controlled feature like a sequential folding process at collapse, as in concertina or diamond modes. Furthermore, it is deduced that the length of a tube must have some bearing on the recorded energy for tubes of identical section geometry, this is consistent with Euler's theory for buckling of struts which relates the buckling load to the length of the strut.

Figure 4.13 does not, however, differentiate between tube lengths in the tests performed. This may account for the considerable spread in the recordings obtained. Due to the non-linearity of the problem, isolation of the length parameter in determination of its overall effect on the magnitude of the energy absorbed makes this problem one of complex nature. This may constitute a subject of further theoretical study with a possible power law relationship to be established for the proposed relationship of Figure 4.13, account having been taken of the effects of different tube lengths.

## 4.5 Numerical Results and Discussion

### 4.5.1 Summary of experimental regression results

The results of the linear and curvilinear regressions carried out for the energy relationships of Sections 4.2, 4.3 and 4.4 are collectively presented below;

Notation

$A$ = net section area of tube in $mm^2$

Notation (continued)

$V_{no}$ = nominal mean volume of a fold in $mm^3$

$V_{tr}$ = true mean volume of a fold in $mm^3$

$E_f$ = fold energy in Joules

Square root relationships apply to the complete range of tube geometry considered in each figure. Logarithms are in base 10.

Concertina mechanism

(a) First fold (Figures 4.1 & 4.3)

$$\log(E_f) = -2.5476 + 2.2515 \log(A) \quad \text{for} \quad A < 120 \text{ mm}^2$$

$$\log(E_f) = -4.8648 + 4.7384 [\log(A)]^{\frac{1}{2}} \qquad (4.5.1)$$

$$\log(E_f) = -2.6060 + 1.5255 \log(V_{no}) \quad \text{for} \quad V_{no} < 1000 \text{ mm}^3$$

$$\log(E_f) = -4.9098 + 3.8964 [\log(V_{no})]^{\frac{1}{2}} \qquad (4.5.2)$$

(b) Mean of fold energies over a set of folds (Figures 4.5, 4.6 & 4.8)

$$\log(E_f) = -2.8537 + 2.4215 \log(A) \quad \text{for} \quad A < 120 \text{ mm}^2$$

$$\log(E_f) = -4.8533 + 4.7267 [\log(A)]^{\frac{1}{2}} \qquad (4.5.3)$$

$$\log(E_f) = -2.5715 + 1.5087 \log(V_{no}) \quad \text{for} \quad V_{no} < 1000 \text{ mm}^3$$

$$\log(E_f) = -4.9077 + 3.8935 [\log(V_{no})]^{\frac{1}{2}} \qquad (4.5.4)$$

$$\log(E_f) = -2.5512 + 1.4535 \log(V_{tr}) \quad \text{for} \quad V_{tr} < 1000 \text{ mm}^3$$

$$\log(E_f) = -5.0965 + 3.9443 [\log(V_{tr})]^{\frac{1}{2}} \qquad (4.5.5)$$

Diamond mechanism

Mean of fold energies over a set of folds (Figures 4.10 & 4.11)

$$\log(E_f) = -2.1696 + 2.5032 \log(A) \quad \text{for} \quad A < 150 \text{ mm}^2$$

$$\log(E_f) = -4.8063 + 4.7039 \left[\log(A)\right]^{\frac{1}{2}} \qquad (4.5.6)$$

$$\log(E_f) = -1.5690 + 1.1038 \log(V_{no}) \quad \text{for} \quad V_{no} < 1000 \text{ mm}^3$$

$$\log(E_f) = -4.9535 + 3.8709 \left[\log(V_{no})\right]^{\frac{1}{2}} \qquad (4.5.7)$$

Eulerian mechanism

Energy absorbed up to the point of axial buckling, $E_u$ (Figure 4.13)

$$\log(E_u) = -3.8527 + 2.7563 \log(A) \quad \text{for} \quad A < 120 \text{ mm}^2$$

$$\log(E_u) = -6.8336 + 6.0256 \left[\log(A)\right]^{\frac{1}{2}} \qquad (4.5.8)$$

## 4.5.2 Discussion and relative comparison of energy absorptions for different collapse modes

It was suggested in Section 4.2 that because of the high axial load initially required to trigger failure in the concertina mode, the energy absorbed in formation of the first fold for a given tube would be expected to be higher than the mean of energies per fold over a number of them. The comparison is made below by considering the relevant curvilinear equations. First, equations (4.5.1) and (4.5.3) are rewritten as follows:

$$E_f \text{ (first fold)} = 1.365 \times 10^{-5} \times 10^{4.7384 \left[\log(A)\right]^{\frac{1}{2}}}$$

$$E_f \text{ (mean)} = 1.402 \times 10^{-5} \times 10^{4.7267 \left[\log(A)\right]^{\frac{1}{2}}} \qquad (4.5.9)$$

In the light of the expected trend we require to inspect the following inequality from (4.5.9) :

$$\frac{E_f \text{ (first fold)}}{E_f \text{ (mean)}} = 0.974 \times 10^{0.0117[\log(A)]^{\frac{1}{2}}} \rangle 1 \qquad (4.5.10)$$

The above expression is equal to unity when

$\log(A) = 0.9661$ i.e. $A = 9.25\ mm^2$

Hence for all section areas, $A \rangle 10\ mm^2$ (and observing the much higher test range of areas considered) the expected trend has been verified. For the energy-volume relationships obtained, curvilinear equations (4.5.2) and (4.5.4) both based on nominal volumes may be compared in similar fashion. Manipulation reveals that for all fold volumes $V_{no} \rangle 3.5\ mm^3$ (an essentially hypothetical figure for this mechanism), a higher absorbed energy is associated with the first fold further confirming the above trend.

Next, comparison is made between concertina and diamond modes for the mean energies absorbed per axial fold ($E_m$). Since the mean tube length per fold ($L_m$) differs for the two modes (see Tables A1.5 & A1.6, App. I), the author was interested to obtain and compare the values of the $E_m/L_m$ ratio. Table 4.1 shows the results obtained indicating the absence of a trend for this ratio from one mode of collapse to another. Reverting to the curvilinear relationships obtained in Section 4.5.1, equations (4.5.3) and (4.5.6) combine to indicate that for all $A \langle 17760\ mm^2$, a figure outside the test range studied, the diamond mode absorbs more energy per fold than the concertina. This is surprising in view of the findings in

Comparison of mean fold energies absorbed per fold length for concertina and diamond mechanisms

Notation

$L_m$ = mean shortening of tube per fold (see Tables A1.5 & A1.6, Appendix I)

$E_m$ = mean energy absorbed per fold (see Tables A1.5 & A1.6, Appndx I - $E_m = E_{mean}$)

| Tube Set | Concertina Mechanism | | | Diamond Mechanism * | | | |
|---|---|---|---|---|---|---|---|
| | $L_m$ (mm) | $E_m$ (Joules) | $E_m / L_m$ (Joules/mm) | $L_m$ (mm) | $E_m$ (Joules) | $E_m / L_m$ (Joules/mm) | |
| 4 in. (D') X 16 SWG (t) | 19.53 | 360.5 | 18.46 | 24.12 | 473.4 | 19.63 | |
| | | | | 23.80 | 424.0 | 17.82 | (3-lobe) |
| 3 in. (D') X 16 SWG (t) | 17.33 | 268.3 | 15.48 | 26.01 | 423.4 | 16.28 | |
| | | | | 22.95 | 348.6 | 15.19 | (3-lobe) |
| 1 in. (D') X 1/32 in. (nom. t) | 6.37 | 13.2 | 2.07 | 10.40 | 28.2 | 2.71 | |
| | | | | 7.68 | 15.5 | 2.02 | (3-lobe) |
| 1.5 in. (D') X 18 SWG (t) | 13.83 | 174.4 | 12.61 | 16.82 | 177.2 | 10.54 | |
| 0.75 in. (D) X 0.5 mm (nom. t) | 6.67 | 14.7 | 2.20 | 7.92 | 19.2 | 2.42 | |
| | | | | 5.91 | 14.3 | 2.42 | (3-lobe) |
| 1 in. (D') X 20 SWG (t) | 8.36 | 35.3 | 4.22 | 12.22 | 45.3 | 3.71 | |
| 1 in. (D') X 1 mm (nom. t) | 8.72 | 38.1 | 4.37 | 10.38 | 40.9 | 3.94 | |
| | | | | 9.51 | 37.5 | 3.94 | (3-lobe) |
| 0.75 in. (D) X 0.75 mm (nom t) | 7.15 | 31.4 | 4.39 | 10.59 | 41.7 | 3.94 | |
| 2.5 in. (D') X 0.125 in. (t) | 24.81 | 1184.9 | 47.76 | 32.41 | 1460.0 | 45.05 | |
| 2 in. (D') X 0.125 in. (t) | 19.47 | 945.2 | 48.55 | 28.48 | 1076.6 | 37.80 | |
| 2.5 in. (D') X 3/16 in. (t) | 29.72 | 2550.7 | 85.82 | 42.17 | 2859.6 | 67.81 | |
| 2.25 in. (D') X 3/16 in. (t) | 26.43 | 2382.2 | 90.13 | 30.33 | 2608.3 | 86.00 | |

*2-lobe diamond, unless otherwise indicated

Table 4.1

Chapter 3 regarding 'specific energy absorption' which favoured the latter mode. However, at discrete values in the experimental range of tube section areas, A, the respective energies per fold have been evaluated from the relevant curvilinear equations and their ratios are found to indicate that, despite the high value of A at which transition occurs from one mode in favour of the other, the relative differences in energy are small. These results are presented in Table 4.2 indicating the decreasing significance of this energy difference (by an increase in the energy ratio), as A is increased.

Extending the comparison to the more important energy-volume relationships, equations (4.5.4) and (4.5.7) are next considered. However ,because of the numerical values of the regression constants in these equations a rigorous mathematical manipulation cannot be made here since an undefined expression (a negative logarithm) will be encountered. Hence ,again a set of discrete points within the experimental ranges are considered and from the above equations the respective energies are evaluated and compared at these points. These results are shown in Table 4.3 and collectively associate the concertina mode with higher dissipation of energy within the range considered.

The above energy comparison is based on nominal fold volumes and it was noted in Section 4.3 that, for a given tube, the difference between the nominal mean and true mean volume of a fold is more appreciable for collapse in the diamond mode than in the concertina mode This sheds further light on the observed trend in the above comparison, further favouring the concertina mode in higher absorption of energy.

PAGE NUMBERING AS IN THE ORIGINAL THESIS

Comparison of energy absorption capacities for concertina and diamond mechanisms of collapse at discrete values of tube geometry

Notation

$A$ = net section area of tube

$V_{no}$ = nominal mean volume of a fold

$E_c$ = mean energy absorbed per concertina fold

$E_d$ = mean energy absorbed per diamond fold

| $A$ ($mm^2$) | $E_c$ equation (4.5.3) (Joules) | $E_d$ equation (4.5.6) (Joules) | Ratio $E_c/E_d$ |
|---|---|---|---|
| 50 | 20.31 | 21.13 | 0.961 |
| 100 | 67.81 | 70.15 | 0.967 |
| 200 | 207.35 | 213.36 | 0.972 |
| 500 | 816.54 | 834.68 | 0.978 |
| 1000 | 2155.68 | 2193.28 | 0.983 |
| 1500 | 3719.05 | 3773.97 | 0.985 |
| 2000 | 5426.46 | 5496.57 | 0.987 |

Table 4.2

| $V_{no}$ ($mm^3$) | $E_c$ equation (4.5.4) (Joules) | $E_d$ equation (4.5.7) (Joules) | Ratio $E_c/E_d$ |
|---|---|---|---|
| 200 | 9.96 | 8.29 | 1.202 |
| 500 | 30.81 | 25.46 | 1.210 |
| 1000 | 68.56 | 56.38 | 1.216 |
| 5000 | 380.68 | 309.95 | 1.228 |
| 10000 | 757.36 | 614.19 | 1.233 |
| 50000 | 3406.29 | 2738.37 | 1.244 |
| 100000 | 6286.81 | 5036.11 | 1.248 |

Table 4.3

chapter are assumed, for mathematical simplicity, to follow square-root functions. In essence, the true relationships are predicted to be in the form of power series, so that the functions assumed here provide a guidance in the relative ranking of tube geometry and mode of axial collapse for energy absorption.

## 4.6 Conclusion

1. The introduction of 'fold energy indices' provides a direct method of relating energy absorption (in Joules) to dimensions of a tube. This is in contrast to specific energy absorption (see Chapter 3) which (measured in units of length) is a function of tube geometric ratio, t/D'.

2. The empirical nature of the relationships introduced is recognized. However, comparison of relative energies indicate that the concertina mode dissipates the greatest amount of energy per unit volume of tube material.

3. [illegible]

# CHAPTER 5

## ANALYSIS OF THE THEORY BY J.M. ALEXANDER ON CONCERTINA MECHANISM OF COLLAPSE

# Chapter 5 - Synopsis

A rigid-plastic theory for the concertina collapse mechanism of cylindrical tubes is reviewed and investigated. Discrepancies are noticed in predictions of material yield stress from this theory with observed test results. Inspection reveals, in particular, the significance of omission of strain hardening, which is a distinct feature of the annealed aluminium tested. For a work hardening material, the theory thus underestimates the internal work done at collapse.

Subsequent inclusion of strain hardening in the theory is shown to produce empirical solutions that are in better agreement with the test data. The theory is further modified by imposing the condition of material incompressibility during the formation of a concertina fold, and a new collapse model is introduced in an attempt to represent the post-buckling configuration. Results, though empirical, suggest the existence of a preferred configuration at collapse on the basis of a minimum internal work expended in its development.

## 5.1 Basis of Theory and Assumptions

In his approximate theory on the quasi-static axial failure of cylindrical shells in the concertina mechanism, Alexander (1) adopted the instability configuration represented in Figure 5.1(i). The assumptions made in this theory are as follows;

1. Material behaviour is rigid-plastic, so that elastic strains and work hardening effects are neglected.
2. The folding process occurs sequentially and fully externally, in relation to the original diameter of the tube.
3. Von Mises criterion governs the condition of yielding of the tube material.
4. Deformation of the tube in rotation at the fold hinges by an increment $d\theta$ proceeds 'under substantially plane strain conditions'.
5. Internal work done at collapse is the sum of the work done in bending at the fold hinges and that required in hoop extensions between & at these hinges. External work done is the product of the mean collapse load, $\overline{P}$ and the axial distance by which the tube shortens, which, for the complete formation of a fold is $2h$, where $h$ denotes the half-wavelength of a fold.

By equating internal and external work defined in assumption 5 for the complete development of a fold, Alexander derived the following expression relating $\overline{P}^{*}$ to material yield stress, Y and tube geometry.

$$\frac{\overline{P}}{Y} = \underset{\text{(axial)}}{\frac{\pi t^2}{\sqrt{3}}\left(\frac{\pi D}{2h} + 1\right)} + \underset{\text{(circumferential) work entities}}{\pi h t} \qquad (5.1.1)$$

and $\frac{d(\overline{P}/Y)}{dh} = 0$ gives,

---

*see, P.107 for definition

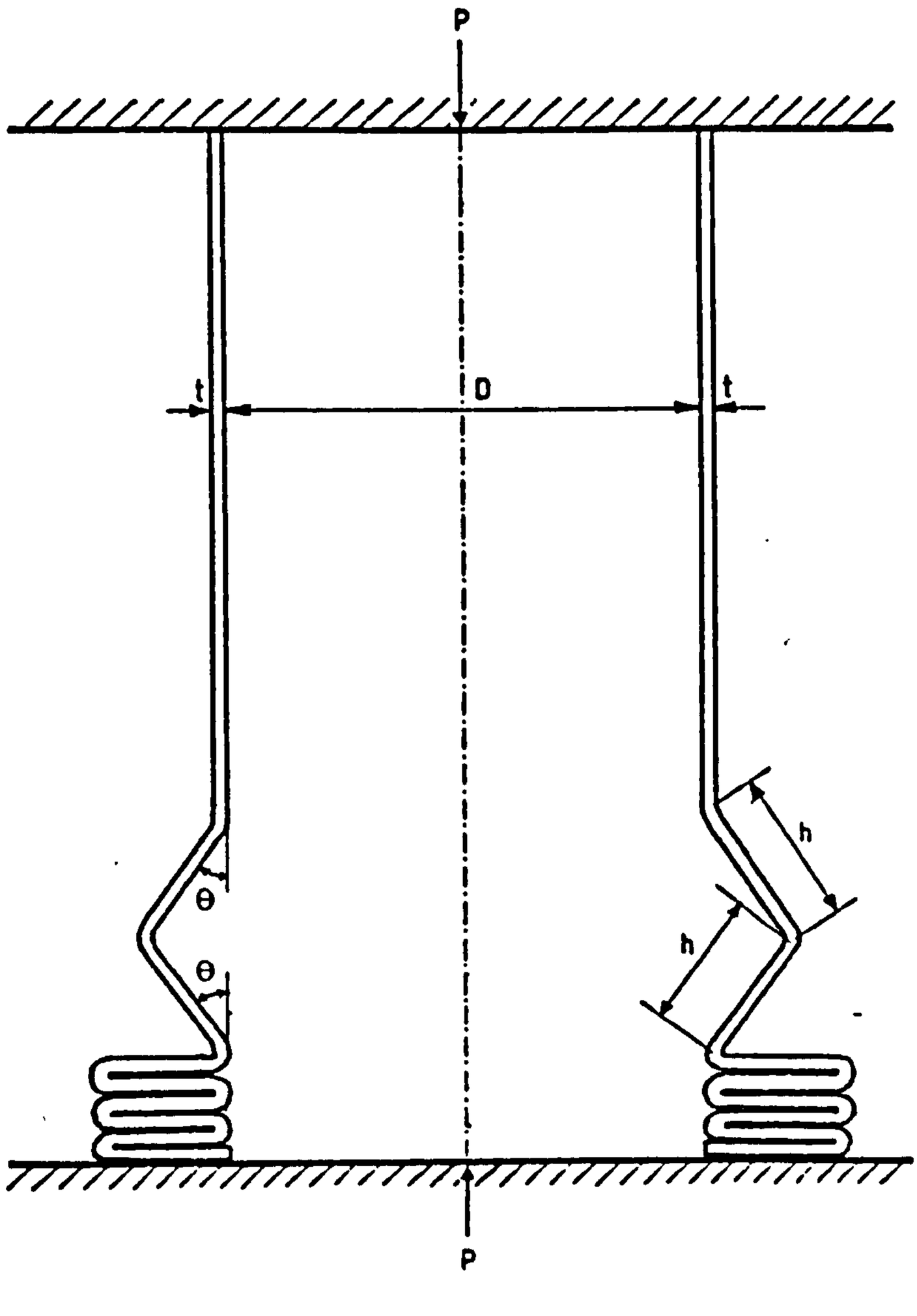


(i)

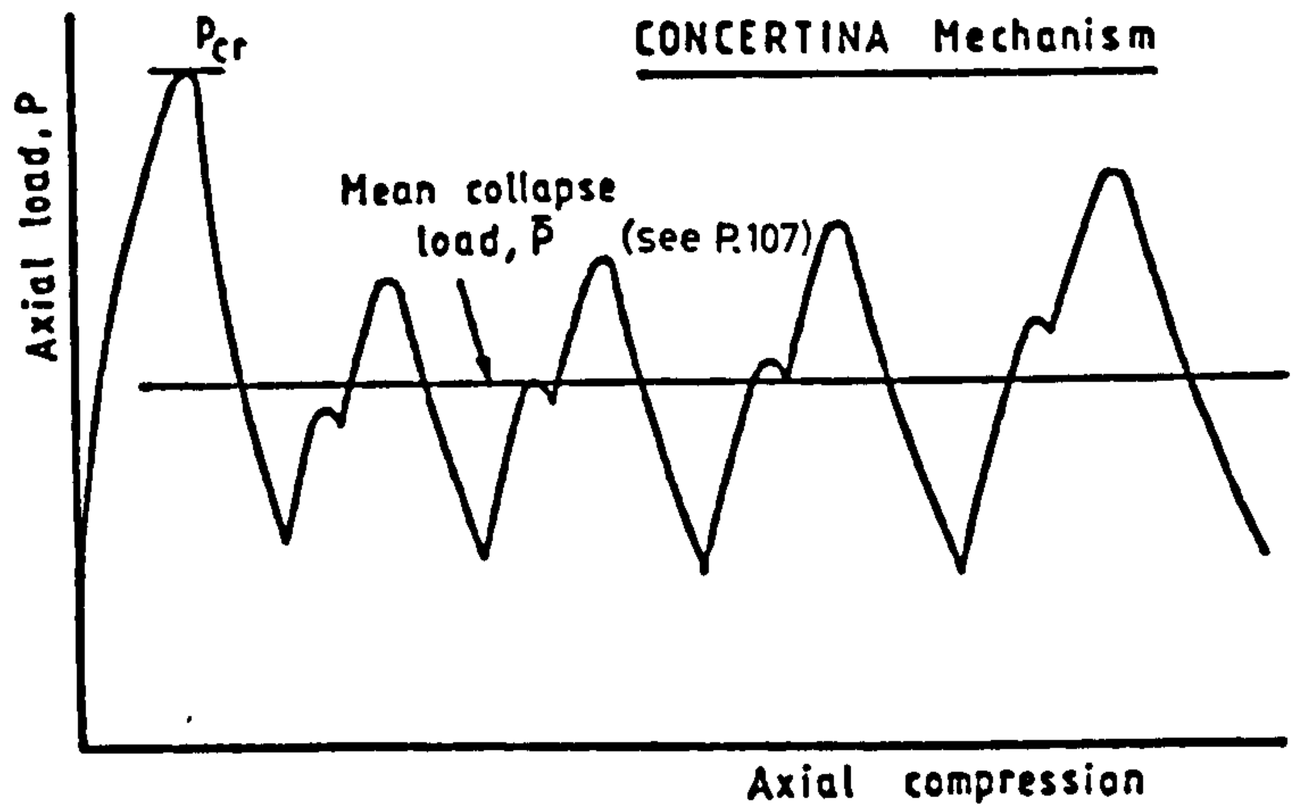


(ii)

Collapse model proposed by Alexander (1)

Figure 5.1

$$h = k\,(D\,t)^{\frac{1}{2}} \qquad \text{where} \quad k = \left(\frac{\pi}{2\sqrt{3}}\right)^{\frac{1}{2}} = 0.953 \qquad (5.1.2)$$

Substitution of the above expression for h into (5.1.1) gives,

$$\frac{\bar{P}}{Y} = \left(\frac{\pi^2}{2\sqrt{3}\,k} + \pi k\right) t^{1.5} D^{0.5} + \frac{\pi t^2}{\sqrt{3}} \qquad (5.1.3)$$

In the second part of the theory, by considering the case of full internal folding in contrast to assumption 2, Alexander derived the following expression;

$$\frac{\bar{P}}{Y} = \left(\frac{\pi^2}{2\sqrt{3}\,k} + \pi k\right) t^{1.5} D^{0.5} - \frac{\pi t^2}{\sqrt{3}} \qquad (5.1.4)$$

Observing that the true collapse configuration, in practice, is somewhere between the two extreme cases considerd, Alexander considered the mean of equations (5.1.3) and (5.1.4) in proposing the following relation.

$$\bar{P} = C\,Y\,t^{1.5}\,D^{0.5} \qquad \text{where} \quad C \simeq 6 \qquad (5.1.5)$$

## 5.2 Application to Experiment

For a given tube failing in the concertina mode, the geometric parameters D, t and h are fixed and the mean load $\bar{P}$ may be obtained experimentally from the axial load-compression curve, as indicated in Chapter 3 and shown in Figure 5.1 (ii). Hence equation (5.1.1) can provide, upon rearrangement, a theoretical value for the yield stress, Y for the material tested. This value may then be compared with that observed experimentally from a separate yield test on a tube specimen of the same annealed aluminium material.

This section presents the comparisons made in summarized form by indicating, as ranges, two sets of results for Y :

(a) those obtained from this theory using equation (5.1.1)

(b) those obtained from direct strain gauged tests, defined as 0.1% proof stress (see Figure (5.1(iii)).

The two ranges of results are as follows:

Equation (5.1.1) (theory) : $0.149 \leqslant Y \leqslant 0.200$ (KN/mm$^2$)
(for individual results see Table A2.1, Appendix II)

Direct yield test (experiment) : $0.032 \leqslant Y \leqslant 0.079$ (KN/mm$^2$)
(for individual results see Table A2.5, Appendix II)

(5.2.1)

The results obtained for direct yield tests on as-received (non-annealed) tubes fall in the range below:

$0.22 \leqslant Y \leqslant 0.29$ (KN/mm$^2$) (see Table A2.4, Appendix II)

The uniformity of the latter range as distinct from the annealed experimental range of (5.2.1) suggests that annealing may have caused local variations in material behaviour for stresses up to the yield; but as may be observed later in this section, the ultimate stress, reflected in the peak load an annealed tube can sustain prior to collapse, is independent of these variations at low magnitudes of stress. Nevertheless, in spite of the notable scatter within each of the two ranges in (5.2.1), the appreciable gap between the two sets of results

Determination of the compressive yield stress of annealed HT30-aluminium alloy tubing

Experimental load-strain curve obtained from strain gauge test on annealed tube specimen :

6 in.(L) x 0.75 in.(D) x 1.5 mm (nom.t)

$E = 34.17\ KN/mm^2$

$E_p = 2.05\ KN/mm^2$

Cross-section area, $A = 97.5\ mm^2$

Yield stress (as 0.1% proof stress) $Y = \frac{3.2}{A} = 0.0328\ KN/mm^2$

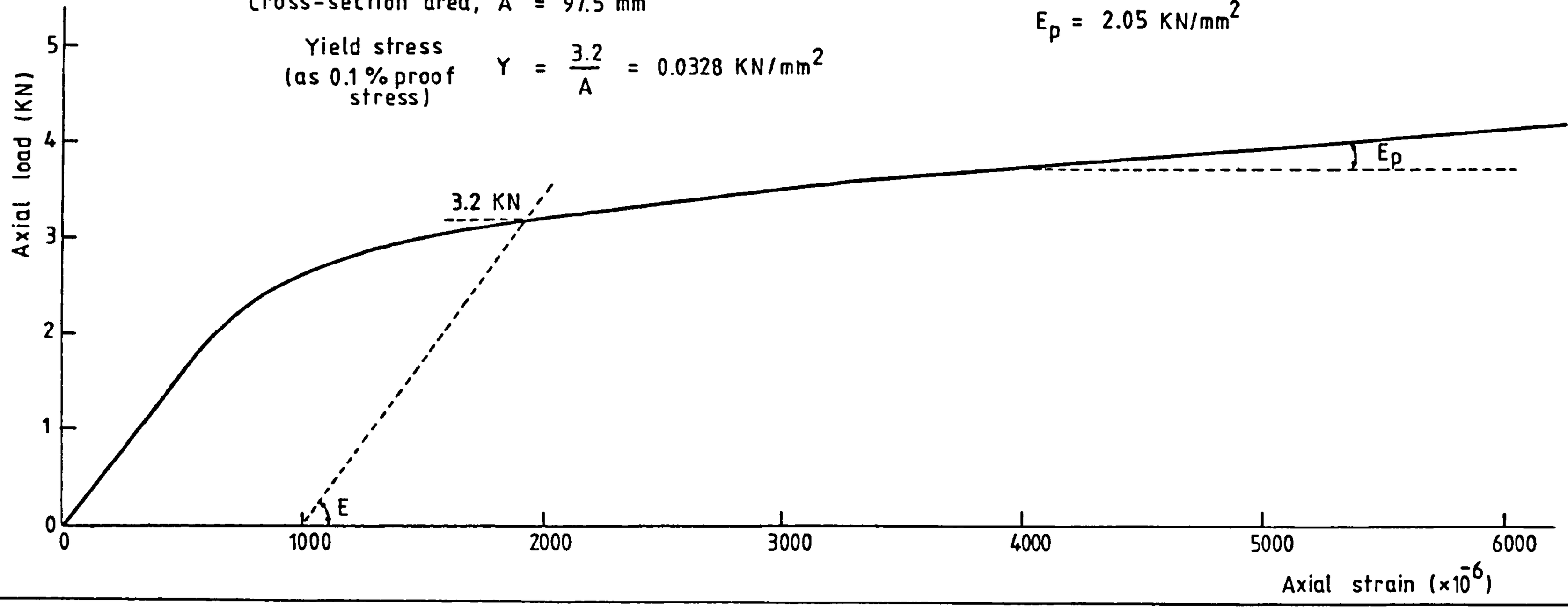


Illustration of the trend typically observed in annealed yield tests

Figure 5.1 (iii)

is clearly apparent.

Attempt has been made by the present author to determine the parameters within the theory associated with the above discrepancy. First, on a geometric note, Figure 5.2 inspects the relationship of equation (5.1.2) for the experimental data obtained for the arm-lengths of a fold, $h^*$ by performing a best-fit regression of the same general form as that of (5.1.2). The constant K is found to be 1.1334 in good agreement with theory. Parameter h has been calculated by the method introduced in Chapter 4 in the context of the true mean volume of a fold. It was shown that, as distinct from direct measurement, the mean fold geometry over a number of folds may be determined by means of the mean axial shortening of the tube over a fold (recorded from the load-compression curve) with a wall thickness correction term incorporated. The mean arm--length, h is thus one half of this mean axial shortening over a fold.

The scatter and deviation of the test data in Figure 5.2 from a smooth curve is deduced to be largely associated with the thickness, t of the different tubes tested. It is observed that for thick tubes the finite length of the tube at the hinges becomes significant. This is confirmed by those recordings in this figure in close agreement to Alexander's curve, which correspond to large diameter tubes, but with low geometric ratios of t/D (0.0165 and 0.0223)*; whereas for the thick tubes tested with high ratios of t/D (0.08 - 0.10), the recordings appear even above the experimental curve, suggesting a deviation

*Details of individual data points are presented in Table A2.2, Appendix II

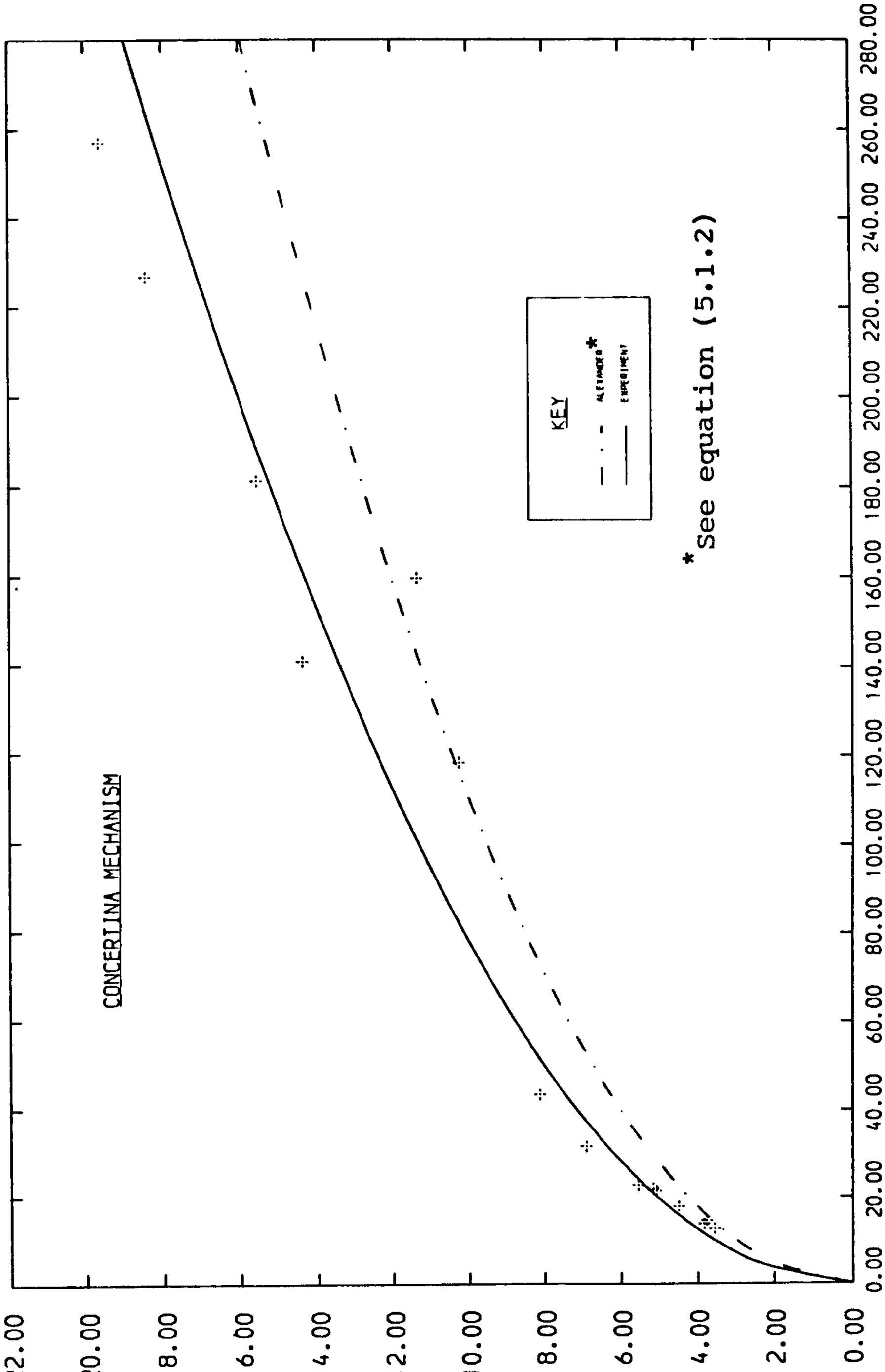
COMPARISON OF ALEXANDER'S THEORY WITH EXPERIMENT
CONCERTINA MECHANISM
PRODUCT D.T (MM²)
ARM-LENGTH OF A FOLD, H (MM)
0.00
20.00
40.00
60.00
80.00
100.00
120.00
140.00
160.00
180.00
200.00
220.00
240.00
260.00
280.00
22.00
20.00
18.00
16.00
14.00
12.00
10.00
8.00
6.00
4.00
2.00
0.00
KEY
ALEXANDER*
EXPERIMENT
*See equation (5.1.2)

Figure 5.2

from (5.1.2) for larger values of Dt. In the absence of exact definition of the arm-length h in the theory, it is apparent that this finite length has been neglected, so that ideally a family of curves is predicted to exist for the relationship of Figure 5.2 for different geometric ratios t/D. However, with the general trend of the experimental data obeying that of the theory and the good correlation obtained in the values of K in equation (5.1.2), it is realised that this equation and the minimization by which it is derived do not account for the discrepancy observed in (5.2.1) .

Examination of the validity of the assumptions used in the theory reveals assumption 4 to be incorrect; this is because for folding of an axially loaded tube, any local deviation from verticality during collapse (e.g. in deformation through angle $d\theta$ ) results in the development of hoop stresses acting in a direction perpendicular to that of the axial load, thus invalidating the condition of plane strain. This assumption was used together with assumption 3 in order to raise the yield parameter Y by a factor of $2/\sqrt{3}$ in evaluation of the internal work done in bending. However, as the right hand side of equation (5.1.1) is a function of the total internal work done, it is deduced that these assumptions cannot be responsible for the observed discrepancy in (5.2.1), as the elimination of the above multiplier would result in higher discrepancies.

Figure 5.3 inspects the experimental data obtained here* for the relationship of equation (5.1.5) by comparing two best-fit linear regressions, one through the origin as in the theory

*Details are presented in Table A2.1, Appendix II

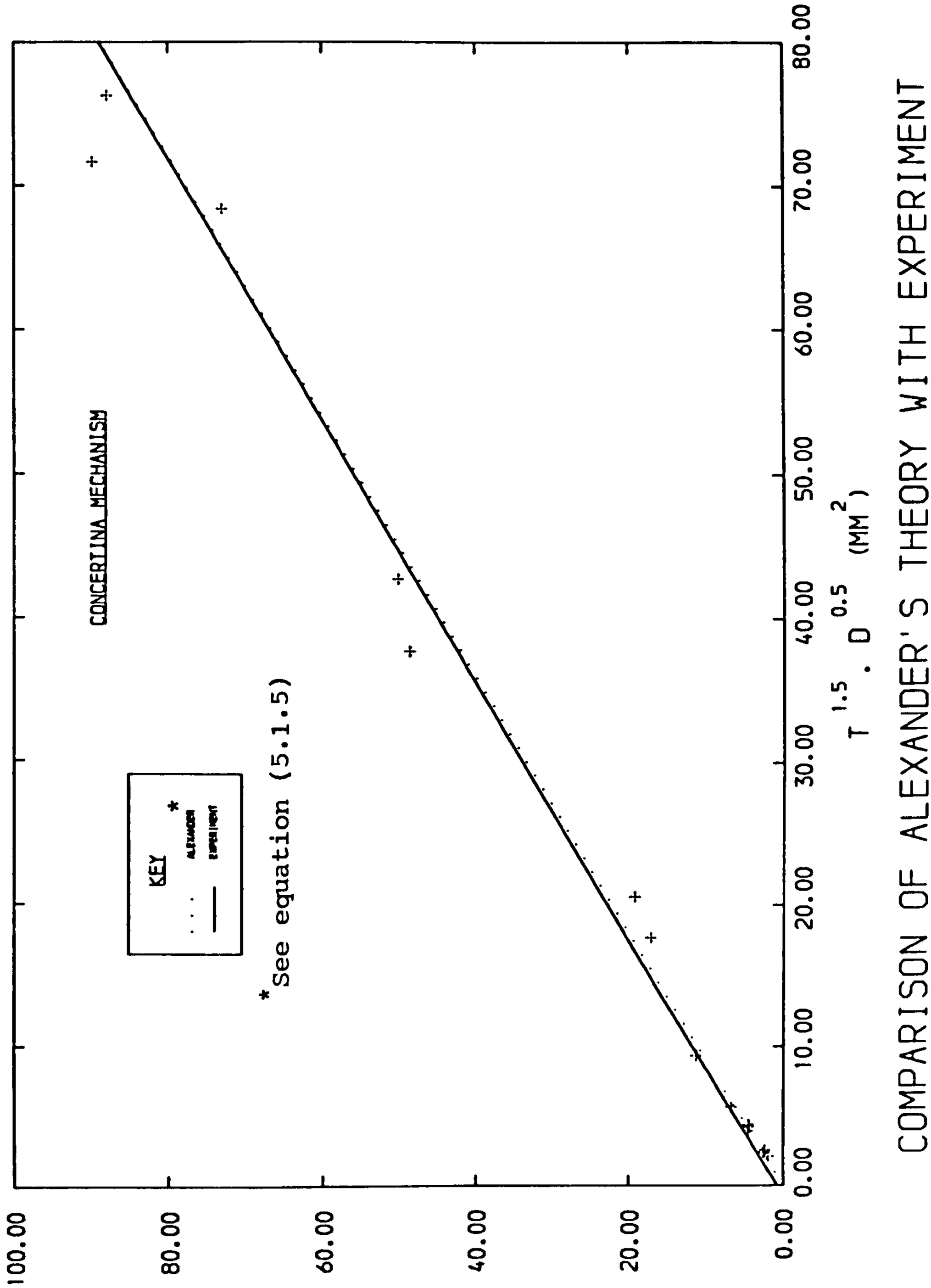
COMPARISON OF ALEXANDER'S THEORY WITH EXPERIMENT
CONCERTINA MECHANISM
KEY
ALEXANDER
EXPERIMENT
*See equation (5.1.5)
MEAN COLLAPSE LOAD, $\bar{P}$ (KN)
$T^{1.5} \cdot D^{0.5}$ ($MM^2$)
0.00
10.00
20.00
30.00
40.00
50.00
60.00
70.00
80.00
100.00
80.00
60.00
40.00
20.00
0.00

Figure 5.3

and the other of the more general form, $y = ax + b$ . The constants of these regressions are found from Figure 5.3 to be:

$$\bar{P} = 1.1103\ t^{1.5} D^{0.5} \qquad (5.2.2)$$

$$\bar{P} = 0.828 + 1.1019\ t^{1.5} D^{0.5} \quad \text{(experiment)}$$

In view of the scatter of test data, the apparently excellent correlation is deduced to be fortuitous. Furthermore, by dividing the gradients of these graphs by the suggested value of $C = 6$ in equation (5.1.5), a mean value of $Y = 0.184$ KN/mm$^2$ is found which is in the theoretical range of $Y$ in (5.2.1) thus disclosing the same previous discrepancy. Figure 5.3 therefore confirms only the form of the proposed relation of equation (5.1.5) .

The results shown project an inconsistency which is in part attributable to the presence of strain hardening for the aluminium material tested . However, in order to check the validity of the criteria on which the internal work is based in assumption 5, an axial test has been performed on a single annealed tube with dimensions : 151 mm (L) X 57.2 mm (D) X 3.175 mm (t)*, in which a regular pattern of slots were cut through the wall prior to testing so as to minimize the development of hoop stresses during collapse. This was done in order to reduce to a minimum the internal work done in hoop stretching (and compression) of the material between & at the hinges, since as already indicated, the folding process is not wholly external, thus resulting also in compressive hoop stresses. Details of the pattern of the drilled holes are shown in Figure 5.4 . Plate 5.1 indicates the various stages

*This tube corresponds to the unpierced 6 in.(L) tube in the test series of Table 2.9 (Ch.2,P.75) shown in Plate 2.9,P.87

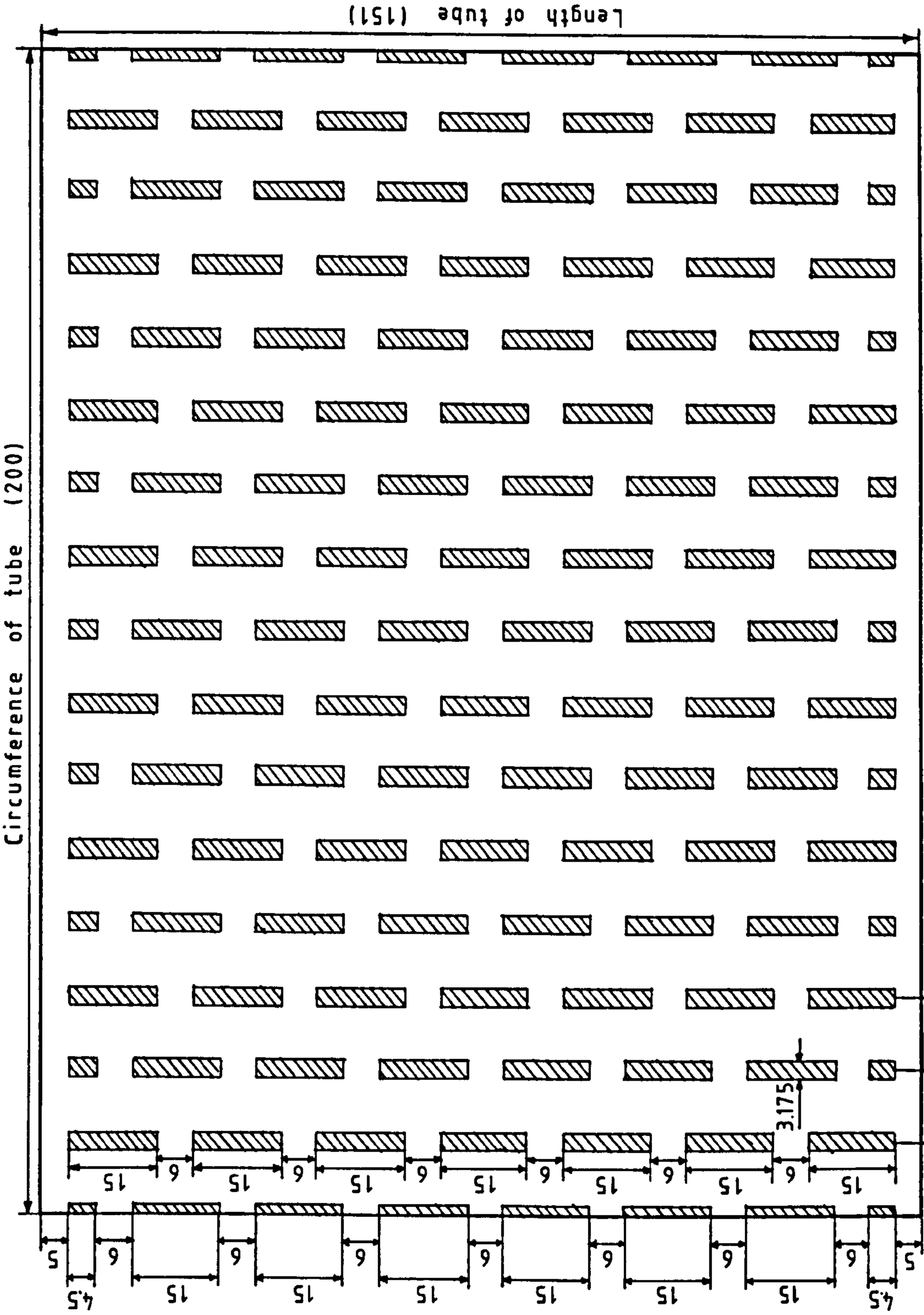


Pattern and dimensions of slots cut in a tube prior to its collapse in axial compression
(Actual shape of each slot has semi-circular ends)
(Dimensions in mm)
Figure 5.4

during collapse of this tube from its original cylindrical shape. The pattern of the holes drilled did not extend to the ends of the tube. This was chosen to ensure collapse, in an axisymmetric manner - in the concertina mode - as in the corresponding unpierced tube (see tube with L = 6 in. in the test series of Table 2.9, P.75). The identical collapsed shape of the above pierced tube with the equivalent unpierced tube may be inspected by comparing Plate 5.1 with Plate 2.9, P.87 (5th tube from right). A mean value of $\bar{P}$ = 22.5 KN has been obtained in this test; (c.f. $\bar{P}$ = 50.1 KN in the corresponding unpierced test series, as shown in Table A2.1, P.346).

In applying theory (1) to determine the internal work done (IWD) in bending at the hinges for this tube, account has been taken of the volume of voids by multiplying the IWD in bending for one fold for the otherwise intact tube by the volume factor $(1 - \frac{V_v}{V_T})$ where $V_v$ denotes the volume of voids and $V_T$ the total net volume of the tube. Although some residual internal work must have been expended in circumferential deformations between the hinges, this is neglected, particularly in view of the fact that no tearing (or squashing by closing-in) of the holes took place indicating the suitability of the width of the holes drilled. Hence for the test carried out, equation (5.1.1) takes the following modified form:

$$\frac{\bar{P}}{Y} = \frac{\pi t^2}{\sqrt{3}} \left( \frac{\pi D}{2h} + 1 \right) \left( 1 - \frac{V_v}{V_T} \right) \qquad (5.2.3)$$

Using equation (5.2.3), a value of $Y = 0.188$ KN/mm$^2$ has been obtained which is in the same previous theoretical range and

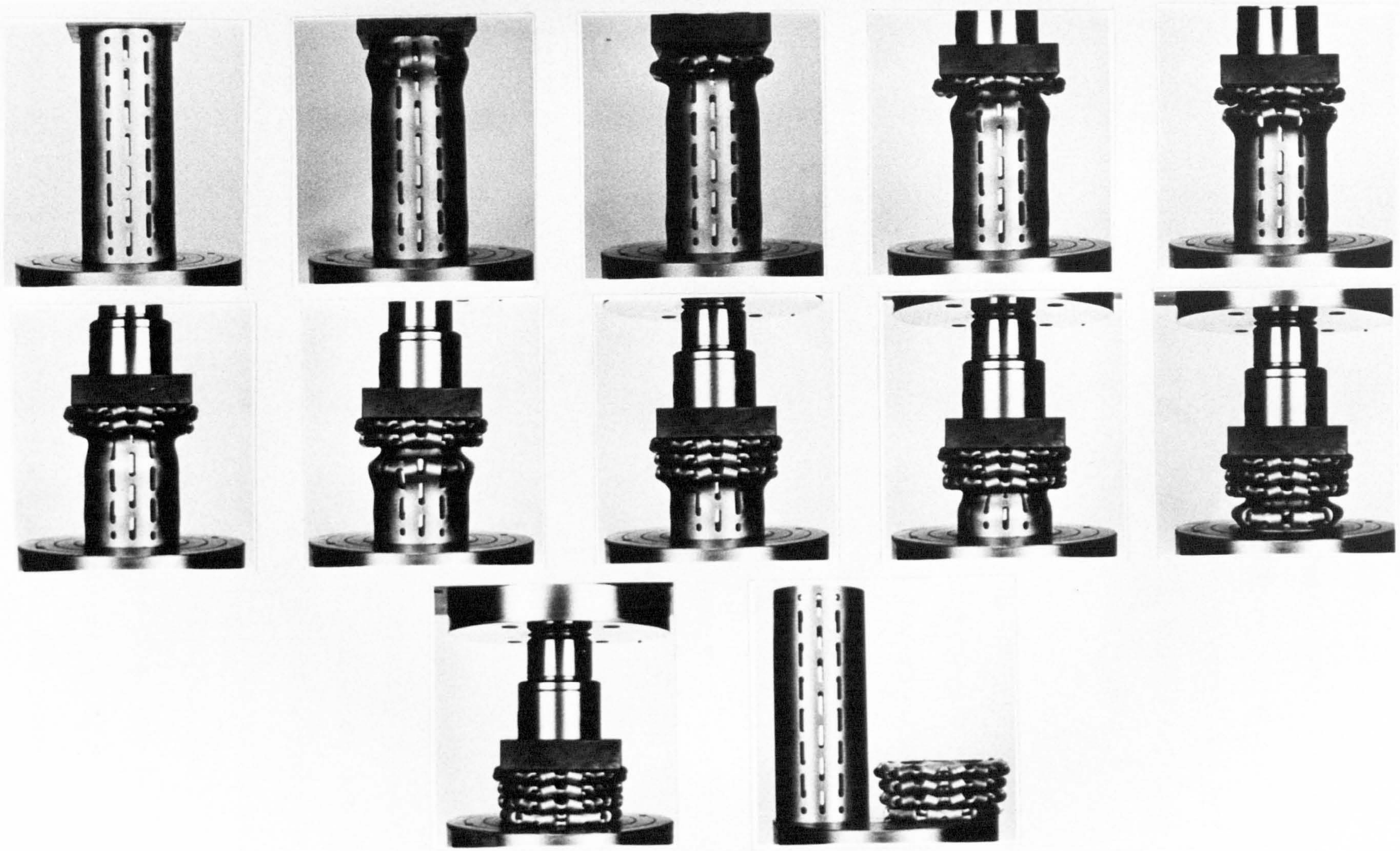

Plate 5.1 Deformation stages of the single drilled tube in axial compression

in conflict with the experimental range of (5.2.1). The test therefore confirms the entities in Alexander's theory constituting the internal and external work done, as defined in assumption 5. The observed discrepancy raises further scepticism about the applicability of the theory to a material such as the aluminium tested, in which work hardening is a prominent feature, as seen in Figure 5.1(iii).

It is concluded from inspection of the form of equation (5.1.1) that neglect of strain hardening in the theory is the key factor responsible for the discrepancies obtained between the two ranges for yield stress $Y$ in (5.2.1). For a work hardening material, the theory thus underestimates the internal work expended in bending and stretching of the tube, since the stresses beyond yielding of the material are not constant as have been assumed. This is reflected in the trend of equation (5.1.1); As the magnitude of the right hand side of this equation (a function of internal work) is raised by incorporating strain hardening, then $Y$ would have to be reduced (for work equilibrium) for the same external work done. This would have the effect of reducing the gap observed in the ranges for $Y$ in (5.2.1). It cannot be argued that this discrepancy is due to the fully external folding model chosen in derivation of equation (5.1.1), since inspection of equations (5.1.3) and (5.1.4) reveals that maximum internal work is associated with this model, so that any alteration to the model in this theory would result in even higher inconsistencies between the two ranges for parameter $Y$.

The above deduction that strain hardening must be accounted for in this theory for general experimental applicability of this theory is shared to some extent in the single criticism of this theory the present author encountered in Reference 98; It is suggested that the term yield stress Y should be replaced by $Y_u$, the ultimate stress of the material. But the suggestion on its own is observed to fall short of modifying the rigid-plastic model introduced in the theory, since for this material behaviour, $Y_u = Y$ as indicated below.

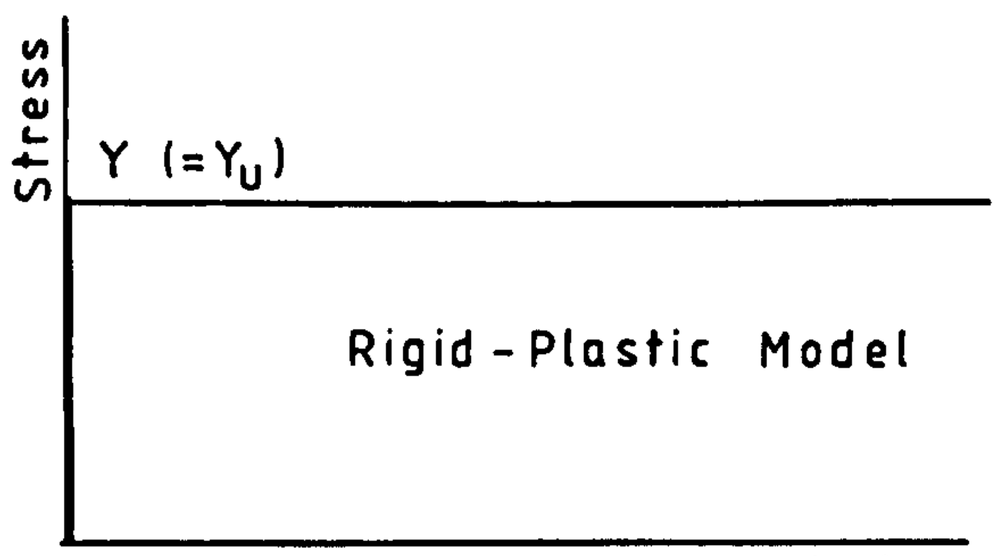


Hence it must be assumed that in the reference quoted the authors discarded the above model and replaced Y by $Y_u$ in accordance with their own model.

The ultimate stress is defined as the peak stress a material can endure. This, coupled with the above suggestion to replace Y by $Y_u$, may be checked for the experimental data obtained. Figure 5.5 illustrates the relation between the initial peak load, $P_{cr}$, a tube can withstand prior to collapse and its net section area, A. As expected, a fairly linear trend exists and the mechanisms of collapse are separated.* The gradients of these graphs thus represent an estimate of the ultimate stress, $Y_u$ for the different modes. These gradients are as follows;

---

*Details of individual data points are presented in Tables A2.2 & A2.3, Appendix II

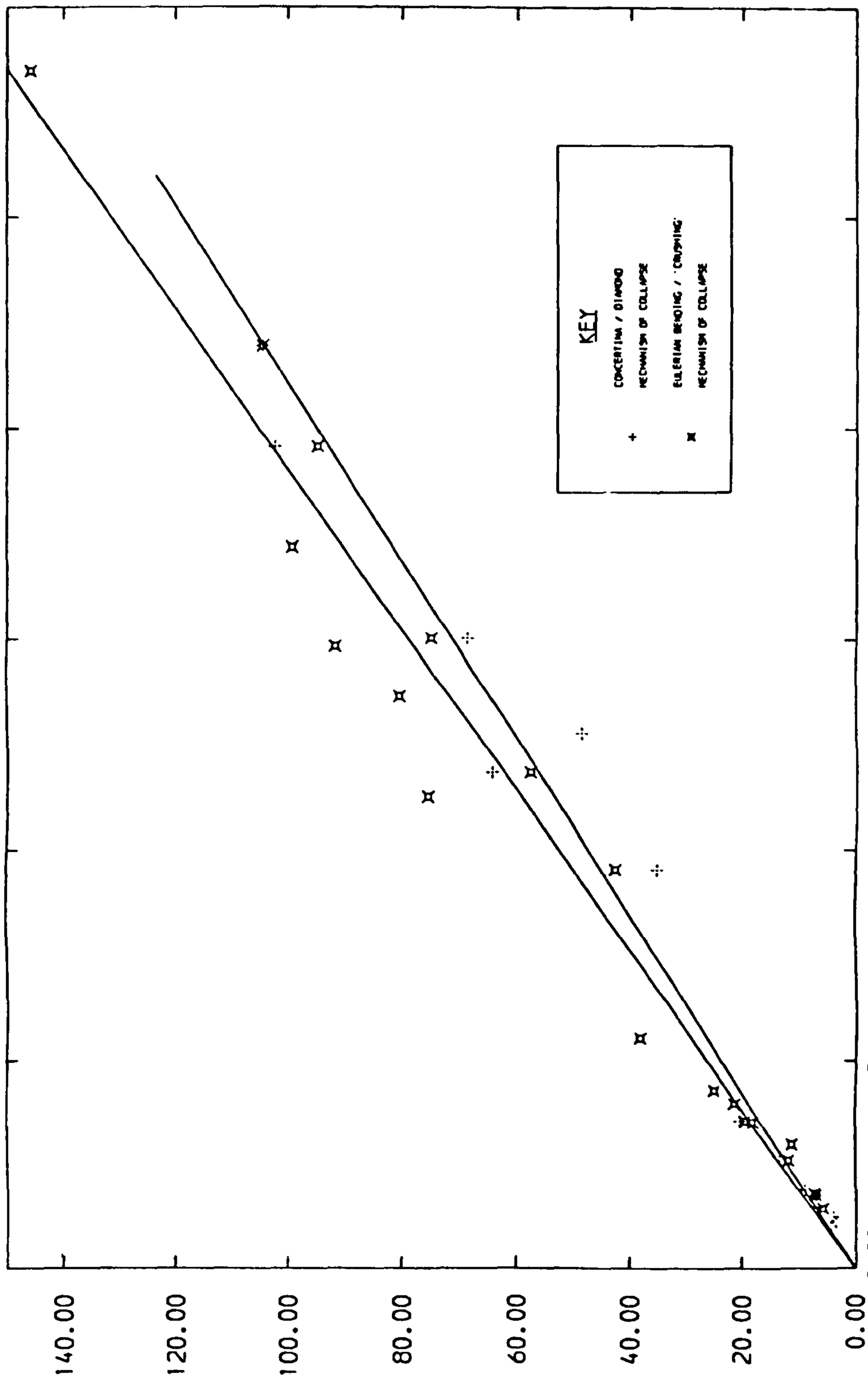


DETERMINATION OF THE ULTIMATE AXIAL COMPRESSIVE STRESS OF ANNEALED HT-30 ALUMINIUM ALLOY TUBES

Figure 5.5

$P_{cr} = Y_u A$ where

$Y_u = 0.1187$ KN/mm$^2$ (concertina / diamond mechanisms)

$Y_u = 0.1314$ KN/mm$^2$ (Eulerian bending/crushing mechanisms)

(5.2.4)

Observation shows that for the concertina mode the values obtained for $Y_u$ fall below the theoretical range of solutions for Y in (5.2.1) . This verifies that the suggested replacement of Y by $Y_u$ is inadequate in modification of Alexander's analysis for better description of the test results obtained.

The author concludes that the rigid-plastic model must be replaced in this case by one which incorporates work hardening; also, as distinct from a straight replacement of the yield parameter Y , the extra internal work quantity due to this process must be calculated as a continuous intergration of the area under the curve of the new model, in accordance with the large deformations that are involved during collapse.

## 5.3 Proposed Model I : Incorporation of Strain Hardening

It was shown in Section 5.2 that in the annealed state, the alloy material tested exhibits strain hardening and in a fairly linear manner, beyond the yield region. This section presents an attempt to incorporate this phenomenon in Alexander's theory in an empirical manner, for a closer evaluation of the internal work done in the concertina folding of a tube.

### 5.3.1 Assumptions

The following assumptions are made as illustrated in Figures

5.6 and 5.7 .

1. Material behaviour is represented by a rigid-linearly--strain-hardening model and is identical in tension and compression.

2. Fully plastic section is defined as the condition in which material fibres at the neutral axis of the section just reach the yield condition.

3. Plastic hinges are assumed to be circular and rotate about a fixed point at midsurface of the tube (see Fig. 5.7 ii).

4. Strains on the surface of the hinges are taken as the mean of axial strains along the length (2h) of a concertina fold.

5. Total work done in bending at the hinges, ($W_H$) = sum of the individual work terms for each hinge, ($W_h$), considered in isolation and calculated using the mean strains defined in '4'. No interaction of strains/stresses between hinges is * assumed.

### 5.3.2 Theory

Calculation of the work done in bending at fold hinges A, B and C in Figure 5.7 (i) ;

(i) End hinges A and C

Because of symmetry, the conditions for these two hinges are identical so that considering one of them, hinge A, for rotation of AB through angle $\theta$, the extension/compression on the outer surfaces of the hinge are

$$\delta_A = \tfrac{1}{2} t \theta \qquad (5.3.1)$$

From assumption 4 and Figure 5.7 (i) defining the axial length of fold ABC, the surface strains of hinge A are as follows:

$$\varepsilon_A = \frac{2h + \delta_A - 2h}{2h} = \frac{t\theta}{4h} \qquad (5.3.2)$$

*It is realised that strains in adjacent hinges, as defined here, overlap. In reality, $W_H < \sum W_h$ and superposition of work terms is invalid, as the work terms depend upon total strains and not the mean strains defined in assumption 4.

Rigid - linearly - strain-hardening material model

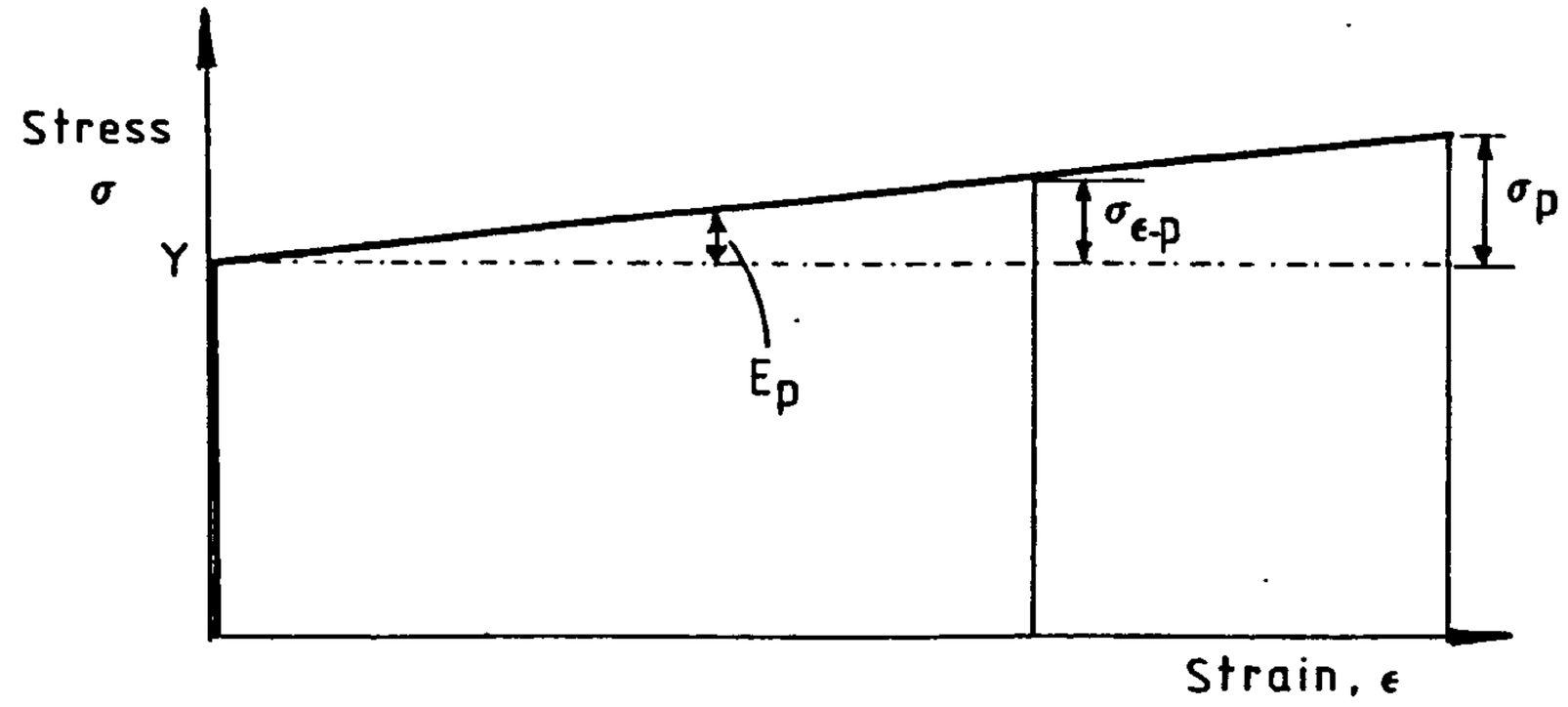


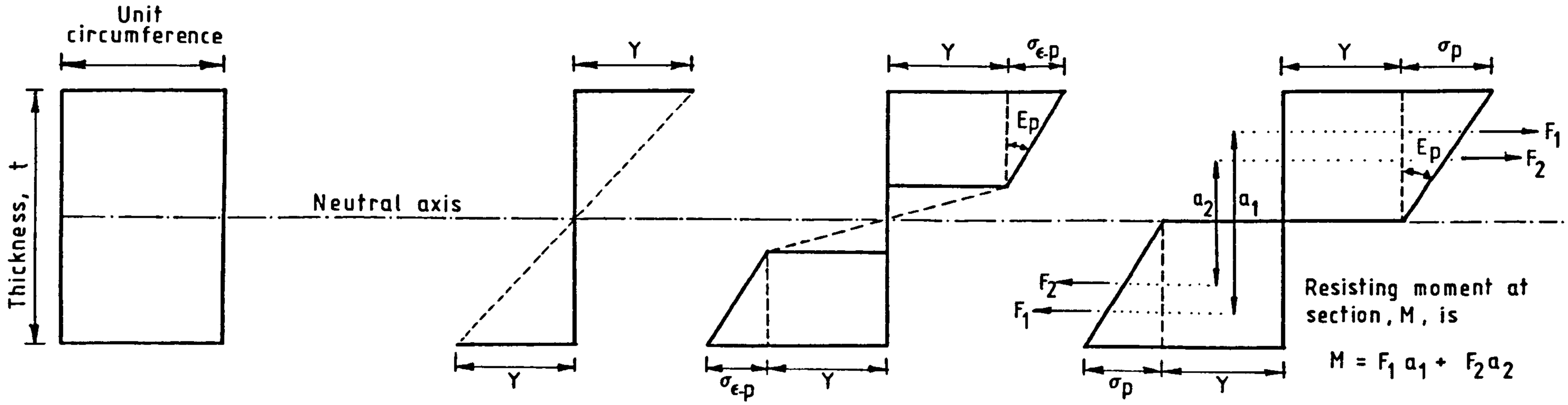


Tube section

Elastic [i]

Elasto-plastic [ii]

Plastic [iii]

Proposed Model I : material behaviour

Figure 5.6

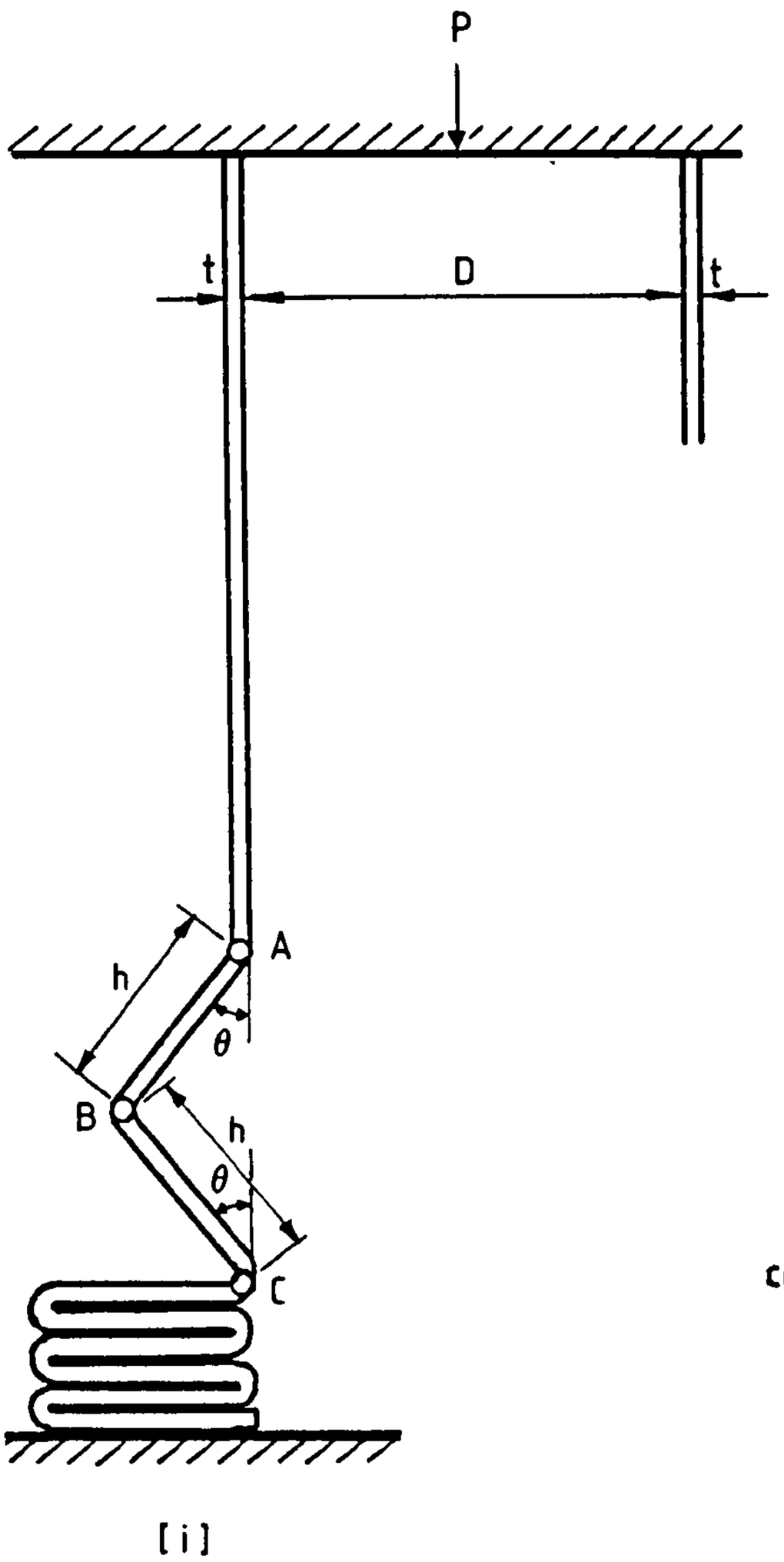


[i]

Hinge Rotations

(Hinge A)

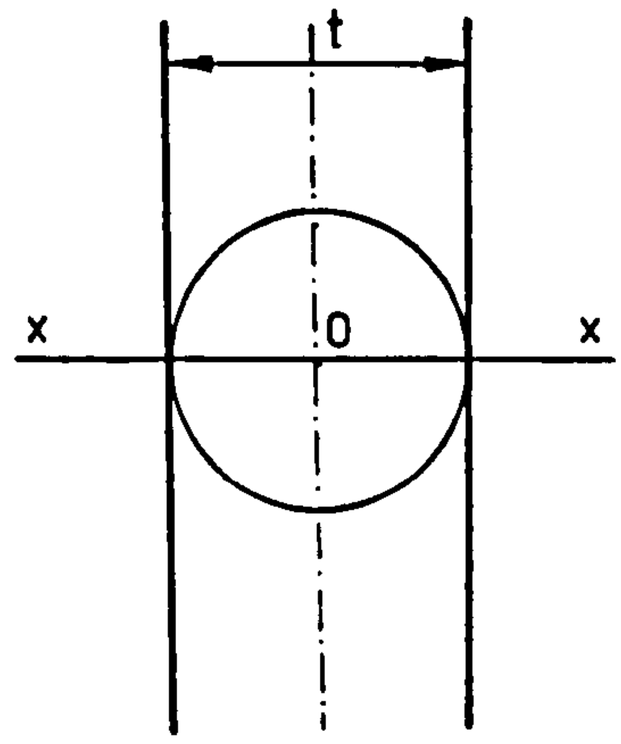





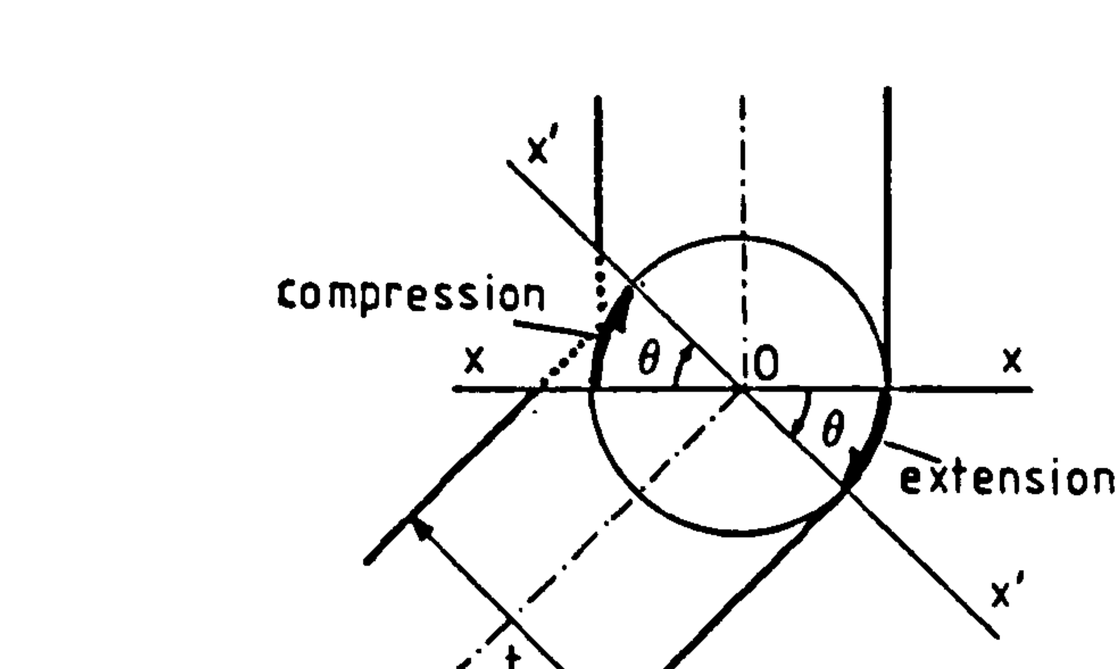


[ii]

Proposed Model I : rotations at a fold hinge

Figure 5.7

In relation to the material model used, this represents the following stress on the hinge surfaces.

$$\sigma_A = Y + E_p \varepsilon_A \quad (E_p \text{ defined in Figure 5.6}) \qquad (5.3.3)$$

Assuming for simplicity the trapezoidal stress block of Figure 5.6 (iii) applies to this rotation (as distinct from Figure 5.6 (ii) ) with the above stress denoting the stresses at the edges of the block, the resisting moment at A, $M_A$ per unit circumferential length of the tube can be shown to be the following. (The assumption imposed is considered to be reasonable since in evaluation of the moment, the overestimated area of the stress block is balanced to some extent by the reduction in the moment arm of the trapezoidal block).

$$M_A = \tfrac{1}{4} t^2 \left( Y + \frac{E_p \theta t}{6h} \right) \quad \begin{matrix}\text{(see Figure 5.6(iii) -} \\ \text{here, } \sigma_p = \frac{E_p \theta t}{4h}, \therefore f_1 = \frac{E_p \theta t^2}{16h} \text{ )}\end{matrix} \qquad (5.3.4)$$

Considering the deformation of the hinge through an increment of rotation $d\theta$, the increment of work done in bending is

$$dW_A = \pi D M_A \, d\theta \qquad (5.3.5)$$

where $\pi D$ denotes the circumference of the tube at A. By substituting (5.3.4) into (5.3.5), the total bending work at hinge A for the complete folding of ABC is the subsequent integration of the latter between limits of $\theta$ : 0 and $\frac{1}{2}\pi$ radians. This gives

$$W_A \ (= W_C) = \frac{\pi^2 D t^2}{8} \left( Y + \frac{\pi E_p t}{24 h} \right) \qquad (5.3.6)$$

(ii) Central hinge B

For rotation of hinge A (or C) through $\theta$, hinge B rotates through $2\theta$ so that the following corresponding expressions are derived leading to the work done in bending at this hinge;

$$\delta_B = t\,\theta$$

$$\varepsilon_B = \frac{t\,\theta}{2h}$$

$$\sigma_B = Y + E_p\,\varepsilon_B$$

(The sign of these 4 expressions is of opposite sense to those for hinge A; also $\varepsilon_B$ and $\varepsilon_A$ overlap *)

$$M_B = \tfrac{1}{4}\,t^2\left(Y + \frac{E_p\,\theta\,t}{3h}\right)$$

$$dW_B = 2\pi M_B\,(D + 2h\sin\theta)\,d\theta$$

$$W_B = \tfrac{1}{2}\pi t^2\left[\tfrac{1}{2}\pi D\left(Y + \frac{\pi E_p t}{12h}\right) + 2h\left(Y + \frac{E_p t}{3h}\right)\right]$$

(5.3.7)

The total work done in bending, $W_{bend}$ is the sum of $W_A$, $W_B$ and $W_C$ giving,*

$$W_{bend} = \tfrac{1}{4}\pi^2 D\,t^2\left(2Y + \frac{\pi E_p t}{8h}\right) + \pi t^2 h\left(Y + \frac{E_p t}{3h}\right)$$

(5.3.8)

Calculation of the work done in stretching of material between the hinges in the circumferential direction

Again, due to symmetry, only one arm-length of a fold, say AB in Figure 5.7 (i) need be studied. Let x be measured from hinge A along AB. Before deformation of AB through $\theta$ the circumference of the tube at any position x is $C_{xo}$, where $C_{xo} = \pi(D + t)$. After deformation to the configuration shown this is increased to the following;

*see assumption 5 & footnote on P.171

$$C_{x\theta} = \pi ( D + t + 2 x \sin\theta ) \qquad (5.3.9)$$

Hence the circumferential strain and stress at x are

$$\varepsilon_{x\theta} = \frac{2 x \sin\theta}{( D + t )} \qquad (5.3.10)$$

$$\sigma_{x\theta} = Y + E_p \varepsilon_{x\theta} \qquad (5.3.11)$$

Considering deformation of AB through an increment of rotation $d\theta$, the change in circumferential strain at x is,

$$d\varepsilon_{x\theta} = \frac{\pi (D + t + 2 x \sin (\theta + d\theta) ) - \pi(D + t + 2 x \sin\theta)}{\pi(D + t + 2 x \sin\theta)}$$

For small $d\theta$, $\cos d\theta \simeq 1$ and $\sin d\theta \simeq d\theta$. This gives

$$d\varepsilon_{x\theta} \simeq \frac{2 x \cos\theta \; d\theta}{D + t + 2 x \sin\theta} \qquad (5.3.12)$$

Thus, the increment of work done in stretching AB at position x is the product of equations (5.3.9), (5.3.11), (5.3.12) and wall thickness t of the tube, i.e.

$$dW_{x\theta} = 2 \pi x t \cos\theta \; \sigma_{x\theta} \, d\theta \qquad (5.3.13)$$

Total work done in stretching of AB from vertical to the horizontal position is the integration of the above with respect to x and $\theta$ between limits : $0 < x < h$, $0 < \theta < \frac{1}{2}\pi$. This gives

$$W_{AB} = \pi h^2 t \left( Y + \frac{2 h E_p}{3 (D+t)} \right) \qquad (5.3.14)$$

Hence for a complete fold (2 arm-lengths, AB and BC) total stretching work, $W_{str}$ is,

$$W_{str} = 2\pi h^2 t \left( Y + \frac{2h}{3} \frac{E_p}{(D+t)} \right) \qquad (5.3.15)$$

Total internal work, $W_I$ is the sum of equations (5.3.8) and (5.3.15) . Thus

$$W_I = \tfrac{1}{4}\pi^2 D t^2 \left(2Y + \frac{\pi E_p t}{8h}\right) + \pi h t \left[ Y(t+2h) + \frac{E_p}{3}\left(\frac{t^2}{h} + \frac{4h^2}{(D+t)}\right)\right] \qquad (5.3.16)$$

The external work done for folding of ABC , $W_E$ is that given in Alexander's theory, namely

$$W_E = 2 \bar{P} h \qquad (5.3.17)$$

By equating the latter two expressions, the following relation for the yield stress Y of the material is obtained;

$$Y = \frac{\bar{P} - \frac{\pi E_p t}{6}\left\{\frac{3\pi^2 D t^2}{32 h^2} + \frac{t^2}{h} + \frac{4h^2}{(D+t)}\right\}}{\frac{\pi t^2}{2}\left(\frac{\pi D}{2h} + 1\right) + \pi h t} \qquad (5.3.18)$$

5.3.3 Discussion and comparison with experiment

Inspection of this solution reveals that if $E_p = 0$ is considered (rigid-plastic material) and the von Mises factor is then introduced on the first term in the denominator, the above reduces to Alexander's expression, namely equation (5.1.1). As it stands, the equation exhibits the favourable trend of a reduction in the magnitudes of Y that would be predicted if the internal work during strain hardening were to be incorporated in Alexander's theory. The worth of equation (5.3.18) is that, if a value of the strain hardening modulus

$E_p$ for the alloy tested is substituted into this equation, it may be used to predict a value of the yield stress Y . This in turn may then be checked against the experimental range given in (5.2.1).

For the annealed aluminium tested, the hardening modulus, $E_p$ has been found by assuming a linear variation of strain beyond the yield region on the stress-strain curves (see Figure 5.1(iii)). This is in close agreement with the actual experimental trend. These results lie in the range: $0.94 \leqslant E_p \leqslant 2.9$ (KN/mm$^2$) giving a mean of $E_p = 2$ KN/mm$^2$. The scatter shown by this range is largely a reflection of the scatter forming the experimental range of yield stresses in (5.2.1). The individual recordings for $E_p$ are presented in Table A2.6, Appendix II.

For the set of tubes tested, i.e. fixed D, t, h & $\bar{P}$ (see Table A2.1, Appendix II) and the mean value of $E_p = 2$ KN/mm$^2$, application of equation (5.3.18) generates the following range of empirical solutions for yield stress parameter, Y. These are compared with the ranges in (5.2.1) as follows:

| | | |
|---|---|---|
| Equation (5.3.18) (for $E_p$=2 KN/mm$^2$) | (proposed model I) | : $-0.0065 \leqslant Y \leqslant 0.0515$ (KN/mm$^2$) |
| Direct yield test | (experiment) | : $0.032 \leqslant Y \leqslant 0.079$ (KN/mm$^2$) |
| Equation (5.1.1) | (Alexander) | : $0.149 \leqslant Y \leqslant 0.200$ (KN/mm$^2$) |

(5.3.19)

Comparison suggests the possibility that the model introduced

overestimates the internal work done at collapse. Observation reveals this finding as consistent with the geometry changes in the collapse model introduced into Alexander's theory and used here. It has been implicitly assumed that during collapse, bending and circumferential stretching of the tube proceed with no change in the original thickness of the tube. Hence by assuming the same initial thickness throughout collapse, it is predicted that the calculated internal work done exceeds the actual value.

In the next section account is taken of this feature where, (in accordance with theories of plasticity) the condition of incompressibility is imposed on the empirical solution obtained.

## 5.4 Proposed Model II : Condition of Material Incompressibility Superimposed onto Model I

### 5.4.1 Theory

The condition of incompressibility is introduced by providing a relationship between the original thickness, t of a tube before deformation and that during collapse through angle $\theta$, denoted as t'. Figure 5.8 indicates the geometry of a fold before and during development. The respective volumes of this fold, $V_f$ are given below.

$$\text{Initially} : \quad V_f(i) = 2\pi h\, t\, (D + t) \qquad (5.4.1)$$

$$\text{At collapse} : \quad V_f(ii) = 2\pi h\, t'(D + t + h\sin\theta) \qquad (5.4.2)$$

For the condition of no volume change, the above may be equated to provide the following relation:

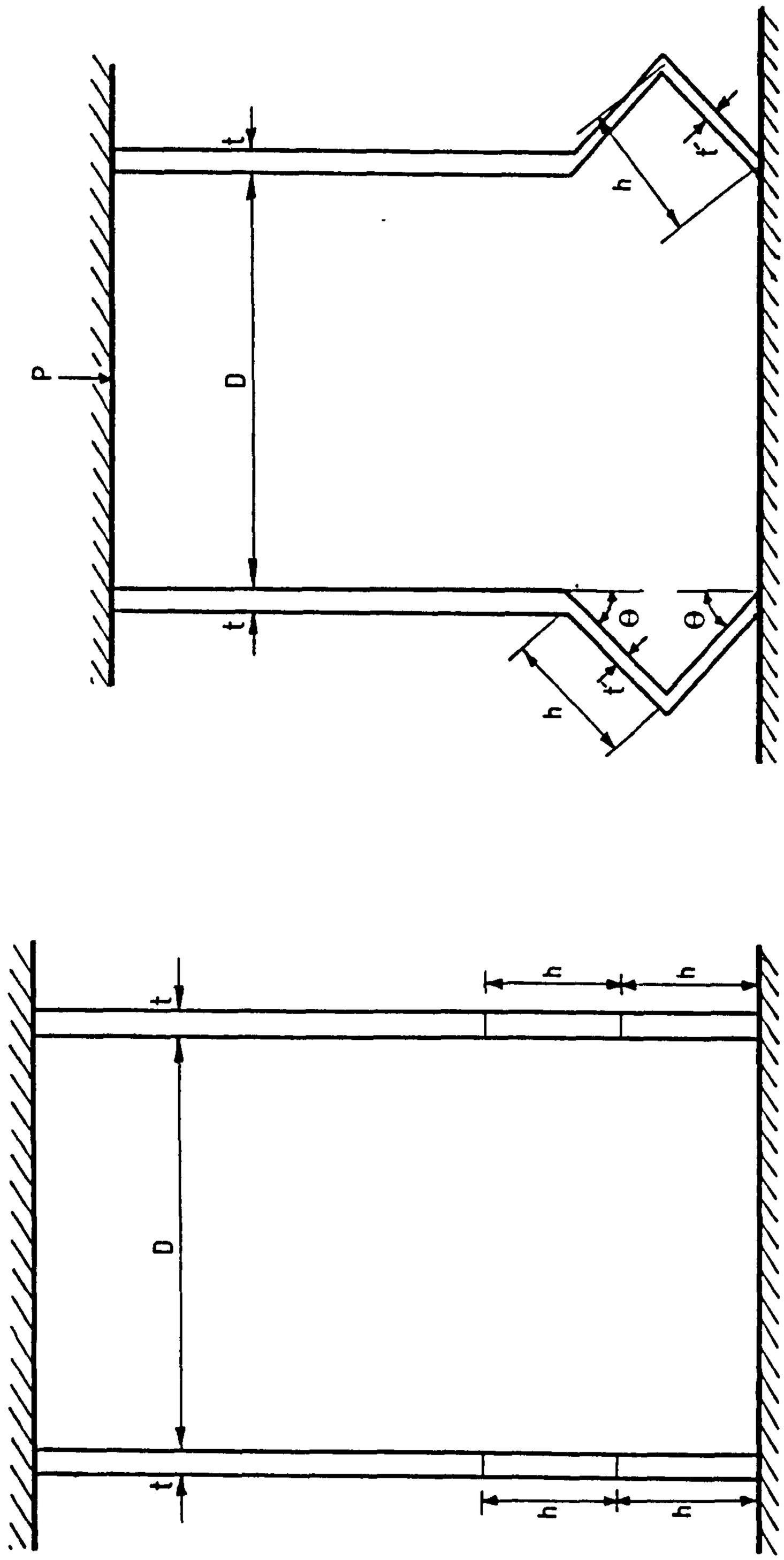


(i) Condition of Material Incompressibility (see equation (5.4.3))

(ii) Proposed Model II

Figure 5.8

$$t' = \frac{t\ (D + t)}{D + t + h \sin\theta} \qquad (5.4.3)$$

This expression is to replace $t$ in the functions obtained in the previous solution of Section 5.3 for certain components of the internal work, as illustrated below.

(i) Work done in bending at the fold hinges

Equation (5.3.6) remains unchanged for the work done at the end hinges A and C since the thickness does not alter at these points during rotation of these hinges. However, for the central hinge B, the increment of work done in rotation through $d\theta$ is modified as follows;

$$dW_B = \frac{\pi t^2 (D+t)^2 (D + 2h\sin\theta)}{2\ (D + t + h\sin\theta)^2} \left[ Y + \frac{E_p\, \theta\, t\ (D + t)}{3h\ (D + t + h\sin\theta)} \right] d\theta \qquad (5.4.4)$$

Total bending work at B is the integration of the above for $\theta$ between limits : 0 and $\frac{1}{2}\pi$ radians. Together with the work done in hinges A and C, the total modified internal bending work, $W_{bend}$ is

$$W_{bend} = \tfrac{1}{4}\pi^2 D t^2 \left[ Y + \frac{\pi E_p t}{24 h} \right] + \tfrac{1}{2}\pi t^2 (D+t)^2 \left[ Y A(\theta) + \frac{E_p t\ (D+t)}{3h} B(\theta) \right] \qquad (5.4.5)$$

where

$$A(\theta) = \int_0^{\pi/2} \frac{D + 2h\sin\theta}{(D + t + h\sin\theta)^2}\, d\theta \qquad (5.4.6)$$

$$B(\theta) = \int_0^{\pi/2} \frac{(D + 2h\sin\theta)\ \theta}{(D + t + h\sin\theta)^3}\, d\theta \qquad (5.4.7)$$

(ii) Work done in extension in the circumferential direction

Replacing t by t' in equation (5.3.13) giving the increment of work done in stretching of the tube at point x along AB, total work done in stretching along AB is

$$W_{AB} = 2\pi t\,(D+t)\int_0^{\pi/2}\int_0^{h}\left[Y + \frac{2\,x\sin\theta\;E_p}{(D+t)}\right]\frac{x\,\cos\theta\quad d\theta\;dx}{(D+t+h\sin\theta)} \qquad (5.4.8)$$

This gives

$$W_{AB} = \pi ht(D+t)\log_e\left(\frac{D+t+h}{D+t}\right)\left(Y - \frac{4\,E_p}{3}\right) + \frac{4}{3}\pi h^2 t\,E_p \qquad (5.4.9)$$

Hence the total work done in stretching, $W_{str}$ (that is for 2 fold-lengths) is

$$W_{str} = 2\pi ht\left[(D+t)\log_e\left(\frac{D+t+h}{D+t}\right)\left(Y - \frac{4\,E_p}{3}\right) + \frac{4h\,E_p}{3}\right] \qquad (5.4.10)$$

The total internal work done in this modified solution is the sum of equations (5.4.5) and (5.4.10) . By equating this to the previous external work done in (5.3.17) which remains unaltered, the following expression for the yield stress Y of the material is newly obtained;

$$Y = \frac{\bar{P} - \frac{\pi t\,E_p}{6}(C_1 + C_2)}{C_3 + C_4} \qquad (5.4.11)$$

where

$$C_1 = \tfrac{1}{2}\left(\frac{t}{h}\right)^2\left[\frac{\pi^2 D}{16} + (D+t)^3\,B(\theta)\right]$$

$$C_2 = 8h\left[1 - \frac{(D+t)}{h}\log_e\left(\frac{D+t+h}{D+t}\right)\right]$$

$$C_3 = \frac{\pi t^2}{4h}\left[\tfrac{1}{2}\pi D + (D+t)^2\,A(\theta)\right] \qquad (5.4.12)$$

$$C_4 = \pi t\,(D+t)\log_e\left(\frac{D+t+h}{D+t}\right)$$

and integrals $A(\theta)$ and $B(\theta)$ given in (5.4.6) and (5.4.7) are to be solved by a numerical method. For known tube geometry, Simpson's rule is used to evaluate these two integrals numerically for 50 increments of angle $\theta$ between 0 and $\frac{1}{2}\pi$ radians.

### 5.4.2 Comparison with experiment

Application of equation (5.4.11) to the set of tubes tested (see Table A2.1, Appendix II) for mean experimental Ep (= 2 $KN/mm^2$) results in the prediction of the following range of empirical solutions for the yield parameter, Y. These are compared with the ranges in (5.2.1) as follows:

| | | |
|---|---|---|
| Equation (5.4.11) (for $E_p$ = 2 $KN/mm^2$) | (proposed model II) | : $0.0332 \leqslant Y \leqslant 0.0671$ $(KN/mm^2)$ |
| Direct yield test | (experiment) | : $0.032 \leqslant Y \leqslant 0.079$ $(KN/mm^2)$ |
| Equation (5.1.1) | (Alexander) | : $0.149 \leqslant Y \leqslant 0.200$ $(KN/mm^2)$ |

(5.4.13)

The solution range obtained above for the model introduced, is observed to be fully encompassed within the experimental range. These results also confirm the suggestion stated in Section 5.3.3 that the empirical solutions predicted from equation (5.3.18) reflect an overestimation of the internal work done at collapse in the formation of a concertina fold.

## 5.5 Proposed Model III : Establishment of a more Representative Collapse Configuration Model

The previous sections disclosed the significance of material

data in Alexander's theory and the importance of the large deformations involved during collapse. In this section a new collapse model which incorporates part internal and part external folding is introduced. The strain hardening behaviour of equation (5.3.3) in Section 5.3.1 is used in conjunction with the previous assumptions regarding plastic hinges.

Figures 5.9 (i) - (iv) indicate the proposed collapse model in relation to the midsurface of the tube (thicknesses not shown for clarity of representation).

### 5.5.1 Assumptions

1. Collapse of the tube proceeds as a heavily damped wave, as shown in Figure 5.9 (ii), but the folding process remains sequential.
2. For a given arm-length $h$ of a fold, the proportion of external folding is $\lambda$.
3. Figure 5.9 (iii) denotes the configuration of a general fold ABC at the initial point of collapse, and model (iv) denotes the complete development of this fold. The two fold lengths collapse independently of each other so that angles $\theta$ and $\phi$ are independent.
4. For a given tube geometry, angle $\alpha$ is fixed and, $\lambda = \sin\alpha$.
5. For complete folding of ABC the internal work done between the hinges is the sum of that in the circumferential compression of AB and part extension and part compression of BC. Work done in bending is the sum of that in rotation of hinge A through $\theta = \frac{1}{2}\pi - \alpha$ radians, hinge B through $\theta + \phi = \pi - \alpha$ radians and C through $\phi = \frac{1}{2}\pi$ radians. External work done

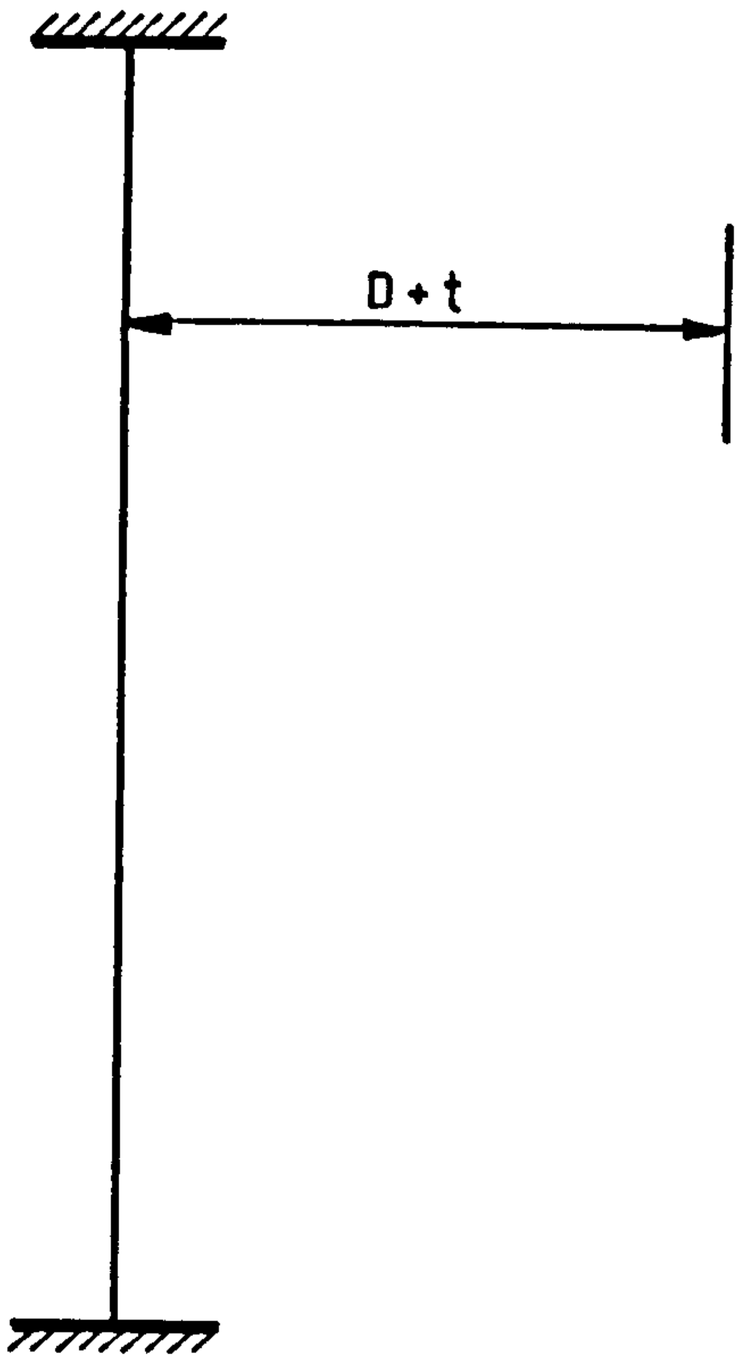


[i]

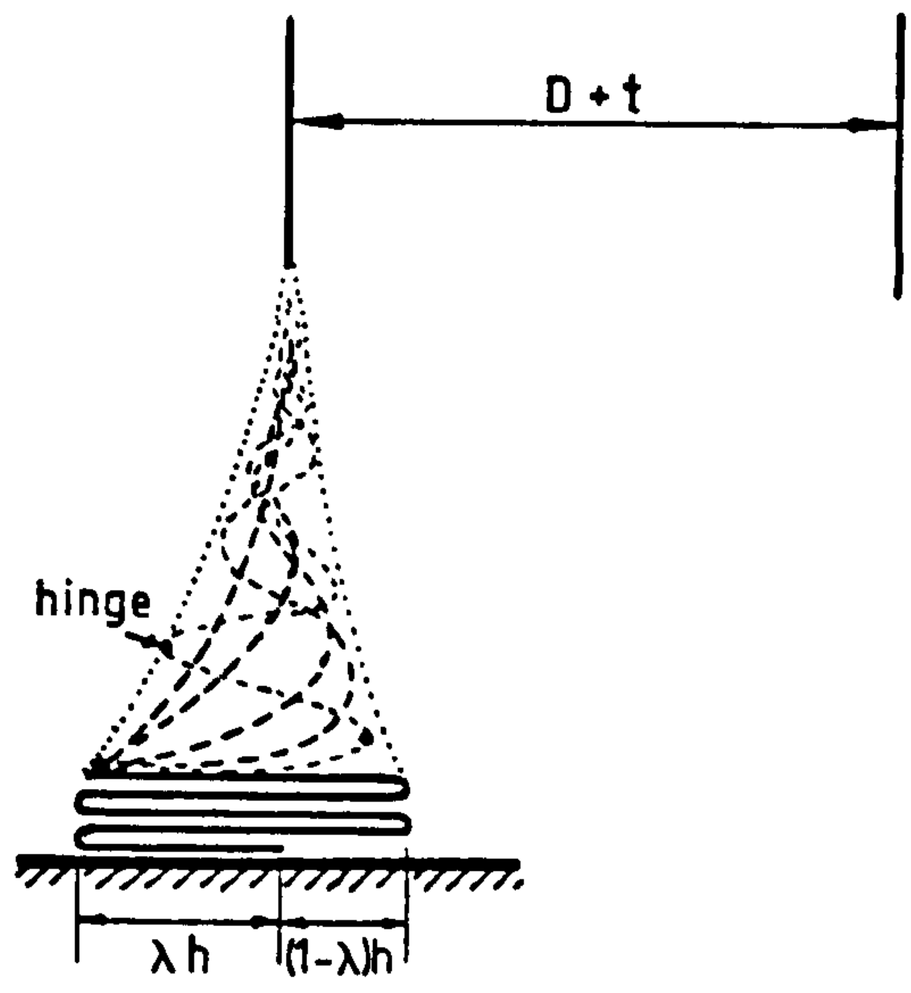


[ii]

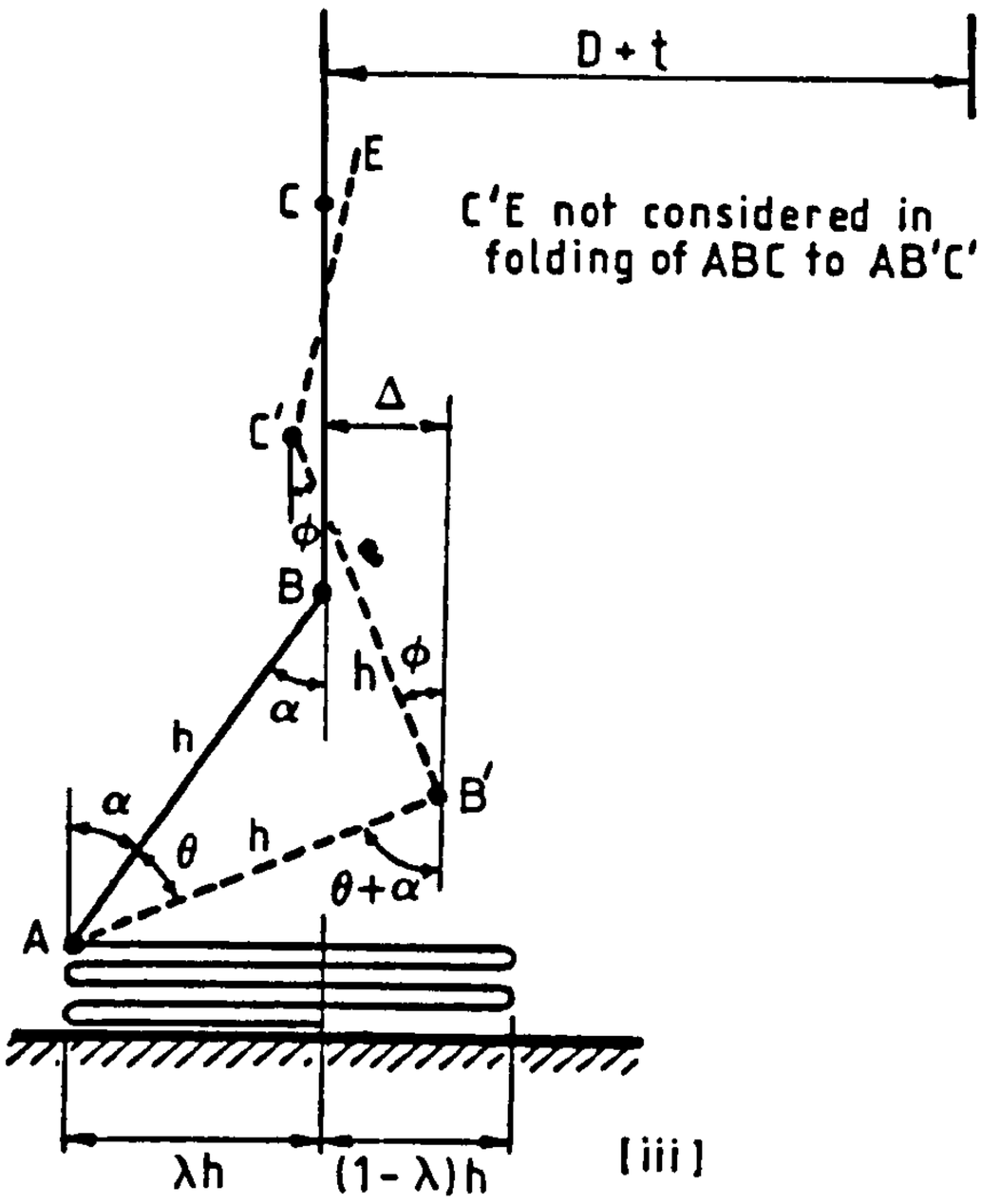


[iii]

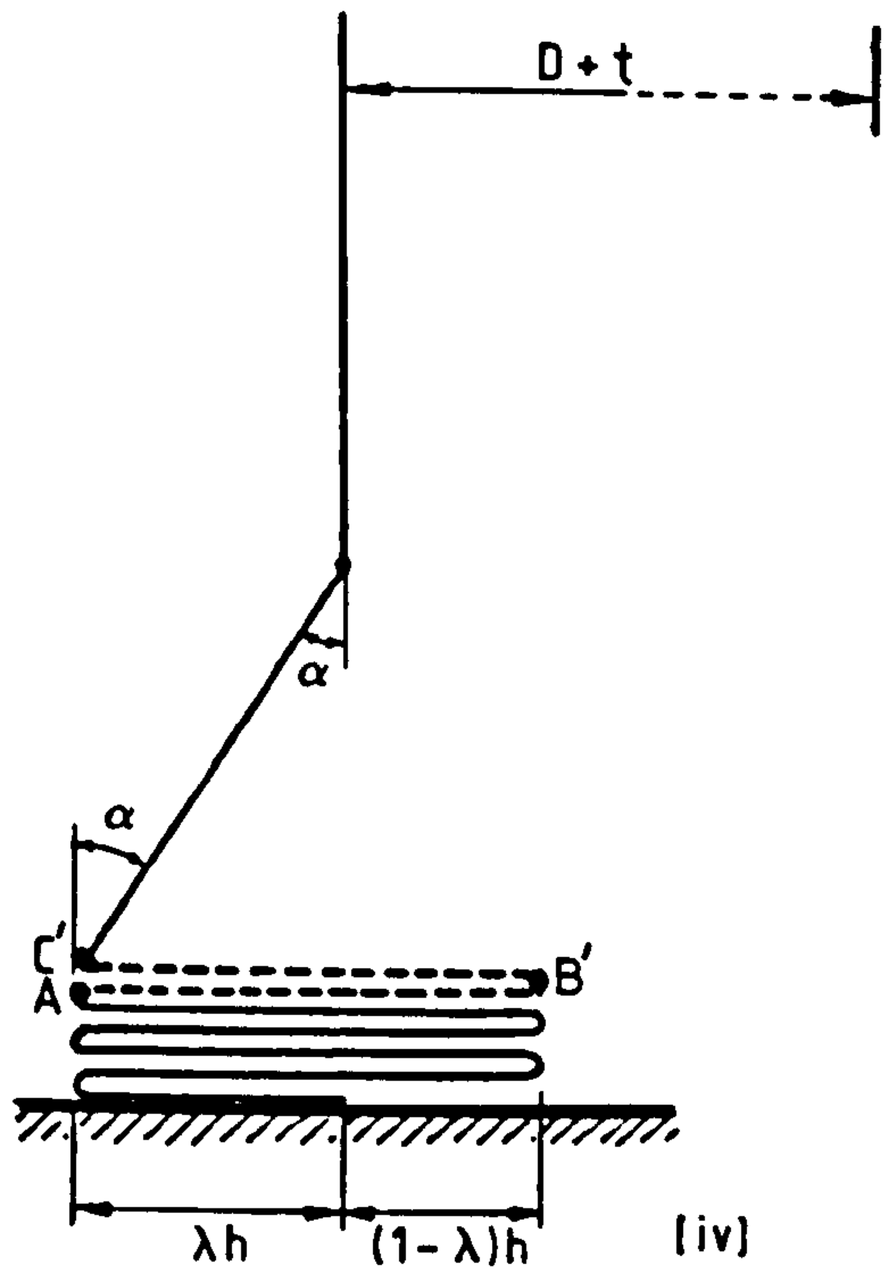


[iv]

PART EXTERNAL AND PART INTERNAL FOLDING MODEL (III)
PROPOSED FOR CONCERTINA COLLAPSE MECHANISM

Figure 5.9

is the product of the mean axial load, $\overline{P}$ and the vertical projection of length ABC .

5.5.2 Theory

From Assumption 5 the external work done, $W_E$ in complete folding of ABC is

$$W_E = \overline{P}\, h\, (1 + \cos \alpha) \qquad (5.5.1)$$

Calculation of the internal work done in bending at the hinges

(i) Hinge A

As before, a circular hinge is assumed with deformations in rotation as multiples of one half the thickness t . Considering fold ABC , the original length of this fold on the inner surface is $2h + \frac{1}{2}t\alpha$ . After rotation of AB through $\theta$ this increases by $\frac{1}{2} t \theta$ . Using the same previous notation, it is found that

$$\varepsilon_A = \frac{t\,\theta}{4h + \alpha t}$$

$$\sigma_A = Y + E_p\, \varepsilon_A \qquad (5.5.2)$$

$$M_A = \tfrac{1}{4} t^2 \left\{ Y + \frac{2\, E_p\, \theta\, t}{3\, (4h + \alpha t)} \right\}$$

$$dW_A = \pi\, (D + t + 2\, \lambda\, h)\, M_A\, d\theta \qquad (5.5.3)$$

Total work done in bending at this hinge is the integration of the above between limits of $\theta$ : 0 and $(\frac{1}{2}\pi - \alpha)$ radians. Thus

$$W_A = \tfrac{1}{4}\, \pi\, t^2\, (D + t + 2\,\lambda h)\, (\tfrac{1}{2}\pi - \alpha) \left\{ Y + \frac{(\pi - 2\alpha)\, E_p\, t}{6\, (4h + \alpha t)} \right\} \qquad (5.5.4)$$

(ii) Hinge B

From Figure 5.9 (iii), it is seen that

$$\Delta = h\{\sin(\alpha+\theta) - \lambda\} \qquad (5.5.5)$$

For rotation of hinge B through angles $\theta$ and $\phi$ the expressions for $\varepsilon_B$, $\sigma_B$ and $M_B$ are equivalent to those given in (5.5.2) for hinge A with $\theta$ replaced by $(\theta + \phi)$. The work done for an increment of rotation is

$$dW_B = \pi (D + t - 2\Delta) M_B \, d\theta \, d\phi \qquad (5.5.6)$$

Thus,

$$W_B = \int_0^{\pi/2} \int_0^{(\pi/2 - \alpha)} \pi M_B (D_1 - 2h \sin(\alpha+\theta)) \, d\theta \, d\phi$$

$$= \frac{\pi^2 t^2}{8} \left[ Y(D_2 - 2h\cos\alpha) + \frac{\pi E_p t}{6(4h+\alpha t)} \left\{ \tfrac{1}{2} D_2 (\tfrac{1}{2}\pi - \alpha) - 2h(1-\lambda) \right\} \right] \qquad (5.5.7)$$

where

$$D_1 = D + t + 2\lambda h$$
$$D_2 = (\tfrac{1}{2}\pi - \alpha) D_1 \qquad (5.5.8)$$

However, inspection of the above solution in (5.5.7) reveals that if $\lambda = 1$ is considered (fully external folding), then $\alpha = \frac{1}{2}\pi$ and this equation yields zero work done which cannot be so. The author affirms at this point that the continuous double integration performed is not permitted so that an alternative approach must be made where collapse through $\theta$ and $\phi$ are considered separately and the work components summed, as follows;

Considering Figure 5.10 (i) for collapse of ABC through $\theta$ only (B'C' remaining vertical) the increment of work done in hinge B, $W_{B(\theta)}$, is that given in (5.5.6) where $M_B = M_A$ in (5.5.2) and increment $d\theta$ is considered only. Subsequent integration between limits of $\theta$ : 0 and $(\frac{1}{2}\pi - \alpha)$ gives

$$W_{B(\theta)} = \tfrac{1}{4}\pi t^2 \left[ Y (D_2 - 2h\cos\alpha) + \frac{E_p t}{3(4h+\alpha t)} \left\{ D_2 (\tfrac{1}{2}\pi - \alpha) - 4h(1-\lambda) \right\} \right] \qquad (5.5.9)$$

Next, collapse of ABC through $\emptyset$ after complete rotation through $\theta$ may be considered as in Figure 5.10 (ii). Here, length AB'C' = $2h + \frac{1}{4}\pi t$. After deformation to AB'C", this is increased by $\frac{1}{2} t \emptyset$. Hence the following expressions are obtained for rotation of hinge B through $\emptyset$.

$$\varepsilon_B = \frac{2\, t\, \emptyset}{8h + \pi t}$$

$$\sigma_B = Y + E_p \varepsilon_B \qquad (5.5.10)$$

$$M_B = \tfrac{1}{4} t^2 \left( Y + \tfrac{2}{3} E_p \varepsilon_B \right)$$

$$dW_{B(\emptyset)} = \pi (D_1 - 2h) M_B \, d\emptyset$$

Integration of the above between limits of $\emptyset$ : 0 and $\frac{1}{2}\pi$ gives,

$$W_{B(\emptyset)} = \frac{\pi^2 t^2}{8} (D_1 - 2h) \left\{ Y + \frac{\pi E_p t}{3(8h+\pi t)} \right\} \qquad (5.5.11)$$

Hence , the total work done in bending at hinge B, $W_B$ is the sum of equations (5.5.9) and (5.5.11), which solution no longer yields zero for the condition of fully external folding.

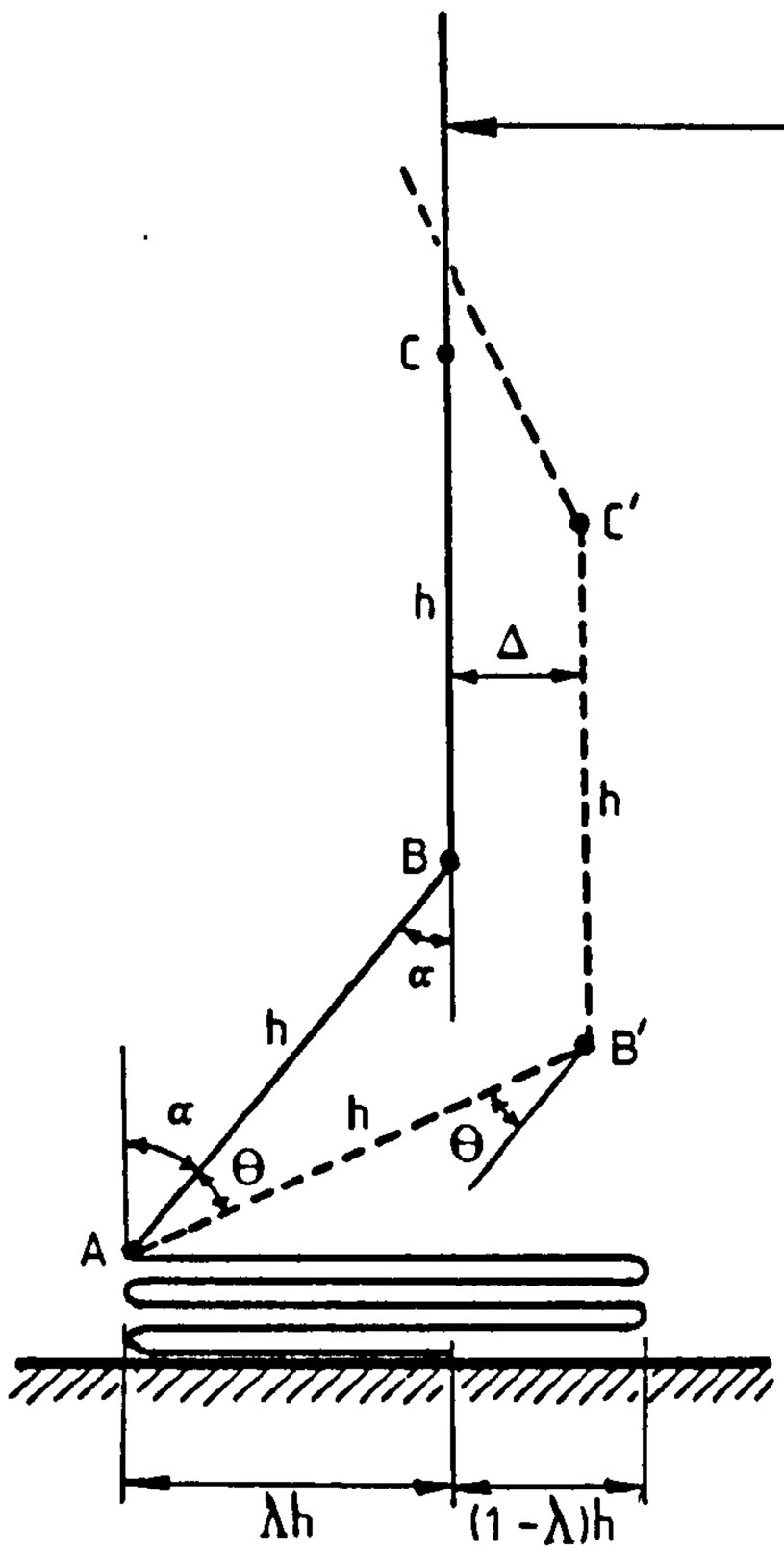


(See Figure 5.9 (iii) :
angle $\phi = 0$ )

[i]

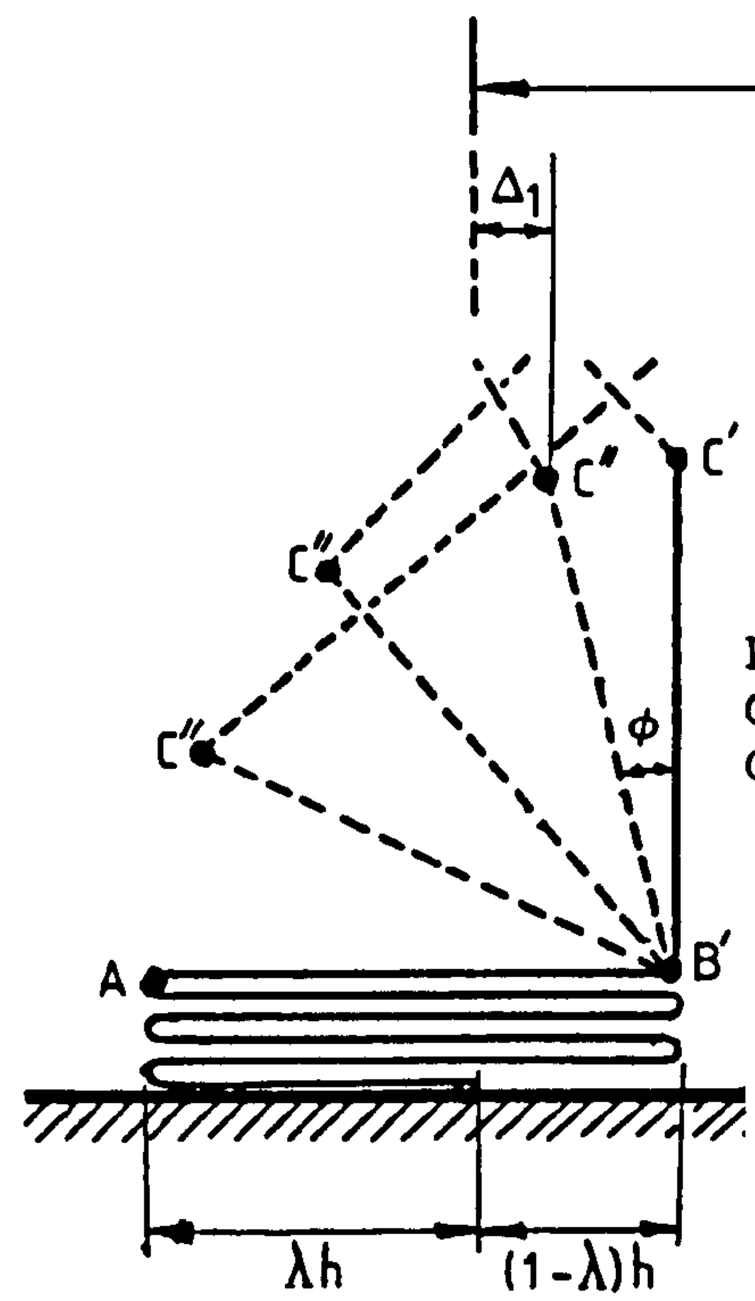


(See Figure 5.9 (iii) :
angle $\theta = \frac{1}{2}\pi - \alpha$ )

Point C' moves to new positions C" (to the left of original hinge C) :
(a) for complete folding of ABC
(b) in order to 'relieve' the tube from 'constriction' (necking) along vertical portion B'C' (B'C' is in complete circumferential compression)

[ii]

Proposed Model III

Figure 5.10

(iii) Hinge C

As in hinge B, rotations through $\theta$ and $\phi$ are separately considered for the work done in bending at this hinge. Considering Figure 5.10 (i) it is observed that for collapse of ABC through $\theta$ alone, no work is done at C as far as fold ABC is concerned. Thus, $W_{C(\theta)} = 0$. Considering rotation through $\phi$ after rotation through $\theta = (\frac{1}{2}\pi - \alpha)$, Figure 5.10(ii) gives

$$\Delta_1 = h(1 - \lambda - \sin\phi) \quad \text{(positive or negative)} \qquad (5.5.12)$$

The expressions for $\varepsilon_C$, $\sigma_C$ and $M_C$ are identical to those for hinge B given in (5.5.10). For an increment of rotation $d\phi$ the increment of work at C is

$$dW_{C(\phi)} = \pi(D + t - 2\Delta_1) M_C \, d\phi \qquad (5.5.13)$$

Hence,

$$W_{C(\phi)} = \tfrac{1}{4}\pi t^2 \left[ Y(D_3 + h(2-\pi)) + \frac{E_p t}{3(8h + \pi t)} (\pi D_3 + h(8-\pi^2)) \right] \qquad (5.5.14)$$

where $D_3 = \frac{1}{2}\pi D_1$ and $D_1$ is given in (5.5.8). Total work done in bending at C, $W_C$ is that given above, since $W_{C(\theta)} = 0$.

With the entities constituting the internal work evaluated, the total internal work done in bending, $W_{bend}$ at the three hinges is the sum of equations (5.5.4), (5.5.9), (5.5.11) and (5.5.14). This gives

$$W_{bend} = \tfrac{1}{4}\pi t^2 \left[ S_1 + \frac{E_p t}{3} (S_2 - S_3) \right] \qquad (5.5.15)$$

where

$$S_1 = 2Y\left\{D_1(\pi - \alpha) + h(1 - \pi - \cos\alpha)\right\}$$

$$S_2 = D_1\left\{(\tfrac{1}{2}\pi - \alpha)^2 K_1 + \pi^2 K_2\right\}$$

$$S_3 = 2h\left\{(1 - \lambda) K_1 + (\pi^2 - 4) K_2\right\} \qquad (5.5.16)$$

$$K_1 = \frac{2}{(4h + \alpha t)}$$

$$K_2 = \frac{1}{(8h + \pi t)}$$

Calculation of the internal work done between the fold hinges in the circumferential direction

Work done in compression of material between hinges A and B

Rotation through $\theta$ is to be considered only so that Figure 5.10 (i) applies. Let $x$ be measured from A along AB. For any $x$ the circumference of the tube at $x$ is, $C_{xo} = \pi(D_1 - 2\lambda x)$. After deformation of AB to AB', the new perimeter at $x$, $C_{x\theta}$, is that in $C_{xo}$ with $\lambda$ replaced by $\sin(\alpha+\theta)$. (Reminder: $\lambda = \sin\alpha$). This gives rise to the following circumferential compressive strain and stress at $x$.

$$\varepsilon_{x\theta} = \frac{2x\,(\sin(\alpha+\theta) - \lambda)}{D_1 - 2\lambda x} \qquad (5.5.17)$$

$$\sigma_{x\theta} = Y + E_p \varepsilon_{x\theta} \qquad (5.5.18)$$

Considering an increment of deformation, $d\theta$, the change in strain at $x$ can be shown to be the following,

$$d\varepsilon_{x\theta} = \frac{2x\cos(\alpha+\theta)\,d\theta}{D_1 - 2x\sin(\alpha+\theta)} \qquad (5.5.19)$$

Hence the increment of work done at $x$ is the product of

equations (5.5.18), (5.5.19), circumference $C_{x\theta}$ and the thickness t of the tube. This gives

$$dW_{AB} = 2\pi x\, t \cos(\alpha+\theta)\, \sigma_{x\theta}\, d\theta \qquad (5.5.20)$$

Total work done along AB is the double integration of the above with respect to x and θ between limits : x = 0 & h, θ = 0 & $(\frac{1}{2}\pi - \alpha)$. Thus,

$$W_{AB} = \pi h^2 t(1-\lambda)\left[ Y + \frac{E_p(1-\lambda)}{2\lambda^2 h}\left\{ \frac{D_1^2}{2\lambda h}\log_e\left(\frac{D_1}{D+t}\right) - (D_1 + \lambda h)\right\}\right] \qquad (5.5.21)$$

In determining the above integration result, it has been necessary to use the following identity :

$$\frac{x^2}{D_1 - 2\lambda x} = \frac{1}{2\lambda}\left[\frac{D_1^2}{2\lambda(D_1 - 2\lambda x)} - x - \frac{D_1}{2\lambda}\right]$$

The above is the source of introduction of λ as a factor in the denominator of the second expression in (5.5.21). It suggests that the solution obtained contains a single discontinuity at the limiting condition : λ = 0 denoting fully internal folding. This may be confirmed by applying L'Hôpital's rule to (5.5.21) which indicates the absence of a limit at λ = 0. It is thought that this anomaly is associated with the collapse model of Figure 5.10(i) which indicates that α = 0 for λ = 0. Nevertheless, the author confirms the solution of (5.5.21) having evaluated separately the work done in AB in the portions lying outside and inside the original tube, $W_{ABo}$ and $W_{ABi}$, respectively and summing the results to obtain equation (5.5.21). For the intersted reader, the key formulae

obtained are presented below;

Evaluation of $W_{ABo}$

x measured from A along AB initially and along AB' after deformation in Figure 5.10(i). Thus,

$$0 \leqslant x \leqslant \frac{\lambda h}{\sin(\alpha+\theta)} \qquad \text{and} \qquad 0 \leqslant \theta \leqslant (\tfrac{1}{2}\pi - \alpha)$$

$$W_{ABo} = 2\pi t \int_0^{\frac{1}{2}\pi-\alpha} \int_0^{\frac{\lambda h}{\sin(\alpha+\theta)}} \sigma_{x\theta}\, x \cos(\alpha+\theta)\, d\theta\, dx$$

$$= \pi h t \left[ Y \lambda h(1-\lambda) + \frac{E_p}{\lambda} \left\{ \frac{D_1^2}{2\lambda^2 h} F(\theta) + \lambda^2 h(1 - \lambda + \log_e \lambda) + D_1 ( \lambda(1 - \log_e \lambda) - 1 ) \right\} \right]$$

where

$$F(\theta) = \int_0^{\frac{1}{2}\pi-\alpha} \log_e \left\{ \frac{D_1(1 - \frac{\lambda}{\sin(\alpha+\theta)})}{D_1} \right\} (\lambda - \sin(\alpha+\theta)) \cos(\alpha+\theta)\, d\theta \qquad (5.5.21(a))$$

Evaluation of $W_{ABi}$

x measured from B along BA originally and from B' along B'A after deformation. Thus,

$$0 \leqslant x \leqslant \frac{\Delta}{\sin(\alpha+\theta)} \qquad \text{where } \Delta \text{ is given in (5.5.5) and}$$

$$0 \leqslant \theta \leqslant (\tfrac{1}{2}\pi - \alpha)$$

$$W_{ABi} = 2\pi t \int_0^{(\frac{1}{2}\pi-\alpha)} \int_0^{\frac{\Delta}{\sin(\alpha+\theta)}} (h - x) \cos(\alpha+\theta) \left\{ Y + \frac{2(h - x)(\sin(\alpha+\theta) - \lambda) E_p}{D_1} \right\} d\theta\, dx$$

$$W_{ABi} = \pi h\, t \left\{ Y(1-\lambda)^2 h + \frac{E_p}{\lambda}\left[ \tfrac{1}{2}(1-\lambda^2)(1-2\lambda)h - 2\lambda h(1-\lambda) - 3\lambda^2 h \log_e(\lambda) \right.\right.$$

$$\left.\left. - (D_1 + 2\lambda h)\left\{ \frac{(1-\lambda)^2}{2\lambda} - (1 - \lambda + \lambda \log_e \lambda) \right\} + \frac{D_1^{\,2}}{2\lambda^2 h}\left( G(\theta) - \lambda J(\theta) \right) \right] \right\}$$

where

$$G(\theta) = \int_0^{\frac{1}{2}\pi - a} \log_e \left\{ \frac{D_1 \left(1 - \frac{\lambda}{\sin(a+\theta)}\right)}{D + t} \right\} \sin(a+\theta)\, \cos(a+\theta)\, d\theta$$

$$J(\theta) = \int_0^{\frac{1}{2}\pi - a} \log_e \left\{ \frac{D_1 \left(1 - \frac{\lambda}{\sin(a+\theta)}\right)}{D + t} \right\} \cos(a+\theta)\, d\theta \qquad (5.5.21(b))$$

The reader may wish to verify that by summing the two part-solutions in (5.5.21(a)) and (5.5.21(b)), equation (5.5.21) will be obtained with the three integrals, $F(\theta)$, $G(\theta)$ and $J(\theta)$ conveniently reducing to the following:

$$F(\theta) + G(\theta) - \lambda J(\theta) = \tfrac{1}{2}(1-\lambda)^2 \log_e\left(\frac{D_1}{D+t}\right)$$

<u>Calculation of the work done in deformation of material between hinges B and C in the circumferential direction</u>

Considering Figure 5.9 (iii), it is observed that collapse of BC into B'C' results in circumferential extensions as well as compressions in this member. If x is measured from B' to evaluate the compression work, then $0 \leqslant x \leqslant \Delta / \sin(\phi)$. The author found that if equations are set up to evaluate this work as a continuous triple integration with respect to $\theta$, $\phi$ and x, the final solution contains the factor $\sin\phi$ in the denominator and hence solution fails at the limit of integration $\phi = 0$. This is consistent with the collapse model in Figure 5.10 (i) where the vertical line B'C' ($\phi$=0) confirms the absence of a limit for the range of x. Hence an alternative

approach is proposed where the work done in BC is calculated separately as the sum of two components : (a) stretching of BC in rotation through Ø alone, and (b) compression of BC in translation through θ after complete rotation through Ø. Figures 5.11 (i)-(ii) indicate the collapse sequence proposed.

(a) Work done in stretching of BC, $W_{BCst}$

For x measured from B along BC in Figure 5.11 (i) the following expressions are obtained;

$$\varepsilon_{x\theta} = \frac{2\ x\ \sin\theta}{D + t}$$

$$\sigma_{x\theta} = Y + E_p\ \varepsilon_{x\theta} \qquad (5.5.22)$$

$$dW_{BCst} = 2\pi\ x\ t\ \sigma_{x\theta} \cos\emptyset\ d\emptyset$$

Hence the work done in stretching of BC to BC' at $\emptyset = \frac{1}{2}\pi$ is the double integration of the above with respect to Ø and x giving,

$$W_{BCst} = \pi h^2 t \left\{ Y + \frac{2\ E_p\ h}{3\ (D + t)} \right\} \qquad (5.5.23)$$

(b) Work done in compression/translation of BC, $W_{BCco}$

Considering Figure 5.11 (ii) with x measured from C' along C'B initially and from C" after translation, the following expressions are derived;

$$\varepsilon_x = \frac{2\ h\ (1 - \lambda)}{D + t + 2(h - x)}$$

$$\sigma_x = Y + E_p\ \varepsilon_x$$

$$d\varepsilon_x = \frac{2\ dx}{D + t + 2(\lambda h - x)}$$

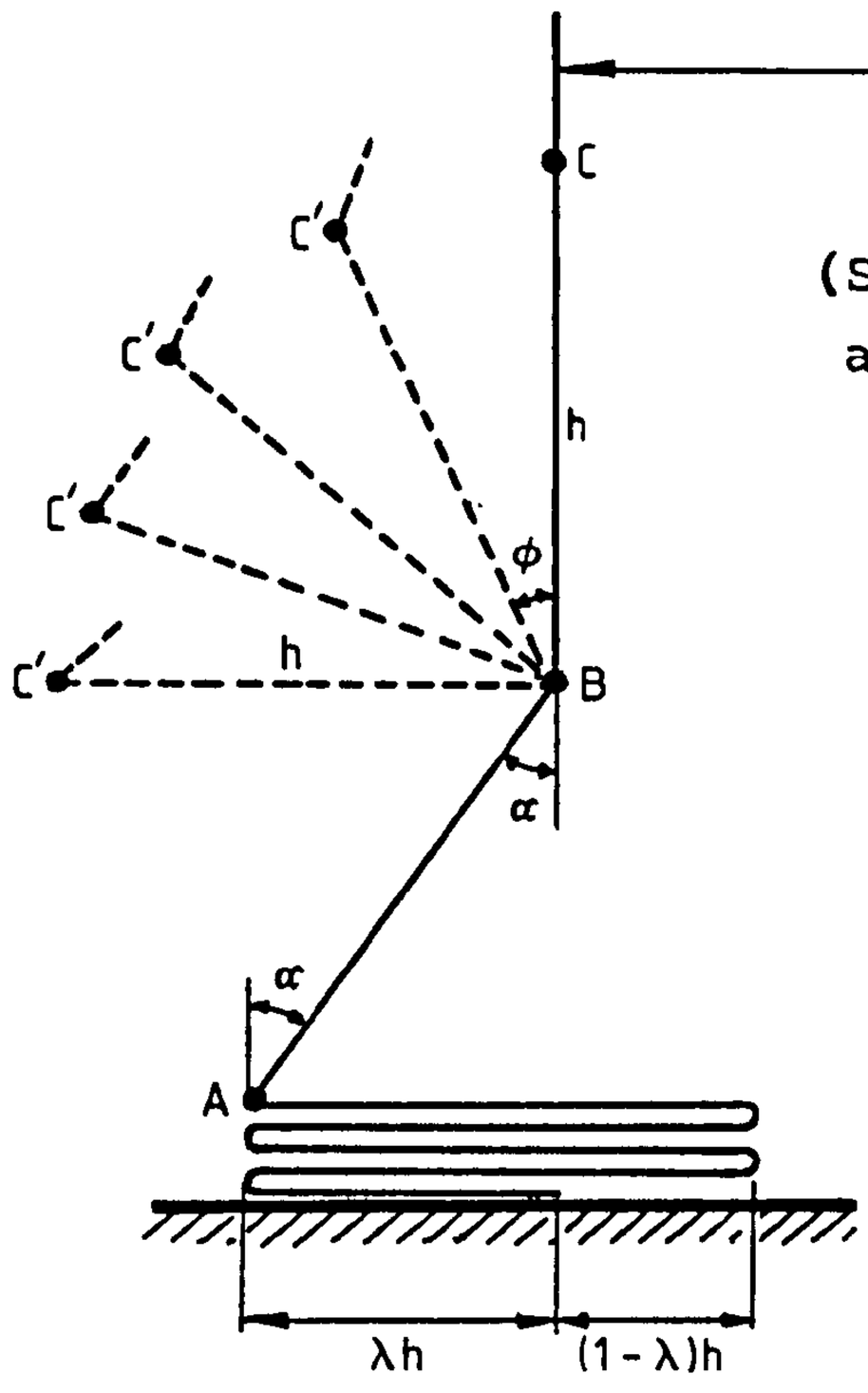


(See Figure 5.9 (iii) :
angle θ = 0)

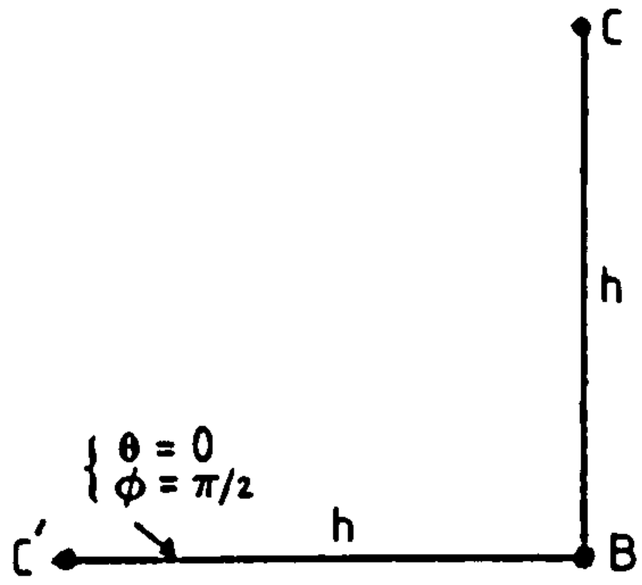


[ i ]

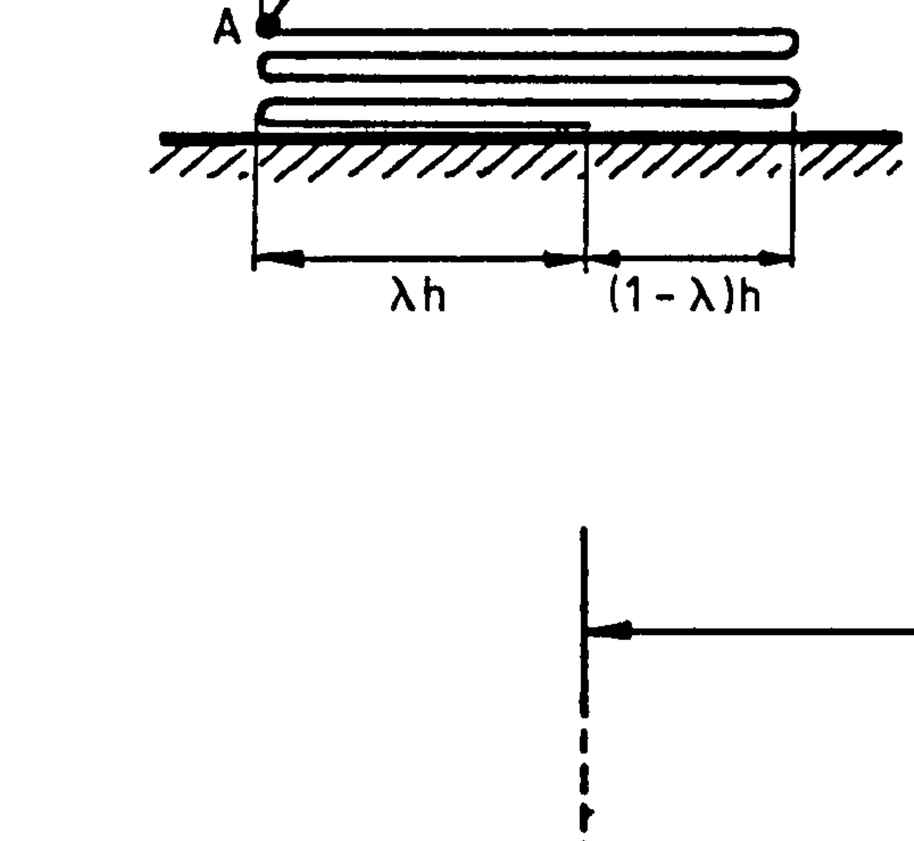


(See Figure 5.9 (iii) :
angle Ø = ½ π)

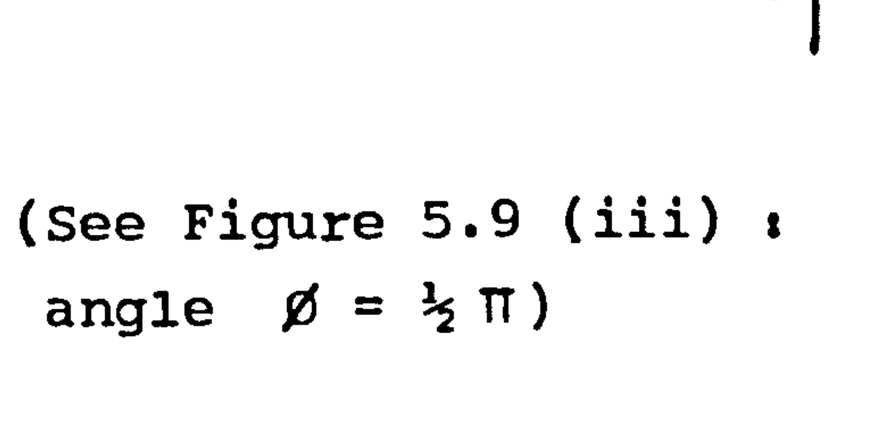


[ ii ]

Proposed Model III
Figure 5.11

$$dW_{BCco} = \pi t \sigma_x d\varepsilon_x \qquad (5.5.24)$$

The required work done is thus the single integration of the above with respect to x between limits of : 0 and h . This gives

$$W_{BCco} = 2\pi ht \left[ Y + (1-\lambda) E_p \log_e \left( \frac{D+t+2h}{D+t} \right) \right] \qquad (5.5.25)$$

Total work done in BC is $W_{BC}$ where

$W_{BC}$ = $W_{BCst}$ (equation (5.5.23)) + $W_{BCco}$ (equation (5.5.25))

Thus,

$$W_{BC} = \pi h t \left[ Y(h+2) + 2 E_p \left\{ \frac{h^2}{3(D+t)} + (1-\lambda) \log_e \left( \frac{D+t+2h}{D+t} \right) \right\} \right] \qquad (5.5.26)$$

With all the entities constituting the internal work done in the collapse of fold ABC evaluated, the total internal work done, $W_I$ is given as follows :

$$W_I = W_{bend} + W_{AB} + W_{BC} \qquad (5.5.27)$$

equations (5.5.15) + (5.5.21) + (5.5.26)

By performing the above sum and equating it to the total external work done, $W_E$ as given in (5.5. 1 ), it can be shown that the following expression for the yield stress parameter Y may be obtained;

$$Y = \frac{\overline{P} - K_3 E_p\{(A_1 - A_2 + A_3 + A_4)\}}{K_3 (A_5 + A_6)} \qquad (5.5.28)$$

where

$$A_1 = \frac{t^2}{12h} D_1 \left\{ (\tfrac{1}{2}\pi - a)^2 K_1 + \pi^2 K_2 \right\}$$

$$A_2 = \frac{t^2}{6} \left\{ (1 - \lambda) K_1 + (\pi^2 - 4) K_2 \right\}$$

$$A_3 = \frac{(1 - \lambda)^2}{2 \lambda^2} \left\{ \frac{D_1^2}{2 \lambda h} \log_e \left( \frac{D_1}{D+t} \right) - (D_1 + \lambda h) \right\}$$

$$A_4 = \frac{2 h^2}{3(D+t)} + 2(1 - \lambda) \log_e \left( \frac{D+t+2h}{D+t} \right)$$

$$A_5 = \frac{t}{2h} \left\{ D_1 (\pi - a) + h(1 - \pi - \cos a) \right\}$$

$$A_6 = h (2 - \lambda) + 2 \qquad (5.5.29)$$

$$K_1 = \frac{2}{(4 h + a t)}$$

$$K_2 = \frac{1}{(8 h + \pi t)}$$

$$K_3 = \frac{\pi t}{(1 + \cos a)}$$

$$D_1 = D + t + 2 \lambda h$$

$$\lambda = \sin a \ .$$

### 5.5.3 Application to experiment

An estimate of the proportion of external folding $\lambda$ has been obtained for each of the different sets of tubes tested that

failed in the concertina mode. This has been evaluated in each case by recording the external diameter of the tubes after collapse, $D^{o}$* and using the following equation,

$$\lambda = \frac{D^{o} - (D + t)}{2h} \qquad (5.5.30)$$

where $h$ is the experimental arm-length of a fold for a given set of tubes tested, as recorded in Figure 5.2 . The results are summarized here to constitute the range : $0.66 < \lambda < 0.73$ with an average of $\lambda \simeq 0.69$ . The individual results obtained are presented in Appendix II , Table A2.2 .

Figure 5.12 indicates the variation of the yield stress $Y$ predicted from (5.5.28) with $\lambda$, for a particular tube tested (data shown on Figure 5.12) using the experimental mean value of the hardening modulus, $E_p$ . Observation shows that for $0.55 < \lambda < 0.95$ (approximately), the values of yield stress obtained for this tube fall within the experimental range recorded in (5.2.1). The peak of the curve in this figure at $\lambda \simeq 0.8$ suggests a failure shape which corresponds to minimum internal work done. This value may be compared with the experimental value of $\lambda \simeq 0.68$ obtained from measurements taken on the experimental tube. The author has observed that the feature of Figure 5.12 with a peak at $\lambda \simeq 0.8$ is common to all the tubes tested; the values of $Y$ predicted from equation (5.5.28) are different, however, because of different $D$, $t$, $h$ and $\overline{P}$.

In spite of its empirical nature, the above feature indicates the possibility of the existence of a 'preferred' collapse

* This is synonymous with $D_1$ in equation (5.5.8)

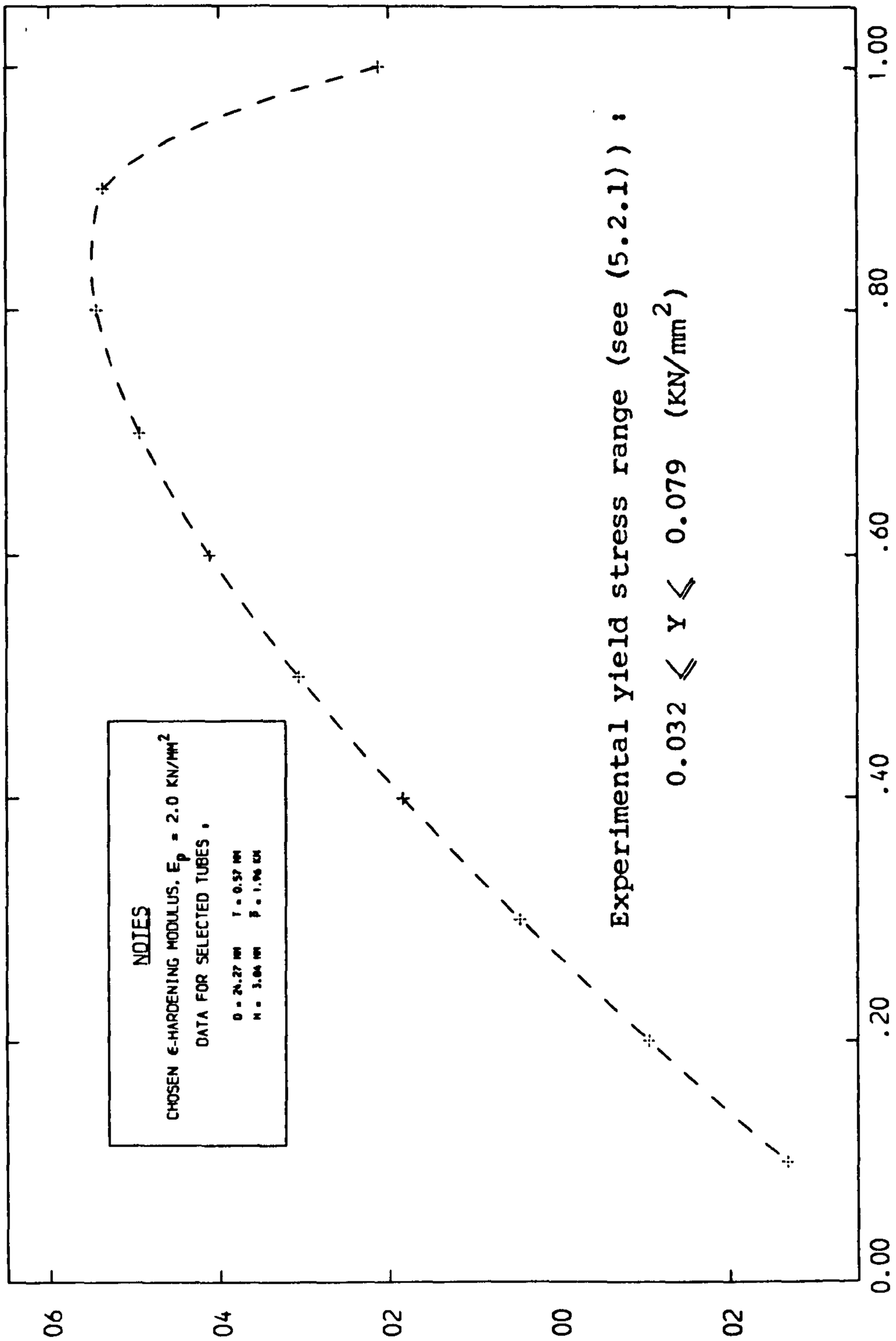
PART EXTERNAL AND INTERNAL COLLAPSE MODEL
PROPORTION OF EXTERNAL FOLDING : λ
CONCERTINA FOLDING
12
Experimental yield stress range (see
0.032 ≤ Y ≤ 0.079 (KN/mm²
NOTES
CHOSEN ε-HARDENING MODULUS, Ep = 2.0 KN/MM²
DATA FOR SELECTED TUBES ,
CALCULATED YIELD STRESS, Y (KN/MM²)
(Equation 5.5.28)
1.00
.80
.60
.40
.20
0.00
.06
.04
.02
0.00
-.02

Figure 5.12

configuration for concertina collapse. For a given tube, this 'preferred' shape is predicted to arise as a result of a minimum internal work expended in the development of a concertina fold.

In summary, it has been illustrated that for a work hardening material, application of Alexander's theory (1) results in solutions which underestimate the internal work done (IWD)† at collapse. An attempt has been made here to incorporate this material feature in the theory, and also to take into account the effects of material incompressibility† and the sensitivity of solutions to collapse shape (as reflected in parameter $\lambda$). The empirical nature of the solutions obtained, however, is reiterated here; this is particularly so in view of the assumptions made concerning the plastic hinges : It was assumed that a plastic hinge is circular in shape and rotates about its centre; surface deformations of a hinge per unit length of tube were assumed to be the product of one half the thickness and the magnitudes of rotation. On this basis, it is concluded that for general application, expressions (5.3.18), (5.4.11) and (5.5.28) provide a guidance in assessing the importance of material input and collapse geometry, towards evaluation of the true IWD at collapse for a concertina fold.

---

†Further experiments may be performed to supplement the theoretical models introduced, by :
(a) measuring circumferential strains (in the evaluation of IWD) from the deformations on a square grid pattern marked or printed on the tube surface
(b) finding variations in tube thickness, t along a concertina fold (to inspect the incompressibility condition) by longitudinal cutting of the collapsed tube and measuring t across the folding.

## 5.6 Conclusion

For the annealed aluminium tubes tested in the experimental study, strain hardening was seen to be a prominent feature.

1. Strain hardening is the main cause of discrepancies in the (high) predictions of yield stress, Y from equation (5.1.1), with observed test values. This reflects an underestimation of the internal work done at collapse, in theory (1).

2. The material model proposed here, together with assumptions on plastic hinges, enabled an alternative formula for prediction of Y to be obtained. Coupled with the condition of material incompressibility, the new formula produced solutions for Y which are fully within the test range.

3. The new collapse model proposed here and applied to test data, suggests the existence of a 'preferred' shape ($\lambda \simeq 0.8$) at collapse (c.f. experimental range : $0.66 < \lambda < 0.73$). Results thus disclose the absence of fully external folding ($\lambda = 1$) assumed in theory (1).

4. The empirical nature of the solutions presented is realised. However, they provide a new guidance in the assessment of material input and collapse shape in theory (1), in evaluating the true internal work done at collapse.

# CHAPTER 6

# INVESTIGATION OF OTHER THEORIES ON THE COLLAPSE BEHAVIOUR OF CYLINDRICAL TUBES

# Chapter 6 - Synopsis

Certain established theories on the axial collapse behaviour of cylindrical tubes are reviewed and investigated. In the first two cases discrepancies are noticed between the solutions of these rigid-plastic theories and experimental results. This is due to strain hardening of the aluminium alloy used. Examination, next, of the classical elastic theory (101) reveals the existence of a bound on the tube geometric ratio, t/R, beyond which theory (101) is inapplicable.

Theories subsequently proposed to improve the classical theory are also investigated and the factors typically suggested as being responsible for the inadequacy of this theory are shown not to account for the actual divergence from test results observed here. The governing factor is the onset of material yield accompanying the collapse of tubes in the geometric range : $0.03 < t/R < 0.18$ considered here and consequently the deviation of theory (101) from the elastic conditions assumed.

## 6.1 Introduction

This chapter presents the comparisons of experimental results with solutions of certain existing theories based on quasi-static axial collapse of circular tubes, and the deductions consequently made regarding the applicability of these and similar theories.

An extension of the theory by Alexander (1) on concertina mechanism, analyzed in Chapter 5, is first examined. This is followed by investigation of a similar rigid-plastic theory (78) on diamond collapse. The discrepancies noticed between the solutions for yield stress, Y, predicted from these theories with observed experimental values is attributed to the presence of strain hardening for the annealed aluminium alloy tested.

A brief review and analysis is presented, next, of an elastic theory predicting the initial axial buckling stress of cylindrical tubes. Proposed by Timoshenko (100), Lorenz (61) and Southwell (92) before the First World War, this linear theory is based on small deflections and its deviation from experimental behaviour has been the subject of extensive study among investigators over the past fifty years. Factors in the order of 2 to 5 for thin-walled tubes have been repeatedly reported as common magnitudes of error associated with solutions of this theory when correlated with experiment. Amongst the influential factors reported are the inevitable presence of geometric imperfections in the otherwise perfect cylinder assumed. This is particularly significant in the case of very thin shells where irregularities, however small,

play a crucial role in reduction of the collapse load of of the tube from that given in the theory. The assumption of infinitesimal deflections, too, has been approached with criticism, since deformations during collapse are of the order of magnitude of the thickness of the tube, and in the case of thin shells, the initial deviations themselves may compare in size with tube thickness.

In the comparisons made here, application of the classical theory to thick-walled tubes is observed to lead to considerably higher discrepancies than those stated above. Imperfections are thus concluded not to be responsible for these deviations. Some of the important theories advancing on the classical theory are also examined and shown to provide little improvement in reducing the magnitudes of discrepancy observed. It is illustrated that the fundamental factor neglected is the inevitable yielding of material for collapse of thick-walled tubes; this is in conflict with the assumption of small deflections and linear elastic behaviour.

## 6.2 Johnson on Concertina Collapse Mechanism

Following Alexander's theory (1) described in Chapter 5 , Johnson et al (48) derived the following equation expressing the mean axial collapse stress, $\bar{\sigma}$ in terms of the geometric ratio, t/D, of a tube failing in the concertina mode:

$$\frac{\bar{\sigma}}{Y} = \left[\frac{2\pi}{\sqrt{3}} \quad (t/D)\right]^{\frac{1}{2}} \qquad (6.2.1)$$

where Y denotes material yield stress in compression. It is believed the above equation was derived by first taking the mean of equations (5.1.3) and (5.1.4) of Chapter 5 denoting, respectively, the conditions for fully external and fully internal folding. This gives

$$\frac{\bar{P}}{Y} = \left( \frac{\pi^2}{2\sqrt{3}\ k} + \pi k \right) t^{1.5}\ D^{0.5} \quad \text{where} \quad k = \left(\frac{\pi}{2\sqrt{3}}\right)^{\frac{1}{2}} \simeq 0.953$$

i.e.,

$$\frac{\bar{P}}{Y} = \left[ \frac{2\pi^3}{\sqrt{3}} \right]^{\frac{1}{2}} t^{1.5}\ D^{0.5} \qquad (6.2.2)$$

Using $A = \pi Dt$ as the approximate net section area of the tube and by dividing both sides of equation (6.2.2) by parameter A, equation (6.2.1) may be obtained.

Figure 6.1 inspects the experimental data obtained here for the proposed relationship of equation (6.2.1) . It is seen that the test data follow a linear trend but not through the origin as the theory implies. This is distinguished by performing two linear regressions with the following values for the constants. (The corresponding details of the individual data points are shown in Table A2.7, Appendix II) .

$$\text{Johnson} : \bar{\sigma} = 0.1916 \left[ \frac{2\pi}{\sqrt{3}} (t/D) \right]^{\frac{1}{2}} \quad KN/mm^2$$

$$\text{Experiment} : \bar{\sigma} = -0.024 + 0.2459 \left[ \frac{2\pi}{\sqrt{3}} (t/D) \right]^{\frac{1}{2}} \quad KN/mm^2 \qquad (6.2.3)$$

The constant obtained in the first relation above denoting the yield stress Y of the material is within the range predicted

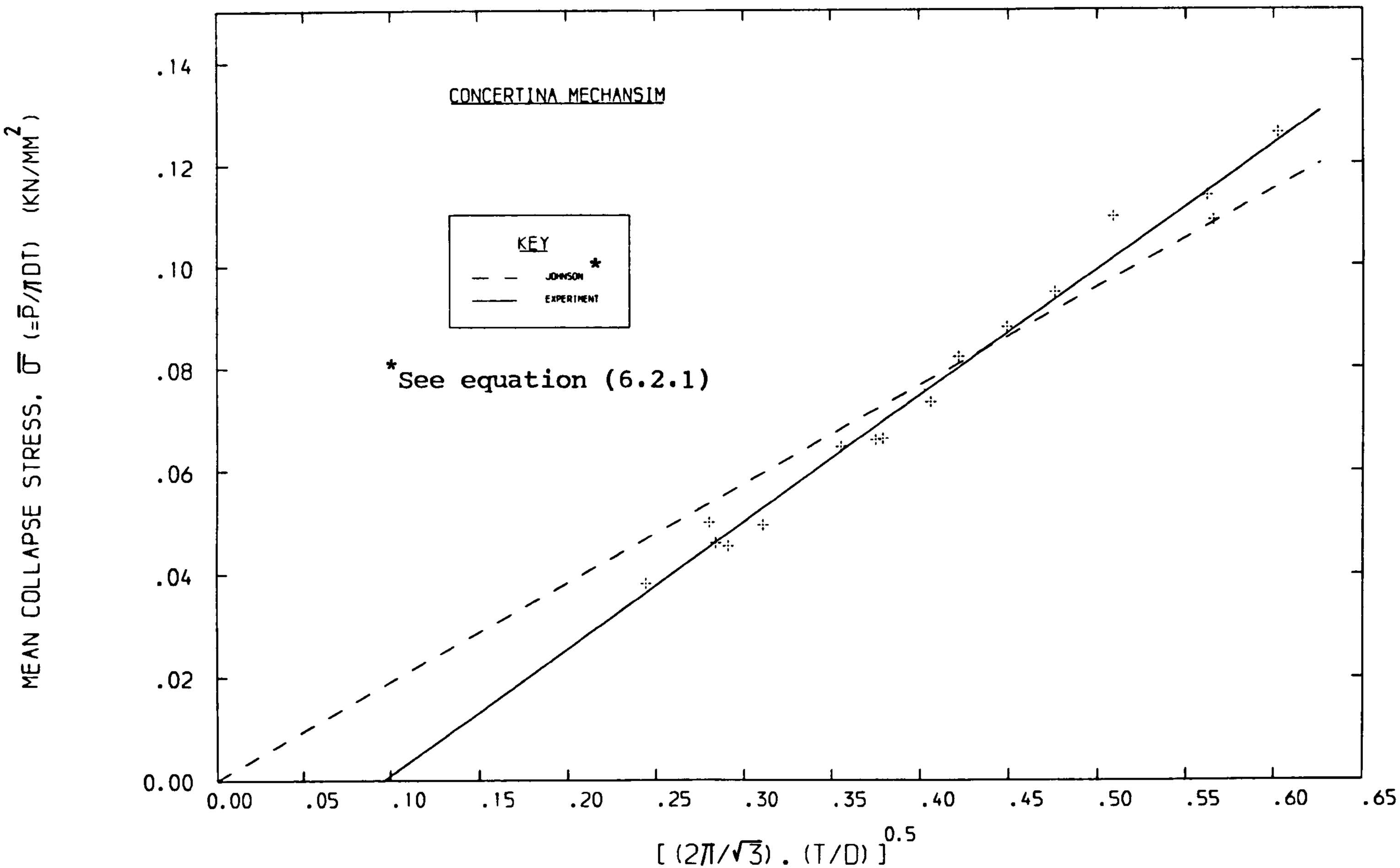


COMPARISON OF JOHNSON'S THEORY WITH EXPERIMENT

**Figure 6.1**

from Alexander's theory (1) (see Chapter 5), as shown below; this value of Y may also be compared with the experimental range of yield stress for the aluminium alloy tested, as follows :

[The value of Y predicted here is an expected result since equation (6.2.1) is derived from theory (1), as stated earlier]

See expressions (5.2.1), Chapter 5

| | | |
|---|---|---|
| Experiment (Direct yield test) | : | $0.032 \leqslant Y < 0.079$ (KN/mm$^2$) |
| Alexander's theory (1) (equation (5.1.1)) | : | $0.149 < Y \leqslant 0.200$ (KN/mm$^2$) |

(6.2.4)

Since equation (6.2.2) is identical to equation (5.1.5) of Chapter 5 and the test data 'obeyed' the latter equation (see Figure 5.3), the question arises as to why the same test data follow a different trend in Figure 6.1 and not in accordance with equation (6.2.1) (derived from (6.2.2)). This is reasoned as follows.

Considering the values of Y predicted from Alexander's theory (1) (see Table A2.1, P.346), it is noticed that Y varies with corresponding tube ratios of t/D. Figure 6.2(i) indicates the curvilinear trend thus obtained. Applying a square-root best-fit regression, it is found that

$$Y = A\,(t/D)^{\frac{1}{2}} + B \qquad \text{where } A = 0.228,\ B = 0.123 \qquad (6.2.5)$$

(A & B have units of KN/mm$^2$)

Substituting the above expression into Alexander's equation (5.1.5) gives,

$$\bar{P} = C\left[At^2 + Bt^{1.5}D^{0.5}\right] \qquad (6.2.6)$$

Figure 6.2(ii) presents the experimental data obtained for the above relationship. Application of a linear regression of

the form, $y = ax + b$ gives,

$$\bar{P} \simeq 6.339\left[At^2 + Bt^{1.5}D^{0.5}\right] + 0.327 \quad \text{(small term - may be neglected)} \qquad (6.2.7)$$

Now, dividing both sides of equation (6.2.7) by tube net section area, $A = \pi D t$ gives,

$$\bar{\sigma} = C\left[A'(t/D) + B'(t/D)^{\frac{1}{2}}\right] \qquad A' = A/\pi = 0.073 \text{ KN/mm}^2 \qquad B' = B/\pi = 0.039 \text{ KN/mm}^2 \qquad (6.2.8)$$

Figure 6.2(iii) shows the results obtained for the above relationship. Application of a similar regression gives,

$$\bar{\sigma} = 6.585\left[A'(t/D) + B'(t/D)^{\frac{1}{2}}\right] - 0.002 \quad \text{(small term - may be neglected)} \qquad (6.2.9)$$

It is inferred that by incorporating the extra term $At^2$, equation (6.2.6) provides the 'complete' relationship between $\bar{P}$, D and t; (c.f. equation (5.1.5)). This extra term emerges as $A'(t/D)$ in (6.2.8) and is responsible for the deviation of the linear trend of test data in Figure 6.1 from the origin.

However, in spite of the deviation from Johnson's graph, the linear trend of the test data in Figure 6.1 may be used as possible experimental evidence for the following finding. Since we are dealing with one particular collapse mechanism, that is the concertina mode, the intercept of this relation with the horizontal axis may be used (as a Southwell plot) to provide a bound on t/D ratios of tubes for collapse in this mode. A figure of $t/D = 0.0026$ is obtained at the intercept. Superposition of this value on the collapse classification chart of Figure 2.1 (Chapter 2) confirms the possibility of this feature as a geometric transition from collapse in concertina to one of purely diamond modes.

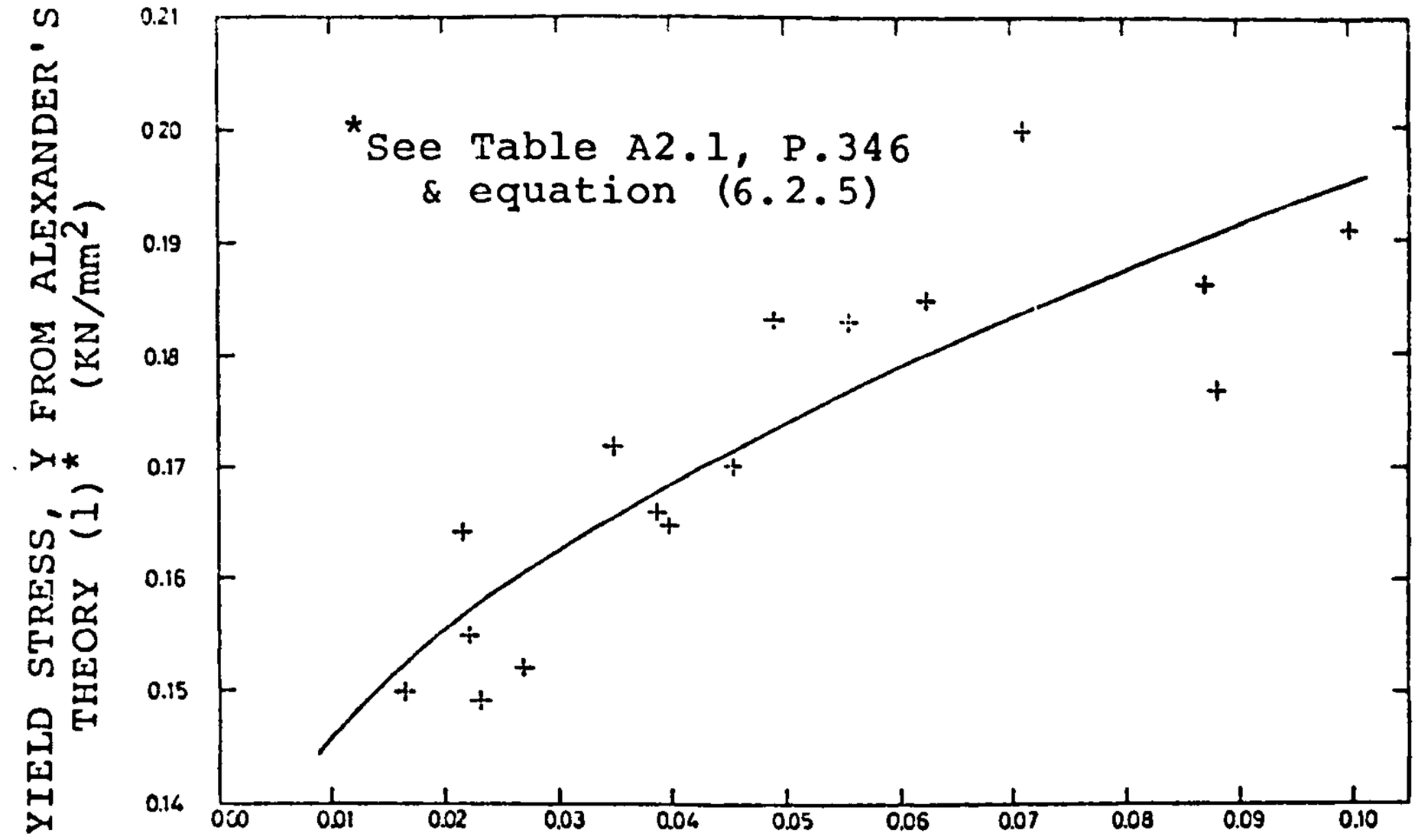


Figure 6.2 (i)

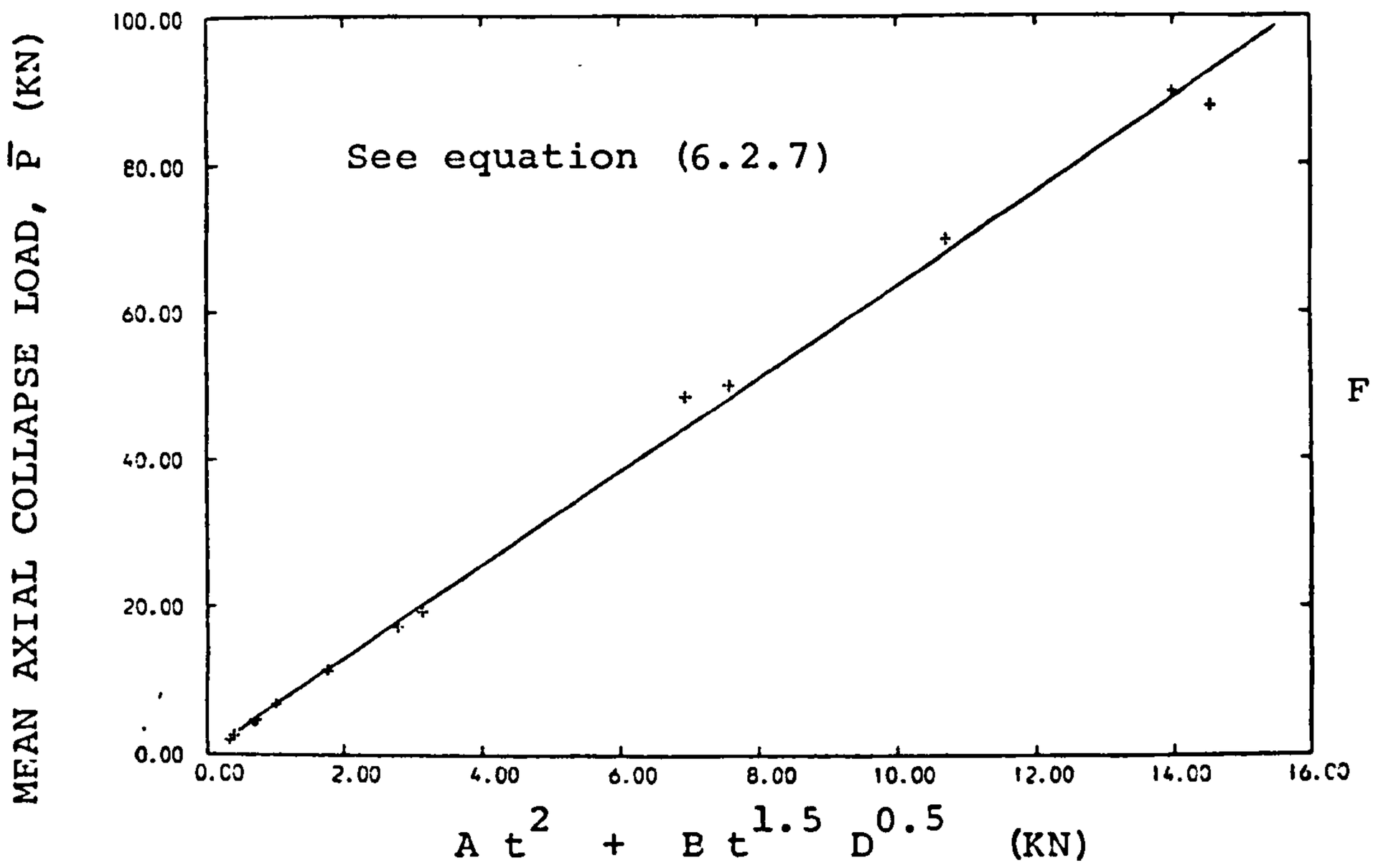


Figure 6.2 (ii)

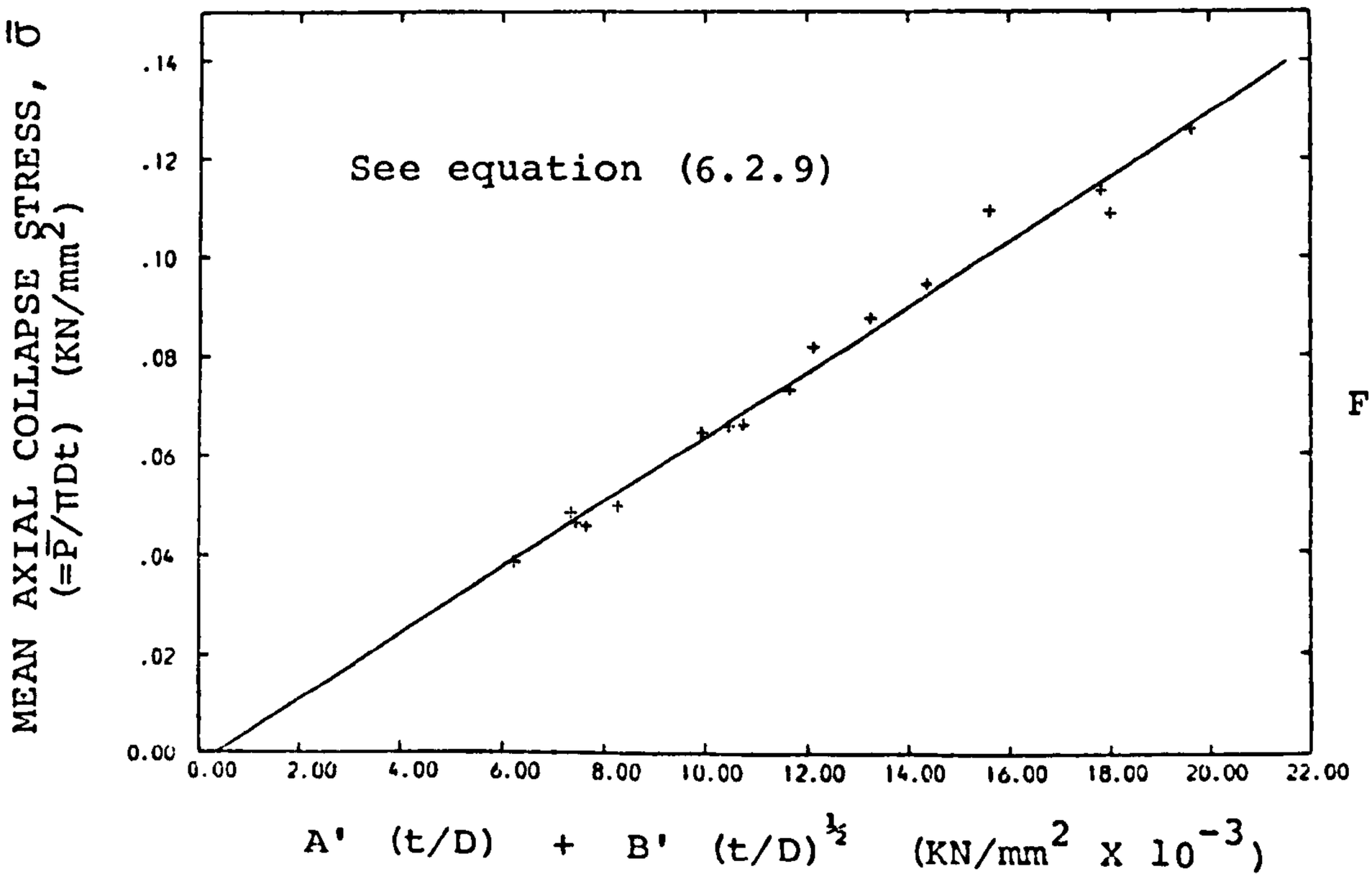


Figure 6.2 (iii)

Figure 6.3 presents an alternative comparison of Johnson's expression (6.2.1) with experiment, by performing a square root regression for the test data and by comparing this curve with those obtained from (6.2.1) for different values of the yield parameter, Y. In this case the true net section areas of the tubes are used $\left[ A = \pi t(D+t) \right]$ in computation of $\bar{\sigma}$; these are only marginally different from the approximate area defined in theory (48). The constant of the square root regression for the experimental curve is found to be 0.3424 ; this produces a value of $Y = 0.180$ KN/mm$^2$ in equation (6.2.1) for the matching of this equation (dotted curves in Figure 6.3) with the experimental curve (c.f. experimental Y in (6.2.4) ).

The present author was interested to observe if a similar square root relationship exists for diamond collapse. Figure 6.4 illustrates the application of a similar regression to the diamond test results obtained here (constant obtained is 0.2815), and compares the levels of resistance for concertina and diamond collapse. For the range considered, the higher collapse stress for the concertina mode reflects a greater efficiency in dissipation of energy. This is consistent with earlier finding favouring this mode (Chapters 3 & 4) as regards the energy absorption capacity of circular tubes.

On the basis of the results presented, the present author concludes by suggesting the inclusion of a term involving parameter t/D on the right hand side of equation (6.2.1), so that, $\bar{\sigma} = \bar{\sigma}((t/D)^{\frac{1}{2}}, (t/D))$; this stems from the observation made here that the values of Y predicted from Alexander's

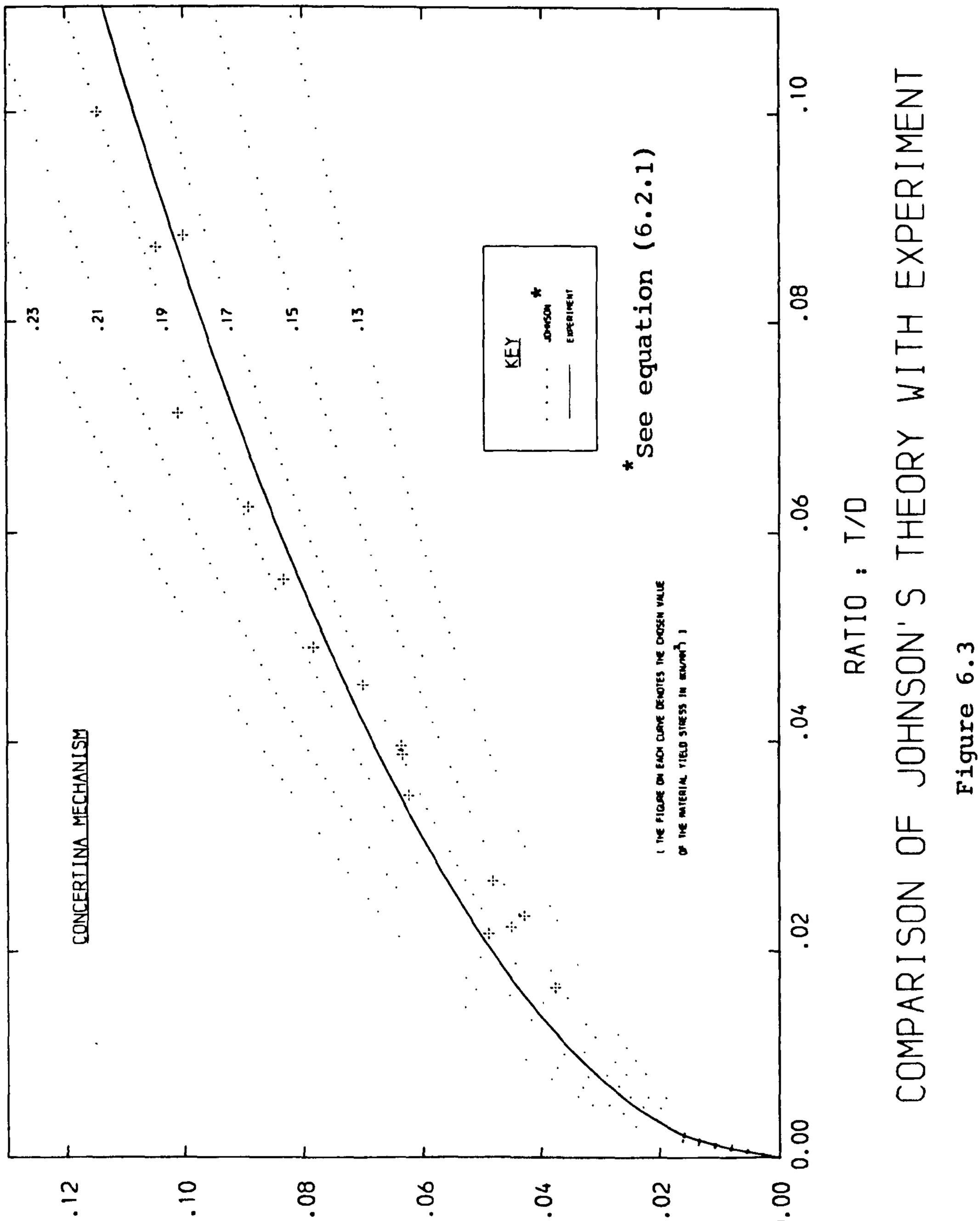


COMPARISON OF JOHNSON'S THEORY WITH EXPERIMENT

Figure 6.3

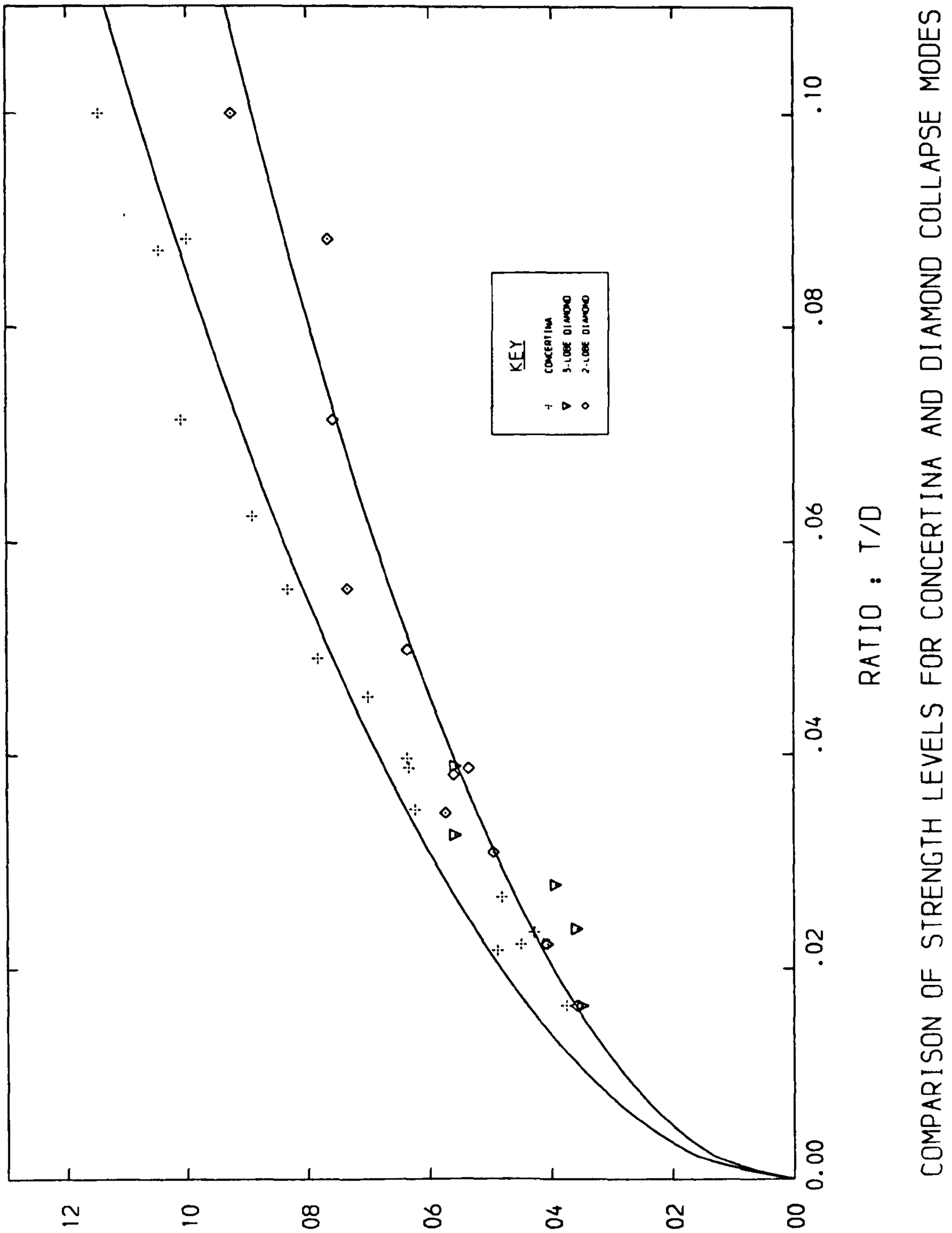
COMPARISON OF STRENGTH LEVELS FOR CONCERTINA AND DIAMOND COLLAPSE MODES
RATIO : T/D
MEAN COLLAPSE STRESS, σ̄ (=F̄/A) (KN/MM²)
KEY
CONCERTINA
3-LOBE DIAMOND
2-LOBE DIAMOND
0.00
.02
.04
.06
.08
.10
.12

**Figure 6.4**

theory (1) exhibit a rising trend with t/D ratio of tubes. Hence, for general application; it is proposed that equation (6.2.8) is used where parameters C, A' and B' are constants for a particular material.

## 6.3 Pugsley on Diamond Collapse Mechanism

For collapse of a circular tube in the diamond mechanism, Pugsley et al (78) proposed and assembled the following energy constituents associated with this instability configuration. Based on rigid-plastic material behaviour, the internal work is that expended in collapsing a diamond fold from an initial square shape, with its diagonals in the axial and circumferential directions, to the final pattern of a folded rhomboid (Figure 6.5). This is in two parts :

1. The work done in folding along the sides and a diagonal of a diamond; this is the product of the full plastic moment per unit fold length, angle of rotation, $\pi$ and the total length of the fold lines
2. The work done in distortion of the diamond shape to a rhombus in the form of plastic shear deformation along the sides of the diamond.

The external work done is the product of the mean resistance, $\bar{P}$ and the axial distance by which folding proceeds. Equating internal and external work, the following general relationship was derived;

$$\bar{P} = 2 k_1 n Y t^2 - 2 k_2 n q t d \qquad (6.3.1)$$

where

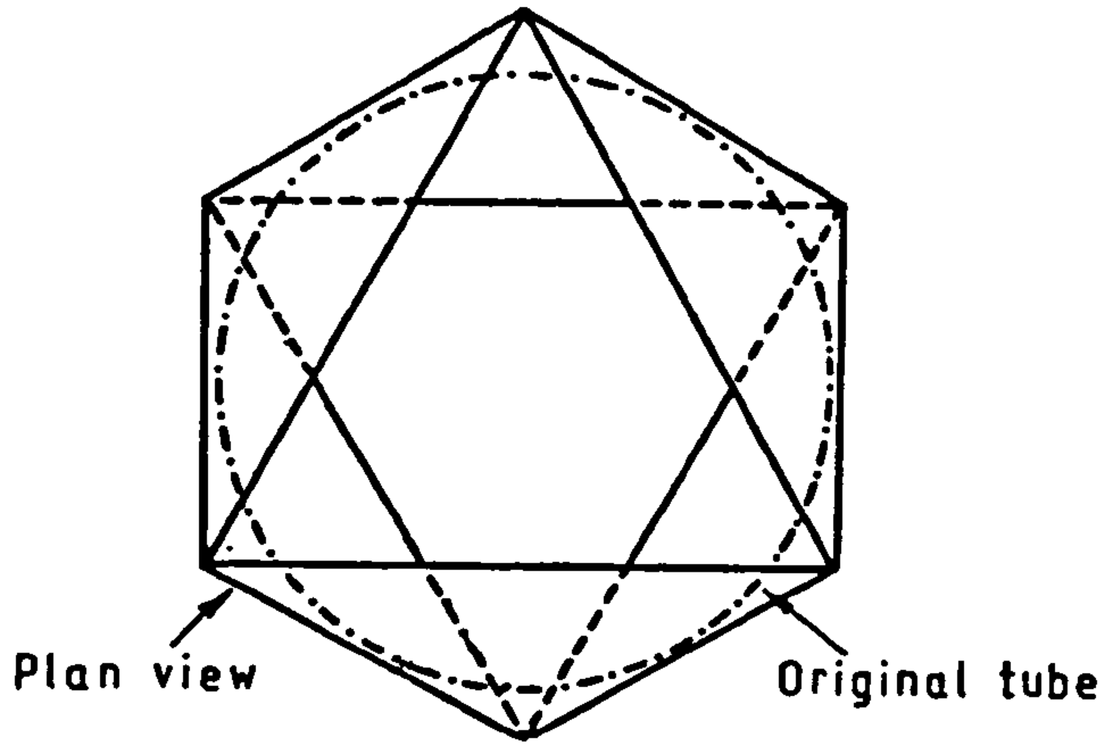


3-lobe diamond

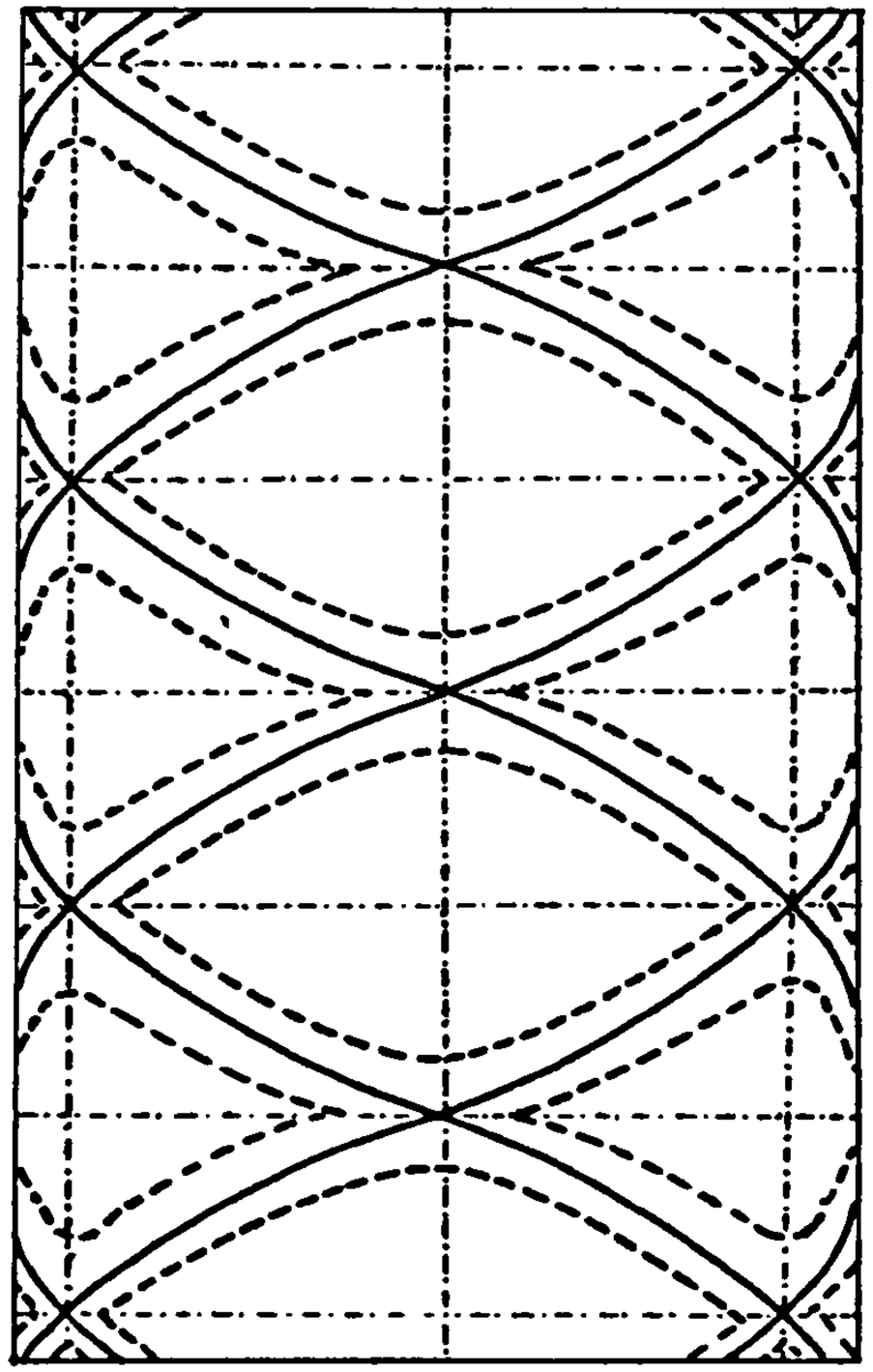

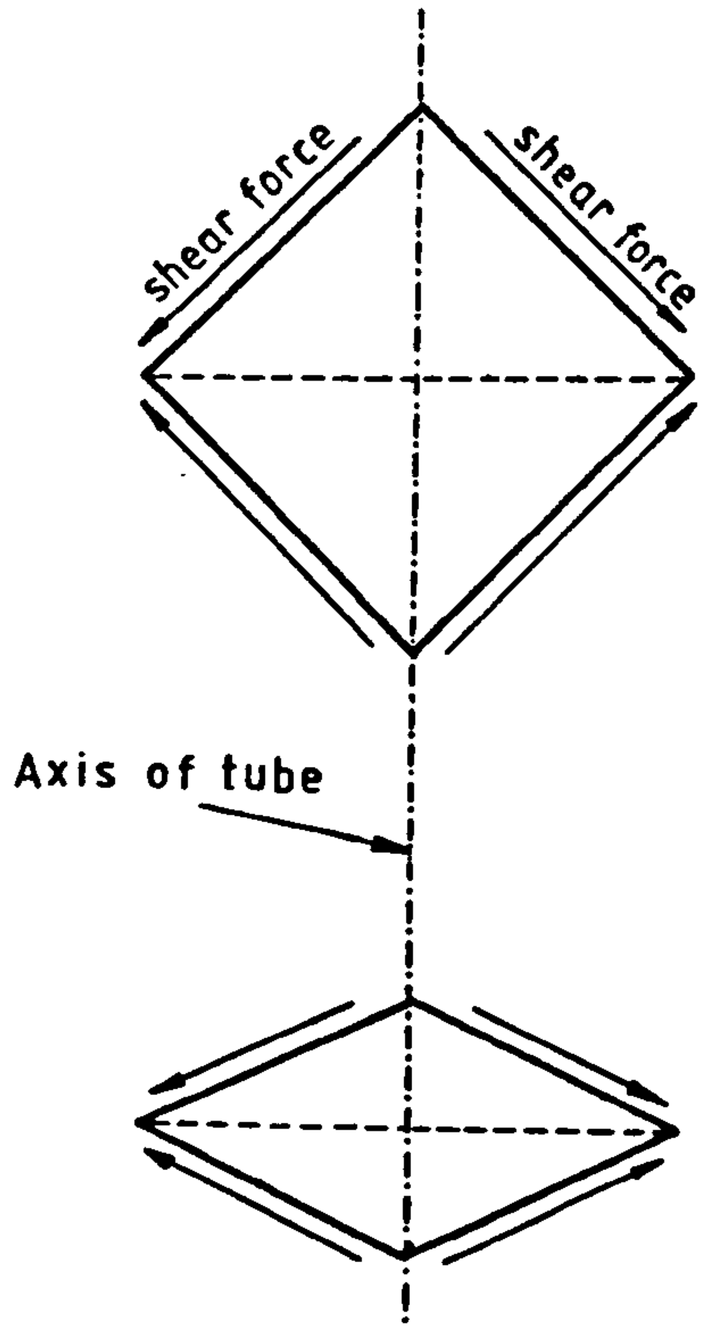


Folding rhomboid

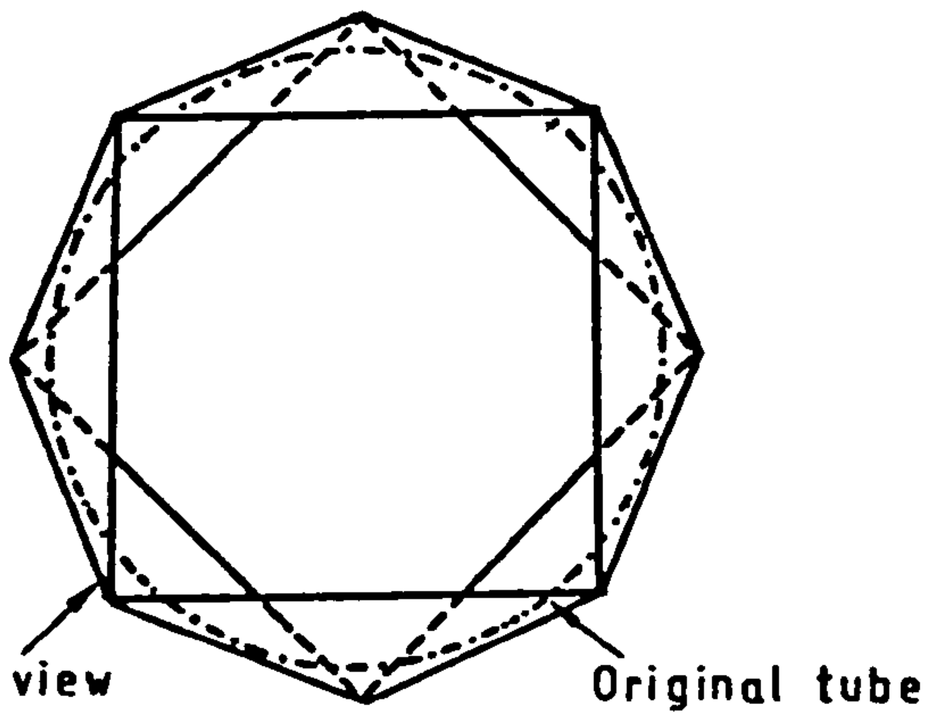


4-lobe diamond

Model proposed by Pugsley for collapse in the diamond mechanism (78)

Figure 6.5

n denotes the number of lobes around the circumference

d is the length of a circumferential diagonal

$k_1$ & $k_2$ are geometric coefficients depending on the shape of the distorted diamond

q is the average shear stress on the side of a diamond.

In the above relation n is restricted to assume integer values larger than and including 3. The authors therefore eliminate the possibility of 2-lobe diamond folding in the reported work. The load $P_o$ that causes yielding of the tube in compression is given as

$$P_o = 2 \pi R t Y \qquad (6.3.2)$$

where R is the mean tube radius. Assuming collapse of the tube is inextensional, that is the buckled pattern conforms to that of the Yoshimura pattern (107), then,

$$n d = 2 \pi R \qquad (6.3.3)$$

With appropriate values of 1.7 and 0.18 for $k_1$ and $k_2$ defined in the theory and $q/Y = 1/3$ as a tentative estimate, Pugsley proposed the following expression for collapse of tubes in the 3-lobe diamond mode,

$$\frac{\bar{P}}{P_o} \left( = \frac{\bar{\sigma}}{Y} \right) = 1.6 \left( \frac{t}{R} \right) + 0.12 \qquad (6.3.4)$$

where $\bar{\sigma}$ denotes the mean collapse stress. Figure 6.6 compares the trend of the experimental data obtained for diamond collapse * against the above equation by performing a hyperbolic regression

*For details of individual data points, see Table A2.8 in Appendix II

of the form : $y = a/x + b$ . The constants obtained are 0.3673 and 0.0262, respectively.

Since many of the data points in Figure 6.6 correspond to the 2-lobe diamond mode and the theoretical set of graphs for equation (6.3.4) are based strictly on the 3-lobe mode, then a direct comparison is essentially inconsistent. However, if the theory is assumed to be equally applicable to the 2-lobe mode, this figure indicates that a value of $Y = 0.228$ $KN/mm^2$ is required for matching of equation (6.3.4) with experiment (c.f. experimental range of Y, shown below). Although the yield condition is defined as a 0.2% proof stress in the reported work, this is only marginally different from the 0.1% proof stress used here to locate the yield condition for the aluminium used. The value of $Y = 0.228$ $KN/mm^2$ required in equation (6.3.4) for description of the experimental trend is in conflict with the experimental range of Y, namely

$$0.032 \leqslant Y \leqslant 0.079 \ (KN/mm^2) \qquad \text{(see (5.2.1), Chapter 5)}$$

and in fact exceeds the theoretical range in Alexander's theory (1) on concertina collapse (see (5.2.1)). It is realised that the rigid-plastic model assumed in theory (78), too, does not permit a full estimate to be made of the magnitude of internal work done at collapse in the case of a strain hardening material, as that of the alloy used. Associated with this deduction is the assumption that the buckled shape is material independent ; Equation (6.3.3) implies that changes in the cross-sectional shape of the tube take

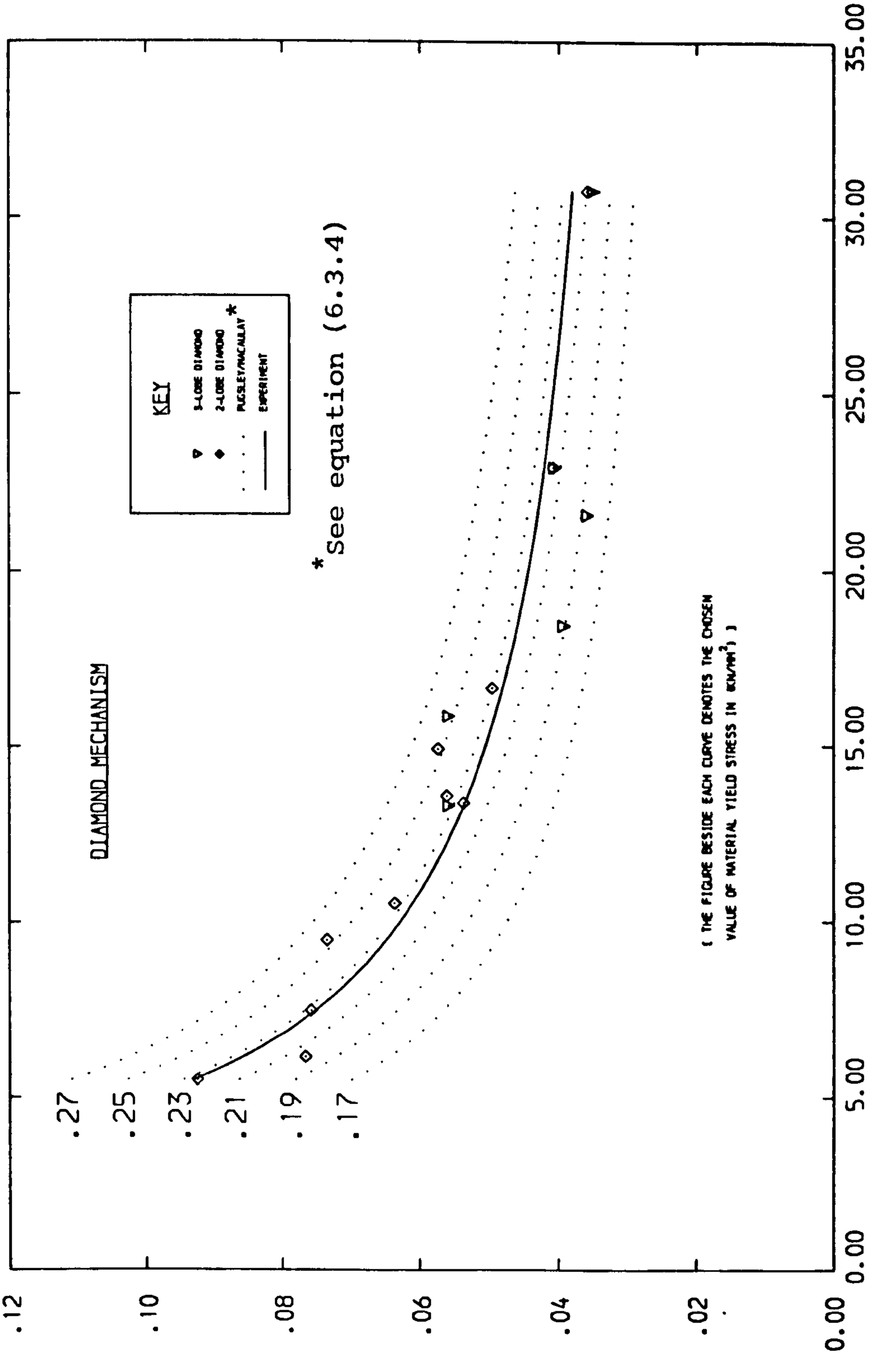
COMPARISON OF PUGSLEY AND MACAULAY'S THEORY WITH EXPERIMENT
RATIO : R/T (R=MEAN RADIUS OF TUBE)
MEAN COLLAPSE STRESS, σ̄ (=F̄/A) (KN/MM²)
0.00
5.00
10.00
15.00
20.00
25.00
30.00
35.00
.12
.10
.08
.06
.04
.02
0.00
.27
.25
.23
.21
.19
.17
DIAMOND MACAULAY
( THE FIGURE BESIDE EACH CURVE DENOTES THE CHOSEN VALUE OF MATERIAL YIELD STRESS IN KN/MM²) )
KEY
3-LOBE DIAMOND
2-LOBE DIAMOND
PUGSLEY/MACAULAY*
EXPERIMENT
*See equation (6.3.4)

Figure 6.6

place without the development of circumferential extensions.

Extending the theory discussed in a work reported later, Pugsley (77) proposed the following relationship for collapse of tubes in the concertina mode;

$$\frac{\bar{P}}{P_o} \quad \left( = \frac{\bar{\sigma}}{Y} \right) \quad = \quad 2 \left( \frac{t}{R} \right)^{\frac{1}{2}} \qquad (6.3.5)$$

The trend of the experimental data obtained for the above relationship has been presented indirectly in Figure 6.4 of the preceding Section with R replaced by D, the tube internal diameter. A value of 0.3424 was obtained in Section 6.2 for the constant of the square root regression in this figure. Hence for correlation of equation (6.3.5) with the experimental data, a value of Y slightly larger than 0.121 $KN/mm^2$ is required in this equation, (since R is the mean radius and not the internal tube radius). This theoretical value of Y is again in discrepancy with the experimental range of Y, as indicated in the preceding paragraph.

The author concludes by sharing, to some degree the criticism of theory 78 as expressed in the work reported in Reference 98, that the assumption of rigid-plastic material behaviour in this theory can lead to significant deviations from experimental observations, for a strain hardening material. However, the deductions made in Chapter 5 regarding criticism of Alexander's theory in this reference apply here too, namely that the suggestion of replacement of Y by $Y_u$, the ultimate stress of the material, is insufficient for representing accurately

the internal work done during collapse.

A similar empirical model to those proposed for concertina collapse mode in Chapter 5 is recommended for the diamond mechanism where the internal work is evaluated in accordance with the true material behaviour; this, for the alloy tested, may be closely resembled by a rigid-linearly-strain-hardening model. Since the stresses are not constant beyond yielding of the material in this model, the effect of the large deformations that accompany collapse would then have to be incorporated in the modified model.

## 6.4 The Classical Elastic Theory of the Buckling of Cylindrical Shells

With the aid of the Ritz method to express the radial deformations in axisymmetric buckling of a cylindrical shell, Timoshenko (101) used the energy method to obtain the critical value of the axial load per unit perimeter length of the shell at which failure precipitates. The collapse configuration assumed is a sinusoidal waveform along the whole length of the tube and is represented in Figure 6.7 .

In this upper bound linear theory, the total strain energy is defined as the sum of the energy in axial compression up to the point of buckling and the extra energy in bending and circumferential deformation of the shell brought about during collapse. Equating this to the work done by the axial load in shortening the tube, and following a minimization procedure, the following equation was derived for the critical stress at collapse;

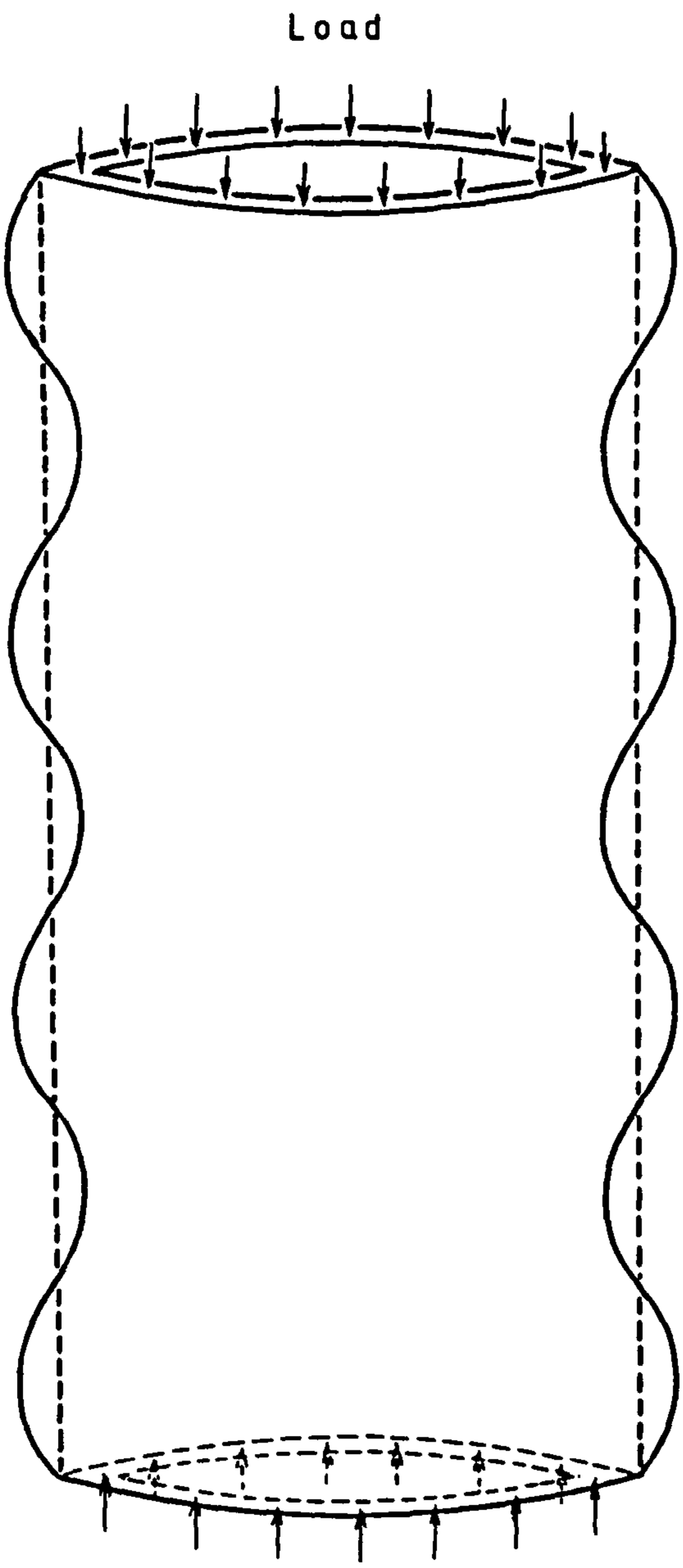


Collapse model proposed by Timoshenko in
the Classical Theory
(101)

Figure 6.7

$$\sigma_{cl} = \frac{E\ t}{R\ \{3(1-\nu^2)\}^{\frac{1}{2}}} \qquad (6.4.1)$$

where $E$ = modulus of elasticity of the shell material

$R$ = mean radius of shell

$\nu$ = Poisson's ratio

From the same minimization, the length of half-waves, $h$ into which the shell buckles is given as

$$h = \pi \left[ \frac{R^2\ t^2}{12(1-\nu^2)} \right]^{\frac{1}{4}} \qquad (6.4.2)$$

It is realised from inspection of Figure 6.7 that for collapse of a tube in the concertina mode, the above expression corresponds to one arm-length of a concertina fold, as has been discussed in Chapter 5, in the context of Alexander's theory (1).

Equations (6.4.1) and (6.4.2) in the classical theory (101) are applicable only to buckling within the elastic limit of the material. This, therefore, confines the use of these expressions to the class of very thin shells. However, quoting from Ref. (101), it is claimed that 'if the shell is not very thin and buckling extends beyond the proportional limit', the above expressions are valid with only a minor modification as follows,

$$\sigma_{cl} = \frac{\{E_r\ E\}^{\frac{1}{2}}\ t}{R\ \{3(1-\nu^2)\}^{\frac{1}{2}}} \qquad (6.4.3)$$

$$h = \pi \left[ \frac{R^2\ t^2}{12(1-\nu^2)} \right]^{\frac{1}{4}} \left[ \frac{E_r}{E} \right]^{\frac{1}{4}} \qquad (6.4.4)$$

where the term $E_r$ is used to denote the reduced modulus of

elasticity but remains undefined in relation to E or the yielding of the tube, in this theory.

From the stress-strain graphs obtained to determine the yield stress (as 0.1% proof stress) of the aluminium alloy tested, a set of values for the modulus of elasticity, E have been obtained and presented in Appendix II, with a mean figure of $E = 33.8\ KN/mm^2$ .*

For the set of tubes tested failing in concertina (axisymmetric) mode as in theory 101, an estimate of the critical stress may be obtained in each case by dividing the axial collapse load, $P_{cr}$, by the net section area of the tube. Figure 6.8 compares these experimental values of critical stress† with those that would have resulted from the linear equation (6.4.1) using the above mean figure of E for different values of Poisson's ratio. If the latter solutions were to be extended over the range of the geometric ratio t/R for the test data considered, the vast overestimation of this experimental range of the critical stress by the linear theoretical set would be revealed! However, for suitable graphic representation these solutions are curtailed at low magnitudes of the tube t/R ratio. For the test recordings a linear regression has been performed giving the following constants:

$$\sigma_{cr} = 0.3018\ (\frac{t}{R}) + 0.0793 \qquad \text{for} \quad 0.03 < \frac{t}{R} < 0.18 \tag{6.4.5}$$

Considering the above limits, equations (6.4.1) and (6.4.5)

* For individual test results for E , see Table A2.6, Appendix II
† Details are presented in Table A2.9, Appendix II

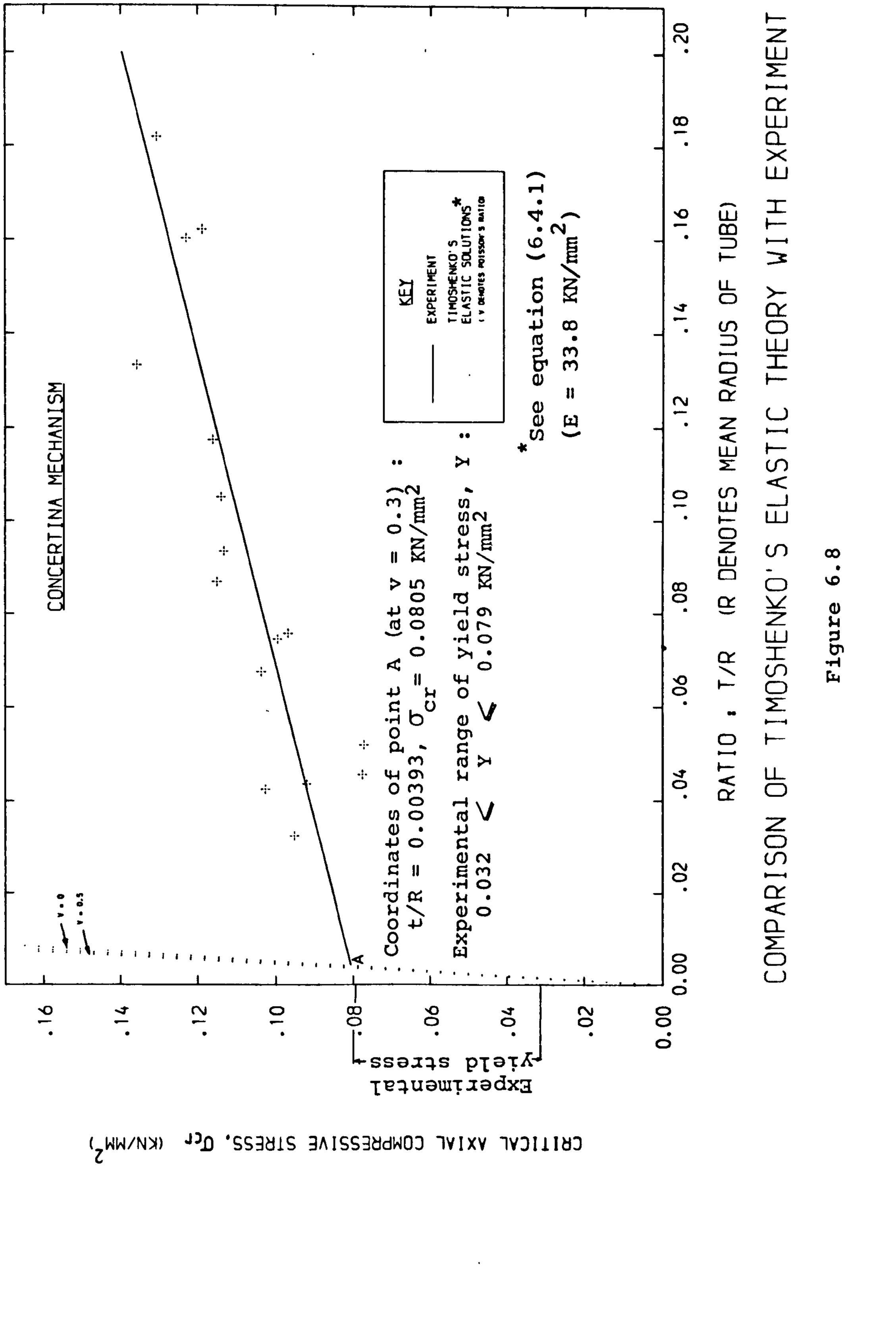
COMPARISON OF TIMOSHENKO'S ELASTIC THEORY WITH EXPERIMENT
CONCERTINA MECHANISM
RATIO : T/R (R DENOTES MEAN RADIUS OF TUBE)
CRITICAL AXIAL COMPRESSIVE STRESS, $\sigma_{cr}$ (KN/MM$^2$)
Experimental yield stress
0.00 .02 .04 .06 .08 .10 .12 .14 .16 .18 .20
0 2 4 6 8 0 2 4 6
A
ν = 0
ν = 0.5
KEY
EXPERIMENT
TIMOSHENKO'S ELASTIC SOLUTIONS* (ν DENOTES POISSON'S RATIO)
Coordinates of point A (at ν = 0.3) :
t/R = 0.00393, $\sigma_{cr}$ = 0.0805 KN/mm$^2$
Experimental range of yield stress, Y :
0.032 ≤ Y ≤ 0.079 KN/mm$^2$
*See equation (6.4.1)
(E = 33.8 KN/mm$^2$)

Figure 6.8

may be combined to indicate that for the geometric range of t/R considered and Poisson's ratio, $\nu = 0.3$, the theory overestimates the actual failure stress by factors ranging from 7 to 27.5 .

These factors exceed considerably the single figures of 2 to 5 commonly reported as the magnitudes of discrepancy. Clearly, geometric imperfections are not responsible for this trend, particularly in view of the relatively thick tubes considered for which irregularities are less influential than in very thin tubes.

Bearing in mind that equation (6.4.1) applies to buckling within the linear elastic range of the material and that the data recorded in Figure 6.8 correspond to tubes failing in concertina mode, that is beyond yielding of the material, the author concludes, from observation of the trends in this figure, that there must exist a limit on the values of the geometric ratio t/R beyond which Timoshenko's theory is inapplicable. This limiting condition is suggested to be the value of t/R at which the critical stress of the corresponding tube coincides with its yield stress. For values of t/R below this critical value, the tube is expected to collapse in an entirely elastic manner with the corresponding critical stress below the yield value. But for t/R above this value, the critical stress is governed by the actual properties of the material beyond the yield condition which is no longer expressed by this linear theory. This would account for the magnitudes of error observed here.

The validity of the above deduction may be confirmed by extrapolating the experimental line in Figure 6.8 to intercept the theoretical set, at the point : $t/R = 0.00393$, $\sigma_{cr} = 0.0805$ KN/mm$^2$, for $\nu = 0.3$ . Two features emerge from this intersection;

1. The above critical stress almost coincides with the upper limit of experimental yield stress range : $0.032 < Y < 0.079$ (KN/mm$^2$), for the alloy used. This result is reminiscent of the Euler theory for a strut in which the hyperbolic relationship between the critical load, $P_E$ and strut length, L is bounded by the ultimate compressive strength of the material at a particular value of L. For struts shorter than this critical length, no gain in load-bearing capacity is obtained as the theory would imply.

2. Considering the fact that elastic buckling is associated with thin tubes failing purely in the diamond mechanism, the critical value of $t/R$ ($\equiv t/D \simeq 0.002$) may be compared with the value of $t/D = 0.0026$ derived in Section 6.2; this value was proposed as a point of geometric transition from collapse in concertina to one of purely diamond modes.

Figure 6.9 compares the values of arm-length of a concertina fold for the tubes tested with the theoretical length of half-waves given in equation (6.4.2) for different values of $\nu$ . These are also compared with Alexander's relation (see Figure 5.2 of Chapter 5). Since the latter is a square root function of product Dt as opposed to product Rt, for direct comparison it has been necessary to re-arrange equation (6.4.2) as follows.

*Details are presented in Table A2.2, Appendix II

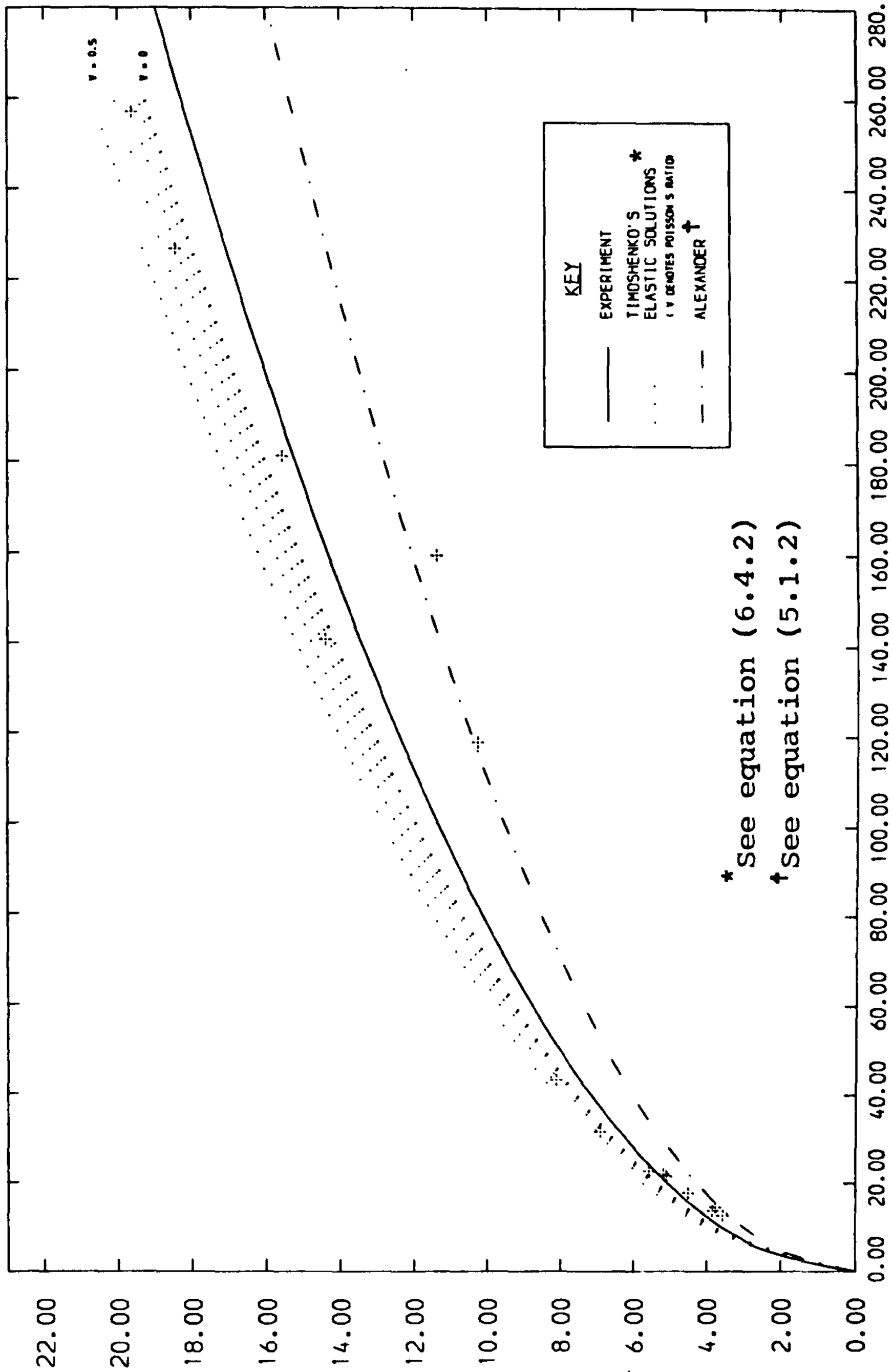
COMPARISON OF TIMOSHENKO'S ELASTIC THEORY WITH EXPERIMENT
ARM-LENGTH OF A CONCERTINA FOLD, H (MM)
PRODUCT D.T (MM²)
KEY
EXPERIMENT
TIMOSHENKO'S ELASTIC SOLUTIONS
( ν DENOTES POISSON'S RATIO)
ALEXANDER †
ν = 0.5
ν = 0
*See equation (6.4.2)
†See equation (5.1.2)
0.00 20.00 40.00 60.00 80.00 100.00 120.00 140.00 160.00 180.00 200.00 220.00 240.00 260.00 280.00
22.00 20.00 18.00 16.00 14.00 12.00 10.00 8.00 6.00 4.00 2.00 0.00

**Figure 6.9**

$$h = \pi \left[ \frac{R^2 t^2}{12(1-\nu^2)} \right]^{\frac{1}{4}} = \frac{1}{2}\pi \frac{\{D\ t\}^{\frac{1}{2}}}{\{3(1-\nu^2)\}^{\frac{1}{4}}} \qquad (6.4.6)$$

The close proximity of the theoretical set of curves with the test curve suggests that the collapse configuration assumed in this theory in the form of a sinusoidal wave has little bearing on the discrepancies in critical stress observed in Figure 6.8 . This is in spite of the fact that true collapse occurs in a sequential manner starting at one end of the tube as distinct from the total wave-like distortion indicated in Figure 6.7 . Furthermore, the tube is assumed to fail in an exact number of half-waves and to form a large number of them. However, in view of the minimization carried out to derive equations (6.4.1) and (6.4.2), these are deduced to be fair assumptions in this upper bound approach.

Having verified that equation (6.4.1) is strictly applicable to linear elastic buckling, the present author was interested to inspect the suitability of equation (6.4.3) for 'buckling beyond the proportional limit'. Assuming this incorporates buckling beyond yielding of the material, equations (6.4.3) and (6.4.5) may be equated to give the following expression for the reduced modulus, $E_r$ for full experimental correlation.

$$E_r = \frac{3\ (1 - \nu^2)}{E} \left\{ 0.0793 \left( \frac{R}{t} \right) + 0.3018 \right\}^2 \qquad (6.4.7)$$

for the experimental range : $0.03 < \left( \frac{t}{R} \right) < 0.18$

Hence, for $\nu = 0.3$, and using $E = 33.8\ KN/mm^2$,

$$0.044 < E_r < 0.70\ KN/mm^2 \qquad (6.4.8)$$

The above values for $E_r$ are exceedingly low in comparison with the mean value of $E = 33.8\ KN/mm^2$ as the linear elasticity modulus for the annealed aluminium used. The plausibility of the assumption of equation (6.4.3) fully representing the true buckling conditions and the validity of the solutions obtained for $E_r$ may be assessed by considering equation (6.4.4) containing the factor $(E_r/E)^{\frac{1}{4}}$. For the range of $E_r$ in (6.4.8) the following range is obtained for this ratio;

$$0.190 \langle \left(\frac{E_r}{E}\right)^{\frac{1}{4}} \langle 0.379 \qquad (6.4.9)$$

It is observed that since equation (6.4.4) differs from the linear elastic equation (6.4.2) only by the introduction of the above factor, the reader is invited to observe that if the above factor were to be incorporated into the theoretical set of curves in Figure 6.9 in order to account for the yield condition, then the range obtained in (6.4.9) would shift this set of curves to new positions far below the experimental curve.

This geometric inconsistency indicates the inadequacy of equation (6.4.3) in Timoshenko's modification of the critical stress for the case of buckling beyond yielding of the shell. It is apparent that a value of $E_r$ fairly close to $E$ is required in (6.4.4) for the geometric correlation; this value of $E_r$, however, produces an inconsistency in the critical stresses by back substitution into (6.4.3).

The classical linear theory, in summary, is deduced to be inapplicable to the class of shells buckling axisymmetrically

and beyond yielding of the material, as in the case of the concertina mode considered here. The extension of this theory accommodating the condition of buckling 'beyond the proportional limit', fails to provide the experimental critical stress for the above class of tubes, so that the extended theory is deduced to apply only to shells buckling beyond the proportional limit but still in the elastic state, i.e. those exhibiting non-linear elastic behaviour.

The author concludes that since axisymmetric collapse of tubes (in the concertina mode) accompanies stresses that exceed material yield (c.f. $\sigma_{cr}$* in Table A2.9, P.355 with experimental range of Y in (5.2.1), P.157), then theory (101) applies to a hypothetical case of buckling where the above configuration at collapse is acheived at stresses below the yield. Elastic buckling or inextensional failure requires little or no alteration to the original circumferential length of a shell after collapse. This pattern is observed in the case of very thin shells which fail essentially in the non-axisymmetric diamond configuration.

## 6.5 Investigation of Previous Studies on the Classical Theory

### 6.5.1 Donnell and von Karman : The Large-Displacement Theory

The first reported attempt to account for the discrepancies commonly observed in solutions of the classical theory with the behaviour of thin shells was made by Donnell (19).

In this work an approximate large-deflection theory is introduced with the assumption that buckling occurs when the critical

---

*This stress, in combination with bending at fold hinges and stretching between (& at) the hinges, promotes significant work in plastic deformations beyond yielding of the material

stress reaches the yield of the material. The influence of geometric imperfections is analyzed by defining their shape as a double harmonic series with waves of equal length in the axial and hoop directions. The paper illustrates that for thin shells, the experimental critical stresses are not only smaller than those predicted by the classical theory (101), but, in fact, exhibit a divergence from the latter values, as ratio R/t is increased; this is because of the imperfections whose influence increase with increases in the above geometric ratio. Thus, a ratio S is introduced in theory (19), of the experimental critical stress, $\sigma_{cr}$, to the corresponding classical value, $\sigma_{cl}$ given by equation (6.4.1) of Section 6.4 . Thus,

$$S = \frac{\sigma_{cr}}{\sigma_{cl}} \qquad (6.5.1)$$

This ratio is shown to be a function of the material properties of the shell expressed by the relation : E/Y and is found to decrease as R/t increases.

In accordance with the above trend and based on the test results obtained and recorded, Donnell proposed the following empirical formula for the axial stress at failure of a circular shell.

$$\sigma_{cr} = \frac{E\{0.6\ (t/R) - 10^{-7}\ (R/t)\}}{1 + 0.004\ (E/Y)} \qquad (6.5.2)$$

For very thin shells (large R/t) it is suggested that if a negative result is obtained in the above equation, then the

stress should be taken as zero without appreciable error. Furthermore, it is claimed that the above relation gives consistent values 'for the extreme material conditions: E/Y = 0 and E/Y = ∞' and that it holds valid also for thick shells (low R/t) and beyond, 'to the extreme condition, R/t = 0'.

An estimate of experimental critical stress for the sets of tubes which collapsed in the concertina mode, has been presented in Figure 6.8 (Section 6.4), by dividing, in each case, the critical load, $P_{cr}$ by the net section area of the tube. Thus, with the knowledge of the corresponding values of R/t and the mean value of $E = 33.8\ KN/mm^2$, equation (6.5.2) may be rearranged, as follows, to predict a set of theoretical values for the yield stress, Y, of the annealed aluminium tested.

$$Y = \frac{0.004\ \sigma_{cr}}{0.6\ (t/R) - 10^{-7}\ (R/t) - (\sigma_{cr}/E)} \qquad (6.5.3)$$

Figure 6.10 presents the theoretical results obtained for Y* against the geometric ratio R/t. Two features are revealed;

1. These solutions fall in the range : $0.005 < Y < 0.023\ KN/mm^2$ which is entirely below the actual range of yield stress for the alloy tested as recorded in Chapter 5, namely, $0.032\ KN/mm^2 < Y < 0.079\ KN/mm^2$.
2. Contrary to the notion that yield stress is a material property and thus independent of any geometric parameter of the stressed shell, these solutions exhibit a marked rising trend with R/t and in a fairly linear manner.

The observed pattern appears to indicate the unsuitability of

* See Table A2.9, Appendix II for individual results

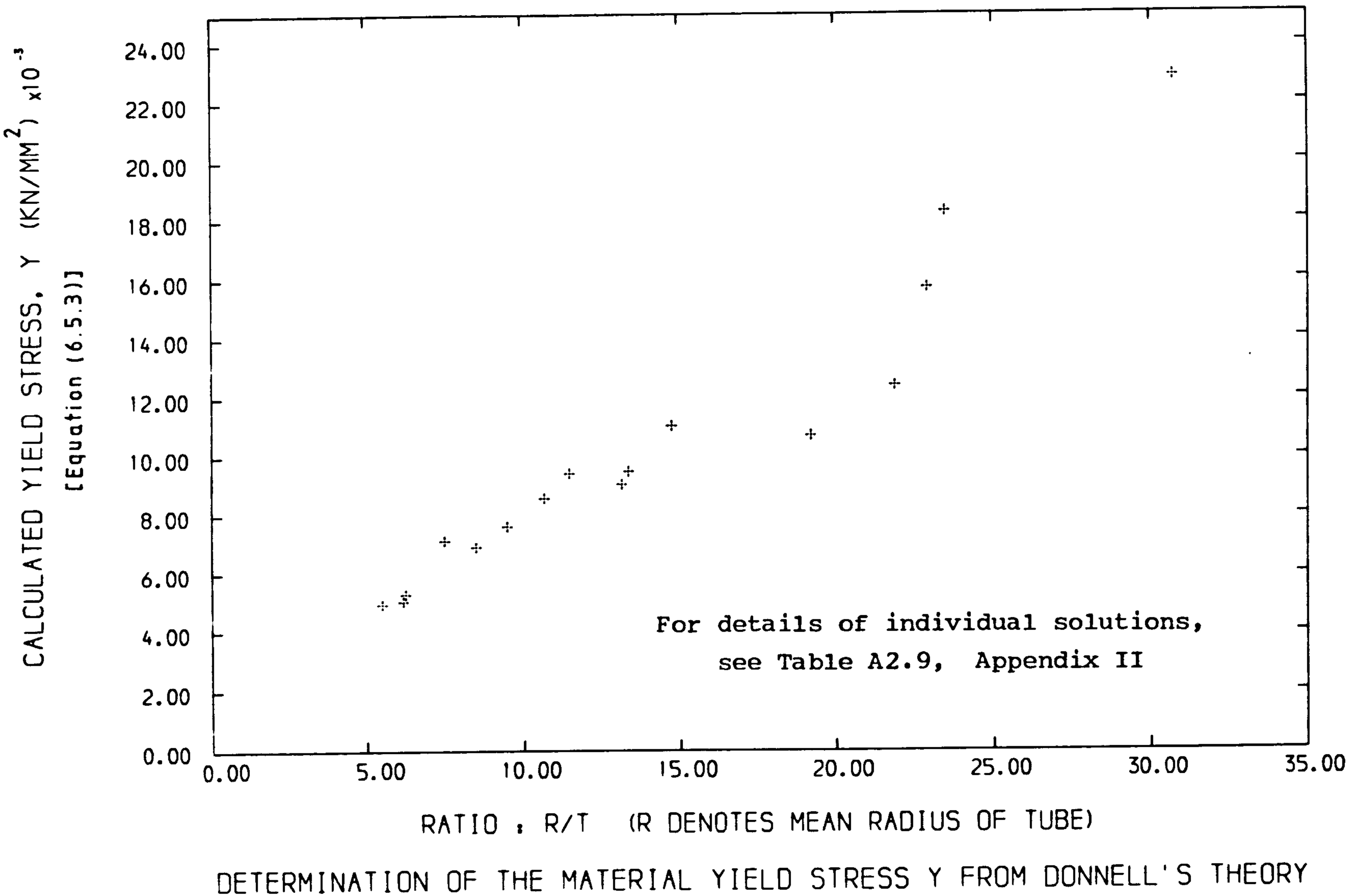
CALCULATED YIELD STRESS, Y (KN/MM$^2$) x10$^{-3}$
[Equation (6.5.3)]
24.00
22.00
20.00
18.00
16.00
14.00
12.00
10.00
8.00
6.00
4.00
2.00
0.00
0.00
5.00
10.00
15.00
20.00
25.00
30.00
35.00
For details of individual solutions,
see Table A2.9, Appendix II
RATIO : R/T (R DENOTES MEAN RADIUS OF TUBE)
DETERMINATION OF THE MATERIAL YIELD STRESS Y FROM DONNELL'S THEORY

**Figure 6.10**

Donnell's expression for application to relatively thick-walled tubes and is thus in conflict with the claim made in the theory that equation (6.5.2) may be applied with reasonable accuracy to this range of shells. The anomaly observed above may be confirmed analytically, as follows.

Substitution of the linear regression result of equation (6.4.5) for experimental critical stress into equation (6.5.2), gives the following result for yield stress, Y .

$$Y = \frac{0.004 \left\{ 0.3018\ (t/R) + 0.0793 \right\}}{0.6\ (t/R) - 10^{-7}\ (R/t) - \frac{1}{E}\left\{ 0.3018(t/R) + 0.0793 \right\}} \qquad (6.5.4)$$

For the geometric range considered, that is, $0.03 \langle (t/R) \langle 0.18$, it is observed that $0.6\ (t/R) \rangle\rangle 10^{-7}\ (R/t)$ so that the latter term may be safely neglected in the above expression thus giving,

$$Y = \frac{1}{c}\left[ a + \frac{b\ c + a\ d}{c\ (t/R) - d} \right] \qquad (6.5.5)$$

where $a = 0.0408$, $b = 0.0107$, $c = 19.978$, $d = 0.0793$

Again, for the range considered, $c\ (t/R) \rangle d$ so that over this range the yield stress in Donnell's theory is seen to be related to ratio R/t in the following approximate linear manner;

$$Y \simeq A\ (\frac{R}{t}) + B \qquad \text{where } A \simeq 5.44 \times 10^{-4},\ B = 2.04 \times 10^{-3} \qquad (6.5.6)$$

This confirms the fairly linear trend of the solutions obtained

in Figure 6.10 . Although a regression has not been performed on these individual solutions for Y in this figure, this trend may be approximated by the relationship of equation (6.5.6) with the above values of A and B.

The inadequacy of Donnell's proposition over the region of thick shells may be represented in an alternative way by direct comparison of the experimental results obtained here for the stress ratio, S and those extrapolated by Donnell over this region. Figure 6.11 presents Donnell's curves obtained from equation (6.5.2) for his test results on brass and copper and for those by Lundquist (62) for duraluminium; (The actual recordings may be observed in Figure 6 of Donnell's paper (19). They fall in the range : $150 < R/T < 1500$ ). These curves are extrapolated to intersect the vertical axis at $S \simeq 0.3$ and $S \simeq 0.5$, respectively. These are compared with the short linear relation in the region : $5 < R/t < 35$ for the test results obtained for the annealed aluminium alloy tested. The latter experimental relation is found by dividing the stress from the experimental linear regression of equation (6.4.5) (Section 6.4) by the corresponding classical theory value with $\nu = 0.3$, for the range of R/t considered. Hence for the experimental line, stress ratio S assumes the expression :

$$S = \frac{0.3018\ (t/R) + 0.0793}{0.605\ E\ (t/R)} \qquad \text{(experimental line of Figure 6.11)}$$

$$\text{for} \quad 5 < R/t < 35 \ , \quad (E = 33.8\ KN/mm^2) \qquad (6.5.7)$$

Hence, $0.034 < S < 0.15$

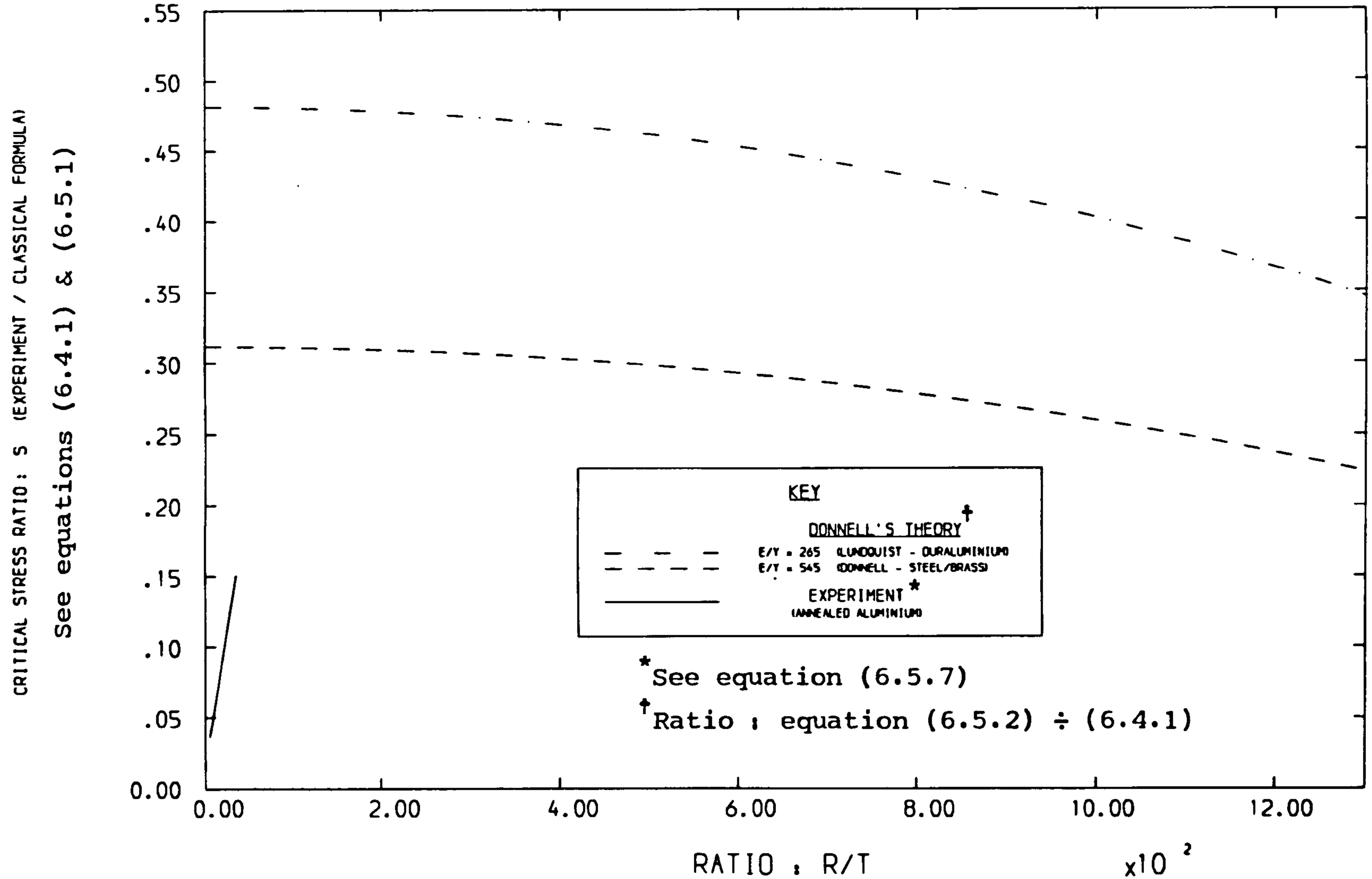


COMPARISON OF DONNELL'S THEORY WITH EXPERIMENT

**Figure 6.11**

Since for thick tubes imperfections play a minor role in reduction of buckling loads, the trends observed in Figure 6.11 cannot be attributed to this feature. Although theory (19) provides an improvement on the classical theory (101) by analyzing the effect of imperfections, it is still based on elastic behaviour. Thus, the present author deduces that extrapolation of the experimental line in Figure 6.11 to Donnell's curves provides, at the intersections, points beyond which, i.e. for smaller R/t, this theory is inapplicable and buckling accompanies yielding of material. This is analogous to the divergence observed in the study of the classical theory (see Figure 6.8), due to material yield.

In the same decade that theory (19) was produced, the subject was studied independently by von Karman and Tsien (50) who developed this theory and considered non-linear displacements at collapse. They indicated that beyond the buckling stress, there is a conspicuous fall in resistance of the cylinder and subsequently smaller loads are required to keep the shell in equilibrium. This was reasoned to be due to the sudden release of elastic energy stored in the shell and imperfections, coupled with vibrations and elastic properties of the testing machine. However, the theory is applicable only to the early stages of buckling and predicts the same buckling loads as in the classical theory (101). Also it failed to indicate the decreasing trend of stress ratio S with increases in the geometric ratio, R/t.

In a second paper, Donnell, jointly with Wan (20), attempted to refine theory (19) by quantifying the magnitudes of initial

imperfections based on pre-determined shapes. He realised by this time that his proposition of equation (6.5.2) may not be extrapolated to cover the region of thick shells. Consistent with the observations made here, he reasoned this to be due to yielding of the shell before the critical stress is reached. Thus, two types of buckling were distinguished : (i) purely elastic, (ii) buckling precipitated by yielding. For the latter type of failure, his analysis (20) accompanies the simulation of a set of curves, similar to the experimental line of Figure 6.11; these are joined to the elastic curves for different magnitudes of imperfections. It is claimed that the higher the yield point and the less the effects of imperfections, the more abrupt is the transition between elastic buckling and one extending into yield. Hence the dotted linear extension of the experimental line to Donnell's curves in Figure 6.11 represents an extreme condition; in reality, because of imperfections at higher R/t, it is likely that a curvilinear extension exists.

The present author concludes by recognizing the approximate nature of the von-Karman - Donnell theories; these are essentially elastic theories based on relatively small displacements during collapse. A restriction must be placed on the geometric ratio R/t for their practical application : Below a critical R/t, buckling accompanies yielding of the material, in which range equation (6.5.2) is inapplicable.

### 6.5.2 Koiter : Imperfections

Simultaneous with the von-Karman - Donnell approach, an independent study was made by Koiter when in 1945 he published

his theory of the stability of thin shells (54).

With particular emphasis on the effects of initial deviations in the development of this theory, Koiter, in a later paper (55) as described by Hoff (33), proposed an analytical formula from which the stress ratio, S (equation (6.5.1) ) may be evaluated if the magnitude of imperfections from perfect cylindrical form could be defined. In order to derive the analytical solution, it was assumed that initial deviations are axisymmetric and the entire length of the shell is covered by an identical set of these eccentricities. This is however in conflict with experimental observation where it is seen that in very thin shells, particularly if clamped at the ends, buckling proceeds in the diamond configuration and is initially a local phenomenon before progressing along the whole length of the tube.

In the reported work two classes of buckling are introduced depending on whether the slope of the curve of axial load vs shortening is positive or negative, as dictated by the shape of the shell. In the first case, the solution of the theory is insensitive to initial deviations and the stress given by the classical theory may be reached or even surpassed even though a practical shell is considered. However, in the second case, imperfections govern the stability of the shell, this resulting in a 'snap-through' with a sudden drop in the axial load which never reaches the classical value.

In order to derive an expression for the maximum practical

stress of a shell at buckling, $\sigma_{max}$, Koiter in the same manner as that of equation (6.5.1), expressed this stress as a proportion of the classical formula (equation (6.4.1)). Thus,

$$\sigma_{max} = S \left\{ 3 \ (1 - \nu^2) \right\}^{-\frac{1}{2}} E \ (t/R) \qquad (6.5.8)$$

where $S$ is called the stress reduction factor and is implicitly defined by the following relation :

$$S \psi = \left\{ 4/27 \ (1 - \nu^2) \right\}^{\frac{1}{2}} (1 - S)^2 \qquad (6.5.9)$$

where $\psi$ is the ratio of the amplitude of the initial deviations to wall thickness, $t$ . In this theory it is assumed that the initial deviation amplitude is proportional to the radius of the shell, so that the amplitude ratio, $\psi$ may in turn be directly related to the geometric ratio $R/t$. This is useful since in combination with equation (6.5.8) it unfolds the increasingly significant role the imperfections play in reduction of buckling loads from the classical formula, as $R/t$ is increased.

Thus, according to this theory, if parameter $\psi$ is quantified, it may then be used in equation (6.5.9) to provide a value of $S$ which, substituted into equation (6.5.8), gives an estimate of the practical stress to be expected at buckling of a shell. In order to differentiate between the probable extent of imperfections present in thin shells associated with the accuracy of the methods by which these are manufactured, Koiter proposed the following values for the amplitude ratio, $\psi$ ;

(a) $\psi = 10^{-4}$ (R/t), (b) $\psi = 4 \times 10^{-4}$ (R/t), (c) $\psi = 10^{-3}$ (R/t)

(6.5.10)

It is recommended that relation (a) is used for shells made with extreme care in the laboratory; (b) for design purposes based on excellent workshop quality; and (c) for least accurate shells particularly in the absence of any statistical information. However, in determination of the maximum stress in (6.5.8) for practical purposes, Koiter proposed a value of $S = 0.5$ as his design limit.

Figure 6.12 indicates the relationship of equation (6.5.9) between the stress reduction factor, S and the geometric ratio R/t, for the recommended values in (6.5.10). These are compared with the linear experimental relation of Figure 6.11 for the annealed aluminium alloy material tested.

It is observed that at the extreme condition $R/t = 0$ the stress factor, S is equal to unity, implying that the theory reduces to the classical theory with imperfections having no effect on the buckling load. As R/t increases, however, the values of S fall steadily in accordance with the magnitudes of imperfections selected.

The discrepancy observed here over the geometric range of R/t considered, is deduced to be the consequence of the same feature as that observed in relation to Donnell's theory, examined in Section 6.5.1; the underlying reason is the neglect of material behaviour at collapse, in that

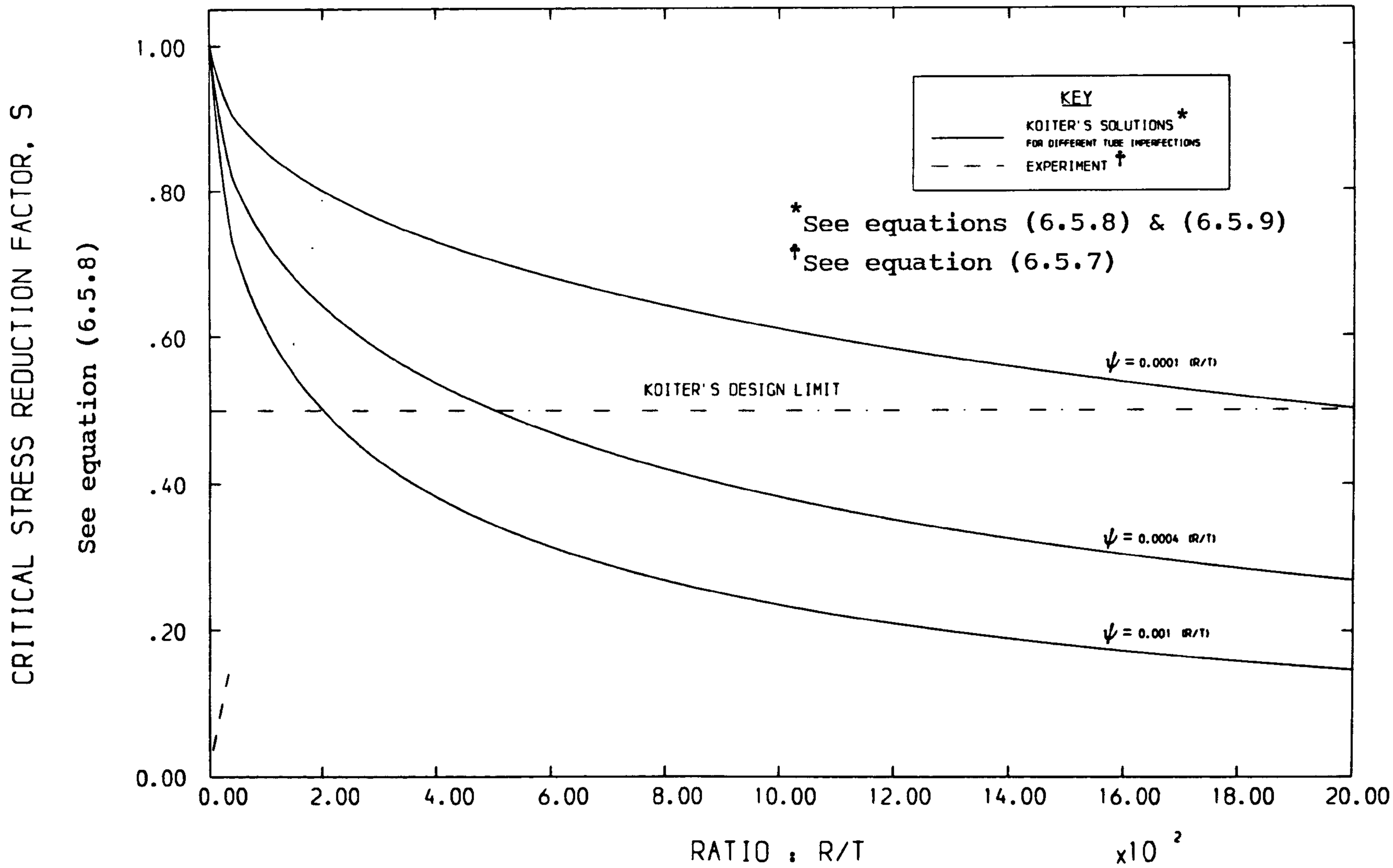


COMPARISON OF KOITER'S THEORY WITH EXPERIMENT

**Figure 6.12**

for thick-walled tubes, buckling accompanies and extends beyond yielding of the material.

It is concluded that despite the assumption of axisymmetric shape for initial deviations in contrast to their actual random pattern, the theory provides a neat representation of the importance of these imperfections; it resembles the experimental pattern of a decreasing trend in the stress ratio, S with a rise in R/t. But the test results here have indicated that this feature is bounded at a particular value of R/t below which buckling progresses beyond yielding of the tube material and the theory is inapplicable for this class of shells.

### 6.5.3 Summary and Review of Further Work on the Classical Theory

The results obtained in the present and the preceding section may be summarized to highlight the importance of differentiation between elastic buckling and buckling that extends beyond yielding of the material. The theories discussed neglect this phenomenon and have thus been shown to produce divergence from test data on critical stresses of tubes. However, it is realised that the theories described, in essence, provide only rough and approximate solutions to a complex problem. A more complete analysis must incorporate the effects of boundary conditions at collapse.

Based on the Donnell - von Karman approach, a series of attempts have since been made by other investigators to

improve the large-deflection theory by considering the boundary conditions at collapse. Detailed literature exists on investigation of the influence of this parameter, notably by : Hoff (27)(28)(30)(31)(32)(33), Hoff et al (34)(35)(36), Nachbar (72), Ohira (73), Kempner (51), Batterman (9)(10), Rehfield (83) and Almroth (5)(6). Their analyses collectively indicate that small changes in fixity conditions at the boundaries of a thin axially loaded shell can have profound effect on the magnitude of the stress ratio, S . The general consensus is that $S = 0.5$ and $S \simeq 0.37$ for axisymmetric and elastic diamond buckling, respectively in the case of simply-supported conditions, whilst it is claimed that the classical load may be reached or even exceeded $(S \rangle 1)$ if the ends of the shell are fully fixed. It is seen here too that the yielding condition associated with axisymmetric (concertina) failure must be imposed on these solutions.

Other factors which are known to reduce the critical load at buckling of thin cylindrical tubes and considered as equivalent geometric deviations in previous investigations are : (i) initial stresses, (ii) accidental lateral loads and vibrations, e.g. sound waves or gust of air; Almroth (7), (iii) non-uniformities in isotropic elastic behaviour as discussed by Tennyson (94), and (iv) elastic characteristics of the testing machine as mentioned by von Karman (50), though this has since been shown by Horton et al (37) to have negligible influence on the buckling load. These are particularly important in the case of very thin shells manufactured from thin sheets of multicrystalline materials where there may be

only a few crystals across the wall thickness.

The influence of geometric imperfections has been studied in other previous investigations, in particular by : Hoff (31)(32), Michielsen (66), Loo (60), Horton and Durham (39), Babcock et al (8), Almroth (6)(7), Thielmann (96), Harris et al (25) and Lee (57). Nevertheless, the need persists for a more accurate representation of shapes and magnitudes of these initial deviations, in order to predict the true buckling loads of thin-walled cylindrical tubes.

## 6.6 Conclusion

1. For the aluminium tested, strain hardening is the source of discrepancies noticed in predictions of yield stress, Y from the theories studied in Sections 6.2 & 6.3; here, these theories underestimate the internal work done at collapse.

2. The interpolation performed on test results here in theory (48) provides a (minimum) bound on the t/D ratio of tubes (t/D = 0.0026) for collapse in the concertina mode.

3. The classical theory (101) fails to distinguish between the material states associated with different collapse modes :

(a) elastic buckling is confined to thin-walled tubes which invariably collapse in the diamond mechanism

(b) axisymmetric buckling, reminiscent of collapse of thick--walled tubes in the concertina mode, accompanies yielding of the material.

Theory (101) is inapplicable to tubes of class (b).

4. Geometric imperfections do not account for the divergence of test results here from theory (101). These are significant for tubes of class (a) above (see Section 6.5).

5. Extrapolation of test results to solutions of theory (101), however, provides a (maximum) bound on the t/R ratio of tubes (t/R = 0.0039) for elastic failure. This bound compares favourably with that in Conclusion 2, confirming a transition from concertina to purely diamond collapse.

# CHAPTER 7

# DESIGN OF CYLINDRICAL TUBES AS ENERGY ABSORBERS WITHIN A PRESCRIBED CRUSHING LAYER

# Chapter 7 - Synopsis

Based on test data, a design method is presented by which the geometry and packing arrangement of cylindrical tubes may be optimized for use, as an assemblage, in an energy - -dissipating application. The possibility of using tube assemblies in different 'rows' (as a series of crushing sublayers) and employing concentric tube sets are also analyzed, in an attempt to locate their optimum arrangement within a prescribed space.

A number of specific conclusions are reached. The general deduction is that, for a given length and total gross volume of crushing tube elements, the energy dissipation capacity of the system may be substantially increased if a large quantity of narrow tubes as distinct from a small number of large diameter tubes are employed. Design efficiency, measured in terms of the cost/weight effectiveness of the arrangement, is also observed to follow this pattern.

## 7.1 Introduction

### 7.1.1 Statement of Pròblem

A space of 10 m X 10 m X 1 m depth within a nuclear power plant is allocated for accommodating a quantity of impact absorbing cylindrical tubes. It is required to design these tubes for axial collapse in a specific mode, arrange them within the space in a specific pattern and determine their quantity such that they absorb maximum energy in deformation up to a total capacity of the order of one Gigajoule of energy. Optimization is to include a measure of cost reflected in tube material weight so that the design aim is towards achieving maximum absorption capacity per unit weight (or net volume) of tube material.

### 7.1.2 Selection of an optimum mechanism of axial collapse

The experimental relationships presented in Chapters 3 and 4 on energy absorption in relation to tube geometry illustrated that concertina mode of collapse is associated with a higher absorption capacity than the diamond mechanism, for a given tube section geometry. Thus the former mode is selected in the design problem. The relatively simple configuration of this mode and the greater knowledge of its geometry in contrast to the diamond modes is predicted to have a considerable computational advantage in determination of the dimensions of the tubes.

Based on the collapse mechanism chosen and the aluminium alloy tested, the following experimental relationships are used here :

1. The collapse mode classification chart of Figure 2.1 in

Chapter 2 which provides bounds on the geometric ratios, t/D and L/D, for tubes to collapse in the selected concertina mechanism.

2. Figure 5.2 of Chapter 5 relating the arm-length of a fold, h to the geometric product Dt.
3. Figure 4.8 of Chapter 4 indicating the mean energy absorbed by a tube per formation of a concertina fold in relation to the true mean volume of a fold.

### 7.1.3 Assumptions

1. Quasi-static axial collapse of tubes is assumed; cylindrical tubes have been known to possess the property of similar collapse behaviour under static and dynamic loading conditions (see Section 8.2.2, Chapter 8).
2. The experimentally bounded concertina zone of Figure 2.1 in Chapter 2, selected here, is closely approximated to a polygon. This permits linear equations to be set up at the zone boundaries thus providing a simple means by which bounds on the L/D ratios may be evaluated at a given section ratio, t/D. Figure 7.1† represents schematically the polygonal zone defined by the nodal coordinates selected with the respective linear equations for the boundaries.
3. Hexagonal close packing is selected for the arrangement of individual tubes within the layer. The chosen pattern, corresponding to maximum packing density, is aimed at gaining maximum energy absorption capacity. However, because of the radial expansion of the tubes during collapse, a clearance of one arm-length of a fold, h is imposed

---

† Figures are presented collectively at the end of chapter (P 286 →)

radially for each tube, where

$$h = k\,(Dt)^{\frac{1}{2}} \qquad (7.1.1)$$

and it is assumed that $k = 1.2$ (experimental $k = 1.133$, as shown in Chapter 5). This envelops the assumption that folding proceeds fully externally in relation to the original tube diameter and is thus on the safe side.

Figure 7.2 indicates the packing arrangement as a consequence of which each tube effectively assumes a plan area of a regular hexagon, $A_{hex}$ within the layer, expressed as follows;

$$A_{hex} = \tfrac{1}{2}\sqrt{3}\,d^2 \quad \text{where} \quad d = D + 2t + 2h \qquad (7.1.2)$$

4. For selected tube geometry, formulae (7.1.2) divided into the square plan area of the layer provides the quantity of tubes required to fill the layer. However, only whole tubes are used in design so that at the boundaries non-whole hexagons are eliminated. The method by which this may be achieved is presented in Appendix III. However, in the next sections the difference in effect by elimination of part hexagons at the boundaries will be observed.

5. Considering single tubes, the volume of a fold developing in a tube, $V_f$ is defined as follows,

$$V_f = 2\,A\,h \qquad (7.1.3)$$

where $A$ is the net section area of the tube and $h$ is given in (7.1.1) . This is a safe assumption since $h$ is on the safe side. Hence for a tube of length L, the total

number of folds that it may develop, $n_f$ is assumed to be

$$n_f = \frac{L\ A}{V_f} = \frac{L}{2\ h} \qquad (7.1.4)$$

6. The energy absorbed per fold by this tube, $E_f$ is calculated from equation (4.5.5) of Chapter 4 for the relationship of Figure 4.8 . This is represented below.

$$\log_{10}(E_f) = -5.0965 + 3.9443 \left\{ \log_{10}(V_f) \right\}^{\frac{1}{2}} \qquad (7.1.5)$$

Total energy absorbed by the tube, $E_t$ is the result of the following product :

$$E_t = E_f\ n_f \qquad (7.1.6)$$

If $n_f$ is not an integer, then the portion $\beta$ ( $\langle$ 1) of a complete fold is assumed to absorb $\beta\, E_f$ amount of energy. Thus the total energy absorbed in layer, $E_T$ is

$$E_T = E_t\ n_t \qquad (7.1.7)$$

where $n_t$ is the number of tubes in the layer. For design $n_t$ is an integer as explained in Assumption 4. This may be compared with the following theoretical (real) number;

$$(n_t)_{Theor} = \frac{C^2}{A_{hex}} \qquad (7.1.8)$$

where C is the span length of the layer. Thus

$$\frac{(E_T)_{Des}}{(E_T)_{Theor}} = \frac{(n_t)_{Des}}{(n_t)_{Theor}} \qquad (7.1.9)$$

Total material volume of tubes used in the layer, $V_T$ is

$$V_T = A\ L\ n_t \qquad (7.1.10)$$

7. On a practical point, it is assumed that the impact energy is transmitted to the tubes via flat plates enclosing them and that the plates are sufficiently thick to deform at stresses above those required to fail the tubes. Coupled with the assumption that irrespective of position the effect of the impact load is uniform on the plate, simultaneous collapse of all the individual tubes in the axial direction is assumed. (The reader is referred to Section 7.9, p.285, for discussion of practical conditions in the nuclear reactor containment application studied here).

## 7.2 Basic Design Relationships

For the given depth of layer L = 1 m in the problem denoting the length of the tubes selected, a range of dimensions for the internal diameter of the tubes may be evaluated from the vertical ordinate range of the zone polygon of Figure 7.1 at a particular t/D ratio of the tubes, and subsequently the respective thicknesses to keep this ratio fixed. Figure 7.3 presents the permissible ranges of both tube dimensions, D and t, at discrete values of t/D as indicated in the inset†.

Figure 7.4 shows the quantity of tubes required to fill the layer for a particular section ratio of all tubes (point O on the zone polygon). The theoretical quantity is evaluated at any point on line EB* of the polygon by calculating the respective diameters and thicknesses of the tubes at this point and using equations (7.1.1), (7.1.2) and (7.1.8) based

---

† The inset shown in this figure and in all others in this chapter represents the polygon of Figure 7.1, P.286

* EB provides the largest ordinate range of L/D in the polygon

on these dimensions. To evaluate the design quantity these dimensions are used in the computer routine described in Appendix III where a particular formulae in this routine is used to evaluate the integer quantity, depending on the boundary conditions.

The horizontal axis of Figure 7.4 is plotted in the scale of L/D (rather than a range for D since L is known) in order to represent identically the vertical range EB on the zone polygon. This illustrates parametrically the expected trend that for a fixed depth, the layer may capacitate either a large number of narrow tubes or a small number of large diameter tubes. The parabolic trend of the theoretical curve is verified below:

$C = 10$ m  $L = 1$ m  $t/D = 0.055$  $L/D = 0.7 \rightarrow 4.8$

$$D = \frac{L}{(L/D)} \qquad t = \frac{L}{(L/D)}\,(0.055) \qquad \text{Thus,}$$

$$\text{from (7.1.1)}, \quad h = 0.2814\ \frac{L}{(L/D)}$$

$$\text{from (7.1.2)}, \quad A_{hex} = 2.425 \left(\frac{L}{(L/D)}\right)^2 \qquad \text{so that}$$

$$\text{from (7.1.8)}, \quad (n_t)_{Theor} = 41.237\ (L/D)^2 \qquad (7.2.1)$$

For the same section ratio of tubes, Figure 7.5 illustrates the relation between the total energy absorbed within the layer and tube geometry corresponding to range EB on the zone polygon. This energy is evaluated from equation (7.1.7) based on equations (7.1.3) to (7.1.6) where the quantity of tubes, $n_t$ assumes real or integer values depending on the boundary conditions considered. The dashed curve represents the lower bound (safe) design relationship obtained by joining the lowest

local points in the design curve. This figure reveals the advantage of a gain in the overall absorption capacity if a large number of narrow tubes (as distinct from a small number of large diameter tubes) are employed - to the extent that for the geometric ratios of tubes considered, the total energy absorption capacity within the layer can be magnified by factors up to six.

Figures 7.6 and 7.7 present, respectively , similar results for the theoretical and design energy relations obtained at other discrete values of t/D covering the range of the zone polygon. The horizontal range of L/D for any curve is identically the vertical ordinate of the zone polygon at the particular value of t/D considered. In Figure 7.7 only the lower bound (safe) design curves are shown, in an effort to minimize local fluctuations (as observed in Figure 7.5) in the discrete relationship, thus avoiding obscurity as far as possible.

These curves collectively indicate that by choosing the narrowest permissible tubes for any t/D within the polygon (from the corresponding highest allowable L/D), the corresponding total absorption capacity reaches a maximum. Furthermore, considering the two extreme points in Figure 7.7 which correspond to points F and B on the polygon, it is observed that by selecting point B in preference to point F in design, a gain in total absorption capacity is obtained by a factor of thirty.

Figures 7.8 and 7.9 illustrate the influence of the boundary

conditions discussed in Assumption 4 in the context of the elimination of non-whole tubes at the boundaries of the layer. This is indicated as a ratio of the energy relationships presented in the two preceding figures in accordance with equation (7.1.9) . Again with the aid of a computer routine devised to store and connect the lowest local points in the discrete functions, lower bound curves are obtained and shown in Figure 7.9 in an attempt to distinguish between the different curves - though some unevenness inevitably remains and will be observed to persist in other relationships that will follow. These figures indicate that the use of narrowest tubes (highest permissible L/D) at any point on lines AB and BC on the zone polygon, not only has the advantage of leading to the highest absorption capacities for the layer, but gives rise to a minimum the energy that is 'lost' as a result of the boundary conditions imposed in design. In Figure 7.9 the combined curvilinear trend of the curves which is convex on the outside, indicates the increasing significance of the boundary conditions and the elimination of non-whole tubes, as ratio L/D is decreased for all tubes, i.e. as larger diameter (but fewer) tubes are selected to fill the layer.

Figure 7.10 presents the relationship obtained from equation (7.1.10) for total design material volume of tubes with section ratios t/D equivalent to point O on the polygon, against the corresponding range of L/D, that is, the vertical ordinate EB. In this figure the upper limit of the discrete function is considered as a safe design estimate. Figure 7.11 indicates the similar results obtained as safe upper limits, for tubes

with other values of t/D. These figures show a steady levelling off, of the total material volume as L/D is increased, but show a declining trend as a small number of large diameter tubes are used. The importance of tube wall thickness reflected in ratio t/D for a given L and D is clearly indicated.

By combining the energy relationship of Figure 7.5 with the corresponding material volume from Figure 7.10 for the selected section geometry of all tubes, the trend of variation of these two parameters is obtained and shown in Figure 7.12 . For safe design, with the aid of a similar computer routine, an attempt was made to isolate and connect the extreme right hand points in the local fluctuations encountered; (the negative gradient at the peak is a graphic aberration and has no physical meaning)

By defining design efficiency as a measure of the energy absorbed per unit material volume (hence material weight†), the factor of cost may now be incorporated as required in the design problem. Hence

$$\text{Design Efficiency} = \frac{\text{energy absorbed in layer}}{\text{corresponding tube material volume}} \qquad (7.2.2)$$

It is observed from Figure 7.12 that the gradient of this curve gives an estimate of the above efficiency. This is a maximum at the peak of the curve (point B on the zone polygon) which happens to coincide with the highest total absorption capacity and the largest required material volume of tubes.

---

† This is synonymous with specific energy absorption

Figure 7.13 shows the similar persisting trends obtained for the lower bound estimates at other values of t/D. In each case the bottom end of the curve corresponds to a point on line FD on the polygon and the peak of each curve to a point on AB or BC as governed by ratio t/D of the tubes.

Figure 7.14 illustrates the variation of the gradient of Figure 7.12 which defines efficiency, with the corresponding range of L/D. This confirms the above deduction that maximum efficiency is obtained at the highest L/D for this particular t/D or any other value of the latter ratio chosen in the polygon.

However, the term efficiency defined in (7.2.2) takes no account of the quantity of tubes, $(n_t)_{Des}$ used to fill the layer, since for the whole layer $n_t$ vanishes as a simple multiple in (7.2.2) . Thus, as noted in Figure 7.14, the term introduced applies to individual tubes essentially. This explains the smooth nature of the curve obtained in this figure since the boundary conditions do not enter the problem.

A new term similar to efficiency is used below which takes account of tube size as distinct from tube net volume and thus indirectly incorporates quantity $n_t$. This is called the energy dissipation density of a tube, $E_{diss}$[↑] defined as follows;

$$E_{diss} = \frac{\text{energy absorbed by tube}}{\text{gross volume of tube}} \qquad (7.2.3)$$

Figure 7.15 shows the identical trend obtained for this

---

[↑] As introduced in Chapter 1

parameter in comparison with the preceding figure. Since a large quantity of narrow tubes (shown to be most suitable in terms of energy absorption capacity) is required to fill the layer, the observed pattern above indicates conclusively that the effect of tube quantity on overall efficiency of the layer enhances the favourable trend obtained by the use of narrow tubes.

On the evidence of the relationships presented, it is concluded that lines AB and BC on the zone polygon of Figure 7.1 constitute the optimum range from which section geometry and hence the quantity of tubes required to fill the layer may be determined.

## 7.3 Variation in Plan Area of the Crushing Layer

This section considers a general case of a square layer in plan with a variable span, C, in order to indicate the variation of some of the relationships shown in Section 7.2 for the particular layer considered (C = 10 m), with this parameter. For all layers the same depth, L = 1 m is considered throughout.

Figure 7.16 presents the lower bound design curves obtained for tubes of a particular t/D ratio, indicating the influence of boundary conditions (on the total energy absorption capacity) in relation to different spans, C. The curve for C = 10 m is identical to Figure 7.8 and the other curves are obtained in a similar manner by replacing this value with the selected spans shown.

It is observed that for layers with spans C = 2 m and C = 1 m,

there is a range of L/D corresponding to large diameter tubes within which range the computed energy ratio is zero. This implies that no such whole tubes can be fitted within these layers or at least if the radial deformation of these tubes are to be confined within these layers. The trend of these curves shows a decreasing importance of the boundary effect as the plan area of the layer is increased. This is expected and reasoned as follows;

Let C denote the unit span of a layer with a square plan area and $A_L$, the area 'lost' in design at any one boundary of this layer as a result of elimination of non-whole tubes. This is illustrated in Figure 7.17 as a result of which the following parametric expressions for the relationships of Figure 7.16 are obtained.

| Plan area of layer | Ratio plotted in Figure 7.16 | |
|---|---|---|
| C X C | $\frac{C^2 - 4 A_L}{C^2}$ | $\frac{\text{(Design area)}}{\text{(Total area)}}$ |
| 2C X 2C | $\frac{4 C^2 - 8 A_L}{4 C^2}$ | |
| nC X nC (for factor n) | $\frac{n^2 C^2 - 4 n A_L}{n^2 C^2}$ | (7.3.1) |

For the trend of Figure 7.16 we have to prove the following:

$$\frac{n^2 C^2 - 4 n A_L}{n^2 C^2} \rangle \frac{C^2 - 4 A_L}{C^2}, \text{ for } n \rangle 1 \qquad (7.3.2)$$

The above is seen to reduce to the inequality, $(-n) \rangle (-n^2)$

which is a valid result for $n > 1$. This confirms the trend observed in Figure 7.16 .

Continuing with square plans at this stage, it is seen that the absorption capacity and the material volume design quantities computed for layers of different spans are at least the appropriate multiples of those for the layer with unit plan area, C X C. Hence if the 'lost' area at one boundary, $A_L$ is computed for one particular square layer for which the design energy, material volume and tube quantities are known, these design parameters may be calculated directly for layers with other square plan areas but of the same depth, since in the optimum condition they accommodate identical tubes.

Therefore, for the layer with sides nC (n greater or less than unity) the design quantities are multiples of those for the layer with sides C (for which the 'lost'area, $A_L$ is also known) in accordance with the following equation;

$$\begin{matrix}\text{Design quantity} \\ \text{for layer of sides} \\ \text{nC X nC}\end{matrix} = (n^2C^2 - 4\,n\,A_L) \cdot \begin{matrix}\text{Design quantity} \\ \text{for layer of sides} \\ \text{C X C}\end{matrix} \qquad (7.3.3)$$

For the particular geometry of all tubes selected, that is point B on the zone polygon of Figure 7.1, Figure 7.18 shows the result of applying equation (7.3.3) to the set of design solutions for C = 10 m in order to determine these quantities for layers with other spans. The marked parabolic trend merely indicates a steady increase in the design quantities as the span is increased but no gain or loss in the overall efficiency

or dissipation density since identical tubes are used in all layers. Below a span of $C \simeq 2m$ zero ratio is observed. This is the limiting condition in which the disregarded areas, $n A_L$ ($A_L$ based on C = 10 m layer) at each boundary of the layer coincide, as distinct necessarily from the condition that no whole tubes can be fitted in the layer. Thus there is a small range of spans within which the above extrapolation is not fully valid.

Finally, it is observed that the above application is not confined to layers with plans of square shape and may be equally extended to rectangular plans of sides nC X mC say; In this case the design quantities would be the appropriate multiples of those for the layer with plan size C X C (for which $A_L$ is again a known quantity), in accordance with the following equation:

$$\begin{matrix}\text{Design quantity} \\ \text{for layer of sides} \\ \text{mC X nC}\end{matrix} = (n\,m\,C^2 - 2\,A_L\,(m+n)) \begin{matrix}\text{Design quantity} \\ \text{for layer of sides} \\ \text{C X C}\end{matrix} \qquad (7.3.4)$$

The above equation reduces to equation (7.3.3), as it should, for the case $m = n$ denoting a square plan.

## 7.4 Variation in Depth of the Crushing Layer

In this section the influence of layer depth, L on the total absorption capacity of the layer is studied for the layer span C = 10 m as in the specific design problem considered.

Figure 7.19 presents the variation of total absorption capacity

with L for all tubes with ratios t/D corresponding to point O on the zone polygon of Figure 7.1 and L/D ratios covering the respective range, EB. The method used to determine the total design energy is that previously described for Figure 7.5 with the selected values of L used in equations (7.1.3) to (7.1.7) . Hence the curve for L = 1 m is identical to that in the latter figure. Figure 7.19 reveals two features for the particular section geometry of tubes selected:

1. There is a minimum depth (L = 20 cm) below which the highest L/D ratio (narrowest permissible tubes) no longer associates with maximum total energy absorption capacity of the layer. The curve for L = 10 cm indicates a slight falling trend beyond L/D = 3 .

2. There is a maximum depth above which the total absorption capacity begins to decline. The curve for L = 5 m is below that for L = 2 m.

The observed pattern is explained as follows;

Consider a fixed value of L/D in the ordinate range EB. For a fixed span C and chosen ratio t/D of all tubes, as depth L is increased so must the chosen diameter D in order to keep L/D fixed at the chosen point. This implies a reduction in the quantity of tubes required to fill the layer, in spite of the fact that each individual tube now absorbs more energy due to its larger size. Thus as L is increased a point is reached when the effect of the reduction in tube quantity outweighs the gain in the energy absorbed by the individual tubes, consequently resulting in an overall decrease in total absorption capacity.

Similar argument applies to the first feature above. For the same layer with a particular depth L, the int. diameter of the tube, D is obtained from the expression, $D = \frac{L}{(L/D)}$, for a chosen L/D ratio in the indicated range. Thus as L is decreased the tube diameters D follow the same trend, implying that a larger quantity of tubes, $n_t$ is required to fill the layer. Now, if the chosen ratio of L/D is increased too, this results in still narrower tubes implying a further increase in quantity $n_t$ - until a point is reached, depending on the value of L, when the large value of $n_t$ no longer compensates the increasing reduction in individual absorption capacities of the tubes as a result of their reduced size.

Figures 7.20 (i) - (vi) indicate the relationship of the preceding figure for other discrete t/D ratios of all tubes selected, against their respective ranges of L/D, as governed by the zone polygon. The deductions made for the trends observed in Figure 7.19 apply to these figures, too. Where zero energy is encountered for all or particular geometric ranges of L/D at a specific depth (as in Figure 7.19, for L = 5 m), no such whole tubes can be fitted in the layer. This is seen to be the extreme condition of feature 2 discussed above.

On the basis of the trends presented, it is concluded that for a fixed layer span, C and tube section geometry, bounds may be placed on the layer depth L if the latter parameter is also a variable to be quantified in a general design problem.

## 7.5 Optimum Design of Identical Tubes

It was concluded in Section 7.2 that lines AB and BC on the zone polygon of Figure 7.1 provide the optimum range from which section geometry and subsequently the required quantity of tubes may be computed for the specific layer considered.

Figure 7.21 shows the permissible range of optimum dimensions for D and t in accordance with the above lines on the polygon. Figure 7.22 indicates the equivalent quantity of tubes required. This is plotted against the ratio t/D of tubes to illustrate parametrically that the shape obtained is a reflection of the trends of lines AB and BC on the polygon; thus, the characteristic peak (corresponding to point B) denotes the narrowest tubes and hence the largest required number of them.

Figures 7.23 and 7.24 show an estimate of the equivalent optimum total absorption capacity and the corresponding total material volume for all t/D ratios within the polygon; As in Figure 7.10, the upper relationship in Figure 7.24 is considered as a safe design estimate. The absence of a peak in Figure 7.24 at t/D equivalent to point O on the polygon, indicates the effect of the tube wall thickness, t reflected in ratio t/D, this resulting in a steady rise in total material volume. Figures 7.23 and 7.24 may be combined to provide the optimum relationship of Figure 7.25 where the minimum energy (and volume) corresponds to point A, maximum energy to point B and maximum volume to point C on the zone polygon. This figure illustrates conclusively the following features:

1. Beyond peak B on the zone polygon, selection of tubes with

geometric ratios falling on line BC results in an increase in the total required tube material volume but a decrease in the total energy absorbed. Hence line BC is not an optimum in comparison with line AB.

2. For the remaining portion of the polygon, the gradient of the curve in Figure 7.25 appears to indicate maximum design efficiency at point B on the polygon.

The above deductions are confirmed in Figure 7.26 which indicates the trend of individual tube efficiencies (identical to total efficiencies of the layer, as discussed in Section 7.2) for tubes with geometric ratios falling on lines AB and BC on the polygon. The peak of this curve which corresponds to point B and the subsequent fall in efficiency beyond this point are clearly distinct.

Thus, it is deduced that the peak (point B) of the zone polygon of Figure 7.1 itself provides an optimum geometric configuration of tubes to be selected if no restriction is placed on the t/D ratio of tubes; Otherwise lines AB and BC provide the complete optimum geometric range. It will be observed in Section 7.7 that geometric restrictions must be imposed in consideration of concentric tube assemblies. But for optimum design of identical tubes in the present section, point B must be selected. Table 7.1 shows the optimum design quantities thus obtained from the relationships presented.

## 7.6 Introduction of Crushing Sublayers

With the optimum geometry and the required quantity of identical tubes determined in the design problem, consideration

Optimum data for the design of identical tubes within the prescribed crushing layer (10 m X 10 m X 1 m depth)

| Design parameter | Symbol | Design quantity |
|---|---|---|
| Tube geometry: Length (Depth of layer) | L | 1000 mm |
| Tube geometry: Internal diameter | D | 208.5 mm |
| Tube geometry: Wall thickness | t | 11.5 mm |
| Tubes to be arranged in hexagonal packing pattern within the layer. Spacing between adjacent tubes = 2 X arm-length of a fold, h as given in equation (7.1.1). | 2 h | 117.5 mm |
| Quantity of tubes required | $n_t$ | 896 |
| Total tube material volume | $V_T$ | 7.1 $m^3$ |
| Total energy absorption capacity of layer | $E_T$ | 264.2 Megajoules |

Table 7.1

is next directed towards the effect on total energy absorption capacity, of subdividing the crushing layer into rows of sublayers each accommodating a quantity of tubes. Thus, assuming a favourable effect, the problem now is to calculate how many sublayers and what depths, L' these should be designed in order to determine the optimum arrangement and geometry of tubes within the crushing layer.

Extending Assumption 7 in Section 7.1, here it is assumed that these sublayers are segregated from each other by flat plates enclosing the tubes ; the plates deform at stresses above those required to fail the tubes. For simplicity the thickness of these plates is omitted in the calculations.

In view of the findings in Section 7.4 regarding different layer depths, a minimum depth of 20 cm is imposed here on all sublayer depths, L'. The geometry of tubes in all sublayers are, of course, optimized to fall on point B of the zone polygon of Figure 7.1 with the actual dimensions governed by the depths selected. Thus, although tubes in different sublayers may be of differing sizes, they all have identical geometric ratios of L/D and t/D.

### 7.6.1 Depth permutations and optimum arrangement

Table 7.2 presents the design quantities obtained for a variety of chosen sublayer depths. Initially a depth difference of 5 cm is imposed in this table in order to observe the trend of these quantities but in the later recordings real values of L' as distinct from integers are chosen, too, the reason

## Design quantities for sublayers at various selected depths

Notation

$L'$ = depth of sublayer

$n_{t'}$ = quantity of tubes required

$V_{T'}$ = total tube material volume

$E_{T'}$ = total energy absorption capacity (Megajoules)

For all sublayers:
- span, C = 10 m (square plan)
- geometry of enclosed tubes corresponds to optimum point B on the zone polygon of Figure 7.1

| $L'$ (cm) | $n_{t'}$ | $V_{T'}$ ($m^3$) | $E_{T'}$ (MJ) | $L'$ (cm) | $n_{t'}$ | $V_{T'}$ ($m^3$) | $E_{T'}$ (MJ) |
|---|---|---|---|---|---|---|---|
| 20 | 23513 | 1.49 | 92.37 | 23.5 | 17010 | 1.75 | 107.84 |
| 25 | 15048 | 1.86 | 114.25 | 24.5 | 15611 | 1.82 | 111.77 |
| 30 | 10450 | 2.23 | 133.65 | 25.5 | 14448 | 1.90 | 116.17 |
| 35 | 7661 | 2.60 | 150.62 | 26.5 | 13330 | 1.96 | 119.75 |
| 40 | 5822 | 2.95 | 164.88 | 20.5 | 22460 | 1.53 | 95.02 |
| 45 | 4599 | 3.32 | 178.72 | 29.5 | 10808 | 2.20 | 131.82 |
| 50 | 3673 | 3.63 | 188.65 | 23.33 | 17273 | 1.74 | 107.24 |
| 55 | 3039 | 4.00 | 200.23 | 26.67 | 13161 | 1.98 | 120.38 |
| 60 | 2538 | 4.34 | 209.37 | 32.33 | 8976 | 2.40 | 141.64 |
| 65 | 2175 | 4.73 | 220.18 | 33.34 | 8465 | 2.48 | 145.40 |
| 70 | 1904 | 5.17 | 232.55 | 34.33 | 7968 | 2.55 | 148.55 |
| 75 | 1613 | 5.38 | 234.29 | 31.33 | 9555 | 2.33 | 138.10 |
| 80 | 1435 | 5.81 | 244.81 | 35.33 | 7487 | 2.61 | 151.10 |
| 22 | 19425 | 1.64 | 101.41 | 30.33 | 10152 | 2.24 | 133.95 |
| 24 | 16303 | 1.78 | 109.92 | 36.33 | 7065 | 2.68 | 153.95 |
| 26 | 13907 | 1.93 | 118.27 | 43.33 | 4978 | 3.21 | 174.89 |
| 28 | 11977 | 2.08 | 125.96 | 46.67 | 4235 | 3.41 | 181.29 |

Table 7.2

for which will be made apparent later. As L' is increased, the corresponding energy and material volume quantities are observed to increase, too, but the tube quantity falls. This is expected because of the increase in tube diameters D (to keep L'/D fixed at point B on the polygon), thus resulting in a reduction in the quantity of tubes required to fill the layer.

Table 7.3 presents a complete set of sublayer depth permutations. In each case the total design quantities are obtained by summing the relevant individual figures from Table 7.2 . These are then used as a ratio to provide an estimate of the efficiency attached to the particular arrangement. It is observed that this is a maximum (62 Megajoules/$m^3$) if the main layer is subdivided into 5 equal sublayers each of minimum imposed depth, L' = 20 cm. In contrast, the case of two sublayers with L' = 80 cm and L' = 20 cm, respectively, provides the lowest efficiency (46 Megajoules/$m^3$), though this is larger than that for the single main layer (37 Megajoules/$m^3$). The total energy absorption capacities, too, follow the same trend. Hence the use of sublayers, as distinct from the single intact layer, is concluded to be advantageous in the design problem.

Inspection of the recordings in Table 7.3 reveals that for a given number of sublayers whose depths total 1 metre, the smaller the differences in the respective depths between these sublayers, the larger would be the overall efficiency of the arrangement. Figure 7.27 confirms the above trend graphically for 2 sublayers by indicating maximum efficiency for identical sublayers and revealing the declining trend in efficiency as

Sublayer permutations with their respective arrangement efficiencies in the main layer

Dimensions of main layer : 10m X 10m X 1m depth

| Sublayer Permutation ($\Sigma L' = L = 1$ m) (cm) | Absorption capacity $E_T$ (MJ) | Material volume $V_T$ ($m^3$) | Design efficiency $E_T/V_T$ ($MJ/m^3$) | Sublayer Permutation ($\Sigma L' = L = 1$ m) (cm) | Absorption capacity $E_T$ (MJ) | Material volume $V_T$ ($m^3$) | Design efficiency $E_T/V_T$ ($MJ/m^3$) |
|---|---|---|---|---|---|---|---|
| 20 + 20 + 20 + 20 + 20 | 461.85 | 7.44 | 62.07 | 30 + 35 + 35 | 434.89 | 7.43 | 58.53 |
| 20 + 20 + 20 + 40 | 441.99 | 7.41 | 59.63 | 30 + 70 | 366.20 | 7.40 | 49.49 |
| 20 + 20 + 25 + 35 | 449.61 | 7.44 | 60.47 | 35 + 65 | 370.80 | 7.33 | 50.62 |
| 20 + 20 + 30 + 30 | 452.04 | 7.44 | 60.75 | 40 + 60 | 374.25 | 7.29 | 51.37 |
| 20 + 20 + 60 | 394.11 | 7.31 | 53.89 | 45 + 55 | 378.96 | 7.32 | 51.80 |
| 20 + 30 + 25 + 25 | 454.53 | 7.44 | 61.08 | 50 + 50 | 377.30 | 7.27 | 51.93 |
| 20 + 30 + 50 | 414.67 | 7.35 | 56.39 | 23.5 + 24.5 + 25.5 + 26.5 | 455.53 | 7.42 | 61.38 |
| 20 + 35 + 45 | 421.71 | 7.40 | 56.97 | 22 + 24 + 26 + 28 | 455.56 | 7.43 | 61.28 |
| 20 + 40 + 40 | 422.13 | 7.38 | 57.17 | 20.5 + 23.5 + 26.5 + 29.5 | 454.43 | 7.44 | 61.12 |
| 20 + 55 + 25 | 406.86 | 7.35 | 55.36 | 20 + 23.33 + 26.67 + 30 | 453.65 | 7.43 | 61.05 |
| 20 + 80 | 337.18 | 7.30 | 46.18 | 32.33 + 33.34 + 34.33 | 435.59 | 7.43 | 58.61 |
| 25 + 25 + 25 + 25 | 457.01 | 7.44 | 61.42 | 31.33 + 33.34 + 35.33 | 434.59 | 7.42 | 58.58 |
| 25 + 25 + 50 | 417.16 | 7.35 | 56.73 | 30.33 + 33.34 + 36.33 | 433.30 | 7.40 | 58.53 |
| 25 + 30 + 45 | 426.62 | 7.41 | 57.59 | 23.33 + 33.34 + 43.33 | 427.54 | 7.42 | 57.61 |
| 25 + 35 + 40 | 429.75 | 7.41 | 58.02 | 20 + 33.33 + 46.67 | 420.06 | 7.37 | 56.96 |
| 25 + 75 | 348.54 | 7.24 | 48.11 | 33.33 + 33.34 + 33.33 | 436.20 | 7.44 | 58.62 |
| 30 + 30 + 40 | 432.18 | 7.41 | 58.30 | 1 X 100 (main layer) | 264.19 | 7.09 | 37.27 |



Table 7.3

the depth margin between the individual sublayers increases. The horizontal scale is a measure of spread from identical depths; Thus, for example, for depths 30 cm and 70 cm the spread defined is 20 cm (deviation of these depths from 50 cm) as distinct from 40 cm which is the difference between the two depths.

In a similar manner, Figure 7.28 presents the results obtained for 3 sublayers showing the same downward trend. Here, the variation of efficiencies obtained is smaller, as is the total permissible spread. But the magnitudes of efficiency are observed to be larger than those for the case of 2 sublayers.

Finally, Figure 7.29 considers 4 sublayers where again the above trend is found to persist despite the much-reduced range of relative efficiencies and the allowable spread. The efficiencies shown exceed the previous cases so that, except for the case of 5 identical sublayers, selection of 4 sublayers provides the optimum design arrangement of tubes in the layer.

### 7.6.2 Inducement of a pronounced load-limiting action

As regards the process of collapse of the tubes in accordance with the above arrangement, a practical point must be incorporated in the selection of sublayers. It was shown in Chapter 5 that the critical axial load for a tube collapsing in the concertina mechanism is directly proportional to its net section area. Thus if identical sublayers are employed, then these would accommodate identical tubes throughout the layer for optimum design, an arrangement which would result

in simultaneous collapse of all tubes in the layer. This is in contrast to the case in which sublayers of differing depths are selected; Here the tubes from one sublayer to the next are different in size (and hence net section area) even though as far as their geometric ratios are concerned, they are congruent, that is to say they all correspond to the peak B on the zone polygon of Figure 7.1 . This implies that the tubes in the sublayer of the smallest depth would fail first (on account of their smallest section areas) and those in the thickest sublayer would fail last.

Therefore, by selecting and arranging the sublayers in an ascending or descending order of depths, a sequential collapse mechanism may be achieved for the overall layer. This manner of global collapse is considered to be beneficial in design since it provides a delaying action from the point at which the layer is struck at impact on one face, to the state in which the forces are transmitted fully effectively to the opposite face. These forces would be expected to be reduced in this process thus causing least damage to the surroundings at the instant of impact. Hence the choice of 4 sublayers with unequal depths not only promotes an increase in the total energy absorption capacity over that for the single layer as a whole, but facilitates a load-limiting action which is an aid towards the safety of the enclosing structure.

On the basis of the above observation, Figure 7.29 thus provides a range of optimum solutions for sublayer depths with a single discontinuity at the highest efficiency corresponding to

identical sublayers. Inspection reveals that the load-limiting function is offset by a loss in total absorption capacity and efficiency. However, because of the very small and almost insignificant differences in the relative efficiencies in Figure 7.29 , the limiting case of sublayer depths(equivalent to maximum spread) is recommended for optimum design. The corresponding design data are shown in Table 7.4 where the significant gain in total absorption capacity for this arrangement over that for the single undivided layer (as recorded in Table 7.1) may be observed.

## 7.7 Introduction of Concentric Tube Assemblies

The design solutions presented in the preceding sections are based on the use of identical tubes in the main layer (or in any one sublayer) and arranged in hexagonal packing pattern at prescribed spacings. In this section the possibility of employing sets of concentric tubes within the main layer is considered and the effect on total absorption capacity of the layer is inspected.

The problem here consists of determining how many concentric tubes and at what optimum section dimensions these should be designed to define a 'set' - and the number of such sets required to fill the layer, assuming hexagonal packing arrangement of these sets. The corresponding design efficiencies of these arrangements are compared with that for the previous cases of identical tubes, as a criterion for suitability of these assemblies for the particular design problem studied.

Optimum design data in the arrangement of tubes within sublayers (all 10m X 10m in plan)

| Design Parameter | Tube geometry | | | Spacing between adjacent tubes (2 X arm-length as in equation (7.1.1) | Table 7.2 | | |
|---|---|---|---|---|---|---|---|
| | Length (Depth of sublayer) (mm) | Internal diameter (mm) | Wall thick-ness (mm) | (mm) | Quantity of tubes in sublayer | Tube material volume ($m^3$) | Energy absorption capacity (Megajoules) |
| Symbol | L' | D | t | 2 h | $n_{t'}$ | $V_{T'}$ | $E_{T'}$ |
| Sublayer 1 | 200 | 42 | 2.3 | 23.5 | 23513 | 1.5 | 92.4 |
| Sublayer 2 | 233 | 48.5 | 2.7 | 27.5 | 17273 | 1.7 | 107.2 |
| Sublayer 3 | 267 | 55.5 | 3 | 31.5 | 13161 | 2.0 | 120.4 |
| Sublayer 4 | 300 | 62.5 | 3.5 | 35 | 10450 | 2.2 | 133.7 |
| Total tube material volume required : 7.4 $m^3$ | | | | | | | |
| Total energy absorption capacity of the layer : 453.7 MJ | | | | | | | |

Table 7.4

### 7.7.1 Determination of optimum dimensions for concentric tubes in a set

Starting with the innermost tube designed to assume section dimensions corresponding to the optimum point B on the zone polygon of Figure 7.1, the next narrowest tube enclosing this tube is determined such that its geometry falls at a point on the optimum line AB on the polygon; (Since depth L is fixed for all tubes in a set, the reader observes that only the innermost tube can have geometry falling on the optimum point B on the polygon). It is assumed that the inner tube, (as before) folds completely externally during collapse by a radial distance $h_i$ (h given in equation (7.1.1), Section 7.1) and that the outer tube folds part internally by amount $\frac{1}{2} h_o$ where $h_o$ (again given by (7.1.1)) indicates the complete arm-length of a concertina fold for the outer tube.

Figure 7.30 (i) indicates the plan view of the arrangement. Assigning suffices i and o for the inner and outer tubes respectively, it is seen that

$$D_o - h_o = D_i + 2t_i + 2h_i \qquad (7.7.1)$$

where

$$h_{i,o} = 1.2\,(D_{i,o}\,t_{i,o})^{\frac{1}{2}} \qquad (7.7.2)$$

and $t_i/D_i = 0.055$, $L/D_i = 4.8$ for the innermost tube.

In the specific design problem, L = 1000 mm (depth of the layer) so that for the innermost tube the following optimum dimensions are obtained, as indicated previously in Table 7.1 :

$$D_i = 208.3 \text{ mm}$$
$$t_i = 11.5 \text{ mm} \qquad (7.7.3)$$
$$h_i = 58.6 \text{ mm}$$

For the geometry of the outer tube falling on line AB of the zone polygon of Figure 7.1, it is observed that

$$L/D_o = 93.333\,(t_o/D_o) - 0.333 \qquad (7.7.4)$$

Thus, combining equations (7.7.1), (7.7.2) and (7.7.3),

$$D_o\,[1 - 1.2\,(t_o/D_o)^{\frac{1}{2}}] = 348.51 \qquad (7.7.5)$$

and equation (7.7.4) gives

$$D_o\,[93.333\,(t_o/D_o) - 0.333] = 1000 \qquad (7.7.6)$$

Equation (7.7.5) divided into (7.7.6) eliminates the unknown $D_o$ giving the following quadratic in terms of one variable only;

$$93.333\ Z^2 + 3.4433\ Z - 3.2027 = 0 \qquad (7.7.7)$$

where $Z = (t_o/D_o)^{\frac{1}{2}}$

Considering the negative sign of the radical in the solution for Z, values of $D_o = 279.8$ mm and $t_o = 11.7$ mm would be obtained which do not satisfy equation (7.7.5) . Hence only the positive sign of the radical is meaningful. This gives

$$\frac{t_{o1}}{D_{o1}} = 0.0281$$

so that,

$$D_{o1} = 436.3 \text{ mm}$$

$$t_{o1} = 12.3 \text{ mm} \qquad (7.7.8)$$

$$h_{o1} = 87.8 \text{ mm}$$

With the optimum geometry of the outer concentric tube evaluated, the above process may be repeated to determine these quantities for the next narrowest permissible outer tube enclosing these tubes. This is achieved by attaching suffix i to the solutions in (7.7.8) and substituting them in equation (7.7.1) to yield a new solution for the right hand side of equation (7.7.5) . The latter equation may then be solved simultaneously with equation (7.7.6) to yield a new quadratic in Z in equation (7.7.7) from which the desired quantities may be computed. These are as follows with suffix 2 denoting the second outer tube.

$$\frac{t_{o2}}{D_{o2}} = 0.0177$$

$$D_{o2} = 757.4 \text{ mm}$$

$$t_{o2} = 13.4 \text{ mm} \qquad (7.7.9)$$

$$h_{o2} = 121.0 \text{ mm}$$

Using the above results, the optimum dimensions of the next outer concentric tube may be calculated again in an identical manner by application of equations (7.7.1), (7.7.5), and (7.7.6) . The following quantities are obtained with suffix 3 denoting the third outer tube.

$$\frac{t_{o3}}{D_{03}} = 0.0126$$

$$D_{o3} = 1186.0 \text{ mm}$$

$$t_{o3} = 15.0 \text{ mm} \qquad (7.7.10)$$

$$h_{o3} = 159.8 \text{ mm}$$

However, in repeating the above process a stage futher, if the above values are used in equations (7.7.1), (7.7.5) and (7.7.6) to determine the optimum geometry of the fourth outer concentric tube, a value of $t_{o4}/D_{o4} = 0.0097$ would be obtained which is outside the permissible range bounded by the zone polygon of Figure 7.1 . Hence for optimum design a maximum of 4 concentric tubes may constitute a set. This is indicated in Figure 7.30 (ii).

It was shown in Section 7.5 that although line BC on the zone polygon provides an optimum range for the region EBCD of the polygon, considering the zone as a whole, this line is not an optimum in comparison with line AB. Nevertheless, starting as before with the innermost tube bearing ratios corresponding to point B, similar computations performed to optimize the geometry of the first outer tube to fall on line BC result in a value of $t_{o1}/D_{o1} = 0.1188$ which is outside the defined polygon. Thus the optimization presented here is in fact restricted to range AB only.

### 7.7.2 Design efficiency and the arrangement of concentric tubes

With the optimum geometry of the concentric tubes forming a set defined above, the corresponding quantities of these sets required to fill the layer are next calculated. Figure 7.31

illustrates the results obtained as a bar chart. The horizontal axis is a measure of the permissible number of concentric tubes forming an optimum set. Thus zero indicates the use of identical tubes throughout the layer and 3 denotes the maximum permissible number of concentric tubes within the outermost tubes in a set. The sharp drop in total quantity of sets in the layer from the case of identical tubes is explained by the fact that in the latter case, the figure shown coincides with the total quantity of individual tubes, whereas in the case of concentric tubes,

$$\begin{array}{c}\text{Total number of}\\ \text{tubes in layer}\end{array} = \begin{array}{c}\text{Total number of}\\ \text{concentric tube sets}\end{array} \times \begin{array}{c}\text{Number of tubes}\\ \text{in each set}\end{array}$$

However, the falling trend observed in Figure 7.31 would persist even if the equivalent quantity of individual tubes throughout the layer is considered, - as inspection of the following corresponding data indicates;

| Arrangement of tubes in layer | Quantity of individual tubes required in layer |
|---|---|
| 1. identical tubes | 896 |
| 2. sets of 2 concentric tubes | 510 (2 X 255) |
| 3. sets of 3 concentric tubes | 270 (3 X 90) |
| 4. sets of 4 concentric tubes | 168 (4 X 42) |

Table 7.5 shows the results obtained for total absorption capacity, total tube material volume and the corresponding design efficiencies of each of the above arrangements, for the layer considered. It is observed that these quantities are a maximum for the case of identical tubes and decrease

Comparison of optimum design efficiencies in the arrangement of concentric tubes within the crushing layer

Length of all tubes, L = depth of layer = 1 m (Layer is 10m X 10m in plan)

| Arrangement of tubes in layer | Tube geometry | | | Quantity of tubes $n_t$ | Tube material volume $V_T$ ($m^3$) | Absorption capacity of layer $E_T$ (MJ) | Design efficiency $E_T/V_T$ ($MJ/m^3$) |
|---|---|---|---|---|---|---|---|
| | Ratio t/D | D (mm) | t (mm) | | | | |
| Identical tubes | 0.0550 | 208.5 | 11.5 | 896 | 7.1 | 264.2 | 37.26 |
| Sets of 2 concentric tubes | 0.0550 | 208.5 | 11.5 | 255 | 2.0 | 75.2 | 31.63 |
| | 0.0281 | 436.5 | 12.3 | 255 | 4.4 | 128.2 | |
| | | | | | 6.4 | 203.4 | |
| Sets of 3 concentric tubes | 0.0550 | 208.5 | 11.5 | 90 | 0.7 | 26.5 | 26.88 |
| | 0.0281 | 436.5 | 12.3 | 90 | 1.6 | 45.3 | |
| | 0.0177 | 757.5 | 13.5 | 90 | 2.9 | 67.9 | |
| | | | | | 5.2 | 139.7 | |
| Sets of 4 concentric tubes | 0.0550 | 208.5 | 11.5 | 42 | 0.3 | 12.4 | 22.84 |
| | 0.0281 | 436.5 | 12.3 | 42 | 0.7 | 21.1 | |
| | 0.0177 | 757.5 | 13.5 | 42 | 1.4 | 31.7 | |
| | 0.0126 | 1186.0 | 15.0 | 42 | 2.4 | 44.4 | |
| | | | | | 4.8 | 109.6 | |

Table 7.5

as the number of concentric tubes constituting a set increases. Figure 7.32 illustrates, as a bar chart, this falling trend in the design efficiencies of concentric tube assemblies.

Thus, on the evidence of the patterns presented, the author concludes, perhaps contrary to previous predictions, that for optimum design, it would be improper to employ sets of concentric tubes in the layer, since the overall efficiency of the respective arrangements reduces from that for a quantity of identical tubes in the layer. This has been shown to be valid for the optimum geometric ratios of all concentric tubes in a set, in accordance with the zone polygon of Figure 7.1, so that, for all other geometric ratios for concentric tubes the above necessarily holds valid.

Furthermore, it can be shown that the solutions presented for the optimum t/D ratios of all concentric tubes in a set are independent of layer depth, L (since equation (7.7.7) would be derived identically for all L). Hence the maximum of 4 concentric tubes with optimum geometry obtained to constitute a set is not restricted to the particular depth specified in the problem. This implies that the conclusion in the preceding paragraph may be extended, by induction, equally to the case of sublayers, each containing concentric tube assemblies. This is because each individual sublayer retains maximum efficiency if it encloses identical tubes.

Therefore, the data presented in Table 7.4 (Section 7.6) provides the optimum set of solutions for the specific design problem studied.

## 7.8 Conclusion

Abbreviations { TE: Total energy absorption capacity (Joules)
DE: Design efficiency : energy absorbed per unit tube material volume (Joules/metre cubed)

1. For a given space to be filled with cylindrical tubes to absorb energy in axial collapse in the (optimum) concertina mode, increases in TE (by factors up to 30) may be gained by using narrow (rather than large) tubes, in accordance with the zone polygon of Figure 7.1 . For all depths $L \geq 20$ cm, both TE and DE reach their peak if tube geometries are selected to fall on optimum point P on this polygon.

2. Boundary conditions (see '4', Section 7.1.3) reduce TE if
(i) a small quantity of large diameter tubes are employed;
(ii) layers of reduced span but identical in depth are used.

3. Division of a layer into N rows of sublayers each containing tubes with optimum ratios defined in '1', results in TE & DE that exceed those for the undivided layer. TE & DE reach their peak for maximum N (& equal depths, L'), obtained from the condition of minimum depth, L' = 20 cm imposed. But for unequal depths, L', the resulting sequential manner of global collapse permits a favourable load-limiting function as well as energy absorption. For optimum design, it is recommended to use maximum N with maximum differences in individual depths (using minimum L'). This signifies a minimum loss in DE.

4. Both TE and DE reduce if sets of concentric tubes are used, even for optimum tube geometries on line AB of the zone polygon. The larger the number of concentric tubes in a set, the greater the drop in DE in the resulting arrangement. This finding is independent of layer depth.

## 7.9 Practical Application

The design method presented in this chapter has been based on highly idealized conditions for (a) axial collapse of the selected tubes and (b) their surrounding environment, in their particular application as an energy-dissipating assemblage in a nuclear reactor plant; the design data may thus be termed 'pseudo-design'. The particular practical factors which will influence the optimum solutions obtained and are worthy of detailed future research are highlighted below.

1. Dynamic loading (see Section 8.2.2, Ch.8) : This promotes an increase in stress with (mean) strain rate and may thus favourably increase the energy dissipation capacity of tubes above their quasi-static quantity.
2. Oblique impact (see assumption 7, P.254): It is most probable that the cover plates of the crushing layer would be impacted in an oblique and non-uniform ('tilting') manner; the resulting off-axis loading on the enclosed tubes would perhaps promote the precipitation of the (undesirable) strut-type (Eulerian) collapse as well as the (selected) concertina mode.
3. Thermal effects : The operating temperatures (~500$\dot{C}$) enhance the 'flow' properties of the tube material and consequently influence the strain rate (see 'Mechanical Properties of Materials at High Rates of Strain', 1979, Inst. Physics Conf. Series No.47)-(and for long-term thermal effects, see Strength of Materials by Timoshenko, Pt.II, 2nd edition, PP.462-473).
4. End-fixity conditions of tubes : The mode of collapse would be influenced depending on whether the tubes are individually 'fixed' on to the cover plates, or are allowed to be shifted within the crushing layer (see Section 8.2.3, Ch.8, for combined effects of '3' and '4').
5. The proportion of the impact energy that is transferred as elastic waves to the whole structure and not dissipated by the tubes in the crushing layer.
6. Special treatments that may be required to remove anisotropic properties of as-received tubes.
7. The corrosive nature of nuclear radiation on the material properties of tubes.

Furthermore, although the present design method has been based on the use of cylindrical tubes in the nuclear reactor application, the author realises that non-circular tubes, in particular square tubes, are also suitable energy dissipators (see Johnson(41)et al(43)(45) and Kukkola(56)).

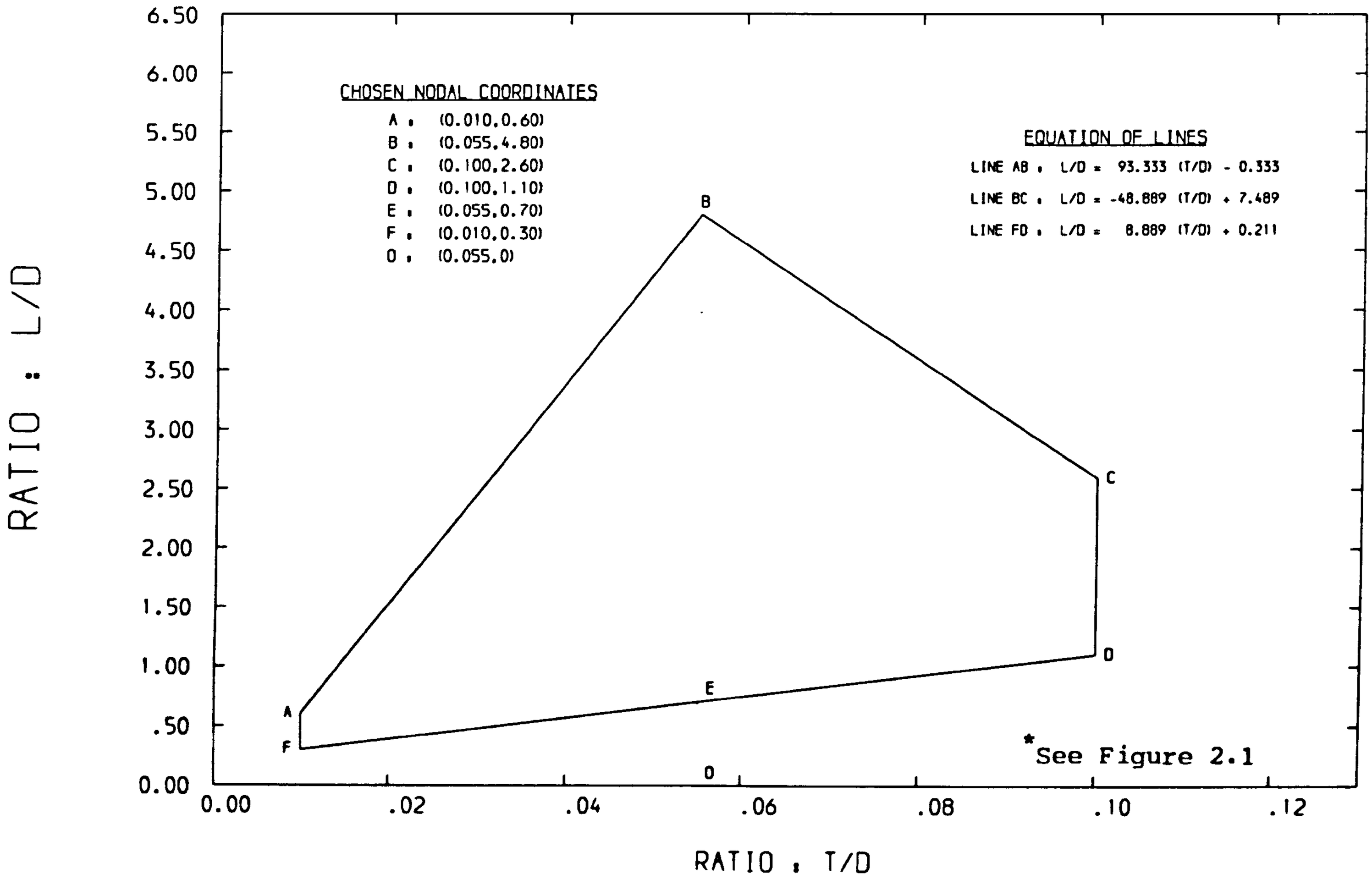


POLYGON DEFINED FOR THE ZONE OF COLLAPSE IN CONCERTINA MODE*

**Figure 7.1**

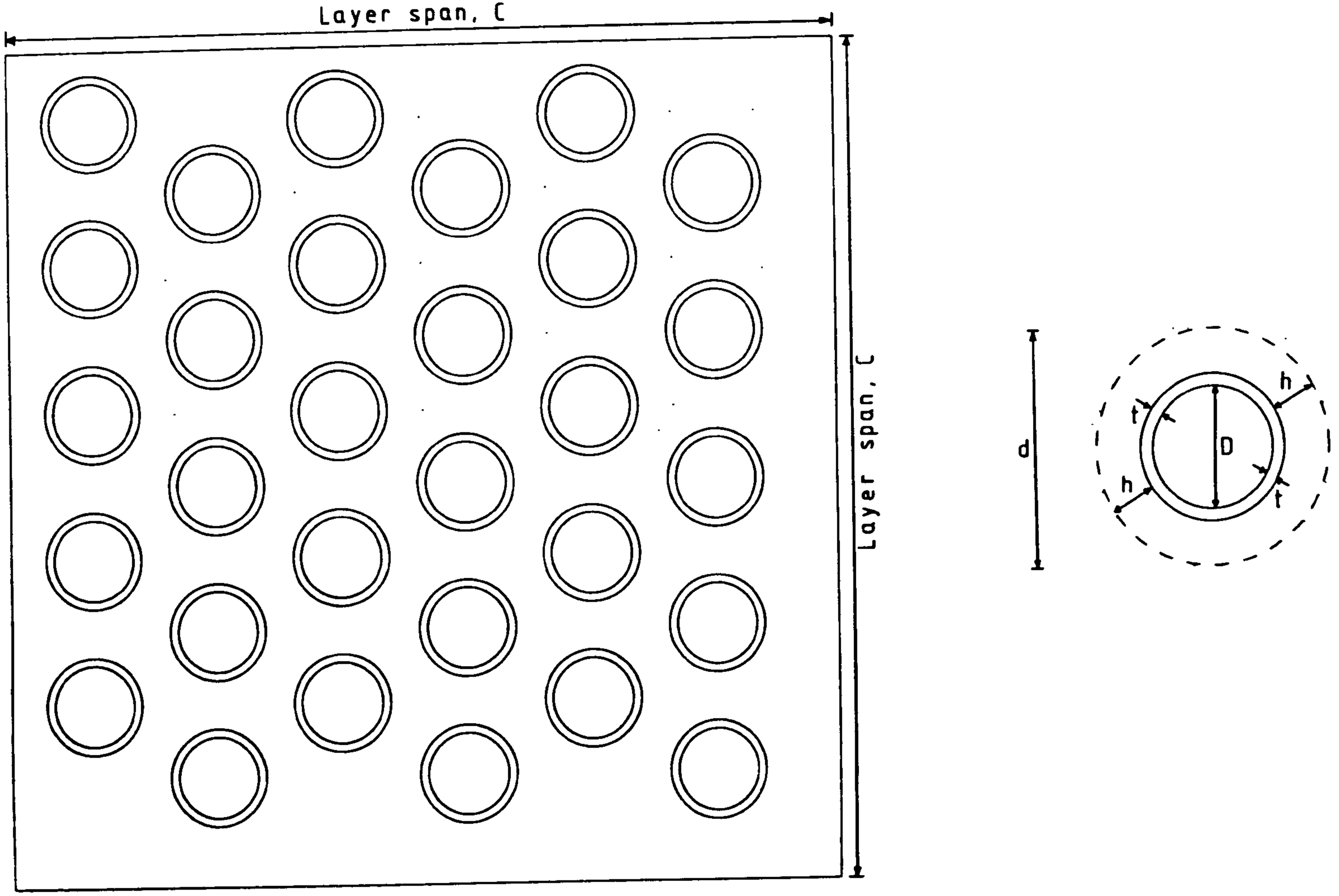


PLAN VIEW OF THE HEXAGONAL PACKING ARRANGEMENT OF TUBES IN LAYER

**Figure 7.2**

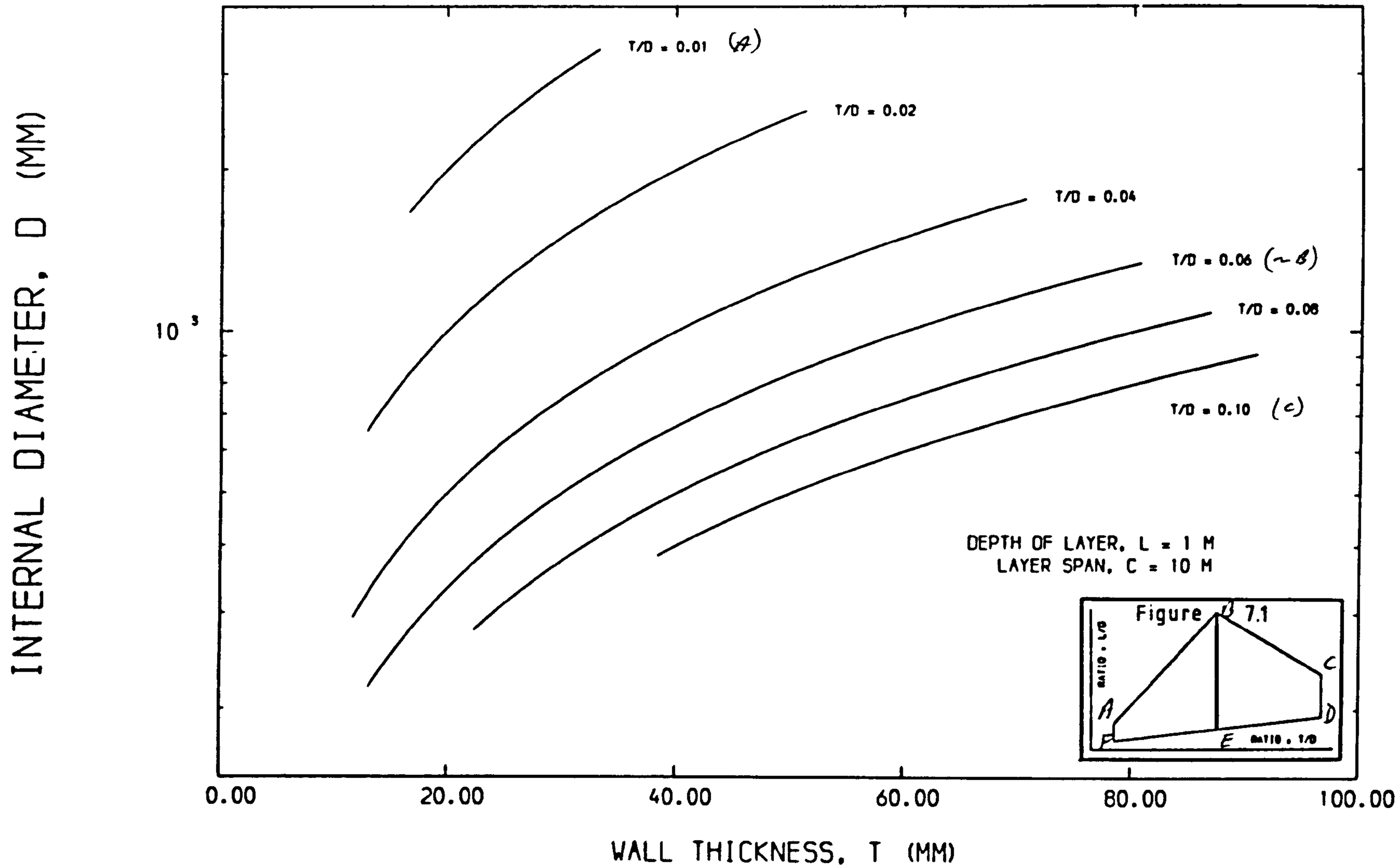


TUBE DIAMETER AND WALL THICKNESS DESIGN RANGES FOR GIVEN LAYER

**Figure 7.3**

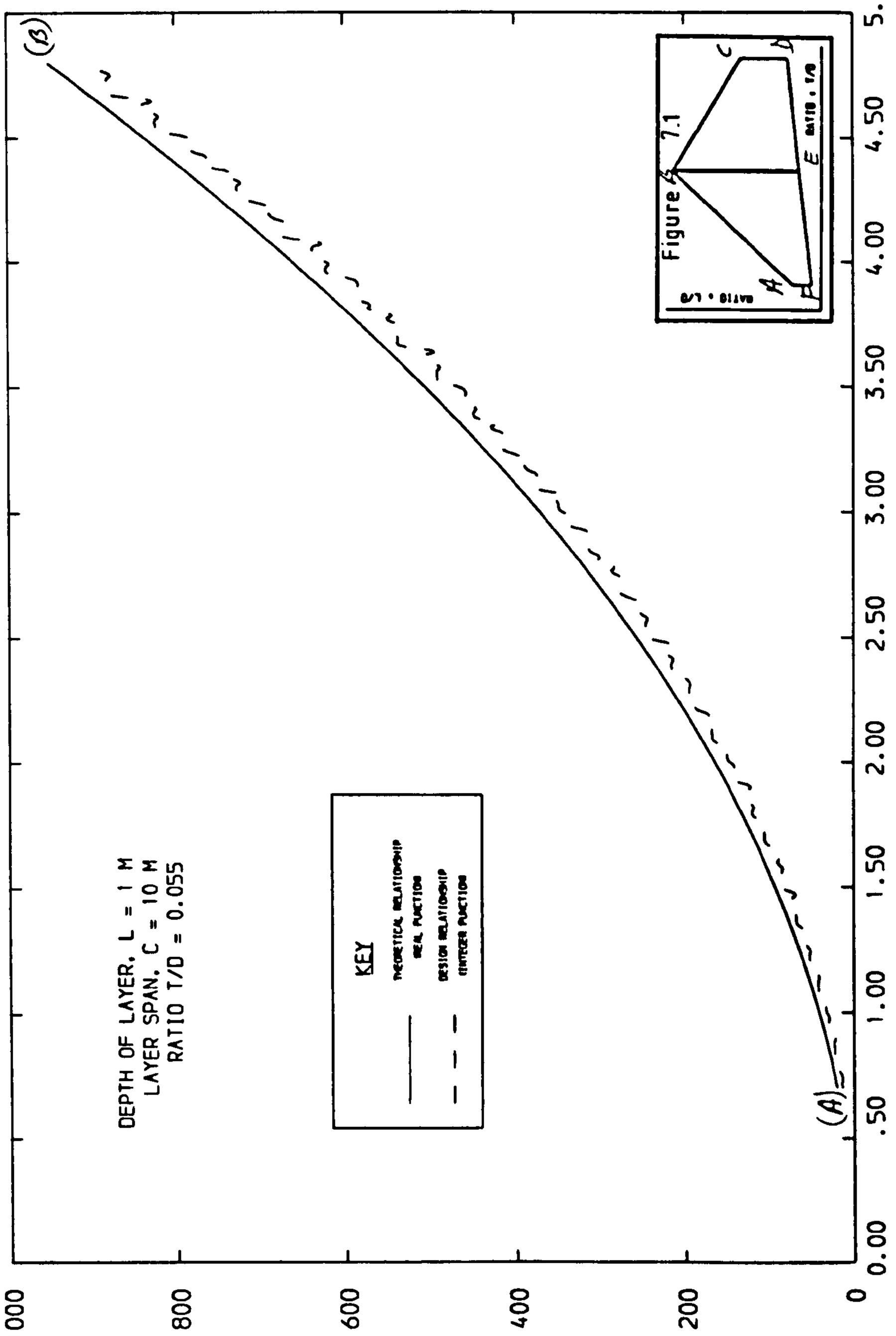
NUMBER OF ENERGY ABSORBING TUBES IN GIVEN LAYER
1000
800
600
400
200
0
DEPTH OF LAYER, L = 1 M
LAYER SPAN, C = 10 M
RATIO T/D = 0.055
KEY
THEORETICAL RELATIONSHIP
REAL FUNCTION
DESIGN RELATIONSHIP
INTEGER FUNCTION
(A)
(B)
0.00
.50
1.00
1.50
2.00
2.50
3.00
3.50
4.00
4.50
5.00
RATIO : L/D
NUMBER OF TUBES WITHIN GIVEN LAYER / TUBE RATIOS
Figure 7.4
Figure 7.1

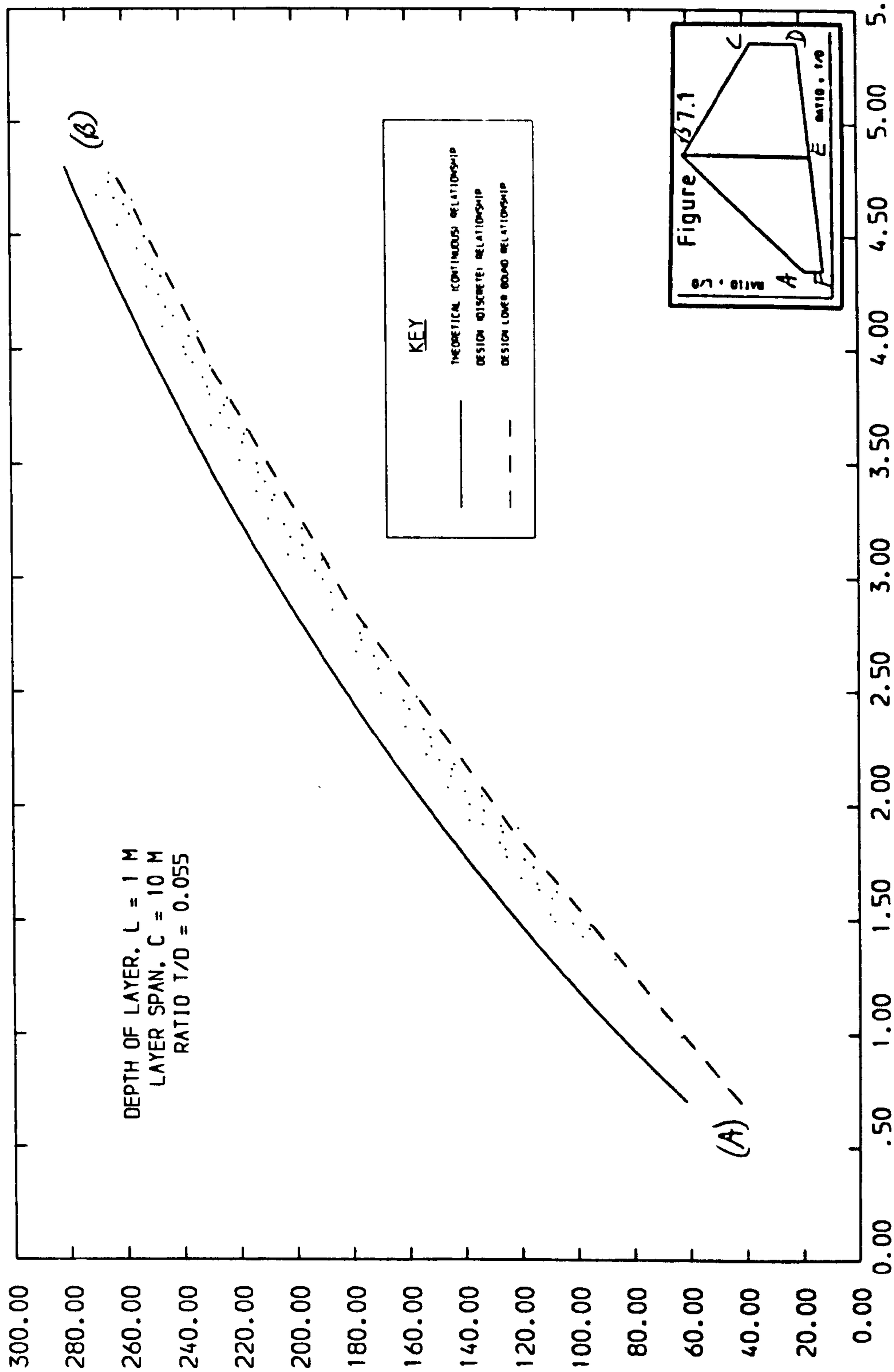
ENERGY ABSORBED FOR GIVEN VOLUME OF LAYER / TUBE RATIOS
RATIO : L/D
TOTAL ENERGY ABSORBED WITHIN GIVEN LAYER (MEGAJOULES)
DEPTH OF LAYER, L = 1 M
LAYER SPAN, C = 10 M
RATIO T/D = 0.055
KEY
THEORETICAL (CONTINUOUS) RELATIONSHIP
DESIGN DISCRETE) RELATIONSHIP
DESIGN LOWER BOUND RELATIONSHIP
(A)
(B)
Figure 7.1
RATIO : L/D
A
D
E
0.00
.50
1.00
1.50
2.00
2.50
3.00
3.50
4.00
4.50
5.00
5.50
0.00
20.00
40.00
60.00
80.00
100.00
120.00
140.00
160.00
180.00
200.00
220.00
240.00
260.00
280.00
300.00

Figure 7.5

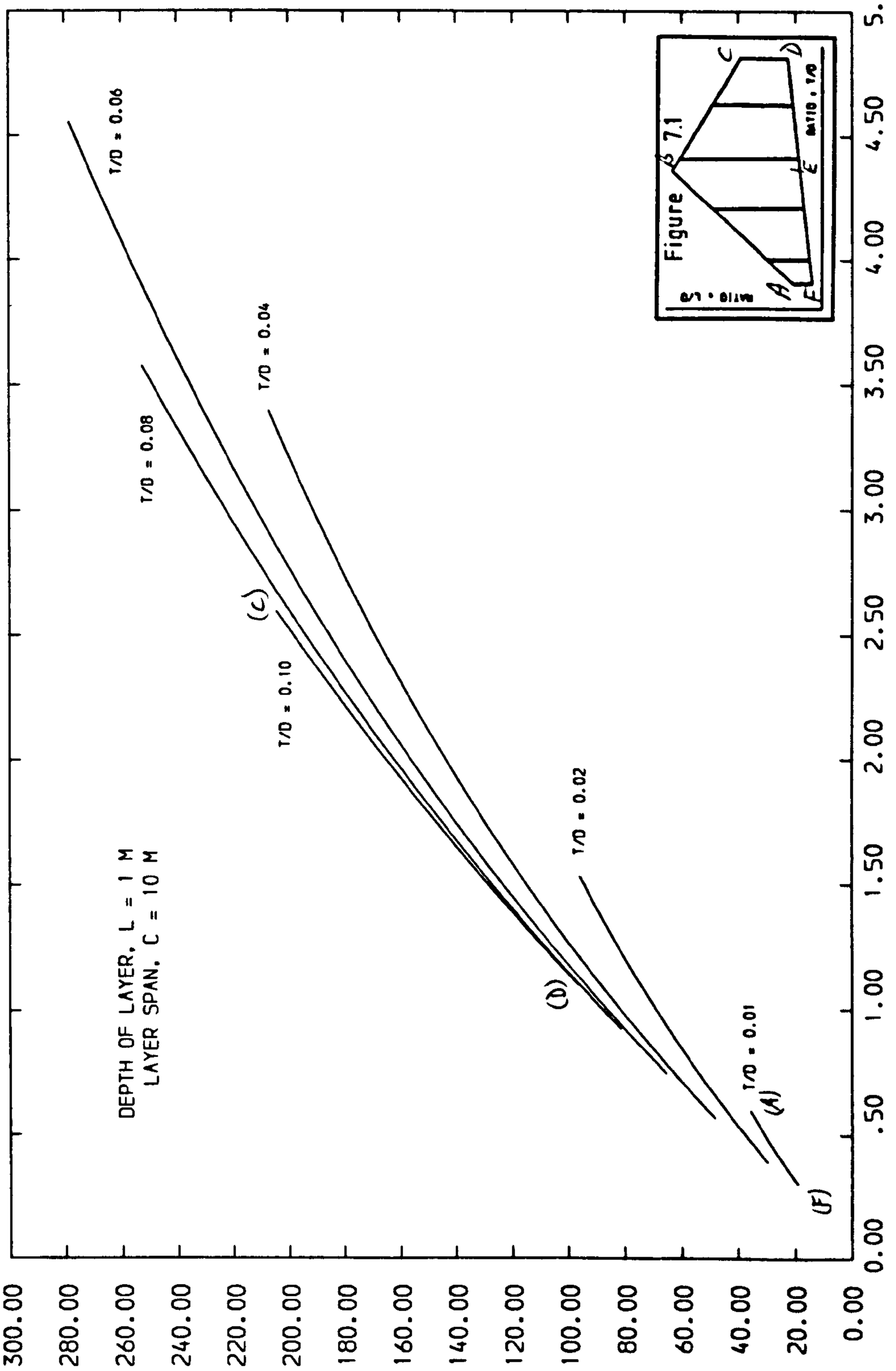
GEOMETRIC RATIOS
Figure 7.1
RATIO : L/D
2.00
2.50
3.00
3.50
4.00
4.50
5.00
THEORETICAL RELATIONSHIPS FOR ABSORBED ENERGY / GEOMETRIC RATIOS
DEPTH OF LAYER, L = 1 M
LAYER SPAN, C = 10 M
T/D = 0.08
T/D = 0.04
T/D = 0.10
T/D = 0.02
T/D = 0.01
(C)
(D)
(A)
(F)
0.00
.50
1.00
1.50
300.00
280.00
260.00
240.00
220.00
200.00
180.00
160.00
140.00
120.00
100.00
80.00
60.00
40.00
20.00
0.00
TOTAL ENERGY ABSORBED WITHIN GIVEN LAYER (MEGAJOULES)

**Figure 7.6**

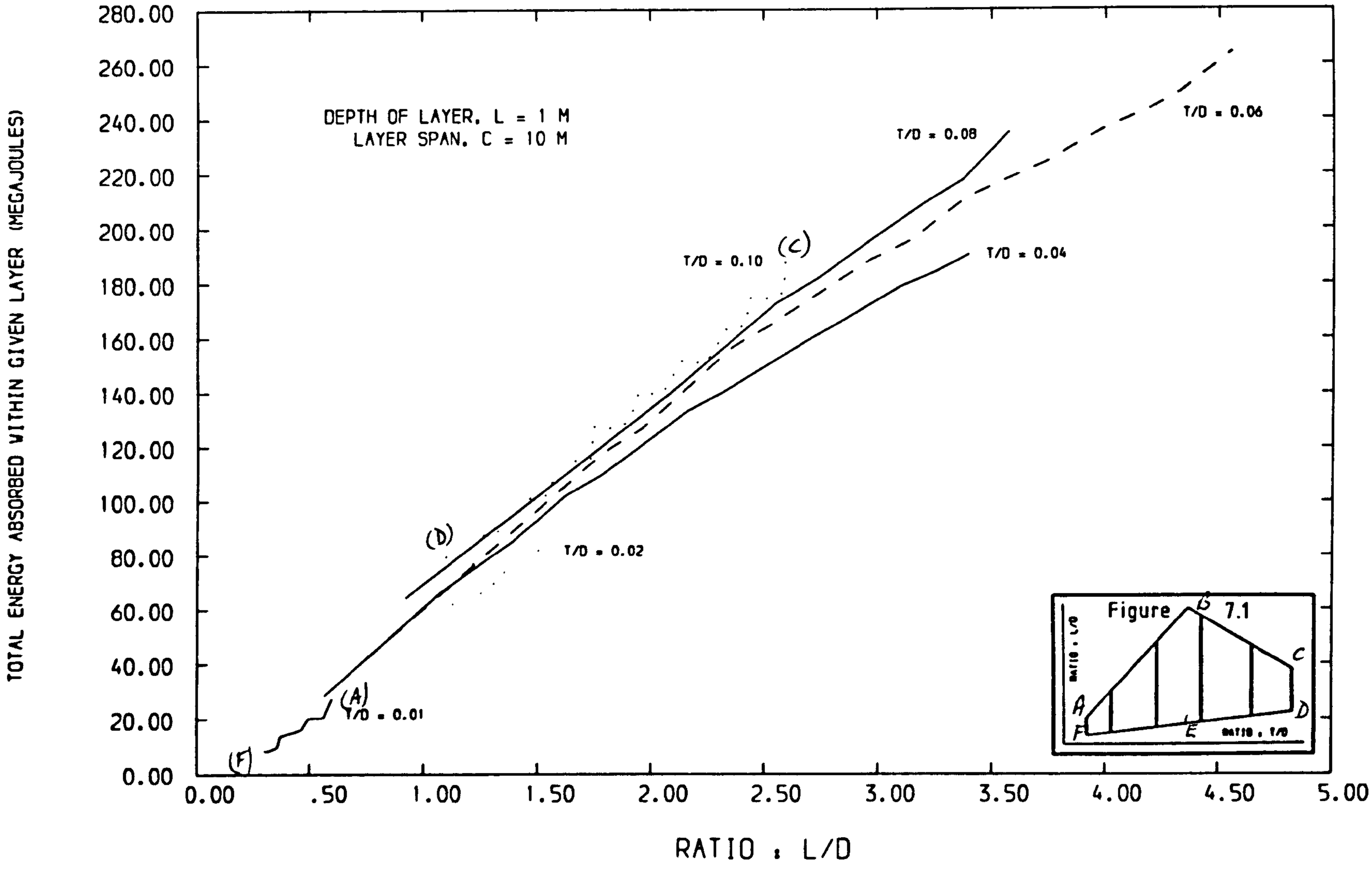


DESIGN LOWER BOUNDS FOR ABSORBED ENERGY / GEOMETRIC RATIOS

**Figure 7.7**

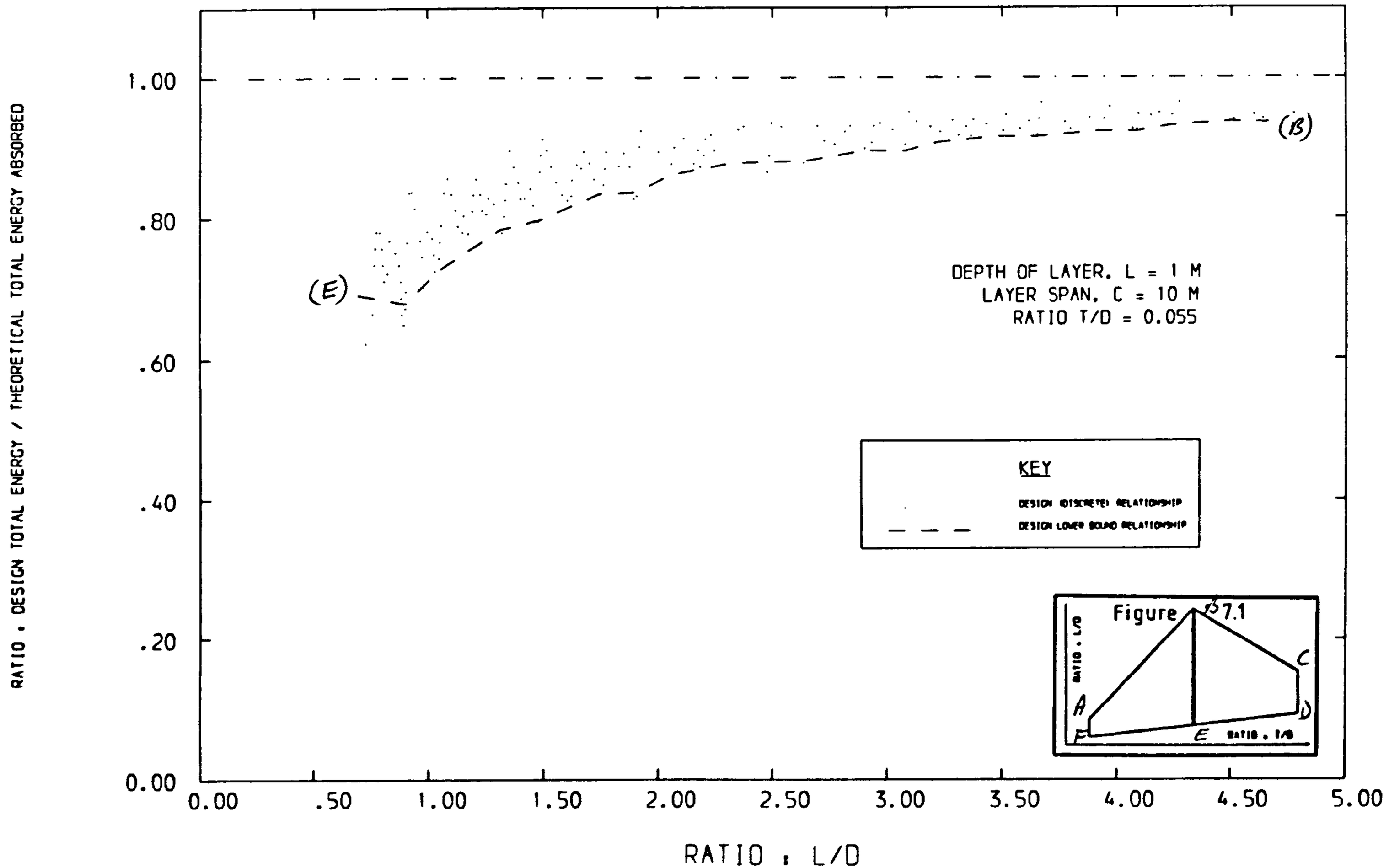


INFLUENCE OF LAYER BOUNDARY EFFECT ON TOTAL ENERGY ABSORPTION

**Figure 7.8**

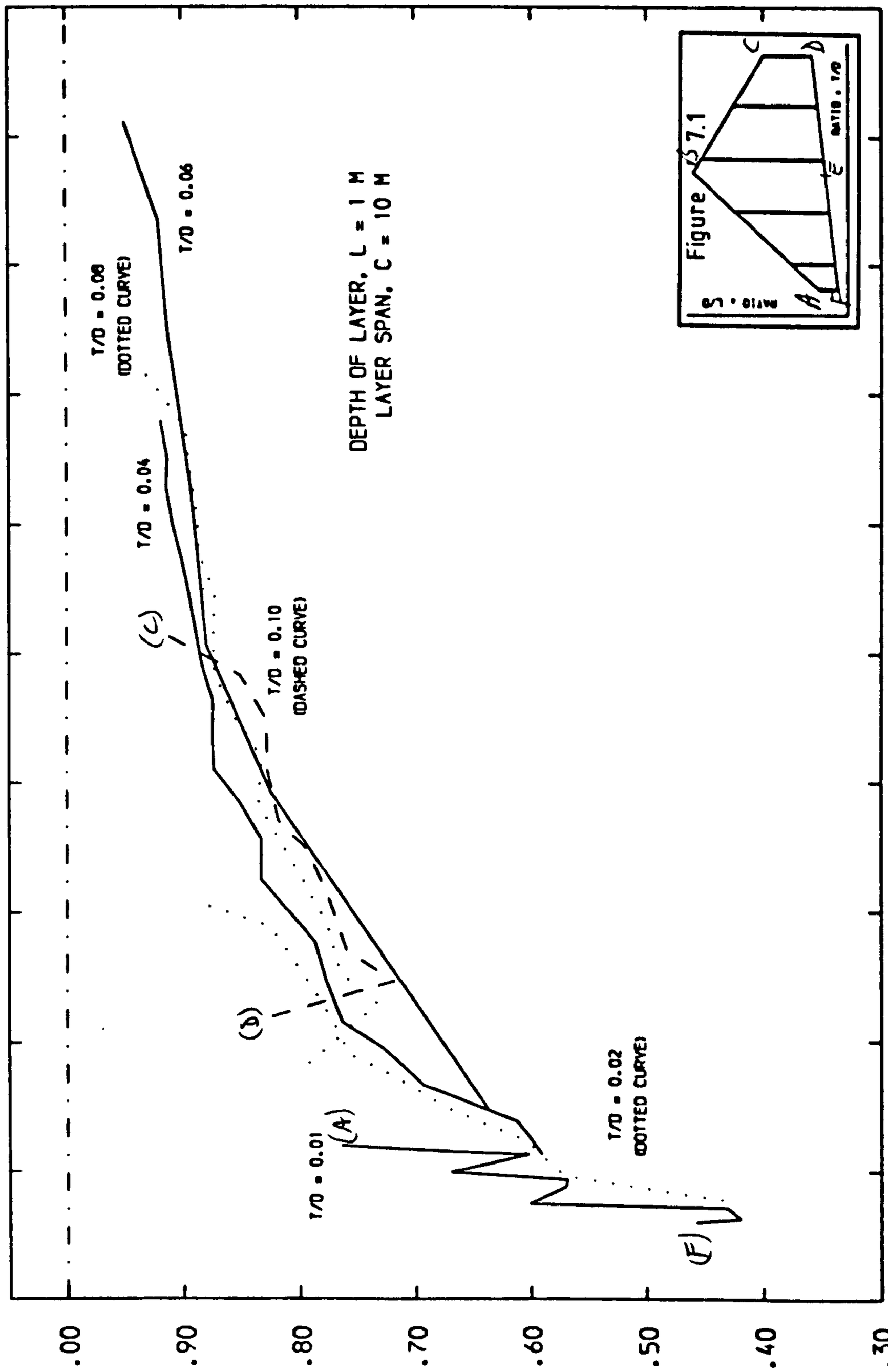
INFLUENCE OF LAYER BOUNDARY EFFECT ON TOTAL ENERGY ABSORPTION
RATIO • L/D
RATIO • DESIGN TOTAL ENERGY / THEORETICAL TOTAL ENERGY ABSORBED
DEPTH OF LAYER, L = 1 M
LAYER SPAN, C = 10 M
T/D = 0.06
T/D = 0.06
(DOTTED CURVE)
T/D = 0.04
T/D = 0.10
(DASHED CURVE)
T/D = 0.01
T/D = 0.02
(DOTTED CURVE)
(A)
(B)
(C)
(D)
(E)
(F)
Figure 7.1
5.00
4.50
4.00
3.50
3.00
2.50
2.00
1.50
1.00
.50
0.00
1.00
.90
.80
.70
.60
.50
.40
.30

Figure 7.9

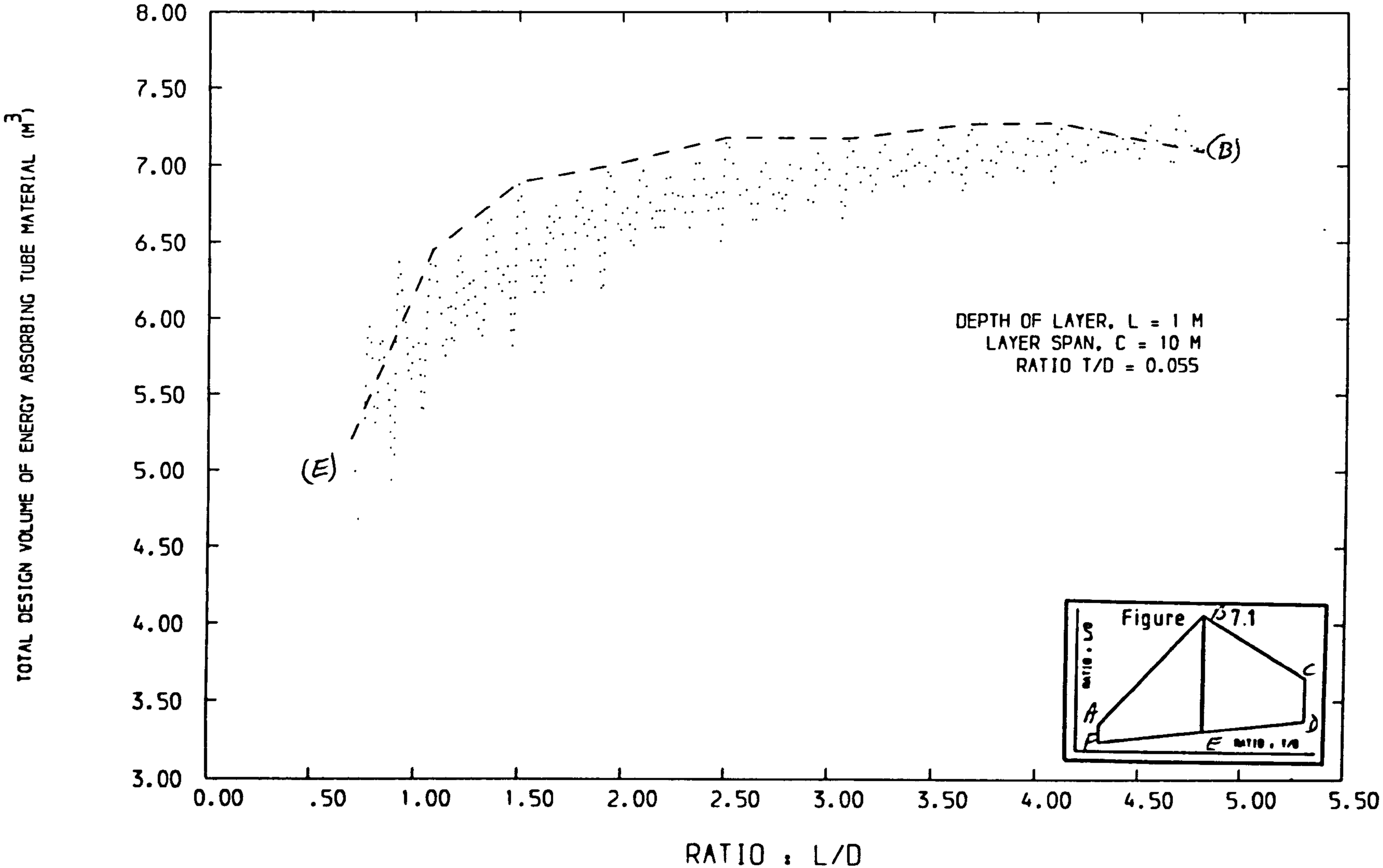


VOLUME OF TUBE MATERIAL / TUBE RATIOS FOR GIVEN LAYER

**Figure 7.10**

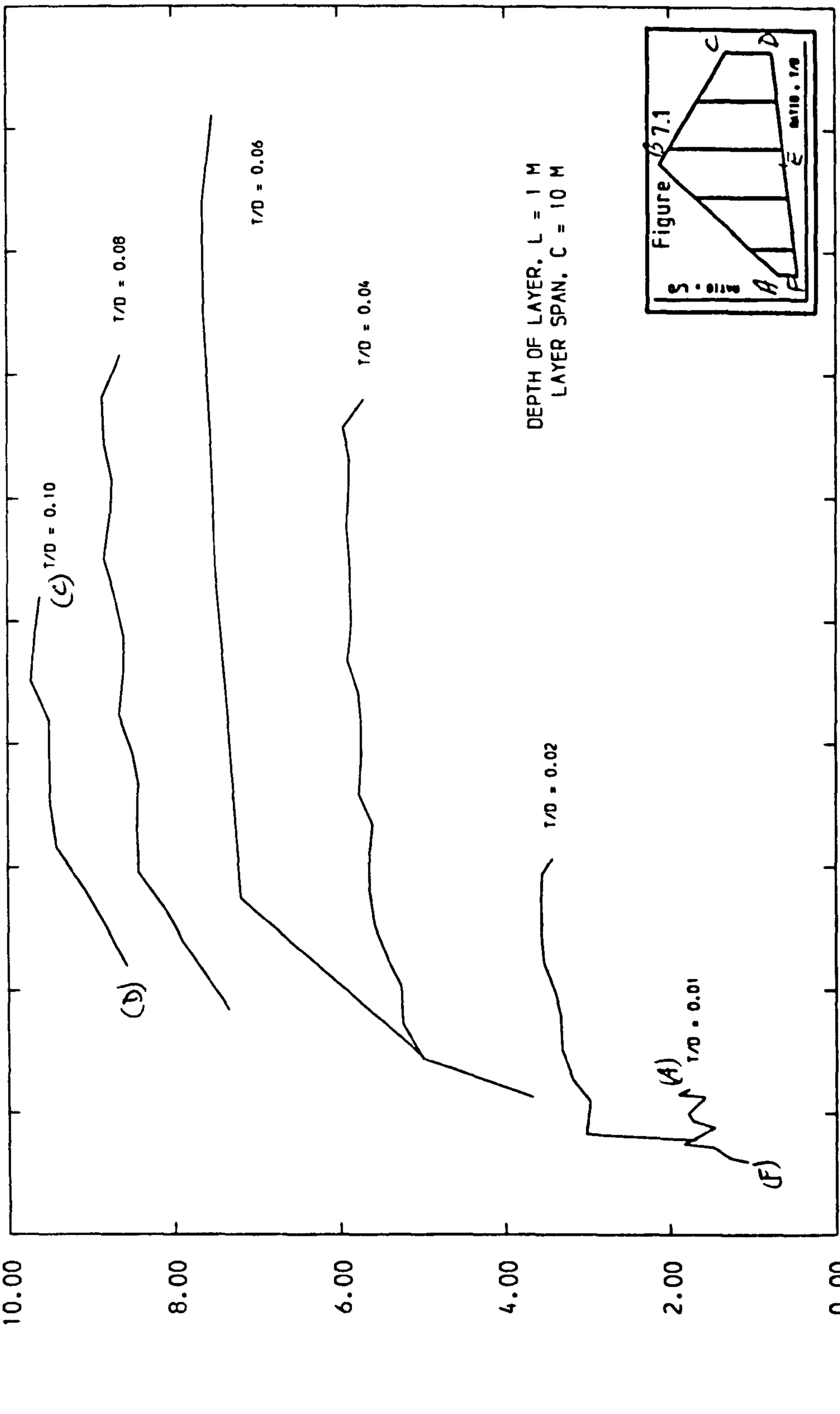
TOTAL DESIGN VOLUME OF ENERGY ABSORBING TUBE MATERIAL (M³)
10.00
8.00
6.00
4.00
2.00
0.00
VOLUME OF TUBE MATERIAL / GEOMETRIC RATIOS FOR GIVEN LAYER
RATIO : L/D
0.00
.50
1.00
1.50
2.00
2.50
3.00
3.50
4.00
4.50
5.00
DEPTH OF LAYER, L = 1 M
LAYER SPAN, C = 10 M
T/D = 0.08
T/D = 0.06
T/D = 0.04
T/D = 0.10
T/D = 0.02
T/D = 0.01
(A)
(B)
(C)
(D)
(E)
(F)
Figure 7.1

Figure 7.11

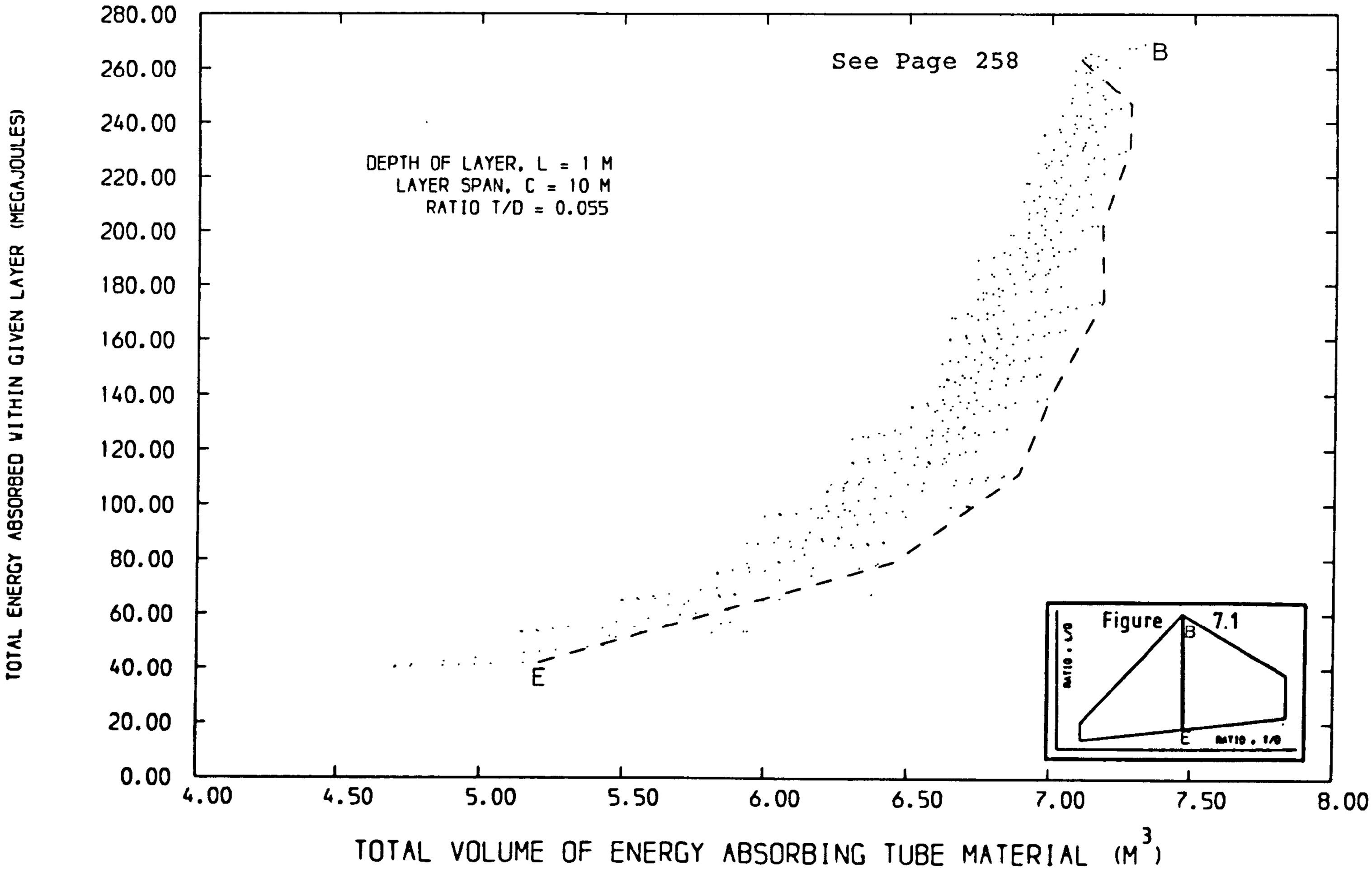


DESIGN LOWER BOUND ENERGY / VOLUME RELATIONSHIP

**Figure 7.12**

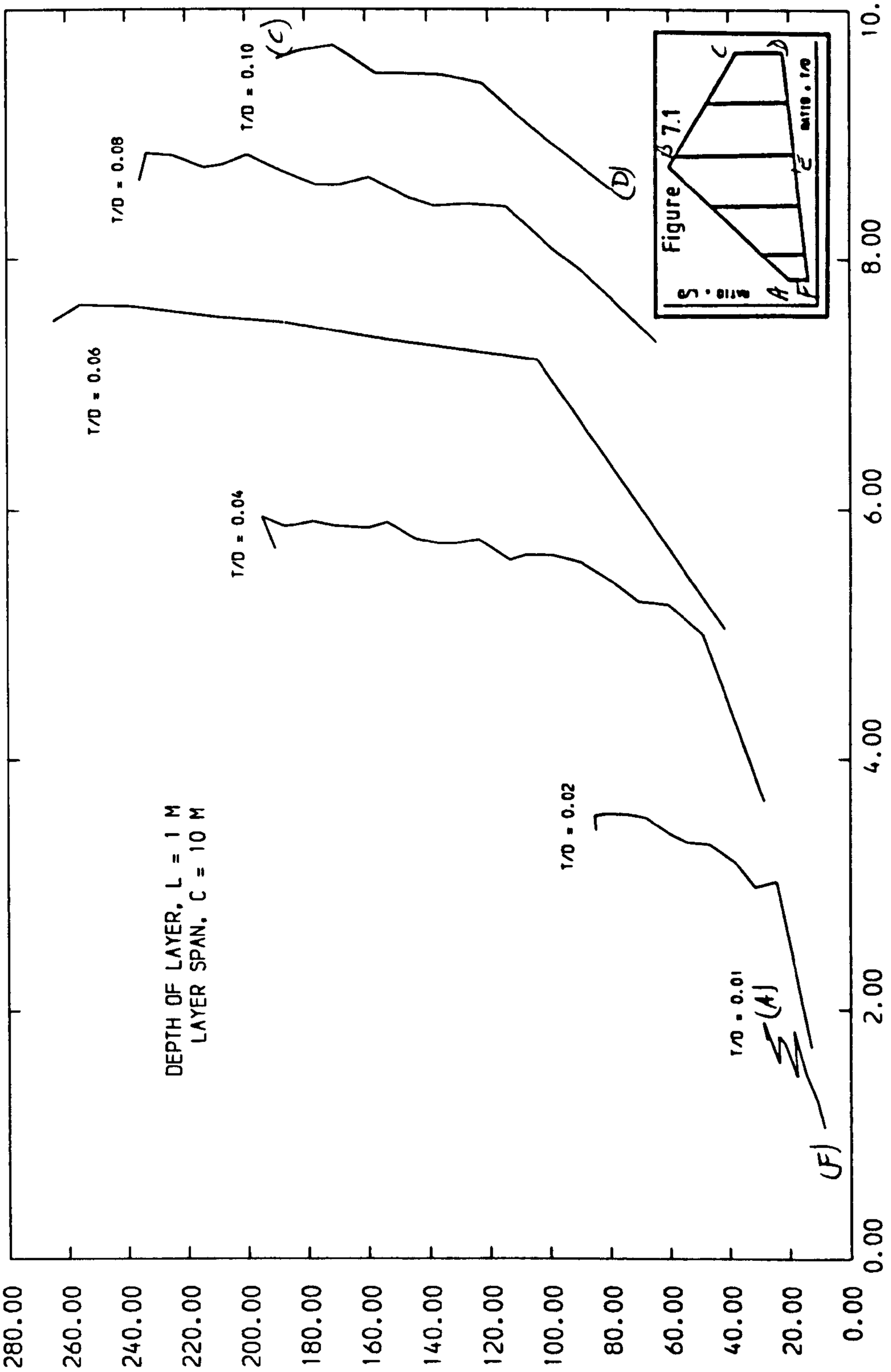
DESIGN LOWER BOUND ENERGY ABSORBING TUBE MATERIAL ENERGY / VOLUME RELATIONSHIPS
TOTAL VOLUME OF ENERGY ABSORBING TUBE MATERIAL ($M^3$)
0.00
2.00
4.00
6.00
8.00
10.00
DEPTH OF LAYER, L = 1 M
LAYER SPAN, C = 10 M
T/D = 0.02
T/D = 0.04
T/D = 0.06
T/D = 0.08
T/D = 0.10
T/D = 0.01
(A)
(C)
(D)
(F)
Figure 7.1
TOTAL ENERGY ABSORBED WITHIN GIVEN LAYER (MEGAJOULES)
280.00
260.00
240.00
220.00
200.00
180.00
160.00
140.00
120.00
100.00
80.00
60.00
40.00
20.00
0.00

**Figure 7.13**

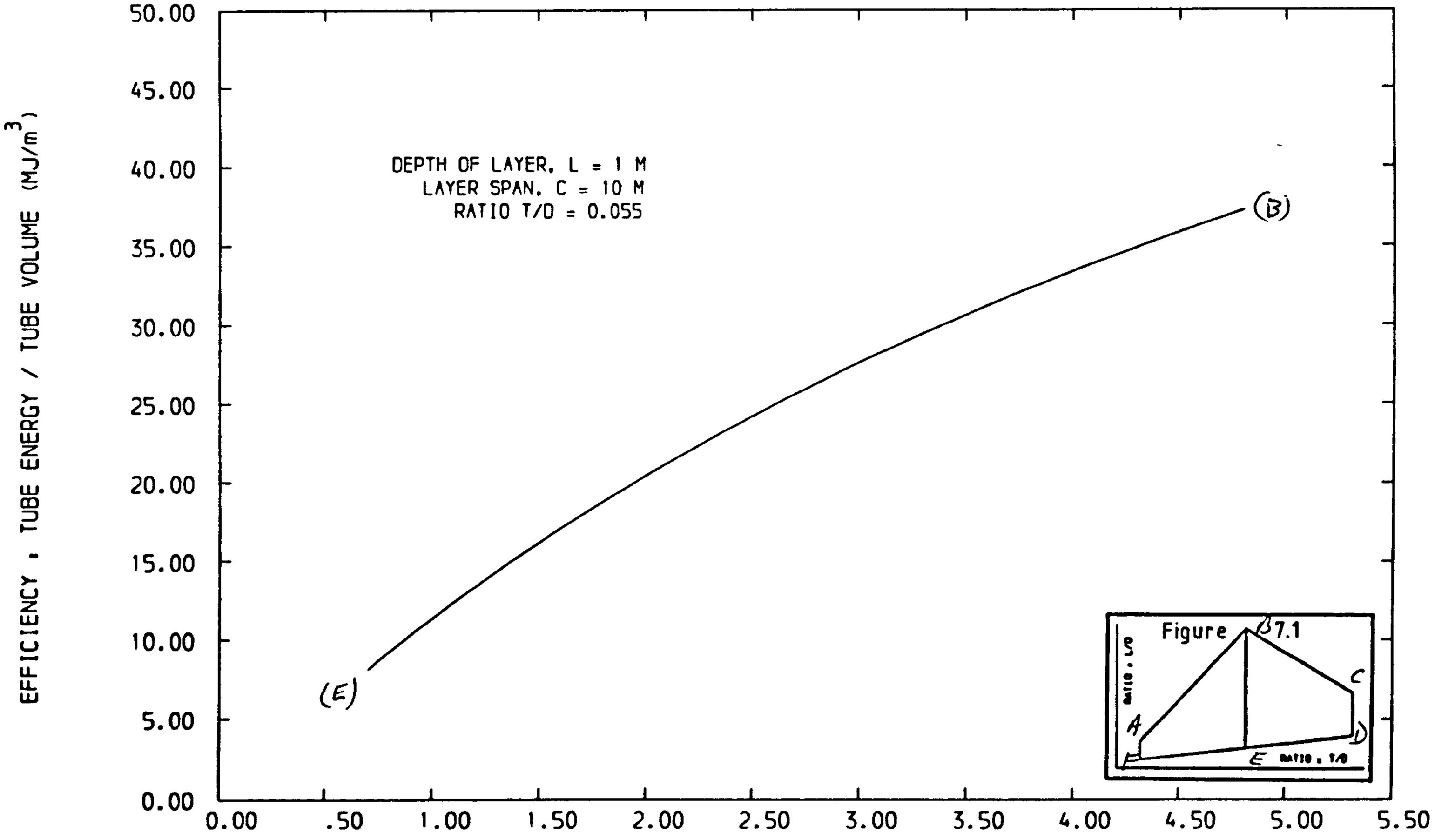


TUBE ENERGY ABSORPTION EFFICIENCY / TUBE GEOMETRY

**Figure 7.14**

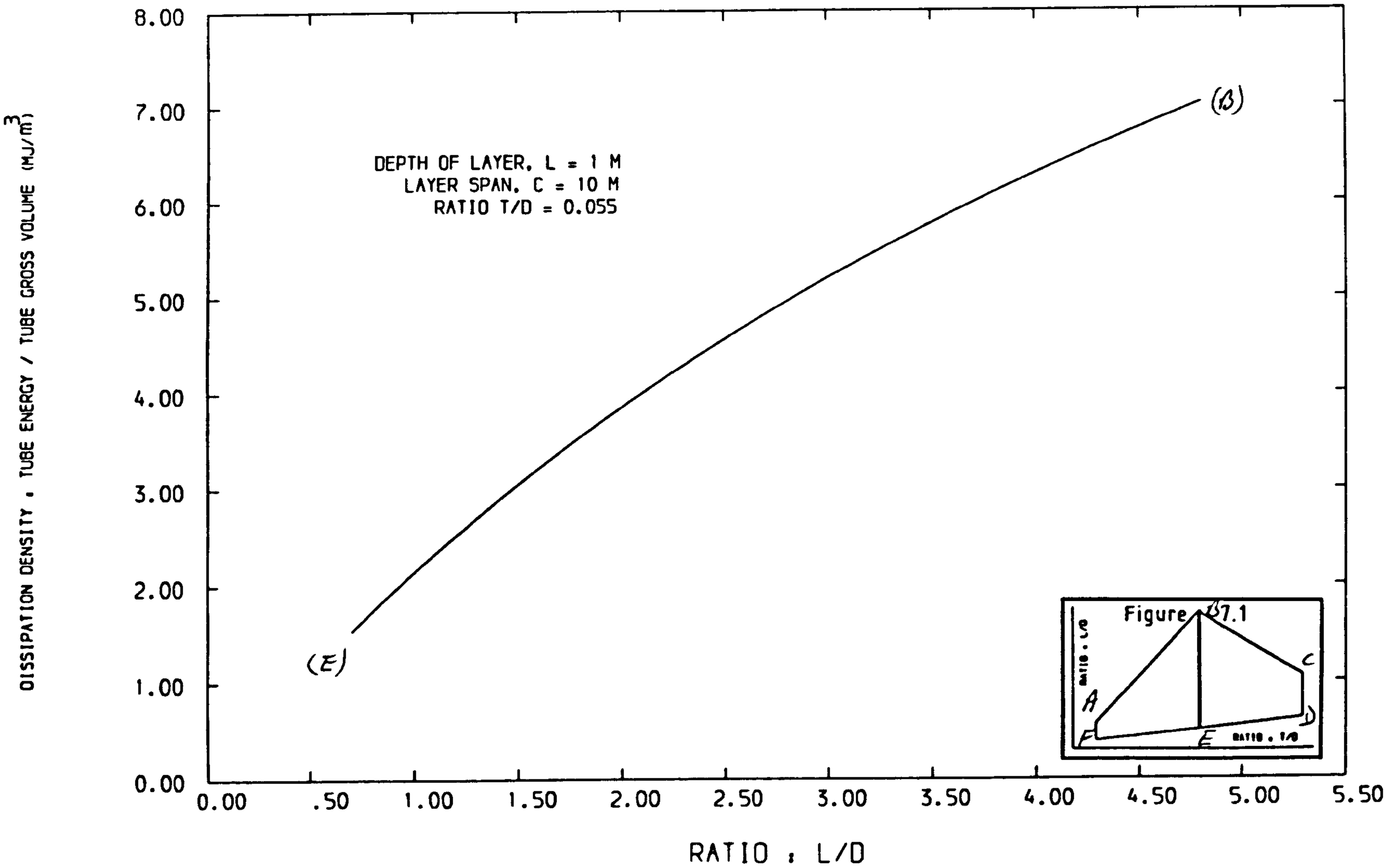


TUBE DISSIPATION DENSITY / TUBE GEOMETRY

**Figure 7.15**

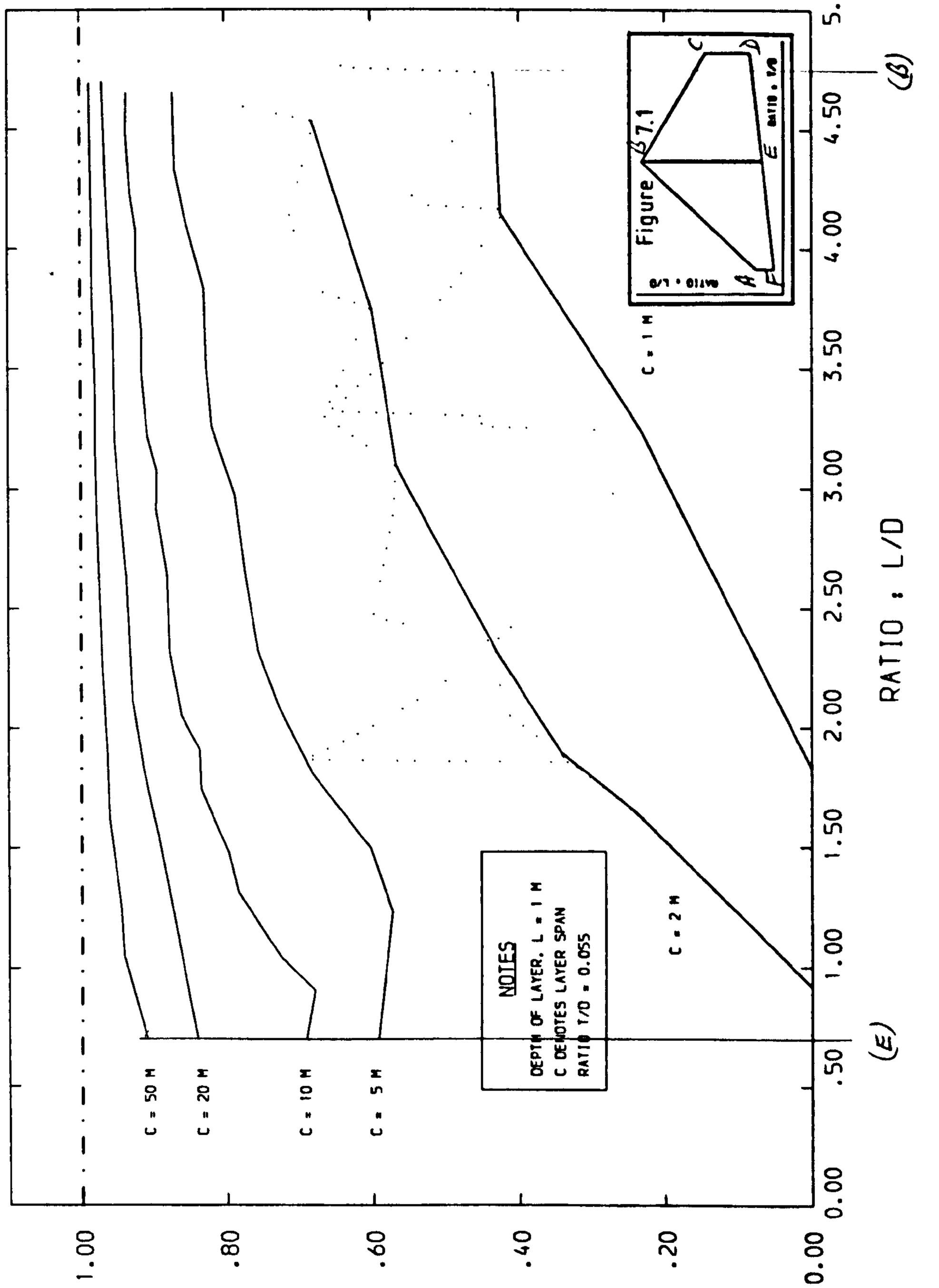
INFLUENCE OF BOUNDARY EFFECT ON DESIGN FOR DIFFERENT LAYER SPANS
RATIO : L/D
(β)
(ε)
RATIO : DESIGN TOTAL ENERGY / THEORETICAL TOTAL ENERGY ABSORBED
Figure 7.1
NOTES
DEPTH OF LAYER, L = 1 M
C DENOTES LAYER SPAN
RATIO T/D = 0.055
C = 50 M
C = 20 M
C = 10 M
C = 5 M
C = 2 M
c = 1 M
2.00
2.50
3.00
3.50
4.00
4.50
5.00
.50
1.00
1.50
0.00
.20
.40
.60
.80
1.00

Figure 7.16

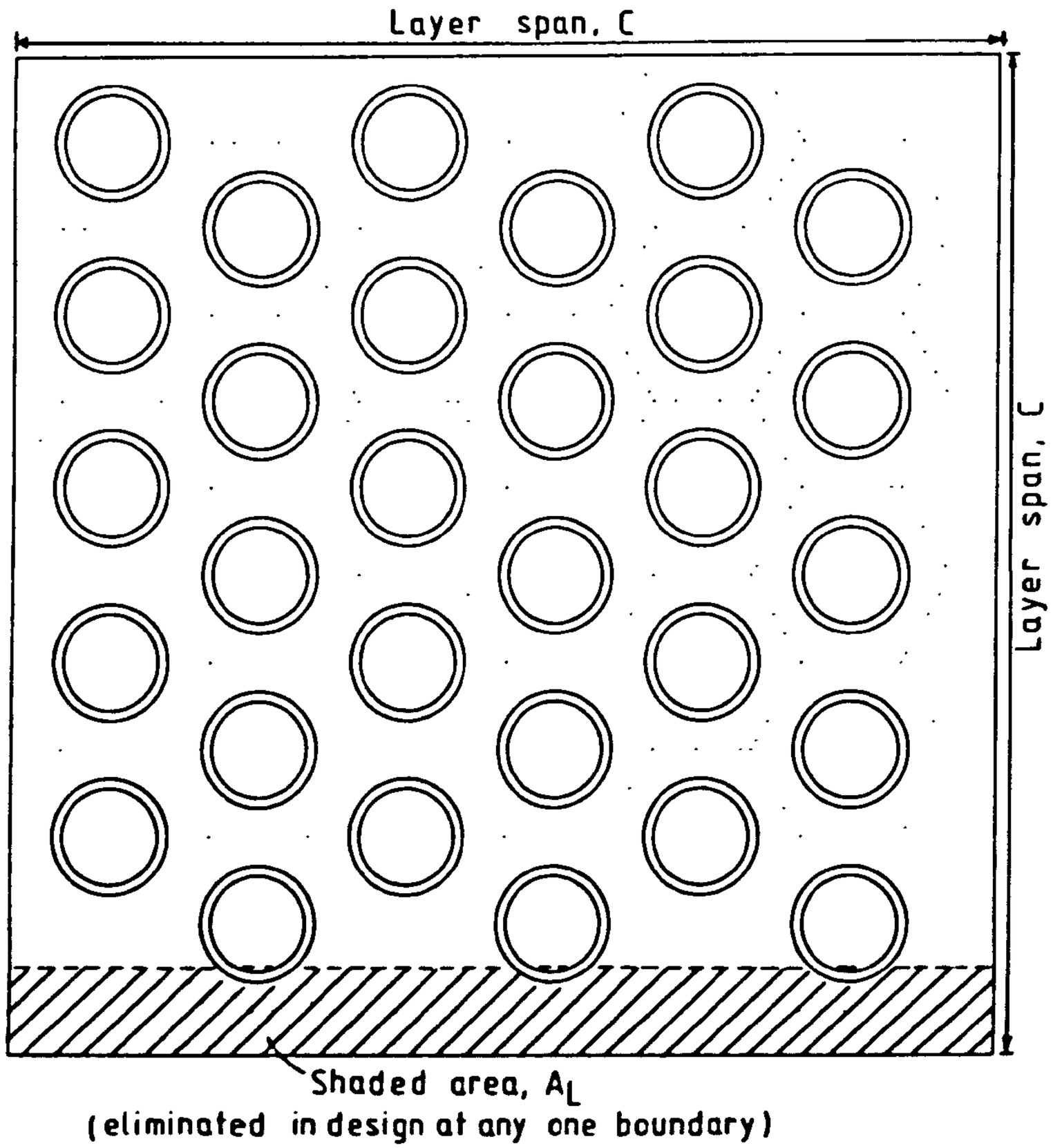


| Plan dimensions of layer | Plan area | Design area |
|---|---|---|
| 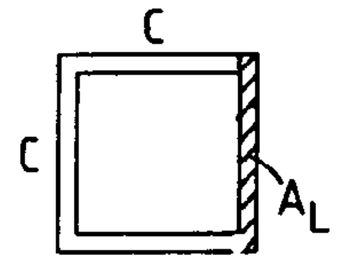  | $C^2$ | $C^2 - 4.A_L$ |
| 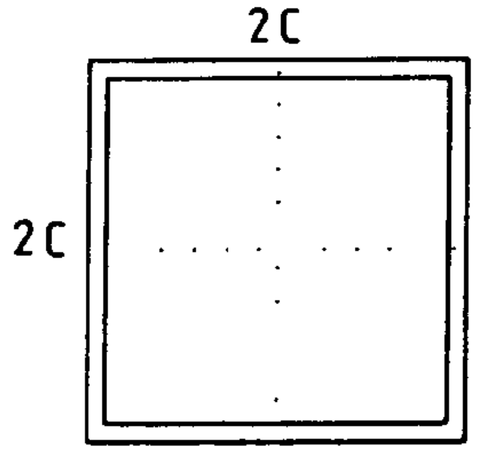  | $4C^2$ | $4C^2 - 8.A_L$ |
| 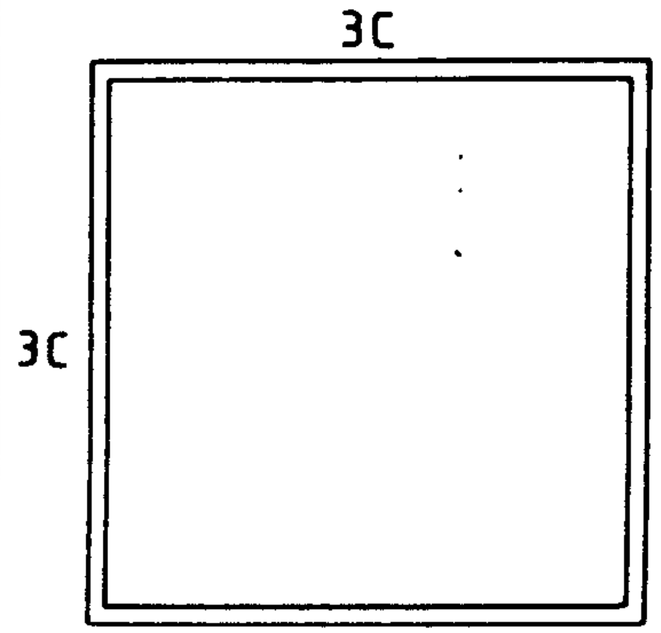  | $9C^2$ | $9C^2 - 12.A_L$ |
| nC X nC | $n^2C^2$ | $n^2C^2 - 4n.A_L$ |

INFLUENCE OF BOUNDARY CONDITIONS IN DESIGN FOR LAYERS OF VARYING SQUARE PLAN AREAS

**Figure 7.17**

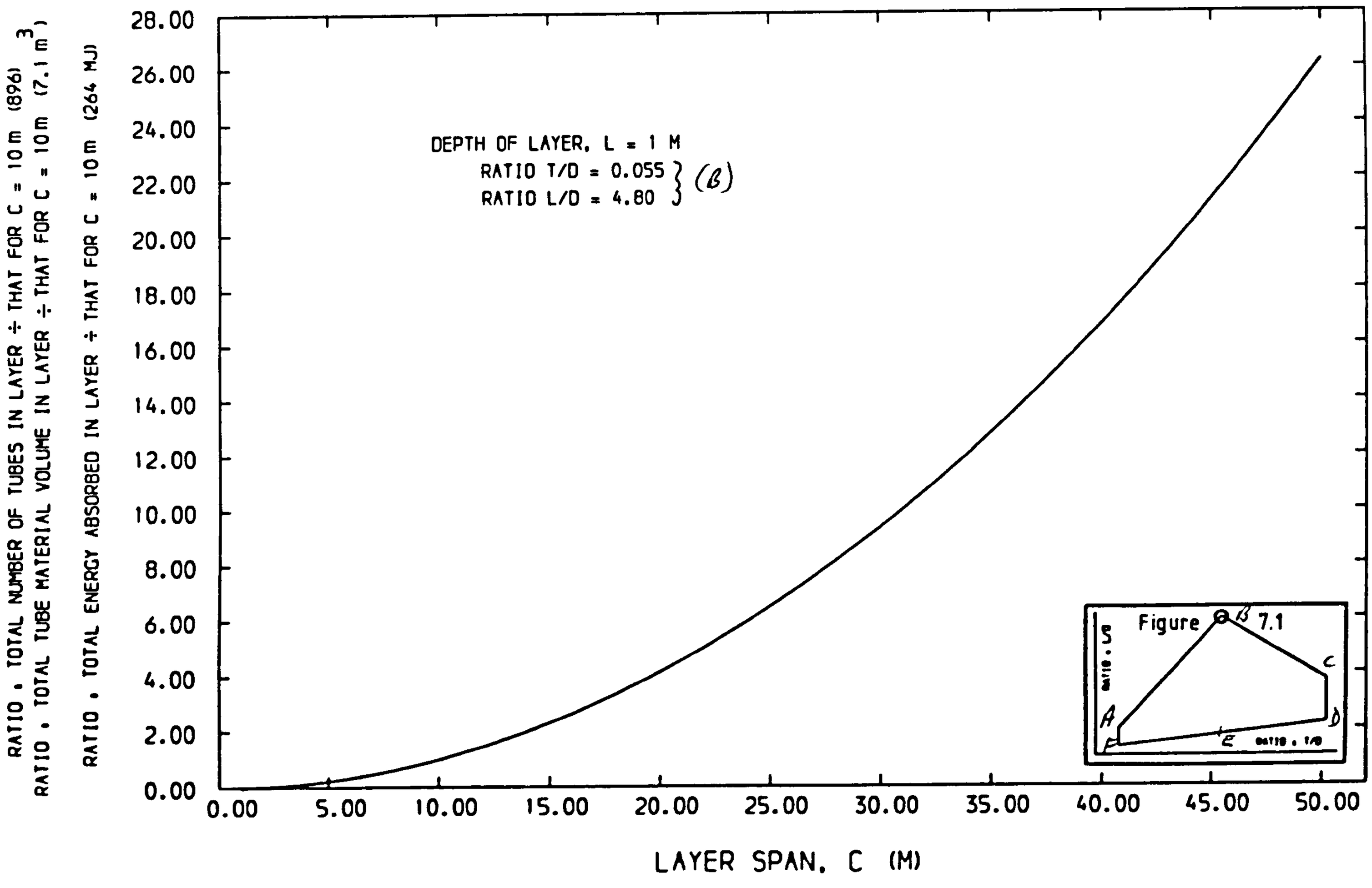


VARIATION OF TOTAL ENERGY ABSORPTION WITH LAYER SPAN

Figure 7.18

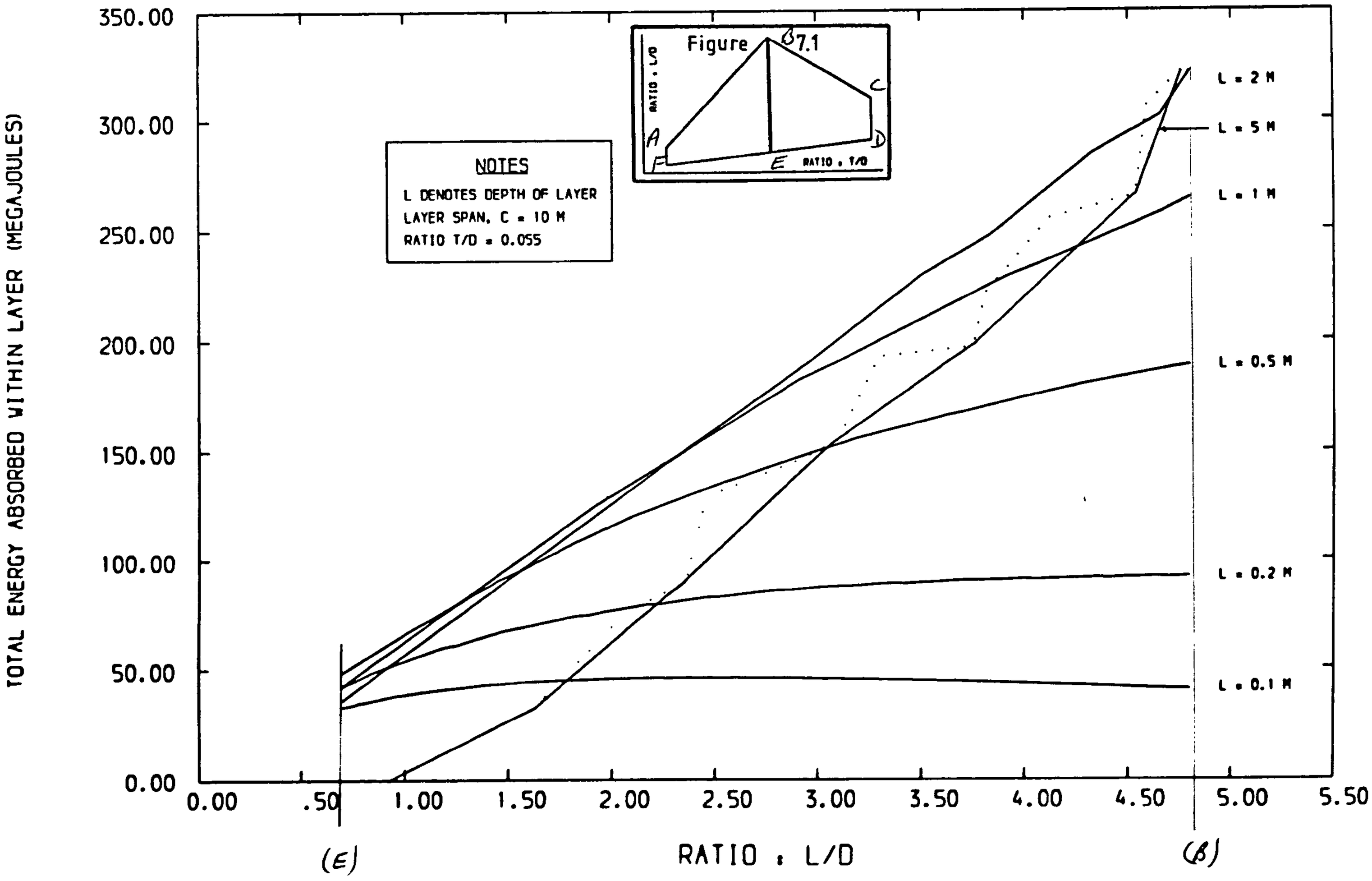


DESIGN LOWER BOUND ENERGY RELATIONS FOR DIFFERENT LAYER DEPTHS

**Figure 7.19**

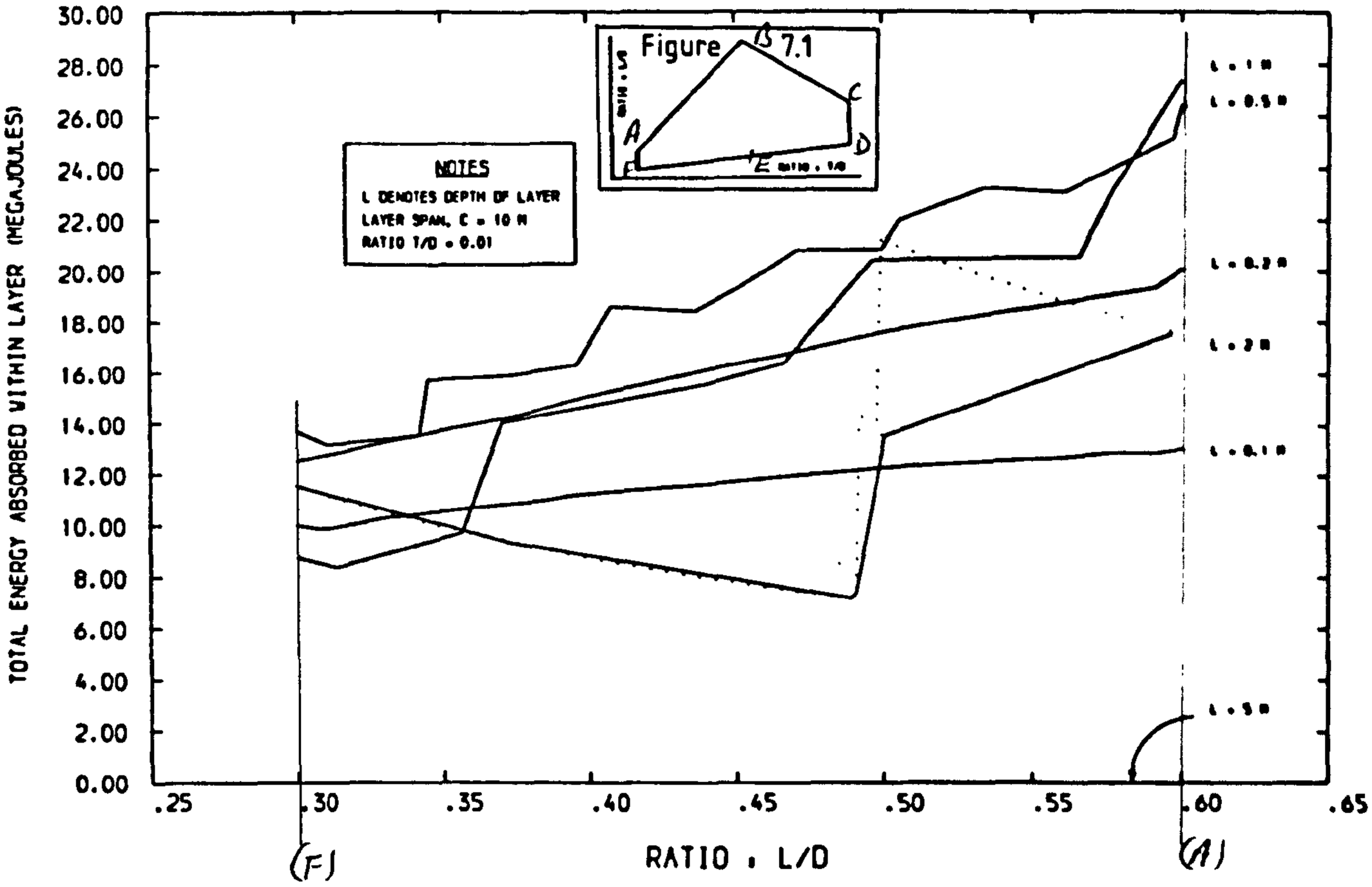


DESIGN LOWER BOUND ENERGY RELATIONS FOR DIFFERENT LAYER DEPTHS

Figure 7.20 (i)

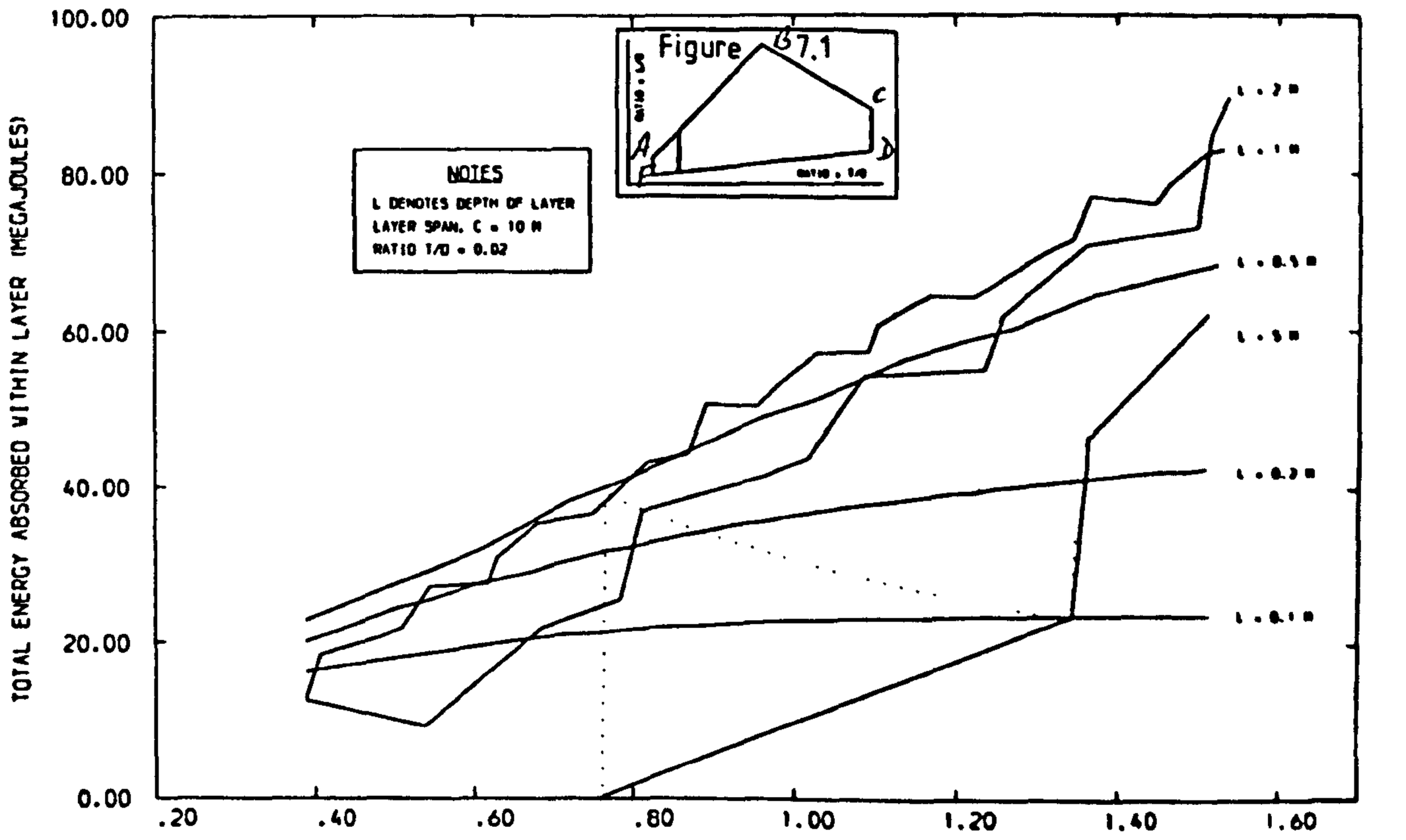


DESIGN LOWER BOUND ENERGY RELATIONS FOR DIFFERENT LAYER DEPTHS

Figure 7.20 (ii)

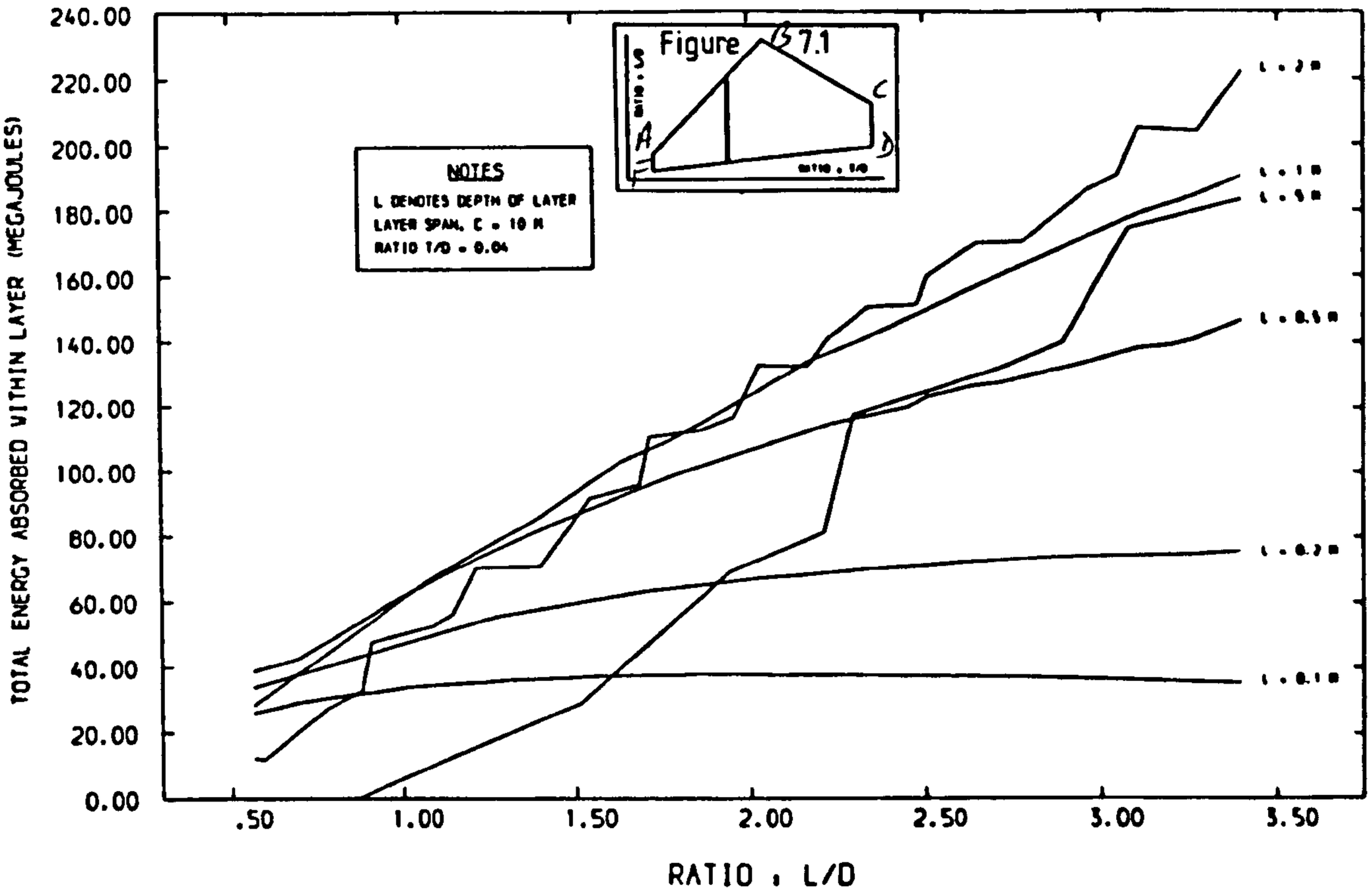


DESIGN LOWER BOUND ENERGY RELATIONS FOR DIFFERENT LAYER DEPTHS

Figure 7.20 (iii)

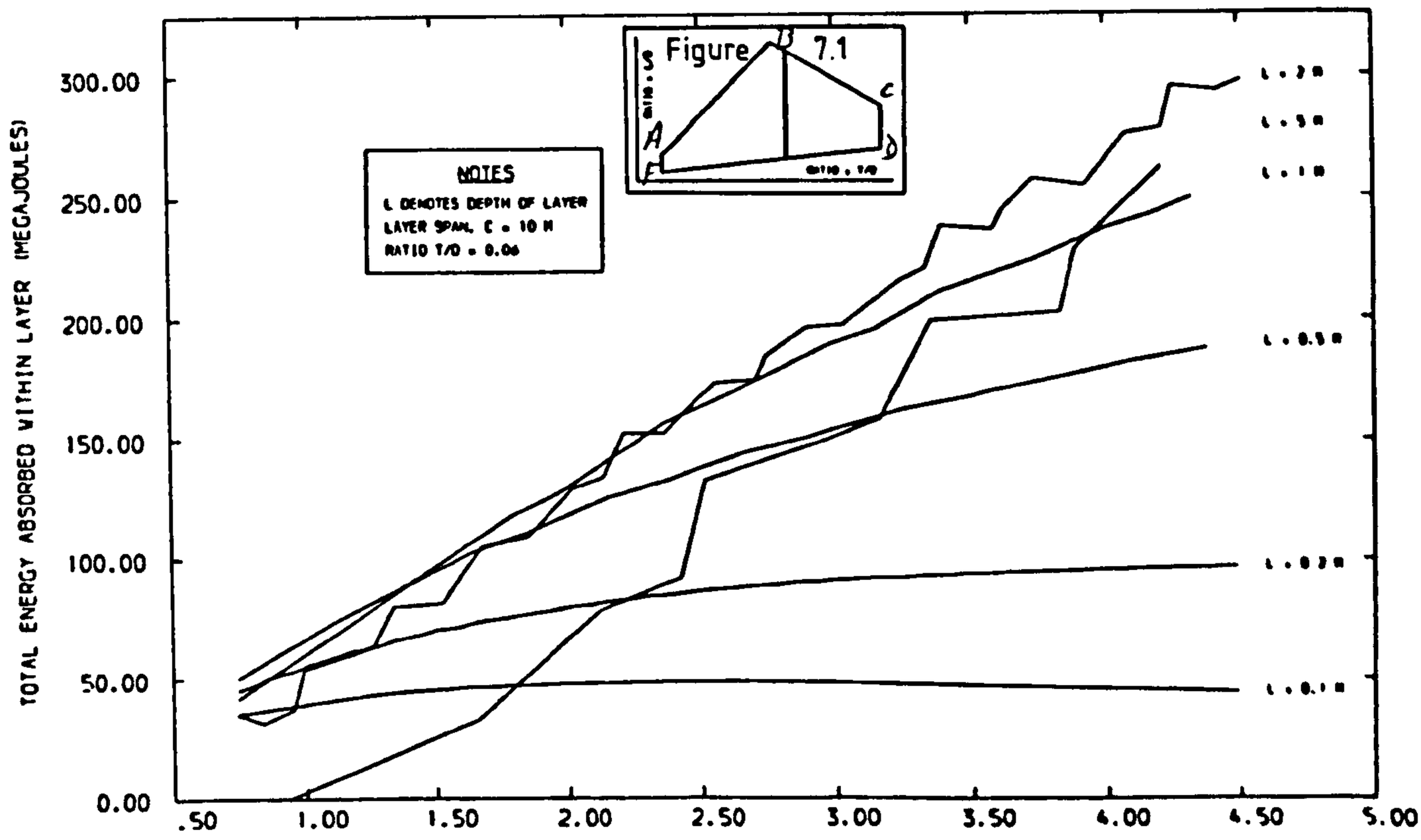


DESIGN LOWER BOUND ENERGY RELATIONS FOR DIFFERENT LAYER DEPTHS

Figure 7.20 (iv)

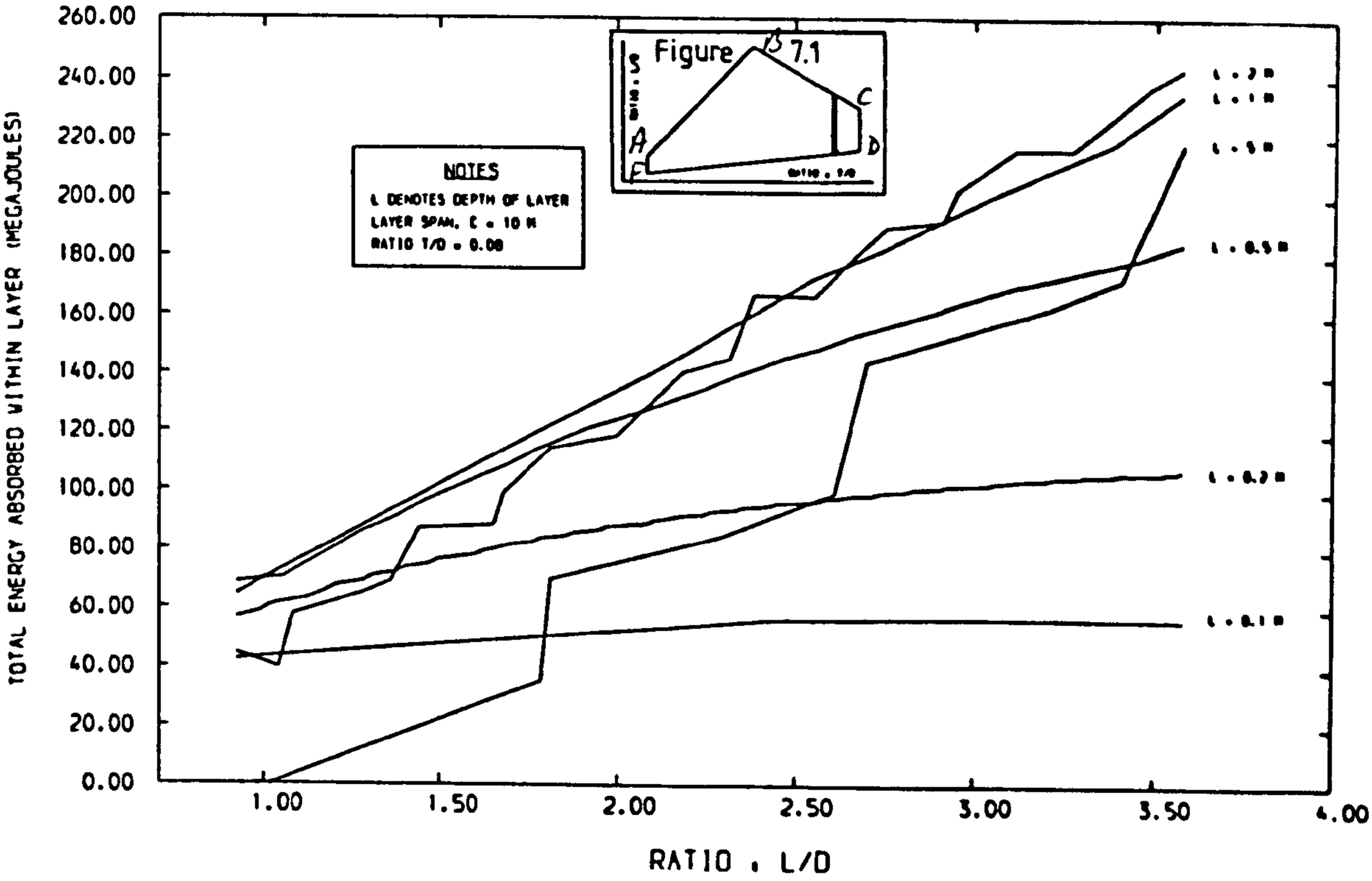


DESIGN LOWER BOUND ENERGY RELATIONS FOR DIFFERENT LAYER DEPTHS

Figure 7.20 (v)

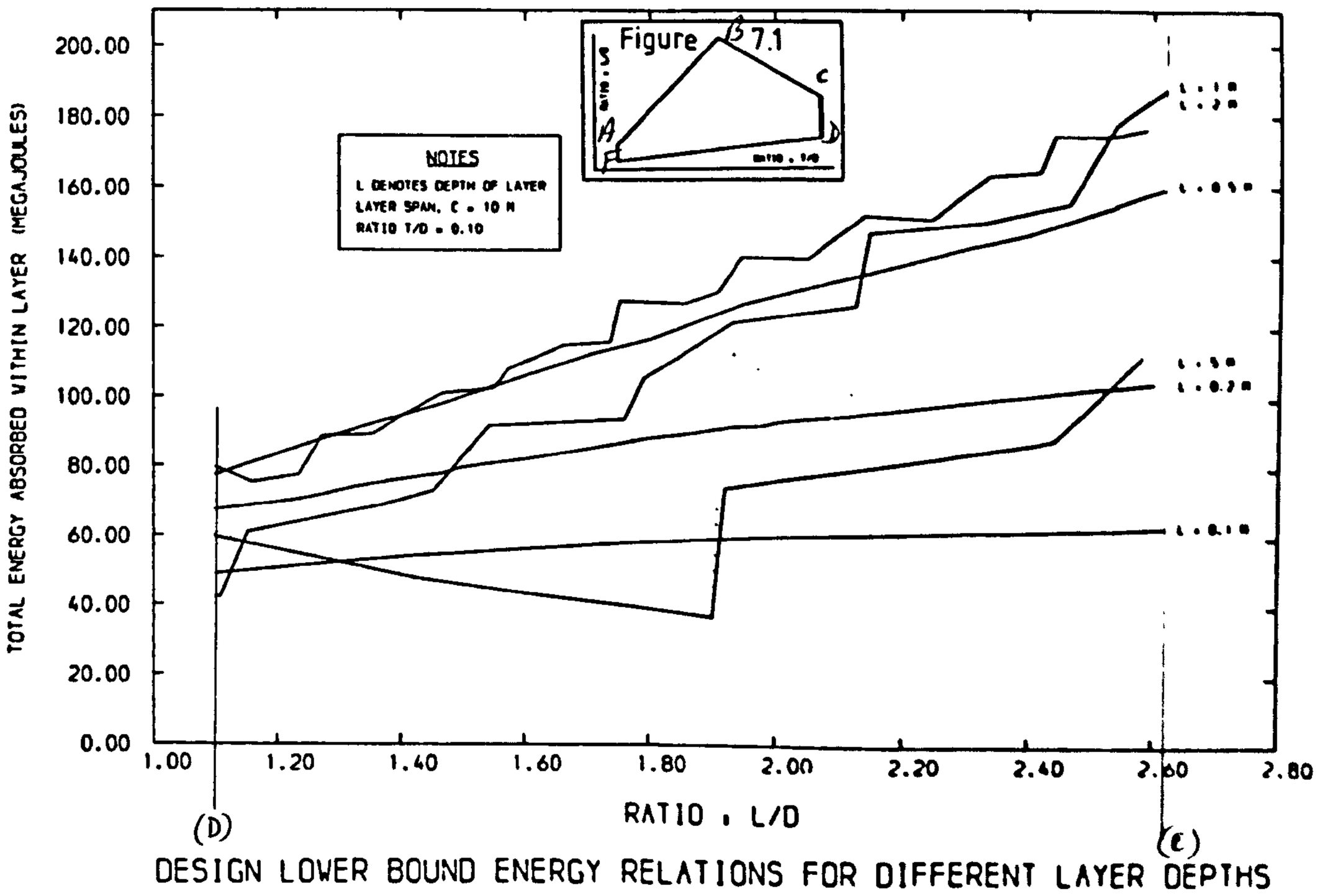


DESIGN LOWER BOUND ENERGY RELATIONS FOR DIFFERENT LAYER DEPTHS

Figure 7.20 (vi)

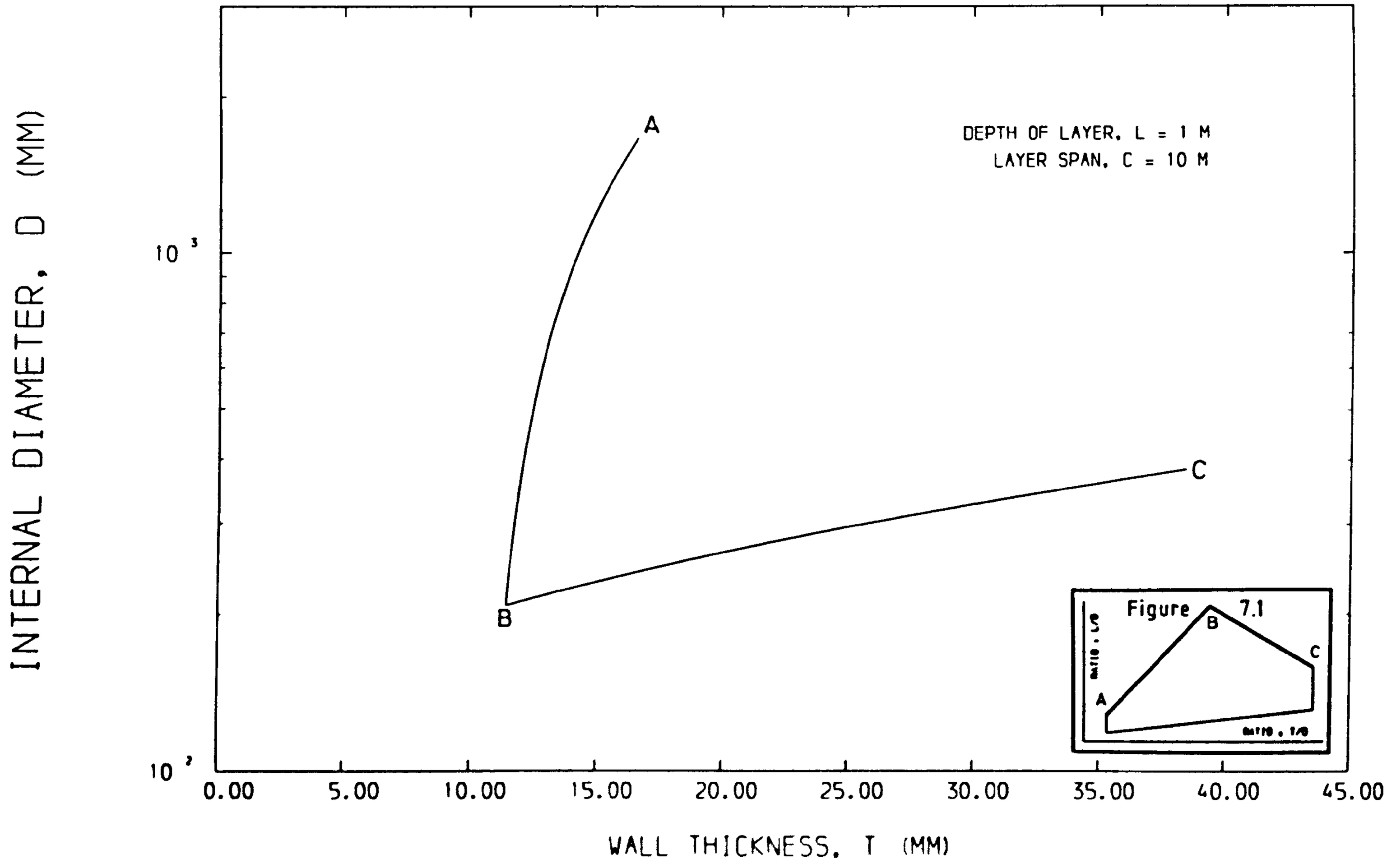


OPTIMUM DESIGN RANGES FOR TUBE SECTION DIMENSIONS

**Figure 7.21**

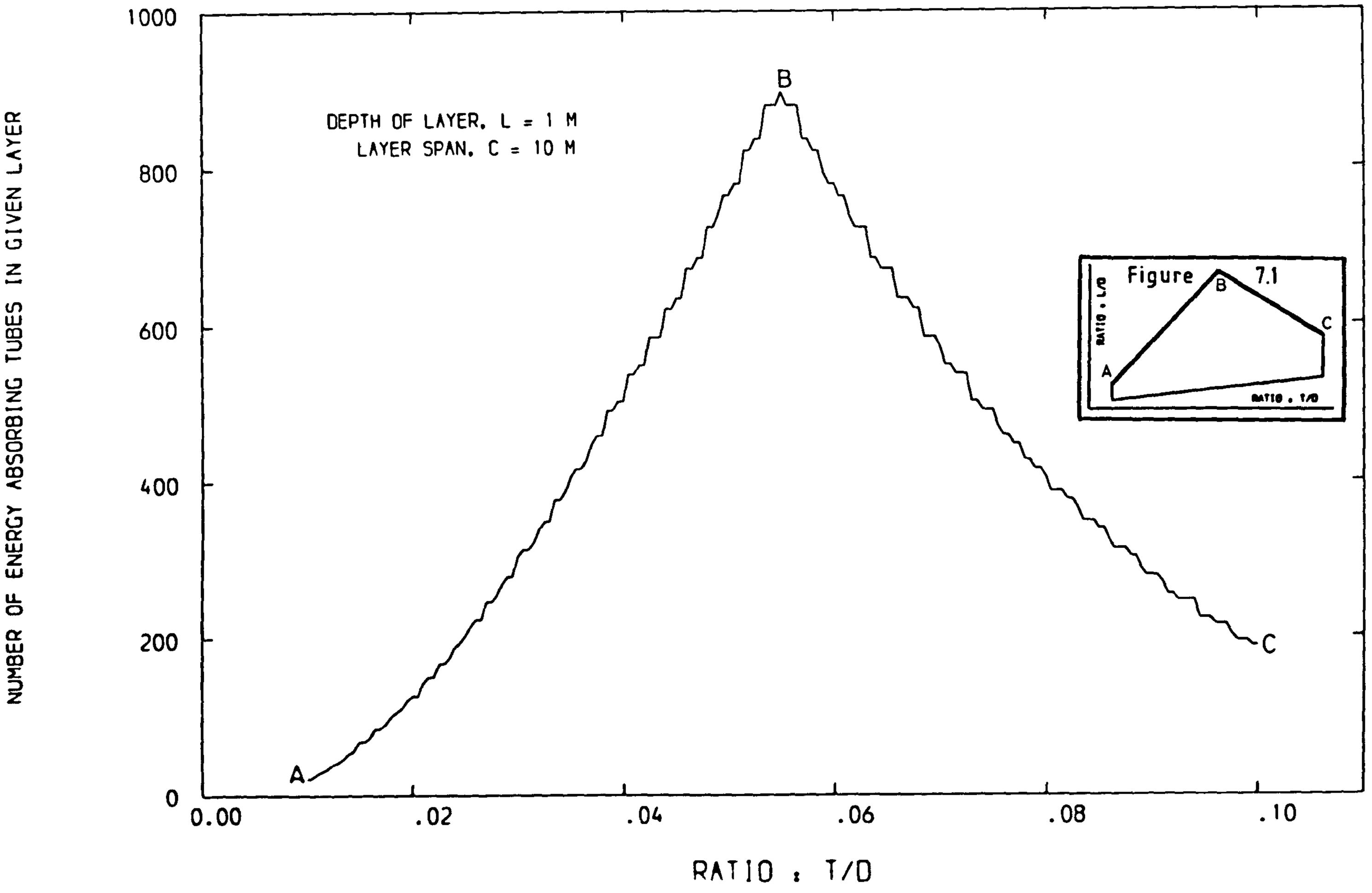


OPTIMUM DESIGN RANGES FOR NUMBER OF TUBES WITHIN GIVEN LAYER

**Figure 7.22**

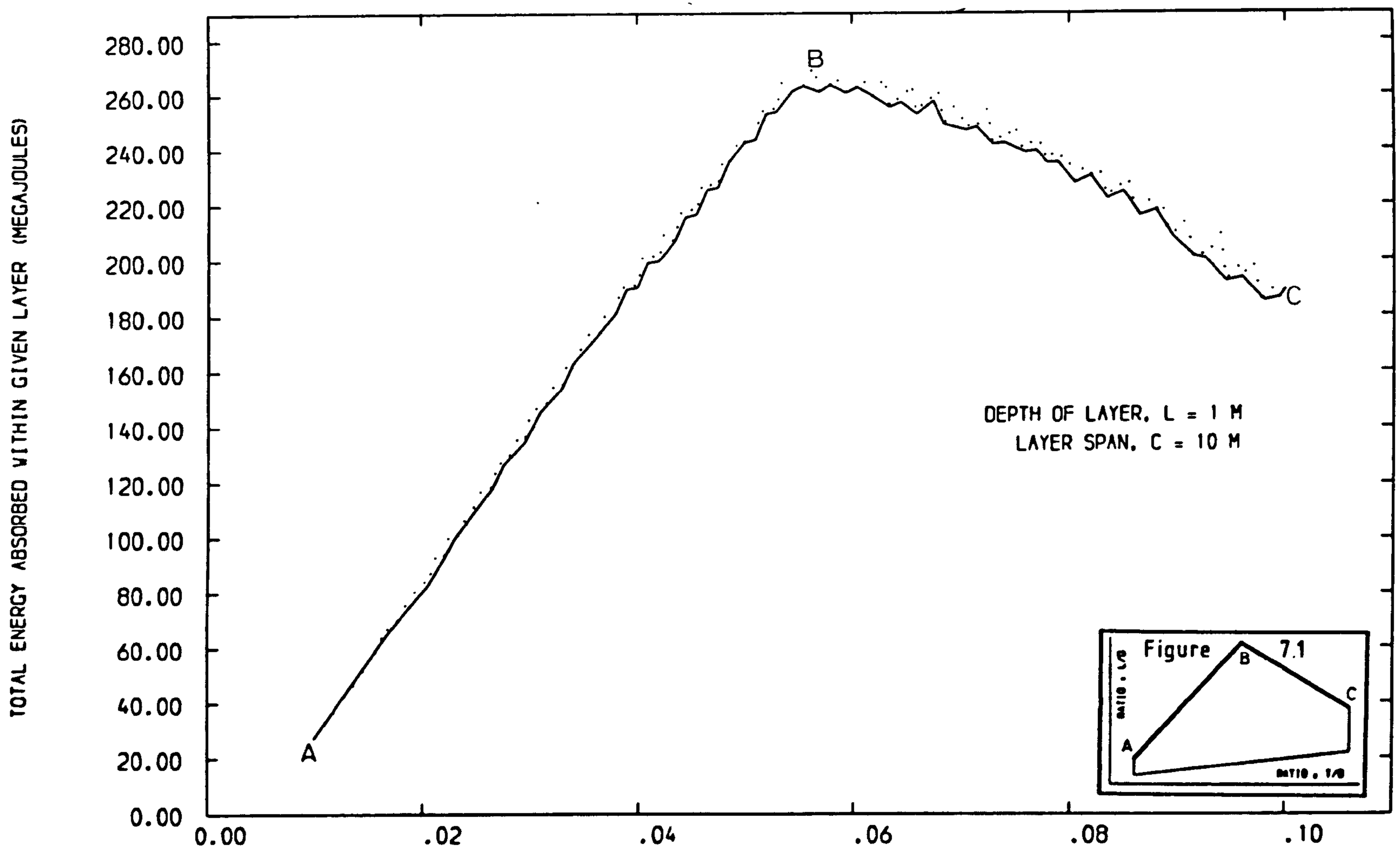


OPTIMUM DESIGN RANGES FOR TOTAL ENERGY ABSORBED WITHIN LAYER

**Figure 7.23**

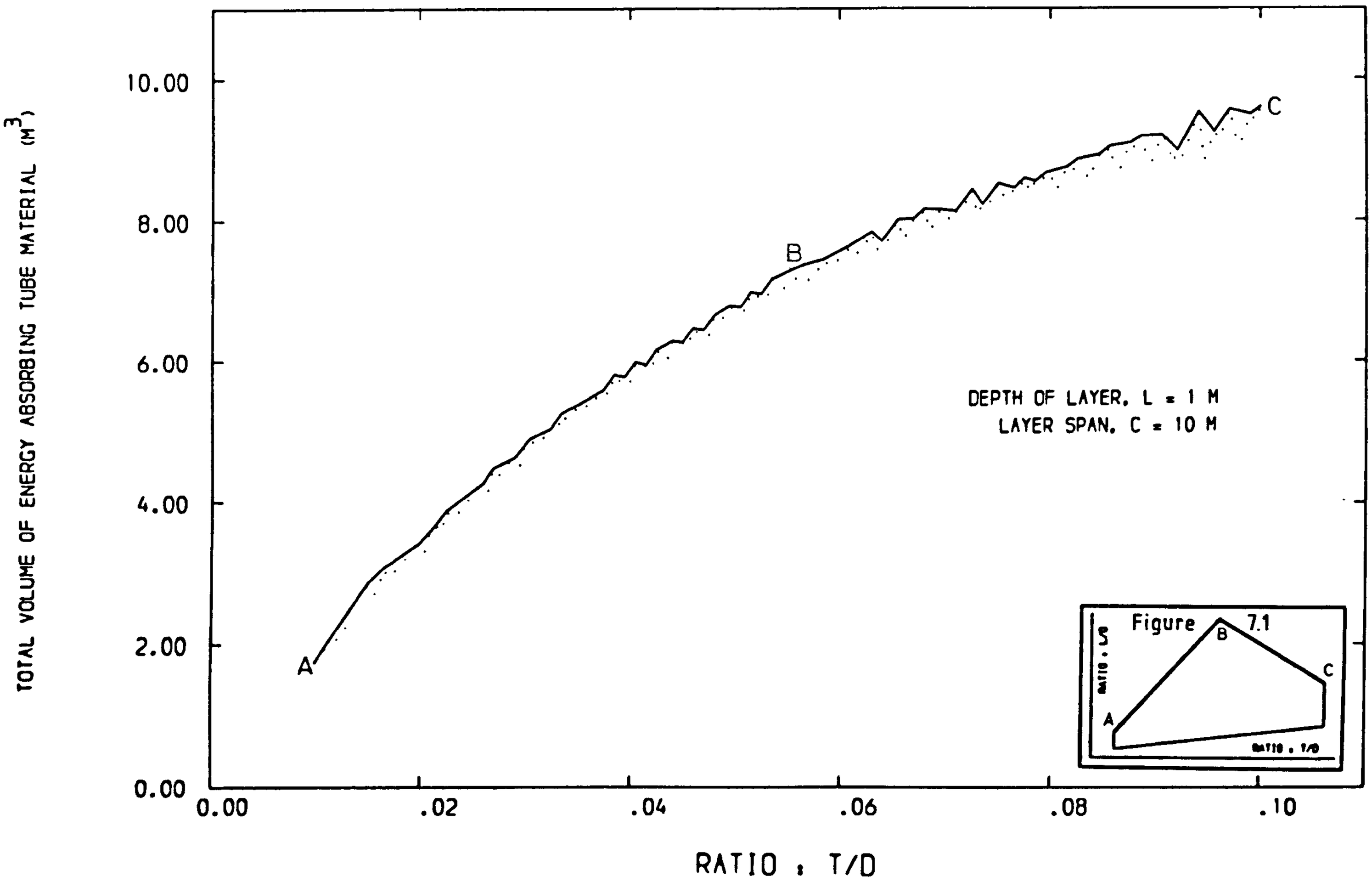


OPTIMUM DESIGN RANGES FOR TOTAL VOLUME OF TUBE MATERIAL IN LAYER

**Figure 7.24**

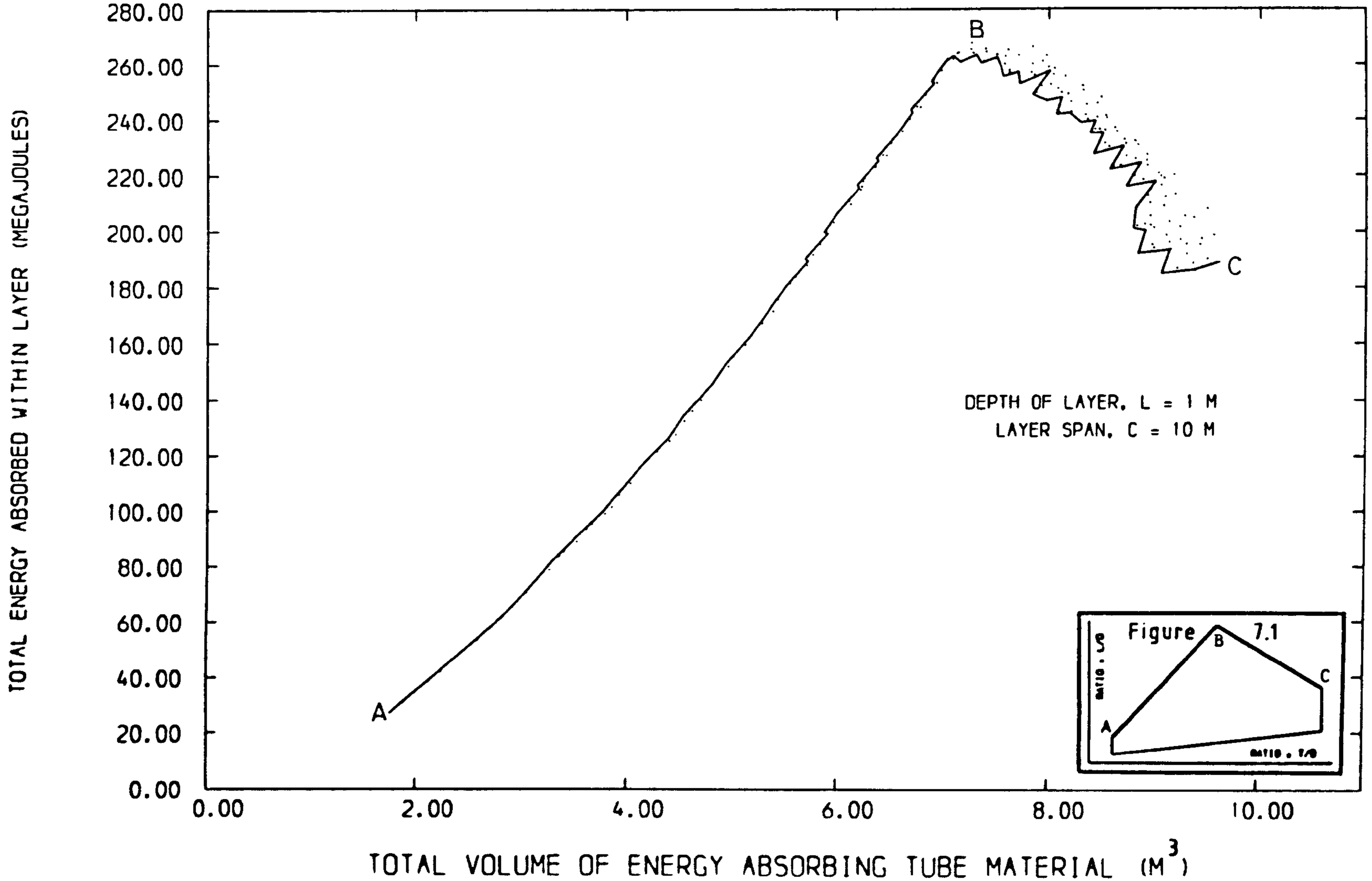


OPTIMUM ENERGY / VOLUME DESIGN RANGES FOR GIVEN LAYER

**Figure 7.25**

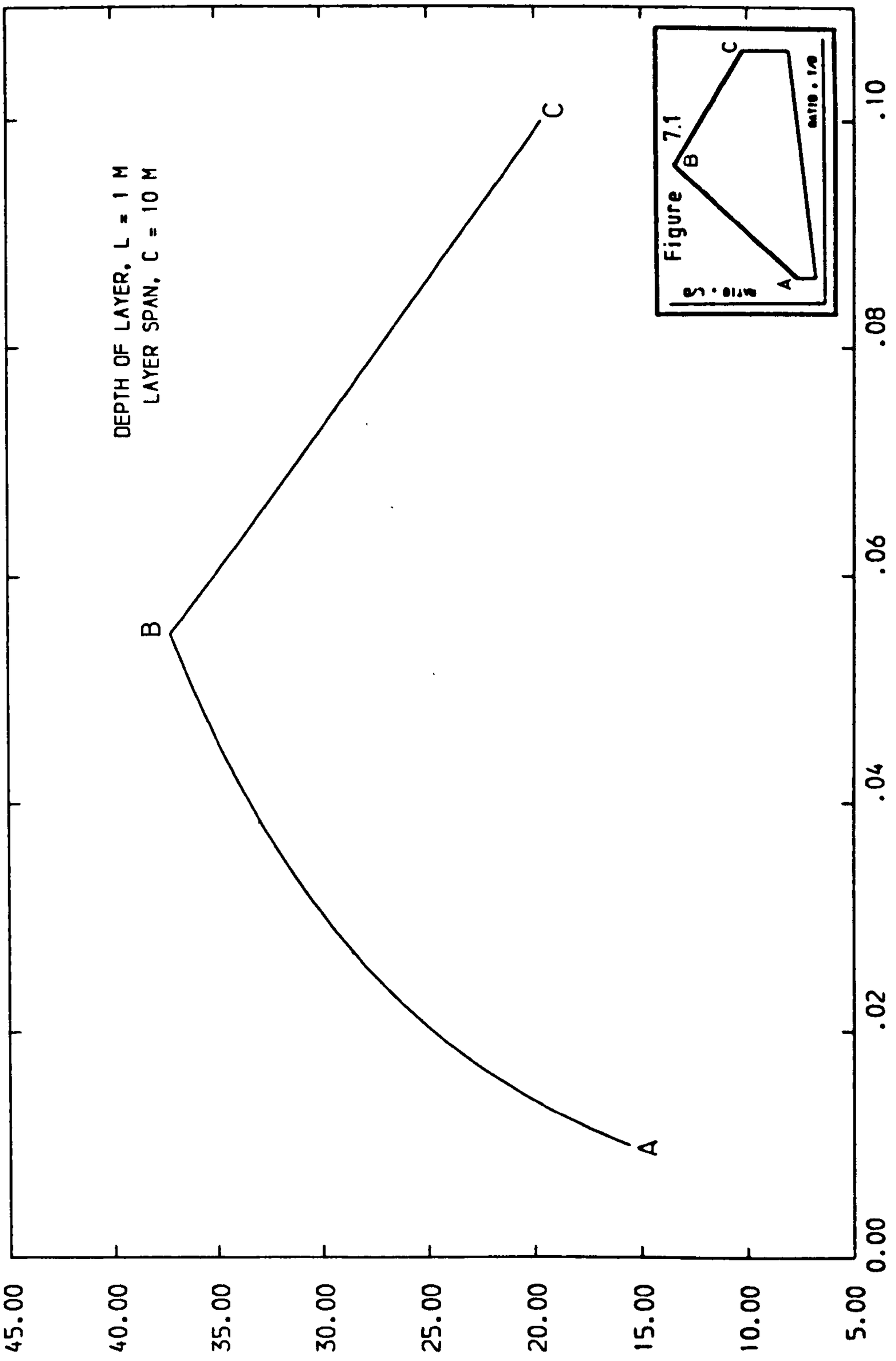
OPTIMUM RANGES FOR ABSORPTION EFFICIENCY OF INDIVIDUAL TUBES
DEPTH OF LAYER, L = 1 M
LAYER SPAN, C = 10 M
RATIO : T/D
EFFICIENCY : TUBE ENERGY / TUBE VOLUME (MJ/m3)
A
B
C
0.00
.02
.04
.06
.08
.10
45.00
40.00
35.00
30.00
25.00
20.00
15.00
10.00
5.00
Figure 7.1

Figure 7.26

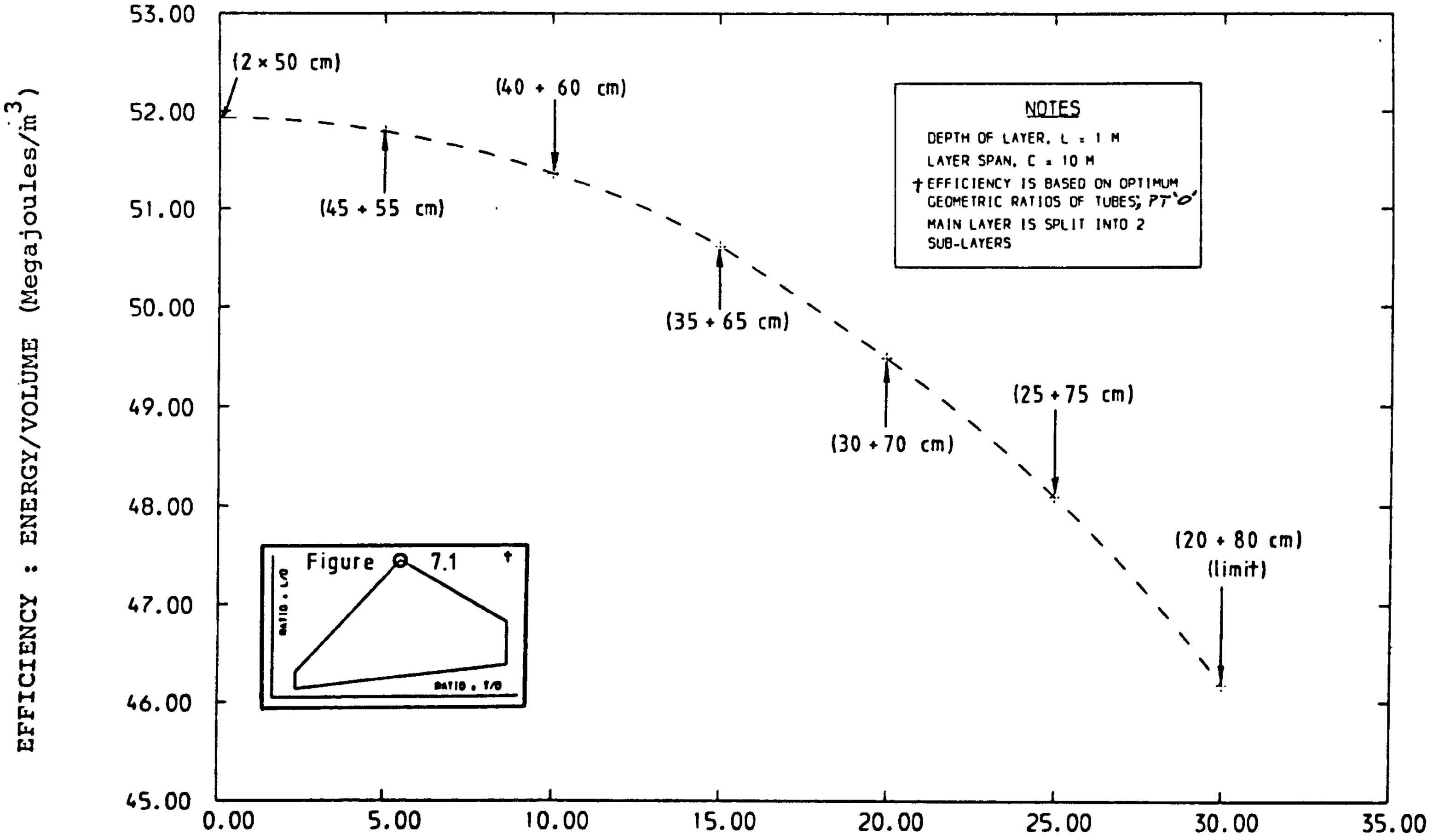


DESIGN EFFICIENCY / RELATIVE DIFFERENCES IN SUB-LAYER DEPTHS

**Figure 7.27**

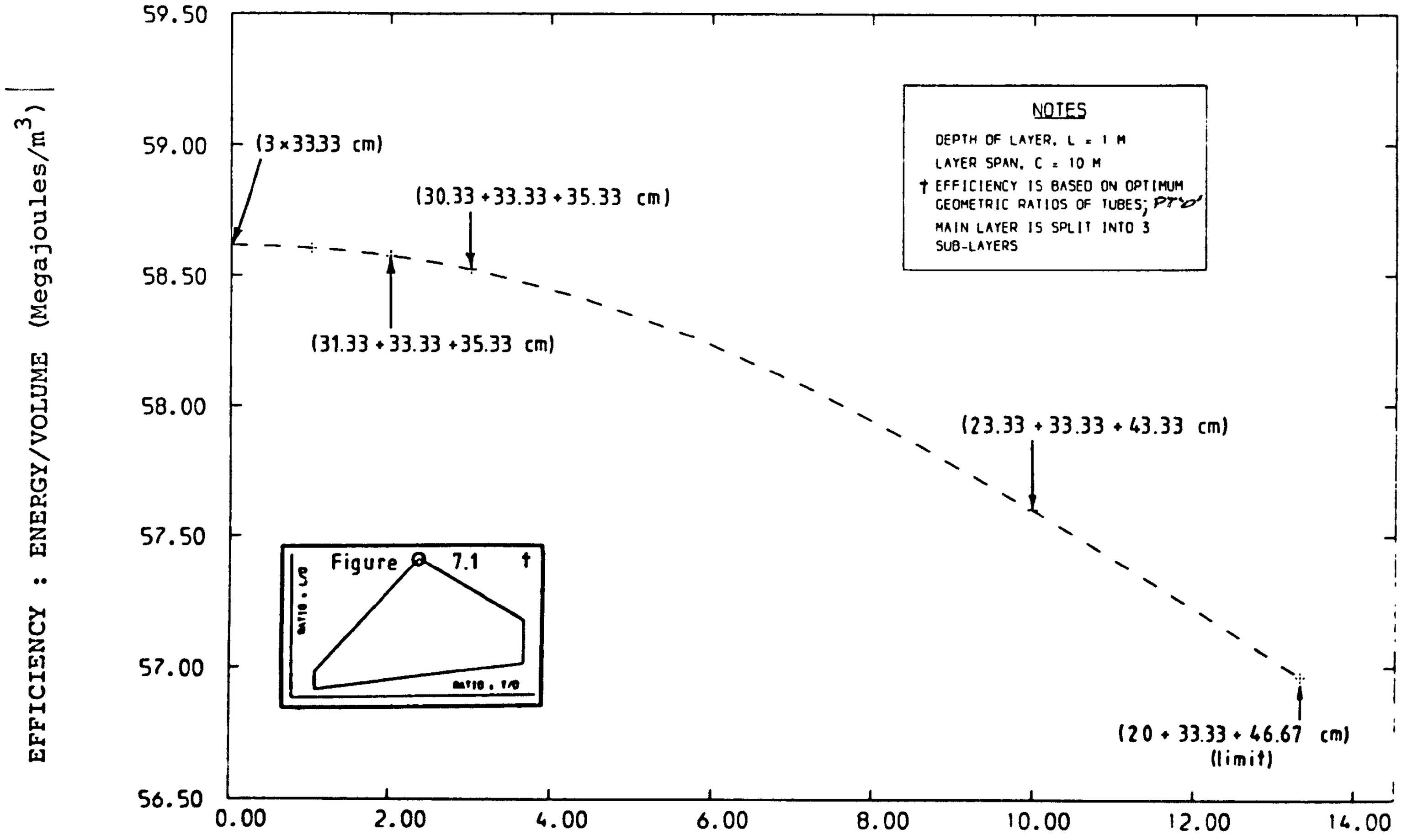


DESIGN EFFICIENCY / RELATIVE DIFFERENCES IN SUB-LAYER DEPTHS

**Figure 7.28**

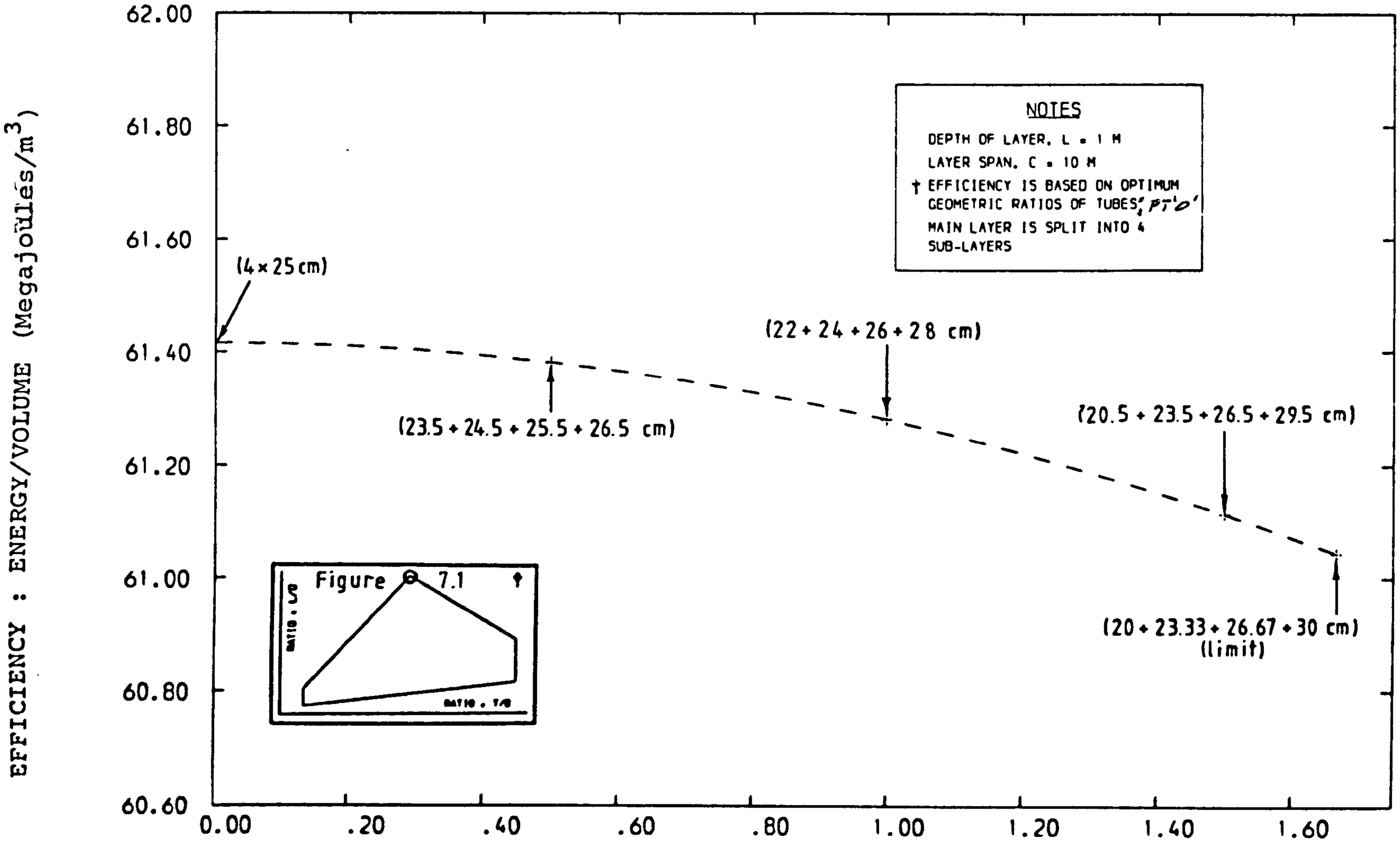


DESIGN EFFICIENCY / RELATIVE DIFFERENCES IN SUB-LAYER DEPTHS

**Figure 7.29**

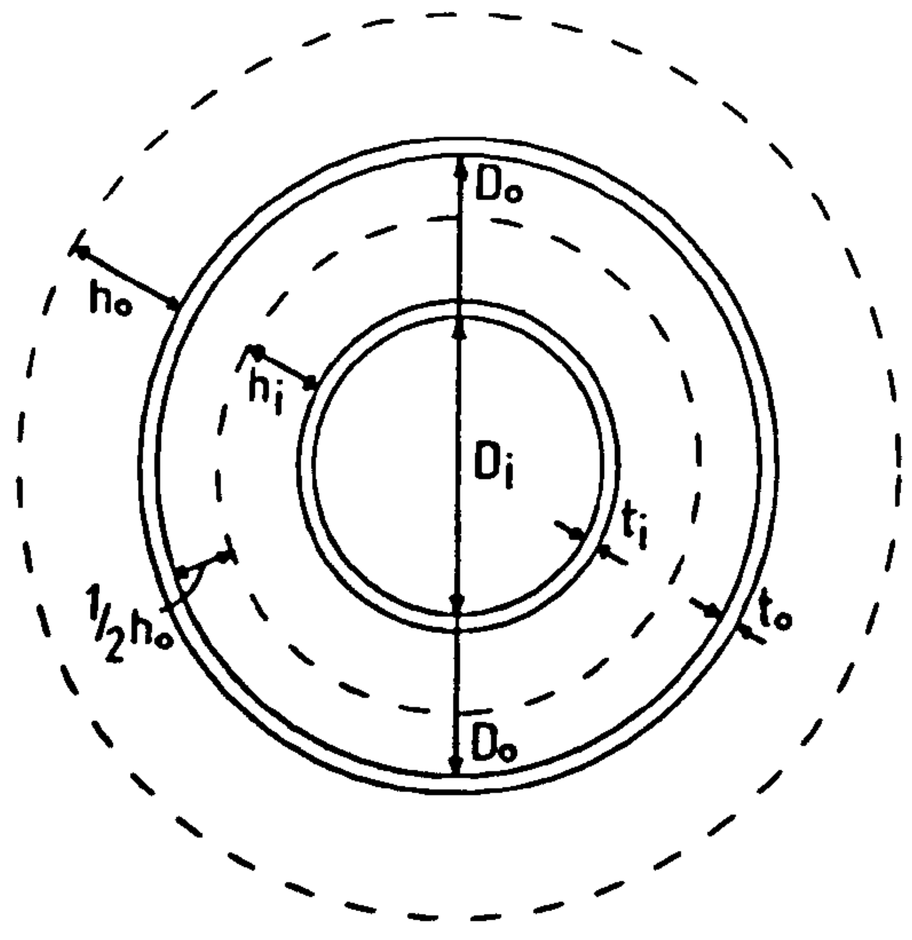


$$h_i = 1.2\sqrt{D_i\, t_i}$$

$$h_o = 1.2\sqrt{D_o t_o}$$

[i]

SPACING PRESCRIBED IN THE ARRANGEMENT OF CONCENTRIC TUBES

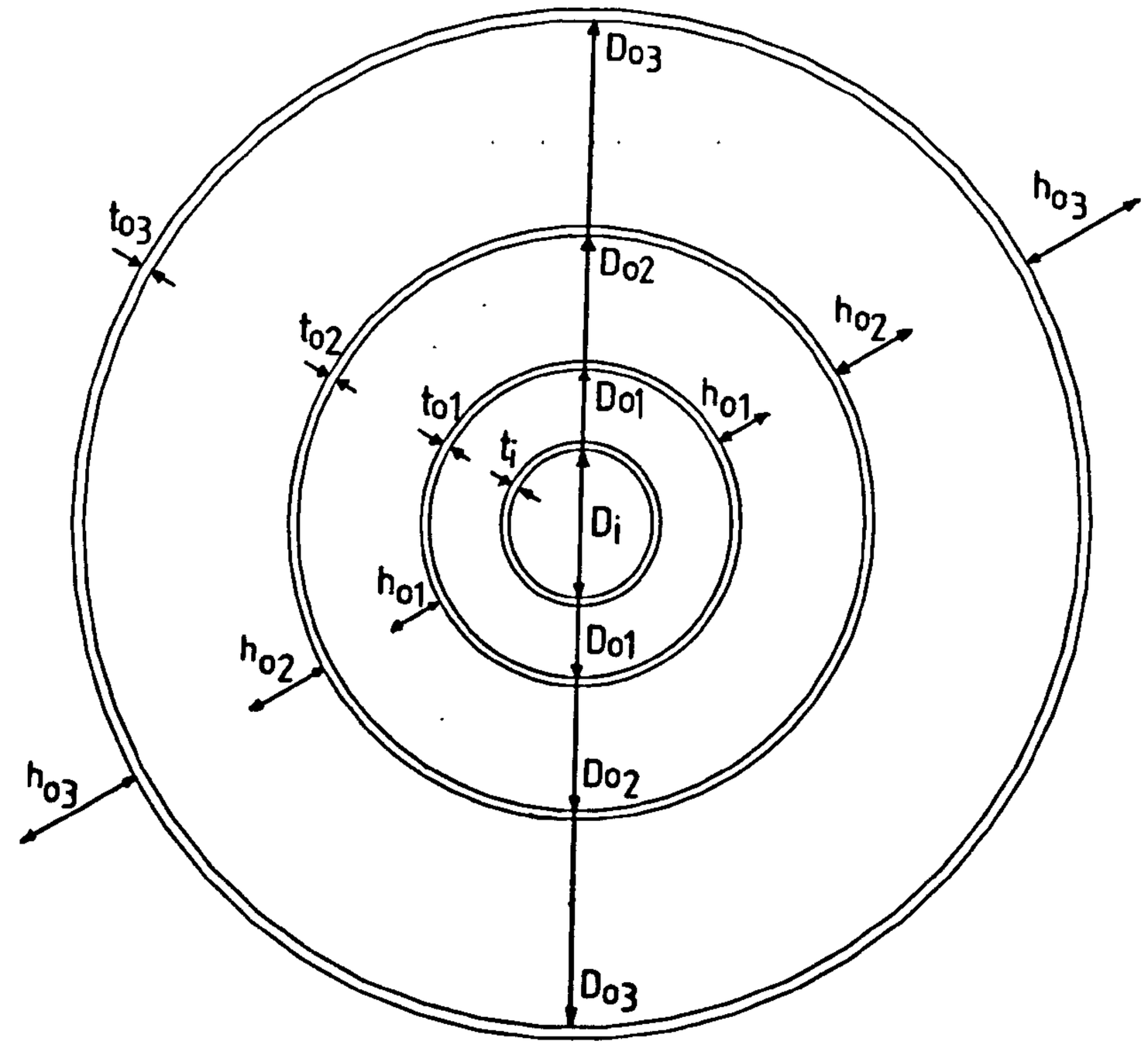


[ii]

CONCENTRIC TUBE SETS UP TO A MAXIMUM OF 4 TUBES IN A SET FOR OPTIMUM DESIGN

**Figure 7.30**

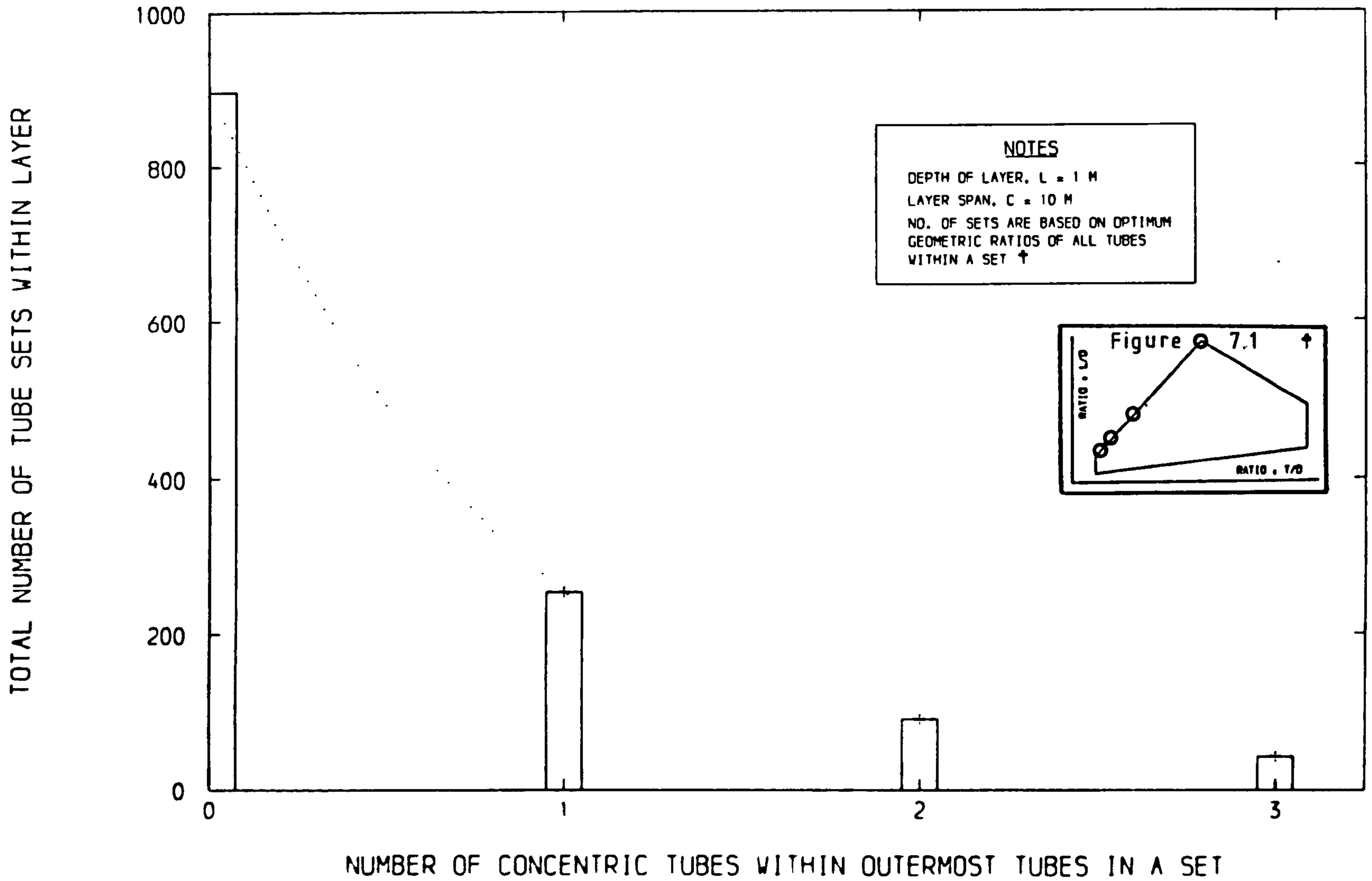
TOTAL NUMBER OF TUBE SETS WITHIN LAYER
1000
800
600
400
200
0
0
1
2
3
NUMBER OF CONCENTRIC TUBES WITHIN OUTERMOST TUBES IN A SET
NOTES
DEPTH OF LAYER, L = 1 M
LAYER SPAN, C = 10 M
NO. OF SETS ARE BASED ON OPTIMUM GEOMETRIC RATIOS OF ALL TUBES WITHIN A SET †
Figure 7.1 †
RATIO, L/D
RATIO, T/D
PACKING ARRANGEMENT OF CONCENTRIC TUBES IN GIVEN LAYER

**Figure 7.31**

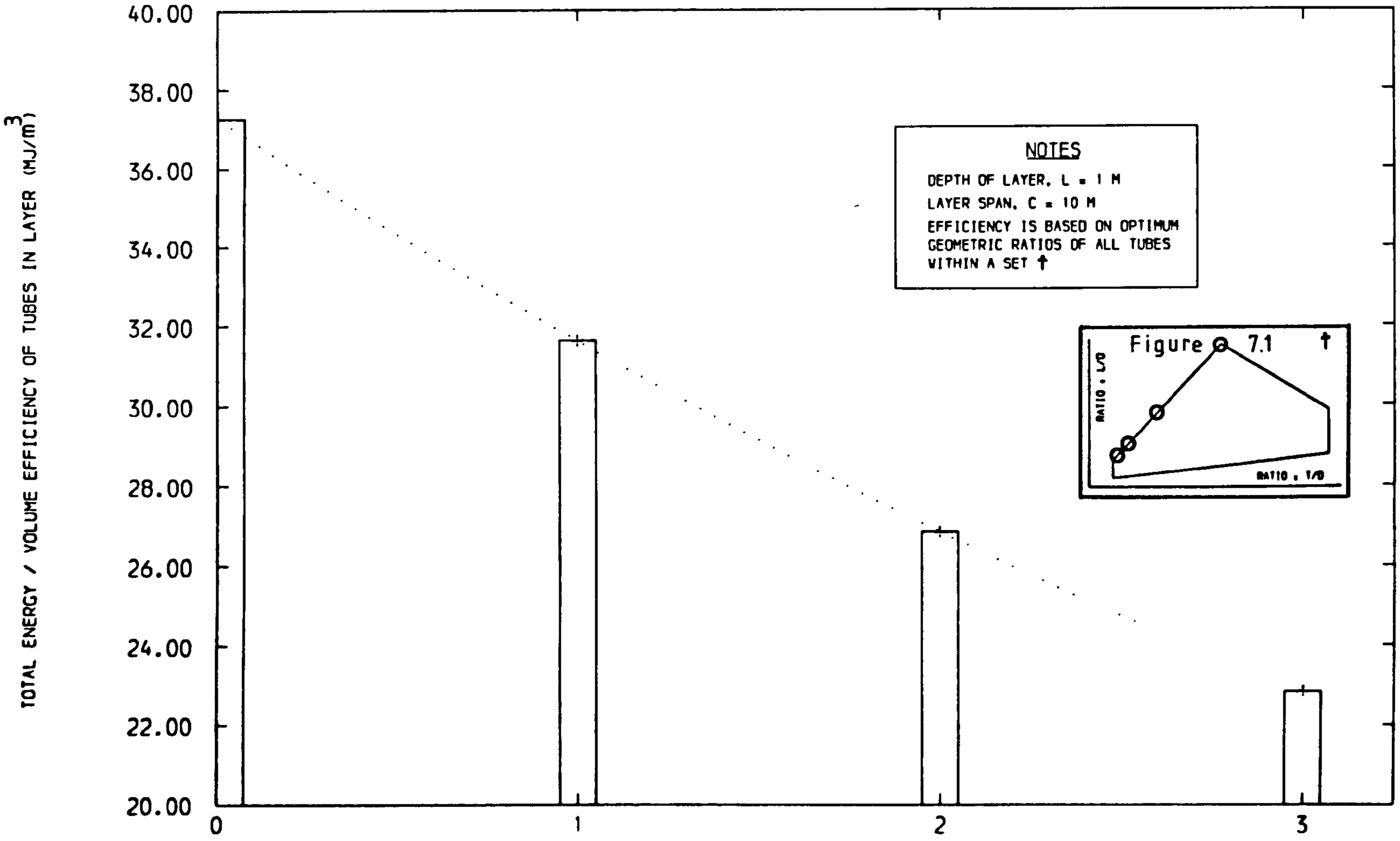


EFFECT OF PACKING ARRANGEMENT OF TUBES ON DESIGN TOTAL EFFICIENCY

**Figure 7.32**

# CHAPTER 8

# CONCLUSIONS, PRACTICAL IMPLICATIONS AND SUGGESTIONS FOR FURTHER RESEARCH

## 8.1 Conclusions

The conclusions made encompassing the results of the work presented in this thesis are classified under 4 categories, as follows : (i) the choice of an energy absorber, (ii) axial collapse of cylindrical tubes and energy dissipation, (iii) inspection of test results obtained against certain theoretical solutions, and (iv) static design of tubes as energy absorbers within an allocated space.

Based on the aluminium alloy material tested, these four categories are considered individually below.

### 8.1.1 The choice of an energy absorber

From the review presented in Chapter 1, of the several energy absorbing (E.A.) devices that are in common use, it can be concluded that no E.A. system exists which possesses the full combination of the following ideal characteristics :

(a) high stroke efficiency

(b) high specific energy absorption

(c) high energy dissipation density

(d) rectangular-type deceleration response, i.e. ideal load uniformity with continuing deformation

(e) adjustable operating pressure for different impact velocities

(f) reliability in terms of predicted behaviour

(g) identical dynamic & quasi-static mechanism of deformation

(h) effective under omnidirectional loading

(i) little or no loss of efficiency if used in repeated applications

(j) low cost, simple configuration and ease of operation

Simultaneously, however, it is recognized to be most improbable that all the above characteristics would be required of a device as justification of its suitability as an energy absorber.

Whilst in general considerations it would be futile to discard any one of the above characteristics as insignificant, the best choice that can be made in selection or design of an E.A. system depends on the specific case considered. In the application to a nuclear reactor containment studied here, the cylindrical tube of a suitably ductile material was chosen, as the best E.A. device, for collapse under axial compression. As studied throughout the chapters, the adherence of this element to many of the above characteristics provides a cheap and efficient method of dissipating energy in their specific large-scale application.

### 8.1.2 Axial collapse of circular tubes and energy dissipation

1. The experimental chart of Figure 2.1 (Chapter 2) featuring the axial collapse mechanisms of tubes as zones on a plot of dimensionless tube ratios, L/D and t/D, provides a first attempt to correlate the mode of axial collapse to all three basic dimensions of a tube. This is of merit in the selection of an optimum collapse mode for circular tubes designed to dissipate maximum energy in an energy absorbing application.

2. Concertina (axisymmetric/ring-type) and diamond (multilobe) modes of collapse constitute the two useful mechanisms in

the context of energy absorption. They provide, as desirable characteristics, a sequential pattern of failure, controlled deformation and consequently a high degree of material participation at collapse.

3. Comparison of the energy dissipation levels associated with the concertina and diamond collapse modes has revealed the former mode as being higher, for a given tube. This is based both on the grounds of 'specific energy absorption' (see Chapter 3) and the 'fold energy indices' introduced by the author (see Chapter 4).

4. Since 'specific energy absorption' is used commonly as a criterion to rank different materials and tube geometries for energy absorption, its use, for a given tube, has been furthered here in the ranking of different modes of collapse (concertina and diamond) in this function.

5. The introduction of fold energy-geometry relationships in Chapter 4 for concertina or diamond collapse, enabled direct empirical estimates to be made of energy absorption (in Joules) in relation to dimensions of a tube (in units of area/volume). This is in contrast to specific energy absorption (see Chapter 3) which, measured in units of length, is a function of the dimensionless tube ratio, t/D' of tubes, for a given material.

6. The increase in energy absorption associated with the concertina mode is concluded to be largely a consequence of the work involved in plastic deformations during the development of hoop stresses, and bending at the fold hinges that accompany folding. This is in contrast to the diamond

mechanism which presents a non-axisymmetric collapse pattern and exhibits globally a less pronounced plastic behaviour.

### 8.1.3 Experimental applicability of the theories studied

For the annealed aluminium used in the experimental study, strain hardening was observed to be a prominent feature. Its occurrence was seen as a fairly linear trend on stress-strain curves beyond yielding of the material.

1. Theories proposed by Alexander (1) for concertina collapse and by Pugsley (78) for the diamond mechanism, are based on rigid-plastic material behaviour. For the test results obtained here, these theories were observed to underestimate the internal work done at collapse, as a consequence of omitting the strain hardening work quantity.

2. Folding in the concertina mode occurs part externally and part internally in relation to the original tube diameter. Thus the fully external folding model adopted in (1) with no change in the original thickness of the tube during collapse, was seen, in this respect, to give rise to an overestimation of the internal work done.

For the material tested here, a rigid-linearly-strain-hardening model was introduced into theory (1), together with simple assumptions regarding plastic hinges. Empirical solutions were obtained by (a) incorporating strain hardening, (b) imposing the condition of material incompressibility, and (c) permitting the concertina collapse shape (reflected in $\lambda$) to be a variable in the problem.

3. Incorporation of features (a) & (b) in theory (1) produced empirical solutions for yield stress, Y, which match fully against test values. Combination of (a) & (c) and minimum internal work resulted in an empirical collapse shape : $\lambda \simeq 0.8$. This compares with the experimental range of $\lambda$ : $0.66 < \lambda < 0.73$, indicating the absence of fully external folding ( $\lambda = 1$) assumed in theory (1).

4. Application of Johnson's theory (48) to test results here produced a bound on geometric ratio t/D (=0.0026) for collapse in the concertina mode. By superimposing this value on the collapse zone chart of Figure 2.1, it was concluded that this bound could be a possible transitional point from concertina failure to one of purely diamond modes of collapse.

5. Timoshenko's classical theory (101), as studied in Chapter 6, is deduced to be applicable only to the class of thin shells that fail purely in elastic manner. If extended to apply also to thick shells, it produces critical stresses that diverge from experimental values. Factors ranging from 7 to 28 were encountered here as magnitudes of discrepancy. Theories subsequently proposed to improve the classical theory, notably by Donnell (19), von Karman (50) and Koiter (55), too, were illustrated and concluded not to represent experimental values, for thick-walled tubes.

However, extrapolation of test data for concertina collapse produced a geometric limit of t/D = 0.002 in (101)for elastic failure. This value compares favourably with that observed in '4' above, confirming the possibility of the existence

of a geometric transition from concertina to diamond collapse.

6. Regarding the theories stated in '5', the following further conclusions are made :

(i) Timoshenko's model presents a hypothetical case in which axisymmetric (concertina) collapse takes place under elastic conditions.

(ii) Tube imperfections, boundary conditions, and other factors which have been recognized in the past to be responsible for the reduction in the buckling loads of thin cylindrical shells from those given in (101), fail to account for the greater discrepancies observed here, for the class of thick tubes tested.

(iii) This divergence of test results from the theories studied is concluded to be due to yielding of material, following collapse in the concertina mode. These theories must incorporate suitable account of post-yield material changes prior to the point of incipient collapse, if they are to provide an accurate representation of the critical axial loads of thick-walled tubes.

### 8.1.4 Design of cylindrical tubes as energy absorbers

By selecting the concertina mechanism (following its verification as the optimum design mode), the corresponding zone on the collapse-geometry chart of Chapter 2 may be approximated to a polygon, as illustrated in Figure 7.1; this provides a simple design chart for determination of tube geometries on the boundaries of the zone. In calculation of optimum design quantities for tubes to collapse within a specified layer,

the following conclusions are made (the reader is referred to Chapter 7 for discussion of other assumptions and more specific conclusions).

1. A gain in energy absorption may be favourably achieved by selecting narrow tubes from the above polygon, and consequently to employ a large number of them to fill the layer; this is distinct from using a small number of large tubes. This applies equally to design efficiency, defined as the energy absorbed per unit tube material volume. Optimum geometry may be derived from peak of the polygon, denoting the narrowest permissible tubes.

2. Boundary conditions (elimination of non-whole tubes at the layer boundaries) are influential in design in promoting a reduction in the energy absorption capacity. This is particularly important if large diameter tubes (away from optimum peak of zone polygon) and consequently fewer of them are considered to fill the layer.

3. By dividing the crushing layer into 'rows' of sublayers, each containing tubes of optimum geometry (see '1' above), the design quantities in '1' may be increased, to an advantage, over those for the single main layer. This increase is a maximum for the maximum permissible number of identical sublayers.

However, in order to obtain a pronounced load-limiting function, i.e. a sequential and delayed action of global collapse by the sublayers as well as one of energy absorption, it is deduced that sublayers of unequal depth must be

chosen. On this account, it is recommended that maximum number of sublayers with maximum difference in depth (as governed by the minimum allowable depth) are selected, as the optimum arrangement in design; this signifies a minimal loss of efficiency.

In the particular problem studied, for the above arrangement, an optimum total energy absorption capacity of 454 Megajoules was obtained; this may be compared with a figure of 264 Megajoules for the single undivided layer.

4. The use of concentric tube assemblies results in an overall reduction in total energy absorption and design efficiency, in relation to the case of identical tubes. This holds valid even if the geometry of all tubes in a concentric set are optimized to correspond to the top edge of the defined zone polygon (narrowest permissible tubes). The greater the number of concentric tubes in a set and consequently the smaller the quantity of sets required, the larger would be this reduction. This deduction has been verified to be independent of layer depth, so that, it applies equally to the case of sublayers, discussed in '3' .

## 8.2 Practical Implications

### 8.2.1 Summary †

For the nuclear reactor containment application studied here, the use of the collapse zone chart of Figure 2.1 in the design study of Chapter 7, together with the location of an optimum (concertina) mechanism of axial tubular collapse, have fulfilled

---

† See also Chapter 7, P.285

the practical aim of optimizing the static energy absorption capacity of the crushing layer. Hence it has been possible to determine the ideal combination of tube geometry, packing arrangement and the quantity of such tubes that would be used in this layer.

However, the dynamic nature of loading in this application is recognized to play an influential role in the design study of Chapter 7. As discussed next, it is predicted that this factor contributes favourably towards an increase in the energy absorption capacity of the layer. But as noted in Chapter 1, the circular tube has been known to possess the desirable feature of the same mechanism of axial collapse under both static and dynamic conditions; this implies little alteration to the geometric parameters in the design method presented. Thus, it is concluded that the design quantities obtained offer a lower bound solution to the total energy absorption capacity of the crushing layer, in the final analysis.

### 8.2.2 Dynamic Response

A literature review is presented of existing studies of the collapse behaviour of circular tubes under dynamic conditions. The general consensus is that tube deformations in an impact are invariably confined to that end of the tube which is impulsively loaded. This is despite the collapse mechanism of the tube remaining largely unaltered from that in the quasi-static state. As observed in the past, notably by Johnson (45), the circular tube amongst all cross-sectional shapes is unique as regards the latter property. The above

dynamic feature is attributed to the effect of longitudinal inertia to crumpling provided by the tube. This inertia is governed by the velocity of impact at a given point on the tube.

Coppa (13) has proposed that a stress wave is created upon impulse which travels away from the struck end of the tube causing progressive collapse for sufficiently high velocities of impact. However, if the velocity is too low to produce failure during the first passage of wave, then instability will occur after a sufficient number of reflections from the rigid end have suitably magnified the total stress to cause failure. In this case, which is reminiscent of static conditions, collapse may occur at either end of the tube depending at which end the stress has reached a critical value.

In discussion of the dynamic behaviour of thin-walled tubes failing in diamond modes, Pugsley (77) has found that at low speeds of impact, the mean resistance to crumpling remains comparable to the static value, but rises to as much as twice the latter figure at 50 ft/sec. . Furthermore, at high speeds the progressive diamond shapes for a tube were found to be smaller than their static equivalent. As confirmed and reasoned by Lindberg and Herbert (59) in discussion of axial wavelengths associated with a collapsing tube, this is because higher modes (shorter wavelengths) respond faster than lower ones in the dynamic condition and thus dominate motion. Considering the respective aspect ratios of tubes (ratios of circumferential to axial wavelengths at collapse), they obtained

values averaging about 3 compared to 1 in static buckling. As suggested by Coppa (13), the rise in the value of this ratio is due to a decrease in the axial length of a diamond fold, rather than necessarily an increase in the number of circumferential lobes. Hence the mechanism of collapse remains essentially unaffected.

For the axisymmetric mode of collapse, Postlethwaite and Mills (76) have obtained half-waves for a concertina fold under dynamic conditions that are in close correlation with their static equivalent. Based on their results for mild steel, these values fall between the Alexander and Timoshenko static wavelengths(as considered in Chapters 5 and 6), and were concluded to imply little or no change in the final collapse configuration mechanism from the quasi-static geometry. Furthermore, they found that the mean collapse stress for a tube is in close agreement with Alexander's expression and the experimental static value and certainly smaller than Pugsley's prediction in the dynamic condition , discussed above.

The correlation discussed is not expected to hold fully for the aluminium alloy material tested in the present study. In their work on the dynamic lateral compression of circular tubes, Reid and Yella Reddy (85) have deduced that for this alloy, strain hardening, which is a prominent feature, increases with strain rate. The latter have also observed a rise in the initial collapse load with an increase in the speed of lateral impact. It is thus predicted that these effects would

give rise to a higher axial mean collapse stress, hence an increase in the energy absorption capacity of a tube of this alloy over the equivalent static quantities.

Postlethwaite and Mills (76) have also investigated the effects of axial non-uniformities, such as cut-outs, on the longitudinal inertia of circular tubes upon axial impact, for their use in automotive applications. Whereas static crashes always produced failure in the region of the discontinuity, they found that in the dynamic case, failure always occurred at the impacted end as in a normal tube, save where the cut-out portion exceeded about 50% of the tube perimeter.

The rise in the initial collapse load of a tube in the dynamic condition has also been verified by Roth and Klosner (89). Considering thin shells with particular emphasis on the influence of imperfections, they have observed that the effect of applying a load for a short time gives rise to a significant increase in the buckling stress of the shell as the time duration of loading is reduced. In the case of a perfect shell with zero imperfections they indicated that this stress could be made to coincide with that obtained from the static elastic theory.

In the allied problem of the buckling of a circular tube under an impulsive radial pressure, similar resistances to loads in addition to those in the static case have been observed. Yao (105) has shown that this effect is more pronounced for a thin tube than for a thick cylinder and

that it increases also with the frequency of loading. Wood and Koval (106) have obtained buckling stresses ranging from 90% to 350% of static collapse stresses. On a geometric point, Florence and Goodier (22) have discussed a theory in which buckling stems from perturbations of uniform initial velocities or displacements and it can predict wavelengths in close agreement with experiment. However, Lindberg (58) has specified that for impulsive loads sufficient to cause large plastic flow, the buckling form is unaltered from the quasi-static mode if the material has a pronounced yield point. It is claimed that the modes of deformation which are dominant are those that respond most quickly to the radial impulse and depend on its magnitude.

The review presented highlights the general characteristics of circular tubes associated with collapse under dynamic conditions. An account of the particular parameters that may have to be re-examined in a further dynamic study of tubes as regards their specific design application is presented in the final section of this chapter.

### 8.2.3 Temperature

Besides the impulsive nature of loading discussed, the other main practical feature concerning the specific use of tubes as energy absorbers is the temperature conditions within the nuclear power station. The operating temperature surrounding the crushing layer is given to be in the region of 500 °C.

A very limited literature exists on previous work analyzing

the combined effects of thermal and mechanical stresses in the study of the collapse behaviour of circular tubes. However, buckling of thin tubes due to a thermal stress alone has been studied in considerable detail. Some characteristics regarding their behaviour are discussed below and their influence on the above application is examined.

Ross et al (88) have illustrated the instability of thin circular shells which were clamped at the ends in a test rig and heated uniformly. The distance between the end sections of the shell was maintained constant so that this restriction to thermal expansion gave rise to axial compressive stresses leading to buckling. Instability occurred as a localized 'snap-through' accompanied by a distinct audible sound this resulting in collapse in the diamond configuration upon further heating. They observed that the buckling stress is the same whether it is caused by the displacement of a moving platen or restriction to thermal expansion. However, the experimental values of buckling temperatures were noted to be appreciably larger than those calculated from a linear theory using the experimental buckling loads. This nonlinear rise in thermal stress with increase of temperature was attributed to geometric changes in the form of 'barrelling' of the tube as a consequence of the end conditions imposing a restriction to both lateral expansion and end rotation. This implies that once the initially straight generators of the shell become curved during heating, they do not shorten in accordance with the linear formula; hence the circular shell can tolerate considerably higher rises in temperature

than would be predicted by a linear theory.

The process of snap-through mentioned above has been examined further by Hoff (29) and Madsen (63) who concluded this feature to be dependent on the rigidity of the testing machine. For an imperfect shell heated in a perfectly rigid rig, snap-through was considered to be absent, whereas it was deduced to be inevitable in the case of a sufficiently elastic testing machine. Experimental buckling temperatures, however, were not predicted in this nonlinear study but were mentioned to be higher, equal, or even lower than those given by the linear theory.

The reader is referred to the list of references provided by Ross et al (88) for further literature on the thermal buckling of thin cylindrical tubes. Directing the above discussion to the specific application of tubes in the present study, the author recognizes the importance of the fixity conditions of the end plates in the crushing layer on the axial stability of tubes that are enclosed within it.* This is in spite of the fact that in the present work unclamped thick-walled tubes have been tested and selected in design for their subsequent application. The implication is that, for maximum stability, restraint to thermal expansion of tubes in the layer by the end plates must be minimized prior to the final effective use of tubes as energy absorbers. This applies equally to the case of sublayers each enclosing a quantity of tubes; here the different 'rows' have again been assumed to be separated by plates which may be held at

* See Assumption 7, Section 7.1.3 (Chapter 7)

fixed positions apart, equivalent to the lengths of the tubes enclosed.

Thus, it is concluded that in the final design arrangement, tolerances may have to be introduced in the positioning of the plates to avoid initiation of premature axial stresses in the tubes enclosed within the crushing layer.

## 8.3 Suggestions for Further Study †

In order to simulate the real operating conditions for the specific application of tubes considered in this study, it is recommended to perform an experimental program of dynamic axial compression of tubes at elevated temperatures. The dynamic feature may be isolated in the first instance by carrying out drop-hammer tests at room temperature on tubes resting on a rigid anvil; alternatively, a compressed-air rifle may be used to fire a projectile whose velocity can be detected by installation of appropriate photoelectric devices. The thermal aspect may be investigated by performing quasi-static tests on tubes whilst they are being heated, at selected temperatures, within a furnace. Subsequently the two features may be superimposed in a further experimental program.

The mode of axial collapse for a circular tube was deduced to be little affected from its ambient quasi-static mechanism following the previous discussions, and it was observed that the main variable in the new conditions would be the mean level of resistance to failure. Since this would reflect a

---

†See also Chapter 7, P.285

change in the energy absorption capacity of a tube, it is recommended to obtain relationships between the fold energy--geometry indices introduced, velocity of impact and the surrounding temperature. Thus, for a selected condition, the appropriate energy relationship may be used to replace that used in the quasi-static design method presented in Chapter 7. The method is otherwise considered to remain largely intact, so that, for the alloy tested, tubes of similar geometry to those considered here may be selected in the tests for collapse in the optimum concertina mode.

The influence of material properties on the energy absorption capacity of a tube and its mode of collapse may be investigated in a further set of tests involving other suitably ductile metals, particularly steels; Type T-316 stainless steel has, in fact, been used as a material in the design of tubes for the specific application considered in this study. Variations in the material selected are expected to lead to variations in the collapse zones in the chart of Figure 2.1 (Chapter 2), for the particular aluminium alloy tested. These results would perhaps enable suitable deductions to be made regarding the trends and causes of these variations in relation to the choice of tube material.

# APPENDICES

# Appendix I

## Experimental Data for the Energy Relationships Presented in Chapters 3 and 4

### Notation

#### Tube geometry

D' = external diameter

D = internal diameter

L = length

t = thickness

nom. t = nominal thickness

SWG = Standard Wire Gauge unit

(see notation in Chapter 2)

A = net section area

#### Other parameters

$\overline{P}$ = mean postbuckling axial collapse load

$\rho$ = material density (= 2.684 X $10^{-8}$ KN/mm$^3$ for the alloy tested)

$E_s^c$ = specific energy absorption in axial compression

$\sigma_n$ = nominal mean axial collapse stress

$L_f$ = axial shortening of tube in formation of the first concertina fold

$L_m$ = mean axial shortening of tube per formation of a fold

$V_{first}$ = nominal net volume of the first concertina fold

$V_{no}$ = nominal mean volume of a fold over a series of folds

$V_{tr}$ = true mean volume of a fold over a series of folds

$E_{first}$ = energy absorbed in formation of the first concertina fold

$E_m$ = mean energy absorbed per formation of a fold

$E_{Euler}$ = energy absorbed up to the initial point of failure in the Eulerian mechanism of collapse

Experimental data for specific energy absorption

Concertina mechanism

| Tube set | t (mm) | D (mm) | Ratio t/D' | A ($mm^2$) | $\bar{P}$ (KN) | $\sigma_n$ (X $10^{-3}$) equation (3.3.1) ($KN/mm^2$) | $E_s^c$ (X $10^6$) (= $\bar{P}/A\rho$) (mm KN force/KN) |
|---|---|---|---|---|---|---|---|
| 4 in.(D') X 16 SWG(t) | 1.63 | 98.35 | 0.0160 | 510.6 | 19.23 | 2.37 | 1.403 |
| 6 in.(D') X 0.125 in.(t) | 3.18 | 146.10 | 0.0208 | 1488.5 | 70.00 | 3.84 | 1.752 |
| 3 in.(D') X 16 SWG(t) | 1.63 | 72.95 | 0.0213 | 380.9 | 17.17 | 3.77 | 1.678 |
| 1 in.(D') X 0.5 mm (nom. t) | 0.57 | 24.27 | 0.0224 | 44.3 | 1.90 | 3.75 | 1.599 |
| 1 in.(D') X 1/32 in.(nom. t) | 0.64 | 24.12 | 0.0253 | 50.0 | 2.42 | 5.23 | 1.797 |
| 0.75 in.(D) X 0.5 mm (nom. t) | 0.67 | 19.05 | 0.0326 | 41.2 | 2.58 | 7.89 | 2.331 |
| 1 in.(D') X 20 SWG(t) | 0.91 | 23.57 | 0.0360 | 70.3 | 4.46 | 8.80 | 2.362 |
| 1 in.(D') X 1 mm (nom. t) | 0.92 | 23.56 | 0.0361 | 70.6 | 4.60 | 9.08 | 2.429 |
| 6 in.(D') X 0.25 in.(t) | 6.35 | 139.70 | 0.0417 | 2913.6 | 204.50 | 11.21 | 2.615 |
| 0.75 in.(D) X 0.75 mm (nom. t) | 0.94 | 19.05 | 0.0447 | 58.7 | 4.60 | 13.38 | 2.916 |
| 2.5 in.(D') X 0.125 in.(t) | 3.18 | 57.15 | 0.0500 | 601.7 | 50.14 | 15.83 | 3.105 |
| 0.75 in.(D) X 1 mm (nom. t) | 1.19 | 19.05 | 0.0556 | 75.7 | 6.75 | 18.71 | 3.324 |
| 2 in.(D') X 0.125 in.(t) | 3.18 | 44.45 | 0.0625 | 475.0 | 48.00 | 23.68 | 3.765 |
| 0.75 in.(D) X 1.5 mm (nom. t) | 1.66 | 19.05 | 0.0742 | 108.0 | 11.30 | 28.75 | 3.898 |
| 2.5 in.(D') X 3/16 in.(t) | 4.76 | 53.97 | 0.0750 | 878.8 | 87.92 | 27.76 | 3.727 |
| 2.25 in.(D') X 3/16 in.(t) | 4.76 | 47.63 | 0.0833 | 783.8 | 89.83 | 35.02 | 4.270 |

Table A1.1

Experimental data for specific energy absorption

Diamond mechanism

| Tube Set | t (mm) | D (mm) | Ratio t/D' | A ($mm^2$) | $\bar{P}$ (KN) | $\sigma_n$ (X $10^{-3}$) equation (3.3.1) ($KN/mm^2$) | $E_s^c$ (X $10^6$) (= $\bar{P}/A\rho$) (mm KN force/KN) |
|---|---|---|---|---|---|---|---|
| | | 2-lobe diamond | | | | | |
| 4 in.(D') X 16 SWG(t) | 1.63 | 98.35 | 0.0160 | 510.6 | 18.40 | 2.27 | 1.343 |
| 3 in.(D') X 16 SWG(t) | 1.63 | 72.95 | 0.0213 | 380.9 | 15.58 | 3.42 | 1.524 |
| 1 in.(D') X 1/32 in. (nom. t) | 0.74 | 23.92 | 0.0291 | 57.3 | 2.85 | 5.63 | 1.852 |
| 0.75 in.(D) X 0.5 mm (nom. t) | 0.66 | 19.05 | 0.0324 | 40.9 | 2.35 | 7.21 | 2.142 |
| 1 in.(D') X 20 SWG(t) | 0.91 | 23.57 | 0.0360 | 70.3 | 3.78 | 7.46 | 2.004 |
| 1 in.(D') X 1 mm (nom. t) | 0.90 | 23.60 | 0.0355 | 69.4 | 3.90 | 7.70 | 2.093 |
| 0.75 in.(D) X 0.75 mm (nom. t) | 0.95 | 19.05 | 0.0453 | 59.7 | 3.80 | 11.20 | 2.372 |
| 2.5 in.(D') X 0.125 in.(t) | 3.18 | 57.15 | 0.0500 | 601.7 | 44.25 | 13.97 | 2.740 |
| 2 in.(D') X 0.125 in.(t) | 3.18 | 44.45 | 0.0625 | 475.0 | 36.00 | 17.76 | 2.824 |
| 2.5 in.(D') X 3/16 in.(t) | 4.76 | 53.97 | 0.0750 | 878.8 | 67.33 | 21.26 | 2.855 |
| 2.25 in.(D') X 3/16 in.(t) | 4.76 | 47.63 | 0.0833 | 783.8 | 72.50 | 28.26 | 3.446 |
| | | 3-lobe diamond | | | | | |
| 4 in.(D') X 16 SWG(t) | 1.63 | 98.35 | 0.0160 | 510.6 | 17.88 | 2.21 | 1.305 |
| 3 in.(D') X 16 SWG(t) | 1.63 | 72.95 | 0.0213 | 380.9 | 15.52 | 3.40 | 1.518 |
| 1 in.(D') X 0.5 mm (nom. t) | 0.58 | 24.25 | 0.0226 | 44.9 | 1.62 | 3.19 | 1.342 |
| 1 in.(D') X 1/32 in.(nom. t) | 0.67 | 24.06 | 0.0264 | 52.1 | 2.05 | 4.05 | 1.467 |
| 0.75 in.(D) X 0.5 mm (nom. t) | 0.62 | 19.05 | 0.0306 | 38.3 | 2.14 | 6.62 | 2.081 |
| 1 in.(D') X 1 mm (nom. t) | 0.92 | 23.56 | 0.0362 | 70.7 | 3.95 | 7.80 | 2.082 |

Table A1.2

## Experimental data for stroke efficiencies

Sequential mechanisms of collapse

(concertina, concertina + diamond)

| Tube set | Stroke efficiency |
|---|---|
| 4 in.(D') X 16 SWG(t) | 0.794 |
| 6 in.(D') X 0.125 in.(t) | 0.780 |
| 3 in.(D') X 16 SWG (t) | 0.776 |
| 1 in.(D') X 0.5 mm (nom. t) | 0.766 |
| 1 in.(D') X 1/32 in.(nom. t) | 0.768 |
| 1.5 in.(D') X 18 SWG(t) | 0.754 |
| 0.75 in.(D) X 0.5 mm (nom. t) | 0.719 |
| 1 in.(D') X 20 SWG(t) | 0.743 |
| 1 in.(D') X 1 mm (nom. t) | 0.758 |
| 6 in.(D') X 0.25 in.(t) | 0.774 |
| 0.75 in.(D) X 0.75 mm (nom. t) | 0.709 |
| 2.5 in.(D') X 0.125 in.(t) | 0.739 |
| 0.75 in.(D) X 1 mm (nom. t) | 0.728 |
| 2 in.(D') X 0.125 in.(t) | 0.646 |
| 0.75 in.(D) X 1.5 mm (nom. t) | 0.719 |
| 2.5 in.(D') X 3/16 in.(t) | 0.689 |
| 2.25 in.(D') X 3/16 in.(t) | 0.679 |

Table A1.3

Crushing mechanisms of collapse
(axisymmetric / 2-lobe diamond crushing, tilting failure)

| Tube set | Stroke efficiency |
|---|---|
| 4 in.(D') X 16 SWG(t) | 0.733 |
| 3 in.(D') X 16 SWG(t) | 0.768 |
| 1.5 in.(D') X 18 SWG(t) | 0.748 |
| 1 in.(D') X 20 SWG(t) | 0.709 |
| 2.5 in.(D') X 0.125 in.(t) | 0.689 |
| 2.5 in.(D') X 3/16 in.(t) | 0.512 |
| 2.25 in.(D') X 3/16 in.(t) | 0.512 |
| 0.75 in.(D) X 2 mm (nom. t) | 0.620 |
| 2 in.(D') X 3/16 in.(t) | 0.587 |
| 2.5 in.(D') X 0.25 in.(t) | 0.627 |
| 0.75 in.(D) X 2.5 mm (nom. t) | 0.605 |
| 1.75 in.(D') X 3/16 in.(t) | 0.570 |
| 1 ¾ in.(D') X 3/16 in.(t) | 0.552 |
| 1 in.(D') X 0.125 in.(t) | 0.628 |
| 1 ¾ in.(D') X 3/16 in.(t) | 0.598 |
| 1.75 in.(D') X 0.25 in.(t) | 0.558 |
| 0.75 in.(D') X 0.125 in.(t) | 0.613 |

Table A1.4

Experimental data for fold energy-geometry indicies

Concertina mechanism

| Tube set | $L_f$ (mm) | $L_m$ (mm) | A ($mm^2$) | $V_{first} = A \cdot L_f$ ($mm^3$) | $V_{no} = A \cdot L_m$ ($mm^3$) | $V_{tr} = A(L_m+2t)$ ($mm^3$) | $E_{first}$ (Joules) | $E_{mean}$ (Joules) |
|---|---|---|---|---|---|---|---|---|
| 4 in.(D') X 16 SWG(t) | 21.10 | 19.53 | 510.6 | 10773.0 | 9974.0 | 11634.3 | 382.3 | 360.5 |
| 6 in.(D') X 0.125 in.(t) | 38.33 | 35.67 | 1488.5 | 57052.4 | 53085.6 | 62537.2 | 2643.3 | 2466.7 |
| 3 in.(D') X 16 SWG(t) | 18.55 | 17.33 | 380.9 | 7066.3 | 6598.4 | 7837.0 | 279.6 | 268.3 |
| 1 in.(D') X 0.5 mm (nom. t) | 6.53 | 6.58 | 44.3 | 289.2 | 291.1 | 341.7 | 11.7 | 11.8 |
| 1 in.(D') X 1/32 in.(nom. t) | 6.65 | 6.37 | 46.4 | 308.8 | 295.1 | 351.2 | 13.2 | 13.2 |
| 1.5 in.(D') X 18 SWG(t) | 14.88 | 13.83 | 141.3 | 2101.4 | 1953.8 | 2298.2 | 182.8 | 174.4 |
| 0.75 in.(D) X 0.5 mm (nom. t) | 6.30 | 6.67 | 41.5 | 261.7 | 276.9 | 332.5 | 16.1 | 14.7 |
| 1 in.(D') X 20 SWG(t) | 9.26 | 8.36 | 70.3 | 651.1 | 588.2 | 716.8 | 39.3 | 35.3 |
| 1 in.(D') X 1 mm (nom. t) | 8.50 | 8.72 | 71.8 | 611.5 | 625.7 | 759.9 | 37.6 | 38.1 |
| 6 in.(D') X 0.25 in.(t) | 55.00 | 57.00 | 2913.6 | 160246.2 | 166073.5 | 203075.8 | 11773.3 | 10910.0 |
| 0.75 in.(D) X 0.75 mm (nom. t) | 7.59 | 7.15 | 58.7 | 445.9 | 419.6 | 529.4 | 32.8 | 31.4 |
| 2.5 in.(D') X 0.125 in.(t) | 25.00 | 24.81 | 601.7 | 15054.2 | 14929.0 | 18749.9 | 1223.3 | 1184.9 |
| 0.75 in.(D) X 1 mm (nom. t) | 8.69 | 8.74 | 75.7 | 657.6 | 661.5 | 841.6 | 57.0 | 56.3 |
| 2 in.(D') X 0.125 in.(t) | 18.50 | 19.47 | 475.0 | 8788.2 | 9248.1 | 12264.6 | 877.6 | 945.2 |
| 0.75 in.(D) X 1.5 mm (nom. t) | 9.20 | 10.53 | 108.0 | 993.6 | 1137.6 | 1496.2 | 103.0 | 124.9 |
| 2.5 in.(D') X 3/16 in.(t) | 28.62 | 29.72 | 878.8 | 25155.6 | 26114.1 | 32688.8 | 2521.9 | 2550.7 |
| 2.25 in.(D') X 3/16 in.(t) | 25.17 | 26.43 | 783.8 | 19725.6 | 20719.5 | 25702.4 | 2325.3 | 2382.2 |

Table A1.5

Experimental data for fold energy-geometry indicies.

Diamond mechanism

| Tube set | $L_m$ (mm) | A ($mm^2$) | $V_{no} = A L_m$ ($mm^3$) | $E_{mean}$ (Joules) |
|---|---|---|---|---|
| 2-lobe diamond | | | | |
| 4 in.(D') X 16 SWG(t) | 24.12 | 510.6 | 12317.5 | 473.4 |
| 3 in.(D') X 16 SWG(t) | 26.01 | 380.9 | 9904.8 | 423.4 |
| 1 in.(D') X 1/32 in.(nom. t) | 10.40 | 57.3 | 596.2 | 28.2 |
| 1.5 in.(D') X 18 SWG(t) | 16.82 | 141.3 | 2375.3 | 177.2 |
| 0.75 in.(D) X 0.5 mm (nom. t) | 7.92 | 40.9 | 323.9 | 19.2 |
| 1 in.(D') X 20 SWG(t) | 12.22 | 70.3 | 859.4 | 45.3 |
| 1 in.(D') X 1 mm (nom. t) | 10.38 | 69.4 | 720.6 | 40.9 |
| 0.75 in.(D) X 0.75 mm (nom. t) | 10.59 | 59.7 | 632.1 | 41.7 |
| 2.5 in.(D') X 0.125 in.(t) | 32.41 | 601.7 | 19501.8 | 1460.0 |
| 2 in.(D') X 0.125 in.(t) | 28.48 | 475.0 | 13529.1 | 1076.6 |
| 2.5 in.(D') X 3/16 in.(t) | 42.17 | 878.8 | 37055.5 | 2859.6 |
| 2.25 in.(D') X 3/16 in.(t) | 30.33 | 783.8 | 23774.9 | 2608.3 |
| 3-lobe diamond | | | | |
| 4 in.(D') X 16 SWG(t) | 23.80 | 510.6 | 12150.7 | 424.0 |
| 3 in.(D') X 16 SWG(t) | 22.95 | 380.9 | 8739.1 | 348.6 |
| 1 in.(D') X 0.5 mm (nom. t) | 7.91 | 44.9 | 355.1 | 12.7 |
| 1 in.(D') X 1/32 in.(nom. t) | 7.68 | 52.1 | 399.7 | 15.5 |
| 0.75 in.(D) X 0.5 mm (nom. t) | 5.91 | 41.5 | 245.1 | 14.3 |
| 1 in.(D') X 1 mm (nom. t) | 9.51 | 70.7 | 672.0 | 37.5 |
| [2-lobe diamond crushing] | | | | |
| 0.75 in.(D) X 2 mm (nom. t) | 10.25 | 144.7 | 1482.8 | 178.6 |
| 2 in.(D') X 3/16 in.(t) | 24.96 | 688.8 | 17191.8 | 2177.2 |
| 1.75 in.(D') X 3/16 in.(t) | 21.00 | 593.8 | 12469.8 | 1922.2 |
| 2.5 in.(D') X 0.25 in.(t) | 32.50 | 1140.1 | 37052.9 | 4366.7 |

Table A1.6

Experimental data for Euler energy index

Eulerian mechanism

| Tube set | A ($mm^2$) | $E_{Euler}$ (Joules) |
|---|---|---|
| 1.5 in.(D') X 18 SWG(t) | 141.3 | 103.6 |
| 1 in.(D') X 20 SWG(t) | 70.3 | 24.0 |
| 0.75 in.(D) X 0.75 mm (nom. t) | 57.7 | 6.9 |
| 2.5 in.(D') X 0.125 in.(t) | 601.7 | 755.9 |
| 0.75 in.(D) X 1 mm (nom. t) | 72.3 | 22.7 |
| 2 in.(D') X 0.125 in.(t) | 475.0 | 747.1 |
| 1 in.(D') X 1/16 in. (nom. t) | 119.0 | 63.5 |
| 0.75 in.(D) X 1.5 mm (nom. t) | 120.5 | 64.7 |
| 2.25 in.(D') X 3/16 in.(t) | 783.8 | 1536.7 |
| 0.75 in.(D) X 2 mm (nom. t) | 138.1 | 121.5 |
| 2 in.(D') X 3/16 in.(t) | 688.8 | 2528.5 |
| 1.75 in.(D') X 3/16 in.(t) | 593.8 | 1683.9 |
| 1 in.(D') X 0.125 in.(t) | 221.7 | 441.1 |
| 1 ¼ in.(D') X 3/16 in.(t) | 451.3 | 2089.6 |
| 0.75 in.(D') X 0.125 in.(t) | 158.4 | 263.3 |

Table A1.7

# Appendix II

## Experimental Data used to Inspect the Solutions of Theories Analyzed in Chapters 5 and 6

### Notation

Tube section geometry

(see notation for Appendix I)

$R$ = mean radius of tube

Other parameters

$h/h_{exp}$ = length of one half-wave of a concertina fold Alexander (theory) / experiment

$Y/Y_{exp}$ = yield stress of annealed HT30-aluminium alloy Alexander, Donnell (theory) / as 0.1% proof stress (experiment)

$Y_n$ = yield stress of the alloy material tested in the non-annealed condition

$\bar{P}$ = mean postbuckling axial collapse load

$D^o$ = external diameter of tube after collapse in the concertina mechanism

$\lambda$ = measure of collapse configuration : proportion of external folding in the concertina mechanism

$P_{cr}$ = critical axial load at failure

$\varepsilon_y$ = strain at yield recorded on the stress-strain curves for the annealed aluminium alloy tested

$E$ = modulus of elasticity of the annealed material

$\Delta P/\Delta \varepsilon_p$ = increments of load / strain recorded beyond yielding on the stress-strain curves of the annealed alloy

$E_p$ = modulus of strain-hardening of the annealed alloy

$\bar{\sigma}$ = mean postbuckling collapse stress

$\sigma_{cr}$ = critical experimental stress at failure

$\sigma_{cl}$ = critical stress from the classical elastic theory

$S$ = critical stress ratio : $\sigma_{cr} / \sigma_{cl}$

Determination of material yield stress from Alexander's theory

Concertina mechanism

| Tube set | t (mm) | D (mm) | A ($mm^2$) | $t^{1.5} D^{0.5}$ ($mm^2$) | $\bar{P}$ (KN) | h equation (5.1.2) (mm) | Y equation (5.1.1) ($KN/mm^2$) |
|---|---|---|---|---|---|---|---|
| 4 in.(D') X 16 SWG(t) | 1.63 | 98.35 | 510.6 | 20.6 | 19.23 | 12.05 | 0.150 |
| 6 in.(D') X 0.125 in.(t) | 3.18 | 146.05 | 1488.5 | 68.4 | 70.00 | 20.52 | 0.164 |
| 3 in.(D') X 16 SWG(t) | 1.63 | 72.95 | 380.9 | 17.7 | 17.17 | 10.38 | 0.155 |
| 1 in.(D') X 0.5 mm (nom. t) | 0.57 | 24.27 | 44.3 | 2.1 | 1.96 | 3.54 | 0.149 |
| 1 in.(D') X 1/32 in. (nom. t) | 0.64 | 24.11 | 50.0 | 2.5 | 2.42 | 3.74 | 0.152 |
| 0.75 in.(D) X 0.5 mm (nom. t) | 0.67 | 19.05 | 41.2 | 2.4 | 2.58 | 3.39 | 0.172 |
| 1 in.(D') X 20 SWG(t) | 0.91 | 23.57 | 70.3 | 4.2 | 4.46 | 4.42 | 0.166 |
| 1 in.(D') X 1 mm (nom. t) | 0.93 | 23.53 | 71.8 | 4.4 | 4.58 | 4.47 | 0.165 |
| 6 in.(D') X 0.25 in.(t) | 6.35 | 139.70 | 2913.6 | 189.1 | 204.50 | 28.38 | 0.170 |
| 0.75 in.(D) X 0.75 mm (nom. t) | 0.94 | 19.05 | 58.7 | 3.9 | 4.60 | 4.02 | 0.183 |
| 2.5 in.(D') X 0.125 in.(t) | 3.18 | 57.15 | 601.7 | 42.8 | 50.14 | 12.84 | 0.183 |
| 0.75 in.(D) X 1 mm (nom. t) | 1.19 | 19.05 | 75.7 | 5.7 | 6.75 | 4.54 | 0.185 |
| 2 in.(D') X 0.125 in.(t) | 3.18 | 44.45 | 475.0 | 37.7 | 48.60 | 11.32 | 0.199 |
| 0.75 in.(D) X 1.5 mm (nom. t) | 1.66 | 19.05 | 108.0 | 9.3 | 11.30 | 5.36 | 0.186 |
| 2.5 in.(D') X 3/16 in.(t) | 4.76 | 53.98 | 878.8 | 76.3 | 87.92 | 15.28 | 0.177 |
| 2.25 in.(D') X 3/16 in.(t) | 4.76 | 47.63 | 783.8 | 71.7 | 89.83 | 14.35 | 0.191 |

Table A2.1

Experimental data for the geometry of folding at collapse

Concertina mechanism

| Tube set | Comparison of fold arm-lengths | | $D^o$ | $\lambda = \frac{D^o - (D + t)}{2 h_{exp}}$ | $P_{cr}$ |
|---|---|---|---|---|---|
| | equation (5.1.2) $h$ (mm) | experiment $h_{exp}$ (mm) | (mm) | | (KN) |
| 4 in.(D') X 16 SWG(t) | 12.05 | 11.39 | 115.37 | 0.675 | 48.7 |
| 6 in.(D') X 0.125 in.(t) | 20.52 | 21.01 | 178.00 | 0.684 | 153.0 |
| 3 in.(D') X 16 SWG(t) | 10.38 | 10.29 | 89.29 | 0.715 | 35.1 |
| 1 in.(D') X 0.5 mm (nom. t) | 3.54 | 3.84 | 30.02 | 0.675 | 3.4 |
| 1 in.(D') X 1/32 in. (nom. t) | 3.74 | 3.77 | 29.82 | 0.672 | 3.9 |
| 1.5 in.(D') X 18 SWG(t) | 6.28 | 8.14 | 48.29 | 0.701 | 20.2 |
| 0.75 in.(D) X 0.5 mm (nom. t) | 3.39 | 3.57 | 24.50 | 0.671 | 4.3 |
| 1 in.(D') X 20 SWG(t) | 4.42 | 5.10 | 31.55 | 0.693 | 7.0 |
| 1 in.(D') X 1 mm (nom. t) | 4.47 | 5.18 | 31.33 | 0.663 | 6.9 |
| 6 in.(D') X 0.25 in.(t) | 28.38 | 34.85 | 193.10 | 0.675 | 335.8 |
| 0.75 in.(D) X 0.75 mm (nom. t) | 4.02 | 4.51 | 26.24 | 0.694 | 6.7 |
| 2.5 in.(D') X 0.125 in.(t) | 12.84 | 15.57 | 82.11 | 0.700 | 68.7 |
| 0.75 in.(D) X 1 mm (nom. t) | 4.54 | 5.56 | 27.73 | 0.673 | 8.8 |
| 2 in.(D') X 0.125 in.(t) | 11.32 | 14.40 | 67.71 | 0.698 | 64.5 |
| 0.75 in.(D) X 1.5 mm (nom. t) | 5.36 | 6.93 | 29.98 | 0.669 | 13.3 |
| 2.5 in.(D') X 3/16 in.(t) | 15.28 | 19.62 | 87.23 | 0.726 | 104.5 |
| 2.25 in.(D') X 3/16 in.(t) | 14.35 | 18.43 | 79.12 | 0.725 | 102.4 |

Table A2.2

Experimental data used in Figure 5.5

Eulerian / crushing mechanisms of collapse

| Tube set | A ($mm^2$) | $P_{cr}$ (KN) |
|---|---|---|
| 3 in.(D') X 16 SWG(t) | 380.9 | 42.5 |
| 1.5 in.(D') X 18 SWG(t) | 141.3 | 19.4 |
| 1 in.(D') X 20 SWG(t) | 70.3 | 7.0 |
| 0.75 in.(D) X 0.75 mm (nom. t) | 57.7 | 5.7 |
| 2.5 in.(D') X 0.125 in.(t) | 601.7 | 75.0 |
| 0.75 in.(D) X 1 mm (nom. t) | 72.3 | 7.2 |
| 2 in.(D') X 0.125 in.(t) | 475.0 | 57.8 |
| 1 in.(D') X 1/16 in.(nom. t) | 119.0 | 11.1 |
| 0.75 in.(D) X 1.5 mm (nom. t) | 103.8 | 11.7 |
| 2.5 in.(D') X 3/16 in.(t) | 878.8 | 104.5 |
| 2.25 in.(D') X 3/16 in.(t) | 783.8 | 95.0 |
| 0.75 in.(D) X 2 mm (nom. t) | 140.3 | 18.0 |
| 2 in.(D') X 3/16 in.(t) | 688.8 | 99.3 |
| 2.5 in.(D') X 0.25 in.(t) | 1140.1 | 145.9 |
| 0.75 in.(D) X 2.5 mm (nom. t) | 171.5 | 25.0 |
| 1.75 in.(D') X 3/16 in.(t) | 593.8 | 91.8 |
| 1 ⅜ in.(D') X 3/16 in.(t) | 546.3 | 80.5 |
| 1 in.(D') X 0.125 in.(t) | 221.7 | 38.4 |
| 1 ⅛ in.(D') X 3/16 in.(t) | 451.3 | 75.7 |
| 0.75 in.(D') X 0.125 in.(t) | 158.4 | 21.3 |

Table A2.3

Experimental data obtained from strain-gauge tests for the yield (0.1 % proof) stress of HT30-aluminium alloy tubing in the non-annealed (as-received) condition

| Tube specimen | A ($mm^2$) | $Y_n$ ($KN/mm^2$) |
|---|---|---|
| 2 in.(L) X 4 in.(D') X 16 SWG(t) | 510.6 | 0.221 |
| 2 in.(L) X 3 in.(D') X 16 SWG(t) | 380.9 | 0.265 |
| 2 in.(L) X 1 in.(D') X 20 SWG(t) | 70.3 | 0.286 |
| 2 in.(L) X 2 in.(D') X 0.125 in.(t) | 475.0 | 0.275 |
| 2 in.(L) X 2 in.(D') X 3/16 in.(t) | 688.8 | 0.238 |
| 2 in.(L) X 2.5 in.(D') X 0.25 in.(t) | 1140.1 | 0.269 |
| 2 in.(L) X 1.75 in.(D') X 3/16 in.(t) | 593.8 | 0.276 |
| 6 in.(L) X 1 in.(D') X 0.125 in.(t) | 221.7 | 0.291 |
| 4 in.(L) X 1 in.(D') X 0.125 in.(t) | 221.7 | 0.277 |
| 2 in.(L) X 1.75 in.(D') X 0.25 in.(t) | 760.1 | 0.274 |

Table A2.4

Experimental data obtained from strain-gauge tests for the yield (0.1 % proof) stress of annealed HT30-aluminium alloy tubing

| Tube specimen | A ($mm^2$) | $Y_{exp}$ ($KN/mm^2$) |
|---|---|---|
| 2 in.(L) X 4 in.(D') X 16 SWG(t) | 510.6 | 0.0760 |
| 2 in.(L) X 3 in.(D') X 16 SWG(t) | 380.9 | 0.0701 |
| 2 in.(L) X 1 in.(D') X 20 SWG(t) | 70.3 | 0.0540 |
| 6 in.(L) X 2.5 in.(D') X 0.125 in.(t) | 601.7 | 0.0357 |
| 4 in.(L) X 2.5 in.(D') X 0.125 in.(t) | 601.7 | 0.0349 |
| 2 in.(L) X 2 in.(D') X 0.125 in.(t) | 475.0 | 0.0453 |
| 6 in.(L) X 0.75 in.(D) X 0.5 mm (nom. t) | 40.9 | 0.0673 |
| 6 in.(L) X 0.75 in.(D) X 0.75 mm (nom. t) | 57.7 | 0.0655 |
| 6 in.(L) X 0.75 in.(D) X 1 mm (nom. t) | 72.3 | 0.0639 |
| 6 in.(L) X 0.75 in.(D) X 1.5 mm (nom. t) | 97.5 | 0.0328 |
| 6 in.(L) X 0.75 in.(D) X 2 mm (nom. t) | 130.8 | 0.0321 |
| 2 in.(L) X 0.75 in.(D) X 0.5 mm (nom. t) | 41.5 | 0.0542 |
| 2 in.(L) X 0.75 in.(D) X 0.75 mm (nom. t) | 59.0 | 0.0686 |
| 2 in.(L) X 0.75 in.(D) X 1 mm (nom. t) | 75.7 | 0.0641 |
| 2 in.(L) X 0.75 in.(D) X 1.5 mm (nom. t) | 110.1 | 0.0758 |
| 2 in.(L) X 0.75 in.(D) X 2 mm (nom. t) | 149.1 | 0.0785 |
| 2 in.(L) X 2 in.(D') X 3/16 in.(t) | 688.8 | 0.0334 |
| 2 in.(L) X 2.5 in.(D') X 0.25 in.(t) | 1140.1 | 0.0347 |
| 6 in.(L) X 1 in.(D') X 0.125 in.(t) | 221.7 | 0.0372 |
| 4 in.(L) X 1 in.(D') X 0.125 in.(t) | 221.7 | 0.0338 |
| 2 in.(L) X 1.75 in.(D') X 0.25 in.(t) | 760.1 | 0.0346 |

Table A2.5

Determination of the compressive yield stress of non-annealed HT30-aluminium alloy tubing

Experimental load-strain curve obtained from strain gauge test on as-received tube specimen :

6 in.(L) x 1 in.(D') x 0.125 in. (t)

Cross-section area, $A = 221.7\ mm^2$

Yield stress, $Y = \frac{64.6}{A} = 0.291\ KN/mm^2$

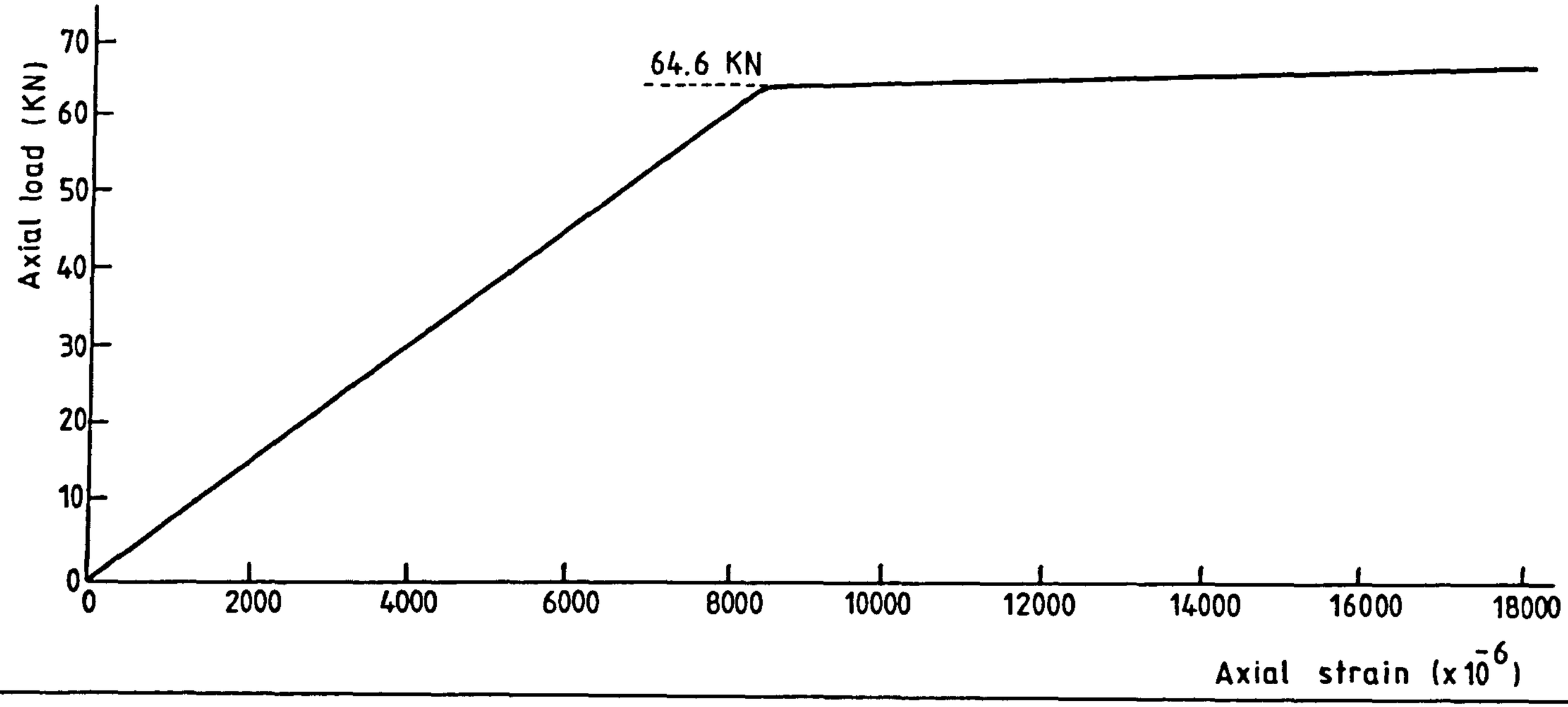


Illustration of the trend typically observed in non-annealed (as-received) yield tests

Figure A2.1

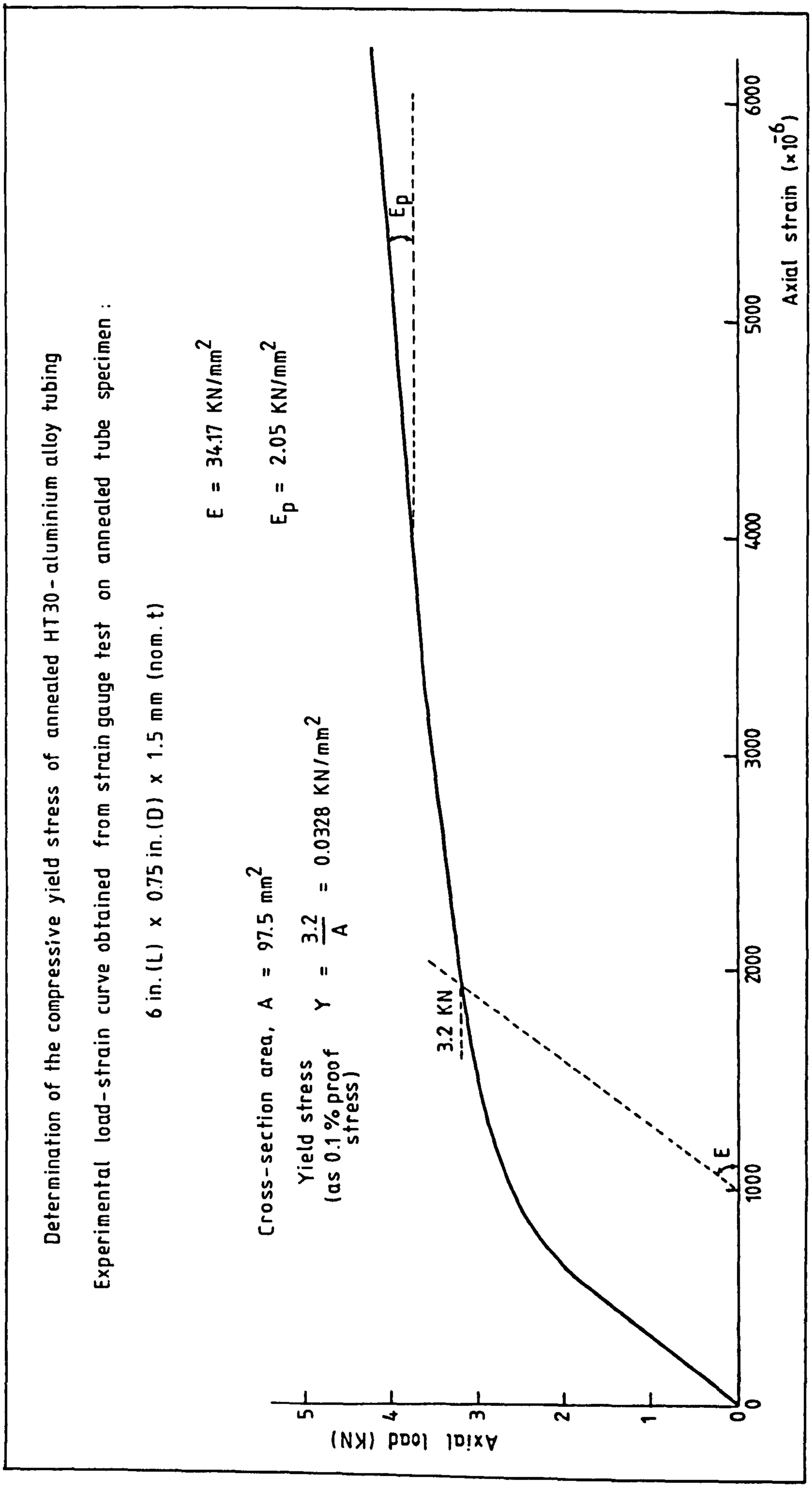


Illustration of the trend typically observed in annealed yield test

Figure A2.2

Experimental data obtained from strain-gauge tests for the moduli of elasticity and strain-hardening of annealed HT30-aluminium alloy tubing

| Tube specimen | A ($mm^2$) | $\varepsilon_Y$ ($\times 10^{-6}$) | E ($= Y/\varepsilon_Y$) ($KN/mm^2$) | $\Delta P$ (KN) | $\Delta \varepsilon_p$ ($\times 10^{-6}$) | $E_p = \Delta P/(\Delta \varepsilon_p A)$ ($KN/mm^2$) |
|---|---|---|---|---|---|---|
| 2 in.(L) X 4 in.(D') X 16 SWG(t) | 510.6 | 3850 | 19.74* | 3.60 | 7500 | 0.94 |
| 2 in.(L) X 3 in.(D') X 16 SWG(t) | 380.9 | 2200 | 31.86 | 5.05 | 10000 | 1.33 |
| 2 in.(L) X 1 in.(D') X 20 SWG(t) | 70.3 | 1570 | 34.40 | 0.20 | 1000 | 2.84 |
| 6 in.(L) X 2.5 in.(D') X 0.125 in.(t) | 601.7 | 1080 | 33.08 | 20.80 | 30000 | 1.15 |
| 4 in.(L) X 2.5 in.(D') X 0.125 in.(t) | 601.7 | 890 | 39.20* | 10.50 | 10000 | 1.75 |
| 2 in.(L) X 2 in.(D') X 0.125 in.(t) | 475.0 | 1230 | 36.83 | 3.75 | 4000 | 1.97 |
| 6 in.(L) X 0.75 in.(D) X 0.5 mm (nom. t) | 40.9 | 1660 | 40.54* | 0.18 | 2000 | 2.14 |
| 6 in.(L) X 0.75 in.(D) X 0.75 mm (nom. t) | 57.7 | 1870 | 35.03 | 0.18 | 1500 | 2.02 |
| 6 in.(L) X 0.75 in.(D) X 1 mm (nom. t) | 72.3 | 1860 | 34.36 | 0.36 | 2500 | 1.99 |
| 6 in.(L) X 0.75 in.(D) X 1.5 mm (nom. t) | 97.5 | 960 | 34.17 | 0.60 | 3000 | 2.05 |
| 6 in.(L) X 0.75 in.(D) X 2 mm (nom. t) | 130.8 | 920 | 34.89 | 0.81 | 2500 | 2.48 |
| 2 in.(L) X 0.75 in.(D) X 0.5 mm (nom. t) | 41.5 | 1520 | 35.66 | - | - | - |
| 2 in.(L) X 0.75 in.(D) X 1 mm (nom. t) | 75.7 | 2000 | 32.05 | - | - | - |
| 2 in.(L) X 0.75 in.(D) X 1.5 mm (nom. t) | 110.1 | 2440 | 31.07 | - | - | - |
| 2 in.(L) X 0.75 in.(D) X 2 mm (nom. t) | 149.1 | 2270 | 34.58 | - | - | - |
| 2 in.(L) X 2 in.(D') X 3/16 in.(t) | 688.8 | 1075 | 31.07 | 5.90 | 4000 | 2.14 |
| 2 in.(L) X 2.5 in.(D') X 0.25 in.(t) | 1140.1 | 1025 | 33.85 | 4.90 | 1500 | 2.87 |
| 6 in.(L) X 1 in.(D') X 0.125 in.(t) | 221.7 | 1360 | 27.35* | 4.0 | 11268 | 1.60 |
| 4 in.(L) X 1 in.(D') X 0.125 in.(t) | 221.7 | 1000 | 33.83 | 4.0 | 10000 | 1.80 |
| 2 in.(L) X 1.75 in.(D') X 0.25 in.(t) | 760.1 | 1065 | 32.49 | 2.20 | 1000 | 2.89 |

* Reading not considered in obtaining a mean value for E

Table A2.6

Experimental data used in inspection of Johnson's theory

Concertina mechanism

| Tube set | t (mm) | D (mm) | Ratio t/D | Product D t ($mm^2$) | $\left\{\frac{2.\Pi.(t/D)}{\sqrt{3}}\right\}^{0.5}$ ($\times 10^{-2}$) | $\bar{P}$ (KN) | $\bar{\sigma}$ ($\times 10^{-2}$) $= \bar{P}/\pi Dt$ ($KN/mm^2$) | $\bar{\sigma}$ ($\times 10^{-2}$) $= \bar{P}/A$ ($KN/mm^2$) |
|---|---|---|---|---|---|---|---|---|
| 4 in.(D') X 16 SWG(t) | 1.63 | 98.35 | 0.0165 | 159.9 | 24.47 | 19.23 | 3.83 | 3.77 |
| 6 in.(D') X 0.125 in.(t) | 3.18 | 146.05 | 0.0217 | 436.9 | 28.06 | 70.00 | 4.81 | 4.70 |
| 3 in.(D') X 16 SWG(t) | 1.63 | 72.95 | 0.0223 | 118.6 | 28.44 | 17.17 | 4.61 | 4.51 |
| 1 in.(D') X 0.5 mm (nom. t) | 0.57 | 24.27 | 0.0234 | 13.7 | 29.11 | 1.96 | 4.55 | 4.30 |
| 1 in.(D') X 1/32 in.(t) | 0.64 | 24.11 | 0.0267 | 15.5 | 31.12 | 2.42 | 4.96 | 4.83 |
| 0.75 in.(D) X 0.5 mm (nom. t) | 0.67 | 19.05 | 0.0349 | 12.7 | 35.58 | 2.58 | 6.47 | 6.25 |
| 1 in.(D') X 20 SWG(t) | 0.91 | 23.57 | 0.0388 | 21.5 | 37.52 | 4.46 | 6.60 | 6.35 |
| 1 in.(D') X 1 mm (nom. t) | 0.93 | 23.53 | 0.0397 | 22.0 | 37.95 | 4.58 | 6.63 | 6.38 |
| 6 in.(D') X 0.25 in.(t) | 6.35 | 139.70 | 0.0455 | 887.1 | 40.63 | 204.50 | 7.34 | 7.02 |
| 0.75 in.(D) X 0.75 mm (nom. t) | 0.94 | 19.05 | 0.0491 | 17.8 | 42.20 | 4.60 | 8.22 | 7.84 |
| 2.5 in.(D') X 0.125 in.(t) | 3.18 | 57.15 | 0.0556 | 181.5 | 44.91 | 50.14 | 8.80 | 8.33 |
| 0.75 in.(D) X 1 mm (nom. t) | 1.19 | 19.05 | 0.0625 | 22.7 | 47.62 | 6.75 | 9.48 | 8.92 |
| 2 in.(D') X 0.125 in.(t) | 3.18 | 44.45 | 0.0714 | 141.1 | 50.89 | 48.60 | 10.96 | 10.10 |
| 0.75 in.(D) X 1.5 mm (nom. t) | 1.66 | 19.05 | 0.0871 | 31.6 | 56.21 | 11.30 | 11.37 | 10.46 |
| 2.5 in.(D') X 3/16 in.(t) | 4.76 | 53.97 | 0.0882 | 256.9 | 56.56 | 87.92 | 10.89 | 10.00 |
| 2.25 in.(D') X 3/16 in.(t) | 4.76 | 47.63 | 0.1000 | 226.7 | 60.23 | 89.83 | 12.60 | 11.46 |

Table A2.7

Experimental data used in inspection of Pugsley's theory

Diamond mechanism

| Tube set | t (mm) | D (mm) | Ratio t/D | R (mm) | Ratio R/t | $\bar{P}$ (KN) | $\bar{\sigma}$ (X $10^{-2}$) = $\bar{P}$ / A ($KN/mm^2$) |
|---|---|---|---|---|---|---|---|
| | | | 2-lobe diamond | | | | |
| 4 in.(D') X 16 SWG(t) | 1.63 | 98.35 | 0.0165 | 49.99 | 30.74 | 18.40 | 3.60 |
| 3 in.(D') X 16 SWG(t) | 1.63 | 72.95 | 0.0223 | 37.29 | 22.93 | 15.59 | 4.09 |
| 1 in.(D') X 1/32 in.(nom. t) | 0.74 | 23.92 | 0.0309 | 12.33 | 16.66 | 2.85 | 4.97 |
| 0.75 in.(D) X 0.5 mm (nom. t) | 0.66 | 19.05 | 0.0346 | 9.86 | 14.93 | 2.35 | 5.75 |
| 1 in.(D') X 20 SWG(t) | 0.91 | 23.57 | 0.0388 | 12.24 | 13.39 | 3.78 | 5.38 |
| 1 in.(D') X 1 mm (nom. t) | 0.90 | 23.60 | 0.0382 | 12.25 | 13.58 | 3.90 | 5.62 |
| 0.75 in.(D) X 0.75 mm (nom. t) | 0.95 | 19.05 | 0.0499 | 10.00 | 10.53 | 3.80 | 6.37 |
| 2.5 in.(D') X 0.125 in.(t) | 3.18 | 57.15 | 0.0556 | 30.16 | 9.50 | 44.25 | 7.35 |
| 2 in.(D') X 0.125 in.(t) | 3.18 | 44.45 | 0.0714 | 23.81 | 7.50 | 36.00 | 7.58 |
| 2.5 in.(D') X 3/16 in.(t) | 4.76 | 53.97 | 0.0882 | 29.37 | 6.17 | 67.33 | 7.66 |
| 2.25 in.(D') X 3/16 in.(t) | 4.76 | 47.63 | 0.1000 | 26.20 | 5.50 | 72.50 | 9.25 |
| | | | 3-lobe diamond | | | | |
| 4 in.(D') X 16 SWG(t) | 1.63 | 98.35 | 0.0165 | 49.99 | 30.74 | 17.88 | 3.50 |
| 3 in.(D') X 16 SWG(t) | 1.63 | 72.95 | 0.0223 | 37.29 | 22.93 | 15.52 | 4.07 |
| 1 in.(D') X 0.5 mm (nom. t) | 0.58 | 24.25 | 0.0237 | 12.41 | 21.59 | 1.62 | 3.60 |
| 1 in.(D') X 1/32 in.(nom. t) | 0.67 | 24.06 | 0.0278 | 12.37 | 18.46 | 2.05 | 3.94 |
| 0.75 in.(D) X 0.5 mm (nom. t) | 0.62 | 19.05 | 0.0325 | 9.84 | 15.86 | 2.14 | 5.59 |
| 1 in.(D') X 1 mm (nom. t) | 0.92 | 23.56 | 0.0390 | 12.24 | 13.32 | 3.95 | 5.59 |

Table A2.8

Experimental data used in inspection of (i) The Classical theory, (ii) Donnell's theory

Concertina mechanism

| Tube set | R (mm) | Ratio t/R | $\sigma_{cr}$ (X $10^{-2}$) ($KN/mm^2$) | $\sigma_{cl}$ (X $10^{-2}$) equation (6.4.1) ($KN/mm^2$) | Ratio R/t | S (= $\sigma_{cr}/\sigma_{cl}$) (X $10^{-2}$) | Y (X $10^{-3}$) equation (6.5.3) ($KN/mm^2$) |
|---|---|---|---|---|---|---|---|
| 4 in.(D') X 16 SWG(t) | 49.99 | 0.0325 | 9.53 | 66.48 | 30.74 | 14.34 | 22.84 |
| 6 in.(D') X 0.125 in.(t) | 74.61 | 0.0425 | 10.28 | 86.94 | 23.50 | 11.82 | 18.29 |
| 3 in. (D') X 16 SWG(t) | 37.29 | 0.0436 | 9.21 | 89.19 | 22.93 | 10.33 | 15.72 |
| 1 in.(D') X 0.5 mm (nom. t) | 12.42 | 0.0457 | 7.78 | 93.49 | 21.90 | 8.32 | 12.40 |
| 1 in.(D') X 1/32 in.(nom. t) | 12.38 | 0.0520 | 7.74 | 106.37 | 19.25 | 7.28 | 10.72 |
| 0.75 in.(D) X 0.5 mm (nom. t) | 9.86 | 0.0677 | 10.38 | 138.49 | 14.78 | 7.50 | 11.07 |
| 1 in.(D') X 20 SWG(t) | 12.24 | 0.0747 | 9.97 | 152.81 | 13.39 | 6.52 | 9.53 |
| 1 in.(D') X 1 mm (nom. t) | 12.23 | 0.0759 | 9.69 | 155.27 | 13.17 | 6.24 | 9.08 |
| 6 in.(D') X 0.25 in.(t) | 73.03 | 0.0870 | 11.53 | 177.97 | 11.50 | 6.48 | 9.46 |
| 0.75 in.(D) X 0.75 mm (nom. t) | 9.99 | 0.0936 | 11.35 | 191.47 | 10.69 | 5.93 | 8.60 |
| 2.5 in.(D') X 0.125 in.(t) | 30.16 | 0.1053 | 11.42 | 215.41 | 9.50 | 5.30 | 7.64 |
| 0.75 in.(D) X 1 mm (nom. t) | 10.12 | 0.1176 | 11.63 | 240.57 | 8.50 | 4.83 | 6.93 |
| 2 in.(D') X 0.125 in.(t) | 23.81 | 0.1333 | 13.59 | 272.69 | 7.50 | 4.98 | 7.16 |
| 0.75 in.(D) X 1.5 mm (nom. t) | 10.36 | 0.1603 | 12.32 | 327.92 | 6.24 | 3.76 | 5.32 |
| 2.5 in.(D') X 3/16 in.(t) | 29.37 | 0.1622 | 11.90 | 331.81 | 6.17 | 3.59 | 5.08 |
| 2.25 in.(D') X 3/16 in.(t) | 26.20 | 0.1819 | 13.07 | 372.11 | 5.50 | 3.51 | 4.97 |

Table A2.9

# Appendix III

## Supplements to Chapter 7

### A3.1 Determination of the total quantity of whole tubes within the crushing layer

By moving a pattern of regular hexagons drawn on a transparent sheet against a square drawn on the background, the author has observed that the largest number of whole hexagons would be obtained in the arrangement whereby a complete hexagon is positioned at one corner of the square with one edge placed at one boundary and one node touching the adjacent boundary of the square.

From this arrangement a total of 4 possible cases arise at the other two boundaries, as illustrated in Figure A3.1 . Proceeding in direction X , it is seen that two cases arise depending on whether the part hexagon in the corner of the third boundary (at $X = C$ ) has a width greater or less than $\frac{1}{2}$ d in the X direction. The total number of whole hexagons in this direction, $|N_X|$ is the absolute value of the ratio $C \div d$ where C is the length of one side of the square layer and d is given in equation (7.1.2) . In the Y direction equivalent hexagons must be considered each of width F where $F = \frac{1}{2}\sqrt{3}\,d$ . In the ideal case where there is an exact number of whole hexagons at the two boundaries parallel to the X direction, the number of equivalent whole hexagons in the Y direction, $|N_Y|$ is equal to the integer quantity given as follows : $\left[C - (d \div (2\sqrt{3}))\right] \div F$ ; otherwise it is the nearest absolute value of this division. The two cases that arise in the Y direction depend on whether $|N_Y|$ is even or odd.

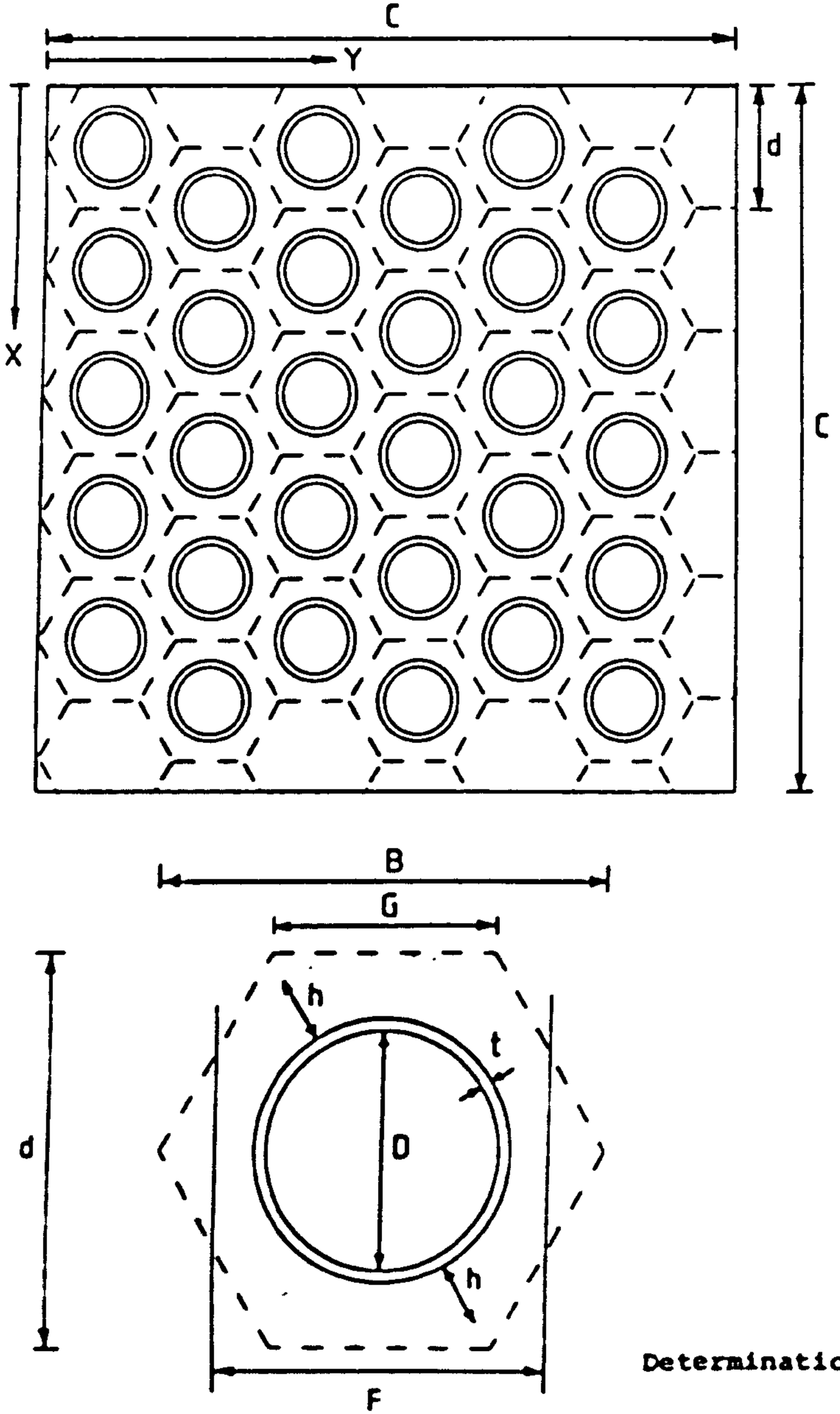


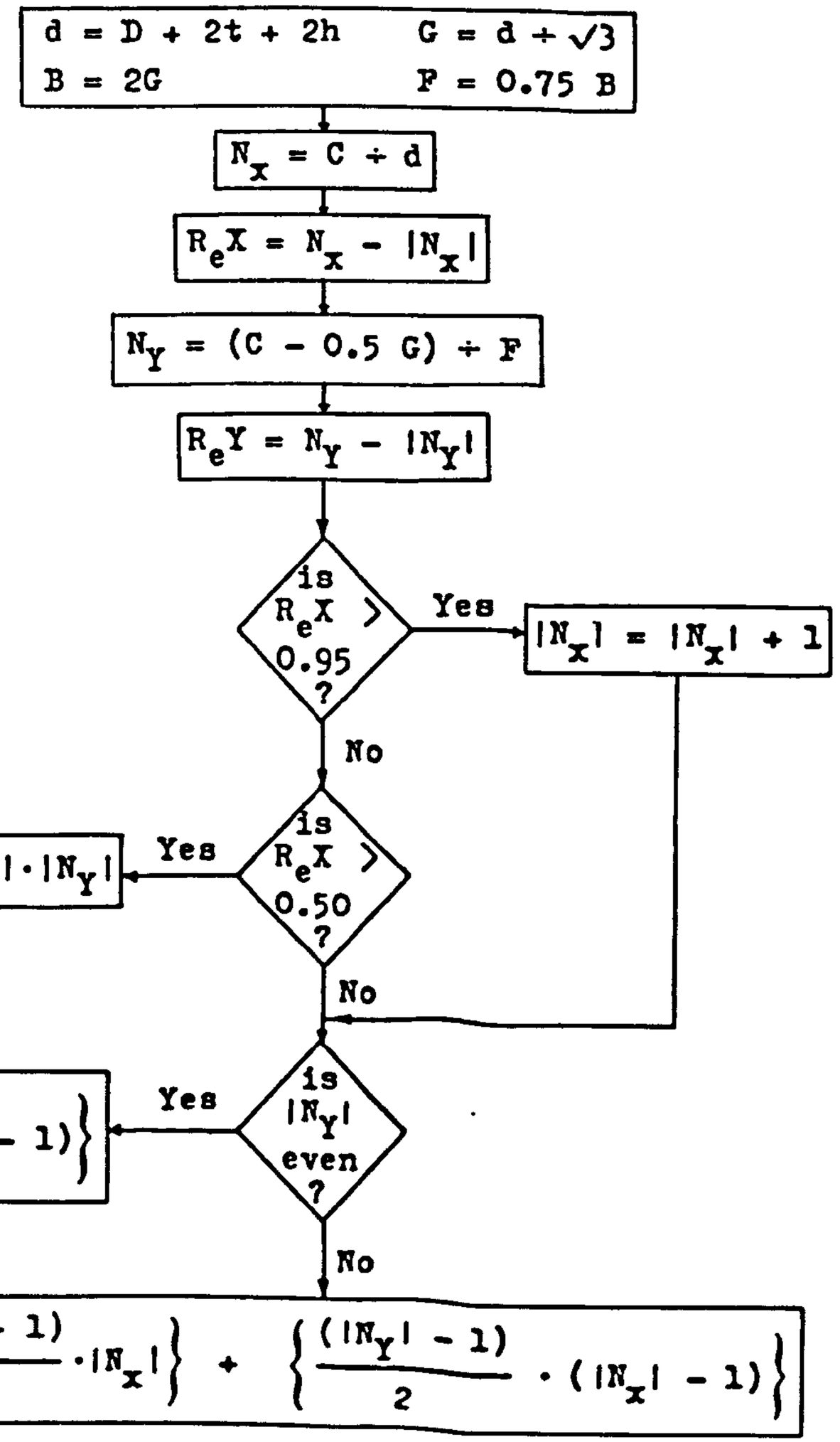


Determination of the quantity of whole tubes within a crushing layer for known tube section dimensions

Figure A3.1

Using a CDC-6600 Computer, a routine was devised to evaluate $|N_x|$ and $|N_y|$ for known quantities C and d in accordance with the above boundary cases from which the total number of tubes required may be evaluated. It is assumed that if the part hexagon encountered in the corner of the square at $X = C$ has a width greater than $0.95\,d$, it may be approximated to a whole hexagon.

Figure A3.1 indicates the flow chart used in this routine together with the expressions for the quantity of whole tubes, $(n_t)_{Des}$ required to fill the crushing layer.

A3.2 Flow chart for the optimum design quantities obtained

Figure A3.2 presents a design flow chart summarizing the sequence of calculations performed in determination of the optimum quantities obtained in the specific design of tubes as energy absorbers.

Notation

L = depth of layer / length of tubes

C = span of layer

D = tube internal diameter

t = tube wall thickness

A = net section area of tube

h = arm-length (one half-wave) of a concertina fold

$V_f$ = net volume of tube in a concertina fold

$E_f$ = mean energy absorbed by tube per concertina fold

$n_f$ = number of concertina folds developed in tube

Notation (continued)

$E_t$ = total energy absorbed by tube in axial compression

$V_t$ = total net volume of tube

$A_p$ = plan area of layer ( = C X C for a square layer)

$A_{hex}$ = hexagonal plan area assumed by tube in layer

$(n_t)_{Th}$ = total theoretical number of tubes in layer (boundary effect not included)

$(n_t)_{Des}$ = total design number of tubes in layer (boundary effect included)

$(E_T)_{Th}$ = total theoretical energy absorbed by layer

$(E_T)_{Des}$ = total design energy absorbed by layer

$V_T$ = total design material volume of tubes in layer

$B_{ndry}$ = influence of boundary conditions as a ratio : $(E_T)_{Des} \div (E_T)_{Th}$

$E_{diss}$ = energy dissipation density ( = $E_t \div$ gross volume of tube )

$E_{ffic}$ = design efficiency - energy absorbed per unit material volume ( = $(E_T)_{Des} \div V_T = E_t \div V_t$ )

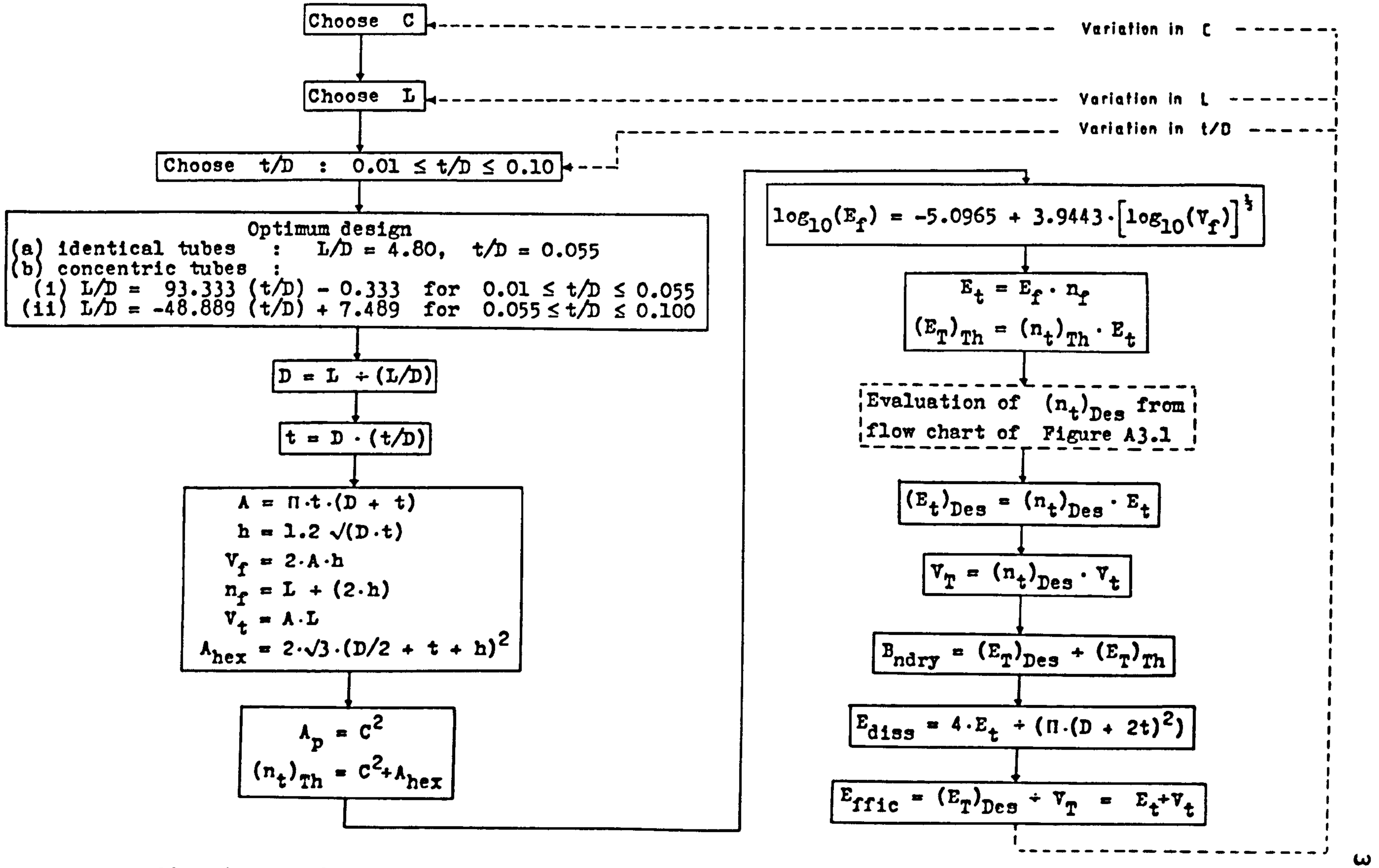


Flow chart used in the design of tubes as energy absorbers within a crushing layer

Figure A3.2

# References

1. Alexander, J.M. An approximate analysis of the collapse of thin cylindrical shells under axial loading. Quarterly J. Mechanics and Applied Mathematics, Vol.13, Part 1, pp 10-15, 1960.

2. Al-Hassani, S.T.S., Johnson, W. and Lowe, W.T. Characteristics of inversion tubes under axial loading. J. Mechanical Engineering Science, Vol.14, No.6, pp 370-381, 1972.

3. Allan, T. Buckling characteristics of axially loaded cylindrical tubes. Ph.D. Thesis, University of Strathclyde, 1967.

4. Allan, T. Experimental and analytical investigation of the behaviour of cylindrical tubes subject to axial compressive forces. J. Mechanical Engineering Science, Vol. 10, No.2, pp 182-197, 1968.

5. Almroth, B.O. Postbuckling behaviour of axially compressed circular cylinders. AIAA Journal, Vol.1, No.3, pp 630--633, March 1963.

6. Almroth, B.O. Influence of imperfections and of edge restraint on the buckling of axially compressed cylinders. AIAA/ASME Seventh Structures and Materials Conference, Cocoa Beach, Florida, 18-20 April 1966.

7. Almroth, B.O., Holmes, A.M.C. and Brush, D.O. An experimental study of the buckling of cylinders under axial compression. Experimental Mechanics, Vol.4, No.9, pp 263-270, September 1964.

8. Babcock, C.D. and Sechler, E.E. The effect of initial

imperfections on the buckling stress of cylindrical shells. Collected Papers on Instability of Shell Structures, NASA TN-D-1510, pp 135-141, December 1962.

9. Batterman, S.C. Plastic buckling of axially compressed cylindrical shells. AIAA Journal, Vol.3, No.2, pp 316--325, February 1965.

10. Batterman, S.C. Free-edge plastic buckling of axially compressed cylindrical shells. J. Applied Mechanics, Vol.35, No.1, Trans. A.S.M.E., Series E, pp 73-79, March 1968.

11. Burton, R.H. and Craig, J.M. An investigation into the energy absorbing properties of metal tubes loaded in the transverse direction. B.Sc.(Eng) Report, University of Bristol, 1963.

12. Conrad, E.W. Non-reusable kinetic energy absorber. U.S. Patent No. 3164222, 5 January 1965.

13. Coppa, A.P. On the mechanism of buckling of a circular cylindrical shell under longitudinal impact. General Electric Co., Missiles and Space Vehicle Dept., Space Sciences Lab., Tech. Inf. Serial No. R60SD494, September 1960.

14. Coppa, A.P. The buckling of circular cylindrical shells subject to axial impact. NASA TN-D-1510, p. 361, December 1962.

15. Coppa, A.P. A porous gas bag device for dissipating landing impact energy. General Electric Co., Missiles and Space Div., Patent Docket No. 39-5D-546, August 1965.

16. Coppa, A.P. New ways to soften shock. Machine Design, Vol.40, No.8, pp 130-140, March 1968.

17. Den Hartog, J.P. Advanced Strength of Materials. McGraw Hill Book Co., New York 1952.

18. De Runtz, J.A. and Hodge, P.G. Crushing of a tube between

rigid plates. J. Applied Mechanics, Vol.30, No.3, Trans. A.S.M.E., Series E, pp 391-395, September 1963.

19. Donnell, L.H. A new theory for the buckling of thin cylinders under axial compression and bending. Trans. Am. Soc. Mech. Engrs., Vol.56, pp 795-806, November 1934.

20. Donnell, L.H. and Wan, C.C. Effect of imperfections on buckling of thin cylinders and columns under axial compression. J. Applied Mechanics, Vol.17, No.1, Trans. A.S.M.E., Vol.72, Series E, pp 73-83, March 1968.

21. Ezra, A.A. and Fay, R.J. An assessment of energy absorbing devices for prospective use in aircraft impact situations. Dynamic Response of Structures, Edited by G. Herrmann and N. Perrone, Pergamon Press, pp 225-246, 1972.

22. Florence, A.L. and Goodier, J.M. Dynamic plastic buckling of cylindrical shells in sustained axial compressive flow. J. Applied Mechanics, Vol.35, No.1, Trans. A.S.M.E. Series E, pp 80-86, March 1968.

23. Garrick, R. Experimental investigations into the buckling and collapse of thin-walled tubes. B.Sc.(Eng) Thesis, University of Strathclyde, 1962.

24. Ghani, E. Optimization of energy absorbing structures. Progress Reports to the Health and Safety Executive, London, 1979-1980.

25. Harris, L.A., Suer, H.S., Skene, W.T. and Benjamin, R.J. The instability of thin-walled unstiffened circular cylinders under axial compression including the effects of internal pressure. J. Aeronautical Sciences, Vol.24, No.8, pp 587-596, August 1957.

26. Hernalsteen, P. and Leblois, L.C. The use of energy absorbers to protect structures against impact loading. Nuclear Engineering and Design, Vol.37, pp 373-406, 1976.

27. Hoff, N.J. The accuracy of Donnell's equations. J. Applied

Mechanics, Vol.22, Trans. A.S.M.E., Vol.77, Series E, pp 329-334, 1955.

28. Hoff, N.J. Buckling of thin shells. Proceedings of an Aerospace Scientific Symposium of Distinguished Lecturers in Honour of Dr Theodore von Karman on his 80th Anniversary, Institute of Aerospace Sciences, New York, N.Y. pp 1-86, 11 May 1961.

29. Hoff, N.J. A non-linear model study of thermal buckling of thin elastic shells. J. Applied Mechanics, Vol.32, No.1, Trans. A.S.M.E., Series E, pp 71-75, March 1965.

30. Hoff, N.J. Low buckling stresses of axially compressed circualr cylindrical shells of finite length. J. Applied Mechanics, Vol.32, No.3, Trans. A.S.M.E., Vol.87, Series E, pp 533-541, September 1965.

31. Hoff, N.J. The perplexing behaviour of thin circular cylindrical shells in axial compression. The Second Theodore von Karman Memorial Lecture of the Israel Society of Aeronautical Sciences, Israel Journal of Technology, Vol.4, No.1, pp 1-28, February 1966.

32. Hoff, N.J. Thin shells in aerospace structures. The Fourth von Karman Lectures of the AIAA, Aeronautics and Astronautics, Vol.5, No.2, pp 26-45, February 1967.

33. Hoff, N.J. Some recent studies of the buckling of thin shells. Aeronautical J. Royal Aeronautical Society, Vol.73, pp 1057-1070, December 1969.

34. Hoff, N.J., Madsen, W.A. and Mayers, J. Postbuckling equilibrium of axially compressed circular cylindrical shells. AIAA Journal, Vol.4, No.1, pp 126-133, January 1966.

35. Hoff, N.J. and Rehfield, L.W. Buckling of axially compressed circular cylindrical shells at stresses smaller than the classical critical value. J. Applied Mechanics, Vol.32, No.3, Trans. A.S.M.E., Vol.87, Series E, pp 542-

-546, September 1965.

36. Hoff, N.J. and Soong, Tsai-Chen. Buckling of circular cylindrical shells in axial compression. International J. Mechanical Sciences, Vol.7, pp 489-520, 1965.

37. Horton, W.H., Bailey, S.C., Cox, J.W. and Smith, S. The influence of test machine rigidity on the initial buckling load for unstiffened circular cylindrical shells. Stanford University Department of Aeronautics and Astronautics Report SUDAAR No. 230 , April 1965.

38. Horton, W.H., Bailey, S.C. and Edwards, A.M. Nonsymmetric buckle patterns in progressive plastic buckling. Experimental Mechanics, Vol.6, No.9, pp 433-444, September 1966.

39. Horton, W.H. and Durham, S.C. Imperfections, a main contributor to scatter in experimental values of buckling load. International J. Solids and Structures, Pergamon, Vol.1, pp 59-72, 1965.

40. Jackson, M.A. Energy absorbing device. U.S. Patent No. 3211260, 12 October 1965.

41. Johnson, W. Impact Strength of Materials. Arnold, London 1952.

42. Johnson, W. An elementary analysis of an energy absorbing device : the rolling torus load-limiter. International J. Mechanical Sciences, Vol.15, pp 357-366, 1973.

43. Johnson, W. and Mamalis, A.G. Crashworthiness of Vehicles. Mechanical Engineering Publications, Inst. Mech. Engrs., London 1978.

44. Johnson, W. and Reid, S.R. The rolling torus : some elastic -plastic considerations. International J. Mechanical Sciences, Vol.16, pp 45-62, 1974.

45. Johnson, W. and Reid, S.R. Metallic energy dissipating systems. Applied Mechanics Reviews, Vol.31, No.3, pp 277--288, March 1978.

46. Johnson, W., Reid, S.R. and Yella Reddy, T. The compression of crossed layers of tubes. International J. Mechanical Sciences, Vol.19, pp 423-437, 1977.

47. Johnson, W., Reid, S.R. and Singh, L.B. Experimental study of the rolling torus load-limiter. International J. Mechanical Sciences, Vol.17, pp 603-615, 1975.

48. Johnson, W., Soden, P.D. and Al-Hassani, S.T.S. Inextensional collapse of thin-walled tubes under axial compression. J. Strain Analysis, Vol.12, No.4, pp 317-330, 1977.

49. Jones, N. On the collision protection of ships. Nuclear Engineering and Design, Vol.38, pp 229-240, 1976.

50. Karman von, Th. and Tsien, H.S. The buckling of cylindrical shells under axial compression. J. Aeronautical Sciences, Vol.8, No.8, pp 303-312, June 1941.

51. Kempner, J. Postbuckling behaviour of axially compressed circular cylindrical shells. J. Aeronautical Sciences, Vol.17, pp 329-342, May 1954.

52. Kirk, J.A. Design of a metal skinning energy absorber for the U.S. Capitol Subway System. International J. Mechanical Sciences, Vol.19, pp 595-602, 1977.

53. Kitching, R., Houlston, R. and Johnson, W. A theoretical and experimental study of hemispherical shells subjected to loads between flat plates. International J. Mechanical Sciences, Vol.17, pp 693-703, 1975.

54. Koiter, W.T. Over de stabiliteit van het elastisch evenwicht. H.J. Paris, Amsterdam - Doctoral Thesis, University of Delft, Holland, 1945.

55. Koiter, W.T. The effect of axisymmetric imperfections on the buckling of cylindrical shells under axial compression. Proceedings of the Royal Netherlands Academy of Sciences, Amsterdam, Series B, Vol.66, No.5, 1963.

56. Kukkola, T. Energy absorbers used against impact loading.

Nuclear Engineering and Design, Vol.37, pp 407-412, 1976.

57. Lee, L.H.N. Inelastic buckling of initially imperfect cylindrical shells subject to axial compression. J. Aerospace Sciences, Vol.29, pp 87-95, January 1962.

58. Lindberg, H.E. Buckling of a very thin cylindrical shell due to an impulsive pressure. J. Applied Mechanics, Vol. 31, No.2, Trans. A.S.M.E., Series E, pp 267-272, June 1964.

59. Lindberg, H.E. and Herbert, R.E. Dynamic buckling of a thin cylindrical shell under axial impact. J. Applied Mechanics, Vol.33, No.1, Trans. A.S.M.E., Series E, pp 105-112, March 1966.

60. Loo, Tsu-Tao. Effects of large deflections and imperfections on the elastic buckling of cylinders under torsion and axial compression. Proceedings of the Second National Congress of Applied Mechanics, Am. Soc. Mech. Engineers, Michigan, pp 345-357, June 1954 - Doctoral Dissertation, Illinois Institute of Technology, Illinois, 1952.

61. Lorenz, R. Achsensymmetrische verzerrungen in dünnwandingen hohlzylindern. Zeitschrift des Vereines Deutscher Ingenieure, Vol.52, p. 1707, 1908.

62. Lundquist, E.E. Strength tests of thin-walled duralumin cylinders. NACA Report, No.473, 1933.

63. Madsen, W.A. and Hoff, N.J. The snap-through and postbuckling equilibrium behaviour of circular cylindrical shells under axial load. Stanford University Department of Aeronautics and Astronautics Report SUDAAR No.227, April 1965.

64. Mallock, A. Note on the instability of tubes subjected to end pressure and on the folds in a flexible material. Proceedings of the Royal Society of London, Vol.81, Series A, pp 388-393, June 1908.

65. Mazelsky, B. Absorbing device. U.S. Patent No. 3369634, 20 February 1968.

66. Michielsen, H.F. The behaviour of thin cylindrical shells after buckling under axial compression. J. Aeronautical Sciences, Vol.15, No.12, pp 738-744, December 1948.

67. Miller, P.M. and Naab, K.N. Basic research in automobile crashworthiness - testing and evaluation of forward structure modification concept. CAL Report No. YB-2684-V-1 , September 1969.

68. Moberg, H.A. Energy absorbing means. U.S. Patent No. 3232383, 1 February 1966.

69. Mutchler, L.D. Energy absorption of aluminium tubing. J. Applied Mechanics, Vol.27, No.4, Trans. A.S.M.E., Series E, pp 740-743, December 1960.

70. McFarland, R.K. Jnr. Hexagonal cell structures under postbuckling axial load. AIAA Journal, Vol.1, No.6, pp 1380-1385, June 1963.

71. McGehee, J.R. Experimental investigation of parameters and materials for fragmenting tube energy absorption process. NASA TN-D-3268, February 1966.

72. Nachbar, W. and Hoff, N.J. On edge buckling of axially compressed circular cylindrical shells. Quarterly J. Applied Mathematics, Vol.20, No.3, p 267, October 1962.

73. Ohira, Hiroichi. Local buckling theory of axially compressed cylinders. Proceedings of the Eleventh Japan National Congress of Applied Mechanics, pp 37-41, 1961.

74. Peterson, G.H. Variable kinetic energy absorber. U.S. Patent No. 3380557, 30 April 1969.

75. Platus, D.L. Energy absorbing device. U.S. Patent No. 3231049, 25 January 1966.

76. Postlethwaite, H.E. and Mills, B. Use of collapsible structural elements as impact isolators with special reference to automotive applications. J. Strain Analysis, Vol.5, No.1, pp 58-73, 1970.

77. Pugsley, A.G. The crumpling of tubular structures under impact conditions. Proceedings of the Symposium on the use of Aluminium in Railway Rolling Stock, Institution of Locomotive Engineers and the Aluminium Development Association, London, pp 33-41, November 1960.

78. Pugsley, A.G. and Macaulay, M. The large-scale crumpling of thin cylindrical columns. Quarterly J. Mechanics and Applied Mathematics, Vol.13, Part 1, pp 1-9, February 1960.

79. Rawlings, B. Energy absorption of dynamically and statically tested mild steel beams under conditions of gross deformation. International J. Mechanical Sciences, Vol. 9, pp 633-649, 1967.

80. Rayfield, J.F. Deceleration device. U.S. Patent No. 2961204, 22 November 1960.

81. Redwood, R.G. Crushing of a tube between rigid plates. Discussion of Reference 18, J. Applied Mechanics, Vol.31, No.2, Trans. A.S.M.E., Series E, pp 357-358, June 1964.

82. Redwood, R.G. On the buckling of thin-walled tubes under axial impact. J. Royal Aeronautical Society, Vol.68, pp 418-419, June 1964.

83. Rehfield, L.W. Further linear and nonlinear considerations in the buckling and postbuckling of axially compressed circular cylindrical shells. Ph.D. Thesis, Stanford University, 1965.

84. Reid, S.R. and Yella Reddy, T. Effect of strain hardening on the lateral compression of tubes between rigid plates. International J. Solids and Structures, Vol.14, pp 213--225, 1978.

85. Reid, S.R. and Yella Reddy, T. Effects of strain rate on the dynamic lateral compression of tubes. Proceedings of the Second Conference on the Mechanical Properties of Materials at High Rates of Strain, Edited by J. Harding, The institute of Physics, Serial No.47, pp 288-298, 28-30

March 1979.

86. Rich, J.W. Shock absorbing buffer. U.S. Patent No. 3284122, 8 November 1966.

87. Robinson, W.H. and Greenbank, L.R. An extrusion energy absorber suitable for the protection of structures during an earthquake. Earthquake Engineering and Structural Dynamics, Vol.4, pp 251-259, 1976.

88. Ross, B., Hoff, N.J. and Horton, W.H. The buckling behaviour of uniformly heated thin circular cylindrical shells. Experimental Mechanics, Vol.6, No.11, pp 529-537, November 1966.

89. Roth, R.S. and Klosner, J.M. Nonlinear response of cylindrical shells subjected to dynamic axial loads. AIAA Journal, Vol.2, No.10, pp 1788-1794, October 1964.

90. Simpson, B.A., Goldsmith, W. and Sackman, J.L. Oblique impact on a head-helmet system. International J. Mechanical Sciences, Vol.18, pp 337-340, 1976.

91. Soper, W.G. and Dove, R.C. Similitude in package cushioning. J. Applied Mechanics, Vol.29, No.2, Trans. A.S.M.E., Series E, pp 263-266, June 1962.

92. Southwell, R.V. On the general theory of elastic stability. Philosophical Transactions of the Royal Society of London, Series A, Vol. 213 , p. 187, 1914.

93. Spielman, J.F. Energy absorbing means. U.S. Patent No. 3059966, 23 October 1962.

94. Tennyson, R.C. A note on the classical buckling load of circular cylindrical shells under axial compression. AIAA Journal, Vol.1, No.2, pp 475-476, February 1963.

95. Thiele, W. Aluminium used as an impact energy absorbing material. Metals and Materials, Vol.6, pp 349-352, August 1972.

96. Thielmann, W. New developments in the nonlinear theories of buckling of thin cylindrical shells. Proceedings of the Durand Centennial Conference, Edited by N.J. Hoff and W.G. Vincenti , Pergamon Press Inc., London, pp 76-119, 1960.

97. Thomas, S.G., Reid, S.R. and Johnson, W. Large deformations of thin-walled circular tubes under transverse loading I : An experimental study of the bending of simply-supported tubes under a central load. International J. Mechanical Sciences, Vol.18, pp 325-333, 1976.

98. Thornton, P.H. and Magee, C.L. The interplay of geometric and materials variables in energy absorption. J. Engineering Materials and Technology, Vol.99, No.2, Trans. ASME, Series H, pp 114-120, April 1977.

99. Tiesenhausen von, G.F. Energy absorbing device. U.S. Patent No. 3381778, 7 May 1968.

100. Timoshenko, S. Einige stabilitätsprobleme der elastizitätstheorie. Zeitschrift für Mathematik und Physik, Vol.58, pp 337-385, 1910.

101. Timoshenko, S. Theory of Elastic Stability. McGraw Hill, New York, pp 439-463, 1936.

102. Watson, A.R., Reid, S.R., Johnson, W. and Thomas, S.G. Large deformations of thin-walled circular tubes under transverse loading II : Experimental study of the crushing of circular tubes by centrally applied opposed wedge-shaped indenters. International J. Mechanical Sciences, Vol.18, pp 387-397, 1976.

103. Watson, A.R., Reid, S.R. and Johnson, W. Large deformations of thin-walled circular tubes under transverse loading III : Further experiments on the bending of simply-supported tubes. International J. Mechanical Sciences, Vol.18, pp 501-509, 1976.

104. Wirsching, P.H. and Slater, R.C. The beer can as a shock

absorber. J. Engineering Materials and Technology, Vol. 95, No.4, Trans. A.S.M.E., Series H, pp 224-226, October 1973.

105. Wood, J.D. and Koval, L.R. Buckling of cylindrical shells under dynamic loads. AIAA Journal, Vol.1, No.2, pp 2576--2582, November 1963.

106. Yao, J.C. Dynamic stability of cylindrical shells under static and periodic axial and radial loads. AIAA Journal, Vol.1, No.6, pp 1391-1396, June 1963.

107. Yoshimura, Y. On the mechanism of buckling of a circular cylindrical shell under axial compression. NACA Tech. Mem. 1390, Washington, July 1955.